Transactions of the ASME

Journal of Heat Transfer (ISSN 0022-1481) is edited and published quarterly at the offices of The American Society of Mechanical Engineers, United Engineering Center, 345 E. 47th St., New York, N. Y. 10017. ASME-TWX No. 710-581-5267, New York. Second-class postage paid at New York, N. Y., and at additional mailing offices.

CHANGES OF ADDRESS must be received at Society headquarters seven weeks before they are to be effective. Please send old label and new address.

PRICES: To members, $25.00, annually; to nonmembers, $50.00. Single copies, $15.00 each. Add $1.50 for postage to countries outside the United States and Canada.

STATEMENT from By-Laws. The Society shall not be responsible for statements or opinions advanced in papers or . . . printed in its publications (B13, Par. 4).

INDEXED by the Engineering Index, Inc.

Journal of Heat Transfer

Published Quarterly by The American Society of Mechanical Engineers
VOLUME 102 • NUMBER 2 • MAY 1980

ANNOUNCEMENTS

TECHNICAL PAPERS

(*continued on page 253*)

TECHNICAL NOTES

DISCUSSION

ERRATA

Heat Transfer Characteristics of a Spark-Ignition Engine

A. C. Alkidas

Engine Research Department,
General Motors Research Laboratories,
Warren, Mich. 48090

Transient heat flux measurements were obtained at four positions on the cylinder head of a four-stroke single-cylinder spark-ignition engine. Tests were performed for both fired and motored operation of the engine. The primary engine operational variable was engine speed. The results showed that the heat flux varies considerably with position of measurement. At fired conditions, the initial high rate of increase of heat flux at each position of measurement correlated with the calculated time of arrival of the flame at that position. Finally, as expected, the peak heat flux was found to increase with increased engine speed.

Introduction

In internal combustion engines, accurate heat transfer information is becoming increasingly important with the great emphasis on engine efficiency and because of the demonstrated strong influence of heat transfer on exhaust emissions. In addition, heat transfer is important in calculating heat release rates and flame propagation from pressure-time data and in other engine simulation studies.

Experimental heat transfer studies in diesel engines have been performed by a large number of investigators, such as Eichelberg [1], Sitkei [2], Annand [3], Woschni [4], LeFeuvre, et al. [5], Whitehouse [6], Flynn, et al. [7], and Dent and Suliaman [8], to name a few.

In contrast, investigations of the heat transfer in spark-ignition engines have been surprisingly few. Overbye, et al. [9], measured the heat flux at several positions on the cylinder head of a CFR engine. Tests were performed at near stoichiometric air-fuel ratio and an engine speed of 830 r/min. The effects of intake manifold pressure, turbulence and wall deposits on surface heat flux were investigated. Overbye presented an empirical heat transfer correlation for the motored operation of the engine. However, this correlation failed when applied to fired conditions. Oguri [10] measured the instantaneous heat flux at one position on the cylinder head of a spark-ignition engine. Comparison of his measurements with calculated results obtained using Eichelberg's correlation [1] showed that this correlation was good in the expansion stroke but failed in the compression stroke. He then proposed an empirical correlation similar to that of Elser's [11], which showed marginal agreement with his experimental results.

Presently, because of the limited number of heat transfer investigations in spark-ignition engines, most of the analytical modeling studies of these engines utilize empirical heat transfer correlations obtained in diesel engines. However, because of the radically different combustion characteristics in these two types of internal combustion engines, one should not necessarily expect the heat transfer correlations obtained in diesel engines to be applicable to spark-ignition engines.

The objective of this investigation was to study experimentally the unsteady heat flux characteristics of a single-cylinder spark-ignition engine. The transient heat flux at four positions on the cylinder head and the transient cylinder gas pressure were measured coincidentally. The primary engine operational variable was engine speed. All tests were performed at constant air-fuel ratio and volumetric efficiency. With the exception of a set of special tests, spark timing was kept at Minimum advance for Best Torque (MBT). In order to determine the influence of combustion on the heat transfer characteristics of the engine, comparative heat flux measurements were made at both motored and fired conditions.

Theory of Heat Flux Measurements

The surface heat flux in the chamber of a reciprocating internal combustion engine consists of two components: the steady-state component, which can be calculated from time-averaged temperature measurements at two known positions within the metal wall (see, e.g., [12]), and the unsteady component, which can be calculated from the cyclic surface temperature variation.

The principal assumption used to calculate the heat flux is that the heat flow through the walls of the combustion chamber is one-dimensional. The method of calculating the unsteady heat flux from transient surface temperature measurements has been well documented in several studies [9, 13]. Briefly, the procedure is as follows:

1 The experimental surface temperature variation during the engine cycle is represented by a Fourier series of the form

$$T_w(t) = \overline{T}_w(0) + \sum_{n=1}^{N} (A_n \cos n\omega t + B_n \sin n\omega t) \tag{1}$$

where $\overline{T}_w(0)$ is the time-averaged surface temperature, and the coefficients of the Fourier series A_n and B_n for $n = 1$ to N are evaluated from the experimental surface temperature-time data. The remaining symbols used in equation (1), along with all the other symbols in this paper, are defined in the Nomenclature.

2 The one-dimensional unsteady heat conduction equation

$$\frac{\partial T}{\partial t} = \alpha \frac{\partial^2 T}{\partial x^2} \tag{2}$$

is solved subject to the following boundary conditions:

$$\left.\begin{aligned} T(0, t) &= T_w(t) \\ T(\delta, t) &= T(\delta) \end{aligned}\right\} \tag{3}$$

where $T(\delta)$ is the steady-state temperature of the solid at a distance δ from the surface ($x = 0$).

From equation (2) with conditions (3) a steady periodic solution was obtained for $T(x, t)$ and, from it, the heat flux at the surface, $x = 0$, was evaluated as follows:

$$q_w(t) = -K \frac{\partial T}{\partial x}(0, t) = \frac{K}{\delta}[\overline{T}_w(0) - T(\delta)] + K \sum_{n=1}^{N} \sqrt{\frac{n\omega}{2\alpha}} [A_n (\cos n\omega t - \sin n\omega t) + B_n (\sin n\omega t + \cos n\omega t)] \tag{4}$$

The first term in the above expression of the surface heat flux is independent of time. It represents the steady-state component of heat flux. The second term is time dependent and represents the unsteady component of heat flux.

Equation (4) is used to calculate the surface heat flux from the harmonic synthesis of the experimental surface temperature fluctuation data. As an example, Fig. 1 shows a typical experimental temperature-crankangle curve and Fig. 2 shows the corresponding calculated variation of heat flux through the engine cycle.

Contributed by the Heat Transfer Division for publication in The JOURNAL OF HEAT TRANSFER. Manuscript received by The Heat Transfer Division August 25, 1979.

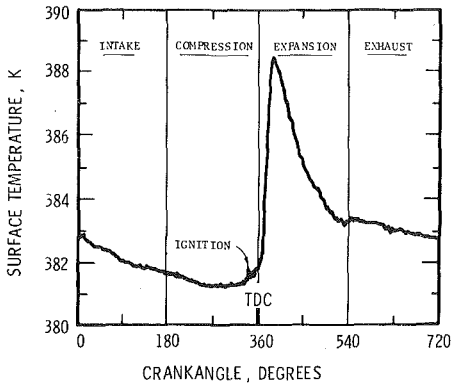

Fig. 1 Measured surface temperature variation with crankangle

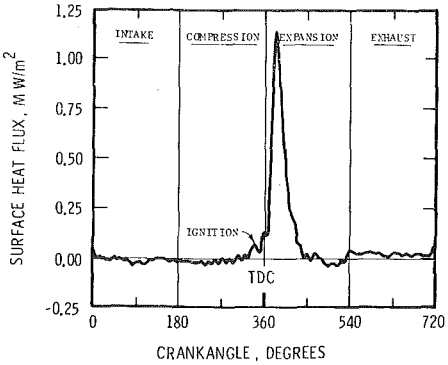

Fig. 2 Calculated heat flux variation with crankangle

Apparatus and Procedure

Engine. The engine was a four-stroke V-8 spark-ignition engine modified to operate on one cylinder. The combustion chamber was disk-shaped with a centrally located spark plug. The principal geometric characteristics of the engine are listed in Table 1.

The cylinder head was modified to allow the insertion of four heat flux probes. The mating holes to these probes were drilled at positions where a solid wall exists along the whole thickness of the head. This required the axis of symmetry of three of the four holes to be at small angles relative to the axis of symmetry of the bore. The locations of the heat flux probes relative to the spark plug and the inlet and exhaust valves are shown in Fig. 3. The probes at positions HT1 and HT2 are near the exhaust valve whereas the probes at positions HT3 and HT4 are near the inlet valve. The distances of the heat flux probes HT1, HT2, HT3 and HT4 from the spark plug are 18.7, 27.5, 37.3 and 46.3 mm, respectively.

Heat Flux Probes. The heat flux probes were designed from commercially available surface thermocouples. Each probe utilizes a second reference thermocouple ("in-depth" thermocouple) located at a known distance, δ, from the tip of the probe to measure the steady-state component of heat flux. The in-depth thermocouple was a 0.50 mm dia. grounded-sheath thermocouple. The position of the thermocouple junction relative to its external surface tip was measured by means of x-ray photography.

The basic construction of the surface thermocouple and its modification to a heat flux probe are shown in Fig. 4. The surface junction was formed by abrading the exposed thermocouple ribbon elements at the probe tip with a very fine Carborundum stone to produce contacts among the microscopic fibers of the ribbons. To minimize distortion of isotherms in the cylinder head, the probe bodies were manufactured from the same material used in making the cylinder head. Furthermore, the in-depth thermocouple was placed as close as possible to the tip of the probe to reduce two-dimensional effects. However, the distance of the in-depth thermocouple from the tip of the probe must be great enough so that it does not experience significant temperature transients during the engine cycle.

Test Conditions. Propane was used as the engine fuel. Both fuel and air were metered by critical flow systems. In this phase of the study, the only engine operational parameter changed was the engine speed. For each engine speed, heat flux measurements were made at both fired and motored conditions. A list of the controlled engine parameters and their values is shown in Table 2.

Analysis of Data. The surface heat flux-crank angle variation at each position of measurement was calculated from surface temperature-crank angle data averaged over 200 cycles.

Table 1 Engine description

Displacement (m^3)	0.82×10^{-3}
Bore (m)	0.1047
Stroke (m)	0.0953
Compression Ratio	8.56
Inlet Valve Opening (°CA)	30 BTDC
Inlet Valve Closing (°CA)	63 ABTC
Exhaust Valve Opening (°CA)	77 BBTC
Exhaust Valve Closing (°CA)	50 ATDC

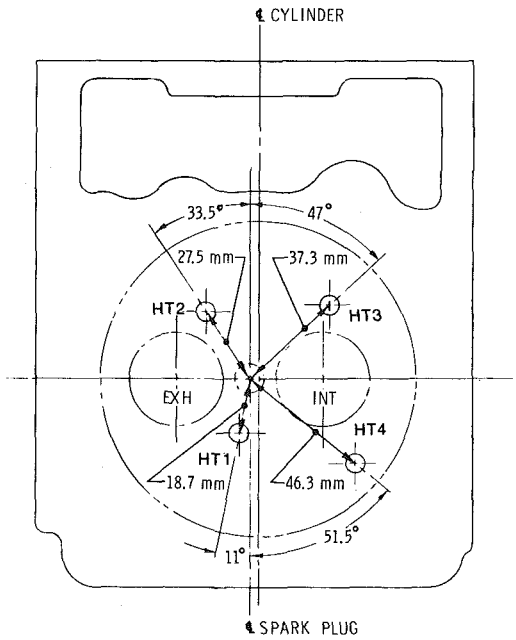

Fig. 3 Location of heat flux probes

Results

As shown in Fig. 2, highest heat transfer rates occur during the compression and expansion strokes near TDC. This is the region of most interest in heat transfer studies. Furthermore, in this region the heat flux measurements are most accurate. During the scavenging strokes the level of heat flux is comparatively very low and large errors may occur in the calculation of heat flux from experimental surface temperature measurements. Therefore, the results presented are limited to the region of the compression and expansion stroke near TDC (about −20 deg BTDC to +50 deg ADTC).

Nomenclature

A_n = coefficient of Fourier cosine series
B_n = coefficient of Fourier sine series
K = thermal conductivity, W/m K
N = number of harmonics
q_w = surface heat flux, W/m^2
t = time, s
T = temperature, K
$\overline{T}_w(0)$ = time-averaged surface temperature, K
x = distance from surface of wall, m
α = thermal diffusivity, m^2/s
δ = distance of the "in-depth" thermocouple from the tip of the probe, m
ω = angular velocity, s^{-1}

Typical variations of heat flux with crank angle at the four positions of measurement on the cylinder head are shown in Figs. 5 and 6 for engine speeds of 1000 and 2000 r/min, respectively. Comparison of these results at each engine speed condition tested shows that the magnitude of the peak heat flux varies with position of measurement. Differences in this magnitude were as high as 1.3×10^6 W/m^2, the highest peak heat flux being 75 percent greater than the lowest. In all cases the peak heat flux was highest at position HT2, which is the position second closest to the centrally located spark plug.

The observed spatial variations of the peak heat flux may be attributed primarily to spatial variations of the temperature and velocity fields in the combustion chamber. Spatial variations of the heat flux on the cylinder head have also been observed by Overbye, et al. [9] in a spark-ignition engine and by Annand and Ma [14], LeFeuvre, et al. [5] and Whitehouse [6] in diesel engines.

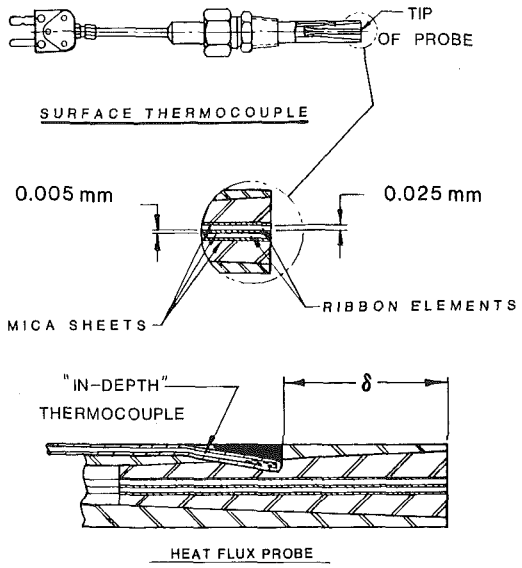

Fig. 4 Design of heat flux probes

Table 2 Test parameters

Air-Fuel Ratio	18
Volumetric Efficiency*	40 percent
Speed	500–2500 r/min
Intake Air Temperature	306 K
Coolant Temperature	358 K
Oil Temperature	364 K

*Defined as the ratio of the actual mass of air supplied to the cylinder per cycle to the theoretical mass of air necessary to fill the displacement volume at 288 K and 101 kPa.

The most significant characteristic of the above results, however, is that the initial high rate of increase in heat flux at each position occurs in the same sequence as the distance of the heat flux probes (measuring position) from the spark plug. Thus, the heat flux rises significantly first at position HT1, followed in sequence by positions HT2, HT3 and finally HT4.

To relate the observed heat flux characteristics to the events occurring in the combustion chamber, flame propagation computations were performed using the heat release model of Krieger and Borman [15] modified by Lancaster [16] to calculate the position of the flame (spherical geometry) at each crank angle. In Figs. 5 and 6, the calculated crank angle for the arrival of the flame at each position is denoted by the full circle on the respective curves, and the crankangle of peak cylinder gas pressure is denoted by p_{MAX}. It is apparent that the calculated arrival of the flame at each position approximately coincides with the beginning of the initial high rate of increase of heat flux at each position. In fact, because the high rate of increase of heat flux at each position must be caused by the arrival of the flame at that position, Figs. 5 and 6 actually suggest that the flame propagates somewhat faster than the computations indicate. Furthermore, the flame apparently does not retain a spherical geometry, but moves faster towards position HT2, as indicated by the measured higher heat flux at the computed time the flame reaches this position in comparison to the other positions.

The location of the flame at a given crankangle computed by the heat release model is influenced by the heat transfer rates calculated from the particular empirical heat transfer correlation used. Low heat transfer rates result in slow burning rates. In general, in accordance with the above observations, the heat transfer rates obtained using Woschni's correlation are lower than the corresponding measurements. This is especially true during the initial stages of combustion as shown in Fig. 7, where the heat flux measured at position HT1 is compared with the "area-averaged" heat flux calculated using Woschni's correlation. The vertical dotted line in Fig. 7 shows the calculated arrival of the flame at position HT1. Before the flame reaches position HT1 the probe is in contact with unburned gas at relatively low temperatures; whereas, after the flame reaches the location of measurement, the probe is in contact with combustion gases at near adiabatic flame temperatures.

The initial high rate of increase of the heat flux and the magnitude of the peak heat flux are strongly influenced by the gas pressure and local burned gas temperature. This is demonstrated in Fig. 8, which shows the variations of surface heat flux at position HT1 with crank angle for three spark timing settings: MBT, 10 deg advanced and 10 deg retarded. As shown in Fig. 8, spark timing strongly influences the rise of the heat flux as well as the magnitude of the peak heat flux. On the other hand, during the last portion of the expansion stroke and

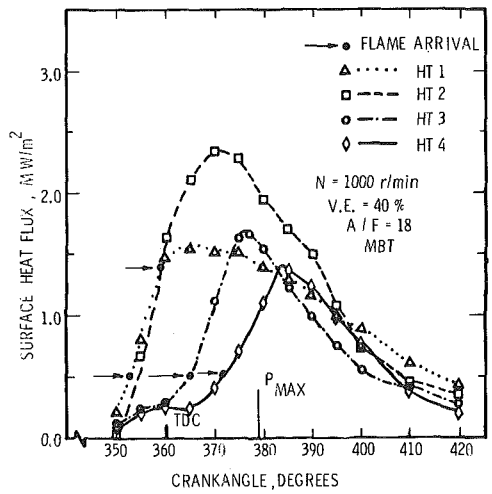

Fig. 5 Variations of surface heat flux with crankangle at the four positions of measurement (1000 r/min, 24 deg BTDC)

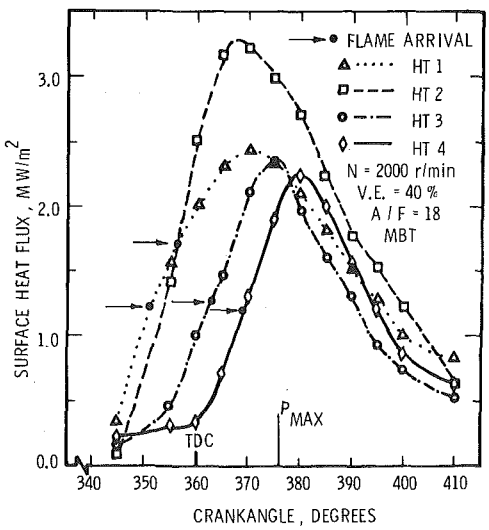

Fig. 6 Variations of surface heat flux with crankangle at the four positions of measurement (2000 r/min, 29 deg BTDC)

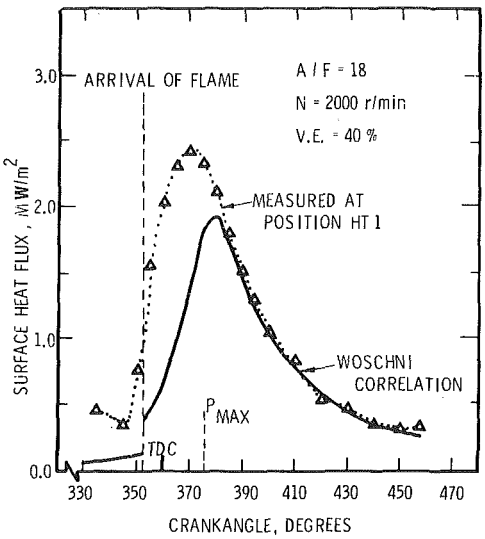

Fig. 7 Comparison of transient heat flux measurements at position HT1 with values calculated using Woschni's correlation

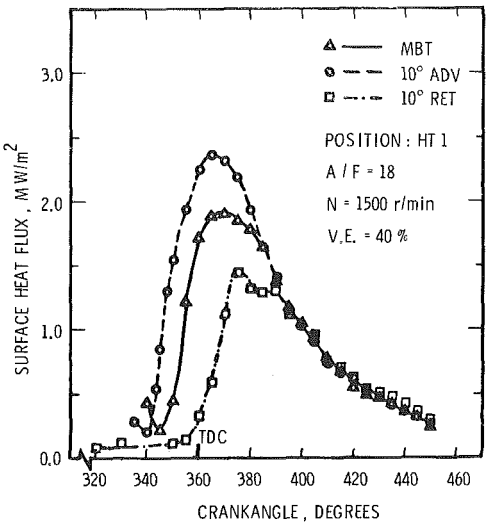

Fig. 8 Effects of combustion timing on surface heat flux at position HT1. (1500 r/min, MBT = 26 deg BTDC)

prior to opening of the exhaust valve the heat flux is relatively unaffected by the spark setting. Advancing the spark setting causes the initial rate of increase of heat flux to occur earlier in the cycle because of the earlier arrival of the flame at the position of measurement. It also augments the initial rate of increase in heat flux and the magnitude of the peak heat flux because of the higher magnitudes of gas pressure and temperature achieved during combustion.

In contrast to fired conditions, for motored operation of the engine, the four heat flux probes do not exhibit the orderly sequence of the initial high rate of increase of heat flux that characterizes the fired conditions. Figure 9 shows the variations of heat flux with crank angle at the four positions of measurement for motored operation of the engine at a speed of 1500 r/min. The increase in heat flux during the compression stroke occurs simultaneously at all positions. In addition, despite random fluctuations in the heat flux results, it also appears that the peak heat fluxes at the four positions on the cylinder head occur at approximately the same crankangle. The irregular fluctuations in the calculated values of the heat flux at motored conditions are caused by the relatively low signal-to-noise ratio of the surface temperature measurement.

In general, the magnitudes of the peak heat fluxes during motored operation of the engine are an order of magnitude less than the corresponding peak heat fluxes during fired operation of the engine.

The effect of engine speed on surface heat flux in a fired engine is shown in Fig. 10. This is a plot of the variation of surface heat flux at position HT1 with crankangle at three different speeds. The surface heat flux increases with increasing engine speed. This increase is more noticeable during the combustion period. During the post-combustion period of the expansion stroke the increase in heat flux with speed is smaller.

Engine speed affects the heat transfer to the surface of the combustion chamber primarily via its effect on the convective heat transfer coefficient. Increasing the engine speed increases the characteristic velocity of the flow [17, 18], which accordingly increases the convective heat transfer coefficient and hence the heat flux.

Conclusions

Based on the transient heat flux measurements presented, the following conclusions were reached:

1 At fired conditions, the beginning of the initial high rate of increase of heat flux at each position of measurement correlates reasonably with the calculated time of flame arrival. In comparison, for motored operation of the engine, the increase of heat flux during the compression stroke occurs simultaneously at the four positions of measurement.

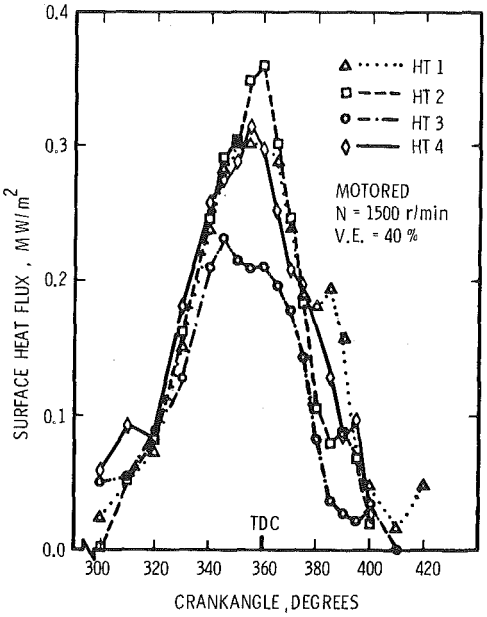

Fig. 9 Variations of surface heat flux with crankangle at the four positions of measurement for motored operation of the engine

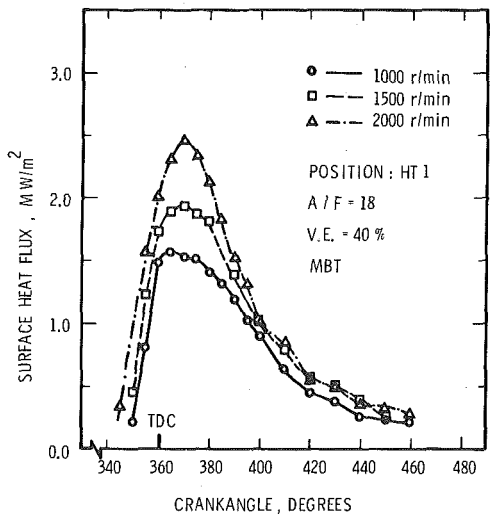

Fig. 10 Effect of engine speed on surface heat flux at position HT1

2 The peak heat flux varies considerably with position of measurement on the cylinder head. This spatial variation is considered to be principally attributable to spatial variations of the temperature and velocity fields in the combustion chamber.

3 Advancing the spark timing increases the peak heat flux and advances the time that this occurs in the engine cycle. During the last stage of the expansion process prior to opening of the exhaust valve, the magnitude of the heat flux is independent of spark setting.

4 The peak heat flux at each position of measurement increases with increasing engine speed.

Acknowledgments

The author would like especially to acknowledge the efforts of J. P. Myers, who initiated the surface temperature measurement program and helped in the design of the heat flux probes, and those of R. W. Bilinsky and D. T. French, who provided the technical support to the experimental program.

References

1 Eichelberg, G., "Some New Investigations on Old Combustion Engine Problems," *Engineering,* Vol. 148, 1939, pp. 463 and 547.

2 Sitkei, G., "Beitrag zur Theorie des Warmeuberganges im Motor," *Konstruktion,* Vol. 15, 1962, p. 67.

3 Annand, W. J. D., "Heat Transfer in the Cylinders of Reciprocating Internal Combustion Engines," *Proceedings of the Institution of Mechanical Engineers,* Vol. 177, No. 36, 1963, p. 973.

4 Woschni, G., "A Universally Applicable Equation for the Instantaneous Heat Transfer Coefficient in the Internal Combustion Engine," *SAE Transactions,* Vol. 76, 1967, p. 3065.

5 LeFeuvre, T., Myers, P. S., and Uyehara, O. A., "Experimental Instantaneous Heat Fluxes in a Diesel Engine and Their Correlation," SAE Paper No. 690464, 1969.

6 Whitehouse, N. D., "Heat Transfer in a Quiescent Chamber Diesel Engine," *Proceedings of the Institution of Mechanical Engineers,* Vol. 185, 1970–1971, p. 963.

7 Flynn, P., Mizusawa, M., Uyehara, O. A., and Myers, P. S., "An Experimental Determination of the Instantaneous Potential Radiant Heat Transfer Within an Operating Diesel Engine," SAE Paper No. 720022, 1972.

8 Dent, J. C., and Suliaman, S. L., "Convective and Radiative Heat Transfer in a High Swirl Direct Injection Diesel Engine," SAE Paper No. 770407, 1977.

9 Overbye, V. D., Bennethum, J. E., Uyehara, O. A., and Myers, P. S., "Unsteady Heat Transfer in Engines," *SAE Transactions,* Vol. 69, 1961, p. 461.

10 Oguri, T., "On the Coefficient of Heat Transfer Between Gases and Cylinder Walls of the Spark-Ignition Engine," *Bulletin of the JSME,* Vol. 3, No. 11, 1960, p. 363.

11 Elser, K., "Der Instationare Warmeubergang in Dieselmotoren," Mitt Inst. Thermodyn., Zurich, No. 15, 1954.

12 Mattavi, J. N., "A Miniature Sensor for Measuring Heat-Transfer Rates in Engines," SAE Paper No. 741078, 1974.

13 Wendland, D. W., "The Effect of Periodic Pressure and Temperature Fluctuations on Unsteady Heat Transfer in a Closed System," NASA Report CR-72323, Mar. 1968.

14 Annand, W. J. D., and Ma, T. H., "Instantaneous Heat Transfer Rates to the Cylinder Head Surface of a Small Compression-Ignition Engine," *Proceedings of the Institution of Mechanical Engineers,* Vol 185, 1971–1972, p. 976.

15 Krieger, R. B., and Borman, G. L., "The Computation of Apparent Heat Release for Internal Combustion Engines," ASME Paper No. 66-WA/DGP-4, 1966.

16 Lancaster, D. R., Krieger, R. B., Sorenson, S. C., and Hull, W. L., "Effects of Turbulence on Spark-Ignition Engine Combustion," SAE Paper No. 760160, 1976.

17 Semenov, E. S., "Studies of Turbulent Gas Flow in Piston Engines," *Combustion in Turbulent Flow,* Ed. L. N. Khitrin, Translated from Russian, 1963.

18 Lancaster, D. R., "Effects of Engine Variables on Turbulence in a Spark-Ignition Engine," SAE Paper No. 760159, 1976.

The Segmented Oxidizing Monolith Catalytic Converter

Theory and Performance

D. W. Wendland

Engine Research Department,
General Motors Research Laboratories,
Warren, Mich. 48090

In an oxidizing monolithic catalytic converter, mass transfer rates to the catalyst sites are greatest in the flow passage entrance regions. Segmenting the monolith, or slicing it normal to the flow direction and separating the pieces, increases conversion efficiency by forcing the species boundary layers to repeatedly redevelop. Models are presented which apply the heat transfer/mass transfer analogy to a developing flow correlation to provide an upper limit to conversion in a general monolith. The models predict that segmenting a small monolith into four pieces decreases hydrocarbon and carbon monoxide residuals by as much as 45 percent and 65 percent, respectively. Engine testing demonstrated 33 and 47 percent residual decreases.

Introduction

The ability of a noble metal-coated monolith to oxidize species in automotive exhaust gas is a complex function of the exhaust stream characteristics, the monolith geometry, and the catalyst properties. The two general mechanisms which limit the rate of conversion of any reactive species are, first, mass transport from the flow passage freestream to the porous wash coat surface and then by diffusion to the catalyst site, and, second, the rate of reaction at the site. For relatively fresh, fully warm, oxidizing catalysts, the rates of reaction of H_2, CO, and many exhaust hydrocarbons (HC) are established primarily by convective transport through the developing laminar species boundary layers in the passages.

Mass and heat transfer rates are higher in the entrance regions of these developing boundary layers than in the fully developed regions. Consequently, segmenting or repeatedly slicing the substrate normal to the flow direction and separating the pieces, improves conversion performance by exploiting the enhanced transport coefficients in the entrance regions. The purpose of this investigation is to quantify, by analysis and experimental test, the impact of segmenting on oxidizing monolith performance.

Two analytical models are described herein. The first provides a means for quickly estimating the mass-transfer-limited (M-T-L) conversion efficiency of reactive species in a segmented monolith of general geometry under arbitrary flow conditions. The second combines catalyst kinetics for alumina-supported platinum with a developing flow correlation in a more detailed treatment of the problem termed the kinetics-mass transfer (K-MT) model.

Experimental tests were run using a test-stand engine with several segmented and one-piece (integral) oxidizing monoliths. Experimental measurements of conversion efficiency are compared with analytical predictions.

M-T-L Model Development

Analytical models have been described by various investigators, e.g., [1–5], delving into different aspects of monolith catalytic converter behavior. Generally involving the numerical solution of the governing conservation equations, these models require a computer for solution. In contrast, a simple M-T-L model is developed to allow rapid estimation of the maximum conversion performance for reactive species in a general oxidizing monolith.

Exhaust gas flow rate, temperature, and species concentrations are assumed to be uniform over the monolith face. The mass transfer rate to the flow passage wall surface, where the reactions are assumed to take place, is proportional to the species concentration potential from the freestream to the surface. The proportionality constant is the location- and species-dependent mass transfer coefficient. A differential mass balance for species i yields:

$$-\frac{w}{\rho A_c}\frac{\partial}{\partial x}C_{i,g}(x,t)-\frac{k_{i,g}}{r_h}[C_{i,g}(x,t) - C_{i,w}(x,t)] = \frac{\partial}{\partial t}C_{i,g}(x,t) \quad (1)$$

For mass-transfer-limited conditions, the concentration at the wall is much less than the freestream concentration, and the full concentration potential is available to drive the mass transfer process. At steady state, the time derivative in equation (1) is set equal to zero. If the equation is nondimensionalized, the solution can be expressed in terms of the conversion efficiency of species i in an integral monolith:

$$\eta_i(x_{mt}{}^+) = 1 - \exp\left[-4\int_0^{x_{mt}{}^+} N_{\mathrm{Sh}}(\xi)\,d\xi\right] \quad (2)$$

where

$$x_{mt}{}^+ = x/4r_h N_{\mathrm{Re}} N_{\mathrm{Sc}_i} \quad (3)$$

$$N_{\mathrm{Sc}_i} = \mu/\rho D_i \quad (4)$$

$$N_{\mathrm{Sh}} = 4r_h k_{i,g}/D_i \quad (5)$$

This efficiency describes an upper bound to conversion since real-world effects such as finite kinetic rates or competition for oxygen at the sites increases the wall surface concentrations of species and deprives the mass transfer process of the full driving potential.

If the integral monolith of dimensionless length $L_{mt}{}^+$ is cut into n equal segments, the hydrodynamic, thermal, and diffusion boundary layers ideally develop anew in each succeeding entrance region, and the conversion limit expression for species i in the n-segment assembly is:

$$\eta_i(L_{mt}{}^+, n) = 1 - \exp\left[-4n\int_0^{L_{mt}{}^+/n} N_{\mathrm{Sh}}(\xi)\,d\xi\right] \quad (6)$$

Sherwood number data may be obtained from published Nusselt number data for simultaneously developing flow in channels by means of the heat transfer/mass transfer analogy. In applying the analogy, however, attention must be paid to the wall boundary condition, the passage shape, and the heat transfer Prandtl number. The boundary condition of prescribed wall temperature Ⓣ for heat transfer or wall concentration Ⓒ for mass transfer is deemed most appropriate to fully warmed-up monolith operation with dilute reactant concentrations. Data have been published for local and/or integrated entrance-region Nusselt numbers for the Ⓣ boundary for simultaneously developing flow in a variety of passage types. A summary of correlations for heat transfer and flow friction is given by Shah and London [6]. Proper

Contributed by the Heat Transfer Division and presented at the 18th AIChE/ASME National Heat Transfer Conference, San Diego, Calif., August 6–8, 1979 of THE AMERICAN SOCIETY OF MECHANICAL ENGINEERS. Manuscript received by the Heat Transfer Division August 25, 1979. Paper No. 79-HT-55.

application of the analogy for the present case requires that the Schmidt and Prandtl numbers must be numerically equal for Sherwood-Nusselt number equivalence. This makes the use of the analogy more than a casual exercise since Schmidt numbers range from 0.2 for hydrogen to over 2 for high molecular weight hydrocarbons. Heat transfer data are not usually available for precisely the right Prandtl number, boundary condition, and passage shape. Thus, engineering judgment must be used in the selection of the best developing flow correlation for most practical applications. Stagnation region mass transfer was not modeled in this study in the interest of developing a simple, easily applied conversion efficiency expression. Leading edge conversion may be significant if care is taken in applying the catalyst and handling the substrate.

A transport augmentation parameter can be defined by:

$$\Phi\,(x_{mt}{}^{+}) = N_{\mathrm{Sh}}\,(x_{mt}{}^{+})/N_{\mathrm{Sh}}\,(\infty),\ \overline{\Phi} = \frac{1}{x_{mt}{}^{+}}\int_{0}^{x_{mt}{}^{+}} \Phi(\xi)\,d\xi \quad (7)$$

where the Sherwood number is normalized by the fully developed Sherwood number, the latter being numerically equal to the Nusselt number for fully developed laminar flow. Figure 1 compares data for the augmentation of mass transfer in passages of several different shapes, all for a Schmidt number of 0.72 appropriate for carbon monoxide or oxygen. Some sensitivity to passage shape is seen. Augmentation curves derived from Hornbeck's [7] circular passage data are chosen for M-T-L model applications since they define augmentation over a relatively broad range of both dimensionless length (0.0005 − 0.1) and Schmidt number (0.7, 2, and 5). This range of Schmidt number precludes consideration of the augmentation of hydrogen mass transfer ($N_{\mathrm{Sc}} = 0.2$). This omission becomes important near stoichiometric air-fuel ratios, where hydrogen oxidation decreases oxygen availability at the catalyst sites, limiting CO and HC conversion.

In order to compare conversion limits from equation (6) for different species on one graph, the species-dependent information is extracted from the independent variable by redefining dimensionless size as the reciprocal Graetz number, expressed in terms of the Lewis number:

$$x^{+} = 1/N_{\mathrm{Gz}} = x/4r_h N_{\mathrm{Re}}\,N_{\mathrm{Pr}} = x_{mt}{}^{+}\,N_{\mathrm{Le}_i} \quad (8)$$

Thus, the mass-transfer-limited conversion of species i in an n-segment monolith of size x^{+}, in terms of the mean augmentation function, is:

$$\eta_i(x^{+}, n) = 1 - \exp\,[-4\,x^{+}\,N_{\mathrm{Nu}}\,(\infty)\,\overline{\Phi}\,(x^{+}/n)/N_{Le_i}] \quad (9)$$

The Lewis number carries species information and, in automotive applications, is independent of pressure and only weakly-dependent on temperature—typically 1 percent per 60 °C. Flow and geometry information are combined in x^{+}, which can be expressed in terms of the ratio of monolith length to gas velocity, or in terms of the ratio of monolith volume to total exhaust flow rate.

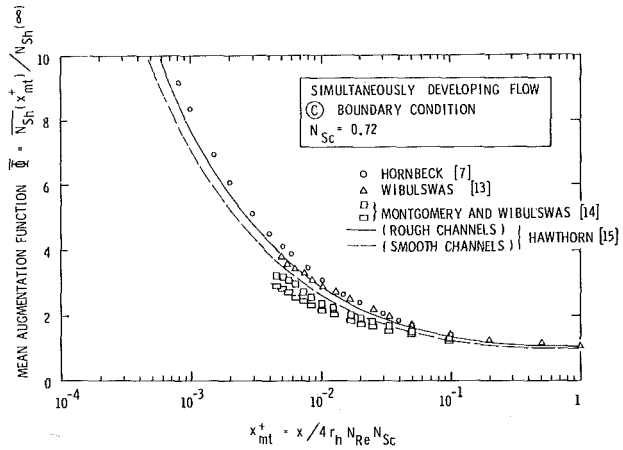

Fig. 1 Mass transfer augmentation function for various passage shapes

The analytical treatment of exhaust hydrocarbons is complicated by the fact that HC consists of a wide variety of species with differing molecular weights, diffusion characteristics, and reactivities. If exhaust HC consists of h different species with relative local concentrations $y_i(x^{+})$ such that:

$$\sum_{i=1}^{h} y_i(x^{+}) = 1, \quad (10)$$

then the exhaust HC conversion limit equation corresponding to the single-species equation (9) is:

$$\eta_{\mathrm{HC}}\,(x^{+}, n) = 1 - \sum_{i=1}^{h} y_i\,(0)\,\exp[-4x^{+}\,N_{\mathrm{Nu}}\,(\infty)\,\overline{\Phi}\,(x^{+}/n)/N_{\mathrm{Le}_i}] \quad (11)$$

A mixture of propylene and methane is taken herein to represent HC, a separation of exhaust HC which has also been used by Kuo, et al. [3], Voltz, et al. [8], and Jackson [9]. Propylene typifies the fully reactive, and methane the less reactive constituents. The low reactivity of methane over alumina-supported platinum is reflected by a low intrinsic rate constant in kinetics proposed by Voltz, et al. [8]. Based on these kinetics, the Lewis number of methane is increased

Nomenclature

A_c = flow area of a passage
C_i = concentration of species i, kg mole i/kg mole exhaust
© = constant concentration boundary condition
DEN = denominator of kinetic rate expression
D_i = diffusivity of species i
$E_{a,i}$, $E_{r,i}$ = activation energies for species i
$k_{a,i}$, $k_{r,i}$, $k_{a,i}{}^{0}$, $k_{r,i}{}^{0}$ = pre-exponential kinetics terms for species i
$k_{i,g}$ = mass transfer coefficient for species i through boundary layer
$k_{i,p}$ = mass transfer coefficient for species i through porous layer
K-MT = kinetics-mass transfer model
$L_{mt}{}^{+}$ = dimensionless mass transfer length
M-T-L = mass-transfer-limited model
M = molecular weight
n = number of segments
N_{Gz} = Graetz number
N_{Le_i} = Lewis number for species i = $N_{\mathrm{Sc}_i}/N_{\mathrm{Pr}}$
N_{Nu} = Nusselt number
N_{Re} = Reynolds number = $4r_h\,w/\mu\,A_c$
N_{Pr} = Prandtl number
N_{Sc_i} = Schmidt number for species i = $\mu/\rho D_i$
N_{Sh} = Sherwood number = $4r_h\,k_{i,g}/D_i$
r = reaction rate
r_h = hydraulic radius
R = universal gas content
S = porous medium total surface area
t = time
T = temperature
Ⓣ = constant temperature boundary condition
w = mass flow rate per flow passage
x = axial distance
x^{+} = dimensionless axial distance, equation (8)
$x_{mt}{}^{+}$ = dimensionless mass transfer axial distance, equation (3)
y = depth into porous solid
y_i = hydrocarbon fraction
η = conversion efficiency
θ = porosity of porous material
μ = viscosity of gas
ρ = density of gas
τ = tortuosity of passage in porous medium
Φ, $\overline{\Phi}$ = augmentation function (local, mean)

Subscripts

CO = carbon monoxide
∞ = fully developed
g = evaluated in the gas stream
h = hydrocarbon index, hydraulic
HC = hydrocarbon
i = species index
p = porous
s = evaluated at the catalyst site
w = evaluated at the wall surface

by an order of magnitude to reflect the low reactivity. From E.P.A. data [10], a 90:10 mixture of propylene:methane is used for engine-out HC.

K-MT Model Development

The M-T-L model, although useful for quick estimates of performance, treated the effects of air-fuel ratio, temperature, and HC reactivity somewhat superficially. A kinetics-mass transfer (K-MT) model using the kinetics of Voltz, et al. [8] for supported platinum was developed for more detailed studies:

$$r = k_{r,i}\, C_{i,s}\, C_{O_2,s}/\mathrm{DEN} \tag{12}$$

$$\mathrm{DEN} = (1 + k_{a,\mathrm{CO}}\, C_{\mathrm{CO},s} + k_{a,\mathrm{HC}}\, C_{\mathrm{HC},s})^2 \tag{13}$$

$$\left.\begin{aligned} k_{a,i} &= k_{a,i}{}^0 \exp\,[-E_{a,i}/RT] \\ k_{r,i} &= k_{r,i}{}^0 \exp\,[-E_{r,i}/RT] \end{aligned}\right\} \tag{14}$$

$$k_{a,\mathrm{CO}}{}^0 = 65.5 \qquad k_{a,\mathrm{HC}}{}^0 = 2080 \tag{15}$$

$$\left.\begin{aligned} k_{r,\mathrm{CO}}{}^0 &= 4.14 \times 10^8 \text{ kg mole/m}^2\text{s} \\ k_{r,\mathrm{CH_4}}{}^0 &= 7.5 \times 10^8 \text{ kg mole/m}^2\text{s} \end{aligned}\right\} \tag{16}$$

$$k_{r,\mathrm{C_3H_6}}{}^0 = 4.3 \times 10^{13} \text{ kg mole/m}^2\text{s} \tag{17}$$

$$E_{a,\mathrm{CO}}/R = -961 \text{ K} \qquad E_{a,\mathrm{HC}}/R = -361 \text{ K} \tag{18}$$

$$\left.\begin{aligned} E_{r,\mathrm{CO}}/R &= 12\,600 \text{ K} \\ E_{r,\mathrm{CH_4}}/R &= 19\,000 \text{ K} \\ E_{r,\mathrm{C_3H_6}}/R &= 14\,560 \text{ K} \end{aligned}\right\} \tag{19}$$

The mass transfer rate for any species i through the developing boundary layer and any porous layer overlaying the catalyst site is:

$$r_i = \frac{\rho}{M_i}\left(\frac{1}{k_{i,g}} + \frac{1}{k_{i,p}}\right)^{-1}(C_{i,g} - C_{i,s}) \tag{20}$$

The boundary layer transport coefficient is derived from equations (4, 7), and (8):

$$k_{i,g} = \mu\, N_{\mathrm{NU}}(\infty)\, \Phi/\rho\, 4r_h N_{\mathrm{Pr}} N_{\mathrm{Le},i} \tag{21}$$

whereas the transport through any inert porous layer of thickness y combines the effects of both ordinary and Knudsen diffusion, as discussed by Satterfield [11]:

$$k_{i,p} = \frac{\theta}{\tau y}\left[\frac{1}{D_i} + \frac{3S\rho_s}{8\theta}\left(\frac{\pi M_i}{2RT}\right)^{1/2}\right]^{-1} \tag{22}$$

Application of the K-MT model is limited to steady-state, lean air-fuel conditions wherein the adiabatic gas temperature rise is normally less than 20 °C, and conditions are approximately isothermal. The method of Reid and Sherwood [12] is used to compute both species diffusivities and Lewis numbers in the exhaust taken as a mixture of CO, H_2, CH_4, C_3H_6, O_2, CO_2, H_2O, NO, and N_2.

At each of 100 axially-spaced nodes, the fluid properties are calculated, and the rate expressions (12) and (20) are iteratively solved for each reactive species. The oxygen concentration at the catalyst is determined from equation (20) and the reaction stoichiometry. Numerical integration of local rates determines streamwise species conversion efficiencies.

Experiment

Experimental work was performed using a test-stand engine with laboratory-coated monoliths in a variety of assemblies, all run as oxidizing converters. All performance comparisons were run using cylindrical monoliths with 0.32 square passages/mm^2 and effective volumes of 0.345 L. Small volumes were used so that outlet emission measurements could be made with enough resolution to discern the effects of parameter changes. In contrast, catalytic converters in current production are in the 3-5 L volume range, with fresh CO and HC conversion efficiencies well in excess of 98 percent. The catalyst was alumina-supported platinum at a representative automotive loading. All uncoated substrates were cut to size and the faces ground before the wash coat and catalyst were applied to insure that the entrance regions were properly coated.

Two four-segment assemblies tested, termed the close-spaced and wide-spaced configurations, had different intersegment spacing values of 3.2 mm and 15.9 mm, respectively. All segments were rotated so as to assure that the developed boundary layers were disrupted between segments.

Monolith assemblies were tested in the exhaust system of a 7.45-L displacement V-8 engine equipped with air injection to the exhaust ports. The exhaust crossover was blocked to isolate the two exhaust banks, and the engine was run on unleaded fuel. Manual valves directed flow from either one or both exhaust banks to the test section. Engine air-fuel ratio was controlled with a pressurized carburetor float bowl. A two-stage air/water intercooler controlled monolith-inlet gas temperature.

Species concentrations (CO, HC, NO_x, O_2, CO_2) and gas temperatures were measured using conventional exhaust emission measurement equipment and radiation-shielded thermocouples. For each test condition, measurements were recorded immediately upstream and downstream of the test section. Exhaust flow rate was determined from the burette-measured fuel flow rate and air-fuel ratio. The latter was established from engine air flow rate measurements and from both oxygen and carbon balances for each emissions sample.

For each of three configurations (integral, close-spaced and wide-spaced four-segment) tested for performance, a set of six randomly sequenced baseline conditions was periodically run to monitor performance degradation. All data reported herein were taken with less than 20 hr exposure of a given monolith to exhaust gas, over which period the conversion efficiencies deteriorated by less than two percentage points. In addition to baseline runs, randomly sequenced runs were made at 16 engine operating conditions over the full cooling range of the intercooler in 30 °C steps, providing a data matrix with sets of runs in which only one of the independent variables (temperature, flow rate, 4/8 cylinders, air-fuel ratio, integral/segmented, close-spaced/wide-spaced) was changed. Engine operating conditions were chosen so that the flow parameters (species concentrations, exhaust flow rates and temperatures) were representative of actual converter applications.

Results

Conversion Efficiency. Figures 2 and 3 show how the experimentally measured CO and HC conversion efficiencies compare with the upper limits for conversion predicted by the models for the wide-spaced four-segment monolith. The ordinates of these and subsequent figures are in an inverted log format, which preserves resolution at high conversion efficiencies. The range in the independent variable x^+ was achieved by varying the exhaust flow rate and temperature. Symbols for experimental data are keyed to temperature. An x^+ of 0.08 corresponds to 0.08 kg/s at 630 °C; an x^+ of 0.20 corresponds to 0.03 kg/s at 480 °C. Error bands are shown which correspond to ±5 ppm CO and ±2 ppm (C6) HC in the monolith outlet emissions measurements. Small fluctuations in outlet measurements and the rapid initial rate of performance deterioration common to fresh catalysts produced much of the data scatter shown.

The solid lines illustrate K-MT model conversion-limit predictions computed for several temperatures. The simple M-T-L model conversion limits are shown as dashed lines. The agreement beetween the data and the K-MT model predictions is reasonably good, but at high CO conversion efficiency, the measured conversion is less than the theoretical ideal at all temperatures. The decrease in CO and HC conversion efficiency associated with low temperature operation can be observed in the analytical curves. The corresponding sensitivity in the experimental data is also seen in the figure but is less definitive because of difficulty in gathering fixed temperature data over wide, overlapping ranges in x^+.

Figure 4 compares CO conversion for four-segment and integral monoliths. The K-MT model conversion-limit lines are shown for both 450 and 650 °C. Since data were not taken at precisely the same x^+ and temperatures for the segmented and integral test series, experimental data are shown as a shaded band, representing about 40 pairs

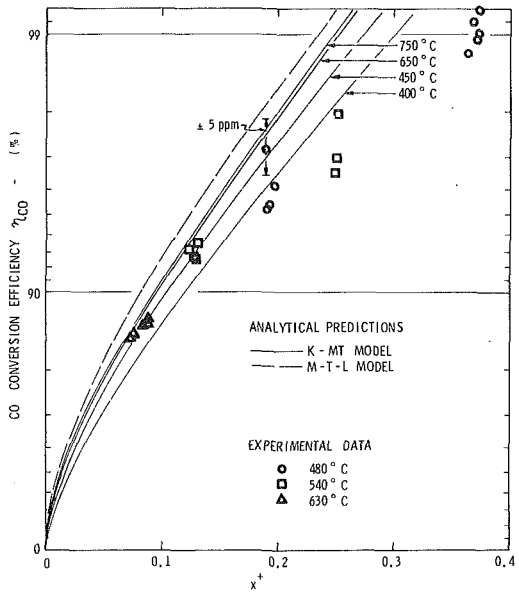

Fig. 2 Four-segment monolith CO conversion—model predictions and experiment

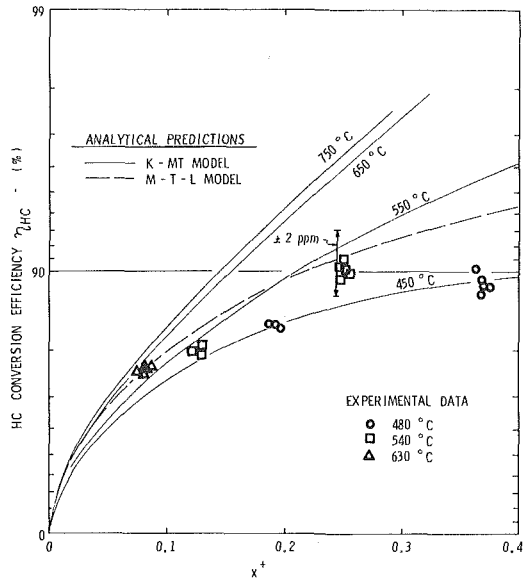

Fig. 3 Four-segment monolith HC conversion—model predictions and experiment

of test runs. The conversion of CO increased with segmenting across the wide range of conditions represented on the figure. Although the limiting theoretical gain was not achieved, the CO residual (unconverted fraction) was typically decreased by 40–48 percent.

Figure 5 is the corresponding comparison for HC. The performance gain due to segmenting into four pieces was substantial: the mean of the data band corresponds to a 33 percent decrease in unconverted HC, somewhat less than the full theoretical potential. The roll-off at high conversion is due primarily to the low reactivity of methane at the low temperatures (350–500 °C) at which these data were acquired.

Several mechanisms could contribute to the inability of the segmented converters to reach their full performance potential, e.g., flow nonuniformity, leakage, leading edge abrasion, and non-ideal boundary layer development. For HC the complications of modeling low-reactivity constituents contributes to discrepancies at high x^+ associated with low temperatures and inert species enrichment. For both CO and HC, minor (<1 percent) leakages of exhaust around the segment peripheral seals contributed to the decline in segmenting advantage at very high conversion.

The conversion benefits of segmenting are summarized in Table 1 for a representative operating condition: 0.04 kg/s flow at 550 °C through 0.345 L of square-passage monolith.

Performance Sensitivity to Parameter Changes. Conversion efficiencies of HC and CO were measured for 87 pairs of test runs for the close-spaced and wide-spaced four-segment configurations. For each test pair, the temperatures, flow conditions, and hours of exposure to exhaust gas were the same. Over a wide range of test conditions for both HC and CO, the conversion efficiencies for the two spacing configurations were scattered within a few percentage points of each other. At high CO conversion (>95 percent), the close-spaced assembly appeared to be slightly inferior, suggesting that the boundary layer redevelopment may be disturbed by close spacing at very low flow rates. It is concluded that, for the conditions tested, the effect of intersegment spacing on conversion was not significant.

The effects of five independent variables on HC and CO conversion for segmented converters were studied. Randomly ordered steady-state tests were run with both the close-spaced and wide-spaced converters at a series of fixed flow rates at controlled temperatures. These tests were run at several exhaust flow rates at different engine speeds (1500 and 2000 r/min), air-fuel ratios (16:1 and 18:1), and number of cylinders exhausting to the monolith (4 and 8). Little or no effect of engine speed, air-fuel ratio, intersegment spacing, or the

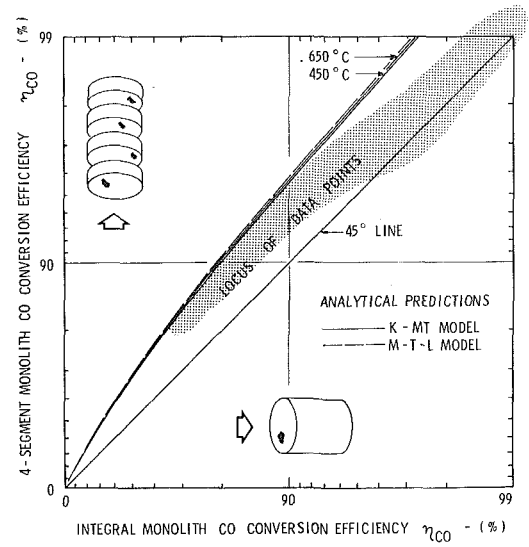

Fig. 4 CO conversion—integral versus four-segment monolith

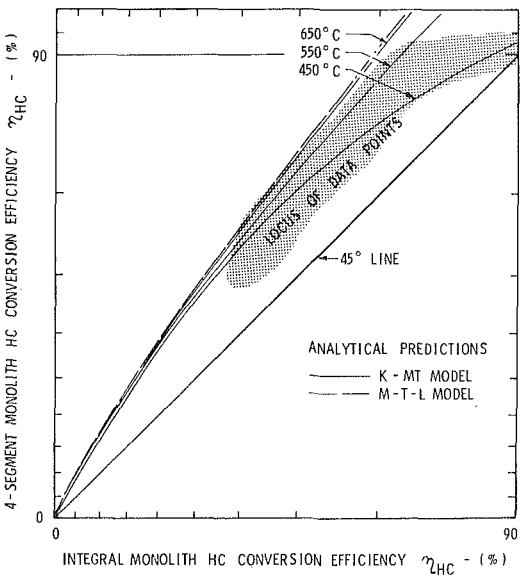

Fig. 5 HC conversion—integral versus four-segment monolith

Table 1 Comparison of conversion efficiencies

	Integral	Four-Segment	Decrease in Residual
M-T-L Model:			
CO	90.0 percent	96.5 percent	65 percent
HC	74.0 percent	85.3 percent	43 percent
K-MT Model:			
CO	89.1 percent	95.2 percent	56 percent
HC	73.2 percent	84.4 percent	42 percent
Measured Efficiency:			
CO	89 percent	94.2 percent	47 percent
HC	73 percent	82.0 percent	33 percent

number of cylinders was observed. There is some concern that the mechanisms responsible for improved conversion in a segmented monolith would also accelerate the rate of poison accumulation in the wash coat, particularly in the leading edge regions. It was beyond the scope of this program to run an extended duration comparison of integral and segmented converter performance. However, data were acquired for 45 hr (equivalent to about 3200 km) on each of the configurations during the test program. The initial, rapid rates of performance decline for both HC and CO were very similar for integral and segmented converters. The long-term durability characteristics of the segmented converter were not determined as part of this study. This aspect, as well as the increased complexity of assembly, would have to be evaluated relative to the integral monolith before the concept could make significant inroads in automotive applications.

Conclusions

1 Segmenting a monolith used as an automotive, oxidizing catalytic converter substantially increases its conversion efficiency. For typical flow conditions with geometrically similar, small integral and four segment monoliths, the CO and HC residuals (unconverted fractions) were decreased by 47 and 33 percent, respectively. For large monoliths, the segmenting advantage would be smaller because of inert species effects and the smaller fraction of the flow passage length occupied by developing boundary layers.

2 A simple model, developed for general flow and monolith geometry and based on mass-transfer-limited conditions in developing flow, provides an upper limit to CO and HC conversion.

3 A more sophisticated model incorporating both external mass transfer and catalyst kinetics is required to demonstrate the effects of lower temperatures at high conversion levels.

4 The long-term durability characteristics and increased complexity of assembly of the segmented monolith would have to be carefully evaluated before the concept could find significant application in automotive catalytic converter systems.

References

1 Heck, R. H., Wei, J., and Katzer, J. R., "Mathematical Modeling of Monolithic Catalysts," *AIChE Journal*, Vol. 22, No. 3, 1976.

2 Ibid., "The Transient Response of a Monolithic Catalyst Support," *Chemical Reaction Engineering—II*, Hugh M. Hulbert, Ed., Advances in Chemistry Series No. 133, American Chemical Society, 1974.

3 Kuo, J. C. W., Morgan, C. R., and Lassen, H. G., "Mathematical Modeling of CO and HC Catalytic Converter Systems," SAE Paper No. 710289, 1971.

4 Young, L. C., and Finlayson, B. A., "Mathematical Modeling of the Monolith Converter," *Chemical Reaction Engineering—II*, Hugh M. Hulbert, Ed., Advances in Chemistry Series No. 133, American Chemical Society, 1974.

5 Sinkule, J., and Hlavecek, V., "Heat and Mass Transfer in Monolithic Honeycomb Catalysts—III—Radiation Model," *Chemical Engineering Science*, Vol. 33, 1978, pp. 829–845.

6 Shah, R. K., and London, A. L., "Laminar Flow Forced Convection Heat Transfer and Flow Friction in Straight and Curved Ducts—A Summary of Analytical Solutions," Stanford University Department of Mechanical Engineering Technical Report No. 75, May 1972.

7 Hornbeck, R. W., "An All-Numerical Method for Heat Transfer in the Inlet of a Tube," ASME Paper No. 65-WA/HT-36, 1965.

8 Voltz, S. E., Morgan, C. R., Liederman, D., and Jacob, S. M., "Kinetic Study of Carbon Monoxide and Propylene Oxidation and Platinum Catalysts," *Ind. Eng. Chem. Prod. Res. Develop.*, Vol. 12, No. 4, 1973.

9 Jackson, M. W., "Effects of Some Engine Variables and Control Systems on Composition and Reactivity of Exhaust Hydrocarbons," SAE Paper 660404, June 1966.

10 "Aldehyde and Reactive Organic Emissions from Motor Vehicles," Part II, APTD-1568b, U.S. Environmental Protection Agency, Emission Control Technology Division, Ann Arbor, Mich., Mar. 1973.

11 Satterfield, C. N., *Mass Transfer in Heterogeneous Catalysis*, M.I.T. Press, Cambridge, Mass., 1970.

12 Reid, R. C., and Sherwood, T. K., *The Properties of Gases and Liquids*, McGraw Hill Chemical Engineering Series, McGraw Hill, New York, 1966.

13 Wibulswas, P., *Laminar Flow Heat Transfer in Non-Circular Ducts*, Ph.D. Thesis, London University, 1966.

14 Montgomery, S. R., and Wibulswas, P., "Laminar Flow Heat Transfer for Simultaneously Developing Velocity and Temperature Profiles in Ducts of Rectangular Cross Section," *Applied Scientific Research 18*, 1967, pp. 247–259.

15 Hawthorn, R. D., "Afterburner Catalysts—Effects of Heat and Transfer between Gas and Catalyst Surface," Shell Development Company Report P-2121 67784, 1970.

M. A. Ait-Ali
D. J. Wilde

Mechanical Engineering Design Division,
Stanford University,
Stanford, CA 94305

Optimal Area Allocation in Multistage Heat Exchanger Systems

In constrained optimization, valuable analytical insight can be gained by focusing attention on the terms of a problem before obtaining any solution particular to the numerical values of the given parameters. The necessary optimality conditions derived from the first semi-log derivatives may give a general result useful as a design rule for all similar problems. This approach is illustrated in the determination of optimal area allocation among the stages of two different multistage heat exchanger systems. This area allocation minimizes the total heat transfer area of the system with respect to: (1) interstage temperature for a given overall temperature change of the process stream; (2) "base area," newly defined here as the ratio of capacity rate to the overall heat transfer coefficient.

Introduction

Problems in optimal design are usually solved numerically using optimization algorithms. This approach rarely gives results as general as those obtainable by analytical methods.

Under suitable conditions, and with constraint and objective functions continuous and twice differentiable, general optimality conditions for the entire class of mathematically similar problems can be derived as follows. The Lagrange multipliers are first eliminated from the necessary optimality conditions given by the first derivatives of the objective function with respect to the design variables. The resulting uncontrained optimality conditions are then expressed in terms of the system operating conditions or groupings of its variables. In this manner, any general parametric relations provided by the necessary conditions which describe the solution for the whole class of similar problems can be exploited. In multistage heat exchanger design, it is convenient to use semi-log derivatives [1] in developing the optimality conditions. Since any relation among the problem terms is preserved by taking first semi-log derivatives instead of the usual derivatives, the same optimality conditions can be expressed in different forms according to the aspect of the solution one wishes to emphasize. The final form constitutes a general result which can be used as a design rule to describe optimality for the whole class of similar problems for which it has been derived.

Derivation of the Necessary Conditions

Consider the N-stage exchanger system of Fig. 1 in which capacity rate (WCp), total temperature change ($T_0 - T_N$) of the process stream and stage overall heat transfer coefficients U_i are assumed given parameters of the problem. The inlet temperatures of the duty streams (T_{i1}, $i = 1, \ldots, N$: cooling or heating) are also assumed given in the problem. The design objective is to minimize the total heat transfer area A_T appropriately choosing the interstage feed stream temperatures $t_1, \ldots, t_{N-1}$.

The solution also maximizes the overall log mean temperature difference of the N-stage system.

Assume that a feed stream with a given capacity rate

$$C_f \equiv (WCp)_f \tag{1}$$

is heated from the temperature T_0 to T_N by passing through a series of N counterflow heat exchanger stages with duty streams of capacity rate

$$C_{d,i} \equiv (WCp)_{d,i} \tag{2}$$

and *base area*, a simplifying concept newly defined here by

$$B_i \equiv (WCp)_{f,i}/U_i = A_i\, \ell m_i/\delta_i \tag{3}$$

where ℓm_i is the log mean temperature difference, and δ_i the temperature change of the feed stream in stage i.

Contributed by the Heat Transfer Division and presented at the Winter Annual Meeting, San Francisco, California, December 10–15, 1978. Manuscript received by the Heat Transfer Division August 7, 1978. Paper No. 78-WA/HT-60.

The total heat transfer area can be expressed as:

$$A_T = \sum_{i=1}^{N} B_i \delta_i/\ell m_i \tag{4}$$

Eliminating the log mean temperature differences and using the stage energy balances gives

$$C_i \delta_i = T_{i,1} - t_{i,2} \tag{5}$$

The total area becomes:

$$A_T = \sum_{i=1}^{N} B_i (C_i - 1)^{-1}\, \ell n(\Delta_i - \delta_i)/(\Delta_i - C_i\delta_i) \tag{6}$$

with

$$\delta_i = t_i - t_{i-1} \tag{7}$$

$$\Delta_i = T_{i,1} - t_{i-1} \tag{8}$$

The first derivative of the total area A_T with respect to the interstage temperature t_i is the sum of the terms $\partial A_i/\partial t_i$ and $\partial A_j/\partial t_i$.

$$\frac{\partial A_T}{\partial t_i} = B_i \Delta_i/(\Delta_i - C_i\delta_i)(\Delta_i - \delta_i) - B_j/(\Delta_j - C_j\delta_j) \tag{9}$$

where $j \equiv i + 1$

Setting this derivative to zero gives

$$B_i/B_j = \frac{(\Delta_i - \delta_i)}{\Delta_i}\frac{(\Delta_i - C_i\delta_i)}{\Delta_j - C_j\delta_j} \tag{10}$$

This is equivalent to

$$B_i/B_j = (\Delta t_{i,\text{out}}/\Delta_i) \cdot (\Delta t_{i,\text{in}}/\Delta t_{j,\text{in}}) \tag{11}$$

per the Nomenclature of the temperature—area diagram of the stage pair shown in Fig. 2.

The second derivative of the total area A_T with respect to the interstage temperature t_i evaluated at the stationary point is positive for consecutive stages with similar values of C_i and B_i in which no constant temperature change is involved. The corresponding stationary point is therefore a minimum and conditions (10) and (11) are optimum.

Thus, at optimality, the ratio of the base areas of a particular stage pair is the product of two temperature ratios. The first is $(\Delta_i - \delta_i)/\Delta_i = 1 - \delta_i/\Delta_i$ where the term δ_i/Δ_i is the heat transfer effectiveness ϵ_i of stage i when $C_f = C_{\min}$, and $1 - \epsilon_i$ is sometimes referred to as the

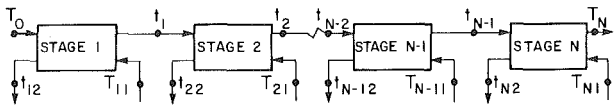

Fig. 1 General N-stage counterflow heat exchanger system

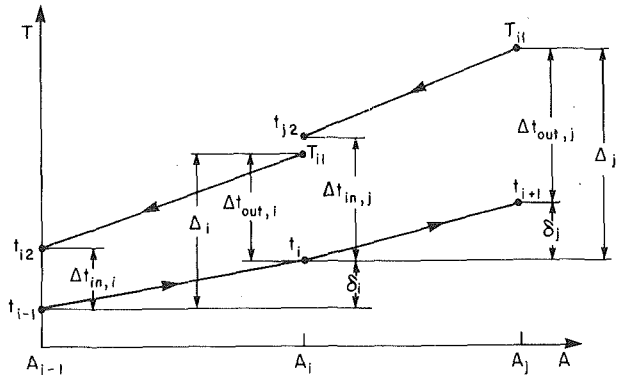

Fig. 2 Stage pair temperature—area diagram

heat transfer *ineffectiveness* ξ_i. The second is the ratio of the temperature differences at the inlet of stage i and stage j. The optimality rule (11) is specialized in Table 1 for heating and cooling process according to the relative values of C_f and C_d, using the concept of heat transfer effectiveness [2].

The cases for which C_f or C_d are infinite either do not fit the problem definition or lead to maximum heat transfer area at the stationary point as in constant temperature boiling refrigerant cascade cycles. In these applications the objective is to minimize refrigeration work by maximizing the overall refrigeration temperature level, and consequently decreasing the log mean temperature difference in the evaporators.

The numerical answer to a particular problem is obtained by solving the set of $(N-1)$ coupled quadratic equations obtained from the optimality conditions (10) by using the temperature difference definitions (7) and (8).

$$t_i^2 - t_i\,[(t_{i-1} - T_{i,1})((1 - C_j)\,B_i/B_j - 1)/C_i + t_{i-1} + T_{i,1}] - [(t_{i-1} - T_{i,1})\,((C_j t_j - T_{j,1})\,B_i/B_j + T_{i,1})/C_i - t_{i-1}T_{i,1}] = 0 \quad (12)$$

This sytem of nonlinear equations is solved by successive substitutions for the interstage temperatures t_i. The total heat transfer area A_T is then obtained by back substitution of equations (7, 8) in equation (6). As written, equations (12) have one sign change. If the coefficients in square brackets are positive, the two roots of each polynomial are real and by the Descartes sign rule on ordered polynomials, only one is positive [3]. Hence the unique local optimum is also globally optimal.

Example 1. The problem is to minimize the heat transfer area of a two-stage gas regeneration system which requires heating a process stream from 311 K (100°F) to 533 K (500°F). The parameters are given in Table 2. This problem has been previously solved by Boas [4] using dynamic programming, Fan and Wang [5] with the discrete maximum principle, and Avriel [6] with a computer program using complementary geometric programming.

The optimal value of t_1^* is obtained by first transforming (10) into:

Table 1 Optimality rule summary process stream

	Heating $C_i = C_f/C_d$	Cooling $C_i = C_d/C_f$
$C_{\min} = C_f$	$\frac{B_i}{B_j} = \xi_i \cdot \frac{\Delta_i}{\Delta_j} \cdot \frac{1 - C_i\epsilon_i}{1 - C_j\epsilon_j}$	$\frac{B_i}{B_j} = \frac{\xi_i}{\xi_j} \cdot \frac{\Delta_i}{\Delta_j} \cdot \frac{C_i - \epsilon_i}{C_i}$
$C_{\min} = C_d$	$\frac{B_i}{B_j} = \frac{\xi_i}{\xi_j} \cdot \frac{\Delta_i}{\Delta_j} \cdot \frac{C_i - \epsilon_i}{C_i}$	$\frac{B_i}{B_j} = \epsilon_i \cdot \frac{\Delta_i}{\Delta_j} \cdot \frac{1 - C_i\epsilon_i}{1 - C_j\epsilon_j}$

Table 2 Example 1 parameters, quantities in parentheses are in British Engineering Units

Stage i	T_{i1}	B_i	C_i	C_f	U_i
1	422 (300)	116 (1250)	1	52740 (10^5)	454 (80)
2	589 (600)	116 (1250)	1	52740 (10^5)	454 (80)

$$t_i = T_{11} - ((T_{11} - T_0)(T_{21} - T_2)B_1/B_2)^{1/2}$$

then substituting for the parameters. The full solution is: $t_1^* = 343.7$ K (158.6°F), $A_1^* = 48.1$ m^2 (518 ft^2), $A_2^* = 396.5$ m^2 (4268 ft^2), $A_t^* = 444.6$ m^2 (4786 ft^2).

Suppose now that we can design the system with either a single stage or three stages to perform the same duty. The single-stage system has no degrees of freedom since $t_1 = T_2 = 533$ K (500°F). The resulting total area is 464.5 m^2 (5000 ft^2).

The solution of the three-stage system, which can be decomposed into two different stage pairs, is given by the two optimality rules of equation (10) transformed into:

$$t_1^* = T_{11} - ((T_{11} - T_0)(T_{21} - t_2^*)B_1/B_2)^{1/2} \quad (13)$$

$$t_2^* = T_{21} - ((T_{21} - t_1)(T_{31} - T_3)B_2/B_3)^{1/2} \quad (14)$$

Using 477.8 K (400°F) for T_{21} and the remaining data of Table 2, we obtain: $t_1^* = 320.3$ K (116.5°F), $t_2^* = 384.2$°K (231.6°F), $A_1^* = 10.4$ m^2 (112.4 ft^2), $A_2^* = 80.3$ m^2 (864.4 ft^2), $A_3^* = 311.7$ m^2 (3355.0 ft^2), $A_T^* = 402$ m^2 (4327 ft^2), thus increasing the number of stages from two to three reduces the heat transfer area by 9.6 percent. However, as suggested by the decreasing value of A_1^*, increasing the number of stages to four while maintaining the overall heat transfer coefficient the same for all stages would result in the area A_1^* approaching zero. That is, the solution vector is no longer an interior point as determined by feasible values of the problem variable, but now lies on a boundary for the value of t_1^*. A larger heat transfer coefficient for the first stage would cause a greater number of stages to be optimal.

Example 2. This example is adapted from [7]. Consider the four-stage cryogenic mixed refrigerant heat exchanger shown in Fig. 3. The pertinent data are given in Table 3. This given design is to be tested for optimality.

Applying equation (10) three times for the three exchanger pairs gives

Nomenclature

A_i = area of exchanger stage i, m^2
A_T = exchanger series total area, m^2
B_i = base area of stage i, $(WCp/U)_i$, m^2
$C_{d,i}$ = duty stream capacity rate, $(WCp)_d$, w/K
$C_{f,i}$ = feed stream capacity rate, $(WCp)_f$, w/K
C_i = feed to duty stream capacity rate ratio, $(C_f/C_d)_i$, dimensionless
$C_{\min}$ = minimum capacity rate (WCp) min, w/K
$C_{\max}$ = maximum capacity rate (WCp) max, w/K
Cp = constant pressure specific heat, J/kg-K
D_k = determinant of order k
ℓm_i = logarithmic mean temperature difference, K
$Ntu_{,i}$ = number of heat transfer units of stage i
t_i = ith stage process stream exit temperature, K
$T_{i,2}$ = ith stage duty stream exit temperatures, K
$T_{i,1}$ = ith stage duty stream inlet temperature, K
U_i = overall heat transfer coefficient of stage i, w/m^2-K
W = feed flow rate, kg/s
Δ_i = maximum temperature difference in exchanger stage i, K
δ_i = feed stream temperature change in stage i, K
$\delta_{i,\max}$ = max (δ_i, C_i δ_i), K
ϵ_i = ith stage heat transfer effectiveness, dimensionless
ξ_i = ith stage heat transfer ineffectiveness, $1 - \epsilon_i$, dimensionless
$\Delta t_{\text{in},i}$ = ith stage inlet temperature difference, K
$\Delta t_{\text{out},i}$ = ith stage exit temperature difference, K

Table 3 Example 2 data

Stage i	B_i	Δ_i	ϵ_i	δ_i	C_i	U_i	t_{i-1}	t_i	T_{i1}	t_{i2}
1	52.0	320.2	0.914	311	0.939	568.	300.	244.	235.4	294.4
	(560)	(116.3)		(100)		(100)	(80)	(−20)	(−36.3)	(70)
2	149.8	312.9	0.921	308	0.490	568.	244.	192.	187.1	213.0
	(1613)	(103.2)		(95)		(100)	(−20)	(−115)	(−123.2)	(−76.6)
3	93.8	320.6	0.916	314	0.978	568.	192.	133.	126.6	186.5
	(1010)	(117.1)		(105)		(100)	(−115)	(−220)	(−232.1)	(−124.8)
4	83.0	276.6	0.868	272	0.965	568.	133.	117.	129.0	129.7
	(893)	(37.8)		(30)		(100)	(−220)	(−250)	(−227.8)	(−226.6)

Equation (10) (not satisfied)	
LHS	RHS
0.347	0.055
1.60	0.312
1.13	0.168

This design is clearly not a minimum area design since equation (10) is not satisfied; i.e. the left hand side is much larger than the right hand side. But this result is not surprising because in low temperature refrigeration minimum cost designs often lead to designs with maximum heat transfer area and minimum refrigeration work.

Sufficient conditions. In the foregoing development it was stated that the stationary point characterized by the optimality rules was a mimimum. The Hessian matrix of second derivatives of the total area with respect to the interstage temperatures evaluated at the stationary point must be positive definite for this to be true. To prove that this is straightforward for a capacity rate ratio of unity, an outline follows.

The matrix is tridiagonal, symmetric with real entries. It can be transformed into a triangular matrix which has its eigenvalues on the main diagonal. These are given by a simple recursion formula. The difference between any two consecutive eigenvalues can be shown to be positive if the ratio of the first two eigenvalues is larger than unity. This is the case if the first interstage temperature t_i is an interior point, i.e. a stationary point, which it is indeed by the necessary conditions. Hence all eigenvalues are positive, the matrix is positive definite, and the point is a local minimum.

Conclusions

Optimal area allocation criteria with respect to the interstage temperatures are derived for multistage heat exchanger systems. They can either be used as optimality rules to verify an existing design for bottlenecks or oversizes, or solved as system of second degree polynomials to specify a new design. Accuracy is not affected by applying a safety factor to the overall heat transfer coefficients (given as parameters), since these appear as ratios for all consecutive stages.

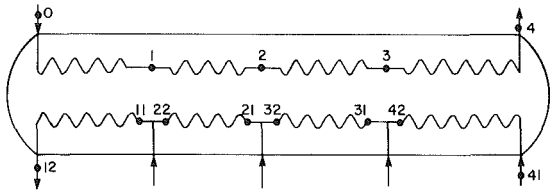

Fig. 3 Cryogenic four-stage heat exchanger (feed side)

Feasible larger numbers of stages (N) lead to smaller total system area, but not necessarily to lower total cost, which can be expected to increase with the resulting system complexity. The optimal stage sequencing requires that the stages with smallest base area be used first in order to obtain the largest stage number N for which the problem has an interior point solution.

Acknowledgments

The research was sponsored by NSF Grant ENG75-00898. The authors wish to express their thanks to Prof. A. L. London for his valuable suggestions.

References

1 Wilde, D. J., *Globally Optimal Design,* Wiley-Interscience, 1978.

2 Kays, W., and London, A. L., *Compact Heat Exchangers,* 2nd edition McGraw-Hill, N.Y. 1964, p. 15.

3 McNeill, B. W., "Tests for Global Optimality and Unboundedness of Engineering Design Polynomials," Ph.D. Thesis, Stanford University, 1976, p. 12.

4 Boas, A. H., "Optimization via Linear and Dynamic Programming," *Chemical Engineering,* Vol. 70, April 1, 1968, pp. 85–88.

5 Fan, L. T., and Wang, C. S., *The Discrete Maximum Principle,* John Wiley and Sons, New York, 1964, pp. 50–53.

6 Avriel, M., Rijckaert, M. J., and Wilde, D. J., *Optimization and Design,* Prentice Hall, Englewood Cliffs, N. J., 1973, pp. 313–315.

7 Ait-Ali, M. A., "Natural gas liquefaction cycles: Irreversibility Analysis," An unpublished Engineer thesis, Stanford University, 1975, pp. 101, 165, 166.

E. M. Sparrow
Fellow ASME

B. J. Lovell

Department of Mechanical Engineering,
University of Minnesota,
Minneapolis, Minn. 55455

Heat Transfer Characteristics of an Obliquely Impinging Circular Jet

Measurements of local heat (mass) transfer coefficients were made on a surface on which a circular jet impinges at an oblique angle. The angle of inclination of the jet relative to the surface was varied from 90 deg (normal impingement) to 30 deg. The Reynolds number and the distance between the jet orifice and the impingement plate were also varied parametrically. To facilitate the experiments, the naphthalene sublimation technique was employed, and the resulting mass transfer coefficients were converted to heat transfer coefficients by the well-established analogy between the two processes. It was found that the point of maximum mass transfer is displaced from the geometrical impingement point, with the extent of the displacement increasing with greater jet inclination. The local coefficients on the uphill side of the maximum point drop off more rapidly than do those on the downhill side, thus creating an imbalance in the cooling/heating capabilities on the two sides. Neither the maximum transfer coefficient nor the surface-averaged transfer coefficient are highly sensitive to the inclination of the jet; during the course of the experiments, the largest inclination-induced decreases in these quantities were in the 15 to 20 percent range.

Introduction

Impinging jets are an established technique for obtaining high local heat transfer coefficients between a fluid and a surface. In the main, the available information on the heat transfer characteristics of impinging jets is restricted to normal impingement. In many applications, owing to the shape of the surface or to constraints on the positioning of the nozzle, the jet impingement may be oblique rather than normal. Furthermore, in numerous situations where normal impingement is intended, the actual impingement may occur at an oblique angle relative to the surface. This is due to the influence of spent air from other jets which causes the jet to be deflected before impingement.

The extensive literature survey by Martin [1] on heat and mass transfer between a jet and an impingement surface contains only two references to inclined jets, and a further search of the archival literature failed to unearth other research papers. One of the two cited references is a study by Korger and Krizek [2] on the impingement of a slot jet. That paper is not directly relevant to the present research, which is concerned with impingement of a circular jet. The other reference is an experimental circular jet study by Perry [3] which, because of its relevance, will be more fully discussed shortly.

In the present study, experiments were performed in which a circular jet of air at room temperature was directed obliquely at a plane impingement surface. The surface was a naphthalene plate which sublimed in response to the air flow passing over it. Highly localized measurements of the mass transfer rates were performed with the aid of a stylus-type instrument. Local mass transfer coefficients were evaluated from the measurements. By making use of the well-established analogy between heat and mass transfer, these coefficients can be employed for heat transfer applications.

The experiments encompassed a range of incidence angles extending from normal impingement (i.e., 90 deg) to 30 deg. Another parameter that was varied during the experiments is the separation distance between the jet-producing orifice and the impingement plate. Separation distances of 7, 10, and 15 jet-orifice diameters were employed. The Reynolds number was also varied over the range from 2500 to 10,000.

The local transfer coefficients were employed to determine a number of important characteristics of the impingement process. For each case, the point of maximum mass transfer on the surface was identified and compared with the point marking the intersection of the geometrical axis of the inclined jet with the surface. Except at normal impingement, these two points were found not to coincide owing to the curvature of the jet axis, as had already been discovered in [2] for the inclined slot jet. The value of the maximum transfer coefficient and the displacement of the maximum point from the geometrical axis are presented as functions of the various independent parameters. The issue of whether or not the point of maximum mass transfer coincides with the stagnation point is examined in the discussion of results. Local transfer coefficient distributions are presented in two perspectives, first as profiles along the main axes of the wall jet and then as complete field contour diagrams.

To supplement the aforementioned local information, consideration will also be given to how the surface-integrated heat/mass transfer characteristics for an inclined jet compare with those for a normal impingement. To this end, the local mass transfer rates for inclined and normal jets are integrated over specified portions of surface centered on the geometrical impingement point. The surface-integrated mass transfer coefficients for inclined jets are then ratioed with that for the corresponding normal jet (i.e., same orifice/plate separation distance and same Reynolds number).

With regard to the work of Perry [3], a basic misconception as well as several experimental inadequacies can be identified. Perry improperly assumed that the point of maximum heat transfer of an inclined jet was coincident with the point of intersection of the geometrical axis of the jet and the impingement surface. Therefore, the reported information for the maximum coefficients is in error, as are contour diagrams normalized by what was improperly purported to be the maximum coefficient. Perry used an imbedded calorimeter to obtain "local" heat transfer coefficients, but the calorimeter diameter was equal to the initial jet diameter and, furthermore, the calorimeter was isolated from the remainder of the impingement plate by an insulating layer only 0.01 cm (0.004 in.) thick. His work was further complicated by the use of high air temperatures (up to 600°C, 1100°F), high velocities (90 m/s, 303 ft/s), and the participation of three temperature levels (i.e., jet, plate, and ambient). It appears that Perry's results cannot be viewed with a high degree of reliability or generality.

Another somewhat relevant work is that of Beltaos [4], who performed a purely fluid mechanic study of an inclined circular jet. In those experiments, pressures were measured on the surface of the impingement plate; the point of maximum pressure was identified with the stagnation point, and its displacement from the geometrical impingement point was reported. These displacements will be compared with those found here for the displacement of the point of maximum heat transfer.

Contributed by the Heat Transfer Division for publication in the JOURNAL OF HEAT TRANSFER. Manuscript received by the Heat Transfer Division June 18, 1979.

The Experiments

Experimental Apparatus. The experiments were performed with the jet impingement plate situated within a test chamber as shown schematically in Fig. 1. Air from the laboratory room is drawn into the chamber through an orifice situated in its upper wall. The jet created by the orifice flow impinges on the naphthalene test plate. Upon traversing the impingement plate, the flow empties into the test chamber proper, from which it is withdrawn by a downstream-positioned blower and is then ducted to a flow meter and finally to an exhaust at the roof of the building.

The impingement surface is pictured in schematic view in Fig. 2. As shown there, the naphthalene test plate is framed by coplanar metallic surfaces. These surfaces permit the hydrodynamic development of the wall jet to continue beyond the active mass transfer region, thereby eliminating end effects. The frame immediately adjacent to the naphthalene plate is part of the mold in which the plate was cast. It serves to house the naphthalene during both the casting process and the impingement experiments. The supplementary frame adds further extension at the two sides and at the downhill end of the impingement surface. Supplementary extension could not be accommodated at the uphill end, nor was it deemed necessary. The overall dimensions of the impingement surface are 17.8 × 20.8 cm (7 × 8.2 in.), with the naphthalene surface area being 7.6 × 15.2 cm (3 × 6 in.).

The impingement surface is positioned on a platform that is suspended from the upper wall of the test chamber by four vertical guide rods. The platform assembly enables precise adjustment of the jet orifice—impingement plate separation distance H that is depicted in Fig. 1. As seen in the figure, H is measured along the centerline of the orifice, and the point P where this line intersects the impingement surface is termed the geometrical impingement point. It should be noted that H is referred to the upper surface of the jet orifice plate because it is there that the jet is initiated.

In addition to vertical positioning, the platform assembly enables the impingement surface to be rotated about an axis which passes through point P and lies in the surface, perpendicular to the plane of Fig. 1. The geometrical impingement point is, therefore, always situated at the same point P, regardless of the inclination of the surface. The protractors governing the inclination were precisely machined and enabled the angle ϕ (Fig. 1) to be set at 15 deg intervals.

The test chamber is an airtight steel enclosure, 127 cm (50 in.) in height and having a (horizontal) square cross section, 61 cm (24 in.) on a side. It is fitted with two removable plexiglass windows which facilitate installation and removal of the impingement plate. The jet orifice plate occupies the central portion of the upper wall of the chamber (Fig. 1). This is a carefully machined stainless steel plate, 0.15 cm (0.060 in.) thick, which houses the jet-producing orifice. The orifice was designed and fabricated according to ASME standards, with a 0.038 cm (0.015 in.) flat and a 60 deg downstream flair. The inlet diameter D of the orifice is 0.635 cm (0.250 in.). The outflow of air from the test chamber was via an exit port at its base.

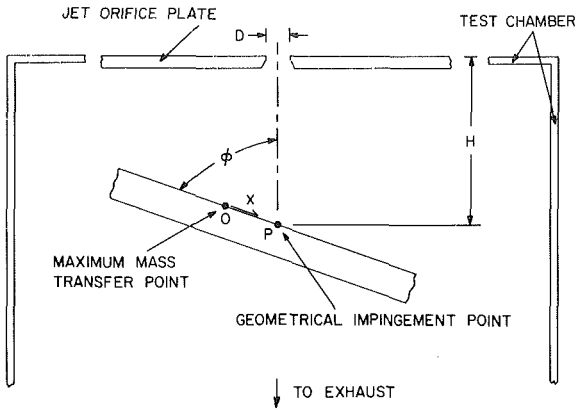

Fig. 1 Side view schematic of the impingement plate in the test chamber

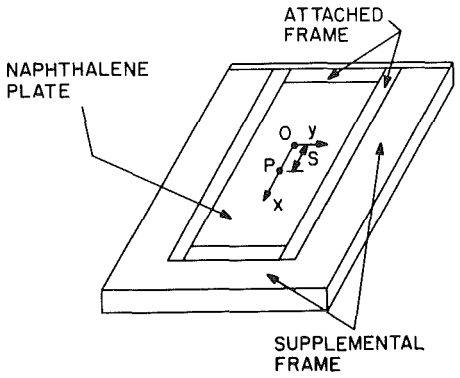

Fig. 2 Pictorial view of the impingement surface

The use of a test chamber enabled the blower to be positioned downstream of the impingement plate, thereby avoiding any preheating of the air which might have occurred had the blower been upstream. In general, the issue of temperature control is of great importance in the use of the naphthalene sublimation technique, since the vapor pressure of naphthalene varies by about 10 percent per °C at room temperature. This consideration also dictated that the experiments by performed in a temperature-controlled room and that the jet velocities be restricted to about 26 m/s (corresponding to Re ~10,000) to limit the temperature rise due to stagnation and recovery. A further measure to obtain well-defined experimental conditions was the outdoor exhaust of the naphthalene-laden air from the test section. This ensured that the air in the laboratory was free of naphthalene vapor, and similarly for the impinging jet.

Naphthalene Test Plates. The naphthalene plates employed in the experiments were cast in a mold consisting of a stainless steel base plate and four aluminum bars which were joined together to form a

Nomenclature

A = integration area
D = jet-orifice diameter, Fig. 1
$\mathcal{D}$ = mass diffusion coefficient
H = separation distance between jet orifice and impingement plate, Fig. 1
h = local heat transfer coefficient
h_0 = maximum heat transfer coefficient
$\bar{h}$ = average heat transfer coefficient
K = local mass transfer coefficient, equation (2)
K_0 = maximum mass transfer coefficient
$\bar{K}$ = average mass transfer coefficient, equation (4)
$\dot{M}$ = surface-integrated mass transfer rate
$\dot{m}$ = local mass transfer per unit time and area
Nu_0 = maximum Nusselt number
$\overline{\mathrm{Nu}}$ = average Nusselt number
Pr = Prandtl number
Re = Reynolds number at jet orifice, $4\dot{w}/\mu\pi D$
S = distance between maximum point and geometrical impingement point, Fig. 2
Sc = Schmidt number
Sh = local Sherwood number, $KD/\mathcal{D}$
Sh_0 = maximum Sherwood number, $K_0D/\mathcal{D}$
$\overline{\mathrm{Sh}}$ = average Sherwood number, $\bar{K}D/\mathcal{D}$
$\dot{w}$ = mass flow rate through jet orifice
x = axial coordinate, Figs. 1 and 2
y = transverse coordinate, Fig. 2
Δ = local sublimation depth
μ = viscosity of air
ν = kinematic viscosity of air
ρ_{nj} = naphthalene vapor density in impinging jet
ρ_{nw} = naphthalene vapor density at plate surface
ρ_s = density of solid naphthalene
τ = duration of data run
ϕ = angle of inclination, Fig. 1

Subscripts

ϕ = at inclination angle ϕ
90 = at normal impingement

frame enclosing a 7.6 × 15.2 cm (3 × 6 in.) rectangle. This frame has already been identified in Fig. 2 during the discussion of the impingement surface. The surface of the base plate was prepared by a succession of lapping and polishing processes which yielded a mirror-like finish.

For the casting process, the frame was placed on the base plate and molten naphthalene was poured into the mold cavity. A secure anchoring of the solidifying naphthalene to the frame was assured by the presence of aluminum pins positioned periodically along the inside surface of the frame. Once complete solidification had occurred, the naphthalene and its enveloping frame were separated from the base plate by a deft hammer blow.

The cast naphthalene surface (i.e., that which had solidified against the base plate) possessed a remarkable degree of smoothness, as sensed both by observation and by touch. The rear face of the naphthalene plate, which had solidified as a free surface, was covered with an impermeable tape. Thus, with this covering of the rear face and with the covering of the edges by the aluminum frame, sublimation mass transfer was limited to the cast face of the naphthalene plate.

Once a casting had been completed, the naphthalene plate and its enveloping frame were placed in the laboratory room to attain thermal equilibrium. During this period, the test surface was covered with a glass plate to prevent natural convection sublimation which might degrade surface quality.

Each of the final data runs was made with a freshly cast naphthalene plate. New (i.e., previously unused) reagent grade naphthalene was used for these castings.

Instrumentation and Experimental Procedure. Measurements of the surface contour of the naphthalene plate, made both before and after an impingement data run, enabled the determination of local mass transfer rates and transfer coefficients. These contour measurements were performed with the plate situated on a movable coordinate table which provided two directions of accurately controlled horizontal travel. The table was equipped with a guide and stops to facilitate horizontal positioning of the plate, the trueness of the positioning being greatly aided by the rigidity of the metal frame which encompassed the plate. In addition, clamps affixed to the table were employed to provide a downward force on the frame, thereby assisting in the establishment of a consistent vertical positioning of the test surface.

The surface contours were measured by instrumentation which converts the movement of a sensor tip (similar to the tip of a dial gage) into an electrical signal that can be read and recorded by a digital voltmeter. The instrumentation includes a sensing head which houses a linear variable differential transformer and signal conditioning electronics. Taken together, the sensor and the voltmeter are able to resolve elevation differences as small as 7.6×10^{-5} cm (3×10^{-5} in.).

The layout of the measurement grid on the naphthalene surface was made with a view toward achieving a higher concentration of points in the region of maximum mass transfer, i.e., in the region of most rapid changes in mass transfer. However, for inclined jets, the point of maximum mass transfer is displaced from the geometric impingement point, so that the former is not known *a priori*. Therefore, for each case (defined by an inclination angle, a Reynolds number, and an orifice—impingement separation distance), two data runs were made. The first of these established the general location of the point of maximum mass transfer and the second, performed with properly deployed measurement stations, yielded the final data.

For each final data run, local elevation measurements were made at between 450 and 550 points on the naphthalene test surface, both before and after the period of jet impingement. In addition, before and after elevation measurements were made at least sixty points on the frame which encompasses the naphthalene plate. As will be explained shortly, the elevation measurements on the frame enable an assessment of the precision of the vertical positioning of the test surface.

The duration of the jet impingement period of each data run extended from 25 to 65 min, depending on the operating conditions. These duration times were selected to ensure that the maximum sublimation depth in any data run did not exceed 0.005 cm (0.002 in.). A careful record was also kept of the time required for the surface contour measurements and for the set-up and disassembly of the impingement surface. In the data reduction procedure, these times are used in conjunction with the results of auxiliary experiments made to determine the mass loss from the test surface during the contour measurements and during the set-up/disassembly periods.

To facilitate closing an overall mass balance in selected data runs, the mass of the test plate was measured before and after the jet impingement period with an analytical balance capable of discriminating to 0.1 mg. Typically, the change of mass during a run was in the range of 100–150 mg.

Data Reduction. The differences between the local surface elevations before and after a data run served as the basis for the local mass transfer rates and mass transfer coefficients. Three corrections, to which allusion was already made in the prior section of the paper, were painstakingly applied to the before/after elevation differences. One of these is a correction which reflects the slight imperfection in vertical positioning inherent in removing and subsequently replacing the test plate on the coordinate table. This correction was made by employing the measured elevations on the frame which encompasses the naphthalene plate. Since the frame does not participate in the mass transfer process, any before/after changes in its elevation are due to vertical positioning imperfections. From the measured elevation changes on the frame, vertical positioning corrections at surface locations on the naphthalene plate were determined by interpolation. Typically, these corrections were on the order of 1.3×10^{-4} cm (5×10^{-5} in.).

The other two corrections were made to account for extraneous mass transfer, due to natural convection and other air currents, during the surface contour measurements and during the set-up/disassembly periods. As noted earlier, these corrections were determined from auxiliary experiments and were, typically, on the order of 1.3×10^{-4} cm (5×10^{-5} in.) and 2×10^{-5} cm (0.8×10^{-5} in.), respectively.

An indication of the efficacy of the aforementioned correction procedure can be obtained from the closure of the overall mass balance. For numerous selected cases, the amount of mass transferred during the jet impingement period was determined by two independent procedures. In one, the corrected local mass transfers were numerically integrated (trapezoidal rule) over the surface of the plate. In the other, the mass transfer was found by differencing direct weighings made immediately before and after the run. Typically, for all the runs so investigated, agreement between the two determinations was within three percent, thereby lending support to the general conduct of the experiment.

If $\Delta(x,y)$ denotes the corrected local sublimation depth at a surface location x,y (see Figs. 1 and 2 for coordinate designations), the local mass transfer per unit time and area follows as

$$\dot{m}(x,y) = \rho_s \Delta(x,y)/\tau \tag{1}$$

where τ is the duration time of the impingement and ρ_s is the density of solid naphthalene (equal to 1.145 gm/cm^3 [5]). For the definition of the local mass transfer coefficient, a concentration difference ($\rho_{nw} - \rho_{nj}$) is used, with ρ_{nw} denoting the concentration of the naphthalene vapor at the impingement surface and ρ_{nj} denoting the naphthalene concentration in the impinging jet. For the present experiments, the latter is zero and the former was evaluated from the Sogin vapor pressure—temperature relation [6] in conjunction with the perfect gas law.

With these inputs, the local transfer coefficient K and its dimensionless counterpart, the local Sherwood number Sh, can be determined from

$$K(x,y) = \dot{m}(x,y)/(\rho_{nw} - \rho_{nj}), \qquad \mathrm{Sh} = KD/\mathcal{D} \tag{2}$$

In defining the Sherwood number, the characteristic dimension is taken as the jet orifice diameter D, and $\mathcal{D}$ is the naphthalene-air diffusion coefficient. Numerical values for the latter were obtained from the defining equation for the Schmidt number, $\mathrm{Sc} = \nu/\mathcal{D}$, where

ν is the kinematic viscosity of air and Sc = 2.5 for the naphthalene-air system [6].

In the presentation of results which follows, the distributions of the local mass transfer coefficient over the plate surface will be expressed in terms of the ratio $K(x,y)/K_0$, where K_0 is the maximum value of $K(x,y)$ for each specific case. The K_0 values for all cases are tabulated in the form $\mathrm{Sh}_0 = K_0 D/\mathcal{D}$.

For design purposes, it is often necessary to know the surface-integrated heat or mass transfer rates. To this end, the measured local mass transfer rates were integrated over a specified part of the impingement surface. In this regard, it was deemed appropriate to center the integration area at the geometrical impingement point P (see Figs. 1 and 2). At a fixed separation distance H, it can be seen from Fig. 1 that a given area (e.g., a square or a circle) centered at this point encompasses the same part of the impingement plate, regardless of the inclination angle ϕ. In contrast, a given area centered at the maximum mass transfer point 0 would encompass different parts of the plate as ϕ changes, since the position of point 0 changes with ϕ.

The integration areas utilized here are squares, respectively four and eight jet-orifice diameters on a side, centered at the geometrical impingement point. If $\dot{M}$ denotes the surface-integrated mass transfer for the selected area A, then

$$\dot{M} = \int\int_A \dot{m}(x,y)dxdy \tag{3}$$

From this, an average mass transfer coefficient $\overline{K}$ and an average Sherwood number can be evaluated from

$$\overline{K} = (\dot{M}/A)/(\rho_{nw} - \rho_{nj}), \qquad \overline{\mathrm{Sh}} = \overline{K}D/\mathcal{D} \tag{4}$$

The average mass transfer coefficients will be presented in terms of the ratio $\overline{K}_\phi/\overline{K}_{90}$. This format highlights the response of $\overline{K}$ to non-normal impingement. Since normal impingement is generally regarded as the most effective impingement orientation, it is relevant to identify the penalty in average transfer performance that is sustained at non-normal orientations. The $\overline{K}_\phi/\overline{K}_{90}$ results are supplemented by a tabulation of $\overline{\mathrm{Sh}}_{90}$.

Although the description of the data reduction procedure and of the presentation parameters has, thus far, been focused on mass transfer, a broader view may be taken by employing the analogy between heat and mass transfer. According to the analogy, the Sherwood and Nusselt numbers at a given Reynolds number are equal when the Prandtl and Schmidt numbers are the same. This result requires that the boundary conditions for the two processes be analogous. Thus, the uniform wall concentration (i.e., ρ_{nw} = constant) of the present experiments translates into uniform wall temperature for the heat transfer case. The analogy will be invoked throughout the presentation of results, and ratios of heat transfer coefficients will be indicated on the graphs along with the analogous ratio of mass transfer coefficients.

The results will be parameterized by three quantities: the inclination angle ϕ, the dimensionless separation distance H/D, and the Reynolds number Re. The latter is based on the jet orifice diameter and the mean velocity passing through the orifice. If the mean velocity is eliminated in favor of the measured airflow rate $\dot{w}$, the Reynolds number takes the form

$$\mathrm{Re} = 4\dot{w}/\mu\pi D \tag{5}$$

which was used in the data reduction.

Results and Discussion

The presentation of results will focus first on local quantities and will then go on to the surface-integrated characteristics. Among the local quantities, results will be given for the displacement of the point of maximum mass transfer from the geometric impingement point and for the distribution of the local transfer coefficient on the impingement surface. In view of the analogy between heat and mass transfer, the phrases *heat transfer* and *mass transfer* will be used interchangeably throughout the presentation and discussion of the results.

The main body of results corresponds to a Reynolds number of 5000 and encompasses inclination angles ϕ of 90, 75, 60, 45, and 30 deg and separation distances H/D of 7, 10, and 15. The influence of Reynolds number was explored by additional runs at H/D = 10 for Re = 2500 and 10,000.

As a prelude to the presentation of results, with a view to establishing the accuracy of the present measurements, comparisons will be made with literature information for the case of normal impingement. For this purpose, average mass transfer coefficients were evaluated in accordance with the definition (4.2) of [1]. The resulting average Sherwood numbers were then compared with those given by the correlation equations (4.10) and (4.11) of that reference.

In general, agreement was found to be in the 10 to 15 percent range, with the present results lying below the correlation. Since, as can be seen in Fig. 8 of [1], the data on which the correlation is based lie in a 50 percent scatter band in the Reynolds number range of interest (Re ~5000), the aforementioned level of agreement is entirely satisfactory. The fact that the present data fall below the correlation is quite reasonable. This is because the turbulence level of a jet produced by suction of air through a sharp-edged orifice should be lower than that in a jet produced by blowing air through a tube or nozzle, as is common in other jet impingement experiments.

Point of Maximum Mass Transfer. For all inclination angles less than 90 deg, the point of maximum mass transfer is displaced uphill as illustrated in Fig. 1. The displacement distance is denoted by S (Fig. 2). The measured displacements have been normalized by the orifice-to-plate separation H and are plotted in Fig. 3 as a function of the inclination angle ϕ. To avoid overlap and attendant confusion, only data for Re = 5000 are shown in the figure; the data for the other Reynolds numbers (Re = 2500 and 10,000) are essentially coincident with those of Fig. 3 (see Fig. 4.2*b* of [7]). The moderate scatter in the data is due primarily to uncertainties in precisely identifying where curves faired through the mass transfer data attain their maxima.

It is seen from the figure that the displacement increases monotonically as the jet becomes more and more inclined. The line passing through the average of the data rises linearly for moderate jet inclinations and then ascends more sharply at larger inclinations. Within the scatter of the data, the normalization of S by H appears to satisfactorily account for the effect of separation distance.

With regard to the magnitude of the displacements, some perspective may be obtained by comparing them to the jet diameter D. At the largest inclination studied, ϕ = 30 deg, the displacements for the separation distances H/D of 7 and 15 are, respectively, 1.05D and 2.25D.

The displacement of the heat or mass transfer maximum for inclined circular jets appears not to have been previously measured, so that direct comparisons of the results of Fig. 3 with the literature are not possible. However, in a purely fluid mechanic study, Beltaos [4] measured static pressures on the surface of an impingement plate and designated the point of maximum pressure as the stagnation point. In that study, both the Reynolds numbers and the separation distances were significantly larger than those of the present investigation, namely, 35,000 $\leq$ Re $\leq$ 100,000 and 15 $\leq H/D \leq$ 47. Furthermore, rather than using the suction mode to induce airflow through an ori-

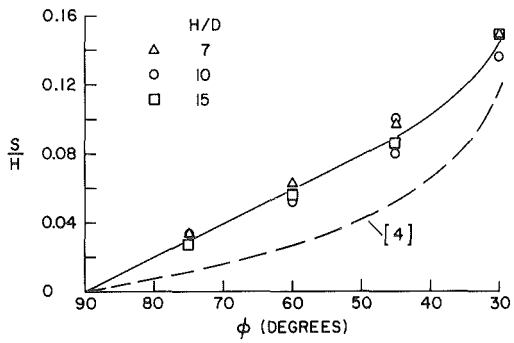

Fig. 3 Displacement distance between the point of maximum mass transfer and the geometrical impingement point

fice, Beltaos operated in the blowing mode and the jet was delivered through a converging nozzle fed by a circular tube. It is likely that this arrangement affected both the jet velocity profile and the turbulence level at exit.

The dashed curve in Fig. 3 is a representation of Beltaos' results for the displacement of the maximum pressure (his designated stagnation point) from the geometric impingement point. It is evident from the figure that the displacements measured by Beltaos are markedly smaller than those found here. The deviations might well be explainable in terms of the differences in the experimental setups and operating ranges noted above. There may, however, be other factors involved. It has been shown that in turbulent flows with skewed velocity fields [8], unsymmetric transport in the neighborhood of a local maximum can cause displacements of the maxima or minima of related quantities. Thus, for instance, in a turbulent wall jet, the point of maximum velocity does not correspond to the point of zero shear [8]. In the present instance, the uphill displacement gives rise to a skewing of the flow; because of this, the maximum pressure point may not coincide with the stagnation point, and neither may coincide with the point of maximum mass transfer.

Local Transfer Coefficient Distributions. The measured local mass (heat) transfer coefficients will be presented from two viewpoints. In the first, the coefficients are plotted as a function of position along the principal axes of the wall jet. The second, to be aired in the next section, shows the coefficients in the form of contour lines (lines corresponding to constant values of the coefficient) superposed on the surface of the impingement plate.

The principal axes of the wall jet are the x and y axes shown in Fig. 2, with the origin O situated at the point of maximum mass transfer for each specific case. The flow field and the transfer coefficients are symmetric about the x-axis, so that there is no need to show results for both positive and negative y. On the other hand, owing to the tilting of the plate, there is no such symmetry with respect to the y-axis. In what follows, transfer coefficient distributions are presented along the x-axis, both for positive and negative x, and along the positive y-axis. For each case (characterized by Re, H/D, and ϕ), the results are normalized by the maximum mass transfer coefficient K_0.

The distribution curves for Re = 5000 are presented in Figs. 4, 5, and 6, respectively for H/D = 7, 10, and 15. In each figure, the results for the various inclination angles (90, 75, 60, 45, and 30 deg) are arranged one above the other. For each inclination angle, the solid line represents the distribution along the x-axis, whereas the dashed line portrays the distribution along the y-axis. On the abscissa, distances along the x- and y-axes are measured in terms of the jet orifice diameter D, while all ordinates are normalized to a maximum value of unity as previously described.

The distribution curves generally display the bell shape that is characteristic of jet impingement, but an increasing asymmetry is apparent as the inclination increases. In particular, the coefficients on the uphill side of the maximum point tend to drop off more rapidly since the jet does not have sufficient momentum to climb very high along the upslope of the plate. On the other hand, the initial momentum of the impinging jet provides a downward thrust, giving rise to higher coefficients on the downhill side. Thus, compared to normal impingement, an inclined jet provides lower transfer coefficients on the uphill side of the maximum point and higher coefficients on the downhill side. The distribution of the transfer coefficients along the spanwise axis (i.e., y-axis) falls between the uphill and downhill distributions for each case.

By comparing Figs. 4, 5, and 6, it is seen that there is a tendency for the distribution curves to drop off more slowly as the separation distance H/D is increased. Furthermore, in the case of inclined jets, the degree of asymmetry tends to diminish with increasing separation.

The effect of Reynolds number on the distribution curves was examined in Figs. 4.5*a* and 4.5*b* of [7], but space limitations preclude their inclusion here. An overview of those figures suggests that the shapes of the distributions are not very sensitive to the Reynolds number. In general, the curves drop off somewhat more slowly as the Reynolds number increases.

Contour Lines of Constant Transfer Coefficient. Contour diagrams showing the deployment of lines of fixed K/K_0 (or h/h_0) on the impingement surface have been prepared for inclination angles of ϕ of 90, 60, and 30 deg and for separation distances H/D of 7, 10,

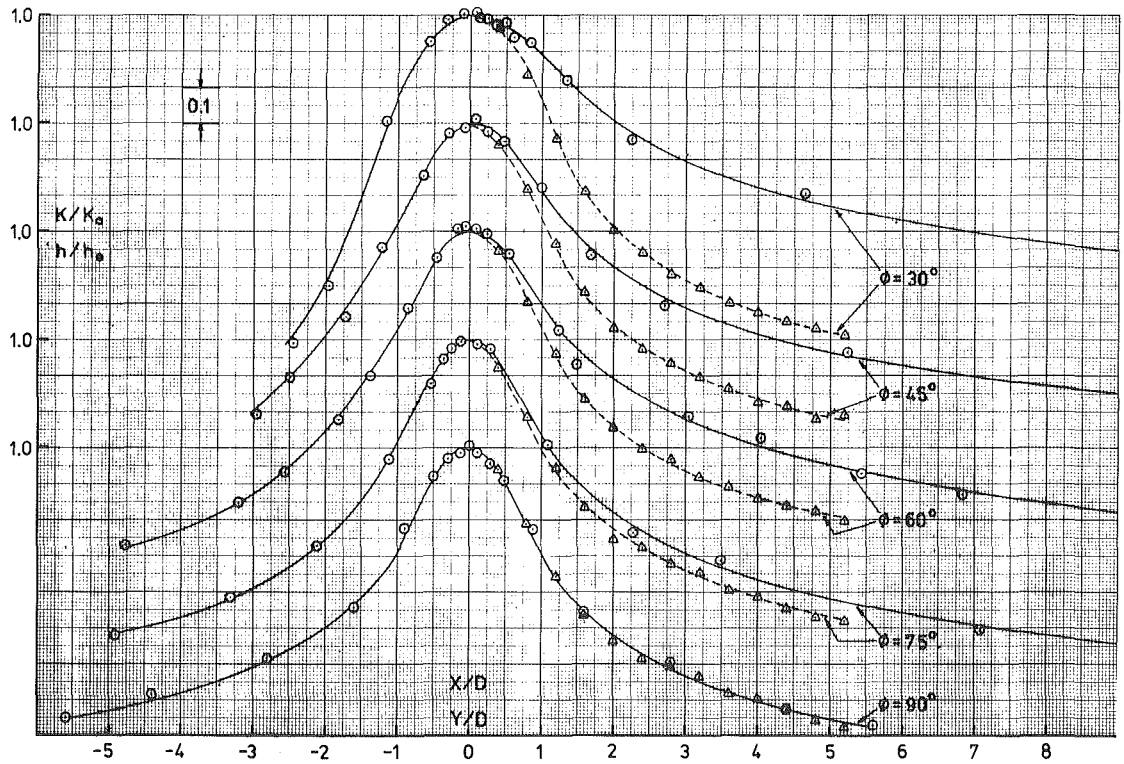

Fig. 4 Distributions of the local transfer coefficient along the principal axes of the wall jet, H/D = 7, Re = 5000

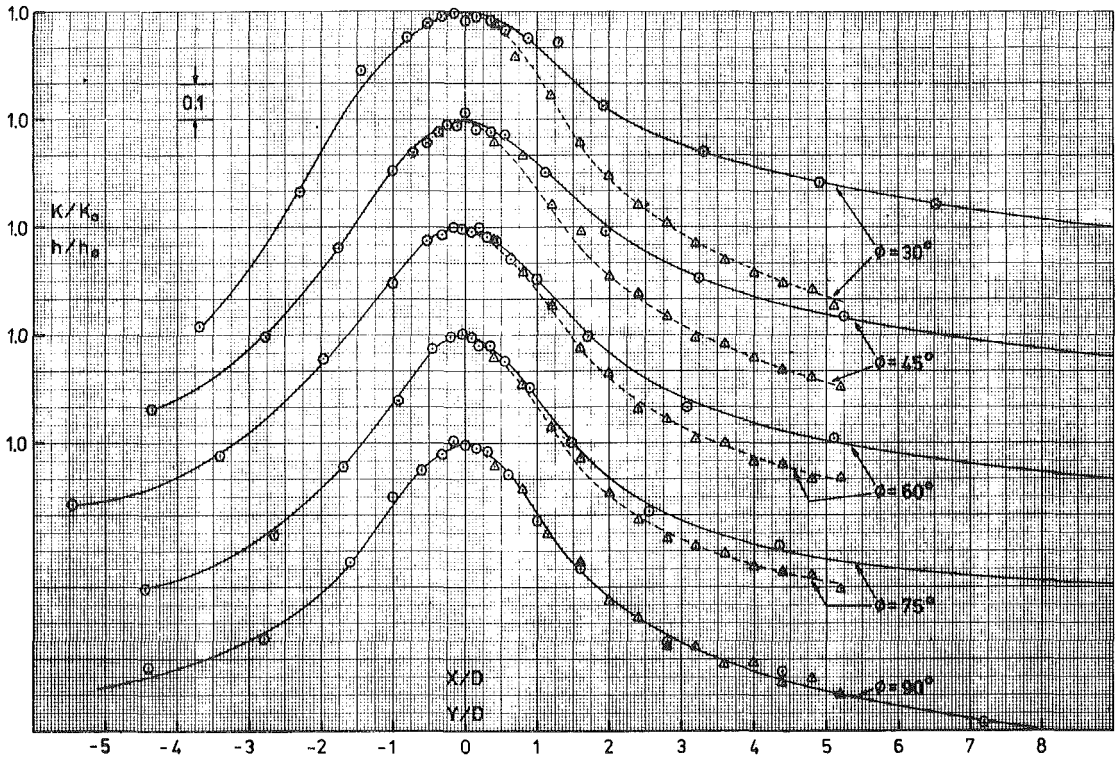

Fig. 5 Distributions of the local transfer coefficient along the principal axes of the wall jet, $H/D = 10$, Re = 5000

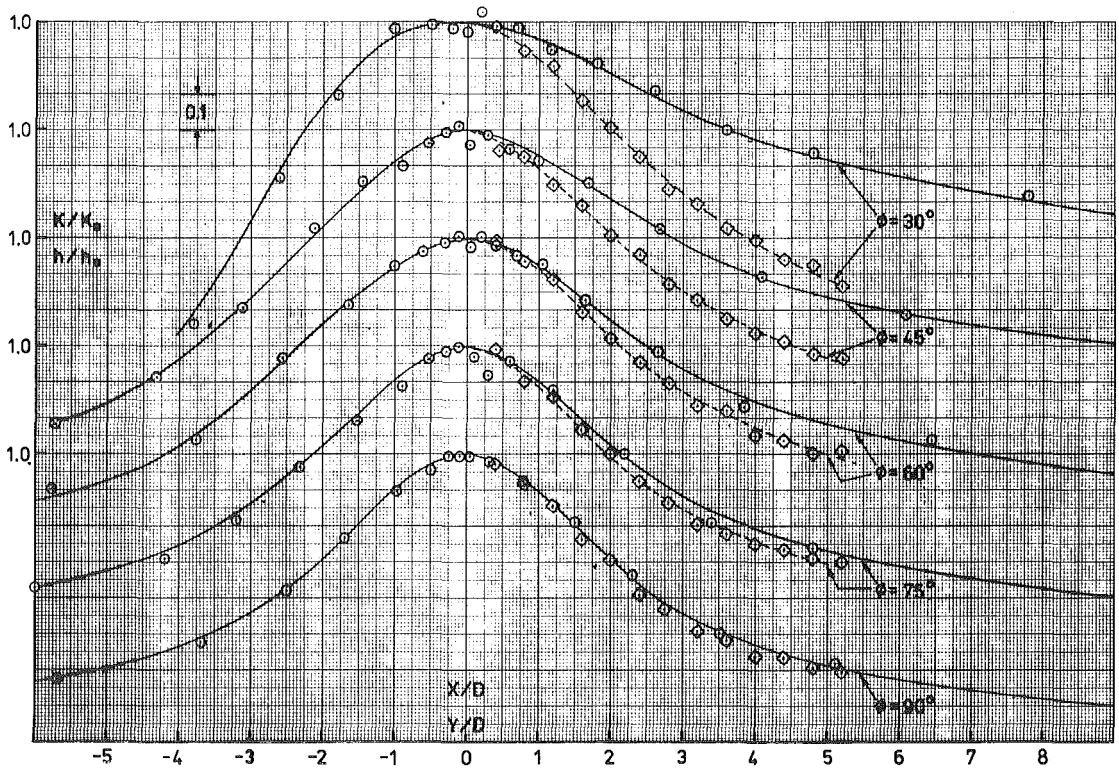

Fig. 6 Distributions of the local transfer coefficient along the principal axes of the wall jet, $H/D = 15$, Re = 5000

and 15. Of these nine figures, three will be presented here (those for $H/D = 10$ and for $\phi = 90$, 60, and 30 deg); the remaining figures can be found in [7].

The contour diagrams, Figs. 7, 8, and 9, are constructed with the abscissa representing the symmetry axis (i.e., the x-axis) and the ordinate representing the span-wise axis (the y-axis). In each figure, contour lines are drawn for $K/K_0 = h/h_0 = 0.9, 0.8, \ldots, 0.4$. As a special feature of Figs. 8 and 9, an arrow has been inserted on the abscissa to indicate the location of the geometrical impingement point.

From Fig. 7, it can be seen that for normal impingement the contour lines are concentric circles. As the inclination increases, the contours tend to compact on the uphill side of the maximum point and spread apart on the downhill side. Thus, on the uphill side, the region of high coefficients contracts while that on the downhill side expands. As a

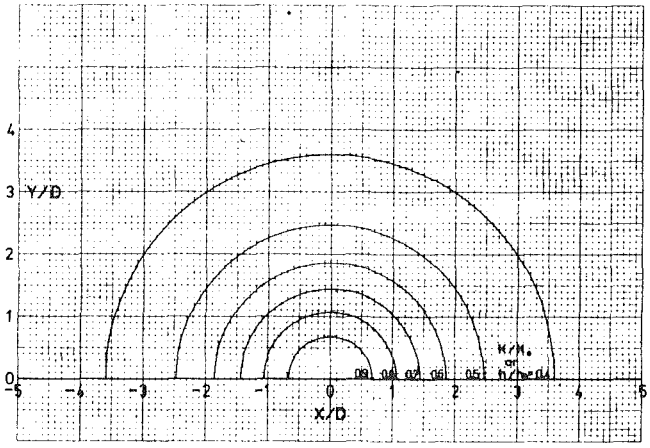

Fig. 7 Contour diagram showing lines of constant mass transfer coefficient, $\phi = 90°$, $H/D = 10$, Re = 5000

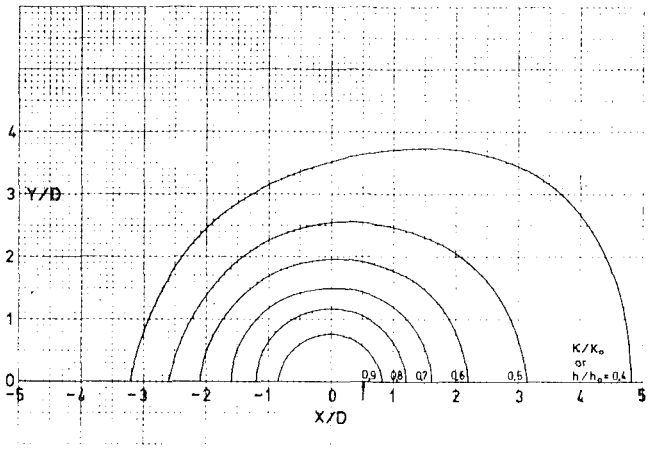

Fig. 8 Contour diagram showing lines of constant mass transfer coefficient, $\phi = 60$ deg, $H/D = 10$, Re = 5000

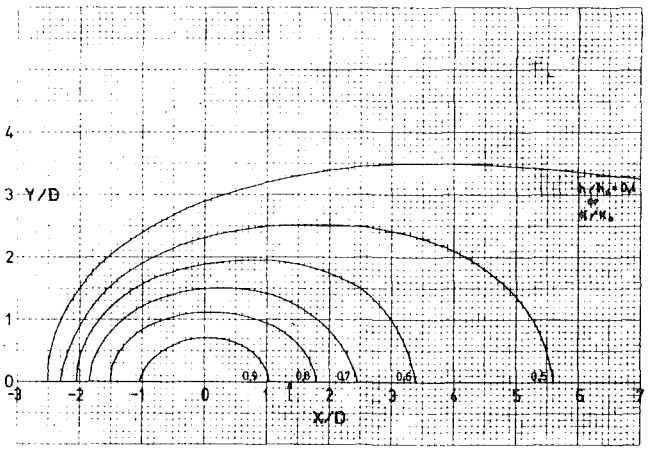

Fig. 9 Contour diagram showing lines of constant mass transfer coefficient, $\phi = 30$ deg, $H/D = 10$, Re = 5000

consequence, there is a significant imbalance in the cooling or heating capabilities of the jet on these two sides. Despite the contracting and expanding on the uphill and downhill sides, the lateral (i.e., spanwise) extent of the plate convered by the contours is not greatly altered by changes in the angle of inclination.

With regard to the effect of changes in separation distance (Figs. 4.7*a*–4.7*i* of [7]), increases in H/D cause a general spreading of the contour lines. This characteristic, which is in evidence for both normal and inclined impingement, indicates a more uniform distribution of the transfer coefficients.

Maximum Transfer Coefficients. The values of the maximum transfer coefficient are of practical interest because they are indicative of the heating/cooling capabilities of the impinging jet. In addition, they are needed here to round out the information that was presented in ratio form in Figs. 4–9.

The measured maximum transfer coefficients are presented in dimensionless form (in terms of Sh_0 or Nu_0) in Tables 1 and 2. In the first of these tables, attention is focused on the effects of jet inclination at various fixed separation distances and at a fixed Reynolds number of 5000. The second table shows the influence of Reynolds number variations.

It can be seen from Table 1 that, aside from modest data scatter (in the 2-4 percent range), there is a clear trend for the maximum transfer coefficient to decrease with increasing inclination. Over the range of angles from 90 to 30 deg, the decrease is in the 15 to 20 percent range. The extent of this decrease, while of some practical significance, is not overpowering, especially when it occurs over such a large range of inclination angles. Over a smaller range, say from 90 to 60 deg, the decrease in Sh_0 (or Nu_0) is on the order of five percent. At the smallest separation distance ($H/D = 7$), the decrease of Sh_0 with ϕ is quite uniform, whereas for $H/D = 10$ and 15 the decrease is relatively gradual for larger angles and becomes sharper for smaller angles.

Further examination of Table 1 indicates that there is a substantial decrease of Sh_0 as the separation distance increases. The Sh_0 values for $H/D = 10$ and 15 are, respectively, about 70 and 45 percent of those for $H/D = 7$. It can be seen from Table 2 that Sh_0 is also quite sensitive to the Reynolds number. A least-squares fit of the data gives the Reynolds number dependence as $Sh_0 \sim Re^{0.6}$.

With a view to generalizing the results to fluids with Prandtl or Schmidt numbers other than 2.5, mention may be made of the analysis of [9] for the stagnation point Sherwood (or Nusselt) number corresponding to normal impingement of a circular jet. There, it was found that for a fixed Reynolds number, $Sh_0 \sim Sc^{0.361}$. In the absence of further information, this same relation may be tentatively adopted for inclined jets. Then, since the results of Tables 1 and 2 correspond to Sc = 2.5, it follows that for other Sc or Pr

$$Sh_0 = (Sc/2.5)^{0.361} Sh_0(\text{table}) \tag{6a}$$

or

$$Nu_0 = (Pr/2.5)^{0.361} Nu_0(\text{table}) \tag{6b}$$

Average Transfer Coefficients. Numerical values of the average mass (heat) transfer coefficient $\overline{K}$ (or $\overline{h}$) were evaluated as described in the text adjacent to equations (3) and (4). The ratio $\overline{K}_\phi/\overline{K}_{90}$ compares the average coefficients for inclined and normal impingement for a given area centered at the geometrical impingement point. Two averaging areas were used: one, a square with a side equal to four jet-orifice diameters and the other a square whose side is eight jet-orifice diameters.

Table 1 Effect of inclination and separation distance on the maximum transfer coefficient (Re = 5000)

ϕ (deg)	H/D =	Sh_0 or Nu_0		
		7	10	15
90		93.0	62.0	43.0
75		91.5	63.1	40.5
60		85.5	60.0	40.2
45		80.0	58.0	39.5
30		75.0	53.8	34.5

Table 2 Effect of Reynolds number on the maximum transfer coefficient ($H/D = 10$)

Re	ϕ =	Sh_0 or Nu_0		
		90 deg	60 deg	30 deg
2500		43.0	39.0	34.5
5000		62.0	60.0	53.8
10,000		101.5	94.5	71.5

The $\overline{K}_\phi/\overline{K}_{90}$ results are plotted in Fig. 10 as a function of the inclination angle ϕ. Results for the four- and eight-diameter averaging squares are respectively presented in the lower and upper graphs, and the data are parameterized by the separation distance H/D. The Reynolds number for all the data is 5000.

From an overview of Fig. 10, it is seen that the average coefficient is not very sensitive to the angle of inclination. From the standpoint of practice, this means that the average cooling (heating) capabilities of the jet are not severely degraded by non-normal incidence. As expected, the deviations of $\overline{K}_\phi/\overline{K}_{90}$ from unity increase with increasing ϕ. Also in evidence is a tendency for these deviations to be smaller as H/D increases, and this is consistent with the more gradual variations of the local coefficients over the surface.

A more detailed tracking of the trends requires consideration of whether the point of maximum mass transfer and its immediate environs falls inside or outside the integration square. If outside, then $\overline{K}_\phi/\overline{K}_{90}$ will register a relatively low value as is evidenced, for example, by the triangle data symbol situated at the lower right in the lower graph of Fig. 10.

As a final note in connection with Fig. 10, mention may be made of the flagged data symbols at $\phi = 75$ deg for $H/D = 10$ and 15. These symbols represent corrected data, with the extent of the corrections being those required to smooth the data scatter for these same cases in Table 1. It is evident that the corrected data fit more harmoniously with the general trends in Fig. 10 than do the uncorrected data.

To complete the presentation of results, the values of $\overline{K}_{90}$, expressed in terms of $\overline{Sh}_{90}$, are listed in Table 3. These results show the expected trends whereby the average coefficient decreases with increasing separation distance and with the size of the averaging area.

Concluding Remarks

The results of the present experiments enable identification of several interesting mass (heat) transfer characteristics of obliquely impinging circular jets. The point of maximum mass transfer is displaced from the geometrical impingement point of the jet, with the extent of the displacement increasing as the inclination increases. The largest displacement encountered during the experiments is about $2\frac{1}{4}$ jet-orifice diameters. The local coefficients on the uphill side of the maximum point drop off more rapidly than do those on the downhill side, and this is accentuated at larger inclinations. Thus, there may be significant imbalances of cooling or heating capability on the two sides of the maximum.

The values of the maximum coefficient decrease with increasing inclination angle, but only moderately. The greatest decreases encountered here are in the 15 to 20 percent range.

Surface-averaged transfer coefficients for inclined jets were compared with those for normal incidence. They, too, were found not to be highly sensitive to inclination, with a maximum decrease of 15 to 20 percent for the extreme conditions of the experiments.

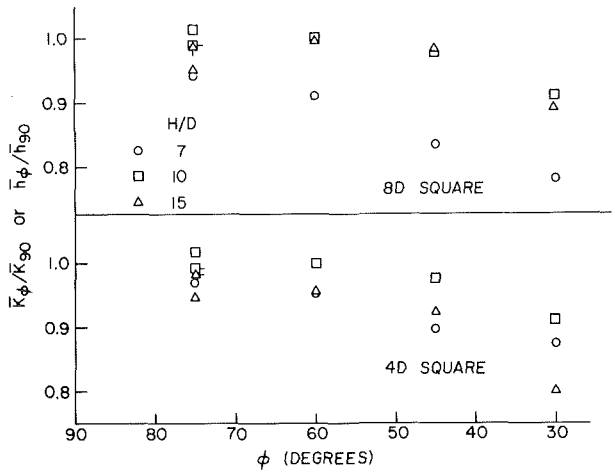

Fig. 10 Comparison of average mass transfer coefficients for inclined and normal impingement, Re = 5000

Table 3 Average coefficients for normal incidence (Re = 5000)

	$\overline{Sh}_{90}$ or $\overline{Nu}_{90}$		
H/D =	7	10	15
4D square	55.7	42.6	33.7
8D square	37.9	29.8	24.6

Acknowledgment

The research reported here was performed under the auspices of NSF grant ENG77-06762.

References

1 Martin, H., "Heat and Mass Transfer Between Impinging Gas Jets and Solid Surfaces," *Advances in Heat Transfer,* Vol. 13, 1977, pp. 1–60.

2 Korger, M. and Krizek, F., "Die Stoffübergangszahlen beim Aufprall schräger Flachstrahlen auf eine Platte," *Verfahrenstechnik,* Vol. 6, 1972, pp. 223–228.

3 Perry, K. P., "Heat Transfer by Convection from a Hot Gas Jet to a Plane Surface," *Proceedings of the Institution of Mechanical Engineers,* Vol. 168, 1954, pp. 775–780.

4 Beltaos, S., "Oblique Impingement of Circular Turbulent Jets," *Journal of Hydraulic Research,* Vol. 14, 1976, pp. 17–36.

5 *International Critical Tables,* Vol. 1, McGraw-Hill, New York, 1926, p. 233.

6 Sogin, H. H., "Sublimation from Disks to Air Streams Flowing Over Their Surfaces," *Trans. ASME,* Vol. 80, 1958, pp. 61–71.

7 Lovell, B. J., "Local Transfer Coefficients for Impingement of an Axisymmetric Jet on an Inclined Surface," Thesis, Department of Mechanical Engineering, University of Minnesota, Minneapolis, Minn., 1978.

8 Bradshaw, P. and Gee, M. T., "Turbulent Wall Jets With and Without an External Stream," *Aeronautical Research Council of London,* R&M 3252, 1960.

9 Scholtz, M. T. and Trass, O., "Mass Transfer in a Nonuniform Impinging Jet," *AIChE Journal,* Vol. 16, 1970, pp. 82–96.

Unit Thermal Performance of Atmospheric Spray Cooling Systems[2]

R. W. Porter
Associate Professor of Mechanical Engineering, Mem. ASME

M. Jain[1]
Research Assistant.

Illinois Institute of Technology, Chicago, Ill.

S. K. Chaturvedi
Assistant Professor of Mechanical Engineering, Old Dominion University, Norfolk, Va., Mem. ASME

Thermal performance of an open atmospheric spray pond or canal depends on the direct-contact evaporative cooling of an individual spray unit (spray nozzle or module) and the interference caused by local heating and humidification. Droplet parameters may be combined into a dimensionless group, number of transfer units (NTU) or equivalent, whereas large-scale air-vapor dynamics determine interference through the local wet-bulb temperature. Quantity NTU were implied from field experiments for a floating module used in steam-condenser spray canals. Previous data were available for a fixed-pipe nozzle assembly used in spray ponds. Quantity NTU were also predicted using the Ranz-Marshall correlations with the Sauter-mean diameter used as the characteristic length. Good agreement with experiments was shown for diameters of 1–1.1 cm (module) and 1.9 mm (fixed-pipe nozzle).

Introduction

It is essential that reliable prediction techniques be available to insure proper cooling capacity for steam-condenser heat rejection to the atmosphere from large electric power plants. Underdesign will result in a decrease in thermal efficiency and, in the extreme, derating of generating capacity. Overdesign adversely affects costs and may even lead to exclusion from further consideration of an otherwise favorable system. Prediction techniques are even more critical for the nuclear ultimate heat sink which is charged with receiving and dissipating energy to the atmosphere in the event of a loss of coolant accident. Spray cooling systems are used in both applications although the configurations and values of parameters differ.

Open spray cooling systems are an alternative to cooling ponds and evaporative cooling towers for supplemental or closed-cycle applications. Factors of land availability, cost, and environmental impact must be considered on an individual basis. The spray canal, wherein floating spray modules are placed in an open channel, has evolved for the condenser application. The channel flow rate is typically 4×10^6 L/min (10^6 gpm) of water with each module spraying about 4×10^4 L/min (10^4 gpm) of about 1-cm-dia drops, and powered by nominally 56-kW (75-hp) motorized pumps. The spray pattern is about 5 m high and extends over 200–600 m^2 of canal surface, depending on the particular design. Both multiple cone-impact (Fig. 1) and single circular-slot nozzle designs have been utilized [1]. The large drop size and relatively massive sprays are compatible with the desire for large flow rates and small drift loss with the prevailing wind substantially in cross flow to the canal. Conversely, the fixed-pipe manifolded system has evolved for the spray pond of the ultimate heat sink and other applications [2]. In this case, order-mm-diameter drops are generated in a finer spray.

The dropwise parameters of the spray may be combined into a dimensionless group denoted by either Number of Transfer Units (NTU) [1] or Spray Energy Release (SER) [3, 4] which may be used to predict spray cooling range in terms of initial liquid temperature, T, and local wet-bulb temperature. The latter may be related to ambient wet-bulb temperature and T through a dimensionless interference allowance, f, which includes localized heating and humidification effects as well as larger-scale convective diffusion in the atmospheric boundary layer, with an imbedded spray matrix producing apparent internal heat and humidity generation [3, 5]. A prediction

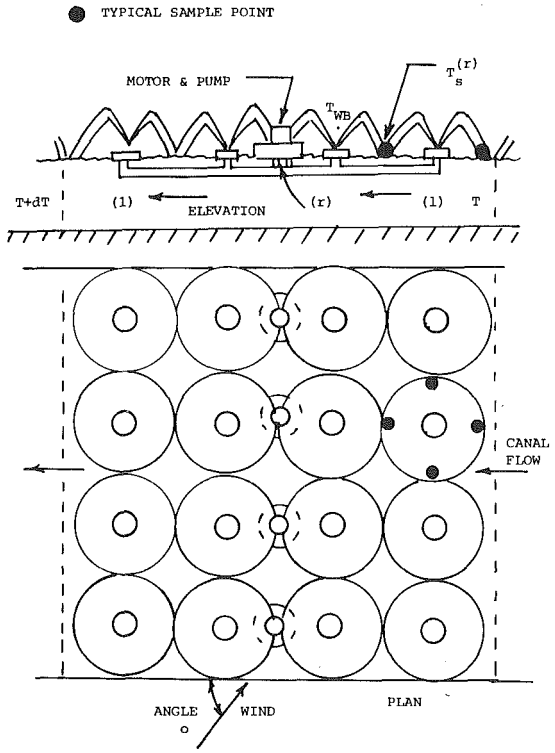

Fig. 1 Typical spray-canal layout with 4-spray modules arranged in four rows

of the local wet-bulb temperature therefore requires a knowledge of the unit performance factor NTU. The entire system can then be analyzed by either analytical [1] or numerical [6] techniques.

Elgawhary and Rowe [7] applied the well-known Ranz-Marshall correlations [8] to unit performance of spray-pond nozzles keeping the unknown drop size as an empirically adjusted parameter. A vapor bubble was envisioned to follow the drop, gaining heat and humidity in the process. Frediani and Smith [9] used a similar approach for floating spray modules, as did Berger and Taylor [10] for spray-pond nozzles oriented at various angles. In the above cases, the analogy between heat and mass transfer was not employed in order to take advantage of the net driving potential, the wet-bulb temperature. Computations were rather involved and computer oriented. Little or no documented experimental data were provided.

By employing the wet-bulb temperature as the driving potential

[1] Present Address: Argonne National Laboratory, Argonne, IL 60439.

[2] This work was supported by U. S. Department of Energy under Contract EC-77-S-02-4531.

Contributed by the Heat Transfer Division for publication in the JOURNAL OF HEAT TRANSFER. Received by the Heat Transfer Division July 27, 1979.

and by combining the dropwise parameters into a dimensionless group denoted either NTU or SER, a convenient bridge may be employed between experimental data and systems analysis similar to that employed in ordinary heat exchangers. Chen and Trezek [11] obtained experimental data for the dimensionless group, implied by temperature measurements on a spray pond using fixed-pipe nozzles and drop sizes up to about 6-mm dia. The Ranz-Marshall correlations were used to predict the dimensionless group using an experimental drop distribution function and an analysis of the drop trajectories. It was assumed that the horizontal drop velocity was in counter flow to the ambient wind.

In the present work we present new experimental data for Ceramic Cooling Tower Company spray modules with order-cm-diameter drop sizes. Field experiments were performed at two operating electric power plants for this purpose. The modules and power plants, Commonwealth Edison Company's Dresden and Quad-Cities Nuclear Stations, are described more fully in references [1, 5] and [6]. We also compare the results of measurements with predictions based on the Ranz-Marshall correlations, but with several modifications: First, the horizontal component of drop velocity is assumed in cross flow to the ambient wind. This accounts for the counter-flow pattern on the upwind half of the umbrella-like spray being compensated by the parallel-flow pattern on the downwind half. Second, mean values are employed for determining the relative drop velocities which avoids a numerical integration. The assumption of free flight gives good agreement for droplet residence time and allows a closed-form representation. Finally, the mass transfer coefficient is evaluated at a mean (Sauter) diameter which is especially convenient when the distribution function is uncertain. Present predictions are also compared with the theory and experiment of Chen and Trezek [11] using Spraco No. 1751 nozzles operated at 0.48-atm gauge pressure.

It should be noted that the Ranz-Marshall correlations were based on single water drops at rest in the laboratory frame with Reynolds numbers up to about 200. They do not include transient effects of freely falling drops [12] or interference of neighboring drops through localized acceleration or wake interaction. Further, droplets greater than about 6 mm in diameter tend to be unstable and might be better described as water globules. In the case of the fixed-pipe spray nozzles, the Reynolds number based on average relative velocity extends up to about 1100, while for the spray modules values up to about 8200 are encountered. Recent laboratory experiments [13, 14] on controlled spray systems using local thermal and dynamical measurements suggest that the Ranz-Marshall correlations may overpredict transport in high-Reynolds-number sprays. Nevertheless, the correlations illustrate the computational approach and appear to give good results for full-scale sprays when used with appropriate drop-size characterization. However, caution should be used in extrapolating to new designs without supporting data.

Theoretical Analysis

The equations of mass and energy transfer for a typical drop of mass, M, and temperature, T_D', are

$$-dM/dt = KA\,[\omega_S\,(T_D') - \omega_a] \tag{1}$$

$$-d\,(Me)/dt = [H\,(T_D' - T_a) + i_g\,(T)\,K\,(\omega_S\,(T_D') - \omega_a)]A \tag{2}$$

where K is mass transfer coefficient based on specific humidity ω [1], A is surface area, e is specific internal energy of liquid water, H is sensible heat transfer coefficient, i_g is specific enthalpy of saturated vapor, S denotes air saturated with vapor, and a denotes the surrounding air-vapor mixture which we assume to be evaluated at an average local state. For practical purposes one may realistically make the following additional approximations [1]: (1) ideal-caloric incompressible liquid water, (2) constant latent heat, and (3) unit psychrometric ratio $H/(c_sK)$ where c_s is specific heat of air and vapor per unit mass of dry air (humid heat). The latter approximation also results in the equivalency of the so-called adiabatic-saturation temperature and the wet-bulb temperature T_{WB} read by a radiation-shielded psychrometer. Indeed, the above equations may be combined and simplified to [1]

$$-c_wMdT_D'/dt = KA\,[h\,(T_D') - h\,(T_{WB_a})] \tag{3}$$

where c_w is specific heat of liquid water and h is the total heat (Carrier's sigma function, the enthalpy i of air and vapor per unit mass of dry air minus the contribution of the moisture present taken as saturated liquid at the adiabatic-saturation temperature, $i - \omega i_f\,(T_{AS})$). When integrated over the drop trajectory, equation (3) is known as Merkel's equation. In order to integrate analytically rather than rely on tabulated data, we approximate $dh\,(T') = b_f\,dT'$ where b_f is evaluated at the mean film temperature $T_f = (T + T_{WB_a})/2$ where T is the initial spray temperature. Quantity b_f is tabulated in previous articles [1, 5] and is of order c_w. Over the cooling range of a drop, it may be assumed constant [1]. Thus

$$-c_w\,MdT_D'/dt = b_fKA(T_D' - T_{WB_a}) \tag{4}$$

Strictly speaking, the value of T_D' on the LHS of (4) refers to the droplet volume average while that on the RHS is the surface average. As shown by Berger and Taylor [10], there is little resulting difference in accounting for the associated internal thermal resistance of a drop.

Of particular interest is the final mass or volume average temperature of the spray. This can be analyzed most rigorously by integrating (4) over the spray trajectory and then computing the volume-average temperature for the drop size distribution. However, this approach does not lead to a convenient formulation of the dropwise parameters and is unnecessary since the sprays of interest tend to have relatively narrow distribution. Further, the time of flight of most drops can be approximated by the uniform free-flight value due to gravitational acceleration, g [15]

$$t_F = (2Z_1/g)^{1/2} + (2Z_2/g)^{1/2} \tag{5}$$

where Z_1 is rise height and Z_2 is fall height. Some sprays have nozzles elevated above the collecting water surface ($Z_2 \geq Z_1$). Free flight is approximated because of the small ratio of drag and gravity forces 3

Nomenclature

A = drop surface area
$b_f = dh\,(T)/dT$ at $T = T_f$
c_s = humid heat
c_w = specific heat of liquid water
D = diameter
f = interference allowance, drop distribution function
g = acceleration of gravity
h = total heat
H = sensible heat transfer coefficient
i = specific enthalpy
k_a = thermal conductivity of air
K = mass transfer coefficient
M = drop mass
NTU = number of transfer units
Nu = Nusselt number
Pr = Prandtl number of air
Re = relative Reynolds number
R_1 = spray radial throw at discharge height
SER = spray energy release
t = time
t_F = time of flight
T = local initial spray temperature
T' = local spray temperature
T_f = film temperature for properties
u = horizontal velocity
V = drop relative velocity
w = vertical velocity
Z_1 = spray rise height
Z_2 = spray fall height
ϵ = psychrometric ratio
η = efficiency
ν_a = kinematic viscosity of air
ρ = density
ω = specific humidity

Subscripts

a = air
C = cold water, canal
D = drop
g = saturated vapor
P = pond
s = spray
S = saturated, surface average
V = volume average
VS = Sauter mean
WB = wet bulb
∞ = ambient

$C_D \rho_a V^2/(2\rho_w Dg)$ where $C_D \approx 0.5$, the drag coefficient, ρ_a is air density, and $V \approx 5$ m/s is the relative drop velocity. The approximation certainly holds for the order-cm-diameter droplets of spray modules. Even in the case of the fine drops of fixed manifolded systems, equation (5) gives good results. For the Spraco No. 1751 nozzle operating at 0.48-atm gauge pressure ($Z_1 = 2.13$ m, $Z_2 = 3.66$ m [15]), the predicted $t_F = 1.52$ s. Chen and Trezek [11] accounted for drag and found a range in $t_F = 1.4$–1.6 s for drop size $D = 1$–6 mm in diameter. In the present experiments discussed in the next section, the Ceramic modules have $Z_1 \approx Z_2 = 5$ m with a predicted $t_F = 2.02$ s.

The above considerations allow a simpler approach where the volume integrated rate of energy change corresponding to the LHS of (4) can be calculated from the surface integrated flux on the RHS. Thus

$$-c_w \rho_w D_V{}^3 dT'/dt = 6b_f \int_0^\infty K(t,D) D^2 (T_D' - T_{WB_a}) f(D) dD \tag{6}$$

where the volume-average temperature

$$T' = D_V{}^{-3} \int_0^\infty T_D'(D) D^3 f(D) dD \tag{7}$$

where f is the normalized drop-diameter distribution function, the fraction of drops from D to $D + dD$. The volume-average drop size is

$$D_V{}^3 = \int_0^\infty D^3 f(D) dD \tag{8}$$

The RHS of (6) can be simplified by assuming that the mean-value of the surface temperature in the flux integral over all drops is equal to the volume-average temperature for all drops, a generalization of the negligible internal resistance concept. Thus (6) is

$$-c_w \rho_w D_V{}^3 dT'/dt = (T' - T_{WB_a})\, 6b_f \int_0^\infty K(t,D) D^2 f(D) dD \tag{9}$$

For the present case, (9) may be integrated from the initial temperature T ($t = 0$) to the final mixed spray temperature T_s ($t = t_F$). Assuming T_{WB_a} is constant at a mean value, the result is

$$(T_s - T_{WB_a})/(T - T_{WB_a}) = \exp(-\text{NTU}\ b_f/c_w) \tag{10}$$

where the number of transfer units

$$\text{NTU} = [6\, t_F/(\rho_w D_V{}^3)] \int_0^\infty D^2 \overline{K}(D) f(D) dD \tag{11}$$

where $\overline{K}$ is the integrated average over the trajectory from time $t = 0$ to t_F. However, the drop distribution functions are not always well known. It is convenient to invoke the mean-value theorem and represent $\overline{K}(D)$ as $\overline{K}(\overline{D})$ evaluated at some mean value. Approximating $\overline{D}$ as the Sauter-mean diameter defined below

$$\text{NTU} = 6\, t_F\, \overline{K}\, (D_{VS})/(\rho_w D_{VS}) \tag{12}$$

where the Sauter-mean diameter is defined

$$D_{VS} = D_V{}^3/D_S{}^2 \tag{13}$$

where

$$D_S{}^2 = \int_0^\infty f(D) D^2 dD \tag{14}$$

Quantity $\overline{K}$ is evaluated at diameter D_{VS} which is the characteristic diameter that gives the proper ratio between total volume and total surface area. In the case of the Spraco No. 1751 nozzle operated at 0.48-atm gauge pressure, Chen and Trezek [11] experimentally found $D_{VS} = 1.6$ mm, although their overall distribution function indicates 1.9 mm. This difference is likely within the accuracy of the photographic method employed. In the case of the Ceramic modules of the present experiments, the distribution function is not available in the open literature. Wilson [16] concluded the effective diameter was 2.21 cm based on observed performance and a numerical predictive analysis. Frediani and Smith [9] used a similar approach but did not report the resulting drop diameter. Guyer and Golay [17] estimated the average drop size as approximately 0.5 in. (1.25 cm) in diameter. We have found $D_{VS} = 1$–1.1 cm gives good agreement with experiments.

Following Chen and Trezek [3, 4, 11] and Yao and Shrock [12] we employ the Ranz-Marshall correlation for Nusselt number Nu rather than Sherwood number, for convenience of property evaluation. Thus

$$K_{VS} \epsilon c_s D_{VS}/k_a = \text{Nu} = 2 + 0.6\, \text{Pr}^{1/3} \text{Re}^{1/2} \tag{15}$$

where k_a is thermal conductivity and Pr is Prandtl number, of air. The relative Reynolds number Re is

$$\text{Re} = V\, D_{VS}/\nu_a \tag{16}$$

where ν_a is kinematic viscosity of air and, for cross flow of ambient wind

$$V^2 = u_D{}^2 + w_D{}^2 + u_\infty{}^2 \tag{17}$$

where u_D and w_D are horizontal and vertical drop velocities and u_∞ is the wind speed which for the present case was taken at the 2-m elevation.

The vertical velocity is estimated from the average of that of free flight over the spray rise and fall distances

$$w_D = [(2gZ_1)^{1/2}/2 + (2gZ_2)^{1/2}/2]/2 \tag{18}$$

while the horizontal drop velocity is taken constant at that of the nozzle discharge. From elementary trajectory analysis, the tangent of angle of the discharge to the vertical is $R_1/(4Z_1)$ where R_1 is spray radial throw at the discharge height. The initial vertical velocity is $(2gZ_1)^{1/2}$. Thus

$$u_D = (2gZ_1)^{1/2} R_1/(4Z_1) \tag{19}$$

Assuming free flight, the drop velocities are determined from observable spray dimensions. For the Spraco nozzle No. 1751 operating at 0.48-atm gauge pressure, $Z_1 = 2.1$ m, $Z_2 = 3.7$ m, and $R_1 = 4.1$ m [15]. For the Ceramic spray module, $Z_1 = Z_2 = 5$ m and $R_1 = 6$ m [1]. The resultant average drop velocity $(u_D{}^2 + w_D{}^2)^{1/2}$ for the Spraco nozzle is 8.08 m/s, and for the Ceramic module it is 10.3 m/s. The wind speed typically varied from 2–6 m/s in the spray-module experiments and 2–8 m/s in the spray-pond case.

Over the typical range of film temperature from 20–40°C, the following properties of air [18] may be assumed: $\epsilon = 0.89$, $k_a = 0.026$ W/m-°C, $\nu_a = 0.000016$ m^2/s, Pr = 0.71 and $c_s = 1000$ J/kg-°C. However tabulated [1, 5] b_f/c_w should be employed in applications of equation (10) because values vary substantially, from 0.78–1.84, over the range 20–40°C.

System Performance

From equation (10), the local efficiency of a spray or spray module is given by

$$\eta_s \equiv (T - T_s)/(T - T_{WB_a}) = 1 - \exp(-\text{NTU}\ b_f/c_w) \tag{20}$$

In a spray pond with all nozzles in parallel, the pond efficiency is

$$\eta_p \equiv (T_H - T_C)/(T_H - T_{WB_\infty}) = (1 - \bar{f})\, [1 - \exp(-\text{NTU}\ b_f/c_w)] \tag{21}$$

where $T = T_H$ is system hot water temperature and $T_s = T_C$ is average system cold water temperature. The interference allowance $\bar{f}$ relates average local and ambient wet-bulb temperatures [3, 5]

$$\bar{f} \equiv (\overline{T}_{WB_a} - T_{WB_\infty})/(T - T_{WB_\infty}) \tag{22}$$

The case of a spray canal can be analyzed by considering mixing of spray flow with canal flow, pass by pass [1]

$$dT/dN = -r\, (T - T_s) \tag{23}$$

where N is number of modules passed and r is ratio of module and canal flow rates. Using the efficiency of equation (20) and the inter-

Table 1 Summary of conditions of field experiments on Ceramic Cooling Tower Co. Powered Spray Modules

Exp.	Station	Type	Date	T_f (C)	Wind (m/s)	Wind (°)*	$\lvert\Delta\rho\rvert/\rho$	Z_B (m)
1	Dresden	Canal	3-17-75	11	3.0	86	0.09	2.4
			3-18-75	18	5.7	62	0.03	2.3
			8-20-75	32	2.8	48	0.06	2.1
			8-21-75	32	3.0	78	0.05	2.1
2	Dresden	Module	6-16-75	24	4.6	10	0.06	2.4
3	Quad-C.	Module	6-30-76	23	4.6	19	0.04	2.0
5a	Quad-C.	Module	9-29-76	20	2.4	81	0.04	2.0

* 90 deg wind angle is normal to canal.

ference allowance of equation (22), and integrating from the hot to the cold end, the resulting canal system efficiency is

$$\eta_C \equiv (T_H - T_C)/(T_H - T_{WB_\infty}) = 1 - \exp[-Nr\,(1 - \bar{f})\,(1 - \exp(-\text{NTU}\; b_f/c_w))] \quad (24)$$

Experimental NTU

As summarized in Table 1, both local spray-module experiments and overall spray-canal experiments were performed. In the former case, local wet-bulb temperature and both initial and final spray temperatures were sensed. In the latter case, canal temperatures at the ends of the run of modules were obtained. Determination of ambient conditions was similar in both cases. A complete tabulation of the data is available in reference [19]. In Table 1, the wind angle to the canal is indicated in degrees; quantity $|\Delta\rho|/\rho$ is the maximum possible fractional density difference of air and vapor when it comes in equilibrium with the spray, a measure of buoyancy effects [1]. Quantity Z_B is bank height over water level. The Dresden data refer to a 40-module two-row-across canal seqment while the Quad-Cities data are for a 176-module four-row segment. In both cases, the individual sprays are placed so that the spray patterns just touch each other at the water surface (Fig. 1). The Commonwealth Edison Company Dresden and Quad-Cities Nuclear Stations are located in northern Illinois.

Canal and spray water temperatures were detected by Atkins thermistor sounding probes and bridges. In experiment (1), the well-mixed canal water temperatures were monitored at the canal-segment intake and discharge ends. In module-NTU measurements (experiments (2–5)), canal water temperature was monitored locally at the test module or immediately upstream. A water collection device was designed and constructed to collect spray water at the end of the flight and measure a radially integrated spray temperature. The collector was a 1-m-dia funnel and floated about 15 cm out of the water when operating. A thermistor was positioned at the throat in a shielded perforated case in about 10 cm of spray water. Measurements were made approximately every 90 deg about the spray pattern proceeding from upwind rows as indicated by the solid dots in Fig. 1. When the collector was properly positioned via cables from shore, the thermistor bridge was switched from the canal temperature sensor to the spray-collector temperature sensor and held for several minutes to get a gust-averaged value. Canal water temperature was monitored below the surface. Experience has shown very little variation in canal temperature at a section.

Wet-bulb and dry-bulb temperatures were obtained from Atkins psychrometer modules and thermistor bridges. Wind run was determined from contact anemometers calibrated in the Illinois Institute of Technology 4 × 6 ft environmental wind tunnel to ±0.1 m/s. Wind direction was obtained with a bivane having a potentiometer element. Ambient meteorological conditions were measured sufficiently upwind to avoid interference and at a 2 m elevation over grade. Bridges and recorders were calibrated in the field using a calibrated decade-resistance substitution device. Recorded temperature data were accurate within ±0.1°C.

In canal-NTU tests, all meterological data were subsequently averaged over the time of flow of each slug corresponding to a hot-water temperature reading. The cold-water temperature was read from the continuous data allowing for time of flow. Canal flow was determined using a Weathermeasure helical propeller contact flow meter and a Heath digital electronic depth sounder (±0.3 m). The canal bottom and banks were defined in contour and velocity-sounded at three equally spaced points each in width and depth. Velocity was first averaged in width and then the vertical profile was integrated graphically allowing for a thin viscous sublayer at the bottom. Resultant canal flow rates agreed with manufacturer's lift-pump specifications to ±5 percent.

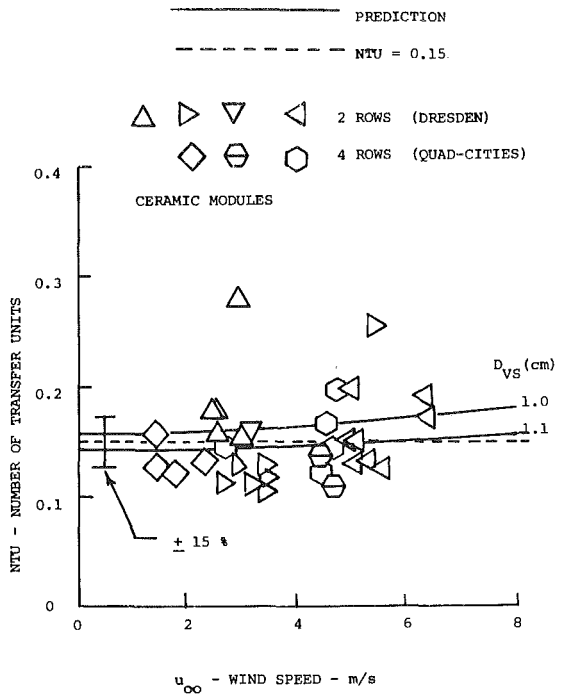

Fig. 2 Correlation of NTU with ambient wind speed at 2-m height

In the module-NTU tests, spray temperature and local wet-bulb temperature were sampled sufficiently long to allow averaging over gusts. Typically, several (three or four) cycles were obtained over a few minutes duration. Canal temperature and ambient conditions were then referred to the test interval. In obtaining average wind speed, wind run was summed over the period. The local wet-bulb temperatures were measured using a psychrometer mounted on the module motor, 2 m over the water level. These data, in terms of the interference allowance factor, were reported in a previous article [5]. It is important to note that the local wet-bulb temperature increases on passing windward through the spray field. Use of ambient rather than local wet-bulb temperatures will give erroneous NTU. In the Dresden-canal NTU tests, theoretical interference allowances were employed [1, 5]. Because the Dresden canal is only two rows wide, the interference effect is small for winds in essentially cross flow.

The NTU based on observed canal cooling performance of Ceramic modules are plotted versus ambient wind speed in Fig. 2. For the purpose of an error analysis of the accuracy of NTU, and for small NTU and $b_f/c_w \approx 1$, $\exp(-\text{NTU}\; b_f/c_w) \approx (1 - \text{NTU})$. Thus, from equation (20), NTU are proportional to the ratio of cooling range to the difference between canal-water and wet-bulb temperatures. A similar result occurs on expanding equation (24) for the relatively short canal segment at Dresden Station. Generally, the numerator of the ratio is accurate to 0.2°C of 1–3°C (7–20 percent) while the denominator is accurate to 0.2°C of about 10–30°C (1–2 percent), which combines to an error from 8–22 percent. Thus, the average experimental error for NTU is estimated within about ±15 percent (Fig. 2).

The experimental evidence points toward NTU of the present spray modules being primarily dominated by dropwise phenomena and independent of conditions when *local* wet-bulb temperature is employed. While there is a slight trend toward greater module NTU at

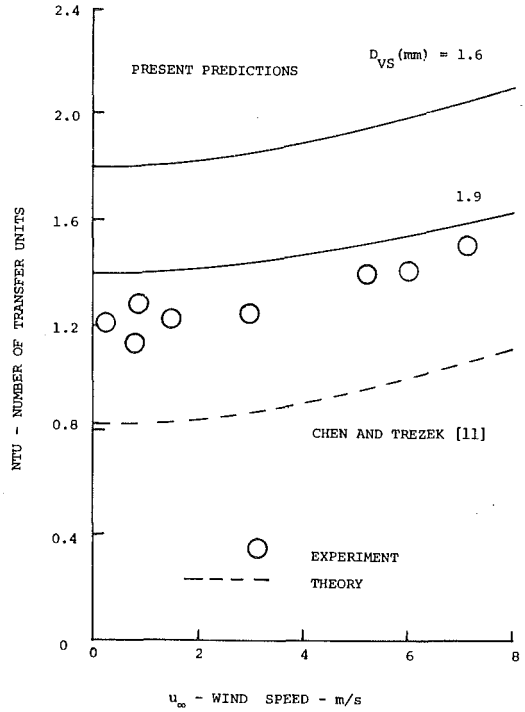

Fig. 3 Comparison of theory and experiment for Spraco No. 1751 nozzle

greater wind speed, the effect is not large. Indeed, NTU = 0.15 with wind speeds from 2–6 m/s with a standard deviation of 24 percent.

Comparison of Theory and Experiment

As noted previously, the drop distribution function for the modules of Ceramic Cooling Tower Company is not documented in the literature. For this reason, equation (11) could not be used for theoretically evaluating NTU. However, by estimating the Sauter-mean drop diameter as 1–1.1 cm in equation (12) we get good agreement with the experiments as shown in Fig. 2. The predictions also show a slight increase in NTU with wind speed as suggested by the experimental data.

The experimental data of Chen and Trezek [11] for the Spraco No. 1751 nozzle at 0.48-atm gauge pressure are shown in Fig. 3. Also shown are their predictions and the present ones (equation (12)), both using the Ranz-Marshall correlations. As noted, there is some contradiction in the Sauter-mean diameters experimentally determined by Chen and Trezek and implied in their drop distribution function. The value suggested by their overall drop distribution function (1.9 mm) appears to give better agreement than the direct experimental value (1.6 mm) which overpredicts transport. However, as noted in the Introduction, we expect the Ranz-Marshall correlations to overpredict transport in the present high Reynolds number range.

In both the spray-module and the spray-nozzle cases, it can be said that use of the Ranz-Marshall correlation with an appropriate Sauter-mean diameter gives good agreement with experiments. In the case of the Ceramic spray modules, the diameter is 1–1.1 cm while for the Spraco No. 1751 nozzle at 0.48-atm gauge pressure, it is 1.9 mm.

Conclusions

It is possible to represent the thermal performance of a spray nozzle or a spray module in terms of Number of Transfer Units (NTU). Predictions of NTU based on the Ranz-Marshall correlations are in good agreement with present experiments for the spray-module case and previous experiments for the spray-nozzle case. The greatest uncertainty is in the value of the Sauter-mean diameter and the requirement to extrapolate the Ranz-Marshall correlations substantially beyond their original Reynolds-number range. The Sauter-mean diameter, while difficult to predict, should be relatively uniform for a given spray unit over a wide range of spray-system configurations and ambient conditions. However, in order for the approach to be more meaningful, the Ranz-Marshall correlations should be extended to higher Reynolds numbers of drops in sprays. Alternatively, one may simply rely on the experimentally determined NTU values.

References

1 Porter, R. W., Yang, U. M., and Yanik, A., "Thermal Performance of Spray Cooling Systems," *Proceedings of the American Power Conference,* Vol. 38, 1976, pp. 1458–1472.

2 Schrock, V. E., Trezek, G. J., and Keilman, L. R., "Performance of a Spray Pond for Nuclear Power Plant Ultimate Heat Sink," ASME *Journal of Engineering for Power,* Vol. 99, No. 4, Oct. 1977, pp. 650–656.

3 Chen, K. H., and Trezek, G. J., "Spray Energy Release (SER) Approach to Analyzing Spray System Performance," *Proceedings of the American Power Conference,* Vol. 38, 1976, pp. 1435–1448.

4 Chen, K. H., and Trezek, G. J., "Thermal Performance Models and Drift Loss Predictions for a Spray Cooling System," ASME JOURNAL OF HEAT TRANSFER, Vol. 99, No. 2, May 1977, pp. 274–280.

5 Chaturvedi, S., and Porter, R. W., "Air-Vapor Dynamics in Large-Scale Atmospheric Spray Cooling Systems," ASME *Journal of Fluids Engineering,* Vol. 100, No. 1, Mar. 1978, pp. 65–72.

6 Porter, R. W., and Chen, K. H., "Heat and Mass Transfer of Spray Canals," ASME JOURNAL OF HEAT TRANSFER, Vol. 96, No. 3, Aug. 1974, pp. 286–291.

7 Elgawhary, A. M., and Rowe, A. M., "Spray Pond Mathematical Model for Cooling Fresh Water and Brine," *Environmental and Geophysical Heat Transfer,* ASME HT, Vol. 4, 1971.

8 Ranz, W. E., and Marshall, W. R., Jr., "Evaporation From Drops," *Chemical Engineering Progress,* Vol. 48, Feb. 1952, pp. 141–146 and 173–180.

9 Frediani, H. A. Jr., and Smith, N., "Mathematical Model for Spray Cooling Systems," ASME *Journal of Engineering for Power,* Vol. 98, No. 2, Apr. 1977, pp. 279–283.

10 Berger, M. H., and Taylor, R. E., "An Atmospheric Spray Cooling Model," *Environmental Effects of Atmospheric Heat/Moisture Releases,* ASME, 1978, pp. 59–64.

11 Chen, K. H., and Trezek, G. J., "The Effect of Heat Transfer Coefficient, Local Wet Bulb Temperature and Droplet Size Distribution Function on the Thermal Performance of Sprays," ASME JOURNAL OF HEAT TRANSFER, Vol. 99, No. 3, Aug. 1977, pp. 381–385.

12 Yao, S. C., and Schrock, V. E., "Heat and Mass Transfer from Freely Falling Drops," ASME JOURNAL OF HEAT TRANSFER, Vol. 98, No. 1, Feb. 1976, pp. 120–126.

13 Dunn, W. E., "Heat, Mass and Momentum Transfer in Multidrop Systems," Dissertation in Mechanical and Industrial Engineering, University of Illinois, Urbana, 1977.

14 Jain, M., "Heat, Mass and Momentum Transfer Through Sprays," Dissertation in Mechanical and Aerospace Engineering, Illinois Institute of Technology, Chicago, Dec. 1979.

15 Hebden, W. E., and Shah, A. M., "Effects of Nozzle Performance on Spray Ponds," *Proceedings of the American Power Conference,* Vol. 38, 1976, pp. 1449–1457.

16 Wilson, D. E., "Thermal Performance of Powered Spray Modules," M. S. Thesis in Mechanical and Industrial Engineering, University of Illinois, Urbana, 1972.

17 Guyer, E. C., and Golay, M. W., "A Model for Salt Drift Deposition from Spray Ponds," *Environmental Effects of Cooling Systems at Nuclear Power Plants,* International Atomic Energy Agency, IAEA-SM-187/37, Vienna, 1975, pp. 331–345.

18 Threlkeld, J. L., *Thermal Environmental Engineering,* Prentice-Hall, Englewood Cliffs, NJ, 1970.

19 Yang, U. M., and Porter, R. W., "Thermal Performance of Spray Cooling Systems—Theoretical and Experimental Aspects," IIT Waste Energy Management Technical Report TR-76-1, Illinois Institute of Technology, Chicago, Dec. 1976.

Enhancement of Natural Convection Heat Transfer by a Staggered Array of Discrete Vertical Plates

E. M. Sparrow
Fellow ASME

C. Prakash
Department of Mechanical Engineering,
University of Minnesota,
Minneapolis, Minn. 55455

An analysis has been performed to determine whether, in natural convection, a staggered array of discrete vertical plates yields enhanced heat transfer compared with an array of continuous parallel vertical plates having the same surface area. The heat transfer results were obtained by numerically solving the equations of mass, momentum, and energy for the two types of configurations. It was found that the use of discrete plates gives rise to heat transfer enhancement when the parameter $(D_h/H)Ra > \sim 2 \times 10^3$ *(D_h = hydraulic diameter of flow passage, H = overall system height). The extent of the enhancement is increased by use of numerous shorter plates, by larger transverse interplate spacing, and by relatively short system heights. For the parameter ranges investigated, the maximum heat transfer enhancement, relative to the parallel plate case, was a factor of two. The general degree of enhancement compares favorably with that which has been obtained in forced convection systems.*

Introduction

The use of enhancement techniques is a commonly accepted design principle for forced convection heat transfer devices. Such techniques may involve boundary layer trips, surface interruptions, roughness elements of various forms, corrugations, twisted tapes, spiral grooves, etc. In general, the heat transfer enhancement is accomplished by the modification of the pattern of fluid flow, so that the increased heat transfer capability is generally accompanied by a penalty in pressure drop and/or pumping power. A rational basis for assessing the benefits of the enhancement, taking account of pressure drop and pumping power considerations, has recently been developed [1–3].

It is noteworthy that in the extensive literature on heat transfer enhancement, there is very little work on natural convection (i.e., a few papers on roughness effects and a single experimental study of discrete plates). The paucity of natural convection enhancement studies is remarkable in that a great many heat transfer devices involve natural convection cooling or heating, for instance, the cooling of electronic equipment. From practical considerations, there is a clear motivation to examine the efficacy of enhancement techniques for natural convection. The present research is a study of natural convection enhancement, using analysis and numerical techniques as the investigatory tools.

When contemplating the use of enhancement techniques in natural convection, it is useful to contrast the response of an enhanced natural convection system with that of an enhanced forced convection system. Suppose, in a forced convection situation, that the enhanced system provides higher heat transfer coefficients than a reference (unenhanced) system operated at the same flow rate, but at the price of higher pressure drop and pumping power. If it is desired to maintain the same pumping power in the two systems, the mass flow through the enhanced system may be reduced until pumping power equality is achieved. The decrease in flow rate will also decrease the heat transfer coefficient of the enhanced system, but under favorable conditions it might still be higher than that of the reference system. In such an instance, the enhancement technique would be regarded as being successful in that it provides higher heat transfer coefficients than a reference system operating at the same pumping power (but at a different mass flow).

The point of the foregoing discussion is that in those forced convection systems where the flow rate can be varied independently, trade-offs can be made between the magnitude of the heat transfer coefficient and the magnitude of the pumping power (or pressure drop). This capability greatly enlarges the possibilities of attaining a desired design goal subject to given constraints.

In a natural convection situation, the rate of fluid flow through a system cannot be independently controlled. Rather, the flow rate is established by a dynamic balance between the buoyancy and the friction forces. Thus, in an enhanced natural convection system, the flow rate cannot be independently adjusted to achieve some desired relationship with an unenhanced system. Rather, the system adjusts itself in accordance with whatever changes have occurred in buoyancy and friction as a result of the implementation of the augmentation technique.

The absence of independent control of the flow rate in natural convection removes some of the flexibilities which may enable the fulfillment of performance goals in forced convection. On the other hand, the concerns about pumping power and pressure drop that are inherent in forced convection are irrelevant in natural convection because no pump or blower is needed. Therefore, the evaluation of an enhancement technique in natural convection may be based on heat transfer performance, without concern about fluid flow issues.

Thus, although there are fewer design options in natural convection enhancement than in forced convection enhancement, the design goals and constraints are also fewer and simpler.

The foregoing discussion is intended to form a bridge between the well-developed methodology of forced convection enhancement and the still to be developed methodology for natural convection. Attention will now be turned to the specifics of the present research.

The enhancement technique to be investigated here is the use of an array of discrete-plate segments as the heat transfer surface in lieu of a continuous uninterrupted surface. A motivation for the investigation of the natural convection characteristics of discrete-plate arrays is their widespread use in forced convection heat transfer devices. A diagram of the contemplated discrete-plate heat transfer array is shown in the left-hand portion of Fig. 1. As seen here, the heat exchanger consists of an assembly of vertical columns of plate segments. In each column, the successive plates, each of length L, are separated by a gap equal to the plate length. The spacing between adjacent columns is s, and the plates in adjacent columns are offset vertically by a plate length. Because of this offset, the entire assembly may properly be termed a staggered array.

The relationship between such a discrete-plate array and an array of continuous vertical plates of equal surface area can readily be established with the aid of the right-hand diagram of Fig. 1. That diagram shows a representative subset of the discrete-plate array. Suppose, as indicated by the arrows in the diagram, that the plates of the second and fourth columns are shifted leftward into the re-

Contributed by the Heat Transfer Division for publication in the JOURNAL OF HEAT TRANSFER. Manuscript received by the Heat Transfer Division October 4, 1979.

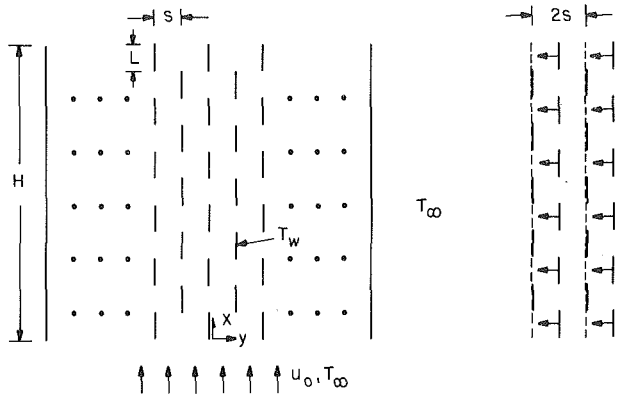

Fig. 1 Discrete-plate array (left-hand diagram). Relation between discrete-plate and parallel plate arrays of equal surface area (right-hand diagram)

spective gaps in the first and third columns. The consequence of this shifting is that the first and third columns have become continuous vertical plates with an interplate spacing of $2s$.

If such a shifting were envisioned as being performed throughout the entire discrete-plate array, the result would be an array of vertical, parallel plate channels of spacing $2s$. The original discrete-plate array (transverse spacing s) and its counterpart parallel plate array (transverse spacing $2s$) have the same heat transfer surface area. All of the comparisons made here between discrete-plate and continuous-plate systems will be for identical heat transfer surface areas—this being a condition commonly employed in the literature on enhancement.

The motivation to consider a discrete-plate array in lieu of a continuous-plate array comes from prior experience with heat transfer in boundary layer flows and developing duct flows. In those cases, it is well established that the highest heat transfer coefficients correspond to thin thermal boundary layers. When the boundary layer thickens or when a duct flow becomes thermally developed, the coefficients are relatively low. Therefore, it is logical to seek a configuration in which thermal development is not permitted to proceed too far.

This objective is fulfilled by the discrete-plate array of Fig. 1. The relatively short plate length (compared with a parallel plate channel) does not permit extensive boundary development, and the gap downstream of each plate enables a degree of homogenization of the velocity and temperature fields to be attained before the next plate is encountered. At the leading edge of each plate, new boundary layers are initiated.

Clearly, the use of discrete plate segments offers the potential for the enhancement of heat transfer. However, for the same reasons, the skin friction may increase and, since natural convection is self regulating, the flow rate may decrease, tending to reduce the heat transfer.

The foregoing discussion serves to clarify the foci of the present research. One focus is to identify the conditions under which a discrete-plate array provides heat transfer enhancement. The other objective is to determine the quantitative extent of the enhancement for conditions under which enhancement occurs.

To fulfill these objectives, numerical solutions of the coupled conservation equations for mass, momentum, and energy were carried out, both for the discrete-plate array and the parallel plate array. For the discrete-plate problem, the solutions depend on two parameters which, when reduced to simplest terms, can be expressed as the number of plates N in a subchannel formed by two adjacent columns and the product of Rayleigh number and s/H. The solutions encompassed N values from 5 to 100 and a sufficiently wide range of the second parameter to encompass both enhanced and unenhanced situations. The solutions for the paralell plate channel depend only on the second parameter. For both cases, the Prandtl number was fixed at 0.7 with air in mind. The thermal boundary condition for both cases was uniform wall temperature.

A survey of the archival literature did not reveal any prior analytical work on discrete-plate arrays in natural convection. With regard to related analytical work, numerous studies of natural convection in a parallel plate channel have been published, and [4–8] are representative of the literature of the past two decades. The only prior study known to the authors on natural convection in a discrete-plate array are the experiments reported in [9]. These experiments were limited in scope in that only a single plate number $N = 3$ was employed. Also, owing to the thermal boundary condition of the experiments (uniform heat flux), the average heat transfer coefficient was based on a local temperature difference which introduces an uncertainty in the comparison between discrete-plate and parallel plate results. The experimental results indicated that the use of discrete plates can provide enhanced heat transfer.

Analysis

Physical Model. The physical model, which was discussed earlier in general terms, will now be described in greater detail in order to facilitate the analytical formulation. The flow and heat transfer processes are envisioned as being two-dimensional, so that the velocity and temperature variables depend only on the x and y coordinates pictured in the left-hand diagram of Fig. 1. Furthermore, each subchannel defined by two adjacent columns of plates is thermally and hydrodynamically identical to any other subchannel. As a consequence, the analysis need only consider a single subchannel.

As shown in the figure, the array is bounded on each of its lateral extremities by a vertical wall of height H. These walls isolate the fluid within the array from any *lateral* pressure communication with the fluid outside the array. The lateral extent of the array is sufficiently large so that hydrodynamic and thermal perturbations due to the presence of the vertical bounding walls do not affect the array proper.

The function of the vertical bounding walls is to create a pressure difference to induce a vertical upward flow through the array when the plates are at a uniform temperature T_w that exceeds the ambient temperature T_∞. The hydrostatic pressure variation in the ambient

Nomenclature

c_p = specific heat
D_h = hydraulic diameter, $4s$
Gr = Grashof number, $g\beta(T_w - T_\infty)D_h^3/\nu^2$
g = acceleration of gravity
H = overall height of array, Fig. 1
$\hat{H}$ = dimensionless height, $(H/D_h)/\mathrm{Gr}$
L = plate length, Fig. 1
$\hat{L}$ = dimensionless plate length, $(L/D_h)/\mathrm{Gr}$
N = number of plates lining a subchannel
$P(X)$ = dimensionless difference pressure at X, equation (2b)
$P_{\max}$ = maximum value of P
Pr = Prandtl number
p = pressure in array at x
p_∞ = pressure external to array at x
p' = difference pressure at x, $p - p_\infty$
$Q(x)$ = surface-integrated heat transfer between $x = 0$ and $x = x$
$\hat{Q}(X)$ = dimensionless heat transfer, equation (8)
$\hat{Q}$ = value of $\hat{Q}(X)$ at $X = \hat{H}$ for discrete-plate array
$\hat{Q}_*$ = value of $\hat{Q}(X)$ at $X = \hat{H}$ for parallel plates
Ra = Rayleigh number, GrPr
s = transverse spacing across a subchannel, Fig. 1
T = temperature
T_w = wall temperature
T_∞ = ambient temperature
U, V = dimensionless velocities, equation (2b)
U_0 = dimensionless inlet velocity, $(u_0 D_h/\nu)/\mathrm{Gr}$
u, v = velocity components
u_0 = inlet velocity
X, Y = dimensionless coordinates, equation (2a)
x, y = coordinates, Fig. 1
θ = dimensionless temperature, $(T - T_\infty)/(T_w - T_\infty)$
ν = kinematic viscosity
ρ = density
ρ_∞ = density of ambient fluid

fluid imposes a pressure decrease between the inlet and exit planes of the array which is equal to $\rho_\infty gH$. If the plates were also at temperature T_∞, the imposed pressure difference would be precisely in balance with the hydrostatic pressure decrease of the fluid within the array, and there would be no motion.

If, however, $T_w > T_\infty$, the hydrostatic pressure decrease in the array is less than $\rho_\infty gH$, and motion ensues due to the pressure imbalance. In the steady state, the flow rate through the array adjusts itself so that the sum of all flow-related pressure drops equals the imbalance between the internal and external hydrostatic pressure differences. This results in an overall balance of pressure such that the pressure drop between the inlet and exit planes of the array is equal to the externally imposed hydrostatic pressure difference. This model is entirely consistent with that employed in [4–8] for the analysis of the vertical parallel plate channel.

As noted earlier, the plates are assumed to be isothermal at temperature T_w. For concreteness, they may be thought of as fins (efficiency ~ 1) which span the space between isothermal walls positioned parallel to the plane of Fig. 1. In view of the relatively low heat transfer coefficients that are characteristic of natural convection flows, a fin efficiency $\sim$1 is not unreasonable. The plate thickness is taken to be sufficiently small so as not to induce a leading-edge separation bubble or a trailing-edge wake. These phenomena involve fluid recirculation, and to take them into account in a multiplate system must await the next generation of computers.

Mathematical Formulation. The first step in the analysis is to derive the buoyancy and pressure forces that drive the flow, beginning with the terms $(-dp/dx - \rho g)$ that appear in the x-momentum equation. In this connection, it is convenient to introduce a reduced pressure $p'(x)$ which is the difference between pressures $p(x)$ and $p_\infty(x)$ at x, respectively internal and external to the array; furthermore, $p_\infty(x) = p_0 - \rho_\infty gx$. With these inputs, there follows

$$-dp/dx - \rho g = -dp'/dx + g(\rho_\infty - \rho) = -dp'/dx + g\beta\rho(T - T_\infty) \tag{1}$$

where the Boussinesq equation of state has been employed in deriving the last term. The difference pressure p' appearing in equation (1) is zero both at the inlet and outlet cross sections of the array. Equation (1) will be employed in conjunction with the x-momentum equation.

Before stating the governing equations, it is appropriate to introduce dimensionless variables. For the characteristic dimension, use will be made of the hydraulic diameter D_h defined by Kays and London [10] for the complex flow passages of compact heat exchangers. That definition gives D_h as four times the product of the free flow area and the streamwise flow length divided by the heat transfer surface area. The evaluation of this definition for the staggered array depicted in the left-hand diagram of Fig. 1 gives $D_h = 4s$.

Dimensionless variables are then introduced as

$$X = (x/D_h)/\mathrm{Gr},\ Y = y/D_h,\ \theta = (T - T_\infty)/(T_w - T_\infty) \tag{2a}$$

$$U = (uD_h/\nu)/\mathrm{Gr},\ V = vD_h/\nu,\ P = p'(D_h{}^2/\rho\nu^2\mathrm{Gr}^2) \tag{2b}$$

where

$$\mathrm{Gr} = g\beta(T_w - T_\infty)D_h{}^3/\nu^2 \tag{2c}$$

With these and with equation (1), the equations of mass, momentum, and energy conservation become

$$\partial U/\partial X + \partial V/\partial Y = 0 \tag{3}$$

$$U(\partial U/\partial X) + V(\partial U/\partial Y) = -dP/dX + \theta + \partial^2 U/\partial Y^2 \tag{4}$$

$$U(\partial\theta/\partial X) + V(\partial\theta/\partial Y) = (1/\mathrm{Pr})\partial^2\theta/\partial Y^2 \tag{5}$$

The boundary conditions are as follows

$$U = V = 0,\ \theta = 1 \text{ on all solid surfaces} \tag{6a}$$

$$\partial U/\partial Y = \partial\theta/\partial Y = V = 0 \text{ on all symmetry lines} \tag{6b}$$

$$\theta = 0 \text{ at } X = 0 \tag{6c}$$

$$P = 0 \text{ at } X = 0 \text{ and at } X = (H/D_h)/\mathrm{Gr} \equiv \hat{H} \tag{6d}$$

It may be noted that the pressure is overspecified in that there are two boundary conditions for a variable for which only a first derivative appears in the governing equations. On the other hand, the presence of $\partial U/\partial X$ in the governing equations requires that $U \equiv U_0$ be specified at $X = 0$; however, as can be seen from equations (6), U is *a priori* unknown at that station. Fortunately, the extra boundary condition on P enables U_0 to be determined.

Examination of the foregoing equations and boundary conditions reveals the presence of two parameters: Pr and $\hat{H} = (H/D_h)/\mathrm{Gr}$. There is an additional parameter which may be specified either as the number of plates N which line a subchannel or the dimensionless plate length $\hat{L} = (L/D_h)/\mathrm{Gr}$. As will be demonstrated shortly, it is advantageous to employ one set of parameters to facilitate the numerical solutions whereas a different set of parameters is more appropriate for the reporting of the results.

Solution Methodology. The solution method to be employed here is a marching procedure, beginning at $X = 0$ and proceeding upward along the subchannel with increasing X. Such a procedure requires that the velocity, pressure, and temperature fields be given as input data at $X = 0$. The temperature and pressure are specified by equations (6*c*) and (6*d*). The velocity, which is actually an unknown, can be treated as a computational parameter. That is, a value of the dimensionless inlet-section velocity U_0 is given and the corresponding solution run on the computer. Once this solution is obtained, it is examined to see if it yields a value of $\hat{H}$ in the desired range. If not, another U_0 value is selected and the procedure repeated.

Another feature of the marching procedure is that the dimensionless plate length $\hat{L}$ has to be specified (rather than the number of plates N). Thus, a given computer run requires input values of U_0 and $\hat{L}$, as well as the value of the Prandtl number which was fixed at 0.7 (air) for all cases.

As the marching procedure propels the solution from $X = 0$ toward larger X, the dimensionless difference pressure P decreases from its initial value of zero, attains a minimum, and then increases towards zero. The value of P is monitored, and when $P = 0$ is encountered the solution is terminated. The X value where $P = 0$ is taken to be equal to $\hat{H}$, since, according to equation (6*d*), $X = \hat{H}$ when $P = 0$.

Also, during the marching, the accumulated heat transfer Q between $X = 0$ and $X = X$ is evaluated from

$$Q(X) = \int_0^s \rho u c_p(T - T_\infty)dy \tag{7}$$

or, in dimensionless terms,

$$\hat{Q}(X) = Q(X)/k(T_w - T_\infty)\mathrm{PrGr} = \int_0^{1/4} U\theta dY \tag{8}$$

The value of $\hat{Q}$ at $X = \hat{H}$ is the overall rate of heat transfer from one subchannel to the fluid.

At the completion of each computer run, the values of $\hat{H}$ and $\hat{Q}(\hat{H})$ are recorded along with the input values of U_0 and $\hat{L}$.

The actual numerical computations were performed by employing the Patankar-Spalding method [11]. This is a fully implicit finite difference scheme that is so well documented in the literature as not to require further elaboration here. An extensive step size study was undertaken to identify the values of ΔX and ΔY that would yield solutions of high accuracy. Depending on the parameters, 250 to 400 grid points were used to span the transverse distance between $Y = 0$ and $Y = 1/4$, while the number of axial steps ranged from about 1000 to 2000.

Parallel Plate Channel. For comparison purposes, computer runs were also performed for the parallel plate channel. As noted earlier, a discrete-plate array with transverse interplate spacing s has the same heat transfer surface area as an array of parallel plate channels with spacing $2s$. Since subsequent comparisons between the two arrays are to be made for equal surface area, the parallel plate solutions performed here correspond to an interplate spacing of $2s$. The hydraulic diameter for this case, whether evaluated from the

conventional definition or from the Kays-London definition, is $4s$, which is identical to the hydraulic diameter for the discrete-plate array.

The dimensionless variables and parameters of equations (2*a*)–(2*c*) were also used for the parallel plate channel, and the governing differential equations are identical to equations (3–5). If note is taken of the symmetry which exists about the centerline of each channel, then the boundary conditions may be written as

$$U = 0, \theta = 1 \text{ at } Y = 0 \tag{9a}$$

$$\partial U/\partial Y = \partial\theta/\partial Y = V = 0 \text{ at } Y = 1/4 \tag{9b}$$

while equations (6*c*) and (6*d*) apply as before. The accumulated heat transfer from one plate of a channel over the length $X = 0$ to $X = X$ is given by equations (7) and (8). The heat transfer computed in this way is appropriate for subsequent comparisons since the surface area of one face of a parallel plate is equal to the area of the walls bounding a subchannel in the discrete-plate array.

The solutions for the parallel plate channel were carried out by employing an approach identical to that described for the discrete-plate array, the one difference being that only U_0 (rather than U_0 and $\hat{L}$) need be prescribed along with Pr. Each solution yields values of the channel height $\hat{H}$ and the heat transfer $\hat{Q}(\hat{H})$ corresponding to the given value of U_0.

Results and Discussion

As discussed in the Introduction, the main focus of the research is to compare the performance of a discrete-plate array with that of a parallel plate array having the same heat transfer surface area. Performance-related information will, therefore, receive top billing in the presentation of results. This will be followed by results for the mass flow and for the axial distributions of the heat transfer and pressure drop.

Heat Transfer Performance. There are a variety of performance comparisons that can be made between competing heat exchange systems, depending on the goals to be achieved and the constraints that are imposed. As was pointed out earlier, goals and/or constraints related to pressure drop and pumping power are not relevant to natural convection systems since the rate of fluid flow cannot be independently controlled. Therefore, in such systems, thermal and geometrical quantities comprise the goals and constraints.

In the present instance, the heat transfer rates for the discrete-plate and parallel plate systems will be compared to determine which yields the higher value under the conditions that the following quantities be the same in the two systems:

1 overall height, H
2 heat transfer surface area
3 temperature difference, $T_w - T_\infty$
4 thermophysical properties

On a dimensionless basis, the foregoing performance goal and constraints take the form of a comparison of $\hat{Q}(\hat{H})$ values for the two systems when $\hat{H} = (H/D_h)/\text{Gr}$ and Pr are the same for each system.[1] For compactness, let $\hat{Q}(\hat{H}) \equiv \hat{Q}$ for the discrete-plate array and $\hat{Q}(\hat{H}) \equiv \hat{Q}_*$ for the parallel plate array. From the computer solutions discussed in the preceding part of the paper, values of $\hat{Q}$ and $\hat{Q}_*$ can be obtained at the same $\hat{H}$ (and for Pr = 0.7) in a manner to be described shortly. Then, the ratio $\hat{Q}/\hat{Q}_*$ can be plotted as a function of $\hat{H}$ in order to determine whether or not there is a range of $\hat{H}$ where $\hat{Q}/\hat{Q}_* > 1$. In that range, the discrete-plate array is superior to the parallel plate array in heat transfer performance.

Although $\hat{H} = (H/D_h)/\text{Gr}$ is a satisfactory variable against which to plot the results, it is not the conventional variable. Therefore, to fit more closely with convention, the variable

$$(D_h/H)\text{Ra} = \text{Pr}/\hat{H} \tag{10}$$

will be employed, where Ra = GrPr.

[1] Here and in what follows, it will be assumed that the geometrical relationship between the two systems is as shown in the right-hand diagram of Fig. 1.

Another point to be noted is that the $\hat{Q}$ values for the discrete-plate array depend not only on $\hat{H}$ but also are a function of the number of plates N per subchannel (or, alternatively, of the dimensionless plate length $\hat{L}$). Thus, to explore the relative heat transfer capabilities of discrete-plate and parallel plate arrays, $\hat{Q}/\hat{Q}_*$ will be plotted as a function of $(D_h/H)\text{Ra}$ for parametric values of N.

The method used to construct the aforementioned plot by employing the numerical solutions of the preceding part of the paper will now be briefly described. For the parallel plate channel, the solutions yield a curve of $\hat{Q}_*$ versus $(D_h/H)\text{Ra}$ as represented by the solid line in Fig. 2. For the discrete-plate array, $\hat{Q}$ versus $(D_h/H)\text{Ra}$ curves were obtained for fixed values of the dimensionless plate length $\hat{L}$ equal to 5×10^{-5}, 10^{-5}, 5×10^{-6}, 2.5×10^{-6}, 10^{-6}, 5×10^{-7}, 10^{-7}, and 5×10^{-8}. Each of these curves was plotted on a separate logarithmic graph with as large a scale as possible to permit subsequent accurate reading. Three of these curves are shown in Fig. 2 for illustrative purposes. It might be noted that if an average Nusselt number were to be defined as $(Q/H\Delta T)H/k$, then $\hat{Q} = \text{Nu}/\text{Ra}$ and similarly for $\hat{Q}_*$.

In Fig. 2, it may be observed that the curves extend over different ranges of the abscissa. This follows from the fact that $\hat{H} = N\hat{L}$ and, for preselected values for N, the values of $\hat{H}$ will be smaller when $\hat{L}$ is smaller. Since the abscissa variable $\sim 1/\hat{H}$, smaller $\hat{L}$ will yield larger abscissa values, as can be seen from the figure. Figure 2 provides a preview of what is to come because it shows that $\hat{Q} > \hat{Q}_*$ for a substantial range of the abscissa ($>2 - 3 \times 10^3$) and that shorter plates generally yield larger values of $\hat{Q}$.

Suppose now that attention is focused on a specific number of plates N. For that N, the value of $(D_h/H)\text{Ra}$ for each $\hat{L}$ follows as

$$(D_h/H)\text{Ra} = \text{Pr}/N\hat{L} \tag{11}$$

and the corresponding $\hat{Q}$ values can be read from the aforementioned large-scale graphs. Also, the $\hat{Q}_*$ value corresponding to each $(D_h/H)\text{Ra}$ value can be read from Fig. 2. Then, the ratio of $\hat{Q}/\hat{Q}_*$ can be evaluated at each $(D_h/H)\text{Ra}$. These operations are repeated for other values of N.

The results of these calculations yield the heat transfer performance comparisons shown in Fig. 3. In this figure, $\hat{Q}/\hat{Q}_*$ is plotted against $(D_h/H)\text{Ra}$ for parametric values of the number of plates N. In appraising the figure, it should be noted that $\hat{Q}/\hat{Q}_* > 1$ signals the fact that a discrete-plate array yields better heat transfer performance than does a parallel plate array having the same surface area.

Inspection of the figure indicates that over a wide range of the abscissa variable, the use of discrete plates leads to a substantial heat transfer enhancement. The extent of the enhancement is accentuated with increasing numbers of plates and at large values of $(D_h/H)\text{Ra}$. An increase of N at a fixed value of $(D_h/H)\text{Ra}$ implies shorter plates, while an increase of $(D_h/H)\text{Ra}$ at fixed H and fixed number of plates implies a larger transverse spacing s. Thus, heat transfer enhancement

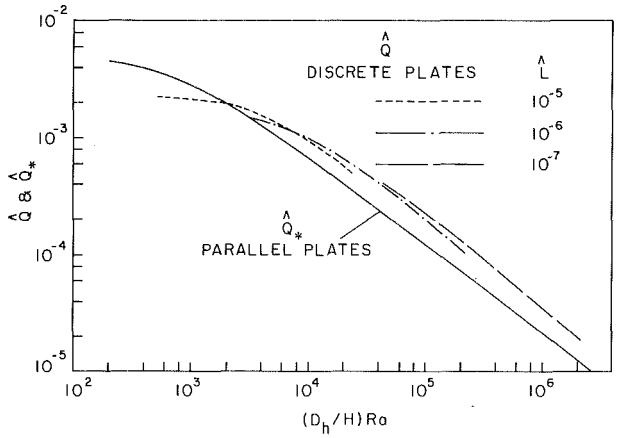

Fig. 2 Overall heat transfer results for discrete-plate and parallel plate arrays

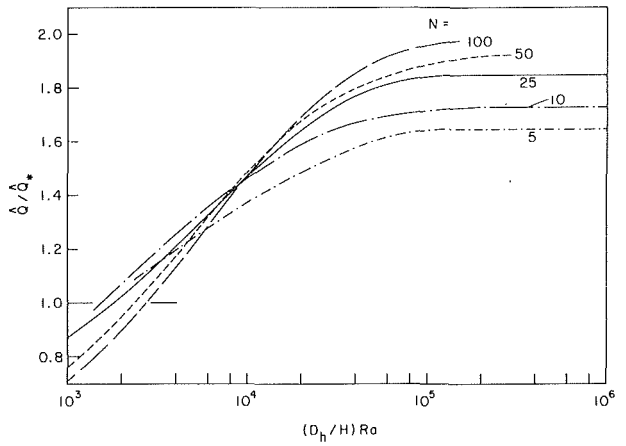

Fig. 3 Comparison of heat transfer performance of discrete-plate and parallel plate arrays

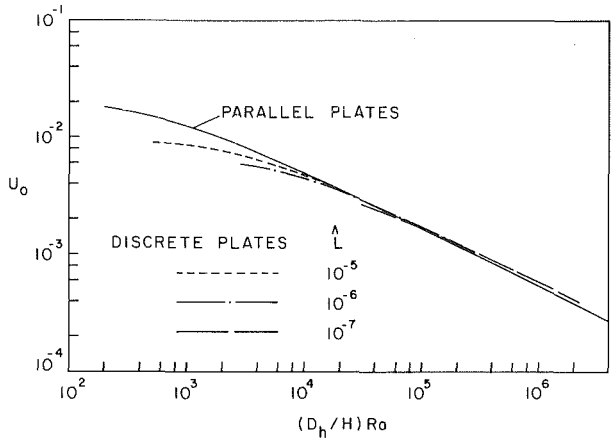

Fig. 4 Inlet velocity results for discrete-plate and parallel plate arrays

is favored by shorter, more numerous plates with relatively large transverse spacing.

An increase in $(D_h/H)\mathrm{Ra}$ at fixed D_h (i.e., fixed s) implies smaller values of the overall height H. Enhancement is, therefore, greater when H is small. This finding is consistent with the fact that the fluid experiences an increasing amount of thermal saturation as it passes upward through the array. When the array is tall, the relatively small temperature differences in the upper reaches of the array result in correspondingly small heat transfer rates, but the frictional resistance in that part of the array is unabated. Under these conditions, the successive boundary layer restartings of the discrete-plate array are not effective in enhancing heat transfer.

For the ranges of N and $(D_h/H)\mathrm{Ra}$ investigated here, the maximum heat transfer enhancement is about a factor of two. Generally, the degree of enhancement in evidence in Fig. 3 compares favorably with that which has been accomplished in forced convection systems. The region of enhancement is defined by

$$(D_h/H)\mathrm{Ra} > 2 \times 10^3 \tag{12}$$

For operating conditions which yield lower values of this parameter, the use of discrete plates rather than continuous plates leads to a decrease in the heat transfer rate.

To provide perspective for the aforementioned threshold value of $(D_h/H)\mathrm{Ra}$, consider the illustrative conditions $s = 0.635$ cm (¼ in.), $H = 30.5$ cm (1 ft), $(T_w - T_\infty) = 55.6°\mathrm{C}$ (100°F), $T_\infty = 21°\mathrm{C}$ (70°F), $p = 1$ atm. For these values, $(D_h/H)\mathrm{Ra} = 7 \times 10^3$, for which $\hat{Q}/\hat{Q}_* = 1.3 - 1.4$.

Mass Flow; Axial Distributions of $\hat{Q}$ and P. An indication of the rate of flow through the array is given by the magnitude of U_0, the dimensionless velocity at the channel inlet. A comparison between the U_0 values for the parallel plate channel and those for several representative discrete-plate arrays is presented in Fig. 4. The figure shows that for small and intermediate values of $(D_h/H)\mathrm{Ra}$, the rate of flow through a discrete-plate array is smaller than that through a parallel plate array, whereas the reverse relationship is in evidence at larger $(D_h/H)\mathrm{Ra}$. Thus, the failure of the discrete-plate array to enhance heat transfer at smaller $(D_h/H)\mathrm{Ra}$ is due to the decrease in mass flow relative to that for the parallel plate channel. The disappearance of this mass flow deficit at larger values of $(D_h/H)\mathrm{Ra}$ is an important factor in the enhancement evidenced in Fig. 3.

The results presented thus far have been focused on the overall performance of the system. Attention will now be turned to an exposition of representative local results. Specific consideration will be given to the axial distributions of the surface-integrated heat transfer Q and of the difference pressure P.

Figure 5 was prepared to illustrate how the distribution of the surface-integrated heat transfer is affected by the number of plates when everything else (i.e., H, D_h, ΔT, fluid properties) is held fixed. In this figure, the ordinate is the ratio of the heat transfer between $x = 0$ and $x = x$ to that transferred between $x = 0$ and $x = H$. This ratio is plotted as a function of the distance along the array, measured in the upward direction from the inlet cross section.

The three curves shown in the figure correspond respectively to parallel plates and to discrete-plate arrays with $N = 10$ and 101. For all three cases, $(D_h/H)\mathrm{Ra} \simeq 6.95 \times 10^4$. Although all curves are normalized to unity at $x = H$, the actual values of $\hat{Q}(H)$ are quite different: respectively, 1.57×10^{-4}, 2.66×10^{-4}, and 2.99×10^{-4} for the parallel plates and for the $N = 10$ and 101 discrete-plate arrays.

Perhaps the most interesting feature of Fig. 5 is the wavy curve representing the $N = 10$ case. This waviness is due to the variation of the heat transfer rate along the individual plates. The heat transfer is seen to be highest at the leading edge of each plate and to decrease along the plate; then, the next plate is encountered and the pattern is repeated. The waviness diminishes in the downstream direction as the general level of the heat transfer rate decreases. Neither the curves for the parallel plates nor the $N = 101$ discrete plates exhibit waviness; a minute waviness does exist for the latter case, but it is too small to be shown in the scale of Fig. 5.

The axial distribution of the dimensionless difference pressure P is plotted in Fig. 6 for the same cases for which heat transfer results were given in Fig. 5. The ordinate of Fig. 6 is the ratio of the local values of P at x to the maximum value for the case in question; all curves, therefore, have a maximum ordinate of unity. The values of $P_{\max}$ are -6.3×10^{-7}, -8.6×10^{-7}, and -1.1×10^{-6}, respectively, for parallel plates and for the $N = 10$ and 101 discrete-plate cases. The negative value of $P_{\max}$ indicates that P is also negative since $P/P_{\max}$ is positive throughout.

In general, P decreases with x in the lower part of the array, attains a minimum, and then increases toward zero in the upper part of the array. In interpreting these trends, it should be noted that P represents, in dimensionless terms, the difference between the pressure internal to the array and that external to the array, both at a station x. It should also be recalled that the external pressure decreases with increasing x. In this light, the P versus x distribution indicates that the internal pressure decreases more rapidly than the external pressure in the lower part of the array, with an opposite relationship in the upper part of the array.

The pressure curve for the $N = 10$ discrete-plate array exhibits a waviness similar to its heat transfer counterpart of Fig. 5. This waviness results from the relatively high pressure drop near the leading edge of each plate and the lesser pressure drop downstream of the leading edge. A slight waviness could be seen in the computer listing for the $N = 101$ discrete-plate array, but it was too slight to be perceptible in the figure.

Concluding Remarks

The work performed here has provided a set of analytically based results for heat transfer enhancement in natural convection systems. The solutions obtained for staggered discrete-plate arrays and parallel plate arrays of equal heat transfer surface area yielded definitive

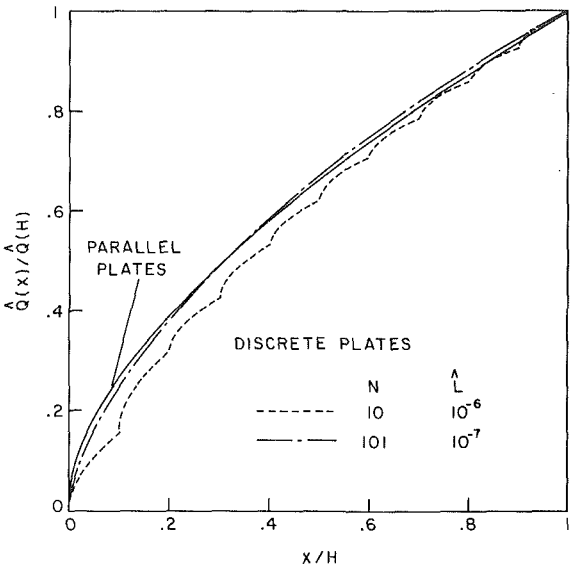

Fig. 5 Axial distributions of surface-integrated heat transfer ($(D_h/H)\mathrm{Ra} \simeq 6.95 \times 10^4$)

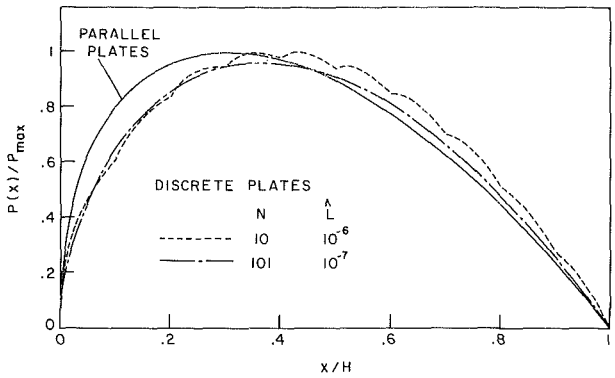

Fig. 6 Axial distributions of inner-outer pressure difference ($(D_h/H)\mathrm{Ra} \simeq 6.95 \times 10^4$)

comparisons between the two types of configurations. The use of discrete plates in lieu of continuous plates gives rise to heat transfer enhancement when $(D_h/H)\mathrm{Ra} > 2 \times 10^3$. The degree of enhancement increases with increasing values of both the number of plates and $(D_h/H)\mathrm{Ra}$. In physical terms, enhancement is favored by numerous, short plates, by larger transverse spacing, and by relatively short system heights.

For the parameter ranges investigated, the maximum heat transfer enhancement was a factor of two. The general degree of enhancement compares favorably with that which has been accomplished in forced convection systems. The failure of the discrete-plate array to enhance heat transfer at smaller $(D_h/H)\mathrm{Ra}$ is due to a decrease in mass throughflow relative to that for the parallel plate array.

References

1 Bergles, A. E., "Survey and Evaluation of Techniques to Augment Convective Heat and Mass Transfer," in *Progress in Heat and Mass Transfer*, Vol. 1, Pergamon Press, Oxford, 1969, pp. 331–424.

2 Bergles, A. E., Blumenkrantz, R. R., and Taborek, J., "Performance Evaluation Criteria for Enhanced Heat Transfer Surfaces," *Proceedings, Fifth International Heat Transfer Conference*, Vol. II, Paper FC6.3, 1974, pp. 239–243.

3 Bergles, A. E., Junkhan, G. H., and Bunn, R. L., "Performance Criteria for Cooling Systems on Agricultural and Industrial Machines," Report HTL-6, Department of Mechanical Engineering, Iowa State University, Ames, Iowa, Dec. 1974.

4 Tao, L. N., "On Combined Free and Forced Convection in Channels," ASME JOURNAL OF HEAT TRANSFER, Vol. 82, 1960, pp. 233–238.

5 Bodoia, J. R. and Osterle, J. F., "The Development of Free Convection Between Heated Vertical Plates," ASME JOURNAL OF HEAT TRANSFER, Vol. 84, 1962, pp. 40–44.

6 Aung, W., "Fully Developed Laminar Free Convection Between Vertical Plates Heated Asymmetrically," *International Journal of Heat and Mass Transfer*, Vol. 15, 1972, pp. 1577–1580.

7 Aung, W., Fletcher, L. S., and Sernas, V., "Developing Laminar Free Convection Between Vertical Flat Plates with Asymmetric Heating," *International Journal of Heat and Mass Transfer*, Vol. 15, 1972, pp. 2293–2308.

8 Carpenter, J. R., Briggs, D. G., and Sernas, V., "Combined Radiation and Developing Laminar Free Convection Between Vertical Flat Plates with Asymmetric Heating," ASME JOURNAL OF HEAT TRANSFER, Vol. 98, 1976, pp. 95–100.

9 Sobel, N., Landis, F., and Mueller, W. K., "Natural Convection Heat Transfer in Short Vertical Channels Including the Effects of Stagger," *Proceedings, Third International Heat Transfer Conference*, Vol. II, 1966, pp. 121–125.

10 Kays, W. M. and London, A. L., *Compact Heat Exchangers*, second ed., McGraw-Hill, New York, 1964.

11 Patankar, S. V. and Spalding, D. B., *Heat and Mass Transfer in Boundary Layers*, second ed., Intertext Books, London, 1970.

Experiments on Natural Convection from Vertical Parallel Plates with Either Open or Closed Edges

E. M. Sparrow
Fellow ASME

P. A. Bahrami

Department of Mechanical Engineering,
University of Minnesota,
Minneapolis, Minn. 55455

Natural convection heat transfer from the face-to-face surfaces of parallel, square vertical plates was investigated experimentally. The experiments encompassed three types of hydrodynamic conditions along the lateral edges: (1) fully open to ambient, (2) blockage of one of the edge gaps, (3) blockage along both of the edge gaps. Measurements were made for ten interplate spacings. Use of a mass transfer measurement technique (the naphthalene sublimation technique) instead of direct heat transfer enabled elimination of radiation effects, extraneous convective/conductive heat losses, and variable property effects. The results for the fully open-edged case cast substantive doubt on the oft-quoted data of Elenbaas in the low range of the parameter (b/H)Ra, where b is the interplate spacing and H is the plate height. Uncertainties in Elenbaas' results owing to large fluid property variations are also demonstrated (the present results correspond to constant properties). Suppression of fluid flow along one lateral edge gap generally has only a modest effect on the transfer coefficients and no effect for (b/H)Ra > 4. When both edges are blocked, 30 percent (or more) reductions in the coefficients occur at lower (b/H)Ra. When (b/H)Ra > 10, the lateral edge conditions do not affect the results.

Introduction

Natural convection heat transfer from an array of vertical parallel plates is encountered in applications as diverse as electronic equipment cooling and fin-tube baseboard heaters. These applications have motivated a substantial body of research on natural convection in parallel plate configurations but, as will be discussed shortly, numerous important issues remain unresolved. The bulk of the work has been directed toward unobstructed parallel plates, i.e., without tubes. Such systems are also the focus of the present study, and the forthcoming discussion of background literature will reflect this focus.

Analytical studies of natural convection between vertical parallel plates have, in all cases, employed a two-dimensional mathematical model. Such a model takes no cognizance of the lateral edges of the plates and of possible inflows and outflows adjacent to those edges when they are open to the ambient. Since open lateral edges are commonly encountered in practice, for example, in plate fin arrays, it is relevant to establish when edge phenomena (e.g., three-dimensional flows) play an important role. Representative contributions to the analytical literature on the subject may be found in [1–4], and a survey of earlier work is available in [5].

With regard to experiment, the earliest and most-quoted study is that of Elenbaas [6] who worked with a system consisting of a pair of square plates open to the ambient along all edges (lateral, top, and bottom). Elenbaas' results are frequently used as the basis of optimization calculations for vertical plate fins (e.g., [7, 8]) and are often compared with analytical results for parallel plate channels. Neither of these uses of the Elenbaas results is strictly consonant with the open lateral edges of his experiments—vertical fins are attached to a wall and a parallel plate channel has no lateral edges. This matter will be revisited later, during the discussion of the present results.

Careful scrutiny of Elenbaas' paper reveals a number of concerns. At small values of the interplate spacing, the corrections for extraneous heat losses were very much larger than the actual natural convection heat transfer (e.g., by a factor of 20 or more in some cases). This puts into serious question the accuracy of the small-spacing results. Furthermore, in many of the experiments, the plate-to-ambient temperature differences were large, up to about 330°C (~600°F), thereby activating both variable property effects and thermal radiation. Finally, the correlation parameter employed by Elenbaas was deduced from an examination of the governing equations for a parallel plate channel, and its applicability to cases characterized by significant lateral edge effects is open to question.

The foregoing discussion of the available analytical work and the experiments of Elenbaas provides a backdrop for the present research. We are concerned here with the heat transfer response to edge-related phenomena, with heat transfer results for closely spaced plates, and with the avoidance of extraneous heat losses, variable property effects, and radiative transfer. To fulfill these objectives, an experimental program was undertaken based on the use of the analogy between heat and mass transfer, whereby the actual experiments were performed with the naphthalene sublimation technique.

This technique enables average heat (mass) transfer results to be determined with a much higher level of accuracy than is attainable in corresponding heat transfer experiments. The mass transfer results are uninfluenced by radiative transfer and variable property effects, and extraneous losses can be readily reduced to a negligible level. Of particular relevance is the easy adaptability of the mass transfer apparatus to facilitate the study of various hydrodynamic boundary conditions at the lateral edges of the plates.

All told, experiments were carried out for three types of lateral-edge boundary conditions. Among these, the first case is that in which all edges are fully open to the ambient. In the second case, fluid flow was suppressed along one of the lateral edges of the array, whereas in the third case flow was suppressed along both of the lateral edges. These experiments are believed to be the first in which various lateral-edge hydrodynamic conditions have been systematically studied under conditions where everything else in the apparatus and in the ambient is unchanged.

The experiments were performed utilizing a pair of square plates, 7.620 cm (3.000 in.) on a side. The spacing between the plates, expressed as a ratio with the side, ranged from 0.042 to 0.333 and encompassed a total of ten spacings. Natural convection mass transfer was permitted to occur only at the face-to-face surfaces of the plates, with no mass transfer whatsoever at any other parts of the plates. To attain the desired accuracy, the apparatus was situated in a temperature-controlled enclosure within which extraneous air currents were carefully suppressed.

The results reported here are in terms of the average Sherwood number, which is the mass transfer analogue of the average Nusselt

Contributed by The Heat Transfer Division for publication in the JOURNAL OF HEAT TRANSFER. Manuscript received by The Heat Transfer Division August 10, 1979.

number. By using the analogy between heat and mass transfer, the Sherwood numbers can be used directly as Nusselt numbers.

Although the already cited work of Elenbaas constitutes the most relevant background literature for the present study, there are other experiments which represent important contributions to the subject. Aside from Elenbaas' experiments, those of Levy [9] appear to be the only ones involving plates open to the ambient along all edges. The Levy experiments covered the upper end of the range of the Elenbaas correlation parameter (in effect, the larger interplate spacings). Comparisons of the present results with those of Levy and of Elenbaas will be made later.

A number of experiments have been carried out to study the performance of an array of parallel plate fins attached to a heated wall (e.g., [10–12]). In effect, this configuration corresponds to the case of fluid flow suppressed along one of the lateral edges of the array. In [13], experiments were performed for the case in which fluid flow was suppressed along both lateral edges. These studies provide valuable information for design but do not deal with the issues which, as discussed earlier, provided the motivation for the present investigation.

The Experiments

The experimental apparatus encompassed the naphthalene test plates at which the mass transfer occurred and a support assembly for holding and positioning the plates. Other essential elements of the test facility included a baffle system to shield the plates from extraneous air currents and a test chamber to create a controlled environment for the experiments. The various components of the apparatus and the test facility will now be described, as will the experimental procedure. A special feature of the apparatus is its ability to provide an arbitrary spacing between the test plates. Owing to its uniqueness, this feature will be described in some detail. Additional information may be found in [14].

Experimental Apparatus. A schematic diagram of the experimental apparatus is shown in Fig. 1. As seen there, a U-shaped main frame carries the naphthalene test plates along with their supporting and positioning devices. The main frame, fabricated from 2.5-cm (1-in.) thick aluminum plate, was designed to be massive and to possess strong clamp-like qualities. A V-groove was machined into each of the top edges of the U. The function of the V-grooves is to house and guide the support rods A and B to which the naphthalene plates are attached. A cap, equipped with thumb screws and alignment pins (not shown), is fitted atop each groove; tightening of the thumb screws serves to lock the respective rods in place.

The rods, each 0.953 cm (0.375 in.) in diameter and 25.4-cm (10-in.) long, were cut from specially chosen straight and uniformly ground drill rod stock. A flange was fitted to one end of each rod and, as shown in Fig. 1, each flange mated with a corresponding flange situated on the back face of a naphthalene plate.

The setting of the spacing between the naphthalene plates was accomplished with the aid of stop sleeves A and B and spring B. The sleeves were machined so that they would just slide freely over the rods. Each sleeve was equipped with a thumb screw which, when tightened, served to fix the sleeve to the rod. Thus, when the thumb screw on stop sleeve A is tightened, leftward motion of rod A is arrested. Similarly, the thumb screw of stop sleeve B prevents leftward motion of rod B. It may also be noted that spring B tends to move rod B to the left so that, if the thumb screw on stop sleeve B is tightened,

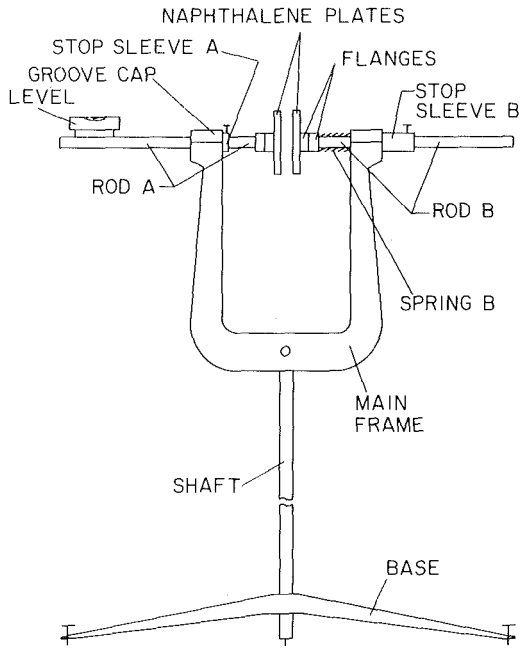

Fig. 1 Schematic diagram of experimental apparatus

the sleeve is forced against the side of the main frame.

The setting of the interplate spacing will now be described. To begin, the thumb screw on stop sleeve A is loosened, allowing rod A to slide freely. At the same time, the thumb screw on stop sleeve B is tightened so that rod B is positioned by the tension in spring B. Then, a precisely machined brass spacer having a desired thickness is inserted between the plates, and rod A is moved so that there is loose contact between the plates and the spacer. Next, stop sleeve A is positioned against the side of the mainframe and its thumb screw tightened. The thumb screw on stop sleeve B is then loosened, allowing the tension in spring B to force intimate contact between the plates and the spacer.

To preserve the thus-established interplate spacing, stop sleeve B is positioned against the side of the main frame and its thumb screw tightened. The spacer is then removed by sliding rod B to the right (while compressing spring B). The spring tension, in conjunction with stop sleeve B, assures that the desired interplate spacing is attained when rod B is release. The foregoing operations were performed with care to assure that no scratching of the naphthalene surfaces would occur.

Spacer disks, 2.54 cm (1 in.) in diameter, having thicknesses of 0.254, 0.318, 0.476, 0.635, 1.15, and 1.27 cm (0.100, 0.125, 0.1875, 0.250, 0.453, and 0.500 in.) were prepared. By employing these spacers either singly or in combinations, interplate spacings of 0.318, 0.476, 0.635, 0.953, 1.111, 1.151, 1.270, 1.524, 1.746, 2.159, and 2.54 cm (0.125, 0.1875, 0.250, 0.375, 0.4375, 0.453, 0.500, 0.600, 0.6875, 0.850, and 1.000[1] in.) were obtained. The spacers were fitted with handles to

[1] Obtained by using two 0.250 in. spacers and a 0.500 in. spacer.

Nomenclature

A = transfer surface area
b = interplate spacing
$\mathcal{D}$ = naphthalene-air diffusion coefficient
Gr = Grashof number—for mass transfer, equation (6); for heat transfer, $g\beta(T_w - T_\infty)b^3/\nu^2$
g = acceleration of gravity
H = plate height (equal to width)
K = mass transfer coefficient, equation (1)
M_a = molecular weight of air
M_n = molecular weight of naphthalene
$\dot{M}$ = mass transfer rate
Nu = Nusselt number
Pr = Prandtl number
Ra = Rayleigh number, GrSc or GrPr
Sc = Schmidt number
Sh = Sherwood number, $Kb/\mathcal{D}$
T_w = wall temperature
T_∞ = ambient temperature
β = thermal expansion coefficient
ρ = density
ρ_{nw} = naphthalene vapor density at wall
$\rho_{n\infty}$ = naphthalene vapor density in ambient
μ = viscosity
ν = kinematic viscosity

enable them to be positioned in the central region of the plate surface when a desired interplate spacing was being established.

As is shown in Fig. 1, the main frame is attached to a vertical shaft which, in turn, is supported by a three-legged base equipped with leveling screws. The shaft and frame serve to elevate the naphthalene plates about 165 cm (65 in.) above the floor of the laboratory room.

Vertical alignment of the surfaces of the naphthalene plates was verified by a level attached to rod A (see Fig. 1), with adjustments being made with the leveling screws on the three-legged base. To ensure that the upper and lower edges of the plates are horizontal, a carefully machined flat surface fitted with a level was placed atop both plates; the two plates were rotated together until the horizontal orientation was attained. At this point, rods A and B were locked in place by tightening thumb screws on the respective caps.

The Naphthalene Plates. Each test plate was a composite consisting of a layer of naphthalene backed by a stainless steel plate. Pictorial and side view schematics of a test plate are shown in the upper and lower diagrams of Fig. 2. The backing plate and its fittings were fabricated prior to the initiation of the experiments, whereas a fresh naphthalene coating was applied by a casting process for each data run. Two identical backing plates were fabricated, one for each of the test plates.

Each stainless steel backing plate is square, 7.620 cm (3.000 in.) on a side. To attain the desired flatness (to better than 0.0025 cm, 0.001 in.), the plate was painstakingly ground, with the final thickness being 0.1092 cm (0.0430 in.). Subsequent to the grinding, three small holes were drilled and tapped at locations 120 deg apart, as shown in Fig. 2. A sharp-tipped screw was inserted in each hole. The three screws, with their tips resting on a surface plate, were adjusted with the aid of a dial gage so that the plane defined by their tips was 0.635 cm (0.250 in.) from the steel plate. The screws were then locked in place.

The backing plate was also fitted with a brass flange affixed to its rear face. The flange contains a center hole aligned with a corresponding hole in the center of the plate. As indicated in Fig. 2, the center hole serves as an access through which molten naphthalene is poured during the casting process. Also, when the test plates are positioned in the experimental apparatus (see Fig. 1), the center hole facilitates attachment of the plate to its support rod.

The casting process used to prepare the naphthalene test surfaces will now be described. Casting was performed in a multi-part mold which includes the backing plate, a large stainless steel plate with a hand-lapped surface, and four highly polished brass bars. In assembling the mold, the sharp-tipped screws of the backing plate were allowed to rest on the hand-lapped surface, and the bars were deployed so as to block the openings along the four edges. This arrangement served to define an enclosed rectangular space within the mold into which molten naphthalene was poured through the hole in the flange of the backing plate. The pouring was facilitated by a funnel fitted to the flange hole.

Once solidification had occurred, the solid naphthalene was separated from the lapped surface and from the bars but not from the backing plate—resulting in the test plate configuration of Fig. 2. The separated surfaces of the naphthalene possessed a remarkable degree of smoothness, corresponding to the surface finish of the stainless steel plate.

Since the experiments were concerned with natural convection mass transfer at the square face of the cast plate and not at the four 0.635-cm (0.250-in.) thick edges of the casting, the latter were covered with a pressure-sensitive tape (0.005 cm or 0.002 in. thick) which fully suppressed sublimation. The application of the tape was facilitated by a guide which insured precise coverage of the thickness of the edge but avoided any overlapping of the tape onto the mass transfer surface. The taping procedure is described in [14].

Reagent grade naphthalene was employed for the casting. For each data run, a new pair of naphthalene plates was prepared using fresh (i.e., previously unused) naphthalene.

The Test Environment. It is well known that natural convection is extremely sensitive to extraneous flows and disturbances in the environment. Furthermore, naphthalene sublimation is quite responsive to temperature level since its vapor pressure increases by about ten percent per °C. Therefore, to insure consistent and highly accurate data, it was necessary to control the conditions in the environment.

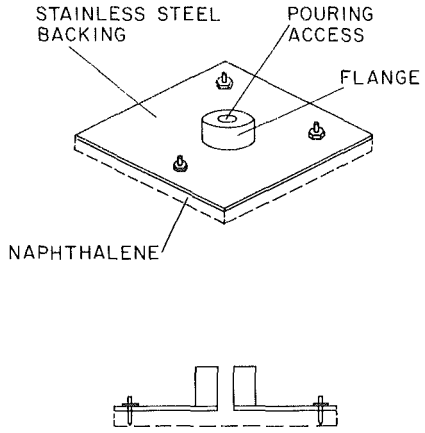

Fig. 2 Diagram of a test plate

To this end, a temperature-controlled, windowless laboratory was chosen as the site of the experiments. However, owing to the forced draft heating and cooling system, the air currents were judged to be unacceptable for natural convection experiments. To achieve the benefits of the controlled temperature without the penalties of the extraneous air currents, a large free-standing test chamber was constructed in the laboratory. The chamber, which is, in fact, a room within a room, had dimensions 3.65 × 2.45 × 2.45 m (12 × 8 × 8 ft)—length × width × height. The ceiling and the four walls of the test chamber were made of 2½-cm (1-in.) thick polystyrene building insulation sheets, and fiberglass batts were placed on the floor. Polystyrene sheets, suitably framed for support, were also used for the access door to the chamber.

As a further precaution against extraneous air currents within the test chamber, a baffle system was set up in the neighborhood of the experimental apparatus. The baffles were designed to shield the apparatus from possible extraneous currents while not interfering with the natural convection flows induced by the mass transfer at the naphthalene plates. Thus, impermeable shields were deployed in directions where no induced flow was expected to occur and screening was situated in those directions where induced flow was expected. The layout of the baffle system is detailed in [14].

During the course of a data run, the test chamber was kept sealed. The outputs of thermocouples positioned adjacent to the naphthalene plates were recorded by a data acquisition system situated outside the test chamber.

Experimental Procedure. Various aspects of the experimental procedure have already been described in the preceding sections, and further information will be given here.

Subsequent to the casting and taping of the naphthalene plates, they were wrapped in plastic and placed in the temperature-controlled laboratory in order to attain thermal equilibrium. Prior to the setup of the apparatus for a data run, the mass of each test plate was measured with a Sartorius analytical balance capable of being read to 0.1 mg. The setup operations were described earlier and need not be repeated. The duration of a data run ranged from 6 to 26 hr, the time being selected so that the mass transfer at each naphthalene plate would be about 30 mg (which corresponds to a mean recession of the surface of about 0.0005 cm (0.0002 in.)). During the run, temperatures were sensed by two thermocouples positioned just below the test plates (naphthalene vapor is heavier than air and the corresponding natural convection motion is downward); the emf's were recorded periodically by the data logger situated outside the test chamber.

The masses of the test plates were measured immediately upon the conclusion of a data run. Then, an additional procedure was executed

in order to determine a correction for extraneous mass transfer which occurs during the setup and disassembly of the apparatus. To this end, subsequent to the weighing at the conclusion of the data run, the setup and disassembly processes were repeated without the natural convection mass transfer period, after which the plates were weighed once again. Typically, the mass transfer during setup and disassembly was about 0.5 mg.

Once all measurements associated with a data run had been completed, the air in the test chamber was exhausted to the roof of the building with the aid of a blower, thereby purging any naphthalene vapor from the chamber.

The first set of experiments was performed with the gaps along the lateral edges of the array fully open to the ambient, as pictured in Fig. 1. In the second set, the gap along one of the lateral edges was blocked while in the third set the gaps along both of the lateral edges were blocked. The blockage was accomplished by taping across the gap, with the blocking tape being anchored on the already taped edges of the test plates. The tape, while inactive in the mass transfer process, was impermeable to fluid flow.

Data Reduction

The results will be presented in terms of the mass transfer coefficient K and the Sherwood number Sh which are, respectively, defined as

$$K = (\dot{M}/A)/(\rho_{nw} - \rho_{n\infty}), \quad \mathrm{Sh} = Kb/\mathcal{D} \tag{1}$$

The quantity $\dot{M}$ is the mass transfer rate (i.e., the sublimation rate) and A is the surface area at which the mass transfer takes place. The denominator of K contains the density difference which drives the mass transfer, where ρ_{nw} and $\rho_{n\infty}$, denote the naphthalene vapor density at the plate surface and in the ambient, respectively. In the Sherwood number, b represents the interplate spacing (b is Elenbaas' symbol for the spacing), and $\mathcal{D}$ is the naphthalene-air binary diffusion coefficient.

For each data run, the $\dot{M}$ value for each plate was determined by differencing the weighings before and after the run, subtracting the extraneous mass transfer during the assembly-disassembly periods, and then dividing by the duration time of the run. In general, as is to be expected on the basis of symmetry, the $\dot{M}$ values for the two plates were virtually identical. These values were, therefore, averaged, and it is the average that was used in evaluating K and Sh.

The naphthalene vapor density at the wall ρ_{nw} was calculated from the vapor pressure—temperature relation for naphthalene [15] in conjunction with the perfect gas law. The ambient naphthalene vapor density $\rho_{n\infty}$ was assumed to be effectively zero, and the validity of this assumption was verified by auxiliary experiments in which mass transfer coefficients for data runs of significantly different durations were compared. In no case did the data differ by more than two percent, which is the range of the general scatter of the data. A computation based on the model of a well-mixed ambient affirmed this finding.

The diffusion coefficient $\mathcal{D}$ appearing in the Sherwood number can be expressed in terms of the Schmidt number Sc, which is the counterpart of the Prandtl number,

$$\mathrm{Sc} = \nu/\mathcal{D} \text{ or } \mathcal{D} = \nu/\mathrm{Sc} \tag{2}$$

The Schmidt number for naphthalene-air diffusion is 2.5 [15]. Furthermore, in view of the minute concentrations of naphthalene vapor, ν can be evaluated as the kinematic viscosity of pure air.

A key dimensionless parameter for the correlation of natural convection heat or mass transfer results is the Rayleigh number. For the two modes of transfer, the respective Rayleight numbers are

$$\mathrm{Ra} = \mathrm{GrPr}, \quad \mathrm{Ra} = \mathrm{GrSc} \tag{3}$$

The basic definition of the Grashof number Gr is the same for heat and mass transfer

$$\mathrm{Gr} = g\rho|(\rho_w - \rho_\infty)|b^3/\mu^2 \tag{4}$$

where ρ_w and ρ_∞ refer specifically to densities at the wall and in the ambient, while μ and ρ are evaluated at a suitable reference state. For heat transfer, $|\Delta\rho|$ is replaced by $|\beta\rho\Delta T|$, and the conventional form of the Grashof number follows immediately from equation (4).

To specialize equation (4) to mass transfer, it should be noted that, in general, ρ_w, ρ_∞, and ρ denote mixture densities (i.e., densities of the mixture of air and naphthalene vapor), although in the present instance ρ_∞ corresponds to pure air. By employing Dalton's law of partial pressures and the perfect gas law, it is easily shown that

$$\rho_w - \rho_\infty = \rho_{nw}(M_n - M_a)/M_n \tag{5}$$

where M_n and M_a denote the molecular weights of naphthalene and air.

Upon introducing (5) into (4), there follows

$$\mathrm{Gr} = \frac{g\rho\rho_{nw}b^3}{\mu^2}\frac{M_n - M_a}{M_n} \tag{6}$$

It is important to note that both ρ and μ, as they appear in equation (6), are indistinguishable from those of pure air. There are, in fact, no variable property decisions to be made in the evaluation of the Grashof number for the present experiments.

If guidance is taken from the analysis of the parallel plate channel, e.g., [1], a correlation can be sought in the form

$$\mathrm{Sh} = f((b/H)\mathrm{Gr},\mathrm{Sc}), \quad \mathrm{Nu} = f((b/H)\mathrm{Gr},\mathrm{Pr}) \tag{7}$$

where, in accordance with the heat/mass transfer analogy, the function f is the same for heat and mass transfer. The quantity H is the height of the channel. As an alternate to equation (7), the Rayleigh number may be employed, so that

$$\mathrm{Sh} = F((b/H)\mathrm{Ra},\mathrm{Sc}), \quad \mathrm{Nu} = F((b/H)\mathrm{Ra},\mathrm{Pr}) \tag{8}$$

where the function F is common to both heat and mass transfer.

When the Rayleigh number is used in natural convection correlations, it is usual to ignore the separate dependence on Sc or Pr. In that case

$$\mathrm{Sh} = F'((b/H)\mathrm{Ra}), \quad \mathrm{Nu} = F'((b/H)\mathrm{Ra}) \tag{9}$$

Comments on the omission of the Sc and Pr dependence will be made later, and the applicability of forms such as (7–9) to situations involving lateral-edge phenomena will be discussed.

As a final note, attention should be called to the fact that the mass transfer situation investigated here corresponds to isothermal plates in the analogous heat transfer problem. If heat transfer fins are being considered, then the present results correspond to fins with an efficiency of unity.

Results and Discussion

As a supplement to the main body of experiments involving two parallel plates, auxiliary experiments were performed for the classical case of a single vertical plate. A total of five single-plate data runs were conducted, spanning a period of slightly over a year. Two of these runs were made with baffles attached to the lateral edges, and the other three were made without baffles. The repeatability of the data was very good, generally within ±2 percent of the average. The Rayleigh number for these runs, based on the plate height as the characteristic dimension, was about 1.35×10^4.

The experimentally determined single-plate Sherwood numbers were compared with the recent correlation of Churchill and Chu [16] for natural convection heat transfer from isothermal vertical plates. The comparison showed that the present data were about 10 percent above the correlation. When the data were plotted in Fig. 1 of Churchill and Chu, it was observed that they were well within the deviations of the data that had been assembled by those authors and plotted on the graph to establish the correlation.

It can, therefore, be concluded that the present data for the single vertical plate are in agreement with prior experiments and with the Churchill-Chu correlation. This finding lends support to the methodology of the present experiments.

Attention will now be turned to the results for the parallel plate experiments.

All Edge Gaps Open to the Ambient. The experimental data for natural convection from square parallel plates with all edge gaps open to the ambient are presented in Fig. 3. The ordinate variable is the Sherwood number Sh or, in accordance with the heat-mass transfer analogy, the Nusselt number Nu. The abscissa variable is (b/H)Ra. Since this quantity is proportional to b^4, it is very responsive to changes in the interplate spacing b, and the ten clusters of data distributed along the abscissa correspond to the ten interplate spacings used in the experiments. It can be seen from the figure that the data are remarkably free of scatter and that replicate data runs were always in good agreement. A curve has been faired through the data to provide continuity.

In addition to the present data, Fig. 3 also shows the experimental results of Elenbaas [6] taken from Fig. 11 of his paper. These results are depicted by a correlation line (solid line) and dashed lines delineating the data band.

From the figure, it can be seen that whereas there is generally good agreement between the two sets of results at the larger values of the abscissa variable (b/H)Ra, there are growing deviations as (b/H)Ra decreases. Apart from possible experimental inaccuracies, there are more fundamental factors which might be responsible for the modest deviations in evidence at larger (b/H)Ra, and these will be addressed shortly. The growing deviations with decreasing (b/H)Ra are a more pressing matter and merit prompt discussion.

Two factors may be identified as being responsible for the large deviations. One of these is a highly questionable assumption in Elenbaas' data reduction procedure, and the other relates to the validity of (b/H)Ra as a sufficient correlation parameter at small interplate spacings.

Consideration may first be given to the data reduction procedure used by Elenbaas and, specifically, to the method of determining the heat transfer attributable to natural convection. At a given plate spacing, the electric power (supplied to embedded heaters) needed to maintain the plates at a given temperature level was measured. The power input encompassed both the natural convection heat transfer from the plate faces and the extraneous losses, the latter being determined from auxiliary experiments in which the interplate spacing was reduced to zero and the temperature level was maintained as before. From an abbreviated table given by Elenbaas, it can be seen that as (b/H) Ra decreased, the magnitude of the losses tended to overwhelm the natural convection heat transfer. Thus, at a value of $(b/H)\text{Ra} \simeq 0.6$, the apportionment of the total power input of 46 W was 2 W for natural convection and 44 W for extraneous losses!

At this same (b/H)Ra, the value of Sh from the present experiments exceeds the Nusselt number of Elenbaas by a factor of five. However, had the extraneous losses actually been 18 percent less than the value used by Elenbaas, then his Nu value would be increased by a factor of five[2] and would agree with the present value of Sh.

The tabulated information given by Elenbaas does not include his smallest (b/H)Ra values and highest temperature levels, so that the most extreme cases characterized by overwhelming extraneous losses are not available. It can be conjectured that in those cases, the losses may have been 50 to 100 times the natural convection from the plate faces.

Further consideration of the situation suggests that Elenbaas was not correct in assuming that the extraneous losses corresponding to a spacing b are equal to the total power input at $b = 0$. This is because the natural convection flow adjacent to the 0.6- or 1-cm (0.25- or 0.40-in.) thick edges of the plates will differ depending on whether or not there is a gap between the plates. Furthermore, at small spacings, the heat losses from these edges is large compared with that from the faces of the plates, so that a change in flow pattern adjacent to the edges can be decisive.

In light of the foregoing, there appears to be ample reason to believe that Elenbaas' results are subject to increasing errors as (b/H)Ra decreases and that this is primarily responsible for the deviations in evidence in Fig. 3.

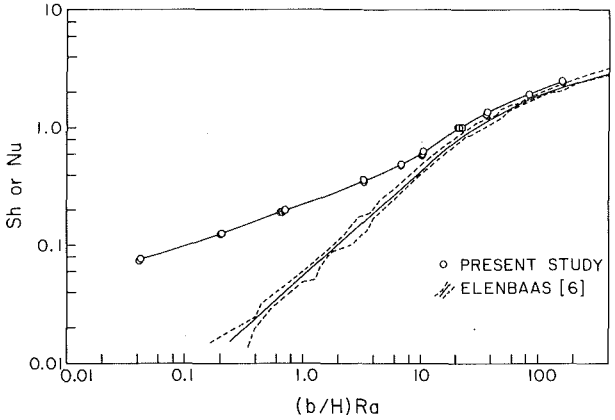

Fig. 3 Sherwood and Nusselt number results for square parallel plates with all edge gaps open to ambient

Another factor, which must remain conjectural for the present, is that the deviations are, in part, somehow related to the inadequacy of (b/H)Ra as a correlating parameter when b/H is small. As the spacing decreases, the frictional resistance encountered by the fluid moving vertically through the channel proper necessarily increases. As a consequence, there will be a decrease in the flow entering the bottom of the channel (for heated plates) and an increase in the flow passing through the open gaps at the lateral edges. When these edge flows are important, the system cannot be regarded as a two-dimensional parallel plate channel, and it is the parallel plate channel analysis that yields (b/H)Ra as the correlating parameter. Rather, a three-dimensional model must be used, and such a model would yield an additional geometrical parameter. These considerations cannot be given quantitative force until numerous additional experiments are performed.

With the completion of the discussion relevant to lower values of (b/H)Ra, attention may be turned to the modest deviations (~15 percent) in evidence in Fig. 3 at the larger (b/H)Ra. There are two issues involved here: (1) variable property effects, (2) the influence of Pr and Sc; these will be discussed successively.

The present results correspond to constant fluid properties. On the other hand, those of Elenbaas are marked by strong variable property effects since wall-to-ambient temperature differences as large as 333°C (~600°F) were employed. The conventional manner of bringing together constant and variable property results is to evaluate the properties in the latter at a suitable reference temperature. Unfortunately, the proper reference temperature for the parallel plate situation has not yet been identified. Therefore, any procedure that is employed for evaluating the properties is necessarily somewhat arbitrary. Elenbaas chose to evaluate all fluid properties at the wall temperature T_w, except that the thermal expansion coefficient β was evaluated as $1/T_\infty$. On the other hand, Levy [9] evaluated all properties at the mean of T_w and T_∞.

To provide further perspective about the properties issue, Fig. 4 has been prepared. The figure, which covers the upper range of (b/H)Ra, shows the data of Levy (open circles) along with those data of Elenbaas that are available in tabular form (blackened triangles). Lines depicting the distribution of the present data and the correlation of Elenbaas are also included for reference purposes. As plotted, the Levy data are supportive of both the present results and those of Elenbaas.

It is of interest to place the data of Elenbaas and Levy on the same property base. To this end, the tabulated data of Elenbaas were recast by evaluating all fluid properties at the arithmetic mean of T_w and T_∞, and the results are shown as open triangles in Fig. 4 (the triangles are connected by a dashed line for continuity).

It may be observed that when the data are brought to the same property base, the apparent agreement between the Elenbaas and

[2] Eighteen percent of Elenbaas' 44 W heat loss estimate is 7.9 W. This value, when added to his 2 W convective heat transfer estimate, increases the Nusselt number by a factor of five.

Levy experiments is not as good as before, especially at smaller (b/H)Ra. Thus, the method of evaluating properties is seen to affect the comparison between different sets of data. Without a well-founded reference temperature rule, there is no reason to expect precise agreement between data for constant properties (present results) and data for variable properties (Elenbaas results).

Variable properties aside, it is relevant to raise the issue of whether the use of the Rayleigh number as a correlating parameter, in lieu of the Grashof number, eliminates the Prandtl (or Schmidt) number as a separate parameter. For the classical vertical plate problem, the Churchill-Chu correlation contains a separate Pr (or Sc) dependence even though the Rayleigh number is the correlating parameter. For a given Rayleigh number, that correlation predicts a Nusselt (or Sherwood) number for Pr (or Sc) = 2.5 which is 12 percent higher than that for Pr (or Sc) = 0.7. In view of this, it is reasonable to expect that in the absence of variable property effects, the present results (which are for Sc = 2.5) should lie on the order of ten percent higher than those of Elenbaas (which are for Pr = 0.7). However, as indicated earlier, the variable property effects preclude a precise comparison.

Flow Blockage along One Lateral Edge Gap. The Sherwood numbers for natural convection from square parallel plates with flow suppressed along one lateral edge gap are presented in Fig. 5. These data are depicted by the triangle symbols (which have been interconnected by a smooth curve for continuity). Also shown in the figure is a solid line which represents the data of Fig. 3 for the case in which all edge gaps are open to the ambient. The ordinate and abscissa variables and scales are identical to those of Fig. 3.

Examination of Fig. 5 shows that the Sherwood number is not significantly affected by the suppression of flow along one of the lateral edge gaps. In fact, for (b/H)Ra > 4, there is no difference between the results for fully open edges and for flow suppressed along one lateral edge. At lower values of (b/H)Ra, some deviations are in evidence, but these are no greater than 15 percent.

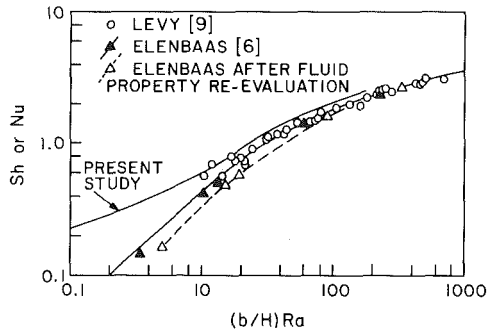

Fig. 4 Effect of fluid property evaluations on the comparison of results for the open gap case

The foregoing finding is of considerable practical significance, since an array of vertical plate fins attached perpendicular to a vertical wall corresponds to the case of flow blockage along one lateral edge. Furthermore, there is evidence [10, 12] that (b/H)Ra > 4 for many applications involving such fin arrays. Thus, for these situations, Nusselt numbers needed for design may be taken as being equal to the Nusselt numbers for plates with fully open lateral edges. Even for (b/H)Ra < 4, the results for the open-edge case should be sufficient for the design of attached fin arrays.

Another ramification of the aforementioned finding is that there is relevance in comparing results from fully open-edged configurations and one-edged blocked configurations. As noted in the Introduction, such comparisons have been made in the past, but without a firm basis.

It is interesting to consider the possible causes of the insensitivity of the Nusselt (Sherwood) number to the blockage of one of the lateral edge gaps. When the interplate spacing is relatively large (i.e., larger values of (b/H)Ra), very little fluid inflow or outflow occurs along the lateral edges of an open-edged configuration. Therefore, blocking of a lateral edge gap should have a negligible effect on the heat (mass) transfer coefficients. At smaller spacings (i.e., smaller (b/H)Ra), fluid flow through the lateral edge gaps becomes more important. For heated plates with all edges open, fluid enters the interplate space through three openings—through the bottom and the two lateral edge gaps. When one of the lateral edges is blocked, there is partial compensation due to an increase in the flow passing through the remaining two openings. Owing to this compensation, the decrease in heat transfer is quite limited.

Flow Blockage along Both Lateral Edges. When flow through both of the lateral edge gaps is suppressed, the mechanism inducing the flow is somewhat different from that which operates when the lateral edges are open. The closed-edge case is, in a sense, a pressure-driven flow, with the pressure difference between the top and bottom of the plates playing a key role. In instances such as this, the flow is said to be induced by the chimney effect. When the lateral edges are open, the chimney effect does not operate.

The Sherwood numbers for the case of doubly closed lateral edge gaps are plotted as square data symbols in Fig. 6. Also shown in the figure are lines respectively representing the results for the cases of fully open edge gaps and of the singly blocked lateral edge gap.

From the figure, it is seen that blocking both lateral edges reduces the Sherwood number in the range of (b/H)Ra < 10. Over most of this range, the reduction, compared with the fully open case, is on the order of 30 percent, with larger deviations at the very low (b/H)Ra. The incremental reductions in Sh caused by blocking the second lateral edge gap are greater than the incremental reductions that occurred when the first lateral edge gap was blocked.

The extent of the reductions is controlled by the complex interaction of two conflicting factors. One of these, the complete suppression of fluid ingress along the lateral edges, requires that all the flow en-

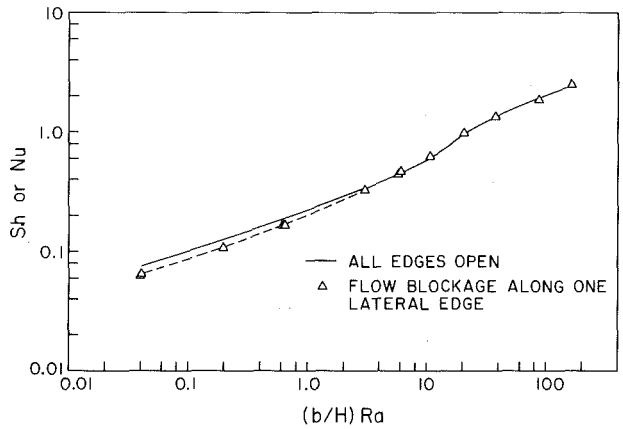

Fig. 5 Sherwood and Nusselt number results for square parallel plates with flow blockage along one lateral edge

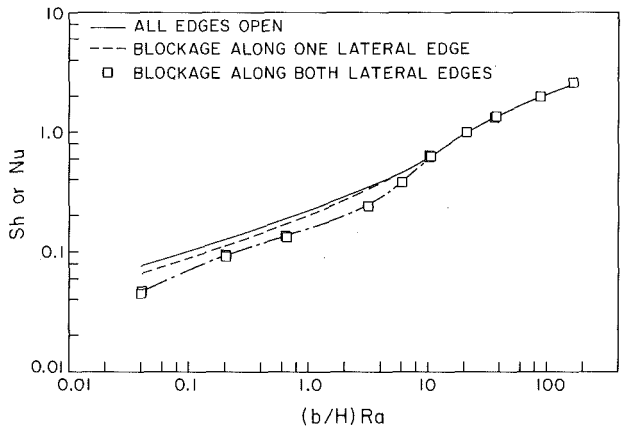

Fig. 6 Sherwood and Nusselt number results for square parallel plates with flow blockage along both lateral edges

tering the interplate space (i.e., through the bottom) traverse the entire plate height. This tends to diminish the natural convection flow. The second factor is the chimney effect, which tends to augment the flow. Evidently, the edge gap blockage plays a greater role than the chimney effect.

For $(b/H)\mathrm{Ra} > 10$, the results for both the singly and doubly blocked configurations are coincident with those for the fully open configuration. Thus, for this range, it can be concluded that phenomena related to the lateral edges play a negligible role, and the system can be treated as if it were a parallel plate channel.

Concluding Remarks

The main results of this investigation will now be summarized. For the case where all edge gaps are open to the ambient, a detailed comparison was made between the present results and the widely referenced results of Elenbaas. In the range of $(b/H)\mathrm{Ra} > 20$, there is satisfactory agreement (15 – 20 percent) between the two sets of results. The deviations can be attributed to two factors: variable property effects and differences in Prandtl (Schmidt) number. The property variations in Elenbaas' experiments were large (temperature differences up to 333°C, 600°F), and it was shown that this causes an uncertainty about how to evaluate the property values. At lower $(b/H)\mathrm{Ra}$ (smaller spacings), there are very substantial deviations between the two sets of results. It was demonstrated that, in all likelihood, these deviations are due to the massive corrections that were employed by Elenbaas to account for extraneous heat losses.

Another issue that may be relevant at small spacings is the inadequacy of $(b/H)\mathrm{Ra}$ as a correlating parameter. Fluid flow through the lateral edge gaps is important at small spacings, and such flows are not included in the two-dimensional model which yields $(b/H)\mathrm{Ra}$ and Pr as the only parameters. A three-dimensional model, accounting for edge-gap flows, would yield an additional geometrical parameter.

The suppression of fluid flow through one of the lateral edge gaps had only a modest effect on the heat (mass) transfer results. For $(b/H)\mathrm{Ra} > 4$, the Nusselt (Sherwood) numbers are identical to those for the unblocked case, and for $(b/H)\mathrm{Ra} < 4$ the maximum deviations (a decrease) are 15 percent. This finding is of direct practical importance, since vertical plate fins attached to a vertical wall correspond to a case of blockage along one of the lateral gaps.

When both lateral edges are blocked, deviations from the free-edge case occur when $(b/H)\mathrm{Ra} < 10$, with the decrease being 30 percent or more for $(b/H)\mathrm{Ra} < 3$. For $(b/H)\mathrm{Ra} > 10$, the heat (mass) transfer results are independent of whether the edges are fully open, blocked along one lateral edge gap, or blocked along both lateral edge gaps. Thus, in this range, lateral edge effects are of no consequence. Because of this, valid comparisons can be made between experimental results corresponding to various lateral edge conditions and analytical results for a vertical parallel plate channel.

Acknowledgment

This research was performed under the auspices of NSF Grant ENG77-06762.

References

1 Bodoia, J. R., and Osterle, J. F., "The Development of Free Convection Between Heated Vertical Plates," ASME JOURNAL OF HEAT TRANSFER, Vol. 84, 1962, pp. 40–44.

2 Quintiere, J., and Mueller, W. K., "An Analysis of Laminar Free and Forced Convection Between Finite Vertical Parallel Plates," ASME JOURNAL OF HEAT TRANSFER, Vol. 95, 1973, pp. 53–59.

3 Aung, W., Fletcher, L. S., and Sernas, V., "Developing Laminar Free Convection Between Vertical Flat Plates with Asymmetric Heating," *International Journal of Heat and Mass Transfer*, Vol. 15, 1972, pp. 2293–2308.

4 Carpenter, J. R., Briggs, D. G., and Sernas, V., "Combined Radiation and Developing Laminar Free Convection Between Vertical Flat Plates with Asymmetric Heating," ASME JOURNAL OF HEAT TRANSFER, Vo. 98, 1976, pp. 95–100.

5 Ostrach, S., "Laminar Flows with Body Forces," in *Theory of Laminar Flows, F. K. Moore*, ed., Princeton University Press, Princeton, *N. J., 1964.*

6 Elenbaas, W., "Heat Dissipation of Parallel Plates by Free Convection," *Physica*, Vol. 9, 1942, pp. 1–28.

7 Fitzroy, N. D., "Optimum Spacing of Fins by Free Convection," ASME JOURNAL OF HEAT TRANSFER, Vol. 93, 1971, pp. 462–463.

8 Bar-Cohen, A., "Fin Thickness for an Optimized Natural Convection Array of Rectangular Fins," ASM E JOURNAL OF HEAT TRANSFER, Vol. 101, 1979, pp. 564–566.

9 Levy, E. K., Eichen, P. A., Cintani, W. R., and Shaw, R. R., "Optimum Plate Spacings for Laminar Natural Convection Heat Transfer from Parallel Vertical Isothermal Flat Plates: Experimental Verification," ASME JOURNAL OF HEAT TRANSFER, Vol. 97, 1975, pp. 474–476.

10 Starner, K. E. and McManus, H. N., Jr., "An Experimental Investigation of Free Convection Heat Transfer from Rectangular Fin Arrays," ASME JOURNAL OF HEAT TRANSFER, Vol. 85, 1963, pp. 273–278.

11 Welling, J. R., and Wooldridge, C. B., "Free Convection Heat Transfer Coefficients from Rectangular Vertical Fins," ASME JOURNAL OF HEAT TRANSFER, Vol. 87, 1965, pp. 439–444.

12 Chaddock, J. B., "Free Convection Heat Transfer from Vertical Rectangular Fin Arrays," *ASHRAE Journal*, Vol. 12, August, 1970, pp. 53–60.

13 Sobel, N., Landis, F., and Mueller, W. K., "Natural Convection Heat Transfer in Short Vertical Channels Including the Effects of Stagger," *Proceedings, Third International Heat Transfer Conference*, Vol. II, 1966, pp. 121–125.

14 Bahrami, P. A., "Natural Convection from Open- and Closed-Sided Vertical Plates and from Fin-Tube Configurations," Ph.D. Thesis, Department of Mechanical Engineering, University of Minnesota, 1979.

15 Sogin, H. H., "Sublimation from Disks to Air Streams Flowing Normal to their Surfaces," *Trans. ASME*, Vol. 80, 1958, pp. 61–71.

16 Churchill, S. W., and Chu, H. H. S., "Correlation Equations for Laminar and Turbulent Free Convection from a Vertical Plate," *International Journal of Heat and Mass Transfer*, Vol. 18, 1975, pp. 1323–1329.

Boundary Layer Regime for Laminar Free Convection between Horizontal Circular Cylinders

M. C. Jischke
M. Farshchi[1]

School of Aerospace, Mechanical, and Nuclear Engineering,
University of Oklahoma,
Norman, Okla.

The steady, buoyancy-driven, laminar motion induced in the annulus of two horizontal, concentric, circular cylinders by a difference in the boundary temperatures is studied analytically in the large Rayleigh number limit. The flowfield is divided into five physically distinct regions: (1) an inner free convection boundary layer near the inner cylinder, (2) an outer free convection boundary layer near the outer cylinder, (3) a vertical plume above the inner cylinder, (4) a stagnant region below the inner cylinder, and (5) a core region surrounded by the other four regions. Zeroth-order solutions which account for the coupling of those five regions are obtained in the high Prandtl number limit using a boundary-layer approximation and integral methods. Comparisons of the calculated heat transfer and temperature fields with experiment and numerical finite-difference results are favorable.

Introduction

Natural convection between concentric horizontal cylinders has been studied experimentally since 1931. Kuehn and Goldstein [1] presented a complete history of the many investigations made for horizontal circular cylinders.

Powe, et al. [2] delineated the various flow regimes that occur in air for different Grashof numbers and cylinder radius ratios. Four different flow patterns were observed: a steady crescent-shaped eddy pattern and three unsteady flow patterns which occurred when the Grashof number exceeded a critical value (for a given radius ratio). These results and those of Grigull and Hauf [3] and others suggested a steady, laminar boundary-layer regime is achieved in which most of the motion occurs in thin boundary layers on the cylinders and in a vertical plume above the inner cylinder if the Grashof number was of the order of 10^4 or larger (for air), but still less than the value at which unsteady behavior is observed.

Regular perturbation analyses based on the smallness of the Rayleigh number have been carried out by Mack and Bishop [4], Hodnett [5], Huetz and Petit [6], Rotem [7], and Singh and Elliott [8]. Raithby and Hollands [9] and Kuehn and Goldstein [10] have considered the high Rayleigh number boundary-layer limit with a conduction-layer model. Although these empirical analyses correlate data quite well, they do not allow determination of the temperature and velocity fields. In addition, they ignore the effects of the temperature variation in the core region between the two boundary layers on the inner and outer cylinders as well as the plume above the inner cylinder.

Kuehn and Goldstein [1] carried out measurements of the local heat transfer rate between two isothermal, horizontal, concentric cylinders of radius ratio 2.6 using air and water as the enclosed fluids. These results showed that a steady, laminar, boundary-layer regime exists for Rayleigh numbers (based on inner cylinder radius) between 5×10^3 and 2×10^5. Numerical calculations using a successive over-relaxation technique gave results which compare favorably with these results and the experiments of Powe, et al. [2]. The use of formal boundary-layer methods to analyze natural convection flows between concentric horizontal cylinders remains to be done.

In this paper we shall employ boundary-layer theory to analyze this flow. Our results represent zeroth-order asymptotic solutions, valid for high Rayleigh numbers.

Formulation

Consider the buoyancy-driven flow between two infinitely long, horizontal circular cylinders maintained at different temperatures. We shall assume the inner body at radius r_i to be at a higher temperature, T_i, than that of the outer body, T_o, with radius r_o. To solve for the temperature and velocity fields in the annulus, we will use the asymptotic methods of boundary-layer theory corresponding to the case of large buoyant forces relative to viscous forces; that is, large Rayleigh number. Experiment (e.g., [6] and [7]) suggests that in this high Rayleigh number limit the fluid flow region can be divided into five physically distinct regions (see Fig. 1).

1 *Stagnant Region:* Here the buoyancy forces inhibit fluid motion and heat transfer takes place largely by conduction.

2 *Inner Boundary Layer:* a very thin fluid layer near the inner cylinder in which buoyant forces and viscous forces dominate.

3 *Outer Boundary Layer:* another very thin fluid layer on the outer cylinder, in which buoyant forces and viscous forces dominate.

4 *Core Region:* an adiabatic, inviscid region bounded by the other four regions.

5 *Plume:* occurs between the bodies along the vertical line of symmetry above the inner cylinder; it is driven by buoyant forces and joins the inner boundary layer to the outer boundary layer.

Because of symmetry we consider only the right half of the annulus. In addition, we assume the flow to be two-dimensional and steady (see Fig. 2); $\mathbf{V}(r, \theta) = u(r, \theta)\hat{e}_r + v(r, \theta)\hat{e}_\theta$. It is convenient to introduce the following normalized flowfield variables,

$$\mathbf{V}' = \frac{\mathbf{V}}{(g\beta_*(T_i - T_o)r_i/\mathrm{Pr})^{1/2}}, \quad p' = \frac{p}{\rho_* g\beta_*(T_i - T_o)r_i} \tag{1}$$

$$T' = \frac{T - T_o}{T_i - T_o}, \quad r' = \frac{r}{r_i}$$

This temperature normalization is dictated by the imposed boundary conditions. The pressure normalization then follows from the requirement of a pressure-buoyancy force balance in the core where, for high Rayleigh number, viscous forces are relatively unimportant. If we further require that viscous and buoyant forces balance in any thin boundary layer and that convection and conduction of energy balance there also, the above scaling for the velocity results as does the conclusion that the boundary layer thickness scales as $r_i\ \mathrm{Ra}^{-1/4}$ and the Rayleigh number Ra, as well as the Prandtl number Pr, emerge as the appropriate nondimensional parameters. The above velocity scale is necessarily a boundary layer scale; the resulting normalized velocity takes on its largest value in the boundary layer where it is of order unity. The velocity scale in the core is of order $\mathrm{Ra}^{-1/4}$ relative to that in the boundary layer since the core motion is a consequence of the feeding and draining of the boundary layers.

[1] Present address: Mechanical Engineering Department, University of California at Berkeley, Berkeley, Calif.

Contributed by The Heat Transfer Division for publication in the JOURNAL OF HEAT TRANSFER. Manuscript received by the Heat Transfer Division September 21, 1979.

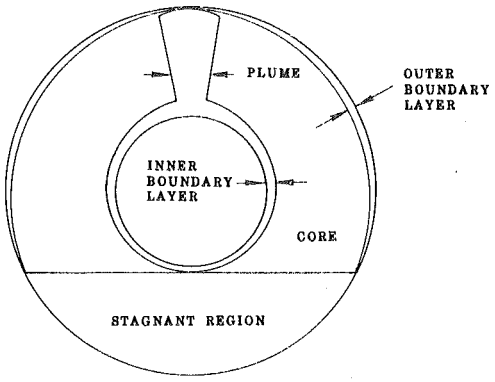

Fig. 1 Flow regions in the annuli of concentric cylinders at high Rayleigh numbers

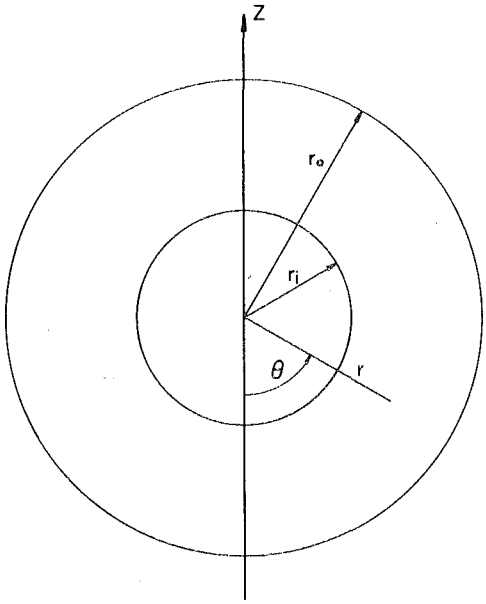

Fig. 2 Flow geometry

The equations expressing conservation of mass, Newton's second law, and the first law of thermodynamics now become, dropping the prime notation for convenience,

$$\nabla \cdot \mathbf{V} = 0 \tag{2}$$

$$\mathrm{Pr}^{-1}\mathbf{V} \cdot \nabla \mathbf{V} = -\nabla p + T\hat{e}_z + \mathrm{Ra}^{-1/2}\nabla^2 \mathbf{V} \tag{3}$$

$$\mathbf{V} \cdot \nabla T = \mathrm{Ra}^{-1/2}\nabla^2 T \tag{4}$$

Here we have employed the usual Boussinesq approximation and have ignored viscous dissipation which is appropriate for most free convection problems. The associated boundary conditions are

$$r = 1: \mathbf{V} = T = 0 \tag{5}$$

$$r = R: \mathbf{V} = 0, T = 1 \tag{6}$$

Here $R = r_o/r_i$ is the radius ratio and $\mathrm{Ra} = g\beta\Delta T r_i^3/\nu\alpha$ is the Rayleigh number. $\mathrm{Pr} = \nu/\alpha$ is the Prandtl number. To proceed, we will take advantage of the largeness of the Rayleigh number and develop simplified equations for each of the five distinct regions of the flow. The results for these five regions will then be coupled by means of a matching procedure from which the entire flowfield may be deduced.

Core Region. The core region has a velocity scale of order $\mathrm{Ra}^{-1/4}$ determined by entrainment into and extrainment out of the boundary layers. Thus, we introduce core variables, denoted by a subscript c, as

$$\mathbf{V}_c = \mathrm{Ra}^{1/4}\mathbf{V}, p_c = p, T_c = T \tag{7}$$

which are of order unity in the limit of infinite Rayleigh number. Rewriting the conservation equations in terms of these new core variables, and taking the limit $\mathrm{Ra} \to \infty$, we then obtain the lowest-order core equations as

$$\nabla \cdot \mathbf{V}_c = 0 \tag{8}$$

$$0 = -\nabla p_c + T_c\hat{e}_z \tag{9}$$

$$\mathbf{V}_c \cdot \nabla T_c = 0 \tag{10}$$

the solution of which is

$$p = p_c(z), T = T_c(z), \mathbf{V} = \mathbf{V}_c(z) \tag{11}$$

where the functions of z are unknown and remain to be determined.

Introducing the streamfunction ψ such that $\mathbf{V} = \hat{e}_x x \nabla\psi$, we find that the streamfunction in the core is of the order of $\mathrm{Ra}^{-1/4}$ and can be expressed as $\psi = \mathrm{Ra}^{-1/4}\psi_c(z)$. Equations (11) imply that the core is stratified in the vertical direction. The result for the streamfunction implies plugging; that is, the streamlines are all horizontal in the core and the velocity in the core does not have a vertical component. Thus, the velocity of a fluid particle emerging from the outer boundary layer must be equal to the velocity of the same fluid particle as it is entrained into the inner boundary layer (or plume) at the same elevation, z. This result will be important in the subsequent analysis.

Inner Boundary Layer. The core solution cannot be made to satisfy the boundary conditions on the inner and outer surfaces. The infinite Rayleigh number limit is singular in that the order of the governing equations is reduced from six to two. This dilemma is a familiar one and can be resolved with the introduction of thin boundary layers and shear layers in which the effects of viscous forces and heat conduction are important.

Nomenclature

a,b = constants (see equation (35))
A = boundary layer velocity profile parameter
C = constant (see equations (57, 58))
$\hat{e}_r,\hat{e}_\theta$ = unit vectors in cylindrical coordinate system
$\hat{e}_y,\hat{e}_z$ = unit vectors in rectangular coordinate system
$\hat{e}_x$ = unit vector perpendicular to plane of flow
F,G = velocity profile functions
g = gravitational acceleration
k = thermal conductivity
Nu = Nusselt number, $qr_i/k\Delta T$
p = pressure
Pr = Prandtl number, ν/α
q = radial heat flux
r,θ = radial and polar cylindrical coordinates, respectively
R = radius ratio (r_o/r_i)
Ra = Rayleigh number, $r_i^3 g\beta\Delta T/\nu\alpha$
T = temperature
u,v = velocity components in r,θ directions, respectively
$\mathbf{V}$ = total velocity
V,W = velocity components in y,z directions, respectively
y,z = horizontal and vertical cartesian coordinates, respectively
α = thermal diffusivity
β = volumetric coefficient of expansion
δ = reference boundary layer thickness
Δ = measure of boundary layer thickness
ΔT = reference temperature difference
ζ = normalized boundary layer coordinate
ν = kinematic viscosity
ξ = normalized plume variable
ρ = density
ψ = streamfunction

Subscripts

c = core variable
cond = conduction value
conv = convection value
$\mathbb{C}$ = plume centerline
i = inner boundary layer
o = outer boundary layer
p = plume
$*$ = reference condition

As noted earlier, in laminar free convection flows the thickness of vertical free convection boundary layers is proportional to $Ra^{-1/4}$. Thus, to study the boundary layer on the inner cylinder we introduce inner variables r_i, u_i, v_i, T_i, and p_i as

$$r_i = Ra^{1/4}(r-1), u_i = Ra^{1/4}u, v_i = v, T_i = T, p_i = p, \psi_i = Ra^{1/4}\psi \tag{12}$$

which are of order unity in the inner boundary layer compared to $Ra^{-1/4}$ as $Ra \to \infty$. Substituting these expressions into equations (2–4) and letting $Ra \to \infty$ with the inner variables held fixed, we obtain the lowest-order inner boundary-layer equations as

$$\frac{\partial u_i}{\partial r_i} + \frac{\partial v_i}{\partial \theta} = 0 \tag{13}$$

$$Pr^{-1}\left(u_i\frac{\partial v_i}{\partial r_i} + v_i\frac{\partial v_i}{\partial \theta}\right) = (T_i - T_c)\sin\theta + \frac{\partial^2 v_i}{\partial {r_i}^2} \tag{14}$$

$$u_i\frac{\partial T_i}{\partial r_i} + v_i\frac{\partial T_i}{\partial \theta} = \frac{\partial^2 T_i}{\partial {r_i}^2} \tag{15}$$

with boundary conditions

$$r_i = 0 : u_i = v_i = 0, T_i = 1$$
$$r_i \to \infty : v_i \to 0, T_i \to T_c \tag{16}$$

The boundary conditions for $r_i \to \infty$ are derived from the asymptotic matching of the boundary layer and core region solutions. We have eliminated the pressure gradient from (14) by making use of the fact that the pressure does not vary, to lowest order, across the boundary layer and is given by the core solution.

Outer Boundary Layer. Here we define outer variables

$$r_o = Ra^{1/4}(R - r), u_o = -Ra^{1/4}u, v_o = v$$
$$T_o = T, p_o = p, \psi_o = Ra^{1/4}\psi \tag{17}$$

which are of order unity in the outer boundary layer in the limit $Ra \to \infty$.[2] Substituting these expressions into equations (3–5) and letting $Ra \to \infty$ with the outer variables held fixed, we obtain the lowest-order outer boundary-layer equations as

$$\frac{\partial u_o}{\partial r_o} + \frac{1}{R}\frac{\partial v_o}{\partial \theta} = 0 \tag{18}$$

$$Pr^{-1}\left(u_o,\frac{\partial v_o}{\partial r_o} + \frac{v_o}{R}\frac{\partial v_o}{\partial \theta}\right) = (T_o - T_c)\sin\theta + \frac{\partial^2 v_o}{\partial {r_0}^2} \tag{19}$$

$$u_o\frac{\partial T_o}{\partial r_o} + \frac{v_o}{R}\frac{\partial T_o}{\partial \theta\partial} = \frac{\partial^2 T_o}{\partial {r_o}^2} \tag{20}$$

with boundary conditions

$$r_o = 0 : u_o = v_o = T_o = 0$$
$$r_o \to \infty : v_o \to 0, T_o \to T_c \tag{21}$$

Plume. Experiments suggest the existence of a plume above the inner cylinder. This plume links the boundary layers on the inner and outer surfaces. For the cylindrical annulus we envision a two-dimensional vertical plume above the inner cylinder. We introduce cartesian coordinates y and z perpendicular to and along the plume centerline which is in the vertical direction through the highest point on the inner cylinder. The y and z velocity components are denoted V and W, respectively. Conservation of mass for this two-dimensional flow requires that the plume thickness be of the same order of magnitude as the boundary layer thickness on the inner cylinder (e.g., of the order $Ra^{-1/4}$). Thus, we introduce cartesian plume variables y_p, z_p, V_p, W_p, T_p, p_p, ψ_p as

$$y_p = Ra^{1/4}y, z_p = z, V_p = Ra^{1/4}V, W_p = W$$
$$T_p = T, p_p = p, \psi_p = Ra^{1/4}\psi \tag{22}$$

which are of order unity compared to $Ra^{-1/4}$ as $Ra \to \infty$. Substituting these expressions into the governing conservation equations and letting $Ra \to \infty$ with the plume variables held fixed, we obtain the lowest order equations for the plume as

$$\frac{\partial V_p}{\partial y_p} + \frac{\partial W_p}{\partial z_p} = 0 \tag{23}$$

$$Pr^{-1}\left(V_p\frac{\partial W_p}{\partial y_p} + W_p\frac{\partial W_p}{\partial z_p}\right) = T_p - T_c + \frac{\partial^2 W_p}{\partial {y_p}^2} \tag{24}$$

$$V_p\frac{\partial T_p}{\partial y_p} + W_p\frac{\partial T_p}{\partial z_p} = \frac{\partial^2 T_p}{\partial {y_p}^2} \tag{25}$$

with boundary conditions

$$y_p = 0 : V_p = \frac{\partial W_p}{\partial y_p} = \frac{\partial T_p}{\partial y_p} = 0$$
$$y_p \to \infty : W_p \to 0, T_p \to T_c \tag{26}$$

The latter two conditions at the plume centerline follow from symmetry there.

We have now derived the equations governing the various flow regions. These equations are coupled to each other and cannot be solved independently. In particular, the driving force in the boundary layers and plume is the difference between the local temperature T and the core temperature $T_c(z)$, which is unknown a priori. To proceed, we shall first develop solutions for the inner and outer boundary layers and plume for arbitrary core conditions. Then, invoking a global matching condition where, at every elevation z, the temperature and streamfunction at the edges of the boundary layers and plume are equated, equations governing the core temperature and streamfunction are developed and subsequently solved. The boundary-layer and plume solutions are then completely determined and other quantities of interest such as the heat transfer can be evaluated.

Approximate Solution by Means of an Integral Method ($Pr \to \infty$)

To preceed, we must develop solutions for the boundary layers and plume for arbitrary core conditions. There appears to be no known exact analytical method for explicitly solving the boundary-layer and plume equations for arbitrary core conditions. There are, however, several approximate methods, of which we have chosen the integral method due to Blythe and Simpkins [11] for its simplicity and generality.

We shall assume in our analysis that the fluid has a large Prandtl number. Many important fluids (e.g., glycerin and most oils) possess a large Prandtl number and are accurately described by an infinite Prandtl number approximation. By taking the Prandtl number to infinity, we drop the nonlinear convection terms in the momentum equation and thereby simplify the governing equations.

The inner boundary-layer equations (13–15), can be rewritten for infinite Prandtl number as

$$\frac{\partial u_i}{\partial r_i} + \frac{\partial v_i}{\partial \theta} = 0 \tag{27}$$

$$0 = (T_i - T_c)\sin\theta + \frac{\partial^2 v_i}{\partial {r_i}^2} \tag{28}$$

$$\frac{\partial}{\partial r_i}(u_iT_i) + \frac{\partial}{\partial \theta}(v_iT_i) = \frac{\partial^2 T_i}{\partial {r_i}^2} \tag{29}$$

with boundary equations given by equations (16). To develop the integral form of these equations, we first integrate (27) across the boundary layer (e.g. from $r_i = 0$ to $r_i = \infty$) and obtain

$$\psi_c = \int_0^\infty v_i dr_i \tag{30}$$

[2] The fact that we have assumed a similar scaling, with respect to the Rayleigh number, for the velocity and streamfunction in the inner and outer boundary layers does not mean the velocities have the same scaling with respect to the radius ratio R. Indeed, mass conservation requires the velocity in the outer boundary layer to be lower than that in the inner boundary layer by a factor of R^{-1}.

A similar integration of (29) across the boundary layer gives, after some manipulation,

$$\psi_c \frac{dT_c}{d\theta} + \frac{d}{d\theta}\int_0^\infty v_i(T_i - T_c)dr_i = -\left.\frac{\partial T_i}{\partial r_i}\right)_{r_i=0} \tag{31}$$

Multiplying (28) by $v_i/\sin\theta$ and integrating the result across the boundary layer, we have, after an integration by parts,

$$\int_0^\infty v_i(T_i - T_c)dr_i = \frac{1}{\sin\theta}\int_0^\infty \left(\frac{\partial v_i}{\partial r_i}\right) dr_i \tag{32}$$

Eliminating the integral of $v_i(T_i - T_c)$ from (31) by means of (32), we have

$$\psi_c \frac{dT_c}{d\theta} + \frac{d}{d\theta}\left[\frac{1}{\sin\theta}\int_0^\infty \left(\frac{\partial v_i}{\partial r_i}\right) dr_i\right] = \left.\frac{1}{\sin\theta}\frac{\partial^3 v_i}{\partial {r_i}^3}\right)_{r_i=0} \tag{33}$$

where we have eliminated $\partial T_i/\partial r_i$ by evaluating the r_i derivative of (28) at $r_i = 0$. Equation (33) has the virtue of involving the tangential velocity profile v_i only. The temperature T_i has been eliminated.

It is possible to use the boundary conditions given by (16) and the governing equations to obtain boundary conditions on the tangential velocity v_i. These boundary conditions are

$$r_i = 0 : v_i = 0, \frac{\partial^2 v_i}{\partial {r_i}^2} = -(1 - T_c)\sin\theta, \frac{\partial^4 v_i}{\partial {r_i}^4} = 0$$

$$r_i \to \infty : v_i, \frac{\partial v_i}{\partial r_i}, \ldots \to 0 \tag{34}$$

To proceed, we must assume a profile for the tangential velocity v_i; we use $v_i(r_i, \theta) = A_i(\theta)F(\xi_i)$ where A_i is positive and $\xi_i = r_i/\Delta_i(\theta)$. Here Δ_i measures the inner boundary layer thickness. The function F describes the assumed velocity profile shape. We shall normalize F so that the integral of F across the boundary layer equals unity. Substituting the profile for v_i into (30), we obtain $A_i = \psi_c/\Delta_i$. Evaluating (28) at $r_i = 0$, we also have ${\Delta_i}^3 = F''(0)\psi_c csc\theta/(1 - T_c)$. Thus, the parameters describing the velocity profile, A_i and Δ_i, can be expressed in terms of the a priori unknown core streamfunction ψ_c and temperature T_c. Substituting the assumed form for v_i into (33) and eliminating A_i and Δ_i, we have

$$a\frac{d}{d\theta}[\psi_c(1 - T_c)] = b{\psi_c}^{-1/3}(1 - T_c)^{4/3}(\sin\theta)^{1/3} - \psi_c\frac{dT_c}{d\theta} \tag{35}$$

where the constants a and b depend on the chosen profile function F and are given by

$$a = \frac{\int_0^\infty F'^2 d\xi_i}{-F''(0)}, \quad b = \frac{F'''(0)}{(-F''(0))^{4/3}}$$

The boundary conditions on the tangential velocity v_i lead to conditions on the profile function F,

$$F(o) = F^{(4)}(o) = 0$$

$$F(\infty) = F'(\infty) = F''(\infty) = \ldots = 0 \tag{36}$$

In addition, F must satisfy the normalization condition. Motivated by linear theory results, we choose $F = 2e^{-\xi i}\sin\xi_i$. This choice for F yields $a = 1/4$ and $b = (1/4)^{1/3}$.

Thus, the structure of this inner boundary layer depends upon the solution of (35) which involves the two unknowns ψ_c and T_c. In the usual boundary-layer calculation for external flows, T_c is known and ψ_c can then be calculated. In internal flows, both T_c and ψ_c are unknown and thus, by itself, (35) cannot be used to determine the inner boundary-layer solution. Rather, a similar analysis for the outer boundary layer will yield a second equation involving ψ_c and T_c which, together with (35), allows determination of the core solution and then the associated boundary-layer solutions.

It is convenient here to develop the expression for the surface heat transfer. In dimensional form, the surface heat flux q is given by

$$q = -k\left.\frac{\partial T}{\partial r}\right)_{r=r_i} \tag{37}$$

In terms of nondimensional inner variables, we have

$$q = -\frac{k\Delta T \mathrm{Ra}^{1/4}}{r_i}\left.\left(\frac{\partial T_i}{\partial r_i}\right)\right)_{r_i=0} \tag{38}$$

where ΔT is the difference in the temperatures of the inner and outer cylinders. We define the Nusselt number Nu as $qr_i/k\Delta T$. Evaluating the r_i derivative of (28) at $r_i = 0$, we obtain, after manipulation,

$$\mathrm{Nu}\,\mathrm{Ra}^{-1/4} = 4^{-1/3}{\psi_c}^{-1/3}(\sin\theta)^{1/3}(1 - T_c)^{4/3} \tag{39}$$

An analysis of the outer boundary layer, identical to that used to derive equation (35) yields

$$a\frac{d}{d\theta}[\psi_c T_c] = -bR{\psi_c}^{-1/3}{T_c}^{4/3}(\sin\theta)^{1/3} + \psi_c\frac{dT_c}{d\theta} \tag{40}$$

Equation (40) is a second equation relating the core streamfunction and temperature. Thus for $z^2 \leq 1$, corresponding to the region where the outer boundary layer extrains fluid through the core into the inner boundary layer, (35) and (40) can be solved for ψ_c and T_c. For $z > 1$, we cannot use the inner boundary-layer equation (35), but most instead use an analogous result for the plume.

The lowest-order equations for the plume, (23–25), become in the infinite Prandtl number limit,

$$\frac{\partial V_p}{\partial y_p} + \frac{\partial W_p}{\partial z_p} = 0 \tag{41}$$

$$0 = T_p - T_c + \frac{\partial^2 W_p}{\partial {y_p}^2} \tag{42}$$

$$\frac{\partial}{\partial y_p}(V_p T_p) + \frac{\partial}{\partial z_p}(W_p T_p) = \frac{\partial^2 T_p}{\partial {y_p}^2} \tag{43}$$

with boundary conditions given by (26). To apply the integral method, we integrate these equations across half of the plume (from $y_p = 0$ to $y_p = \infty$). After some manipulation, we obtain

$$\psi_c\frac{dT_c}{dz} + \frac{d}{dz}\int_0^\infty \left(\frac{\partial W_p}{\partial y_p}\right)^2 dy_p = 0 \tag{44}$$

and

$$\psi_c = \int_0^\infty W_p dy_p \tag{45}$$

The boundary conditions and plume equations give the following boundary conditions on the vertical velocity W_p,

$$y_p = 0 : \frac{\partial W_p}{\partial y_p} = \frac{\partial^3 W_p}{\partial {y_p}^3} = \frac{\partial^5 W_p}{\partial {y_p}^5} = 0$$

$$y_p \to \infty : W_p, \frac{\partial W_p}{\partial y_p}, \frac{\partial^2 W_p}{\partial {y_p}^2}, \ldots \to 0 \tag{46}$$

To proceed, we assume the vertical velocity W_p has the form $A_p(z)$-$G(\xi)$, where $\xi = y_p/\Delta_p(z)$. Here Δ_p measures the half-width of the plume. The profile shape function G is normalized so that its integral over half the plume (from $\xi = 0$ to ∞) equals unity. The boundary conditions on W_p require that G satisfy

$$\xi = 0 : G' = G''' = G^{(5)} = 0$$

$$\xi \to \infty : G, G' = G'' \to 0 \tag{47}$$

A suitable function G that satisfies these conditions is $2e^{1/4}e^{-\xi^2}\cos\xi/\sqrt{\pi}$. Substituting for W in (45) and (42) (evaluated at $y_p = 0$), we have $A_p = \psi_c/\Delta_p$ and ${\Delta_p}^3 = -\psi_c G''(o)/(T_\ell - T_c)$, where $T_\ell = T_p(0, z_p)$ is the plume centerline temperature. Substituting the expression for W into (44), eliminating A_p and Δ_p, we obtain

$$\psi_c\frac{dT_c}{dz} + a_p\frac{d}{dz}[\psi_c(T_\ell - T_c)] = 0 \tag{48}$$

where the constant a_p is given by

$$a_p = -\frac{\int_o G'^2 d\xi}{G''(0)} \tag{49}$$

Using the above expression for the function G, we find that $a_p = 0.3945$.

Equation (48) involves the plume centerline temperature T_ℓ which is unknown. An equation for T_ℓ can be developed by first differentiating the momentum equation twice with respect to y_p, eliminating $\partial^2 T_p/\partial {y_p}^2$ using the energy equation, and then evaluating the result at $y_p = 0$. The resulting equation is

$$\left.\frac{\partial^2 W_p}{\partial {y_p}^4}\right)_{y_p=0} = -\left. W_p\right)_{y_p=0} \frac{dT_\ell}{dz} \tag{50}$$

Substituting for W_p and eliminating A_p and Δ_p, we finally have

$$\frac{dT_\ell}{dz} + b_p \left[\frac{T_\ell - T_c}{\psi_c}\right]^{4/3} = 0 \tag{51}$$

where the constant b_p is given by

$$b_p = \frac{G^{(4)}(0)}{G(0)(-G''(0))^{4/3}} \tag{52}$$

Using the given expression for the function G, b_p takes the value 3.5242.

Equations (48) and (51) provide two ordinary differential equations for the three unknowns T_c, T_ℓ, and ψ_c. When coupled with (40) from the outer boundary-layer analysis, they provide a means for determining the core solution in the region above the inner cylinder ($1 \leq z \leq R$).

The analysis of this high Rayleigh number, boundary-layer-driven flow in the annulus of two horizontal concentric cylinders has now been reduced to the solution of a system of ordinary differential equations for the core streamfunction $\psi_c(z)$, the core temperature $T_c(z)$, and the plume centerline temperature $T_\ell(z)$. In the region $z^2 \leq 1$ (e.g., the region bounded by horizontal planes tangent to the high and low points of the inner cylinder), (35) and (40) can be solved for T_c and ψ_c. In the region $1 \leq z \leq R$, (40), (48), and (51) can be solved for T_c, ψ_c, and T_ℓ. It is important conceptually to recognize that the coupling of the outer bounday-layer equation with the inner boundary-layer equation for $z^2 \leq 1$ and with plume equations for $1 \leq z \leq R$ is equivalent to a global matching condition. That is, the core conditions at the outer edge of the inner boundary layer and plume must be the same as the core conditions at the outer edge of the outer boundary layer *at the same elevation* z since the core solution depends on z only.

It is therefore convenient to rewrite (35) and (40) in terms of z rather than θ. On the inner cylinder $z = -\cos\theta$ while on the outer cylinder $z = -R\cos\theta$. Using these results, we can rewrite (35) and (40) as

$$a\frac{d}{dz}[\psi_c(1 - T_c)] + \psi_c \frac{dT_c}{dz} = b{\psi_c}^{-1/3}(1 - T_c)^{4/3}(1 - z^2)^{-1/3} \tag{53}$$

$$a\frac{d}{dz}[\psi_c T_c] - \psi_c \frac{dT_c}{dz} = -bR{\psi_c}^{-1/3}{T_c}^{4/3}(1 - z^2/R^2)^{-1/3} \tag{54}$$

which govern the core region in $z^2 \leq 1$. In the region $1 \leq z \leq R$, we replace (53) with (48) and (51). Once these equations are solved, the structure of the boundary layers and plume can be determined and the heat transfer evaluated. To complete the formulation, we must specify initial conditions.

In the high Rayleigh number limit, the thickness of any interior shear layer, such as that between the core and stagnant region, must go to zero. Thus, to lowest order, continuity of the temperature and streamfunction require

$$\psi_c(z = -1) = T_c(z = -1) = 0 \tag{55}$$

which provide initial conditions for (53) and (54) at $z = -1$. However, these equations are singular at $z = -1$ and asymptotic solutions valid near $z = -1$ must be obtained. Adding (53) and (54), we obtain near $z = -1$,

$$\psi_c \sim \left(\frac{b}{a}\right)^{3/4}(2(1 + z))^{1/2} \tag{56}$$

Near $z = -1$, the right-hand-side of (54) is negligibly small. Integration of (54) then yields

$$T_c \sim C{\psi_c}^{a/1-a} \tag{57}$$

where C is an arbitrary constant of integration. Note that the initial conditions (55) are satisfied for any choice of C. Indeed, it appears that there is no condition at $z = -1$ that can be imposed to determine C. We will return to the question of the determination of C shortly.

We also required initial conditions at $z = 1$ for the integration of the plume and outer boundary-layer equations. Continuity of the core streamfunction and temperature give

$$\psi_c(z = 1+) = \psi_c(z = 1-),\ T_c(z = 1+) = T_c(z = 1-) \tag{58}$$

In addition, the initial value of the plume centerline temperature, $T_\ell(1)$, is needed. To determine $T_\ell(1)$, we assume the energy flux convected out of the top of the inner cylinder boundary layer must equal the energy flux convected into the plume. Thus,

$$\int_0^\infty v_i(T_i - T_c)dr_i = \int_0^\infty W_p(T_p - T_c)dy_p \text{ at } z = 1 \tag{59}$$

Using (26) and (42), and some minor manipulation, we can rewrite this energy flux continuity condition as,

$$T_\ell(z = 1) = \frac{a}{a_p} + \left(1 - \frac{a}{a_p}\right) T_c(z = 1) \tag{60}$$

Since $T_c(1) < 1$, we have that $T_\ell(1) > T_c(1)$. Thus, the plume is initially warmer than the core, and the fluid in the plume is driven upward by the buoyant force. Equations (54) and (60) provide the necessary initial conditions for the core region above the inner cylinder.

Except for the determination of the constant C, our formulation of the problem is now complete. Indeed it is possible to determine a solution of the equations that satisfies the given initial conditions for any value of C. Thus, to render the calculation completely determinate, we must find an additional condition so that C can be determined.

To see how this might be done, it is instructive to first consider how the constant C affects the solution. If C is greater than a critical value, the plume generated above the inner cylinder stops rising at some point between the two cylinders. Presumably the fluid above this elevation is stagnant with a temperature equal to that of the cool outer cylinder. This is, of course, an unstable situation which is unlikely to occur at steady state. If the constant C is less than the critical value, the plume reaches the outer cylinder with a finite velocity. The transition to zero vertical velocity at the top of the outer cylinder would have to occur through a "shock-like" boundary layer for which there is no experimental evidence. In addition, it is unlikely that fluid with an infinite Prandtl number could have such a shock-like structure. There is, however, a critical value of C for which the plume ceases rising just as it meets the outer cylinder. In this case there is neither an unstable temperature distribution nor a need for a shock-like transition near the top of the outer cylinder. Thus, we propose to determine the constant C by requiring that $W_p(z = R) = 0$. This is equivalent to requiring the plume centerline temperature T_ℓ to be equal to the core temperature T_c at $z = R$ or having ψ_c vanish there. Numerical results show that it is always possible to choose C so that this condition is satisfied.

The numerical procedure used was to first fix R and guess C. Equations (53) and (54) were integrated from $z = -1+$ to $z = +1$ by means of a fourth-order Runge Kutta method. Equations (56) and (57) were used for the initial conditions at $z = -1+$. The values of T_c and ψ_c thus obtained at $z = 1$ along with (60) provided initial conditions for the numerical integration of (48, 51), and (54) near $z = 1$ to $z = R$. If the values of T_c and T_ℓ differ at $z = R$, a new value of C is chosen and the process is repeated. This is continued until the dif-

ference between T_c and T_t at $z = R$ is less than some small amount.

Results and Discussion. Numerical results have been obtained for cylinder radius ratios R varying from 1.5 to 10. In all cases, it was possible to determine a value of C for which the terminating condition is satisfied. Figure 3 shows the variation of C with R. As the radius ratio increases, C decreases. It is interesting to note that $W_p(R)$ has a very sensitive dependence upon C. It was necessary to determine C to six decimal places in order to have $W_p(R)$ less than 0.001.

The variation of the core streamfunction ψ_c and temperature T_c with height z are shown in Figs. 4 and 5 for $R = 2.6$ (a case for which Kuehn and Goldstein [1] have conducted experiments and carried out numerical solutions using finite difference methods). The maximum value of the core streamfunction is achieved at $z = 1.23$ which is somewhat less than the value 1.36 measured by Kuehn and Goldstein in air for $\mathrm{Ra} = 4.7 \times 10^4$. Note that the calculated core temperature does not reach the outer cylinder temperature. Presumably this difference is resolved through a thin thermal boundary layer near the top of the outer cylinder.

While the calculated core streamfunction and temperature are continuous, their derivatives are not. These derivatives correspond to the horizontal velocity and the vertical heat flux. Both ψ_c and T_c possess infinite derivatives at $z = -1$ and $z = R$, corresponding to the usual singular behavior of boundary layers near leading and trailing edges. Similar results are obtained by Gill [12] at the leading and trailing edges of the vertical walls of a rectangular cavity. The derivatives of ψ_c and T_c are discontinuous at $z = 1$, the plane tangent to the top of the inner cylinder. As discussed by Jischke and Doty [13], these discontinuities arise when the cross-sectional area of the fluid region has a discontinuous derivative. In practice, the singularities at $z = \pm 1, R$ are made finite by internal shear layers in which diffusive phenomena are important. Nonetheless, the large values of the horizontal velocity near $z = -1, R$ imply most of the mass transport occurs near these locations.

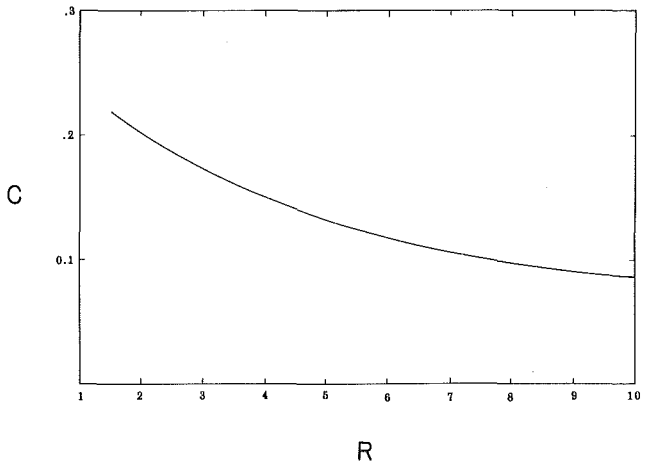

Fig. 3 Variation of the constant C with the cylinder radius ratio R

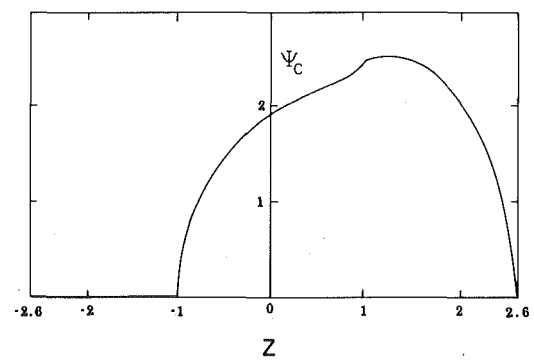

Fig. 4 Core streamfunction versus height ($R = 2.6$)

Comparisons of theory with experiment are most readily made for the heat transfer. Figure 6 shows the variation of the heat transfer with angle θ on the inner cylinder. The heat transfer is given in terms of the Nusselt number for free convection, $\mathrm{Nu}_{\mathrm{conv}}$, relative to the value of the Nusselt number for pure conduction, $\mathrm{Nu}_{\mathrm{cond}} = (\ln R)^{-1}$. Figure 6 shows the present infinite Prandtl number theory result (the solid line) and the Kuehn and Goldstein experimental results for a cylindrical annulus ($R = 2.6$) with air as the working fluid. The Prandtl number of air is 0.706 which is not large. Nonetheless, the trend of the variation with θ is given correctly by the theory. The discrepancy between the present theory and experiment can be reduced by correcting the present theory for finite Prandtl number. To do so, we use the empirical correlation developed by Raithby and Hollands [9],

$$\frac{\mathrm{Nu}}{\mathrm{Nu}_{\mathrm{Pr}=\infty}} = \left(\frac{\mathrm{Pr}}{0.861 + \mathrm{Pr}}\right)^{1/4} \tag{61}$$

The corrected results for the heat transfer are shown as a dashed line in Fig. 6. The comparison between the corrected theory and experiment is now rather good and suggests the high-Rayleigh-number flow structure we have calculated is correct in its essential features. The discrepancy near $\theta = 0$ is likely due to the inaccuracy with which the stagnation point condition is calculated. We have ignored both the effects of the internal shear layer near $z = -1$ and the different character of the tangential velocity profile near the stagnation point. Both effects likely contribute to the error. Also shown in Fig. 6 are the numerical results of Kuehn and Goldstein [1] for $\mathrm{Ra} = 5 \times 10^4$, $R = 2.6$, and $\mathrm{Pr} = 5$. While the trend of the heat transfer remains the same, the present theory is roughly 25 percent above these numerical results.

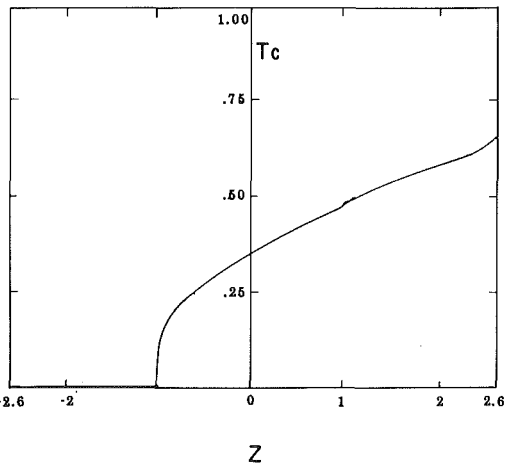

Fig. 5 Core temperature versus height ($R = 2.6$)

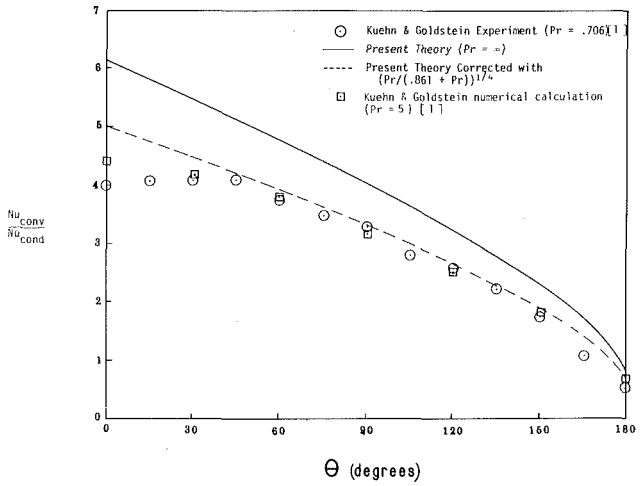

Fig. 6 Variation of the local Nusselt number with θ on the inner cylinder (Ra $= 4.7 \times 10^4$, $R = 2.6$)

A similar discrepancy occurs between the experimental measurements of the overall heat transfer for water in reference [1] and their numerical results.

A comparison of the local heat transfer rate on the outer cylinder with the experimental results of Kuehn and Goldstein [1], shown in Fig. 7, is not nearly as good. The overall heat transfer rate is still accurately predicted because it is constrained to be equal to that on the inner cylinder. We attribute the inaccuracy of the calculation of the distribution of the heat transfer on the outer cylinder, at least in part, to the neglect of the effects of the initial thermal boundary layer at the top of the outer cylinder due to plume impingement there. It is likely that the outer cylinder boundary layer near $\theta = \pi$ has a double layer structure that is rather complex in detail.

Figure 8 gives the theoretically calculated average Nusselt number for free convection, $\overline{\mathrm{Nu}}_{\mathrm{conv}}$,

$$\overline{\mathrm{Nu}}_{\mathrm{conv}} = \frac{1}{\pi}\int_0^{\pi} \mathrm{Nu}_{\mathrm{conv}} d\theta$$

(relative to the Nusselt number for pure conduction) and compares this result with experimental data from Kraussold [14] for oils with Prandtl numbers between 100 and 800, experimental data from Kuehn and Goldstein [1] for water with Prandtl number equal to 5.6, an empirical correlation due to Itoh, et al. [15], which in the present notation is

$$\mathrm{Ra}^{-1/4}\frac{\overline{\mathrm{Nu}}_{\mathrm{conv}}}{\mathrm{Nu}_{\mathrm{cond}}} = 0.20\, R^{3/8}(\ln R)^{3/4}$$

and an approximate theoretical result due to Raithby and Hollands [9], which is

$$\mathrm{Ra}^{-1/4}\frac{\overline{\mathrm{Nu}}_{\mathrm{conv}}}{\mathrm{Nu}_{\mathrm{cond}}} = 0.649(1 + R^{-3/5})^{-5/4}\ln R$$

The comparison of the present with Kraussold's experiments, Kuehn and Goldstein's experiments, and the empirical correlation of Itoh, et al. is excellent over the range of R calculated. Kuehn and Goldstein's experimental result for the overall heat transfer in water is about nine percent greater than our theoretical value (0.2888 compared to 0.2656), which we take to be rather good agreement. The trend exhibited by the Raithby and Hollands theory is similar to the other results although it appears to be somewhat high and thus less accurate.

In the limit $R \to \infty$, we expect the inner cylinder heat transfer to approach that of an isolated cylinder. If we take $T_c = 0$ near the inner cylinder, as it would be with $C \to 0$ when $R \to \infty$, the inner boundary layer equation, (53), can be solved explicitly for ψ_c, from which the average Nusselt number can be evaluated. The result is

$$\mathrm{Ra}^{-1/4}\overline{\mathrm{Nu}}_{\mathrm{conv}} = 0.402$$

which can be compared with the empirical value of 0.436 quoted by Kuehn and Goldstein [10].

The generally good comparison between theory and experiment lead us to conclude that the high Rayleigh number, boundary-layer model we have proposed is correct in its essential features. While certain details such as the internal shear layers near $z = \pm 1$ and the thermal boundary layer at the top of the outer cylinder remain to be explored, the basic structure of the flow is well understood.

It is perhaps worth noting again that experimental observations [2] and numerical calculations [1] show the flow in the annulus of two concentric, horizontal circular cylinders becomes unsteady when the Rayleigh number exceeds some critical value. As the present approach appears to give steady solutions for all values of the radius ratio R, the origins of the unsteadiness may well lie in the stability of the flow calculated herein. In particular, the horizontal shear layers near $z = \pm 1$ and the plume are likely locations for instabilities to occur. This is a topic that requires further analysis and is currently under investigation.

Any other two-dimensional annular region should have a five-region steady flow structure similar to that of the circular cylinders provided the geometry does not introduce singularities such as might occur with

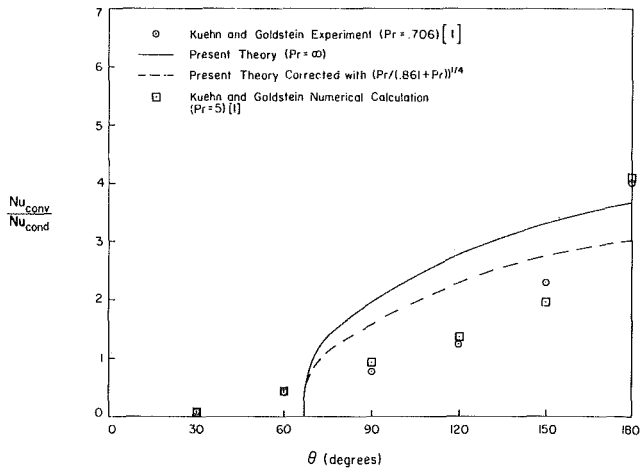

Fig. 7 Variation of the local Nusselt number with θ on the outer cylinder (Ra $= 4.7 \times 10^4$, $R = 2.6$)

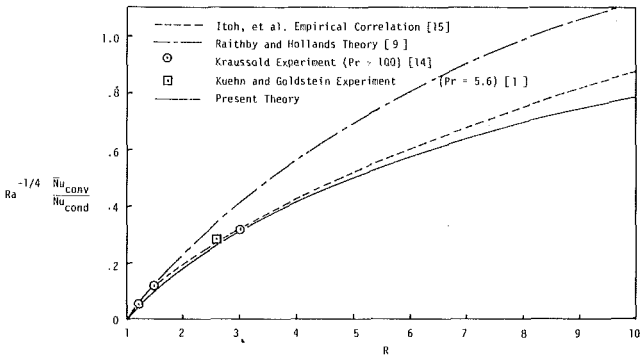

Fig. 8 Variation of Nusselt number with cylinder radius ratio

corners. The only differences will occur in the inner and outer boundary layers where the driving buoyancy force $(T - T_c)|\hat{n} \times \hat{e}_z|$ depends on the orientation of the surface. Given the geometry of the annulus, these boundary layers are easily computed with the integral method employed herein.

Concluding Remarks

A general means for analyzing high Rayleigh number free convection flows in two-dimensional annuli has been developed. While the details of the method are developed for concentric horizontal cylinders, the approach for any other two-dimensional annulus would be nearly identical. Comparison of the results obtained for cylinders with experiment suggest the essential features of the flow have been captured in this boundary-layer analysis. While certain higher-order features, such as internal shear layers, have been ignored, the basic flowfield structure and the heat transfer has been elucidated.

Acknowledgment

This research was performed under the auspices of NSF grant ENG-7410833.

References

1 Kuehn, T. H. and Goldstein, R. J., 1976, "An Experimental and Theoretical Study of Natural Convection in the Annulus Between Horizontal Concentric Cylinders," *Journal Fluid Mechanics*, Vol. 74, pp. 695–719.

2 Powe, R. E., Carley, C. T., and Bishop, E. H., 1969, "Free Convective Flow Patterns in Cylindrical Annuli," ASME JOURNAL HEAT TRANSFER, Vol. 91, pp. 310–314.

3 Grigall, V. and Hauf, W., 1966, W., 1966, "Natural Convection Between Horizontal Cylindrical Annuli," *Third International Heat Transfer Conference*, Chicago, Vol. 2, pp. 182–195.

4 Mack, L. R. and Bishop, E. H., 1968, "Natural Convection Between Horizontal Concentric Cylinders for Low Rayleigh Numbers," *Quarterly Journal Mechanics and Applied Mathematics*, Vol. 21, pp. 223–241.

5 Hodnett, P. F., 1973, "Natural Convection Between Horizontal Heated Concentric Circular Cylinders," *Journal Applied Mathematical Physics*, Vol. 24, pp. 507–516.

6 Huetz, J. and Petit, J. P., 1974, "Natural and Mixed Convection in Concentric Annular Spaces—Experimental and Theoretical Results for Liquid Metals," *Fifth International Heat Transfer Conference*, Tokyo, Vol. 3, pp. 169–172.

7 Rotem, Z., 1972, "Conjugate Free Convection from Horizontal Conducting Circular Cylinders," *International Journal Heat Mass Transfer*, Vol. 15, pp. 1679–1693.

8 Singh, S. N. and Elliott, J. M., 1979, "Free Convection Between Horizontal Concentric Cylinders in a Slightly-Thermally Stratified Fluid," *International Journal of Heat Mass Transfer*, Vol. 22, pp. 639–646.

9 Raithby, G. D. and Hollands, K. G. T., 1975, "A General Method of Obtaining Approximate Solutions to Laminar and Turbulent Free Convection Problems," *Advances in Heat Transfer*, Vol. 11, pp. 266–317.

10 Kuehn, T. H. and Goldstein, R. J., 1976, "Correlating Equations for Natural Convection Heat Transfer Between Horizontal Circular Cylinders," *International Journal of Heat Mass Transfer*, Vol. 19, pp. 1127–1134.

11 Blythe, P. A. and Simpkins, G. P., 1977, "Thermal Convection in a Rectangular Cavity," Presented at the Levich Conference, Oxford.

12 Gill, A. E., 1966, "The Boundary Layer Regime for Convection in a Rectangular Cavity," *Journal Fluid Mechanics*, Vol. 26, 3, pp. 515–536.

13 Jischke, M. C. and Doty, R. T., 1975, "Linearized Buoyant Motion in a Closed Container," *Journal Fluid Mechanics*, Vol. 71, 4, pp. 729–754.

14 Kraussold, H., 1934, "Wärmeabgabe von zylindrischen Flüssigkeitschichten bei natürlicher Konvection," *Forschung im Ingeniurerwesen*, Vol. 4, pp. 186–191.

15 Itoh, M., Fujita, T., Nishiwaki, N., and Hirata, M., 1970, "A New Method of Correlating Heat-Transfer Coefficients for Natural Convection in Horizontal Cylindrical Annuli," *International Journal of Heat Mass Transfer*, Vol. 13, pp. 1364–1368.

B. L. Turner
Senior Systems Engineer,
Advanced Technology, Inc.,
McLean, Va. 22102
Assoc. Mem. ASME

R. D. Flack
Assistant Professor,
Department of Mechanical and
Aerospace Engineering,
University of Virginia,
Charlottesville, Va. 22901
Assoc. Mem. ASME

The Experimental Measurement of Natural Convective Heat Transfer in Rectangular Enclosures with Concentrated Energy Sources

Heat transfer rates were experimentally measured for laminar convection air flows in rectangular enclosures with one isothermal heated vertical wall, a concentrated cooling strip on the opposing wall, and adiabatic top and bottom plates. Both local and overall heat transfer data were obtained by the use of a Wollaston prism schlieren interferometer. The aspect ratio of the enclosure and size and location of the cooling strip were parametrically varied for Grashof numbers of 5×10^6 to 9×10^6. Results are compared to previously available theoretical predictions for low Grashof numbers (10^5). Correlations are presented such that the theoretical predictions can be extended to Grashof numbers up to 10^7. The present data also indicate the dependence of heat transfer rates on the geometric parameters.

Introduction

In recent years, the study of natural convection in enclosures has become increasingly important. In particular, with the development of complex, high power electronics packaging and with the increasing demands on exhausting energy supplies, the understanding of free convective flows within rectangular enclosures heated by concentrated heat sources has become warranted.

Previously, many investigators studied free convection in various two-dimensional enclosures. Simple rectangular enclosures (one side uniformly and isothermally cooled, and the opposing side uniformly and isothermally heated, and isothermal or adiabatic top and bottom) have been examined both theoretically and experimentally for wide ranges of Rayleigh numbers and aspect ratio [1–10]. Cylindrical and spherical enclosures are geometries which have also been studied [11–12]. Triangular enclosures are another geometry which has received recent attention [13].

In modern electronic equipment, a large number of high power dissipating components such as transistors, resistors, and power transformers are being packaged in modular rectangular enclosures. The applications of these packages are often such that space, weight, and external cooling sources are minimal. Such applications are in sophisticated aircraft or missile systems. In these cases, the placement of the high power dissipating components within an electronic package should be optimized as to maximize the natural convection heat transfer within the enclosure, thus possibly totally eliminating the need for forced cooling. Similarly, with the need for increased efficiency in building heating, the proper placement of a "baseboard" type heater in a room to maximize the heat transfer is important. This will be increasingly more important as solar heating is developed to assure optimum utilization of all of the available energy.

The work of Chu and Churchill [14] represents a major contribution to two-dimensional enclosures with concentrated heat sources. In this reference a finite difference solution was used to solve the transient equations for a rectangular geometry as shown in Fig. 1. In general the relationship governing the heat transfer is:

$$\mathrm{Nu} = \mathrm{Nu}\,(\mathrm{Gr}, \mathrm{Pr}, H/W, L/H, S/H) \tag{1}$$

The solutions presented in reference [14] are for aspect ratios of 0.4 to 5, Grashof numbers from 0 to 10^5 and a Prandtl number of 0.7. The size and location of the heater strip was also varied. The authors qualitatively evaluated the accuracy of their solution by experimentally examining smoke flow patterns in a 2.54 cm × 2.54 cm enclosure. Unfortunately, many practical applications warrant the need for solutions with larger Rayleigh numbers and often turbulent flow.

The aim of this paper is to present experimental laminar heat transfer data for two-dimensional rectangular enclosures which have a concentrated energy source on one side wall. Both local and overall heat transfer data for Grashof numbers ranging from 5×10^6 to 9×10^6 were obtained using a Wollaston prism schlieren interferometer. Similarities are identified between the data presented herein and the theoretical predictions of Chu and Churchill and other simple rectangular enclosure data. The present work is intended to cover large Grashof number flows, yet below the onset of turbulence.

Apparatus

The air filled, rectangular enclosure consisted of one isothermally heated side wall, an insulated side wall with an isothermally cooled strip, an isothermally heated top wall, and an isothermally cooled bottom, as shown in Fig. 2(*a*). It was necessary to control the temperatures of the top and bottom plates to effectively insulate them

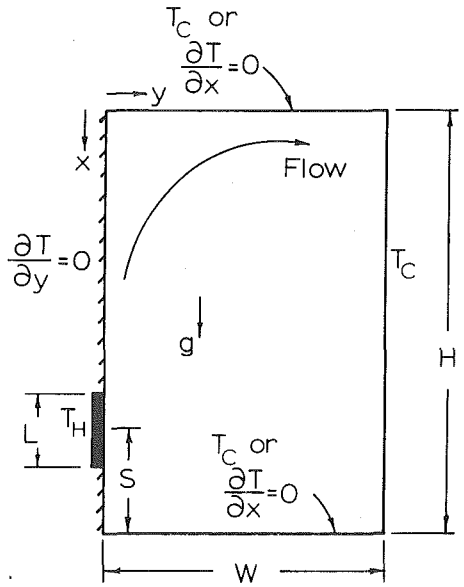

Fig. 1 Geometry studied by Chu and Churchill [14]

Contributed by the Heat Transfer Division for publication in the JOURNAL OF HEAT TRANSFER. Manuscript received by the Heat Transfer Division September 19, 1979.

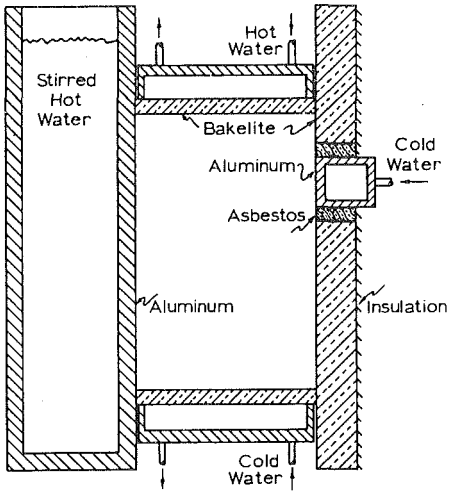

Fig. 2(*a*) Enclosure schematic

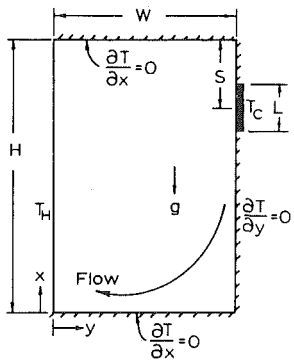

Fig. 2(*b*) Idealized enclosure

Fig. 2 Enclosure with heated wall and cooled strip

and maintain adiabatic conditions similar to that done by Sernas and Lee [7]. This apparatus is represented by the ideal geometry presented in Fig. 2(*b*).

One should note that the present ideal geometry is the "inverse" of the geometry studied by Chu and Churchill [14]. Originally, a geometry similar to that in reference [14], was utilized. However, two problems arose. First, analyzing the fringes near the heater strip was difficult due to the congestion of fringe shifts in the area. Thus, the accuracy was significantly impaired. Second, analyzing the fringe data near the cold wall became difficult due to refraction effects [15], particularly for large Grashof numbers since the light rays were bent into the cold wall. To increase the accuracy as much as possible the inverse geometry was studied herein. It should be noted that the solutions to both the Chu and inverse geometries bear a one-to-one relationship for the velocity and temperature fields for constant property fluids. For example, $T_{Chu}(x, y) = T_{inv}(H\text{-}x, W\text{-}y)$ and $\partial T_{Chu}/\partial y = dT_{inv}/\partial(W\text{-}y)$. Thus, the total heat transfer rates are identical for the two geometries so that this modification has minimal bearing on the comparability of the two sets of results.

Table 1 Geometries used

L/H	S/H	H/W
0.125	0.500	1.0
0.250	0.125	0.5, 1.0, 2.0
0.250	0.313	0.5, 1.0, 2.0
0.250	0.500	0.5, 1.0, 2.0
0.250	0.875	0.5, 1.0, 2.0
0.500	0.500	1.0

The heated wall was polished aluminum 1.27 cm thick with a hot water tank mounted on the outside. The bath was constantly stirred to assure uniform temperature distribution. The top and bottom plates were 0.95 cm thick Bakelite with aluminum heat exchangers attached to them. Water was circulated through the two exchangers by means of two centrifugal pumps. The wall with the concentrated cooling source was made of two 2.54 cm thick pieces of Bakelite bolted to both sides of an aluminum channel. Asbestos sheeting was used as a gasket between the aluminum and Bakelite to reduce the conduction between the two. Water was circulated through the channel by the same pump used to cool the bottom of the enclosure. The source of the cold water was an external ice bath which was constantly replenished with ice during the testing. Urethane foam was installed on the back of the Bakelite plate.

A total of 35 copper constantan thermocouples were mounted in the enclosure: 15 in the heated plate, five in the cooling strip, five in the Bakelite side wall, five in the top surface and five in the bottom surface. The thermocouples were imbedded in the walls within 0.16 cm of the faces and the isothermal walls were uniform within 0.5° C.

Double pane, optically flat glass was sealed onto the ends of the enclosure with silicon sealant/adhesive. The air filled thermalpane had a 0.64 cm gap between the 0.64 cm glass plates and was used to reduce the heat transfer through the ends. Previously, only single pane windows were typically used. Studies with the present apparatus indicate that by using double pane glass the end wall heat transfer is reduced by 10 to 35 percent of the total heat transfer between the side walls, particularly for large values of Grashof numbers [16].

Three sizes of tops and bottoms were used (corresponding to three values of W) so that the effect of aspect ratio could be determined; and three different size cooling strips were used to examine their effect. The apparatus was also designed to easily allow the change of the cooling strip location, so that this effect could be determined. Table 1 summarizes all of the geometries used in the study. The height (H) and length (Z) of the test section were 10.16 cm and 25.25 cm, respectively.

The Wollaston prism schlieren interferometer used by Flack, et al. [13] was utilized to make the heat transfer measurements. A diagram

Nomenclature

f = focal length of spherical mirrors, see Fig. 3
g = acceleration due to gravity
Gr, $\overline{\text{Gr}}$ = local and overall Grashof numbers, see equations (3, 6)
h, $\bar{h}$ = local and average heat transfer coefficients, see equations (3, 5, 6)
H = height of enclosure
K = Gladstone-Dale constant
k = thermal conductivity of air
L = length of cooled strip
n_e, n_o = extraordinary and ordinary indices of refraction of Wollaston prism
Nu, $\overline{\text{Nu}}$ = local and overall Nusselt numbers, see equations (3, 6)
p = pressure in enclosure
Pr = Prandtl number
R = ideal gas constant
S = position of cooled strip, see Fig. 2
T = temperature
u = distance defined in Fig. 3
W = width of enclosure
w = distance defined in Fig. 3
x = vertical direction, see Fig. 2
y = horizontal direction, see Fig. 2
Z = length of test section, see Fig. 3
α = wedge angle of Wollaston prism
β = volumetric coefficient of expansion
δ = angle between the reference interference fringes and y
ϵ = relative fringe shift
λ = wavelength of light
ν = kinematic viscosity

Subscripts

C, H = refer to conditions at the cold and hot side walls
CL = elevated at the center plane, $y/w = 0.50$
m = evaluated at the mean temperature, $T_m = (T_H + T_C)/2$
r = evaluated at the reference temperature, see equation (3)
1,2 = refer to methods of correlating data, see equations (3–6)

of the system is shown in Fig. 3. The light source was a 5 mw HeNe Laser (λ = 6328A). Two polarizers oriented at 90 deg to each other were used as well as two spherical mirrors with focal lengths (f) of 164.5 cm and diameters of 20.3 cm as shown. The Wollaston prism had a wedge angle (α) of 3 deg and indices of refraction (n_e, n_o) of 1.55178 and 1.54272. Interferometric images of the enclosure were projected on to a large ground glass screen and photographed with a 35mm camera onto high resolution film.

Experimental Procedure

Each geometric configuration was run at six different hot bath temperatures and at least two different fringe orientations were used in the data analysis. Before each of these tests was run, however, the parallel reference fringes were recorded (i.e., both baths and bottom plate were at ambient conditions. See Fig. 4 (a)). These fringes were necessary to analyze the shifted fringe data when one bath was heated and the other cooled (See Fig. 4 (b).).

The cold bath temperature was held constant at approximately 0°C,

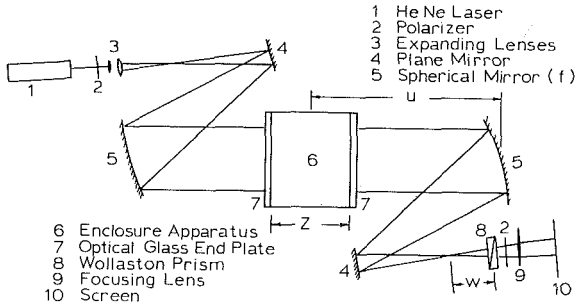

Fig. 3 Wollaston prism schlieren interferometer

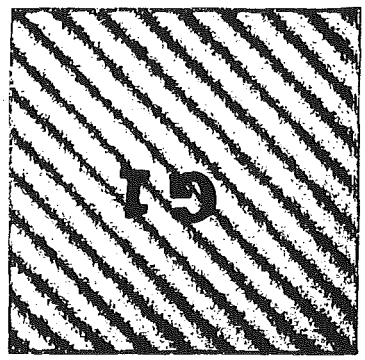

Fig. 4(a) Unshifted fringes

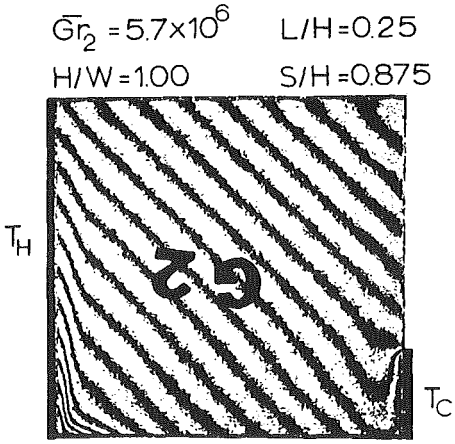

Fig. 4(b) Shifted fringes

Fig. 4 Photographs of typical interferograms

while six temperatures were used for the hot bath; approximately 35, 45, 55, 65, 75, and 80°C. Photographs of the fringes were taken during transient periods. By analyzing and comparing the transient patterns, it was found that waiting periods of more than one hour were necessary for steady-state conditions to be established.

To obtain nearly adiabatic conditions at the top and bottom, heat guards, described in the previous section and discussed in reference [7] were used. The bottom plate was held at the cooling strip temperature and the top plate temperatures were controlled separately and adjusted so that the fringe pattern indicated adiabatic conditions at the top surface. The temperatures of the top plate were within 5°C of the heated side wall.

To analyze the data recorded on film, an X-Y measuring microscope was used. The reference fringe interferogram was first analyzed to determine the exact fringe spacing and angles between the fringes and the various surfaces. A single reference fringe was also marked on this intergerogram and this fringe was observed and continuously remarked during any transient conditions (during temperature changes). Thus, by knowing the initial and final positions of one fringe, one could measure the relative motions of other fringes. The reference fringe was marked near the center of the enclosure where very little shifting of fringes occurred.

Sernas, et al. [17] showed that the local temperature gradient was proportional to the relative fringe shift. Equations are also derived in this reference which allow the calculation of temperature gradient normal to a wall ($\partial T/\partial y$) and the heat transfer rate once the fringe shift is measured. For example, the thermal gradient evaluated at the surface is given by:

$$(\partial T/\partial y)_s = -(\lambda R T_s^2/p \sin \delta)\,[2KZ\,(n_e - n_o) \times \tan \alpha(f + w - wu/f)]^{-1}\epsilon \quad (2)$$

where R, K, p, δ, ϵ, w, and u are defined in the Nomenclature and Fig. 3.

Measurement uncertainties are described in reference [13] and are due to the measurement of the center of the fringes on the reference and shifted interferograms and numerical integration techniques to find the total heat transfer. For local and average heat transfer quantities the uncertainties are 6 and 7 percent, respectively.

Also, at worst, 3 percent of the total heat transfer was occurring on the upper, lower, and insulated sidewalls as indicated by analyses of the fringe patterns on these surfaces. Holding the heat guards at a uniform temperature does not produce exactly the same temperature distribution on the top and bottom walls as a truly adiabatic surface. However, the boundary conditions at these walls do closely approximate those for ideal walls as indicated by the very low heat transfer rates. Since the boundary conditions for the actual experiment and ideal geometry are almost identical, the resulting temperature and velocity fields should be nearly identical. Previous to these tests, plain Bakelite plates were used for the top and bottom walls; however, typical heat transfer rates from the horizontal surfaces were 20 percent of the total heat transfer. Thus, from a practical standpoint, the present apparatus represents the best approximation to the ideal case. Furthermore, another set of ideal theoretical predictions can be made and compared to the present results. For example, the method of Chu and Churchill [14] could be modified to incorporate the isothermal boundary conditions with the upper wall at T_H and the lower wall at T_C.

Finally, less than 2 percent of the total heat transfer was lost through the end plates. This is significantly lower than reported in references [7] and [13] and is due to the thermal panes.

Analysis of Data

Two types of data are presented in this paper. First, local heat transfer data along the hot surface are presented for several configurations and Grashof numbers. These data are compared to theoretical results for vertical isothermal plates with a local Nusselt number versus local Grashof number plot. Second, the overall (or average) heat transfer data are presented and compared to the the-

oretical predictions of Chu and Churchill [14] for low Grashof numbers.

First, the local data are presented. To present results for rectangular enclosures in a form comparable to vertical plate data, Eckert and Carlson [1] utilized the temperature at the center plane ($y/W = 0.50$) to represent the temperature at infinity. For the present analysis, a similar technique was used and the local heat transfer coefficient was calculated using the temperature at the center plane, T_{CL}. This temperature was obtained by numerical integration of the experimental temperature gradient in the flow field. In the "core" of the enclosure a significant amount of stratification was found as will be discussed later.

To account for temperature dependent properties, the suggestions by Sparrow and Gregg [18] were used to correlate the data. That is, a reference temperature at 38 percent of the fluid-wall temperature difference was used, and the volumetric coefficient of expansion was evaluated at T_{CL}. Therefore, for the present local data the correlating parameters which are used for each wall are:

$$\left.\begin{aligned} h_1 &= k_H\,(\partial T/\partial y)_H/(T_H - T_{CL}) \\ \mathrm{Nu}_1 &= h_1 x/k_r \\ \mathrm{Gr}_1 &= g\beta(T_H - T_{CL})\,x^{\,3}/\nu_r{}^2 \\ \beta &= 1/T_{CL} \end{aligned}\right\} \qquad (3)$$

$$T_r = T_H - 0.38(T_H - T_{CL})$$

The present experimental data are compared to the commonly accepted theoretical correlations for laminar free convection over an isothermal heated flat plate in an isothermal fluid [19, 20]:

$$\mathrm{Nu} = F(\mathrm{Pr})[\mathrm{Gr}]^{1/4} \qquad (4)$$

where $F(\mathrm{Pr}) = 0.357$ for $\mathrm{Pr} = 0.72$.

Overall heat transfer data are presented and compared to large aspect rectangular enclosure data [1] and the theoretical predictions of reference [14]. The authors of reference [1] used different correlating parameters to present their overall results. The overall temperature difference was used, $T_H - T_C$, and properties were evaluated at an average temperature, T_m. Therefore,

$$h_2 = k_H(\partial T/\partial y)_H/(T_H - T_C) \qquad (5)$$

The average heat transfer coefficient was then correlated by:

$$\left.\begin{aligned} \overline{h}_2 &= \int_0^1 h_2(x)d(x/H) \\ \overline{\mathrm{Nu}_2} &= \overline{h}_2 H/k_m \\ \overline{\mathrm{Gr}_2} &= g\beta(T_H - T_C)H^3/\nu_m{}^2 \\ \beta &= 1/T_m \end{aligned}\right\} \qquad (6)$$

$$T_m = (T_H + T_C)/2$$

For the present study, the value of $\overline{\mathrm{Gr}_2}$ ranged from 5.0×10^6 to 9.0×10^6. By observing the interferograms during the test runs, one noted that the temperature gradient field at steady state was motionless. This indicates that for all of the data presented herein, the flow was steady and laminar since turbulent eddies would have resulted in fluctuating fringe patterns.

Results and Discussion

Two types of measurements were made in this study: local and average. Local results are presented to indicate the similarity of the data for different configurations and overall results are presented to provide engineering design guidelines. The parameters Gr, H/W, L/H and S/H were varied in the studies.

Local Data. To evaluate the local heat transfer coefficient Eckert and Carlson [1] found that by using the center plane temperature results agreed well with simple flat plate correlations. In Fig. 5, typical temperature profiles are presented. These profiles represent a square enclosure with $L/H = 0.25$. Each curve presented in Fig. 5 is a least squares curve fit to six data cases (different values of $\overline{\mathrm{Gr}_2}$). Individual temperatures were determined using numerical integration of the temperature gradient data similar to that used in reference [13]. For large values of S/H the curves are nearly linear, whereas for the small values of S/H the curve is slightly parabolic. Eckert and Carlson ($L/H = 1.00$) also found for large Grashof numbers and aspect ratios of 2.5 the temperatures were nearly linear at the center plane.

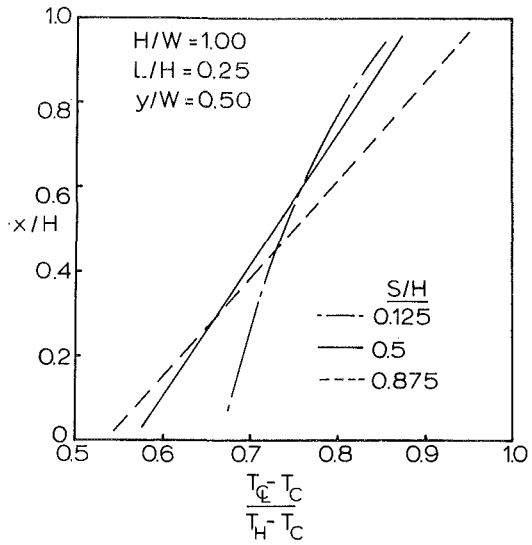

Fig. 5 Typical nondimensionalized center plane temperature profiles

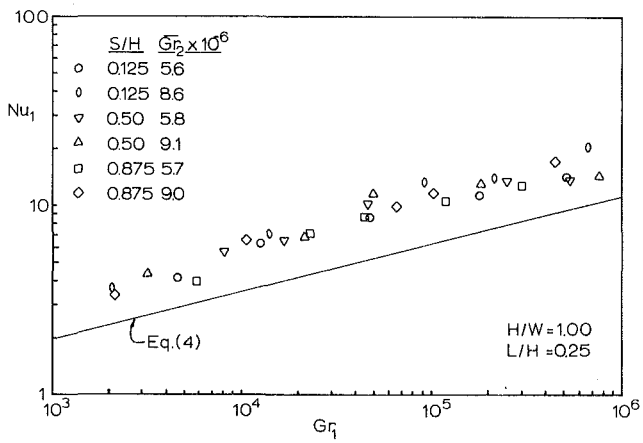

Fig. 6 Local Nusselt number variation for the heated wall

Local Nusselt numbers along the hot wall for six data sets ($H/W = 1.00$, $L/H = 0.25$) are presented in Fig. 6. Also presented in Fig. 6 is the accepted correlation for vertical isothermal surfaces from equation (4). As can be seen, the present data approximate one curve regardless of the value of $\overline{\mathrm{Gr}_2}$ and S/H. Also, the present data are also higher than the simple correlation by typically 60 percent. Similar results were also obtained for $H/W = 0.50$ and 2.00, and $L/H = 0.125$ and 0.50. A least squares fit to the data yields:

$$\mathrm{Nu}_1 = 0.524\,\mathrm{Gr}_1^{0.26} \qquad (7)$$

The difference between the local data and the simple correlation is attributed to the thermal stratification in the core as evidenced by the temperature profile in Fig. 5. Yang, et al. [21] theoretically predicted the effect of thermal stratification of the free stream medium on the heat transfer rates of vertical plates. Using these results one can approximately determine the increase in heat transfer for specific cases. For a typical stratification ($S/H = 0.5$, Fig. 5) the results of reference [21] predict an increase in heat transfer of 55 percent over an isothermal free stream case. This agrees well with the experimentally observed difference (60 percent).

Overall Data. Also, the overall Nusselt numbers were experi-

mentally determined and these data are presented in Figs. 7–10. Previous to the present effort the most thorough examination of concentrated energy sources in enclosures was that of Chu and Churchill [14]. This analysis was conducted up to Grashof numbers of approximately 10^5. Thus, the first objective of the present study was to compare the experimental data herein ($Gr \sim 10^7$) to the predictions of Chu and Churchill ($Gr \sim 10^5$). Such a comparison is made in Fig. 7 for a square enclosure with a centrally located energy source. Results for three values of L/H are presented as well as the experimental results of Eckert and Carlson [1]. Evidently, the current experimental results indicate that one can linearly extrapolate the results in reference [14] to the higher Grashof numbers. Very good agreement is found, with the current data agreeing at worst within 10 percent of the extensions. The data of reference [1] are also seen to agree with an extension of the results of reference [14]. The present data and the other results can be correlated for $S/H = 0.5$ and $H/W = 1.00$ by

$$\overline{Nu_2} = C_1(\overline{Gr_2})^{C_2} \tag{8}$$

where C_1 and C_2 are functions of L/H and are given in Table 2. The agreement with prior results is encouraging but the extrapolation indicated in Fig. 7 is subject to considerable uncertainty and should not be considered a critical test of the present work or that of references [1] and [14].

Typical parameter studies are also presented. The first is the influence of the size of the cooled strip centrally located in a square enclosure and results are presented in Fig. 8. In Fig. 8 one can see that by increasing L/H the heat transfer is increased. However, as L/H increases for values greater than 0.25, the overall Nusselt number increases by only 9 percent for the two values of $\overline{Gr_2}$ presented. Similarly, for low Grashof numbers, Chu and Churchill [14] predicted that only small increases in Nu would be present as L/H increased above 0.20. A typical curve from reference [14] is presented in Fig. 8 for qualitative comparison.

Next, the effect of the variation of the strip location in a square enclosure with $L/H = 0.25$ is presented in Fig. 9. Experimentally, the most heat transfer occurred for values of S/H of approximately 0.4, although the heat transfer rates were nearly identical for $S/H = 0.313$ and 0.50. Chu and Churchill [14] similarly predicted the maximum values of $\overline{Nu_2}$ to occur near 0.4 for low Grashof numbers. Experimental tests were also performed for $H/W = 0.50$ and 2.00 and the optimum location was again determined to be for S/H of approximately 0.4. These figures are not presented for the sake of brevity.

Finally, the results from the variation of the aspect ratio are presented in Fig. 10. In this study L/H was 0.25 and the strip was centrally located. As can be seen variation of $\overline{Nu_2}$ with H/W is very small and is not measurable. This is in agreement with the experimental data of Sernas and Lee [7], who found that for aspect ratios of 0.4 to 1.0 (with $L/H = 1.00$) the dependence of $\overline{Nu_2}$ on H/W was within the

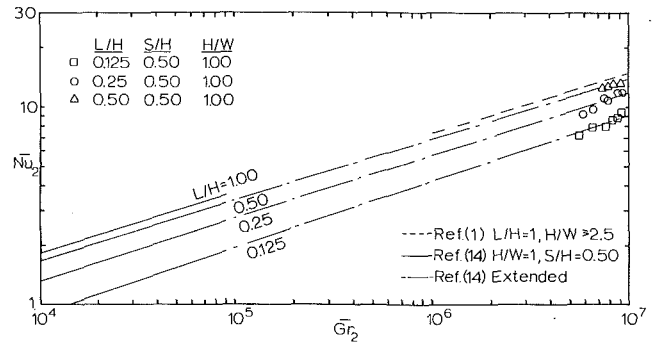

Fig. 7 Overall Nusselt number variation as compared to low Grashof number predictions [14] and other experimental data [1]

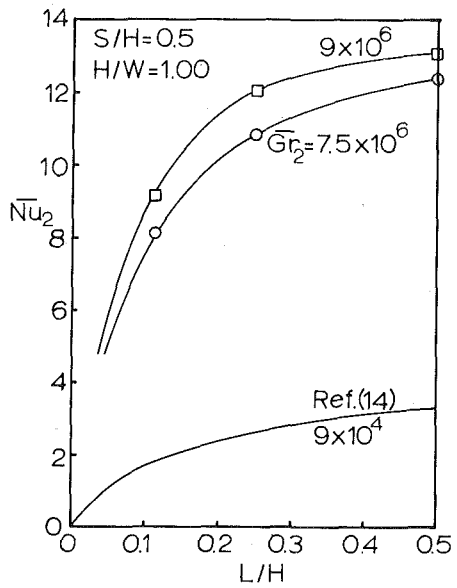

Fig. 8 Influence of strip size on overall Nusselt number

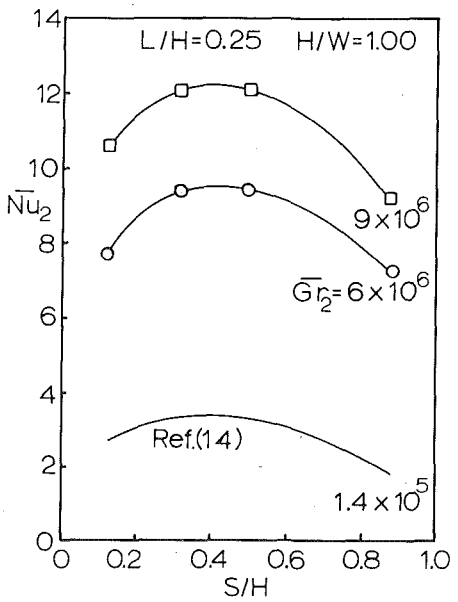

Fig. 9 Influence of strip location on overall Nusselt number

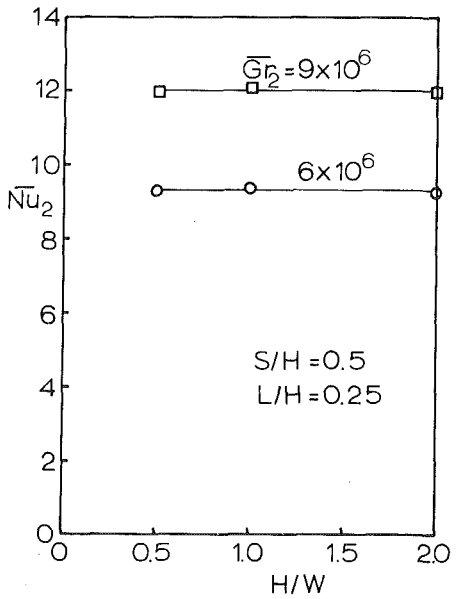

Fig. 10 Influence of aspect ratio on overall Nusselt number

Table 2 Coefficients for equation (8), $H/W = 1.00$, $S/H = 0.50$

L/H	C_1	C_2
0.125	0.045	0.33
0.25	0.069	0.32
0.50	0.097	0.31
1.00	0.119	0.30 from [1]

limits of measurement error. Similar studies were made with S/H = 0.125, 0.313, and 0.875, but again the dependence of $\overline{Nu_2}$ on H/W was smaller than the measurement error; these results are not presented for the sake of brevity.

Conclusions

Free convection heat transfer data were experimentally determined for rectangular enclosures which had one vertical heated wall and a concentrated cooling strip on the opposing wall. The overall Grashof number was varied from 5×10^6 to 9×10^6 and the aspect ratio, strip size and strip location were parametrically varied. Such a class of enclosures had not been experimentally studied previously. Specific conclusions include: (1) Correlations are presented to extend the range of applicability of the predictions in reference [14] from Grashof numbers of 10^5 to 10^7. (2) The size of the strip influences $\overline{Nu_2}$, but the dependence of $\overline{Nu_2}$ on L/H is small for L/H greater than 0.25. (3) The optimum location of the strip is $S/H \simeq 0.4$ for $L/H = 0.25$ and for H/W from 0.5 to 2.0. (4) The effects of variations in aspect ratio from 0.5 to 2.0 are negligible for $L/H = 0.25$ and S/H from 0.125 to 0.875. (5) The local data along the heated wall are in qualitative agreement with simple vertical plate correlations and differences of approximately 60 percent are attributable to the thermal stratification in the core.

Acknowledgments

The authors gratefully acknowledge the support of the Department of Mechanical and Aerospace Engineering, University of Virginia, for the experimental apparatus. The authors also acknowledge G.-S. Wang's helpful correspondence concerning the one-to-one relationship between the Chu and inverse geometries.

References

1 Eckert, E. R. G., and Carlson, W. O., "Natural Convection in an Air Layer Enclosed Between Two Vertical Plates with Different Temperatures," *International Journal of Heat Mass Transfer,* Vol. 2, Nos. 1/2, Mar. 1961, pp. 106–120.

2 MacGregor, R. K., and Emery, H. A., "Free Convection Through Vertical Plane Layers—Moderate and High Prandtl Number Fluids," ASME JOURNAL OF HEAT TRANSFER, Vol. 91, 1969, pp. 391–403.

3 Newell, M. E., and Schmidt, F. W., "Heat Transfer by Laminar Natural Convection Within Rectangular Enclosures," ASME JOURNAL OF HEAT TRANSFER, Vol. 92, No. 1, Feb. 1970, pp. 159–168.

4 Boyack, B. E., and Kearney, D. W., "Heat Transfer by Laminar Natural Convection in Low Aspect Ratio Cavities," ASME Paper No. 72-HT-52, presented at the AIChE-ASME Heat Transfer Conference, Denver, Colo., Aug. 1972.

5 Taborrok, B. and Lin, R. C., "Finite Element Analysis of Free Convection Flows," *International Journal of Heat and Mass Transfer,* Vol. 20, No. 9, Sept. 1977, pp. 945–952.

6 Briggs, D. G., "Numerical Solutions of High Rayleigh Number Two-Dimensional Free Convection in Enclosures With An Aspect Ratio of One," *Proceedings of AICA International Symposium on Computer Methods for Partial Differential Equations,* Lehigh University, Bethlehem, Penn., June 1975.

7 Sernas, V., Lee, E. I., "Heat Transfer in Air Enclosures of Aspect Ratio Less Than One," ASME Paper 78-WA/HT-7, presented at the ASME Winter Annual Meeting, San Francisco, CA, Dec. 1978.

8 Ozoe, H., Sayama, H., and Churchill, S. W., "Natural Convection in an Inclined Rectangular Channel at Various Aspect Ratios and Angles—Experimental Measurements," *International Journal of Heat and Mass Transfer,* Vol. 18, No. 12, Dec., 1975, pp. 1425–1431.

9 Buchberg, H., Catton, I., and Edwards, D. K., "Natural Convection in Enclosed Spaces—A Review of Application to Solar Energy Collection," ASME JOURNAL OF HEAT TRANSFER, Vol. 98, No. 2, May 1976, pp 182–188.

10 Clomburg, L. A. "Convection in an Enclosure-Source and Sink Located Along a Single Horizontal Boundary," ASME Paper 76-HT-22, presented at the ASME-AIChE Transfer Conference, St. Louis, Mo., Aug. 1976.

11 Powe, R. E. Carley, C. T., and Bishop, E. H., "Free Convective Flow Patterns in Cylindrical Annuli," ASME JOURNAL OF HEAT TRANSFER, Vol. 91, No. 3, Aug. 1969, pp. 310–314.

12 Yin, S. H., Powe, R. E., Scanlan, J. A. and Bishop, E. H., "Natural Convection Flow Patterns in Spherical Annuli," *International Journal of Heat and Mass Transfer,* Vol. 16, No. 9, Sept., 1973, pp. 1785–1795.

13 Flack, R. D., Konopnicki, T. T., and Rooke, J. H., "The Measurement of Natural Convective Heat Transfer in Triangular Enclosures," ASME JOURNAL OF HEAT TRANSFER, Vol. 101, No. 4, Nov. 1979, pp. 648–654.

14 Chu, H. H., Churchill, S. W., "The Effect of Heater Size, Location, Aspect Ratio, and Boundary Conditions on Two Dimensional, Laminar, Natural Convection in Rectangular Channels," ASME JOURNAL OF HEAT TRANSFER, Vol. 98, No. 2, May 1976, pp. 194–201.

15 Mehta, J. M. and Black, W. Z., "Errors Associated with Interferometric Measurement of Convective Heat Transfer Coefficients," *Applied Optics,* Vol. 16, No. 6, June 1977, pp. 1720–1726.

16 Turner, B. L., "An Experimental Study of Natural Convection in Rectangular Enclosures with Concentrated Energy Sources," M. S. Thesis, University of Virginia, Charlottesville, Va., Aug. 1979.

17 Sernas, V., Fletcher, L. S., and Aung, W., "Heat Transfer Measurements with a Wollaston Prism Schlieren Interferometer," ASME Paper No. 72-HT-9, Presented at the AIChE-ASME Heat Transfer Conference, Denver, Colo., Aug. 1972.

18 Sparrow, E. M., and Gregg, J. L., "The Variable Fluid Property Problem in Free Convection," *Trans. ASME,* Vol. 80, 1958, pp. 879–886.

19 Ostrach, S., "An Analysis of Laminar Free Convection Flow and Heat Transfer About a Flat Plate Parallel to the Direction of Generating Force," NACA Report, 1111, 1953.

20 Gebhart, B., *Heat Transfer,* McGraw-Hill, New York, 1971.

21 Yang, K. T., Novatny, J. L., and Cheng, Y. S., "Laminar Free Convection From a Nonisothermal Plate Immersed In a Temperature Stratified Medium," *International Journal of Heat and Mass Transfer,* Vol. 15, No. 5, 1972, pp. 1097–1109.

R. F. Bergholz
Department of Mechanical and Industrial Engineering,
University of Illinois at Urbana-Champaign,
Urbana, IL 61801

Natural Convection of a Heat Generating Fluid in a Closed Cavity

Thermal convection of a heat generating fluid in a rectangular enclosure, cooled at the side walls, is investigated in the boundary-layer regime at large internal Rayleigh numbers. A boundary-layer analysis is employed to derive a system of equations valid near the vertical walls and a corresponding system valid in the core of the enclosure. The boundary-layer equations were solved using a modified Oseen linearization method. It was found that the primary convective flow consists of a bicellular circulation in which the cold, descending boundary layers at the lateral walls generate a nearly uniform, upward flow in the core. In addition, a strong, stable, vertical temperature gradient is established in the core by the process of upward transport of heat. The side-wall heat flux distribution shows that most of the heat generated within the cavity is removed along the upper one-half of each vertical wall. It is expected that the results of this work can be applied in studies of the containment of heat generating radioactive materials and in analyses of convection driven by electrical currents or exothermic chemical reactions.

Introduction

Most studies of natural convection in volumetrically heated fluids focused on the case of a horizontal fluid layer, with uniform internal heat generation, cooled at the upper and lower boundaries. In contrast, there have only been a few investigations of natural convection of heat generating fluids in cavities cooled predominantly at the *side* boundaries. Some of these dealt analytically or experimentally with the flow of an internally heated fluid in a long vertical tube cooled at the wall [1–5], while others have treated the convection problem numerically for containers of cylindrical or spherical shape with cooling on all of the surfaces [6–7]. However, the rather interesting case of convection at large Rayleigh numbers, driven by strong internal boundary-layer flows on cooled vertical walls, has not been considered.

There are a number of practical situations in which lateral cooling will play a dominant role in the convection process within a contained, heat generating fluid. In the field of nuclear reactor safety, there is considerable interest in the heat transfer characteristics of molten, internally heated fuel pools and of liquid suspensions of radioactive wastes. Liquid nuclear fuel elements also have been proposed as a possible alternative to solid fuel rods. Finally, natural convection can be important in fluids undergoing electrolytic processes or exothermic chemical reactions.

The purpose of this communication is to examine the general features of natural convection of a heat generating fluid in a rectangular enclosure cooled at the vertical walls. Approximate solutions were obtained for the velocity and temperature distributions in the core and in the side-wall boundary layers. The variations of the boundary layer thickness and the local Nusselt number at a side wall also are described. As such, this study represents a useful adjunct to a full scale numerical solution of the problem.

Analysis

A schematic illustration of the convection pattern of a heat generating fluid in a rectangular cavity cooled at the vertical walls and insulated at the horizontal walls is shown in Fig. 1. It is assumed that either the volumetric heat generation rate, Σ, or the separation, D, between the walls is sufficiently large to give a boundary layer-core structure to the flow. The cold, descending side-wall boundary layers generate horizontal and vertical velocities in the core by direct interaction with the core fluid, and also indirectly through the formation of stagnation boundary layers at the horizontal surfaces. As a result of symmetry considerations, and under the assumptions that the flow is steady and two-dimensional in the x-z plane, the vertical centerline of the enclosure must be a stagnation streamline dividing the flow into two counter rotating circulation cells, one each in the left and right halves of the cavity. In addition, the vertical convection of heat creates a stable vertical temperature distribution within the core. The exis-

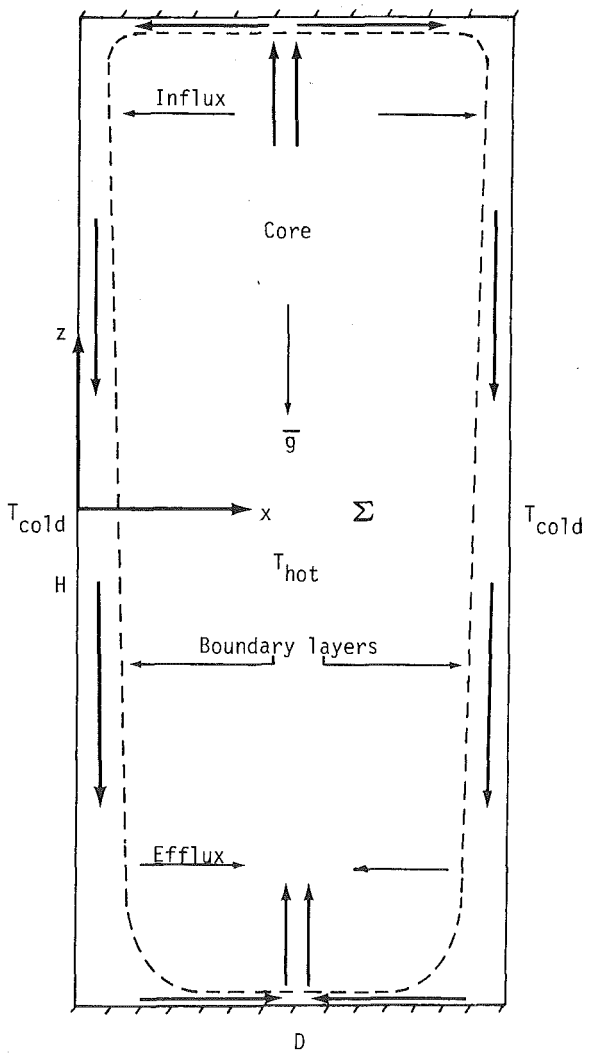

Fig. 1 Schematic illustration of the problem geometry

Contributed by the Heat Transfer Division and presented at the Winter Annual Meeting, San Francisco, Calif. December 10–15, 1978 of THE AMERICAN SOCIETY OF MECHANICAL ENGINEERS. Revised manuscript received by the Heat Transfer Division February 8, 1979. Paper No. 78-WA/HT-6.

tence of a stable core stratification has been demonstrated experimentally and numerically in several related problems (e.g., convection in rectangular cavities and in horizontal cylinders with lateral heating and cooling), as discussed in [8, 9].

Governing Equations and Scaling. The equations governing two-dimensional fluid flow, under the Boussinesq approximation, are the vorticity equation,

$$u^*(\partial\zeta^*/\partial x^*) + w^*(\partial\zeta^*/\partial z^*) = \nu[\partial^2\zeta^*/\partial x^{*2}) + (\partial^2\zeta^*/\partial z^{*2})] + g\beta(\partial T^*/\partial x^*), \quad (1)$$

in which

$$u^* = -\partial\Psi^*/\partial z^*, \qquad w^* = \partial\Psi^*/\partial x^*, \quad (2)$$

$$\zeta^* = (\partial^2\Psi^*/\partial x^{*2}) + (\partial^2\Psi^*/\partial z^{*2}), \quad (3)$$

and the thermal energy equation

$$u^*(\partial T^*/\partial x^*) + w^*(\partial T^*/\partial z^*) = \kappa[(\partial^2 T^*/\partial x^{*2}) + (\partial^2 T^*/\partial z^{*2})] + \Sigma/\rho c_p. \quad (4)$$

The above system is reduced to dimensionless form by introducing the following *core* scales relating dimensional and nondimensional quantities:

$$\left.\begin{aligned} x^* = (D/2)\,x, \quad z^* = Hz, \quad u^* = (\Psi/H)\,u, \quad w^* = (2\Psi/D)\,w, \\ \zeta^* = (4\Psi/D^2)\,\zeta, \quad T^* - T_w = (\Delta T)T, \quad \Psi = (\kappa H/\ell), \\ \Delta T = \Sigma D\ell/(2k), \quad \ell = (2\nu\kappa kH/g\beta\Sigma D)^{1/5}. \end{aligned}\right\} \quad (5)$$

Note that the conduction temperature scale, ΔT, is defined implicitly in terms of the average wall heat flux, $\Sigma D/2$, and a nominal thickness, ℓ, of one of the vertical boundary layers. The length scale ℓ was derived from (2) and (4), assuming a convective balance in the core, and from (1), assuming a balance of convection, buoyancy and diffusion in the boundary layer. Thus, ΔT and ℓ are definite, fixed scales, whereas the actual dimensional quantities $\Delta T^*(z^*)$ and $\ell^*(z^*)$ are unknown and must be determined in the course of the analysis. The resulting nondimensional system corresponding to equations (1)–(4) becomes

$$\mathrm{Pr}^{-1}(u\zeta_x + w\zeta_z) = \overline{\mathrm{Ra}}_I{}^{-1/5}[\zeta_{xx} + (1/4h^2)\zeta_{zz}] + \overline{\mathrm{Ra}}_I{}^{2/5}T_x \quad (6)$$

$$\zeta = \Psi_{xx} + (1/4h^2)\Psi_{zz}, \qquad u = -\Psi_z, \qquad w = \Psi_x, \quad (7)$$

$$uT_x + wT_z = \overline{\mathrm{Ra}}_I{}^{-1/5}[T_{xx} + (1/4h^2)T_{zz}] + 1. \quad (8)$$

The aspect ratio, h, the Prandtl number, Pr, and the *modified internal* Rayleigh number, $\overline{\mathrm{Ra}}_I$, are now the dimensionless parameters governing the problem. The boundary conditions for equations (6–8) are simply

$$\Psi = \Psi_x = T = 0 \text{ on } x = 0,2; \quad \Psi = \Psi_z = T_z = 0 \text{ on } z = \pm 1/2 \quad (9)$$

If $\overline{\mathrm{Ra}}_I$ is sufficiently large, the most significant vertical flow in the enclosure will be confined to relatively thin boundary layers along the lateral walls. Consequently, the full system of governing equations can be approximated by two simpler sets of equations, one governing the flow in the core and the other that in the boundary layers. However, the core equations are unlike those for the exterior potential flow in the case of external boundary layers in that they cannot be solved a priori, even in the lowest order approximation, without explicit consideration of the boundary-layer solutions.

The Core Equations. The zeroth-order equations governing the flow in the interior of the enclosure are obtained by formally taking the limit $\overline{\mathrm{Ra}}_I \to \infty$ in the system (6–8). This gives

$$T_{0_x} = 0, \qquad W_0\,T_{0_z} = 1, \quad (10a,b)$$

from which it immediately follows that $W_0 = W_0(z)$ and $T_0 = T_0(z)$. From equations (7) and (10) and the symmetry of the boundary conditions, we obtain

$$\Psi_0(x,z) = W_0(z)(x - 1). \quad (11)$$

The unknown functions $W_0(z)$ and $T_0(z)$ cannot be specified arbitrarily but must be determined through the solutions for the side-wall boundary layers.

Physically, equation (10b) states that all of the heat generated within the core is convected upward by a horizontally uniform, vertical flow. The heated core fluid then is transported to the downward flowing boundary layers at the vertical walls by way of stagnation boundary layers at the top and bottom surfaces. The entire process is dominated by convection, conduction in the core being negligible in the lowest order approximation. Also, $T_{0_z} > 0$, that is, the vertical temperature distribution within the core is everywhere stabilizing.

The Boundary-Layer Equations. The boundary-layer equations for the vertical walls are obtained by employing the stretching transformations

$$\eta = \overline{\mathrm{Ra}}_I{}^{1/5}\,x, \qquad w \to \overline{\mathrm{Ra}}_I{}^{1/5}\,w, \qquad \zeta \to \overline{\mathrm{Ra}}_I{}^{2/5}\,\zeta$$

in the complete governing system (6–8) and taking the limit $\overline{\mathrm{Ra}}_I \to \infty$. The transformation applied to the horizontal coordinate implies that the dimensionless boundary layer thickness, $\delta = 2\ell/D$, is $0(\overline{\mathrm{Ra}}_I{}^{-1/5})$. This estimate in terms of the modified internal Rayleigh number is consistent with the definition of $\overline{\mathrm{Ra}}_I$ and with the assumed balances in the core and boundary layers. To facilitate the analysis,

Nomenclature

c_p = specific heat
D = width of enclosure
$f(z)$ = even function of z (equation (24a))
g = gravitational acceleration
H = height of enclosure
h = aspect ratio of enclosure, H/D
i = imaginary unit
K_0 = core temperature (constant) at mid-height of enclosure
k = thermal conductivity
ℓ = boundary-layer thickness scale, $(2\nu\kappa kH/g\beta\Sigma D)^{1/5}$
Nu = local sidewall Nusselt number, $-(\theta_\eta)_{\eta=0}$
Pr = Prandtl number, ν/κ
$p(z)$ = odd function of z (equation (24b))
Ra_I = internal Rayleigh number, $(g\beta/\nu\kappa)(\Sigma D^2/64k)D^3$
$\overline{\mathrm{Ra}}_I$ = modified internal Rayleigh number, Ra_I/h
T = temperature
T_0 = core temperature
$\overline{T}'(z)$ = η-averaged vertical temperature gradient
ΔT = temperature scale between core and wall, $\Sigma D\ell/(2k)$
U_0 = horizontal core velocity
u = horizontal velocity
$\overline{u}(z)$ = η-averaged horizontal velocity
W_0 = vertical core velocity
w = vertical velocity
x = horizontal coordinate
z = vertical coordinate
Σ = uniform volumetric heat generation rate
Ψ = stream function scale, $\kappa H/\ell$
Ψ_0 = core stream function
ζ = vorticity in x-z plane
β = coefficient of thermal expansion
κ = thermal diffusivity
ν = kinematic viscosity
ρ = density
Θ_0 = odd part of core temperature distribution
θ = boundary-layer temperature
η = horizontal coordinate (boundary-layer), $\overline{\mathrm{Ra}}_I{}^{1/5}\,x$
δ = dimensionless nominal boundary-layer thickness, $2\ell/D$
$\lambda_{1,2}$ = complex exponential decay rates (boundary-layer)
$\gamma = \lambda_1 + \lambda_2$
$\xi = \lambda_1\,\lambda_2$

Subscripts

w = wall value
x,z = partial differentiation
0 = core value

Superscripts

* = dimensional quantity
′ = ordinary differentiation
r = real part of a complex quantity

it is also assumed that $\mathrm{Pr} \to \infty$, in which case the nonlinear convection terms in the vorticity equation are eliminated. The assumption of infinite Prandtl number actually is not a severe restriction, because previous predictions in which this approximation was used have shown it to be valid even for values of Pr near 1.

The field equations and boundary conditions for the boundary layer on the left-hand wall are written as follows:

$$w_{\eta\eta} + T - T_0(z) = 0, \qquad u\,T_\eta + w\,T_z = T_{\eta\eta}, \tag{12a,b}$$

$$u = w = T = 0, \qquad w_{\eta\eta} = T_0(z) \text{ on } \eta = 0, \tag{13}$$

$$u, w, T \to U_0, W_0, T_0, \eta \to \infty. \tag{14}$$

Equations (12–14) are those for a free-convection boundary layer along an isothermal wall in a thermally stratified ambient environment. The effect of internal heat generation upon the boundary layer flow is small ($0(\ell/D)$) and so does not appear at this level of approximation.

A number of difficulties immediately arise in the treatment of the system (12–14). First, since the unknown function $T_0(z)$ appears explicitly in the momentum equations and in one of the boundary conditions, the boundary-layer solutions are fundamentally coupled to those for the core. This excludes the application of standard asymptotic matching techniques. Secondly, similarity methods cannot be used to solve (12–14) because the appropriate transformations can be derived only for certain specialized variations of the ambient temperature, in this case $T_0(z)$ (e.g., a power law variation in z). Finally, even numerical solutions of the complete boundary-layer equations pose certain problems, the most important being the lack of initial conditions at the "leading edge" (upper left corner) of the vertical wall and the necessity of simultaneously matching the solutions for the boundary layer and core.

The Oseen Approximation. To circumvent the difficulties described above, an analytical approach was chosen which has proven useful in determining the principal features of flows similar to the one studied here. Gill [10] used the method to investigate the boundary-layer regime for natural convection in a rectangular cavity heated at one vertical surface and cooled at the other. Applications of similar techniques can be found in the works of Carrier [11] and Weinbaum [12]. In essence, the approach is based upon a simplification of the convective transport terms in equation (12b) analogous to that accomplished by the method of Oseen linearization in analyses of low Reynolds number flows. In the present situation, the horizontal velocity $u(\eta,z)$ and the vertical temperature gradient $T_z(\eta,z)$ in the boundary layer are approximated by suitable η-averages, $\overline{u}(z)$ and $\overline{T}'(z)$, respectively, at any given level z = constant. For convenience, the boundary-layer temperature T is written as $T(\eta,z) = T_0(z) + \theta(\eta,z)$, in which case equations (12a,b) become

$$w_{\eta\eta} + \theta = 0, \qquad \overline{u}(z)\,\theta_\eta + w\overline{T}'(z) = \theta_{\eta\eta}. \tag{15a,b}$$

Equations (15a,b) can be combined to give

$$w_{\eta\eta\eta\eta} - \overline{u}(z)\,w_{\eta\eta\eta} + \overline{T}'(z)\,w = 0, \tag{16}$$

which is simply an ordinary differential equation whose coefficients are functions of the parameter z. Solutions satisfying the boundary conditions (13) are given by

$$w = [T_0(z)/(\lambda_1^2 - \lambda_2^2)](e^{-\lambda_1\eta} - e^{-\lambda_2\eta}), \tag{17}$$

$$\theta = -[T_0(z)/(\lambda_1^2 - \lambda_2^2)](\lambda_1^2\,e^{-\lambda_1\eta} - \lambda_2^2\,e^{-\lambda_2\eta}), \tag{18}$$

where $\lambda_1 = \lambda_1(z)$ and $\lambda_2 = \lambda_2(z)$ are the roots, with positive real part, of the characteristic equation

$$\lambda^3(\lambda + \overline{u}(z)) + \overline{T}'(z) = 0. \tag{19}$$

Note from (17) that strict matching of $w(\eta,z)$ with the core velocity $W_0(z)$ does not occur in the limit $\eta \to \infty$. This lack of continuity is a result of the averaging process applied to the horizontal velocity, u. Normally, suitable matching procedures would provide the means for finding the unknown functions $W_0(z)$ and $T_0(z)$. However, in applying the Oseen method outlined above, one must resort to more general compatibility conditions relating the core and boundary-layer quantities. These conditions are the global conservation relations for fluxes of mass and heat in the vertical direction, expressed as follows:

$$W_0(z) = -\int_0^\infty w(\eta,z)\,d\eta, \quad d/dz\left\{\int_0^\infty (w\theta)\,d\eta\right\} = 1 - (\theta_\eta)_{\eta=0}. \tag{20a,b}$$

These conservation relations establish the necessary link between $\overline{u}(z)$ and $\overline{T}'(z)$ in the boundary layer and $U_0(0,z)$ and $T'_0(z)$ in the core.

Solutions. Introducing w and θ, from (17) and (18), into the integral relations (20a,b) results in

$$W_0 = T_0/\gamma\xi, \tag{21}$$

$$d/dz(T_0^2/2\gamma^3) = 1 + T_0[(\xi/\gamma) - \gamma], \tag{22}$$

where

$$\gamma = \lambda_1 + \lambda_2, \qquad \xi = \lambda_1\,\lambda_2. \tag{23a,b}$$

A convenient solution of (21) and (22) can be obtained upon the condition that $W_0(z)$ is an even function of z. Whereas this condition was exactly satisfied in Gill's problem, it is only a first approximation in the problem studied here. Since both side-wall boundary layers are downward flowing, one would clearly expect some asymmetry in the distribution of $W_0(z)$. However, the displacement effect should not be too pronounced at large $\overline{\mathrm{Ra}}_I$, when the boundary layers are thin. Note that approximation of $W_0(z)$ as an even function of z in no way implies z-symmetry for the boundary layer velocity $w(\eta,z)$. The integral relations simply demand that the average boundary layer velocity be greater in the thin layers in the top half of the cavity than in the somewhat thicker layers in the bottom half.

Under the approximation that $W_0(z)$ is vertically symmetric, it follows from equation (10b) that $T_0(z) = K_0 + \Theta_0(z)$, where $\Theta_0(z)$ is an odd function of z, and K_0 is an undetermined constant. Also, $\overline{u}(z)$ is an odd function of z and $\overline{T}'(z)$ is an even function of z. It is now possible to use the solution method developed by Gill [10]. First, define the even and odd functions, respectively

$$f(z) = \gamma(z) + \gamma(-z), \; p(z) = \overline{u}(z)/f(z), \tag{24a,b}$$

where $-1 \le p(z) \le 1$, $p(0) = 0$, and $p(\pm\frac{1}{2}) = \mp 1$. Then, using the symmetry properties of equation (19), it is easy to show that

$$\gamma = \tfrac{1}{2}f(1-p), \qquad \xi = \tfrac{1}{8}f^2(1-p^2)(1-p) \tag{25a,b}$$

$$\lambda_{1,2} = \tfrac{1}{4}f(1-p)[1 \pm i\,(1+2p)^{1/2}]. \tag{26}$$

Substituting equations (25a,b) into equation (21), and equating the odd and even parts, gives the following explicit relations for W_0 and T_0 in terms of the functions f and p:

$$W_0 = (16\,K_0)/[f^3(1-p^4)], \qquad \Theta_0 = (-2\,K_0\,p)/(1+p^2). \tag{27a,b}$$

Equations (10b) and (27a,b) can be combined to give the simple differential equation

$$dz/dp = (-32\,K_0^2)/[f^3(1+p^2)^3] \tag{28}$$

Combining equations (25a,b), (27b), and the energy equation (22) and, again, equating the odd and even parts, yields two more differential equations, from which we obtain

$$f = [(1+p^2)(7-p^2)]/[2\,K_0(1-p^2)(1+3\,p^2)]. \tag{29}$$

Equation (28) now becomes

$$dz/dp = -(2\,K_0)^5\,\{[2(1-p^2)(1+3\,p^2)]/[(1+p^2)^2\,(7-p^2)]\}^3. \tag{30}$$

Equation (30) must be integrated numerically to find $z(p)$. Note that the constant K_0 serves as a scale factor for the coordinate z. It could be determined by matching the core solutions to solutions for the boundary layers on the horizontal surfaces. However, it is not

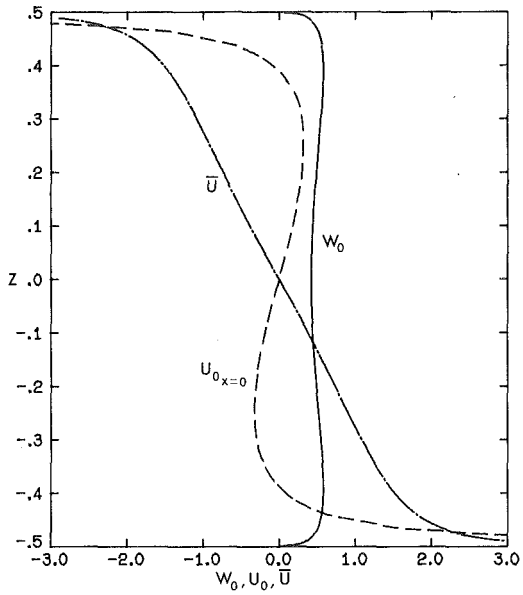

Fig. 2 Variations of W_0, U_0 $(0,z)$, and $\bar{u}$ with z

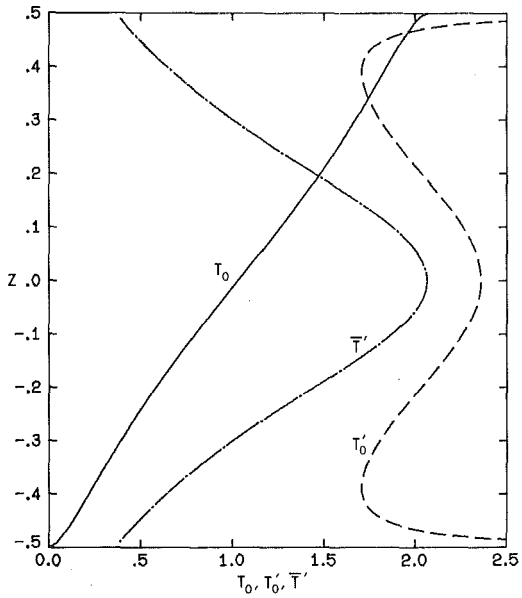

Fig. 3 Variations of T_0, T_0', and $\overline{T}'$ with z

expected that the horizontal layers will be crucial to the overall description of the flow. In a numerical study of Gill's problem, Quon [13] demonstrated that the hydrodynamic boundary conditions at $z = \pm 1/2$ have little influence on the vertical boundary-layer flow. Therefore, it seems justified at the current level of approximation to invoke the *inviscid boundary conditions* $W_0(\pm 1/2) = 0$ as reasonable ones for determining K_0. Equation (30) can now be integrated from $z(0) = 0$ to $z(1) = -1/2$, and a numerical value for K_0 can be calculated a posteriori to insure that $W_0(-1/2) \approx 0$. The result is $K_0 = 1.0321$.

Results and Discussion. Using the numerically defined function $z(p)$ and the constant K_0, it is now possible to compute the distributions of W_0, T_0, and Ψ_0 in the core, and the profiles of w and θ in the boundary layer. Two other quantities of interest are the exponential boundary-layer thickness scale

$$\delta_e(z) = 1/[\lambda^{(r)}(z)], \tag{31}$$

and the local side-wall Nusselt number,

$$\mathrm{Nu}(z) = -(\theta_\eta)_{\eta=0} = (T_0/\delta_e)(1-p). \tag{32}$$

The function $\delta_e(z)$ provides a convenient measure of the variation of the actual boundary-layer thickness $\delta(z)$.

Figures 2 and 3 show the vertical profiles of $W_0(z)$, $U_0(0,z)$, $T_0(z)$, and $T_0'(z)$ in the core, and $\bar{u}(z)$ and $\overline{T}'(z)$ in the boundary layer. The shapes of the vertical and horizontal core velocity distributions are the result of the competing effects of entrainment ($\bar{u}(z) < 0$) or ejection ($\bar{u}(z) > 0$) and the core temperature gradient $T_0'(z)$ in controlling the dynamics of the side-wall boundary layer. As noted by Gill [10], if $T_0' = 0$, then an ejecting boundary layer cannot exist. This is an immediate consequence of equation (19). With $\overline{T}' = 0$, we must have $\bar{u} < 0$ to satisfy the condition of exponential decay ($\lambda > 0$) of w and θ in the boundary layer. In contrast, when $\overline{T}' > 0$, ejection from the boundary layer is possible. For our purposes, it is sufficient to point out that the stable stratification within the core has its most significant influence upon the boundary layer in the domain between the two minima in the curve for $T_0'(z)$. In the regions $z > 0.4$ and $z < -0.4$, where the boundary layer is strongly entraining or ejecting, the core temperature gradient has a much weaker effect. We also expect the boundary layer approximation to break down near the lower boundary.

Though the core temperature distribution in Fig. 3 appears nearly linear in z, there is a variation in T_0' (z) as demanded in equation (10*b*). The dimensionless temperature gradient at $z = 0$ was calculated to be $T_0'(0) = 2.362$. Note that $T_0(z)$ does not satisfy the adiabatic condition $T_{0_z} = 0$ at $z = \pm 1/2$. In addition, U_0 is singular at these points. This happens because the horizontal boundary layers have been ignored in the approximate analysis used here.

The exponential thickness scale of the boundary layer along a lateral wall varies in the manner shown in Fig. 4. The value at $z = 0$ is $\delta_e(0) = 1.18$. The behavior of $\delta_e(z)$ near the upper left-hand corner must be interpreted with caution. Unlike the external free-convection boundary layer along a heated or cooled vertical plate, the leading edge of the boundary layer in the enclosure is modified by the influx from the stagnation layer near the top surface. The effect will be most important very near the corner where the horizontal inflow must join the downward flowing layer. It is possible that a secondary, recirculating flow will occur there under certain conditions, but the prediction of such additional complexities requires a considerably more refined analysis.

The local Nusselt number distribution, $\mathrm{Nu}(z)$, also displayed in Fig. 4, indicates that the great majority of the heat generated in the core is removed along the upper part of the side boundary. There is the familiar singularity in $\mathrm{Nu}(z)$ at $z = 1/2$ (the 'leading edge'), similar to that found in the external free-convection case. If proper account were taken of the conjunction of the horizontal and vertical boundary layers at the corner, then such a singularity would not exist. Note, however, that the steepest rise in $\mathrm{Nu}(z)$ takes place only along the upper 2 to 3 percent of the wall while the predicted values along the rest of the wall remain quite reasonable.

To the author's knowledge, there are no published experimental data in the high Rayleigh number regime with which to compare the theoretical magnitudes for $\mathrm{Nu}(z)$ presented here. Yet, it might be mentioned in passing that the experimental results of Gabor, et al. [14], for rectangular, internally heated *boiling* pools indicate that, for low boiling rates, the local sideward heat flux along the upper 10 to 20 percent of a cooled vertical wall is about twice as great as the average flux over the lower portion of the wall.

The velocity and temperature profiles, $w(\eta,z)$ and $\theta(\eta,z)$, for the boundary layer adjacent to the left-hand wall are shown in Figs. (5*a*,*b*) for three different values of z. These profiles are characteristic of boundary-layer flows under the influence of strong ambient stratification. In particular, note the over-shoots in w and θ near the outer edge of the boundary layer. Both the peak velocity and the wall temperature gradient diminish as the flow traverses the length of the wall from top to bottom.

Contours of the core stream function, plotted in Fig. 6, give the overall convection pattern within the enclosure. The figure shows only the streamlines in the left-half of the enclosure, those in the right-half being obtained by a simple reflection about the vertical axis at $x = 1$. The flow is almost vertical in the center of the cavity near the

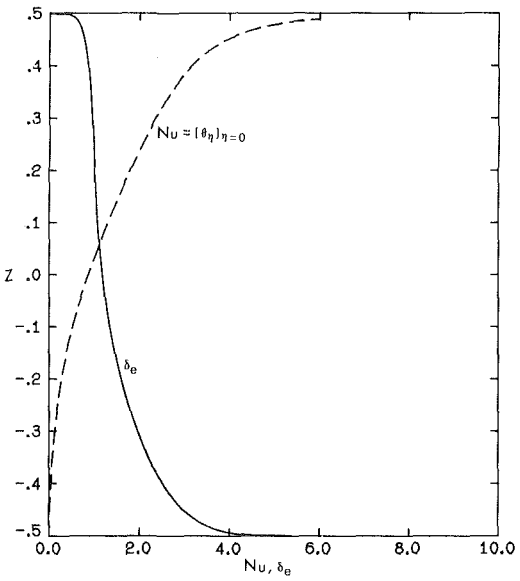

Fig. 4 Variations of δ_e and Nu with z

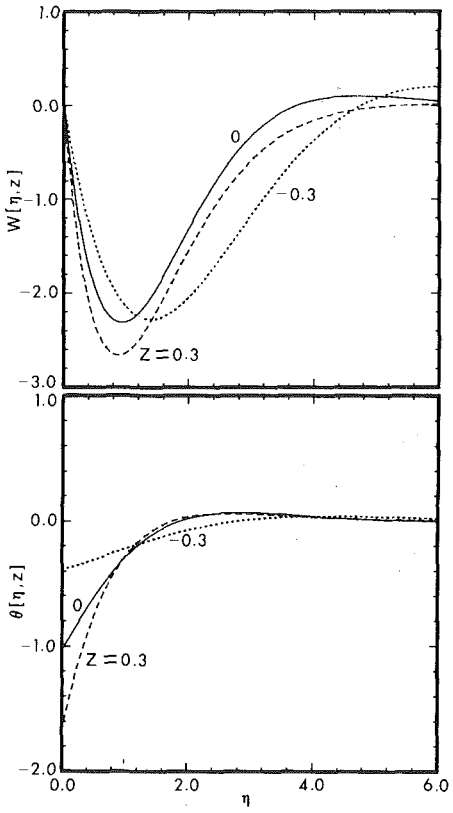

Fig. 5 Boundary-layer velocity and temperature profiles

stagnation streamline. However, as the outer edge of the boundary layer is approached, the core streamlines become more highly skewed owing to the enhanced horizontal flow induced by the boundary layer. The compaction of the streamlines near the top and bottom boundaries indicates an increase in the mass flux in these regions, but, of course, the viscous stagnation boundary layers there will alter the results somewhat.

It is of interest to calculate an approximate lower bound on $\overline{\mathrm{Ra}}_I$ for which the boundary-layer theory is justified. To accomplish this, consider the boundary-layer velocity profile at the level $z = -0.2$, above which nearly all of the heat transfer occurs. A reasonable estimate for the thickness of the boundary layer at this level would be π

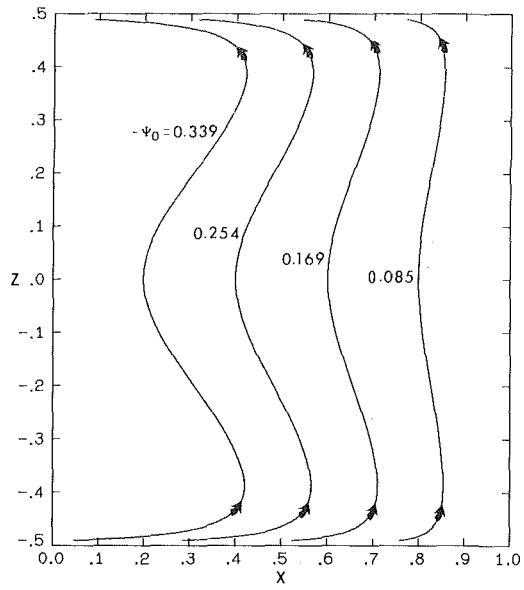

Fig. 6 Core streamlines in left-half of enclosure

$\delta_e(-0.2) = 5.0$, at which point $w = 0$. Thus, it follows from the stretching transformation $\eta = \overline{\mathrm{Ra}}_I^{1/5} x$, with $x = \delta$, that

$$\delta(-0.2) = 5.0\, \overline{\mathrm{Ra}}_I^{-1/5}. \tag{33}$$

In his analysis of natural convection in a rectangular cavity with lateral heating, Gill [10] estimated that $\delta \leq \frac{1}{2}$ should be satisfied for the boundary layers to be relatively distinct and noninteracting. (Recall that δ is just the ratio of the dimensional boundary layer thickness to the half-width of the cavity.) Owing to the close relationship between the present problem and the one studied by Gill, it seems appropriate to use the condition $\delta(-0.2) \leq \frac{1}{2}$ in the computation of a lower bound for $\overline{\mathrm{Ra}}_I$. Hence, from equation (33), we find that

$$\overline{\mathrm{Ra}}_I \geq 10^5 \tag{34}$$

is the tentative requirement for the boundary-layer theory to be meaningful.

Conclusions

The characteristics of natural convection of a heat generating fluid in a rectangular cavity cooled at the side walls have been studied analytically for flow in the boundary-layer regime at large internal Rayleigh number. It was found that the primary convective flow consists of a bicellular circulation in which the cold, downward-flowing boundary layers on the lateral walls generate a nearly uniform, upward flow in the core. In addition, a strong, stable vertical temperature gradient is established in the core by the process of upward convection of heat. The side-wall heat flux distribution shows that most of the heat generated within the enclosure is removed along the upper extremity of each vertical wall, and the Nusselt numbers on each wall were found to vary as $\overline{\mathrm{Ra}}_I^{1/5}$.

Clearly, though, the scope of this theory is limited by the assumptions and approximations employed in the Oseen linearization method. Furthermore, one would expect that there is an upper limit to the magnitude of $\overline{\mathrm{Ra}}_I$ beyond which a transition to unsteady or turbulent flow would occur. Nevertheless, certain extensions and refinements of the analysis would be of interest. For example, explicit consideration of the stagnation boundary layers and the corner flows would allow a quantitative determination of the sidewall Nusselt number near the upper and lower boundaries. Also, experimental data are needed to verify the predicted distributions of $W_0(z)$ and $T_0(z)$ in the core and Nu(z) along the vertical walls. Currently, work is continuing along two paths: (1) modification of the analysis to account for the effects of vertical asymmetry, including more realistic horizontal boundary conditions, and (2) comparison of the analytical results with a complete numerical solution of the problem.

The results of this work should be useful as an analytical counterpart to numerical and experimental investigations in areas such as nuclear reactor safety, the containment of heat generating radioactive wastes, and convection in fluids undergoing exothermic chemical reactions.

References

1 Hammitt, F. G., "Modified Boundary Layer Type Solution for Free-Convection Flow in Vertical Closed Tube with Arbitrarily Distributed Internal Heat Source and Wall Temperature," ASME Paper No. 58-SA-30 presented at the Semi-Annual Meeting, Detroit, Mich., June 15–19, 1958.

2 Hammitt, F. G., "Natural-Convection Heat Transfer in Closed Vessels with Internal Heat Sources–Analytical and Experimental Study," ASME Paper No. 58-A-212, presented at the Winter Annual Meeting, New York, N.Y., Nov. 30–Dec. 5, 1958.

3 Martin, B. W., "Free Convection in a Vertical Cylinder with Internal Heat Generation," *Proceedings of the Royal Society,* Series A, Vol. 301, 1967, pp. 327–341.

4 Murgatroyd, W., and A. Watson, "An Experimental Investigation of the Natural Convection of a Heat Generating Fluid within a Closed Vertical Cylinder," *Journal of Mechanical Engineering Sciences,* Vol. 12, 1970, pp. 354–363.

5 Watson, A., "Natural Convection of a Heat Generating Fluid in a Closed Vertical Cylinder: An Examination of Theoretical Predictions," *Journal of Mechanical Engineering Sciences,* Vol. 13, 1971, pp. 151–156.

6 Jones, D. R., "Convective Effects in Enclosed Exothermically Reacting Gases," *International Journal of Heat Mass Transfer,* Vol. 17, 1974, pp. 11–21.

7 Kee, R. J., C. S. Landram, and J. C. Miles, "Natural Convection of a Heat-Generating Fluid within Closed Vertical Cylinders and Spheres," ASME JOURNAL OF HEAT TRANSFER, Vol. 198, 1976, pp. 55–61.

8 Ostrach, S., "Natural Convection in Enclosures," *Advances in Heat Transfer,* Vol. 8, 1972, pp. 161–227.

9 Elder, J. W., "Laminar Free Convection in a Vertical Slot," *Journal of Fluid Mechanics,* Vol. 23, 1965, pp. 77–98.

10 Gill, A. E., "The Boundary-Layer Regime for Convection in a Rectangular Cavity," *Journal of Fluid Mechanics,* Vol. 26, pp. 515–536.

11 Carrier, G. F., *Proceedings of the 10th International Conference of Applied Mechanics,* 1962.

12 Weinbaum, S., "Natural Convection in a Horizontal Circular Cylinder," *Journal of Fluid Mechanics,* Vol. 18, 1964, pp. 409–437.

13 Quon C., "High Rayleigh Number Convection in an Enclosure—A Numerical Study," *Physical Fluids,* Vol. 15, 1972, pp. 12–19.

14 Gabor, J. D., L. Baker, J. C. Cassulo, and G. A. Mansoori, "Heat Transfer from Heat-Generating Boiling Pools," *AIChE Symposium Series,* Vol. 73, 1977, pp. 78–85.

Steady Thermal Convection from a Concentrated Source in a Porous Medium[1]

C. E. Hickox
Mem. ASME

H. A. Watts

Sandia National Laboratories,
Albuquerque, N.M. 87185

Solutions for the steady, axisymmetric velocity and temperature fields associated with a point source of thermal energy in a fluid-saturated porous medium are obtained numerically through use of similarity transformations. The two cases considered are those of a point source located on the lower, insulated boundary of a semi-infinite region and a point source embedded in an infinite region. Numerical results are presented from which complete descriptions of the velocity and temperature fields can be constructed for Rayleigh numbers of 0.1, 1.0, 10.0, and 100.0.

1 Introduction

In a previous paper, Wooding [1] demonstrated the utility of simple models for the description of geothermal flow processes. Of particular interest in the present context, Wooding considered the case of a point source of thermal energy located on the lower boundary of a semi-infinite, fluid-saturated, porous medium. When vertical gradients of velocity and thermal conduction were negligible compared with horizontal gradients, and the Boussinesq approximation was invoked, Wooding was able to show that similarity solutions for planar or axisymmetric flow could be obtained by direct analogy with the solutions given by Schlichting [2] for planar or axisymmetric, incompressible, laminar jets. The approximations imposed were, generally speaking, valid only for sufficiently large values of the Rayleigh number.

Since point source solutions can be of considerable practical utility, a more complete analysis, which requires no assumptions regarding the relative magnitudes of horizontal and vertical gradients, is developed in the present paper. Two cases, both concerned with axisymmetric flow and valid for any value of the Rayleigh number, are considered. In the first instance, the physical arrangement is identical to that considered by Wooding. The second case treats the problem of axisymmetric flow induced by a point source embedded in an infinite, fluid-saturated, porous medium. Both cases are analyzed through the introduction of similarity transformations resulting in sets of nonlinear ordinary differential equations which are then solved numerically in order to provide descriptions of the velocity and temperature fields.

2 General Theory

In this section, mathematical models are developed for the description of axisymmetric free convection in a fluid-saturated porous medium. The medium is assumed to be rigid, homogeneous, and isotropic, and the fluid incompressible, with density changes occurring only as a result of changes in the temperature according to

$$\rho = \rho_\infty[1 - \beta(T - T_\infty)], \tag{1}$$

where ρ is the density, T is the temperature, β is the coefficient of thermal expansion, and the subscripts refer to reference conditions. In accordance with the usual Boussinesq approximation, density changes are accounted for only in the buoyancy term in the equation of motion. It is also assumed that the fluid and matrix are in thermal equilibrium and that the fluid motion can be adequately described by Darcy's law. Permeability, viscosity, effective thermal diffusivity, and the coefficient of thermal expansion are assumed constant and dispersion effects are neglected.

The steady-state equations of continuity, motion, and thermal transport are then

$$\operatorname{div} \mathbf{v} = 0, \tag{2}$$

$$\frac{\mu}{k}\mathbf{v} = -\operatorname{grad}(p + \rho g h), \tag{3}$$

$$\mathbf{v} \cdot \operatorname{grad} T = \alpha \operatorname{div}(\operatorname{grad} T), \tag{4}$$

where $\mathbf{v}$, k, μ, α, p, and g are, respectively, the velocity vector, permeability, dynamic viscosity, effective thermal diffusivity, pressure, and acceleration due to gravity. The elevation h is measured vertically upward and g is oppositely directed.

In the cases to be considered, thermal energy is released continuously at a finite rate from a point source. Hence, in the absence of any bounding surfaces which can inhibit motion, any deviation from an isothermal state will result in fluid motion. We, therefore, expect no lower limit for the occurrence of natural convective motion.

2.1 Point Source at the Base of a Semi-Infinite Region. Here we wish to consider the axisymmetric flow induced by a point source of strength Q (energy generated per unit time) situated on the lower, insulated boundary of a semi-infinite region. Cylindrical polar coordinates (r, z) with associated velocity components (u, w) are used in the subsequent analysis. The origin of the coordinate system is coincident with the point source, and the z-axis is directed vertically upward.

The basic formulation now proceeds in a straightforward manner from equations (1–4). Equation (1) admits the introduction of a stream function ψ defined by

$$ru = -\frac{\partial \psi}{\partial z}, \; rw = \frac{\partial \psi}{\partial r}. \tag{5}$$

Introduction of the similarity transformations

$$\eta = r/z, \; \psi = \alpha z f(\eta), \; T - T_\infty = \left(\frac{\mu\alpha}{\rho_\infty g k \beta}\right)\frac{\theta(\eta)}{z}, \tag{6}$$

as suggested by Yih [3], allows equations (1–4) to be reduced to the set of nonlinear ordinary differential equations,

$$(\eta^3 + \eta)f'' - f' = \eta^2\theta', \tag{7}$$

$$-(f\theta)' = (\theta'\eta)' + (\eta^2\theta)' + (\eta^3\theta')', \tag{8}$$

where primes denote differentiation with respect to η. An additional requirement obtained upon integration of equation (4) over a plane taken normal to the z-axis is

$$\int_0^\infty (f'\theta + \eta\theta + \eta^2\theta')d\eta = \mathrm{Ra}, \tag{9}$$

where Ra is the Rayleigh number

[1] This work was supported by the U.S. Department of Energy under contract DE-AC04-76DP00789.

Contributed by the Heat Transfer Division and presented at the 18th AIChE/ASME National Heat Transfer Conference, San Diego, Calif., August 6–8, 1979 of THE AMERICAN SOCIETY OF MECHANICAL ENGINEERS. Manuscript received at ASME Headquarters June 18, 1979. Paper No. 79-HT-69.

$$\mathrm{Ra} = Qgk\beta/2\pi\alpha^2\mu c, \tag{10}$$

and c is the specific heat of the fluid. Physically, equation (9) shows that the net energy flux is constant for any plane taken normal to the vertical axis. For future reference, the relationships between velocities and similarity parameters are

$$u = \frac{\alpha}{z}\eta\left(\frac{f}{\eta}\right)', \; w = \frac{\alpha}{z}\left(\frac{f'}{\eta}\right). \tag{11}$$

From physical arguments, it is expected that u, w, and $(T - T_\infty)$ should approach zero for large r. In addition, u as well as the radial gradients of w and T should be zero along the axis of symmetry. These requirements yield the boundary conditions

$$f(0) = 0 = \theta'(0), \tag{12a}$$

$$f'(\infty) = 0 = \theta(\infty). \tag{12b}$$

Solution of equations (7) and (8) subject to the integral relation and boundary conditions given by equations (9) and (12) will provide a complete description of the thermal and flow fields.

2.2 Point Source in an Infinite Medium. In order to analyze the axisymmetric flow field induced by a point source in an infinite medium, it is appropriate to adopt spherical polar coordinates (R, Φ) with associated velocity components (v_R, v_Φ). The angle Φ is measured from the vertical axis (z-axis as introduced in Section 2.1) to the radial position vector $\mathbf{R}$. The velocity component v_R is in the direction of $\mathbf{R}$. The other velocity component v_Φ is normal to $\mathbf{R}$, lies in the plane of R and z, and is positive in the direction of increasing Φ. The origin of coordinates is again taken coincident with the point source.

The formulation for this case, in essence, parallels that presented in the first part of the section. A stream function ψ is defined such that

$$v_R = \frac{1}{R^2 \sin\Phi}\frac{\partial\psi}{\partial\Phi}, \; v_\Phi = \frac{-1}{R\sin\Phi}\frac{\partial\psi}{\partial R}. \tag{13}$$

Based on certain apparent similarities between the present system of equations and those derived by Squire [4] in his study of the round laminar jet, we introduce the following substitutions

$$\eta = \cos\Phi, \; \psi = \alpha R f(\eta), \; T - T_\infty = \frac{\mu\alpha}{\rho_\infty g k\beta}\frac{\theta(\eta)}{R}. \tag{14}$$

The original system of partial differential equations can now be reduced to the system of ordinary differential equations

$$f'' = -(\eta\theta)', \tag{15}$$

$$(f\theta)' = \theta'' - (\eta^2\theta')', \tag{16}$$

where primes denote differentiation with respect to η. Integration of equation (4) over a sphere centered about the origin provides the relation

$$\int_{-1}^{1}(1 - f')\theta d\eta = \mathrm{Ra}, \tag{17}$$

where Ra is the Rayleigh number as defined in equation (10). Velocity components are now given by

$$v_R = -\frac{\alpha}{R}f'(\eta), \; v_\Phi = -\frac{\alpha}{R}(1-\eta^2)^{-1/2}f(\eta). \tag{18}$$

As before, it is expected that v_R, v_Φ, and $(T - T_\infty)$ should approach zero for large R and that the solution should exhibit symmetry about a vertical axis. These physical requirements translate into the conditions

$$f(1) = 0 = f(-1), \tag{19a}$$

$$\theta, \theta' \text{ bounded for } \eta = \pm 1. \tag{19b}$$

Although, in some instances, the notation used in this section is in conflict with that used in the previous section, no confusion should exist so long as the two cases are considered separately.

3 Approximate Analytical Solutions

When the Rayleigh number is sufficiently small, approximate analytical results can be obtained for both cases under consideration. For large Rayleigh numbers, Wooding [1] obtained an approximate solution for the semi-infinite region by analogy with the results of Schlichting [2] for incompressible laminar jets. Presently, we know of no corresponding solution for the point source in an infinite region. The various approximate solutions are presented in the remainder of this section. These results are useful in that they provide bounds for the more general numerical results which will be presented subsequently.

3.1 Point Source at the Base of a Semi-Infinite Region. For small Rayleigh number, solutions to equations (7–9) can be obtained by straightforward expansion of the dependent variables in terms of the Rayleigh number. The leading terms resulting from this process provide the approximations

$$f = -\frac{1}{2}\mathrm{Ra}\,[(\eta^2+1)^{-1/2} - 1], \tag{20}$$

$$\theta = \mathrm{Ra}\,(\eta^2+1)^{-1/2}, \tag{21}$$

where it may be noted that equation (21) produces the steady-state conduction solution associated with a point source.

For a sufficiently large Rayleigh number, Wooding's analysis [1] provides the results

$$f = \frac{3}{8}\mathrm{Ra}\,\eta^2\left(1 + \frac{3}{32}\mathrm{Ra}\,\eta^2\right)^{-1}, \tag{22}$$

$$\theta = \frac{3}{4}\mathrm{Ra}\left(1 + \frac{3}{32}\mathrm{Ra}\,\eta^2\right)^{-2}. \tag{23}$$

3.2 Point Source in an Infinite Medium. For small Rayleigh number, the leading terms of an expansion in terms of the Rayleigh number provide the approximate results [5]

$$f = \frac{1}{4}\mathrm{Ra}\,(1-\eta^2) + \frac{1}{24}\mathrm{Ra}^2\,\eta(1-\eta^2), \tag{24}$$

$$\theta = \frac{1}{2}\mathrm{Ra} + \frac{1}{8}\eta\,\mathrm{Ra}^2, \tag{25}$$

where it may be noted that the first term of equation (25) produces

Nomenclature

F = parameter introduced in equation (36)
f = nondimensional function related to stream function
g = acceleration of gravity
H = vertical transport of fluid particle
h = elevation
k = intrinsic permeability
p = pressure
Q = strength of point source
$\mathbf{R}$ = position vector in spherical polar coordinates
Ra = Rayleigh number
(r, z) = cylindrical polar coordinates
(R, Φ) = spherical polar coordinates
T = temperature
t = time
(u, w) = velocity components in cylindrical polar coordinates
(v_R, v_Φ) = velocity components in spherical polar coordinates
$\mathbf{v}$ = velocity vector
α = thermal diffusivity
β = coefficient of volumetric thermal expansion
η = similarity variable
θ = nondimensional function related to temperature
μ = dynamic viscosity
ρ = density
ψ = stream function
ζ = integration variable

Subscript

∞ = reference conditions far from point source

the steady-state conduction solution associated with a point source.

4 Computational Approach

Although the use of similarity transformations results in simplified formulations for the cases considered, the resulting equations are still of sufficient complexity to warrant the use of numerical techniques in order to obtain general solutions. Efficient, state-of-the-art computer codes, currently under development at Sandia Laboratories [6, 7] and designed specifically for the solution of two-point boundary value problems, were utilized for the numerical solutions. In the remainder of this section, numerical results are presented along with brief descriptions of the techniques employed in the analysis.

4.1 Point Source at the Base of a Semi-Infinite Region [8]. Equations (7) and (8) can be integrated once to provide

$$\left(\eta + \frac{1}{\eta}\right) f' - f = \theta + C_1, \tag{26}$$

$$-f\theta = (\eta^3 + \eta)\theta' + \eta^2\theta, \tag{27}$$

where C_1 is a constant of integration, and the constant of integration associated with equation (27) is equal to zero by virtue of equation (12a). Further integration of the differential equations by analytical methods does not appear feasible.

In order to obtain numerical solutions, equations (26) and (27) could be solved subject to the boundary conditions given by equations (12) for a specified value of the constant C_1. Then C_1 could be varied until the constraint condition given by equation (9) is satisfied. However, it is desirable to automate the entire process within the framework of solving only differential equations. Thus, a differential equation for C_1 is added and equation (9) is modified to provide

$$S(\eta) = \int_0^\eta (f'\theta + \zeta\theta + \zeta^2\theta')d\zeta, \tag{28}$$

where the integration variable is now ζ. The original boundary value problem can now be expressed by the system of first order differential equations

$$\theta'(\eta) = -(\eta + \eta^3)^{-1}(f + \eta^2)\theta, \ \eta > 0, \tag{29a}$$

$$f'(\eta) = \eta(1 + \eta^2)^{-1}(\theta + f + C_1), \tag{29b}$$

$$C_1'(\eta) = 0, \tag{29c}$$

$$S'(\eta) = \eta(1 + \eta^2)^{-1}(\theta + C_1 + 1)\theta, \tag{29d}$$

subject to the boundary conditions

$$f(0) = 0 = S(0), \tag{30a}$$

$$f(\infty) = -C_1, S(\infty) = \mathrm{Ra}. \tag{30b}$$

The condition $\theta'(0) = 0$ is used directly to give proper definition to equation (29a) at the origin. Equation (29d) is obtained upon differentiation of equation (28) and substitution from equations (29a) and (29b). The boundary conditions on S follow directly from consideration of equations (9) and (28). The condition $f'(\infty) = 0$ is automatically satisfied by the differential equation (29b) under the assumption of boundedness for $f(\eta)$ and $\theta(\eta)$. An even stronger condition emerges under our physical constraints—namely, $\lim_{\eta\to\infty} \eta f'(\eta) = 0$. Using this requirement along with the condition $\theta(\infty) = 0$ in equation (29b) leads to the new boundary condition on f, given by $f(\infty) + C_1 = 0$. The motivation for using this condition stems from difficulties encountered in attempting to obtain satisfactory numerical solutions when the condition $\theta(\infty) = 0$ was imposed. It was observed that θ was driven to zero for large η regardless of the acceptability of the other variables. With the alternate boundary condition, the solution algorithm was less sensitive to poor initial guesses for $\theta(0)$ and C_1.

Numerical solutions of equations (29) subject to the boundary conditions given by equations (30) were obtained for Rayleigh numbers of 0.1, 1.0, 10.0, and 100.0. A computer code, SHOOT2 [6], based on a shooting procedure which uses current state-of-the-art variable step size integration methods was employed for the solution of the boundary value problem. The integration was carried out to a value of 1000 for η in all cases. This interval was found to be of sufficient magnitude to ensure the accuracy of solutions in regions of physical interest.

Numerically determined values for $\theta(\eta)$, $f(\eta)$, and $f'(\eta)$ are plotted versus η, with Rayleigh number as a parameter, in Figs. 1–3. For convenience in plotting, it was necessary to scale the various functions. Numerical values of the scaling parameters $\theta(0)$ and $f(\infty)$ are tabulated in Table 1. In Figs. 1–3, the dashed curves are obtained from the large Rayleigh number solutions given by equations (22) and (23). Comparisons are made only for Rayleigh numbers of 10 and 100. For a Rayleigh number of 1.0, the large Rayleigh number approximation is no longer valid, hence no comparison to the numerical results is attempted. The small Rayleigh number approximations, as given by equations (20) and (21), are indistinguishable from the curves for a Rayleigh number of 0.1 as plotted in Figs. 1–3.

If the constant of integration C_1 and the function $\theta(0)$ are known a priori for a specified Rayleigh number, then equations (29) and (30) can be integrated in a straightforward manner. As a guide to the selection of C_1 and $\theta(0)$, values for these parameters are tabulated for selected Rayleigh numbers in Table 1. Since $C_1 = -f(\infty)$, the approximate analytical solutions given by equations (20) and (22) can be used to show that the limiting values for C_1 are $-\mathrm{Ra}/2$ for small Rayleigh number and -4 for large Rayleigh number. Limiting values for $\theta(0)$, as obtained from equations (21) and (23), are Ra for small Rayleigh number and $3\mathrm{Ra}/4$ for large Rayleigh number.

4.2 Point Source in an Infinite Medium. The numerical solution procedure utilized for this problem closely parallels that of the preceding case. The basic differential equations (15) and (16) can be integrated once to provide

$$f' = -\eta\theta + C_2, \tag{31}$$

$$f\theta = (1 - \eta^2)\theta', \tag{32}$$

where C_2 is a constant of integration, and the constant of integration associated with equation (32) is zero by virtue of the boundary conditions given by equations (19). As before, the integral constraint given by equation (17) is rewritten as

$$S(\eta) = \int_{-1}^\eta (1 - f')\theta d\zeta. \tag{33}$$

Now the original boundary value problem can be expressed by the system

$$\theta'(\eta) = (1 - \eta^2)^{-1} f\theta, \tag{34a}$$

$$f'(\eta) = -\eta\theta + C_2, \tag{34b}$$

$$C_2'(\eta) = 0, \tag{34c}$$

$$S'(\eta) = (1 + \eta\theta - C_2)\theta, \tag{34d}$$

subject to the boundary conditions

$$f(-1) = 0 = f(1), \tag{35a}$$

$$S(-1) = 0, S(1) = \mathrm{Ra}. \tag{35b}$$

A complication arises due to the singular nature of equation (34a) at the boundary points. This difficulty is, however, easily removed since a straightforward analysis using equations (34a) and (34b) shows that $\theta'(\pm 1) = \mp(\frac{1}{2})\theta(\pm 1)f'(\pm 1)$. The numerical solution of the differential system given by equations (34) subject to the boundary conditions specified by equations (35) was obtained through use of the computer code SUPOR Q [7] which utilizes quasilinearization techniques coupled with superposition and an orthonormalization process.

Numerically determined values for $\theta(\eta)$, $f(\eta)$, and $f'(\eta)$ are plotted versus the angle Φ, with Rayleigh number as a parameter, in Figs. 4–6. Values for the scaling parameters used in these figures are tabulated in Table 2. The dashed curve in Fig. 4 represents the low Rayleigh number solution given by equation (25). For a Rayleigh number of 0.1, the approximate solution is indistinguishable from the numerical results when plotted in Fig. 4. The approximate results given by

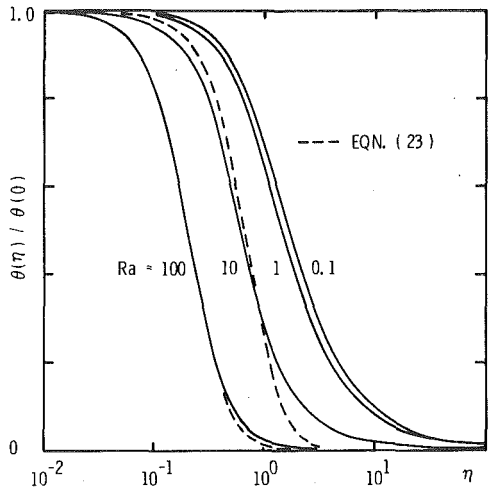

Fig. 1 The function $\theta(\eta)/\theta(0)$ for the semi-infinite region

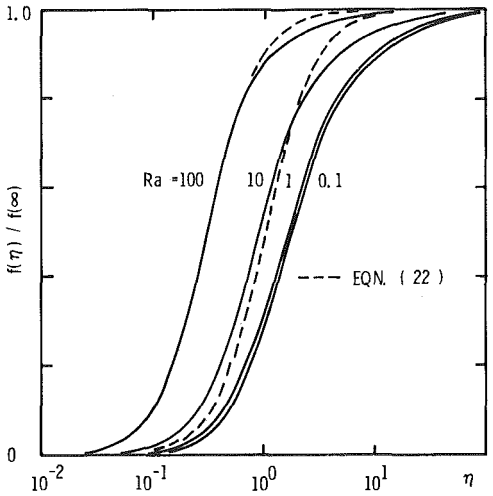

Fig. 2 The function $f(\eta)/f(\infty)$ for the semi-infinite region

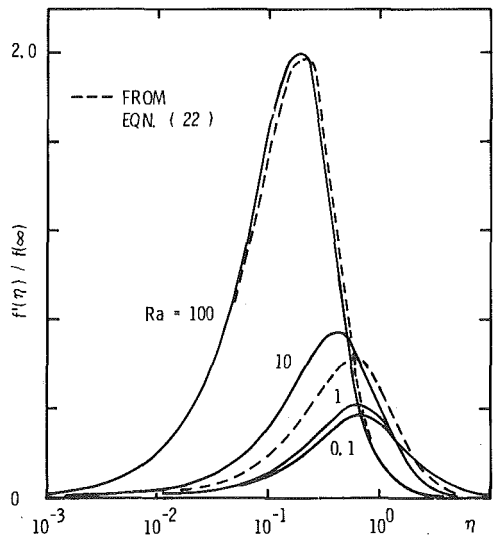

Fig. 3 The function $f'(\eta)/f(\infty)$ for the semi-infinite region

Table 1 Selected numerical results for the semi-infinite region. Tabulated values are accurate to four significant figures

Ra	$\theta(0)$	$-C_1, f(\infty)$	$f''(0)$
0.1	1.0106 E − 1	5.0174 E − 2	5.0889 E − 2
0.5	5.2461 E − 1	2.5274 E − 1	2.7186 E − 1
1	1.0959 E + 0	5.0673 E − 1	5.8917 E − 1
5	6.0983 E + 0	1.9746 E + 0	4.1237 E + 0
10	1.1213 E + 1	2.6640 E + 0	8.5489 E + 0
50	4.2955 E + 1	3.6091 E + 0	3.9346 E + 1
100	8.0541 E + 1	3.7921 E + 0	7.6749 E + 1

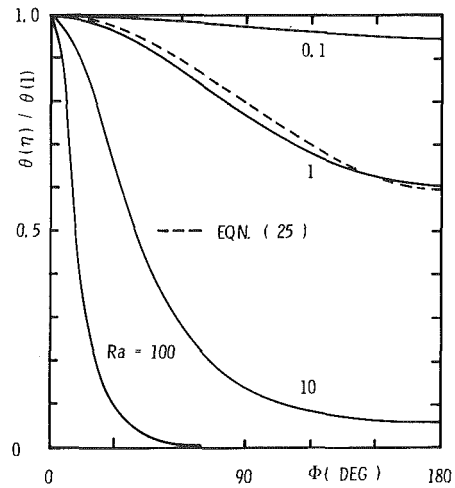

Fig. 4 The function $\theta(\eta)/\theta(1)$ for the infinite region

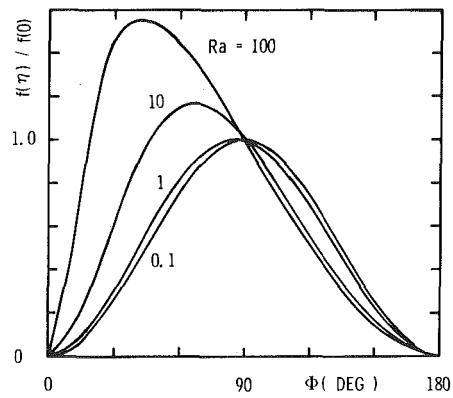

Fig. 5 The function $f(\eta)/f(0)$ for the infinite region

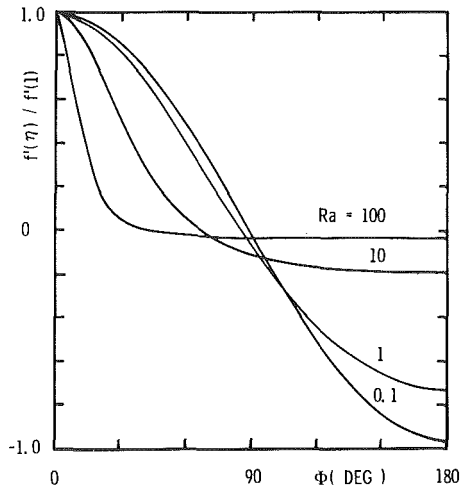

Fig. 6 The function $f'(\eta)/f'(1)$ for the infinite region

Table 2 Selected numerical results for the infinite region. Tabulated values are accurate to four significant figures

Ra	$\theta(1)$	$C_2, f'(0)$	$f(0)$	$-f'(1)$
0.1	5.1246 E − 2	4.1638 E − 4	2.4992 E − 2	5.0829 E − 2
0.5	2.8643 E − 1	1.0244 E − 2	1.2399 E − 1	2.7018 E − 1
1	6.1577 E − 1	3.9074 E − 2	2.4234 E − 1	5.7670 E − 1
5	4.0172 E + 0	4.5916 E − 1	8.4127 E − 1	3.5580 E + 0
10	8.2570 E + 0	8.2643 E − 1	1.1457 E + 0	7.4306 E + 0
50	3.9214 E + 1	1.5531 E + 0	1.6526 E + 0	3.7661 E + 1
100	7.6984 E + 1	1.7289 E + 0	1.7792 E + 0	7.5255 E + 1

equation (24) and its derivative are essentially identical to the numerical results for Rayleigh numbers of 0.1 and 1.0 when plotted in Figs. 5 and 6. For a Rayleigh number of 10, the small Rayleigh number approximation is no longer valid, hence no further comparison is attempted.

A knowledge of the values of C_2 and $\theta(1)$ for a specified Rayleigh number will allow equations (34) and (35) to be integrated in a straightforward manner. Numerical values for these parameters are tabulated for selected Rayleigh numbers in Table 2. Noting that $C_2 = f'(0)$, the approximate solution given by equation (24) can be used to show that the limiting value for C_2 for small Rayleigh number is $Ra^2/24$. Numerical results have been used to establish a limit of approximately 2 for large Rayleigh number. For small Rayleigh number, equation (25) yields a limiting value of Ra/2 for $\theta(1)$, and numerical results indicate a value of approximately 3 Ra/4 for large Rayleigh number.

4.3 Vertical Transport of Fluid Particles. A simple expression can be derived for the vertical transport of a fluid particle which is initially coincident with the point source. From a consideration of equations (11) and (18), it can be shown that the velocity along the axis of symmetry, for both cases considered, is

$$w = \alpha F/z, \tag{36}$$

where the parameter F is given by $f''(0)$ for the semi-infinite region and $-f'(1)$ for the infinite region. These parameters are tabulated for selected values of the Rayleigh number in Tables 1 and 2. If it is assumed that the fluid particle is initially coincident with the point source, then the total vertical transport H in a time interval t is expressed by

$$H = (2\alpha F t)^{1/2}. \tag{37}$$

Limiting values for $f''(0)$ for the semi-infinite region, as established from equations (20) and (22), are Ra/2 for small Rayleigh number and 3 Ra/4 for large Rayleigh number. For the infinite region, equation (24) yields a limiting value of Ra/2 for the function $-f'(1)$ for small Rayleigh number, and numerical results yield an approximate limiting value of 3 Ra/4 for large Rayleigh number.

5 Discussion

Accurate numerical solutions for the steady, axisymmetric velocity and temperature fields associated with a point source of thermal energy in a fluid-saturated porous medium were obtained through use of similarity transformations. The two cases considered were those of a point source located on the lower, insulated boundary of a semi-infinite region and a point source embedded in an infinite region. Representative plots of the isotherms and streamlines for each case considered are presented in Figs. 7 and 8 for a Rayleigh number of 10.

A careful examination of the numerical results indicates that, for a Rayleigh number of 0.1, the temperature distribution is closely approximated by the steady-state conduction solution. Isothermal surfaces are approximately hemispherical or spherical and are centered about the point source. The results for low Rayleigh number given by equations (20, 21, 24), and (25) then closely approximate the numerical solutions. When the Rayleigh number is 100, the solutions exhibit a plume-like behavior in agreement with the boundary layer

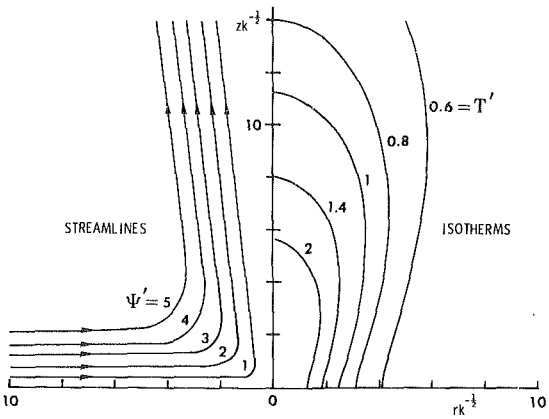

Fig. 7 Streamlines and isotherms for a point source at the base of a semi-infinite region, Ra = 10, $\psi' = \psi/\alpha k^{1/2}$, $T' = (T - T_\infty)\rho_\infty g\beta k^{3/2}/\mu\alpha$

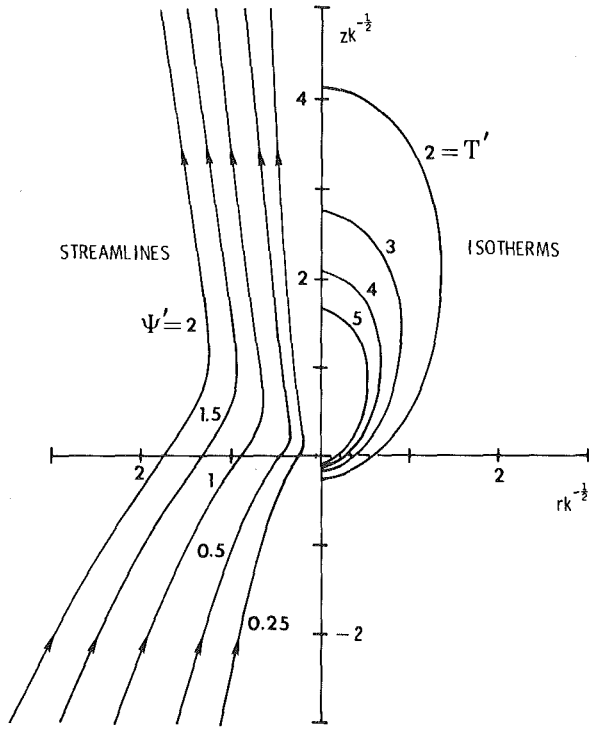

Fig. 8 Streamlines and isotherms for a point source in an infinite region, Ra = 10, ψ' and T' defined in Fig. 7

model proposed by Wooding. For the semi-infinite region, the results for large Rayleigh number given by equations (22) and (23) are found to be reasonably accurate, even for a relatively modest value of 100 for the Rayleigh number. In general, the numerical results exhibit a smooth transition from flows which are conduction dominated at low Rayleigh number to flows with boundary layer behavior at large Rayleigh number.

The plots of the numerical results presented in the paper provide reasonably accurate estimates for the important features of the velocity and temperature fields. If, however, more detailed results are needed, tabulated numerical values for all important parameters are contained in reference [9].

References

1 Wooding, R. A., "Convection in a Saturated Porous Medium at Large Rayleigh or Peclet Number," *Journal Fluid Mechanics*, Vol. 15, 1963, pp. 527–546.

2 Schlichting, H., *Boundary Layer Theory*, 6th ed., McGraw-Hill, New York, 1965.

3 Yih, C.-S., *Dynamics of Nonhomogeneous Fluids*, MacMillan, New York, 1965.

4 Squire, H. B., "The Round Laminar Jet," *Quarterly Journal of Mechanics and Applied Mathematics*, Vol. 4, 1951, pp. 321–329.

5 Bejan, A., "Natural Convection in an Infinite Porous Medium with a Concentrated Heat Source,"*Journal Fluid Mechanics*, Vol. 89, Part 1, 1978, pp. 97–107.

6 Scott, M. R., and Watts, H. A., "A Systematized Collection of Codes for Solving Two-Point Boundary Value Problems," in *Numerical Methods for Differential Systems-Recent Developments in Algorithms, Software, and Applications*, L. Lapidus and W. Schiesser, Eds., Academic Press, New York, 1976.

7 Scott, M. R., and Watts, H. A., "Computational Solution of Nonlinear Two-Point Boundary Value Problems," *Proceedings 5th Symposium of Computers in Chemical Engineering*, Czechoslovakia, 1977, also Sandia Laboratories Report—SAND77-0091, Albuquerque, NM, 1977.

8 Hickox, C. E., and Watts, H. A., "Steady Thermal Convection from a Concentrated Source in a Porous Medium," SAND76-0562, Sandia Laboratories, Albuquerque, NM, 1976.

9 Hickox, C. E., and Watts, H. A., "Numerical Solutions for Steady Thermal Convection from a Concentrated Source in a Porous Medium," SAND79-2214, Sandia Laboratories, Albuquerque, NM, 1979.

Effects of Nonuniform Thermal Gradient and Adiabatic Boundaries on Convection in Porous Media

N. Rudraiah
B. Veerappa
S. Balachandra Rao

Department of Mathematics,
Central College,
Bangalore University,
Bangalore-560001, India

The effects of different combinations of thermally insulated boundaries and nonuniform thermal gradient caused by either sudden heating or cooling at the boundaries or by distributed heat sources on convective stability in a fluid saturated porous medium are investigated using linear theory by considering the Brinkman model. In the case of sudden heating or cooling, solutions are obtained using single-term Galerkin expansion and attention is focused on the situation where the critical Rayleigh number is less than that for uniform temperature gradient and the convection is not maintained. Numerical values are obtained for various basic temperature profiles and some general conclusions about their destabilizing effects are presented. In particular, it is shown that the results of viscous fluid ($\sigma = 0$) and the usual Darcy porous medium ($\sigma \to \infty$) emerge from our analysis as special cases. In the case of convection caused by heat source, since the effect of heat source is not brought out by the single-term Galerkin expansion, the critical internal Rayleigh number is determined using higher order expansion by specifying the external Rayleigh number. It is shown that, for values of $\sigma^2 \geq 2.45 \times 10^5$, the different combinations of bounding surfaces give almost the same Rayleigh number and an explanation, following Lapwood, for this surprising behavior is given. It is found that the heat source's effect on convection decreases for wave numbers up to the value 2.2 and drops suddenly around the critical value of 2.4 and then increases up to 2.5.

Introduction

Recently, Rudraiah, et al. [14] investigated the effect of nonuniform thermal gradient, caused by either sudden heating or cooling at the boundaries or by distributed heat sources, on the convective heat transfer in a fluid saturated porous medium using the Brinkman model specifying isothermal boundary conditions. Their motive was to use the results to understand convection in geothermal regions. In this isothermal case they specified that the perturbation temperature is zero at the boundaries. Physically, this is valid when the wall has high heat conductivity and large heat capacity. In many industrial applications, however, the most effective insulation for a given thermal conduction is provided by porous layer insulation consisting of solid particles and pores. In such situations, to store all the energy within the layer, it is desirable that the layers be bounded by thermally insulating boundaries. Further, the consideration of actual physical situations [15] suggests that the standard thermal boundary conditions of fixed temperature at the surfaces of the fluid layer may be too restrictive; in many real situations, heat can be exchanged between the surface and the environment. If the heat transfer coefficient between the surface and environment is finite, the surface temperature will be perturbed when the quiescent state breaks down. One might also cite various illustrations of the restrictive nature of the fixed temperature boundary conditions. For example, a situation which is of interest for experimental investigation in the laboratory is one of heating the lower surface by passing an electric current. In this case, instead of specifying the temperature at the lower boundary, one has to specify heat flux. These considerations have motivated us to investigate the convective stability with nonlinear basic temperature distribution arising either from sudden heating or cooling of the boundaries or from the internal heat sources, by specifying heat flux at the boundaries. More specifically, we try to answer the following questions: (1) What is the effect of adiabatic boundaries on convection when σ^2 is finite (Brinkman model) and when σ^2 is large (Darcy model)? and (2) using the Brinkman model, can one get the known result of Lapwood [6] viz., the difference in combinations of bounding surfaces has no significant effect on convection when $\sigma^2 \to \infty$ (Darcy porous medium)?

Contributed by the Heat Transfer Division for publication in the JOURNAL OF HEAT TRANSFER. Manuscript received by the Heat Transfer Division August 1, 1979.

In the viscous fluid case, the problem of convection arising from sudden heating or cooling was investigated by Nield [9] by considering adiabatic boundary conditions. Using the infinitely long wavelength approximations, he determined the situation where the critical Rayleigh number is less than that for a linear temperature profile. In particular, he has shown that if the basic temperature gradient is nowhere negative, then the profile which leads to the smallest critical Rayleigh number is the one in which temperature changes stepwise but is otherwise uniform. The problem of convection in the viscous fluid case arising from heat source was investigated by Sparrow, et al. [15] and Roberts [11]. Nield [9] also investigated the problem of convection in a porous medium arising from sudden heating or cooling by considering only Darcy resistance which is the friction offered by the solid particles to the fluid. As shown by Nield [9], this usual Darcy equation results in a fourth order differential equation to govern the onset of convection. Using physical arguments, however, six boundary conditions can be specified. In a mathematical sense, the problem is therefore not properly posed and we have an overspecified system. From a physical point of view, the no-slip condition is as valid as both other conditions and there appears no a priori reason to reject it. In fact, Morales, et al. [8] have shown that boundary conditions resembling no-slip do in fact exist in a sparsely packed porous bed reactor. Therefore, if a porous medium is made up of sparse distribution of particles [5, 17] which is usually the case in chemical and petroleum industrial applications, the usual Darcy equation is not suitable. For, in the case of sparse distribution of particles the porous medium will involve large void spaces which give rise to viscous shear in addition to the usual Darcy resistance. Therefore, to understand the onset of convection in a porous medium made up of sparse distribution of particles one has to take into account the viscous shear, however small it may be, in addition to the Darcy resistance. In other words, instead of considering only the potential nature of the Darcy equation, one has to consider also the boundary layer type of equation as postulated for the first time by Brinkman [2] (hereafter called the Brinkman model) for which a rigorous theoretical justification was given later by Tam [16] and Lundgren [7].

It is of interest to note that the Brinkman model is valid [5] up to magnitude of $k/d^2 \approx 10^{-3}$ or so. For example, if a porous medium made up of sparse distribution of spherical particles is considered,

the value of $k/d^2 \approx 10^{-3}$ corresponds to a considerably high value of d_p/d where d_p is the mean grain diameter and d is the thickness of the porous bed. For these high values of d_p/d the assumption of homogeneity of the medium may become questionable. As regards the theory, however, it must be pointed out that the microscopic state has been homogenized assuming the macroscopic velocity and temperature and the theory has been formulated using the permeability k and the relative thermal conductivity K^* which are both defined for the macroscopic quantities aforementioned. Under these approximations, according to the experiments of Katto and Masuoka [5], it is not unreasonable to assume homogeneity even when d_p/d becomes comparatively high. In fact, in Section 5 it is shown that for large values of σ^2 the results obtained from Brinkman model, suitably defining the Rayleigh number, tend to the results obtained by Lapwood [6]—namely, the different combinations of bounding surfaces have no significant effect on the onset of convection. Thus, we claim that even the Brinkman model gives the qualitative results of Lapwood [6] for large values of σ^2. We note that even when σ^2 is large, we should include the viscous shear, however, small it may be, in addition to the Darcy resistance. This is analogous to the classical boundary layer theory in fluid mechanics.

The basic equations for the Brinkman model and the corresponding boundary conditions are discussed in Section 2. The effect of nonlinear temperature distribution arising from sudden heating or cooling on thermal convection is discussed in Section 3 by considering free-free, rigid-free and rigid-rigid boundaries. In the case of sudden heating or cooling at the boundaries, the eigenvalues are determined following Nield [9] using the single-term expansion in the Galerkin method and the optimum distance at which maximum convection occurs is obtained by considering different temperature gradient profiles. A comparison of our results with those of the viscous fluid case reveals that even a single-term expansion gives accurate results in some cases although the use of single-term expansions is an approximate method.

The effect of nonlinear basic temperature distribution, arising from uniform distribution of internal heat sources, on convection in porous media is investigated in Section 4 by considering the different boundary combinations. It is shown, in general, that the single-term Galerkin expansion fails to bring out the effect of heat source and hence a higher order expansion in the Galerkin technique is resorted to study the heat source effect on convection. Detailed conclusions are drawn in Section 5. It is concluded that the effect of permeability of the medium is to augment the heat source effect and that for large values of σ^2, even in the Brinkman model, the different combinations in the bounding surfaces have no significant contributions on the onset of convection.

2 Mathematical Formulation

The porous material may be thought of as being composed of sparse distribution of particles [17] completely surrounded by Boussinesq fluid. The schematic diagram is shown in Fig. 1. The basic equations of motion for flow through porous media using Brinkman model under the Boussinesq approximation [3, 10] may be taken as

$$\frac{\partial \vec{q}}{\partial t} + (\vec{q} \cdot \nabla)\vec{q} = -\frac{1}{\rho_0}\nabla p + \frac{\rho}{\rho_0} g\hat{k} - \frac{\nu}{k}\vec{q} + \nu\nabla^2\vec{q} \qquad (2.1)$$

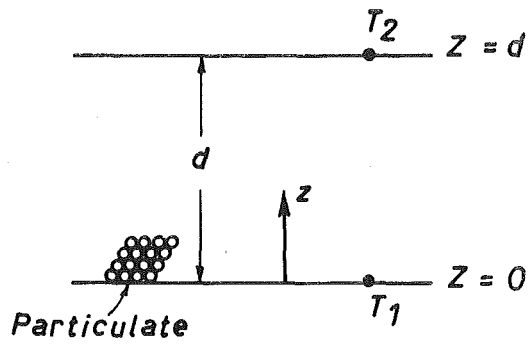

Fig. 1 Schematic illustration of a porous layer

Nomenclature

$a = \sqrt{\ell^2 + m^2}$, resultant horizontal wave number
C_{m_i} = coefficients in the expansion of the general solution for W in (4.7) with $i = 0, 1, 2, 3, 4$
d = thickness of the porous layer
d_p = mean grain diameter

$D = \dfrac{d}{dz}$

$f(z) = -\dfrac{d}{\Delta T}\dfrac{dT_0}{dz}$, nondimensional temperature gradient

g = acceleration due to gravity
$I_0^{nm}, I_i^n, I_5^{nm}, I^n{}_{i+5}{}^n$ = integrals obtained by integrating with respect to z from 0 to 1 the product of each term in (4.8) with $\cos(n\pi z)$
k = permeability (dimension of length squared)
$\hat{k}$ = unit vector in the z-direction
K^* = relative thermal conductivity of the porous medium as defined in (2.6)
K_f = thermal conductivity of the fluid
K_s = thermal conductivity of the solid
l,m = horizontal wave numbers in the directions of x and y axes
$M = (\rho C)^*/(\rho C)_f$
p = pressure
$\mathrm{Pr} = \nu/\kappa^*$, Prandtl number
$\mathbf{q}$ = mean filter velocity with components (u, v, w)
Q = uniformly distributed volumetric internal heat source strength
$\mathrm{R} = g\beta(\Delta T)d^3/\nu\kappa^*$, Rayleigh number

$\mathrm{R_E} = \dfrac{K_f}{K_s}\dfrac{g\beta(\Delta T)d^3}{\nu\kappa^*}$ external Rayleigh number

$\mathrm{R}_I = \dfrac{K_f}{K_s}\dfrac{g\beta Q d^5}{\nu\kappa^* K_s}$ internal Rayleigh number

$\mathrm{R}_L = \mathrm{R}/\sigma^2$, Rayleigh number as defined by Lapwood
T = temperature
T' = ambient temperature
T_0 = basic temperature distribution
T_1 = temperature at the lower boundary
T_2 = temperature at the upper boundary
$\Delta T = T_1 - T_2$, temperature difference between the boundaries
W = w-component of velocity being a function z only
β = coefficient of thermal expansion
ϵ = porosity of the medium
$\kappa^* = K^*/(\rho C)_f$, relative thermal diffusivity
ν = kinematic viscosity
ρ = density
ρ_0 = density at the ambient temperature
$(\rho C)^*$ = relative heat capacity of the porous medium as defined in (2.5)
$(\rho C)_f$ = heat capacity of the fluid
$(\rho C)_s$ = heat capacity of the solid
$\sigma = d/\sqrt{k}$, porous parameter
$\phi = a^2(a^2 + \sigma^2)$
$\psi = 2a^2 + \sigma^2$
ω = frequency

$$\nabla \cdot \vec{q} = 0 \tag{2.2}$$

$$(\rho C)^* \frac{\partial T}{\partial t} + (\rho C)_f (\vec{q} \cdot \nabla) T = K^* \nabla^2 T + Q \tag{2.3}$$

$$\rho = \rho_0 [1 - \beta (T - T')] \tag{2.4}$$

where

$$(\rho C)^* = \epsilon (\rho C)_f + (1 - \epsilon)(\rho C)_s \tag{2.5}$$

$$K^* = \epsilon K_f + (1 - \epsilon) K_s \tag{2.6}$$

It is assumed that the material is of infinite horizontal extent and bounded by two horizontal boundaries below and above which may be both free or both rigid or one free and one rigid, separated by a distance d apart. In dealing with free boundaries, we assume that the surface tension is negligible and that the boundaries are free from shear stresses.

3 Convection Due to Sudden Heating or Cooling

To study the stability of a quiescent state, given by $\partial p_0/\partial z = -g[1 - \beta(T_0 - T')]$ with non-linear basic temperature distribution $To(z)$ arising from the sudden heating or cooling of the boundaries, a small symmetric perturbation is superposed. They applying the usual procedure of linearization to (2.1) to (2.3), we get

$$\frac{\partial \vec{q}}{\partial t} = -\frac{1}{\rho_0} \nabla p - g\beta (T - T') \hat{k} - \frac{\nu}{k} \vec{q} + \nu \nabla^2 \vec{q} \tag{3.1}$$

$$\nabla \cdot \vec{q} = 0 \tag{3.2}$$

$$(\rho C)^* \frac{\partial T}{\partial t} + (\rho C)_f \frac{\partial T}{\partial z} W = K^* \nabla^2 T \tag{3.3}$$

Eliminating the pressure term in (3.1), assuming that all the physical quantities vary in the form

$$F(z) e^{i(lx + my - \omega t)} \tag{3.4}$$

and making the resulting equations dimensionless choosing

$$d,\ d^2/\nu,\ \nu/d,\ \frac{\nu}{ad} \sqrt{\frac{\Delta T}{d} \frac{\nu}{g\beta\kappa^*}}$$

as units of length, time, velocity and temperature respectively, one obtains

$$(D^2 - a^2)[D^2 - a^2 - (\omega + \sigma^2)] W - aR^{1/2} T = 0 \tag{3.5}$$

$$(D^2 - a^2 - M\omega P_r) T + aR^{1/2} f(z) W = 0 \tag{3.6}$$

The nondimensional temperature gradient $f(z)$ must satisfy ${}_0\int^1 f(z)dz = 1$ [9]. The selection of R appearing in (3.5) and (3.6) is convenient to apply the variation principle so that the eigenvalue R becomes insensitive in the Galerkin method used in this paper.

We now apply the Galerkin method as described by Nield [9]. Recently, Rudraiah and Rohini [12] and Rudraiah and Vortmeyer [13] established that overstable motions occur only in the presence of external constraints like rotation and magnetic field and in the absence of these, overstable convection cannot exist. In this paper, since there is no external constraint of rotation or magnetic field, we assume that the principle of exchange of stability is valid and, hence, the time derivatives in (3.5) and (3.6) vanish, i.e., $\omega = 0$. Then, multiplication of (3.5) by W and (3.6) by T and integration of the resulting equations with respect to z from 0 to 1 and using the boundary conditions $W = DW = 0$ in the case of rigid boundaries and $W = D^2W = 0$ in the case of free boundaries with $DT = 0$ on each thermally adiabatic boundary field

$$aR^{1/2} \langle WT \rangle = \langle (D^2W)^2 + (2a^2 + \sigma^2)(DW)^2 + a^2(a^2 + \sigma^2) W^2 \rangle \tag{3.7}$$

$$aR^{1/2} \langle f(z) WT \rangle = \langle (DT)^2 + a^2 T^2 \rangle \tag{3.8}$$

where the angle brackets denote the integration with respect to z from 0 to 1.

Substituting $W = AW_1$ *and* $T = BT_1$ into (3.7) and (3.8) and eliminating A and B and dropping the suffixes for simplicity, we get

$$R = \frac{\langle (D^2W)^2 + (2a^2 + \sigma^2)(DW)^2 + a^2(a^2 + \sigma^2) W^2 \rangle \langle (DT)^2 + a^2 T^2 \rangle}{a^2 \langle WT \rangle \langle f(z) WT \rangle} \tag{3.9}$$

As stated earlier, in the remaining part of this section we will consider situations where the bounding walls are both free or both rigid or lower boundary rigid and upper boundary free.

3.1 Both Boundaries Free. In this section, an estimate for the critical Rayleigh number is obtained when both the boundaries are stress-free and thermally adiabatic, so that the boundary conditions are

$$W = D^2W = DT = 0 \text{ at } z = 0,1 \tag{3.10}$$

We note that although both bounding surfaces being free may not be reliazable in practice, the mathematical analysis gets simplified. We assume the trial functions, satisfying the boundary conditions, to be of the form

$$W = z(1 - z)(1 + z - z^2),\ T = 1 \tag{3.11}$$

Equation (3.9), using (3.11), yields

$$R = \frac{\left\{24 + \frac{17}{7}(2a^2 + \sigma^2) + \frac{31}{126} a^2(a^2 + \sigma^2)\right\}}{\langle f(z)(z^4 - 2z^3 + z) \rangle} \tag{3.12}$$

The minimum value of R, for any given $f(z)$, occurs at $a = 0$ and its value, R_c, is

$$R_c = \frac{\left\{24 + \frac{17}{7}\sigma^2\right\}}{\langle f(z)(z^4 - 2z^3 + z) \rangle} \tag{3.13}$$

For uniform basic temperature gradient $f(z) = 1$,

$$R_c = 120 + (12.143)\sigma^2$$

We note that when $\sigma = 0$(i.e., viscous fluid case), $R_c = 120$. However, when σ is very large, i.e., considering only the Darcy resistance, we have $R_c = 12\sigma^2$ which is the known value (Lapwood's Rayleigh number is defined a little differently from that used in the present analysis [6], see Section 5). In the case of sudden heating or cooling at the boundaries discussed herein the basic temperature gradient is not uniform and we are interested in knowing which temperature profile sets up maximum convection, subject to $f(z) \geqslant 0$ and $Df(z) \leqslant 0$. For this purpose we consider different basic temperature profiles. For piecewise linear profile

$$f(z) = \begin{cases} \gamma^{-1} & 0 \leqslant z < \gamma \\ 0 & \gamma < z \leqslant 1 \end{cases} \tag{3.14}$$

(which approximates the profile for heating from below) gives a lesser critical Rayleigh number than that for a completely linear profile. In this case, we have

$$R_c = \frac{240 + (24.286)\sigma^2}{2\gamma^4 - 5\gamma^3 + 5\gamma} \tag{3.15}$$

As ν increases from 0 to 1, R_c decreases from ∞ to a minimum value of $105.56 + (10.68)\sigma^2$ attained at $\gamma = 0.743$ and then increases to $120 + (12.143)\sigma^2$ at $\gamma = 1$.

A similar variation of R_c with ν was found by Rudraiah, et al. [14] for the case of constant temperature rather than constant flux boundary conditions. They obtained the minimum value $R_c = 3927.31$ attained at $\nu = 0.72$ for $a_c = 2.931$ and for $\sigma^2 = 10^2$. However, for $\sigma = 0$, the minimum value was 550.99 attained at $\gamma = 0.72$ and $a_c = 2.227$. Comparison of these values reveals that the eigenvalue is greater in the case of constant temperature than that of the constant heat flux.

In other words, adiabatic boundaries tend to destabilize the system.

Instead of piecewise linear profile if one selects the Dirac delta function for $f(z)$ in which the basic temperature drops suddenly by an amount ΔT at $z = \gamma$ but is otherwise uniform given by

$$f(z) = \delta(z - \nu) \tag{3.16}$$

one gets

$$R_c = \frac{24 + \frac{17}{7}\sigma^2}{\gamma^4 - 2\gamma^3 + \gamma} \tag{3.17}$$

This has a minimum value of $76.79 + (7.769)\sigma^2$ attained at $\gamma = 0.5$ i.e., midway between the surfaces. Comparison of (3.15) and (3.17) reveals that a greater reduction in R_c is possible if the buoyancy force of the form (3.16) is applied at the middle of the layer away from both the surfaces.

3.2 Lower Boundary Rigid and Upper Boundary Free. In this case the appropriate boundary conditions are

$$\begin{aligned} W = DW = DT = 0 \quad &\text{at } z = 0 \\ W = D^2W = DT = 0 \quad &\text{at } z = 1 \end{aligned} \tag{3.18}$$

The trial functions, satisfying the boundary conditions (3.18), are

$$W = z^2(1 - z)(3 - 2z),\ T = 1 \tag{3.19}$$

Here also, R attains the minimum value when $a = 0$ and we have

$$R_c = \frac{48 + \frac{16}{7}\sigma^2}{\langle f(z)(3z^2 - 5z^3 + 2z^4)\rangle} \tag{3.20}$$

For the linear profile $f(z) = 1$,

$$R_c = 320 + (15.238)\sigma^2$$

For the piecewise linear profile given by (3.14)

$$R_c = \frac{960 + (45.7)\sigma^2}{20\gamma^2 - 25\gamma^3 + 8\gamma^4} \tag{3.21}$$

This has a minimum value of $292.8 + (13.94)\sigma^2$ attained at $\gamma = 0.8208$ (further away from the lower boundary than for the free-free conditions).

For the piecewise linear profile cooled from above given by

$$f(z) = \begin{cases} 0 & 0 \leqslant z < 1 - \gamma \\ \gamma^{-1} & 1 - \gamma < z \leqslant 1 \end{cases} \tag{3.22}$$

we have

$$R_c = \frac{960 + \frac{320}{7}\sigma^2}{8\gamma^4 - 15\gamma^3 + 10\gamma} \tag{3.23}$$

which has a minimum value of $252 + (11.99)\sigma^2$ attained $\gamma = 0.638$ and thus $1 - \gamma = 0.362$. We see that R_c is less when the buoyancy force is applied nearer the free surface rather than the rigid one.

For the Dirac delta function for $f(z)$ given by (3.16), we have

$$R_c = \frac{48 + \frac{16}{7}\sigma^2}{3\gamma^2 - 5\gamma^3 + 2\gamma^4} \tag{3.24}$$

which has a minimum value, $(R_c)_{min} = (184.8) + (8.88)\sigma^2$ attained at $\nu = 0.578$. For large values of σ^2, $R_c/\sigma^2 = 8.88$ which is closer to the value 8 obtained by Nield [9]. From this, we see that the most destabilizing δ-function profile has the step closer to the free boundary than to the rigid one.

3.3 Both Boundaries Rigid. Now, the boundary conditions are

$$W = DW = DT = 0 \text{ at } z = 0, 1 \tag{3.25}$$

We choose the trial functions for W and T as

$$W = z^2(1 - z)^2,\ T = 1 \tag{3.26}$$

R takes the least value when $a = 0$ so that

$$R_c = \frac{24 + \frac{4}{7}\sigma^2}{\langle f(z)z^2(1 - z)^2\rangle} \tag{3.27}$$

For linear temperature profile $f(z) = 1$,

$$R_c = 720 + (17.14)\sigma^2$$

When $\sigma = 0$, we get $R_c = 720$ which is the known exact value. For a piecewise linear temperature profile given by (3.14),

$$R_c = \frac{720 + \frac{120}{7}\sigma^2}{10\gamma^2 - 15\gamma^3 + 6\gamma^4} \tag{3.28}$$

As ν increases from 0 to 1, R_c decreases from ∞ to a minimum value

$$(R_c)_{min} = 600.9 + (14.31)\sigma^2$$

attained at $\gamma = 0.7243$. For the Dirac delta function profile for $f(z)$ given by (3.16),

$$R_c = \frac{24 + \frac{4}{7}\sigma^2}{\nu^2 - 2\nu^3 + \nu^4} \tag{3.29}$$

The minimum value of R_c is given by $(R_c)_{min} = 384 + (9.14)\ \sigma^2$ attained at $\gamma = 0.5$, exactly midway between the boundaries.

We note that Lapwood [6] Nield [9] and others (Joseph [4]) defined the Rayleigh number in the case of porous media as $R_L = g\beta(\Delta T)dk/\nu\kappa$ whereas in the present analysis the Rayleigh number R is defined as $R = g\beta(\Delta T)d^3/\nu\kappa$ so that $R_L = R/\sigma^2$. With this notation, we find that the viscous fluid ($\sigma = 0$) and the usual Darcy porous medium ($\sigma \to \infty$ with R_L) results emerge, as special cases, from our analysis. These results are shown in Table 1 and are in good agreement with the available values for the viscous fluid [9, 15] and the Darcy porous medium [6, 9] cases.

4 Convection Due to Internal Heat Source

In Section 3 we discussed the effect of basic nonlinear temperature distribution on convection in a fluid saturated porous medium arising from sudden heating or cooling at the boundaries. In this section we are concerned with convective energy transfer in a fluid saturated porous medium heated by uniform distribution of heat sources by considering the Brinkman model. The problem of convection in a porous medium arising from internal heat sources with isothermal boundary conditions has been investigated by Gasser and Kazimi [3] and Rudraiah, et al. [14] using the Brinkman model. In this section, we extend their analysis to thermally insulated boundary conditions by considering rigid-rigid, free-free and rigid-free surfaces.

The basic equations of the problem are given by (2.1–2.4). The phenomenon of convection is achieved by assuming that instability occurs by way of perturbation to an existing basic state. In the absence of convection, the basic state is such that heat is transported from layer to layer by conduction only. We consider the basic flow to be in the quiescent state with quadratic basic temperature distribution in the form

$$T_0 = -\frac{Qz^2}{2K^*} + \left[\frac{Qd}{2K^*} - \frac{T_1 - T_2}{d}\right]z + T_1 \tag{4.1}$$

Applying the same procedure as in deriving (3.5) and (3.6) and using d, $\kappa^*\nu/g\beta d^3$ and κ^*/d for the dimensions of length, temperature and velocity, we obtain

$$(D^2 - a^2 - \sigma^2)(D^2 - a^2)W = a^2T \tag{4.2}$$

$$(D^2 - a^2)T = \{R_I(\tfrac{1}{2} - z) - R_E\}W \tag{4.3}$$

To find the solution of these equations we consider a fluid saturated bed bounded below and above by both free surfaces or both rigid

Table 1 Critical Rayleigh numbers for different temperature profiles

Boundary Combinations	Linear Profile			Piecewise Linear Profile				Dirac delta function for f(z)			
	$\sigma = 0$	$\sigma = 10$	$\sigma \to \infty$	$\sigma = 0$	$\sigma = 10$	$\sigma \to \infty$	Optimum distance	$\sigma = 0$	$\sigma = 10$	$\sigma \to \infty$	Optimum distance
	R_c	R_c	R_{L_c}	R_c	R_c	R_{L_c}	κ	R_c	R_c	R_{L_c}	κ
Rigid-Rigid	720	2434	17.14	600.9	2032	14.31	0.7243	384	1298	9.14	0.5
Rigid-Free	320	1844	15.24	292.8	1687	13.94	0.8208	184.8	1073	8.88	0.58
Free-Free	120	1334	12.14	105.5	1174.5	10.68	0.7438	76.79	853.7	7.77	0.5

surfaces or upper boundary free and lower boundary rigid separately when the boundaries are thermally insulated.

4.1 Solution. In this section, thermal convection due to heat source is investigated by considering free-free, rigid-rigid, and rigid-free boundaries which are thermally adiabatic.

Since the single term expansion in the Galerkin method does not bring out heat source effect, we have resorted to higher order expansion. Therefore, to find the solution of (4.2) and (4.3), we apply Galerkin method where we assume the trial solution in form

$$T = \frac{1}{a^2} \sum_m A_m \cos(m\pi z) \tag{4.4}$$

Equation (4.2), using (4.4), becomes

$$(D^2 - b^2)(D^2 - a^2)W = \sum_m A_m \cos(m\pi z) \tag{4.5}$$

where $b^2 = a^2 + \sigma^2$ (4.6)

The general solution of (4.5) is

$$W = \sum_m C_{m0}\{\cos(m\pi z) + C_{m1}\sinh\beta_1 z + C_{m2}\sinh\beta_2 z + C_{m3}\cosh\beta_1 z + C_{m4}\cosh\beta_2 z\} \tag{4.7}$$

where

$$C_{m0} = A_m/(m\pi)^4 + (m\pi)^2\psi + \phi,\ \beta_1^2 = a^2,\ \beta_2^2 = a^2 + \sigma^2$$

and the constants C_{m_i} ($i = 1$ to 4) are determined using the appropriate boundary conditions depending on the nature of the bounding surfaces.

Substituting (4.4) and (4.7) into (4.3), we obtain

$$\sum_m \left(\frac{m^2\pi^2 + a^2}{a^2}\right) A_m \cos(m\pi z) = \left(R_E - \frac{R_I}{2}\right) \sum_m C_{m0}\{\cos(m\pi z) + C_{m1}\sinh\beta_1 z + C_{m2}\sinh\beta_2 z + C_{m3}\cosh\beta_1 z + C_{m4}\cosh\beta_2 z\} + R_I \sum_m C_{m0}\{z\cos(m\pi z) + C_{m1}z\sinh\beta_1 z + C_{m2}z\sinh\beta_2 z + C_{m3}z\cosh\beta_1 z + C_{m4}z\cosh\beta_2 z\} \tag{4.8}$$

Multiplying (4.8) by $\cos(n\pi z)$ and integrating between $z = 0$ and $z = 1$, we get a set of n equations:

$$\sum \left(\frac{m^2\pi^2 + a^2}{a^2}\right) A_m I_0^{nm} = \sum_m C_{m0}\left\{\left(R_E - \frac{R_I}{2}\right)(I_0^{nm} + C_{m_i} I_i^n) + R_I(I_s^{nm} + C_{m_i} I^n{}_{i+5})\right\} \tag{4.9}$$

where $i = 1$ to 4 and the summation convention is followed on repeated subscript. The eigenvalue equation for the nontrivial solution for A_m from (4.9) is

$$\left|\left(\frac{m^2\pi^2 + a^2}{a^2}\right) I_0^{nm} + \frac{1}{(m\pi)^4 + (m\pi)^2\psi + \phi}\left[\frac{R_1}{2}\{I_0^{nm} + C_{m_i} I_i^n - 2(I_5^{nm} + C_{m_i} I^n{}_{i+5})\} - R_E(I_0^{nm} + C_{m_i} I_i^n)\right]\right| = 0 \tag{4.10}$$

We note that the analytical determination of eigenvalues from (4.10) is mathematically complicated even for lower order approximations and hence a numerical procedure is adopted to determine them.

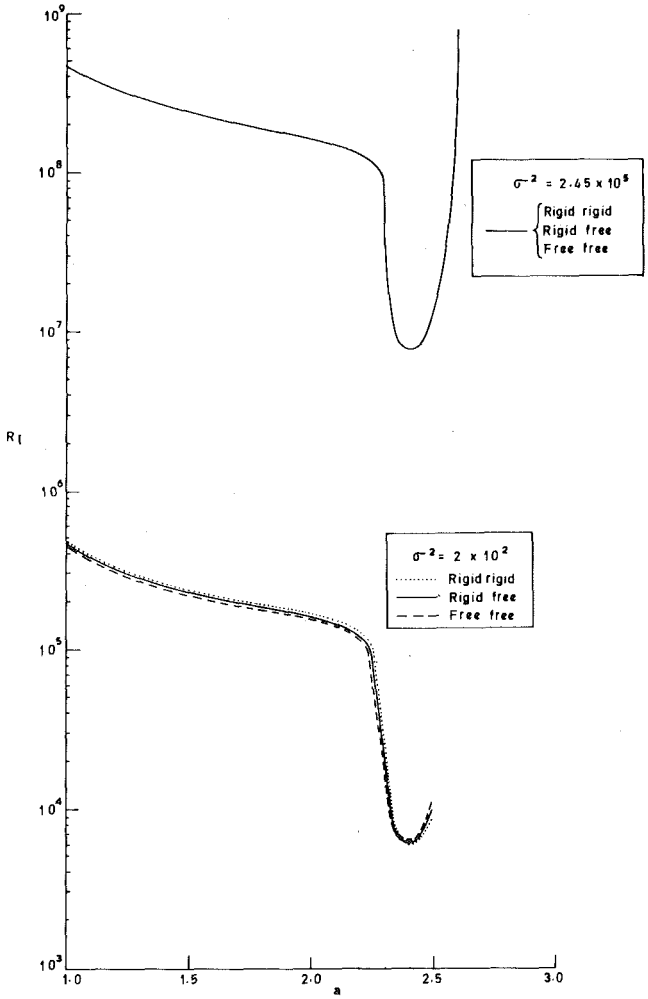

Fig. 2 Variation of internal Rayleigh number R_I with wave number a for $\sigma^2 = 2 \times 10^2$ and $\sigma^2 = 2.45 \times 10^5$

We consider a sixth order ($m = 6$) approximation in the Galerkin expansion. In this case, (4.9) yields a six by six matrix for the coefficients of the A_m terms. For the nontrivial solution of A_m the determinant obtained from the matrix of coefficients of A_m must vanish. These coefficients are functions of the external and internal Rayleigh numbers R_E and R_I, the wave number a and the porous parameter σ.

Since we are considering the Brinkman model which is valid, according to the experimental work of Katto and Masuoka [5], for the values of σ^2 to the order to 10^3, the numerical evaluation is performed with values of $\sigma^2 = 2 \times 10^2$. However, to compare our results with those of Gasser and Kazimi [3] and Rudraiah, et al. [14], the numerical analysis has been carried out also for $\sigma^2 = 2.45 \times 10^5$ and the results are plotted in Fig. 2 for the different values of σ^2. From this figure it is clear that R_I increases with σ^2. Hence the effect of permeability is to augment the effect of heat source.

The numerical evaluation has been carried out for different

Table 2 Comparison of $(R_I)_{min}$ for adiabatic and isothermal cases with different boundary combinations for $\sigma^2 = 2.45 \times 10^5$

WAVE No	Both Boundaries Free		Lower Rigid-Upper Free Boundaries		Both Boundaries Rigid	
a	Adiabatic	Isothermal	Adiabatic	Isothermal	Adiabatic	Isothermal
1.0	4.7538×10^8	5.9327×10^8	4.7538×10^8	5.9327×10^8	4.7539×10^8	5.9328×10^8
1.5	2.4255×10^8	3.0254×10^8	2.4255×10^8	—	2.4255×10^8	3.0255×10^8
2.0	1.6234×10^8	2.0238×10^8	1.6234×10^8	—	1.6234×10^8	1.9780×10^8
2.5	1.2925×10^7	1.5774×10^8	1.2828×10^7	—	1.2842×10^7	1.5554×10^8

Table 3 Comparison of $(R_I)_{min}$ for adiabatic and isothermal cases with different boundary combinations for $\sigma^2 = 2 \times 10^2$

WAVE No	Both Boundaries Free		Lower Rigid-Upper Free Boundaries		Both Boundaries Rigid	
a	adiabatic	Isothermal	Adiabatic	Isothermal	Adiabatic	Isothermal
1.0	4.3892×10^5	5.4661×10^5	4.6727×10^5	5.4649×10^5	4.6815×10^5	5.5023×10^5
1.5	2.2530×10^5	2.8044×10^5	2.3880×10^5	—	2.3921×10^5	1.8199×10^5
2.0	1.5207×10^5	1.8918×10^5	1.6037×10^5	—	1.6062×10^5	4.7473×10^4
2.4	7.2019×10^3	—	6.3839×10^3	—	6.2156×10^3	—
2.5	1.0593×10^4	1.4904×10^5	8.8869×10^3	—	9.0875×10^3	9.2912×10^4

boundary combinations viz., rigid-rigid, free-free and rigid-free boundaries and we found that in contrast to the isothermal case of Rudraiah, et al. [14], the eigenvalues are almost identical in all these cases for $\sigma^2 \geq 2.45 \times 10^5$ as shown in Table 2. The large values of σ^2 imply that the viscous shear in the momentum equation is negligible compared to the Darcy resistance and we have the usual modified Darcy's equation as given by Lapwood [6]. Therefore, for large values of σ^2 the results obtained in this paper are consistent with the results obtained by Lapwood [6]. In other words, even in the case of the Brinkman model, the boundaries have no significant effect on the onset of convection in a porous medium. To know the effect of adiabatic boundaries in contrast to the isothermal ones, the results of the present analysis are compared with those of Rudraiah, et al. [14] for the isothermal case in Tables 2 and 3 and we find that the effect of specifying heat flux at the boundaries is to reduce the heat source effect.

Conclusions

The effect of nonlinear temperature distribution, arising either from sudden heating or cooling at the boundaries or from distribution of heat sources, on thermal convection in a fluid saturated permeable layer is investigated using the Brinkman model. The effect of different temperature gradients on the onset of convection is investigated using various combinations of boundary conditions at the upper and lower thermally adiabatic surfaces. A single term Galerkin expansion reveals that the Dirac delta function profile for the temperature gradient gives the maximum convection attained exactly the midway between the bounding surfaces. The results obtained are compared to the existing values and close agreement is found. The comparison of the results for the three different boundary combinations reveals that the critical Rayleigh number in the case of rigid-rigid surfaces is the highest as expected on physical grounds. Again, the values of the critical Rayleigh number for the thermally adiabatic boundaries are lower than those for the corresponding isothermal cases thereby establishing that the fluid saturated porous layer bounded by adiabatic surfaces is convectively less stable than the one bounded by the isothermal surfaces.

The convection due to internal heat source is also investigated using a single term Galerkin expansion and in that case the effect of heat source is not brought out. In order to bring out the heat source effect, a sixth order approximation which yields a six by six matrix for the coefficients of A_m in (4.9) was employed. The resulting eigenvalue equation is solved numerically as explained in Section 4.1. The numerical algorithm we employed converges very fast. In all the cases of boundary combinations shown in Tables 2 and 3 it is found that the effect of permeability is to augment the heat source effect. Further, for values of $\sigma^2 \geq 2.45 \times 10^5$, Table 2 reveals that the different bounding surfaces give almost the same critical internal Rayleigh number. In other words, for smaller values of σ^2 the difference in boundary combinations has a perceptible effect on the onset of convection and its effect is negligible for large values of σ^2. This result, in the presence of heat source, for large values of σ^2 is similar to the one observed by Lapwood [6] in the absence of heat source. Therefore, for large values of σ^2, our analysis, as demonstrated in Section 3.1, should give qualitatively the results similar to those for the usual Darcy porous medium case in the presence of heat source.

It is of interest to note that the heat source effect decreases for wave number up to the value 2.2 and there will be a sudden decrease up to the value of 2.4 and then increases up to 2.5 having a minimum at $a \approx 2.4$. In other words, there are two stability regions: one for values of a up to 2.2 in which the effect of heat source slowly decreases and the other is the region in which there will be an abrupt reduction in heat source effect in the range of wave number around 2.4. For values of wave number greater than 2.5, oscillatory nature of convection exists. This may be due to the limitation of linear theory and it warrants nonlinear theory.

Acknowledgments:

This work was supported by the Indian National Science Academy under the research project No. 31/BS/P-18/521.

The research by one of the authors (S.B.R.) was supported by the U.G.C., India under its Faculty Improvement Programme. One of us (B.V.) is grateful to the Indian National Science Academy for providing a Fellowship under its research project.

We are indebted to the referees for their valuable comments which improved the paper considerably.

References

1 Beavers, G. S., and Joseph, D. D., "Boundary Conditions at a Naturally Permeable Wall," *Journal Fluid Mechanics*, Vol. 30, 1967, pp. 197–207.

2 Brinkman, H. C., "Calculation of the Viscous Force Exerted by a Flow in Fluid on a Dense Swarm of Particles," *Applied Science Research*, Section A.1, 1947, pp. 27–34.

3 Gasser, R. D., and Kazimi, M. S., "Onset of Convection in a Porous Medium with Internal Heat Generation," ASME JOURNAL OF HEAT TRANSFER, Vol. 98, 1976, pp. 49–54.

4 Joseph, D. D. *Stability of Fluid Motions, I & II*, Springer Tracts in Natural Philosophy, Springer-Verlag, 1976.

5 Katto, Y., and Masuoka, T., "Criterion for the Onset of Convective Flow in a Fluid in Porous Medium," *International Journal of Heat and Mass Transfer*, Vol. 10, 1967, pp. 297–309.

6 Lapwood, E. R., "Convection of a Fluid in a Porous Medium," *Proceedings of the Cambridge Philosophical Society*, Vol. 44, 1948, pp. 508–521.

7 Lundgren, T. S., "Slow Flow Through Stationary Random Beds and Suspensions of Spheres," *Journal Fluid Mechanics*, Vol. 51, part 2, 1972, pp. 273–299.

8 Morales, M., Spinn, C. W. and Smith, J. M., "Velocities and Effective

Thermal Conductivities in Packed Beds," *Industrial and Engineering Chemistry*, Vol. 43, 1951, pp. 225–232.

9 Nield, D. A., "The Onset of Transient Convective Instability," *Journal Fluid Mechanics*, Vol. 71, 1975, pp. 441–454.

10 Prabhamani, R. P. and N. Rudraiah, "Stability of Hydromagnetic and Thermoconvective Flow Through Porous Medium," ASME *Journal of Applied Mechanics*, Vol. 40, No. 4, 1973, 879–884.

11 Roberts, P. H., "Convection in Horizontal Layers with Internal Heat Generation," *Theory Journal Fluid Mechanics*, Vol. 30, 1967, pp. 33–49.

12 Rudraiah, N., and Rohini, G., "Cellular Convection in a Rotating Fluid through Porous Medium," *Vignana Bharathi*, Vol. 1, No. 1, 1975, pp. 23–29.

13 Rudraiah, N., and Vortmeyer, D., "Stability of Finite-Amplitude and Overstable Convection of a conducting Fluid Through Fixed Porous Bed," *Wärme-und Stoffübertragung* 11, 1978, pp. 241–254.

14 Rudraiah, N., Veerappa, B., and Balachandra Rao, S., "Convection in a Fluid saturated Porous Layer with Non-uniform Temperature Gradient," Accepted for publication in *Journal of Fluid Mechanics*, 1979.

15 Sparrow, E. M., Goldstein, R. J., and Jonsson, V. K., "Thermal Instability in a Horizontal Fluid Layer: Effect of Boundary Conditions and Non-Linear Temperature Profile," *Journal of Fluid Mechanics*, Vol. 18, 1964, pp. 513–528.

16 Tam, C. K. W., "The Drag on a Cloud of Spherical Particles in Low Reynolds Number Flow," *Journal of Fluid Mechanics*, Vol. 38, 1969, pp. 537–546.

17 Taylor, G. I., "A Model for the Boundary Condition of a Porous Material," Part I. *Journal of Fluid Mechanics*, Vol. 49, 1971, pp. 319–326.

Thermal Instability of Natural Convection Flow over a Horizontal Ice Cylinder Encompassing a Maximum Density Point

T. Saitoh
Associate Professor,
Mem. JSME and Meteorological Society of Japan

K. Hirose
Graduate Student.

Department of Mechanical Engineering II,
Tohoku University,
Sendai, Japan 980

The problem of three-dimensional thermal instability over a horizontal ice cylinder which occurs in a minimum heat transfer region has been solved. A fully numerical method was applied to the governing equations in the transverse and longitudinal planes, which were simplified to two-dimensional. The perturbation method was employed to obtain the wave number. The appearance of a convexo-concave melting front, which was predicted by a previous experiment, was clearly explained by the convection pattern along the cylinder. The transient process of onset of stable vortices around a cylinder was clarified by streamlines and isotherms. Comparing the wave numbers obtained by the numerical and the small perturbation methods, it is concluded that the perturbation method cannot be effectively applied to problems involving density inversion.

Introduction

Since the pioneering works of Dumoré, et al. [1] and Merk [2], the problem of natural convection heat transfer involving density inversion has been studied by many investigators: e.g., Schechter and Isbin [3], Vanier and Tien [4], Gilpin [5], Watson [6], Forbes and Cooper [7], Cheng and Takeuchi [8], Bendell and Gebhart [9], Saitoh [10, 11], and Saitoh and Hirose [12]. A detailed survey of the literature is found in references [8] and [10].

One of the authors carried out an experiment [10] on the natural convection heat transfer around a horizontal circular cylinder encompassing a maximum density point. The minimum heat transfer region, which was found by Dumoré, et al., has been examined in detail and a comparison was made between the experimental data and the numerical results. Moreover, it was revealed from careful observation in the vicinity of the heat transfer minimum that three-dimensional flow instability is induced. The water temperature over which such instability occurs ranged from approximately 5.5°C to 6.5°C according to the experiment [10]. It was observed that the melting front shape in the longitudinal direction becomes sinusoidal; from this, the onset of a helical vortex around the cylinder was surmised.

Two-dimensional numerical analysis in the plane perpendicular to the cylinder axis was also performed, and it was found that two solutions exist in the vicinity of the convection inversion domain. The multiplicity of the solution for the Navier-Stokes and energy equations were detected by chance during the test calculations in which the spatial mesh length was varied in order to check the degree of accuracy of the numerical solutions. One of the solutions corresponds to the result for a coarse mesh size case, and the other for a finer mesh size case. Melting front contours in the circumferential and axial cross sections, and the Nusselt number distributions are shown in Fig. 1.

In this paper, two methods are employed to elucidate flow instability. The first is a numerical method in which the relevant governing equations are solved in the two cross sections, i.e., in the plane perpendicular to the cylinder axis, and in the plane passing through the stagnation line and the cylinder axis. The latter is the typical perturbation method which has been frequently used in thermal instability analysis. For instance, Cheng and Wu [13] and Nakayama, et al. [14] analyzed thermal instability in plane Poiseuille flows.

A typical perturbation analysis has been made by Sparrow, Goldstein and Jonsson [15] for thermal instability in a horizontal fluid layer, in which the equation for a single velocity component was derived and the resultant homogeneous perturbation function was solved. A similar analysis was extended to the problem involving change of phase by Sparrow, et al. [16]. The perturbation method was also used in the present analysis to check the possibility of its application to the flow instability involving density inversion.

The wave number was selected for the comparison between the numerical and the perturbation solutions. As a consequence, it was concluded that the perturbation method is not sufficient for analyses including density inversion as in the present case.

Further, the mechanism of formation of a wavy melting front shape was clarified by inspection of the Nusselt number distribution along the cylinder surface and the flow patterns.

Governing Equations

The physical model and the coordinate system are schematically shown in Fig. 2. For simplicity, the curvilinear coordinates are employed [10]. No problem will arise by utilizing this coordinate system as long as the cylinder diameter is not too small. The problem is to analyze numerically the transient convection flow around a horizontal circular ice cylinder which is located in quiescent water of constant temperature T_∞. The temperature of the cylinder was initially set at $T_w = 0$.

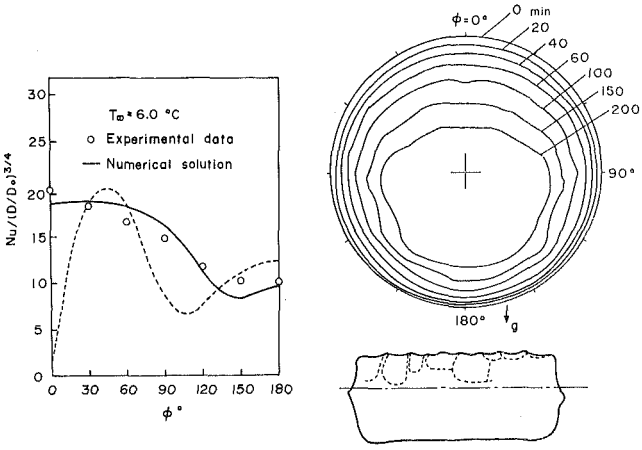

Fig. 1 *Transient melting front contours and Nusselt number distributions around the cylinder, in which two converged numerical solutions are shown,* $T_\infty = 6°C$, *(from reference [10]). A dotted line in the left figure indicates another converged numerical solution corresponding to the coarse mesh size case. Dotted lines in the right figure show the melted region around an ice cylinder*

Contributed by The Heat Transfer Division for publication in the JOURNAL OF HEAT TRANSFER. Revised manuscript received by the Heat Transfer Division November 9, 1979.

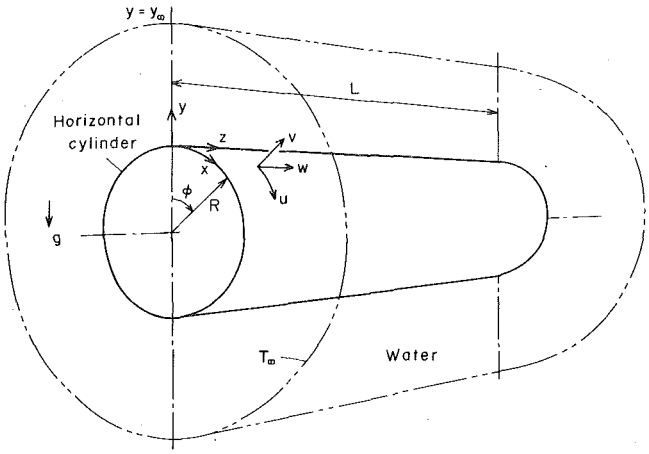

Fig. 2 Schematic numerical model and coordinate system

For the analysis, the following assumptions and restrictions are made.

1 Flow is laminar.
2 Physical properties are constant.
3 Boussinesq approximation is valid.
4 Flow is symmetrical with respect to a vertical plane passing through the axis.

Under these postulations, the governing equations for this problem can be described as follows.

$$(\nabla \cdot \mathbf{v}^+) = 0 \tag{1}$$

$$\frac{\partial \mathbf{v}^+}{\partial t^+} + (\mathbf{v}^+ \cdot \nabla)\mathbf{v}^+ = -\operatorname{grad} p^+ + \mathrm{Pr}\nabla^2\mathbf{v}^+ + \mathrm{PrRa}f(T^+)\begin{bmatrix}\sin\phi\\ \cos\phi\\ 0\end{bmatrix} \tag{2}$$

$$\frac{\partial T^+}{\partial t^+} + (\mathbf{v}^+ \cdot \nabla)T^+ = \nabla^2 T^+ \tag{3}$$

Here, the function $f(T^+)$ is given by

$$f(T^+) = T^+[1 + aT^+ + b(T^+)^2 + c(T^+)^3]. \tag{4}$$

and indicates the variation of density of water. The coefficients a, b and c are obtained, for example, by Fujii's equation [17] which is coincident with Landolt-Börnstein's results [19] up to the last decimal place.

In the above and later equations, use is made of the following nondimensional variables.

$$(x^+, y^+, z^+) = \frac{1}{R}(x, y, z),\ (u^+, v^+, w^+) = \frac{R}{a}(u, v, w)$$

$$T^+ = \frac{T_\infty - T}{T_\infty - T_w},\ p^+ = \frac{R}{\rho a^2}p,\ t^+ = \frac{at}{R^2},\ y_\infty^+ = \frac{y_\infty}{R}$$

$$\mathrm{Pr} = \frac{\nu}{a},\ \mathrm{Gr} = \frac{g\beta_\infty \Delta T R^3}{\nu^2},\ (\Psi^+, \psi^+) = \frac{1}{a}(\Psi, \psi) \tag{5}$$

$$(\Omega^+, \omega^+) = \frac{R}{a}(\Omega, \omega)$$

It is quite difficult to perform a complete numerical analysis in three-dimensions due to the length of computer running time. Therefore, only two analyses were carried out in the present study. First, two-dimensional numerical computations were executed in the (x, y) plane which is perpendicular to the cylinder axis. Secondly, the computations were made in the plane which is parallel to the cylinder axis and contains both upper stagnation line and cylinder axis.

Analysis in the (x, y) Plane.

Using the vorticity and the stream function, the governing equations are written as below:

$$\Omega^+ = \nabla^2\Psi^+ \tag{6}$$

$$\frac{\partial T^+}{\partial t^+} + \frac{\partial(T^+, \Psi^+)}{\partial(x^+, y^+)} = \nabla^2 T^+ \tag{7}$$

$$\frac{\partial \Omega^+}{\partial t^+} + \frac{\partial(\Omega^+, \Psi^+)}{\partial(x^+, y^+)} = \mathrm{Pr}\nabla^2\Omega^+ + \mathrm{PrRa}\left[\sin x^+\left(\frac{\partial f(T^+)}{\partial y^+} - f(T^+)\right) + \cos x^+ \frac{\partial f(T^+)}{\partial x^+}\right] \tag{8}$$

where,

$$\nabla^2 = \frac{\partial^2}{\partial(x^+)^2} + \frac{\partial^2}{\partial(y^+)^2}, \tag{9}$$

$$\frac{\partial(\Omega^+, \Psi^+)}{\partial(x^+, y^+)} = \begin{vmatrix}\partial\Omega^+/\partial x^+ & \partial\Omega^+/\partial y^+\\ \partial\Psi^+/\partial x^+ & \partial\Psi^+/\partial y^+\end{vmatrix}. \tag{10}$$

The velocities u^+ and v^+, and the vorticity Ω^+ are defined by

$$u^+ = \frac{\partial\Psi^+}{\partial y^+},\ v^+ = -\frac{\partial\Psi^+}{\partial x^+}, \tag{11}$$

$$\Omega^+ = \frac{\partial u^+}{\partial y^+} - \frac{\partial v^+}{\partial x^+}. \tag{12}$$

Boundary conditions are listed as follows.

Nomenclature

a = thermal diffusivity
a_f = wave number
$|\boldsymbol{C}|$ = determinant
D = diameter of cylinder
D_0 = reference diameter of cylinder equal to 0.1 m in Fig. 1
g = acceleration of gravity
Gr = Grashof number
h = heat transfer coefficient
$i = \sqrt{-1}$
k = thermal conductivity
L = cylinder length
Nu = Nusselt number = hR/k
p = pressure
Pr = Prandtl number
R = radius of cylinder
Ra = Rayleigh number
t = time
T = temperature
T_∞ = water temperature
T_w = surface temperature of cylinder
T_s = surface temperature of cylinder in the longitudinal direction
$\Delta T = T_\infty - T_w$
u, v, w = velocities in the directions of x, y, and z, respectively
$\mathbf{v}$ = velocity vector
x, y, z = coordinates defined in Fig. 2
$\Delta x, \Delta y$ = mesh length in the directions of x and y, respectively
β_∞ = volumetric expansion coefficient
λ = wave length
ν = kinematic viscosity
ρ = density
ϕ = circumferential angle
Ψ, ψ = stream function of (x, y) plane and (y, z) plane, respectively
Ω, ω = vorticity of (x, y) plane and (y, z) plane, respectively

Subscripts and Superscripts

+ = dimensionless quantity
∞ = infinity value
s, w = cylinder surface
0 = basic quantity
1 = perturbed quantity
2 = perturbed quantity of the (x, y) plane

$$x^+ = 0, 1; \left.\frac{\partial T^+}{\partial x^+}\right|_- = \left.\frac{\partial T^+}{\partial x^+}\right|_+, \Psi^+ = \Omega^+ = 0.$$

$$y^+ = 0; T^+ = 1, \Psi^+ = \frac{\partial \Psi^+}{\partial y^+} = 0, \Omega^+ = \left.\frac{\partial^2 \Psi^+}{\partial (y^+)^2}\right|_{y^+=0}.$$

$$y^+ = y_\infty^+; T^+ = \Omega^+ = 0, \frac{\partial \Psi^+}{\partial y^+} = 0. \tag{13}$$

Analysis in the (y, z) Plane.

Taking account of the symmetry of flow in the vertical plane passing through the cylinder axis, the governing equations can be reduced to two-dimensions and the problem becomes considerably simplified. The governing equations are written as below.

$$\omega^+ = \nabla^2 \psi^+ \tag{14}$$

$$\frac{\partial T^+}{\partial t^+} + \frac{\partial(\psi^+, \omega^+)}{\partial(y^+, z^+)} = \nabla^2 T^+ \tag{15}$$

$$\frac{\partial \omega^+}{\partial t^+} + \frac{\partial(\psi^+, \omega^+)}{\partial(y^+, z^+)} = \mathrm{Pr}\nabla^2 \omega^+ + \mathrm{PrRa}\frac{\partial f(T^+)}{\partial z^+} \tag{16}$$

where,

$$\nabla^2 = \frac{\partial^2}{\partial (y^+)^2} + \frac{\partial^2}{\partial (z^+)^2}, \tag{17}$$

$$\frac{\partial(\psi^+, \omega^+)}{\partial(y^+, z^+)} = \begin{vmatrix} \partial\psi^+/\partial y^+ & \partial\psi^+/\partial z^+ \\ \partial\omega^+/\partial y^+ & \partial\omega^+/\partial z^+ \end{vmatrix}. \tag{18}$$

The function $f(T^+)$ is again expressed by equation (4). The vorticity ω^+ and the stream function ψ^+ are defined by

$$w^+ = \frac{\partial \psi^+}{\partial y^+}, v^+ = -\frac{\partial \psi^+}{\partial z^+}, \tag{19}$$

$$\omega^+ = \frac{\partial w^+}{\partial y^+} - \frac{\partial v^+}{\partial z^+}. \tag{20}$$

Boundary conditions for equations (14) to (16) are

$$z^+ = 0, L^+; \left.\frac{\partial T^+}{\partial z^+}\right|_- = \left.\frac{\partial T^+}{\partial z^+}\right|_+, \psi^+ = \omega^+ = 0.$$

$$y^+ = 0; T^+ = 1, \psi^+ = \frac{\partial \psi^+}{\partial y^+} = 0, \omega^+ = \left.\frac{\partial^2 \psi^+}{\partial (y^+)^2}\right|_{y^+=0},$$

$$y^+ = y_\infty^+; T^+ = \omega^+ = 0, \frac{\partial \psi^+}{\partial y^+} = 0. \tag{21}$$

In the above, L^+ means that

$$L^+ = \frac{L}{R}. \tag{22}$$

Numerical Procedure.

The above equations were solved by utilizing the multipoint explicit finite difference method developed by Saitoh [18] for efficient computation in multidimensional problems. The upwind difference expressions were used for the equations of vorticity and energy. As to the Poisson's equation derived from the continuity equation, the successive over-relaxation method was employed. As a trigger for the initial disturbance, the following surface temperature distribution in the axial direction was assumed.

$$T_s^+ = 1 + \frac{exp\{-A(t^+)^2\}}{B}\cos(3\pi z^+). \tag{23}$$

The values are given for constants such that $A = 1000$, $B = 5$. The surface temperature T_s^+ converges to a given boundary condition when time elapses. The typical computation required some 600 s on NEAC 2200 ACOS 6 SYSTEM 700 TSS, with $\Delta x = 1/12$, $\Delta y = 1/10$.

Results and Discussion.

Figure 3 shows the computed streamlines and isotherms in the case of $T_\infty = 5.6°C$, Pr = 12.4, and Ra = 7750. The outer edge of the computing area on the water side was set as $y_\infty^+ = 1.5$. The accuracy of computation was checked by varying the value of y_∞^+. It is observed that the two clockwise vortices appear at upper and lower portions on the right hand side of the cylinder. The isotherms are considerably influenced by these vortices.

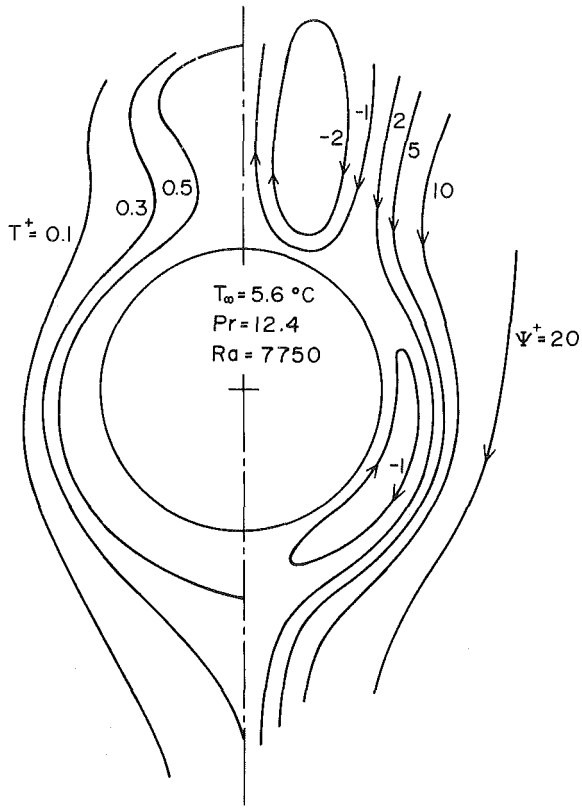

Fig. 3 Streamlines and isotherms around the cylinder for $T_\infty = 5.6°C$, Pr = 12.4, and Ra = 7750

Figure 4 shows the distribution of the Nusselt number under the same conditions as in Fig. 3. A characteristic feature that the Nusselt number has a peak at $\phi \cong 30$ deg can be seen. It seems that this peculiar feature is not detected at water temperatures other than $T_\infty \cong 5.5 \sim 6.5°C$, which was determined by the experiment. However, this temperature range was only partly verified by the present numerical calculations. Namely, at water temperatures 5.0 and 7.0°C, no such instabilities appear. Even if the initial disturbances were introduced, the flows in the (y, z) plane are not induced in such cases. The isotherms and streamlines corresponding to a different water temperature are shown in Fig. 5, in which Pr = 12.3 and Ra = 10425 are used. A tiny vortex appears at the bottom portion of the cylinder.

The Nusselt number distribution is also depicted in Fig. 6 which resembles a boundary layer type profile in the case of high water temperature. However, it is presumed that another type of metastable state exists at this temperature [10]. Stable patterns typical of those described are thought to correspond to two converged solutions that were obtained previously [10].

Transient numerical results in the (y, z) plane, when $T_\infty = 6°C$, Pr = 12.3, Ra = 10425, $L^+ = 2.8$, and $y_\infty^+ = 1.5$, are shown in Figs. 7–9. They were calculated for the Fourier number $t^+ = 0.1$, 0.3, and 0.5, respectively. The streamlines and Nusselt number distribution at the cylinder surface are indicated in the figures, from which the transient process of formation of vortices in the (y, z) plane can be clarified. At an early stage, when the transient computation has just started, double rows of vortices are formed although the strength of the vortices is slight, as illustrated in Fig. 7. The distribution of the Nusselt number is almost constant which implies that the heat transfer from the cylinder to the surrounding water is not affected markedly by the convection.

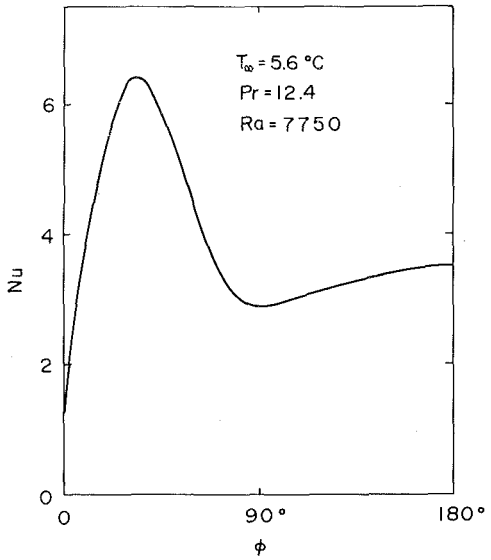

Fig. 4 Nusselt number profile around the cylinder for $T_\infty = 5.6°C$, Pr = 12.4, and Ra = 7750

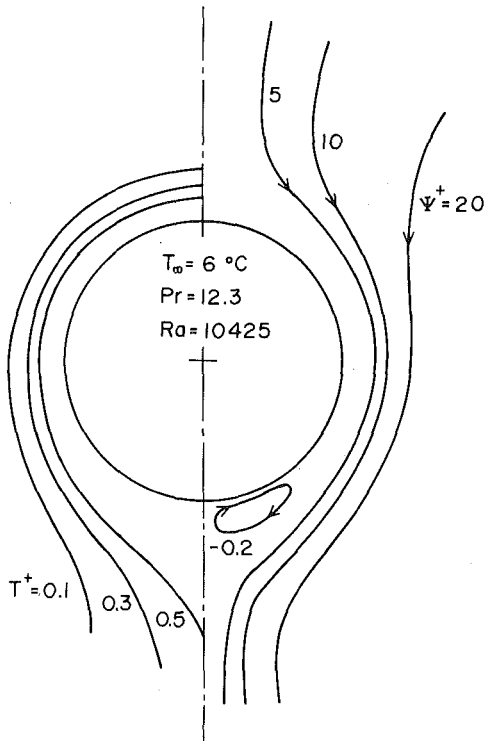

Fig. 5 Streamlines and isotherms around the cylinder for $T_\infty = 6°C$, Pr = 12.3, and Ra = 10425

On the other hand, the flow pattern and the Nusselt number profile when time elapses to $t^+ = 0.3$ are shown in Fig. 8. Notable points are that the outward rows of vortices at an early time stage disappear completely and, in turn, the lower rows with greater strength grow. It is also seen that the Nusselt number distribution has distinct maximum and minimum values.

The streamlines and Nusselt number profile at the final time stage, where no appreciable change is seen, are plotted in Fig. 9. It is found that a pair of vortices with oppositely rotating directions and of approximately the same strength is produced. The pitch between each pair of vortices is about $z_p^+ = 1.9$. It is important to note, however, that velocities and stream function do not vary in sinusoidal fashion as in the case of the perturbation analysis in which the axial variation are often assumed to be $\exp(ia_f z^+)$.

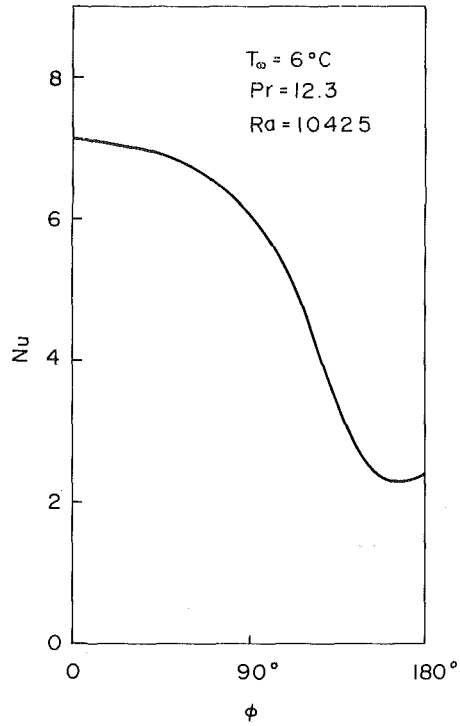

Fig. 6 Nusselt number profile around the cylinder for $T_\infty = 6°C$, Pr = 12.3 and Ra = 10425

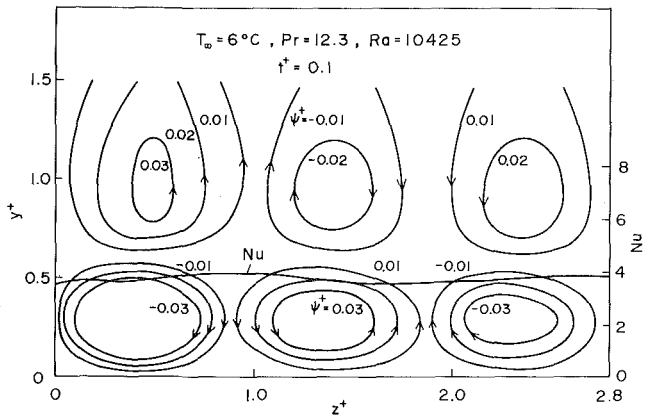

Fig. 7 Transient streamlines and Nusselt number profile in the $x = 0$ plane at Fourier number $t^+ = 0.1$. $T_\infty = 6°C$, Pr = 12.3, and Ra = 10425

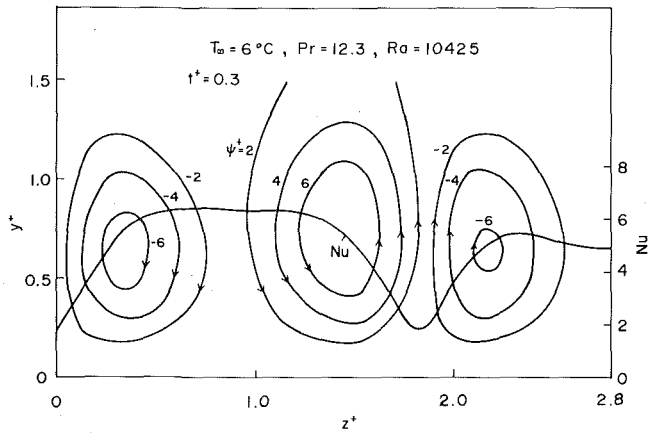

Fig. 8 Transient streamlines and Nusselt number profile in the $x = 0$ plane at Fourier number $t^+ = 0.3$. $T_\infty = 6°C$, Pr = 12.3, and Ra = 10425

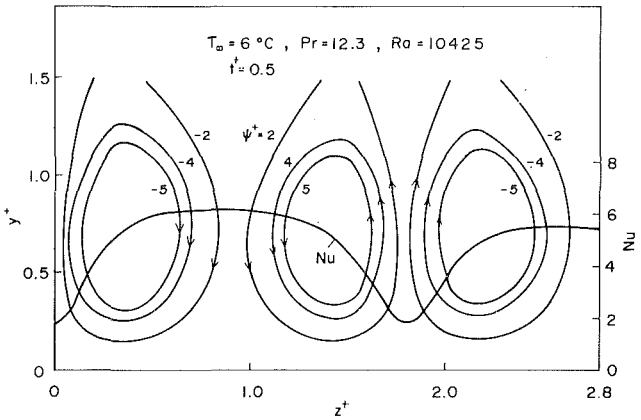

Fig. 9 Steady streamlines and Nusselt number profile at Fourier number $t^+ = 0.5$. $T_\infty = 6°C$, Pr = 12.3, and Ra = 10425

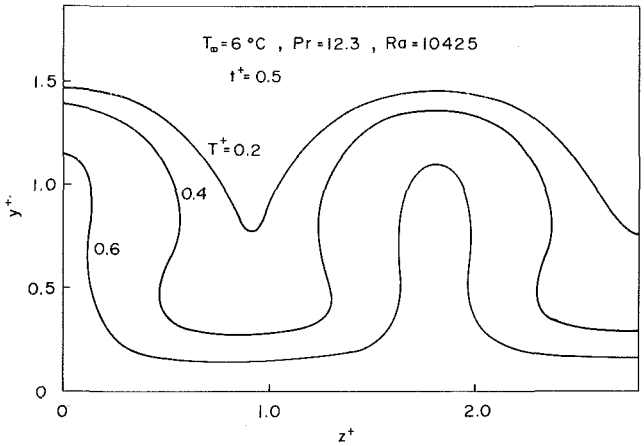

Fig. 10 Steady isotherms at Fourier number $t^+ = 0.5$ for $T_\infty = 6°C$, Pr = 12.3, and Ra = 10425

Next, the cause of formation of a wavy melting front shape is sought; this was found experimentally by one of the authors [10]. An inspection of the Nusselt number profile in Fig. 9 leads to the conclusion that Nu takes maximum and minimum values alternatively in the longitudinal direction. Namely, when the impinging flow toward the cylinder occurs, Nu has a maximum value, and when the outward flow occurs, Nu has a minimum value. These two cases clearly correspond to the melting rate at the cylinder surface, i.e., a concave melting front resulted at high Nusselt number and a convex one at low Nusselt number. As mentioned above, it seems that the mechanism of thermal instability which arose in the previous experiment is definitely clarified.

Figure 10 shows the isotherms in the (y, z) plane at a steady state. It can be seen from the figure that a hot flow goes down to the cylinder surface at high Nusselt number and a cold flow goes up from the cylinder at low Nusselt number.

Roots of the wave number obtained by virtue of the small perturbation method are plotted in Fig. 11. A detailed analysis by the small perturbation method is shown in the Appendix. Comparison of this value ($a_f = 1.795$ or 2.160) with that of the previous numerical result ($a_f = 3.3$) reveals that a large discrepancy exists between the two. This fact indicates that the small perturbation method cannot be applied successfully to the present problem involving density inversion.

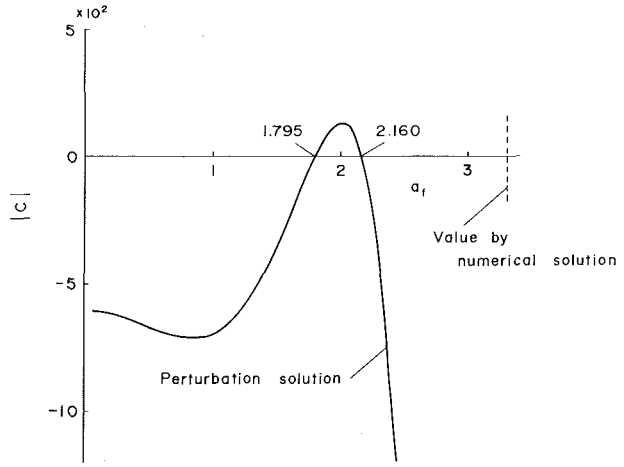

Fig. 11 Wave number roots a_f of matrix equation $|C|$ for the coefficient. Only the first two solutions are indicated

Concluding Remarks

The three-dimensional thermal instability which appears in the natural convection heat transfer around a horizontal ice cylinder passing through a maximum density point was analyzed by utilizing both fully numerical method and the small perturbation method.

The following conclusions can be drawn from the present study.

1 Thermal instability which arises in natural convection flow over a temperature range of about 5.5°C to 6.5°C and which had been predicted in a previous paper [10] was confirmed theoretically. The occurrence of a convexo-concave cross section of the melting front was rigorously explained from the convection pattern along the cylinder.

2 The transient process of formation of steady vortices was clarified when an initial disturbance was given by a periodic temperature variation in the axial direction. Initially, two rows of vortices are generated and then the outward vortices disappear, eventually, the final steady vortices are formed.

3 An analysis was also performed using the small perturbation method. Comparison of wave number obtained from this method with that of the numerical method shows that a significant discrepancy exists between the two. This fact seems to indicate that the perturbation method is not applicable to problems, such as the present case, which involve density inversion. In such a case, the perturbed quantities approach the magnitude of the basic quantities, which makes the method unreliable.

Acknowledgment

The authors extend their sincere thanks to Professor T. Yokobori for his gracious aid and encouragement in these studies. Thanks are also due to the Computer Center of the Tohoku University for the use of NEAC 2200 ACOS 6 SYSTEM 700 Time Sharing System.

Appendix

In this appendix, an analysis via small perturbation method will be presented briefly. The various quantities u^+, v^+, w^+, p^+, and T^+ are split into two parts, namely, the basic quantities (suffix 0) and the perturbed quantities (suffix 1) as below.

$$\Gamma^+ = \Gamma_0 + \Gamma_1 \tag{A1}$$

where, Γ^+ means either of u^+, v^+, w^+, p^+, and T^+.

As basic quantities, the steady two-dimensional quantities in the (x, y) plane perpendicular to the cylinder axis are adopted. After substituting equations (A1) into governing equations (1), (2) and (3), and neglecting the higher order terms of the perturbed quantities, the equations for basic and perturbed quantities can be derived.

1 Equations for Perturbed Quantities. Since the perturbed quantities contain a z-component, the axial dependence is assumed to be approximated by

$$f_1(x, y, z) = f_2(x, y) \cdot \exp(ia_f z), \tag{A2}$$

which is frequently used in perturbation analyses. Here, a_f means the wave number and is defined as

$$a_f = \frac{2\pi R}{\lambda}, \tag{A3}$$

with λ being the wave length. Inserting the equation (A2) into the governing equations, the perturbed equations involving only x and y components may be obtained. However, they are omitted here.

2 **Wave number a_f.** Since laborious work is necessary to solve the perturbation equations, the attention is focused only on the symmetry plane; i.e., the plane of $x = 0$, where the approximation $\partial/\partial x = 0$ hold true, and the resultant wave number a_f may be computed.

The perturbed equations are simplified to:

$$\frac{\partial v_2}{\partial y} + ia_f w_2 = 0 \tag{A4}$$

$$v_0 \frac{\partial v_2}{\partial y} + v_2 \frac{\partial v_0}{\partial y} = -\frac{\partial p_2}{\partial y} + \mathrm{Pr}\nabla^2 v_2 + \mathrm{PrRa}g(T_2) \tag{A5}$$

$$v_0 \frac{\partial w_2}{\partial y} = -ia_f p_2 + \mathrm{Pr}\nabla^2 w_2 \tag{A6}$$

$$v_0 \frac{\partial T_2}{\partial_y} + v_2 \frac{\partial T_0}{\partial y} = \nabla^2 T_2 \tag{A7}$$

where,

$$\nabla^2 = \frac{\partial^2}{\partial y^2} - a_f{}^2. \tag{A8}$$

By virtue of the linearity of the above equations, a higher order ordinary differential equation which is a function of only v_2, can be deduced finally after elimination of variables by turns.

$$F(v_2) = (AD^6 + BD^5 + CD^4 + ED^3 + FD^2 + GD + H)v_2 = 0 \tag{A9}$$

where,

$$D^n = \frac{\partial^n}{\partial y^n} \tag{A10}$$

and A, B, C, E, F, G, and H are the coefficients involving Pr, v_0, a_f, T_0, etc.

Next, v_2 expanded by a series as

$$v_2 = \sum_{n=0}^{\infty} \frac{A_n}{n!} y_n. \tag{A11}$$

Substitution of equation (A11) leads to a recurrence formula with respect to A_n. Taking the boundary condition at $y = y_\infty$ into account, a simultaneous equation pertinent to A_2, A_3, and A_5 is obtained.

$$\begin{bmatrix} c_{11}c_{12}c_{13} \\ c_{21}c_{22}c_{23} \\ c_{31}c_{32}c_{33} \end{bmatrix} \begin{bmatrix} A_2 \\ A_3 \\ A_5 \end{bmatrix} = \begin{bmatrix} 0 \\ 0 \\ 0 \end{bmatrix} \tag{A12}$$

where,

$$c_{11} = \frac{y_\infty{}^2}{2!} + \frac{y_\infty{}^4}{4!}\frac{Dv_0 + 2\mathrm{Pr}a_f{}^2}{\mathrm{Pr}} + \sum_{n=6}^{\infty} \frac{y_\infty{}^n}{n!} B_{n,2}$$

$$c_{12} = \frac{y_\infty{}^3}{3!} + \sum_{n=6}^{\infty} \frac{y_\infty{}^n}{n!} B_{n,3}$$

$$c_{13} = \frac{y_\infty{}^5}{5!} + \sum_{n=6}^{\infty} \frac{y_\infty{}^n}{n!} B_{n,5}$$

$$c_{21} = y_\infty + \frac{y_\infty{}^3}{3!}\frac{Dv_0 + 2\mathrm{Pr}a_f{}^2}{\mathrm{Pr}} + \sum_{n=6}^{\infty} \frac{y_\infty{}^{n-1}}{(n-1)!} B_{n,2}$$

$$c_{22} = \frac{y_\infty{}^2}{2!} + \sum_{n=6}^{\infty} \frac{y_\infty{}^{n-1}}{(n-1)!} B_{n,3}$$

$$c_{23} = \frac{y_\infty{}^4}{4!} + \sum_{n=6}^{\infty} \frac{y_\infty{}^{n-1}}{(n-1)!} B_{n,5} \tag{A13}$$

$$c_{31} = -(Dv_0 + 2a_f{}^2\mathrm{Pr}) + \left(\mathrm{Pr} - v_0 y_\infty - (Dv_0 + 2a_f{}^2\mathrm{Pr})\frac{y_\infty{}^2}{2!}\right)\frac{Dv_0 + 2a_f{}^2\mathrm{Pr}}{2} + \sum_{n=6}^{\infty}\left(\mathrm{Pr}\frac{y_\infty{}^{n-4}}{(n-4)!} - v_0\frac{y_\infty{}^{n-3}}{(n-3)!} - (Dv_0 + 2a_f{}^2\mathrm{Pr})\frac{y_\infty{}^{n-2}}{(n-2)!}\right) B_{n,2}$$

$$c_{32} = -(v_0 + Dv_0 + 2a_f{}^2\mathrm{Pr}) + \sum_{n=6}^{\infty}\left(\mathrm{Pr}\frac{y_\infty{}^{n-4}}{(n-4)!} - v_0\frac{y_\infty{}^{n-3}}{(n-3)!} - (Dv_0 + 2a_f{}^2\mathrm{Pr})\frac{y_\infty{}^{n-2}}{(n-2)!}\right) B_{n,3}$$

$$c_{33} = \mathrm{Pr}y_\infty - v_0\frac{y_\infty{}^2}{2!} - (Dv_0 + 2a_f{}^2\mathrm{Pr})\frac{y_\infty{}^3}{3!} + \sum_{n=6}^{\infty}\left(\mathrm{Pr}\frac{y_\infty{}^{n-4}}{(n-4)!} - v_0\frac{y_\infty{}^{n-3}}{(n-3)!} - (Dv_0 + 2a_f{}^2\mathrm{Pr})\frac{y_\infty{}^{n-2}}{(n-2)!}\right) B_{n,5}$$

$$A_n = B_{n,2} \cdot A_2 + B_{n,3} \cdot A_3 + B_{n,5} \cdot A_5$$

The wave number a_f is obtained from the stipulation that A_2, A_3, and A_5 should have nontrivial solutions, which states

$$|\boldsymbol{C}| = 0. \tag{A14}$$

The matrix $|\boldsymbol{C}|$ contains Pr, Ra and a_f, i.e., the water temperature T_∞, cylinder radius R, and the wave number a_f. Therefore the wave number can be obtained if T_∞ and R are determined.

A numerical example is shown in Fig. 11 for $T_\infty = 6.0°\mathrm{C}$, $y_\infty = 1.5$, and Ra = 10425. It is noted here that the wave number obtained by the perturbation method is considerably smaller than the numerical value, thereby making the perturbation analysis for the problem including density inversion invalid.

References

1 Dumoré, J. M., Merk, H. J., and Prins, J. A., "Heat Transfer from Water to Ice by Thermal Convection," *Nature*, Vol. 172, 1953, pp. 460–461.

2 Merk, H. J., "The Influence of Melting and Anomalous Expansion on the Thermal Convection in Laminar Boundary Layers," *Applied Scientific Research*, Vol. 4, 1953, pp. 435–452.

3 Schechter, R. S., and Isbin, H. S., "Natural-Convection Heat Transfer in Regions of Maximum Fluid Density," *AIChE Journal*, Vol. 4, 1958, pp. 81–89.

4 Vanier, C. R., and Tien, C., "Effect of Maximum Density and Melting on Natural Convection Heat Transfer from a Vertical Plate," *Chemical Engineering Progress Symposium*, Ser. No. 82, Vol. 64, 1968, pp. 240–254.

5 Gilpin, R. R., "Cooling of a Horizontal Cylinder of Water Through Its Maximum Density Point at 4°C," *International Journal of Heat and Mass Transfer*, Vol. 18, 1975, pp. 1307–1315.

6 Watson, A., "The Effect of the Inversion Temperature on the Convection of Water in an Enclosed Rectangular Cavity," *Quarterly Journal of Mechanics and Applied Mathematics*, Vol. 25, No. 4, 1972, pp. 423–446.

7 Forbes, R. E., and Cooper, J. W., "Natural Convection in a Horizontal Layer of Water Cooled From Above to Near Freezing," ASME JOURNAL OF HEAT TRANSFER, Vol. 97, 1975, pp. 47–53.

8 Cheng, K. C., and Takeuchi, M., "Transient Convection of Water in a Horizontal Pipe with Constant Cooling Rate Through 4°C," ASME JOURNAL OF HEAT TRANSFER, Vol. 98, 1976, pp. 581–587.

9 Bendell, M. S., and Gebhart, B., "Heat Transfer and Ice-Melting in Ambient Water Near Its Density Extremum," *International Journal of Heat and Mass Transfer*, Vol. 19, 1976, pp. 1081–1087.

10 Saitoh, T., "Natural Convection Heat Transfer From a Horizontal Ice Cylinder," *Applied Scientific Research*, Vol. 32, 1976, pp. 429–451.

11 Saitoh, T., "An Experimental Study for Two-dimensional Freezing Around a Horizontal Circular Cylinder Passing Through Maximum Density Point," *Refrigeration*, Vol. 53, No. 612, 1978, pp. 891–896.

12 Saitoh, T., and Hirose, K., "Numerical Method for Two-dimensional Freezing Problem Around a Horizontal Cylinder Passing Through Density Inversion Point," *Trans JSME*, Vol. 46, 1980, (to be published).

13 Cheng, K. C. and Wu, R.-S., "Axial Heat Conduction Effects on Thermal Instability of Horizontal Plane Poiseuille Flow Heated From Below," ASME JOURNAL OF HEAT TRANSFER, Vol. 98, 1976, pp. 564–569.

14 Nakayama, W., Hwang, G. J. and Cheng, K. C., "Thermal Instability in Plane Poiseuille Flow," ASME JOURNAL OF HEAT TRANSFER, Vol. 92, 1970, pp. 61–68.

15 Sparrow, E. M., Goldstein, R. J. and Jonsson, V. K., "Thermal Instability in a Horizontal Fluid Layer: Effect of Boundary Conditions and Non-linear Temperature Profile," *Journal of Fluid Mechanics*, Vol. 18, 1964, pp. 513–528.

16 Sparrow, E. M., Lee, L. and Shamsunder, N., "Convective Instability in a Melt Layer Heated From Below," ASME JOURNAL OF HEAT TRANSFER,

Vol. 98, 1976, pp. 88–94.
17 Fujii, T., *Advances of Heat Transfer Engineering,* Vol. 3, p. 66, Yokendo, 1974.
18 Saitoh, T., "A Numerical Method for Two-dimensional Navier-Stokes Equation by Multi-point Finite Differences," *International Journal for Numerical Methods in Engineering,* Vol. 11, 1977, pp. 1439–1454.
19 Landolt-Börnstein, *Physikalisch-Chemisch Tabellen,* 6 Aufl., Bd. II/5a, Springer, Berlin, 1969, p. 551.

Convective Instability of Rotating Radiating Fluids

S. O. Onyegegbu

Department of Mechanical Engineering,
University of Nigeria, Nsukka
Nigeria

The Benard problem of a rotating radiating nongray fluid is examined analytically for both stationary and oscillatory convection. Radiation is modeled by the Milne-Eddington approximation. The time derivatives are retained in the disturbance equations and both types of instability were studied using the same approximating functions. Results presented show that, in the presence of rotation, radiation increases the zone in which overstability is the preferred mode of instability.

Introduction

The combined effect of rotation and radiative transfer on the onset of convection is a phenomenon which is important in a number of engineering, astrophysical and geophysical applications. Components such as gas turbines and helicopter ramjets rotate at high speeds and the associated large centrifugal forces generate strong natural convection currents which, together with radiative transfer, are known to provide the cooling of turbine blades. Also, rotating radiating fluids are known to exist in planetary and solar interiors and an accurate analysis of the interaction between rotation and radiation is useful in the understanding of these interiors.

Many investigators have studied singly the Benard problem with radiative transfer and the Benard problem with rotation. An excellent summary of the former can be found in a paper by Arpaci and Gozum [1]. The results show that, in all cases, instability is in the form of stationary convection only. Chandrasekhar, [2] and Niller and Bishop [3] among others have studied the Benard problem with rotation and their results show that for Prandtl numbers less than 0.67 the onset of instability will be in the form of oscillatory cells, overstability, if the Taylor number exceeds a certain value while for Prandtl numbers above 0.67 only stationary convection can occur. Khosla and Murgai [4] considered the combined effect of radiative transfer and rotation but were primarily concerned with stationary convection and commented only briefly on overstability. This paper reconsiders the Benard problem of radiating fluid with rotation for both cases of stationary and oscillatory convection. Of particular interest is the effect of radiation on the manner of onset of instability.

Governing Equations

Consider a plane layer of absorbing, nonscattering, nongray medium confined between uniform temperature gray planes separated by a distance, d. The fluid is in rotation with a constant angular velocity, Ω, about the vertical axis and is heated from below.

Neglecting the contribution of the radiative energy density to the energy equation and the contribution of the radiative stress to the momentum equation, the Boussinesq formulation of the momentum, energy, and mass equations can be written as

$$\frac{\partial u_i}{\partial t} + u_j \frac{\partial u_i}{\partial x_j} = -\frac{\partial}{\partial x_i}\left(\frac{P}{\rho_0} - {}^1/_2\,\Omega \times xr/2\right) + \left(1 + \frac{\delta\rho}{\rho_0}\right) X_i + \nu\nabla^2 u_i + 2\epsilon_{ijk} u_j \Omega_k \quad (1)$$

$$\frac{\partial T^*}{\partial t} + u_j \frac{\partial T^*}{\partial x_j} = \frac{\kappa \partial^2 T^*}{\partial x_i \partial x_j} + \frac{\alpha_p}{\rho_0 c_v}(j - 4\sigma T^{*4}) \quad (2)$$

$$\frac{\partial u_i}{\partial x_i} = 0 \quad (3)$$

Following Vincenti and Kruger [5], radiation is modeled by the Milne-Eddington approximation which is valid for the entire optical thickness. This approximation is given by

$$\nabla^2 q_i{}^R - 3\alpha_p \alpha_R q_i^R = 4\alpha_p \partial_i E_b \quad (4)$$

where

$$q_i^R = \int_0^{4\pi} \ell_i I d\omega$$

Relating the radiant flux q_i^R to the first moment of radiative intensity, j, and the black body radiation, E_b, to the absolute temperature T^*, this approximation can be written as

$$\nabla^2 j - 3\alpha_p \alpha_R j = -12\alpha_p \alpha_R \sigma T^{*4} \quad (5)$$

where

$$j = \int_0^{4\pi} I\, d\omega$$

The corresponding radiative boundary conditions are $j_w = 4E_{bo} + (\eta/3\lambda\tau)\,\partial j_w/\partial x_3$ for a gray boundary with no temperature jump and $\partial j_w/\partial x_3 = 0$ for a mirror boundary.

The stability problem requires the gradient of the initial temperature distribution, β, which is readily obtained as

$$\frac{\beta}{\beta_0} = A + B\,\text{Sinh}\,\phi\tau z + C\,\text{Cosh}\,\phi\tau z \quad (6)$$

where

$$\beta = -\frac{dT^*}{dx_3},\ \beta_0 = \frac{T_0 - T_1}{d},\ \phi = (3 + 4\chi)^{1/2}$$

$$\chi = \eta/\text{P}\ell,$$

$$A = {}^3/G,\ B = (\phi^2 - 3)E/G,\ C = (\phi^2 - 3)F/G$$

$$E = \frac{[\lambda_1\phi\,\text{Sinh}\,\phi\tau + \eta\,\text{Cosh}\,\phi\tau - \eta]}{[(\eta + \lambda_0\lambda_1\phi^2/\eta)\,\text{Sinh}\,\phi\tau + \phi(\lambda_0 + \lambda_1)\,\text{Cosh}\,\phi\tau]}$$

$$F = \lambda_0\phi E/\eta - 1$$

$$G = [(\phi^2 - 3)\{F\sinh\phi\tau - E(1 - \cosh\phi\tau) - 3\phi\tau\}]/\phi\tau$$

$$\lambda_0 = \frac{\epsilon_0}{2(2 - \epsilon_0)},\ \lambda_1 = \frac{\epsilon_1}{2(2 - \epsilon_0)}$$

The results for black and mirror boundaries are obtained by evaluating these equations for $\epsilon_0, \epsilon_1 = 1$ and $\epsilon_0, \epsilon_1 = 0$, respectively.

The linear stability problem is analyzed in terms of the normal modes applied to the x_3 components of the following disturbance quantities: vorticity, velocity, temperature, and first moment of radiative intensity. If b is any disturbance quantity, then following Finlayson [6] and expressing this quantity as

$$b(x_1, x_2, x_3, t) = B(x_3, t)\exp[i(K_1 x_1 + K_2 x_2)]$$

stationary and oscillatory instability can be studied by means of the same trial functions. In dimensionless form, the disturbance equations are

$$\frac{\partial Z}{\partial t_*} = T^{1/2} DW + (D^2 - a^2)Z \quad (7)$$

$$(D^2 - a^2)\frac{\partial W}{\partial t_*} = -\frac{\text{Ra}^2\kappa}{\beta_0 d^2}\theta + (D^2 - a^2)^2 W - T^{1/2} DZ \quad (8)$$

Contributed by the Heat Transfer Division for publication in the JOURNAL OF HEAT TRANSFER. Manuscript received by The Heat Transfer Division January 15, 1980.

$$\Pr \frac{\partial \theta}{\partial t_*} = \frac{d^2\beta}{\kappa} W + (D^2 - a^2 - 4\chi\tau^2)\theta + 3\chi\tau^2 J \tag{9}$$

$$0 = (D^2 - a^2 - 3\tau^2)J + 4\tau^2\theta \tag{10}$$

where

$a = d\,(K_1^2 + K_2^2)^{1/2}$ is the wavenumber

$$D = \frac{d}{dz}$$

$t_* = \frac{\nu}{d^2}\,t$ is dimensionless time

and J has been dimensionalized by $12\sigma T_m^3$. Equations (9) and (10) can be combined by operating on (9) by $(D^2 - a^2 - 3\tau)$ and using (10) in the resulting equation to obtain

$$\Pr(D^2 - a^2 - 3\tau^2)\frac{\partial \theta}{\partial t_*} = \frac{d^2\beta}{\kappa}(D^2 - a^2 - 3\tau^2)W + \{(D^2 - a^2 - 3\tau^2)(D^2 - a^2 - 4\chi\tau^2) - 12\chi\tau^4\}\theta \tag{11}$$

Equations (7, 8) and (11) govern the stability of the problem subject to the appropriate boundary conditions.

Method of Solution

In the usual Galerkin method the solution is approximated by

$$W(z, t_*) = \sum_{n=1}^{N} A_n(t_*)W_n(z)$$

$$\theta(z, t_*) = \sum_{n=1}^{N} B_n(t_*)\theta_n(z) \tag{12}$$

$$Z(z, t_*) = \sum_{n=1}^{N} C_n(t_*)Z_n(z)$$

where $W_n(z)$, $\theta_n(z)$, $Z_n(z)$ satisfy the boundary conditions.

Considering the case of free boundaries, the boundary conditions are

$$W = D^2W = \theta = DZ = 0 \qquad \text{on } z = 0, 1$$

These conditions suggest solutions of the form

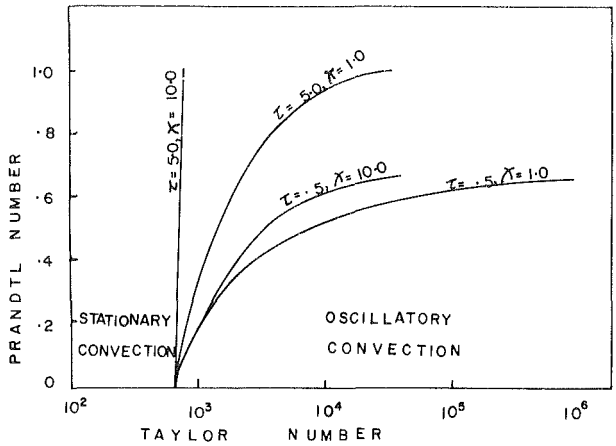

Fig. 1 The effect of radiation on the zones of instability

$$W_n = \text{Sin } n\pi z,\ \theta_n = \text{Sin } n\pi z,\ Z_n = \text{Cos } n\pi z$$

These solutions are substituted into equation (12) and the results substitututed into equations (7, 8) and (11). The residuals are orthogonalized in the spatial domain and the resulting system of $3N$ ordinary differential equations can be written as

$$\overline{E}\frac{d\overline{A}}{dt_*} = \overline{B}\,\overline{A} \text{ or } \frac{d\overline{A}}{dt_*} = \overline{D}\,\overline{A} \tag{13}$$

The stability of the system is governed by either det. $\overline{D} = 0$ for stationary instability or $T_{N-1} = 0$ for oscillatory instability, where T_i are successive determinants formed from the Hurwitz determinants defined in [6]. In terms of the first approximation when $N = 1$ we obtain for stationary convection,

$$R^s = \frac{L\{(\pi^2 + a^2)^3 + \pi^2 T\}}{a^2 SM(\pi^2 + a^2)} \tag{14}$$

for oscillatory convection,

Nomenclature

a = nondimensional wave number
c_v = specific heat at constant volume
d = depth of fluid layer
E_b = black body emissive power
E_{bo} = black body emissive power of the fluid at the boundary
E_{bw} = black body emissive power of the boundary wall
g = gravitational acceleration
I = frequency averaged radiative intensity
j = first moment of radiative intensity
J = amplitude function of the first moment of radiative intensity dimensionalized by $12\sigma T_m{}^3$
k = thermal conductivity
P = fluid pressure
$P\ell$ = Planck number, $\frac{\alpha_m K}{4\sigma T_m{}^3}$
Pr = Prandtl number, ν/κ
Pr* = Prandtl number above which instability occurs as stationary convection for all Taylor numbers
r = position vector from axis of rotation
R = Rayleigh number, $\frac{g\alpha_0\beta_0 d^4}{\kappa\nu}$
$R_c{}^o$ = critical Rayleigh number for overstability
$R_c{}^s$ = Critical Rayleigh number for stationary convection
t = time
T = Taylor number, $\frac{4\Omega^2 d^4}{\nu^2}$
T^* = temperature
T_0 = temperature of bottom layer
T_1 = temperature of top layer
T_m = mean temperature
u_i, u_j = fluid velocity vector
w = fluid velocity vector in the vertical direction
W = amplitude function of the velocity w
x_1 = spanwise coordinate
x_2 = transverse coordinate
X_3 = vertical coordinate
z = dimensionless vertical coordinate
Z = amplitude function of the vorticity
α = coefficient of thermal expansion
α_0 = reference value of the coefficient of thermal expansion
α_m = Root mean square value of absorption coefficient, $(\alpha_p\alpha_R)^{1/2}$
α_p = Planck mean of the absorption coefficient
α_R = Rosseland mean of the absorption coefficient
β = temperature gradient of the initial state
β_0 = temperature gradient of the initial state without radiation
γ = eigenvalues of the characteristic matrix
Γ = overstable oscillation frequency
ϵ = hemispherical (diffuse) emissivity of boundary
ϵ_0 = hemispherical (diffuse) emissivity of the lower boundary
ϵ_1 = hemispherical (diffuse) emissivity of the upper boundary
η = degree of nongrayness of fluid, $\left(\frac{\alpha_p}{\alpha_R}\right)^{1/2}$
θ = amplitude function of the disturbance temperature
κ = thermal diffusivity
ν = kinematic viscosity
ρ_0 = reference value of density
σ = Stefan-Boltzman constant
τ = optical thickness, $\alpha_m d$

$$R^0 = \frac{2(\pi^2 + a^2)^2 L\{2\mathrm{Pr}M(\pi^2 + a^2) + L\} + 2\mathrm{P_r}^2 M^2(\pi^2 + a^2)\{(\pi^2 + a^2)^3 + \pi^2\mathrm{T}\}}{a^2 MS\{\mathrm{P_r}M(\pi^2 + a^2) + L\}} \tag{15}$$

where

$L = \{(\pi^2 + a^2 + 3\tau^2)(\pi^2 + a^2 + 4\chi\tau^2) - 12\chi\tau^4\}$, $\mathrm{M} = (\pi^2 + a^2 + 3\tau^2)$

$$S = \int_0^1 \frac{\beta}{\beta_0} \mathrm{Sin}^2 \pi z$$

When oscillatory instability occurs, the oscillation frequency, Γ, can be obtained by successive substitution of $\gamma = i\Gamma$ and $\gamma = -i\Gamma$ into the polynomial form of the eigenvalue equation, $\det(\overline{D} - \gamma I) = 0$, and solving the resulting two equations for Γ^2. For the first approximation we obtain

$$\Gamma^2 = \frac{2(\pi^2 + a^2)L}{M} - \frac{\mathrm{Ra}^2 S}{(\pi^2 + a^2)} + (\pi^2 + a^2)^2 + \frac{\pi^2 \mathrm{T}}{(\pi^2 + a^2)} \tag{16}$$

Γ, as defined, is dimensionless since time in the governing equations has been nondimensionalized by d^2/ν. If $\tau \to 0$ or $\chi \to 0$ we recover the solutions for the nonradiating problem given by Chandrasekhar for R^s, R^0 and Γ^2. The two Rayleigh numbers are minimized with respect to a^2 and whichever is lower determines the manner of onset of instability for a given condition. The convergence of the approximate technique used was checked by performing computations for the first and second approximations. The results for black and mirror boundaries obtained in terms of the two approximations differed at the most by 2.6 percent for the critical Rayleigh number and 1.1 percent for the critical oscillation frequency. The equations obtained here for critical Rayleigh number are rather long and cumbersome and it may be convenient and instructive to establish the results which are valid for the limiting cases of the thin gas ($\tau \ll 1$), the thick gas ($\tau \gg 1$), and large Taylor number.

Thin Gas

In the optically thin gas approximation, there is a small decay or absorption of emitted radiant energy which implies that the middle term of equation (4) can be neglected and the Milne-Eddington approximation reduces to

$$\nabla q_i^R = 4\alpha_p E_b \tag{17}$$

Using this equation in place of equation (1) and following the steps outlined, the following values for Rayleigh number are obtained.

$$\mathrm{R}^s = \frac{(\pi^2 + \mathrm{a}^2 + 4\chi\tau^2)[(\pi^2 + \mathrm{a}^2)^3 + \pi^2\mathrm{T}]}{a^2(\pi^2 + a^2)S} \tag{18}$$

and

$$\mathrm{R}^0 = \frac{2(\pi^2 + a^2)^2[(\pi^2 + a^2)\mathrm{Pr} + (\pi^2 + a^2 + 4\chi\tau^2)]^2 + 2\pi^2(\pi^2 + a^2)\mathrm{Pr}^2\mathrm{T}}{a^2 S[(\pi^2 + a^2)\mathrm{Pr} + (\pi^2 + a^2 + 4\chi\tau^2)]} \tag{19}$$

For small τ and relatively large Taylor number, R^s and R^0 attain their minimum values at the same values of a^2 as their corresponding nonradiating problems given by Chandrarekhar. Namely, for stationary convection $a_c{}^2 = \frac{1}{2}(\pi^2 T/2)^{1/2}$ and for oscillatory convection, $a_c{}^2 = [\pi^2 \mathrm{Pr}^2 T/2(1 + \mathrm{Pr})^2]^{1/3}$.

The critical values of Rayleigh number become

$$R_c{}^s = \frac{3\left(\frac{\pi^2 T}{2}\right)^{2/3}}{S}\left[1 + \frac{4\chi\tau^2}{\left(\frac{\pi^2 T}{2}\right)^{1/3}}\right] \tag{20}$$

$$R_c{}^0 = \frac{6(1 + \mathrm{Pr})}{S}\left(\frac{\pi^2 \mathrm{Pr}^2 \mathrm{T}}{2(1 + \mathrm{Pr})^2}\right)^{2/3} + \frac{4\chi\tau^2}{S}\left(\frac{\pi^2 \mathrm{Pr}^2 \mathrm{T}}{2(1 + \mathrm{Pr})^2}\right)^{1/3} \tag{21}$$

Clearly, the thin gas problem approaches the nonradiating problem since $S \to 1$ as $\tau \to 0$. The second terms of both equations together with S provide the modifications by radiation to the nonradiating solution.

Thick Gas

In the optically thick gas approximation, emitted radiant energy is absorbed within the immediate neighborhood of the emitting particle and in this case the first term of equation (1) can be neglected and the Milne-Eddington approximation reduces to the Rosseland equation

$$q_i^R = -\frac{4}{3\alpha_R}\partial_i E_b \tag{22}$$

and radiative transfer is entirely diffusive. Using this equation in place of equation (1) and following the steps outlined we obtain

$$\mathrm{R}^s = \frac{(1 + 4\chi/3)\{(\pi^2 + a^2)^3 + \pi^2\mathrm{T}\}}{a^2 S} \tag{23}$$

$$\mathrm{R}^o = \frac{2(\pi^2 + a^2)^3[\mathrm{Pr} + (1 + 4\chi/3)]^2 + 2\pi^2\mathrm{Pr}^2\mathrm{T}}{a^2 S[\mathrm{Pr} + (1 + 4\chi/3)]} \tag{24}$$

For large values of $\mathrm{Pr}^2\mathrm{T}$, R^s attains its minimum value when $a^2 = (\pi^2\mathrm{T}/2)^{1/3}$ while R^o attains its minimum value when $a^2 = \{\pi^2\mathrm{Pr}^2\mathrm{T}/2[\mathrm{Pr} + (1 + 4\chi/3)]^2\}^{1/3}$

Hence

$$\mathrm{R}_c{}^s = \frac{(1 + 4\chi/3)}{S} 3\left\{\frac{\pi^2\mathrm{T}}{2}\right\}^{2/3} \tag{25}$$

$$\mathrm{R}_c{}^o = \frac{6(1 + 4\chi/3)}{S}(\tfrac{1}{2}\pi^2\mathrm{T})^{2/3}\frac{\left\{\frac{\mathrm{Pr}}{1 + 4\chi/3}\right\}^{4/3}}{\left\{1 + \frac{\mathrm{Pr}}{(1 + 4\chi/3)}\right\}^{1/3}} \tag{26}$$

These solutions can be seen to be of the same form as the nonradiating solutions obtained by Chandrasekhar. The stationary convection solution has been modified by $(1 + 4\chi/3)/S$, while the oscillatory convection solution has been modified by the same term and Prandtl number has been effectively reduced by $(1 + 4\chi/3)$.

Results and Discussion

The solutions obtained show that the stability of rotating radiating fluids depends on the following dimensionless parameters: optical thickness, Taylor number, Prandtl number, degree of nongrayness of the fluid, the Planck number which is a measure of the relative importance of conduction to radiation, and the parameter χ defined as $\eta/\mathrm{P}\ell$. Results are presented for optical thickness values ranging from 0.01 (optically thin) to 10 (optically thick) and with Planck number taking on values ranging from 0.01 (radiation dominant) to 1. The conduction dominant cases ($\mathrm{P}\ell \gg 1$) will be identical to the nonradiating problem.

The influence of optical thickness and Planck number on the zones of instability is illustrated in Fig. 1. This figure indicates that the principal influence of radiation is to increase the region of overstability by reducing the Taylor number above which overstability is the preferred mode of instability for a given Prandtl number, and also by increasing the value of the limiting Prandtl number above which only stationary instability can occur. For the optically thin gas cases these radiative effects are small. For the optically thick gas cases the radiative effects are quite significant, particularly the increase in the limiting Prandtl number for overstability. This limiting Prandtl number, obtained for large τ and large T by equating the critical

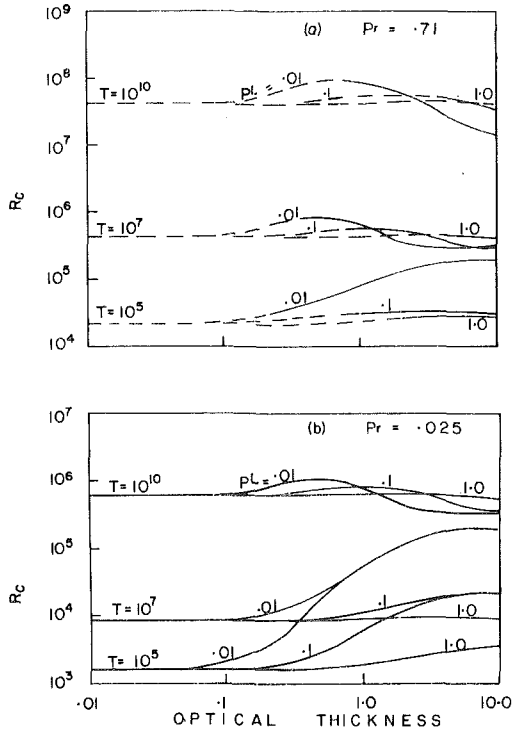

Fig. 2 Influence of Planck number on critical Rayleigh number for the case $\eta = 1.0$: - - - - - -, Stationary convection; —— oscillatory convection: Prandtl numbers (*a*) 0.71 and (*b*) 0.025

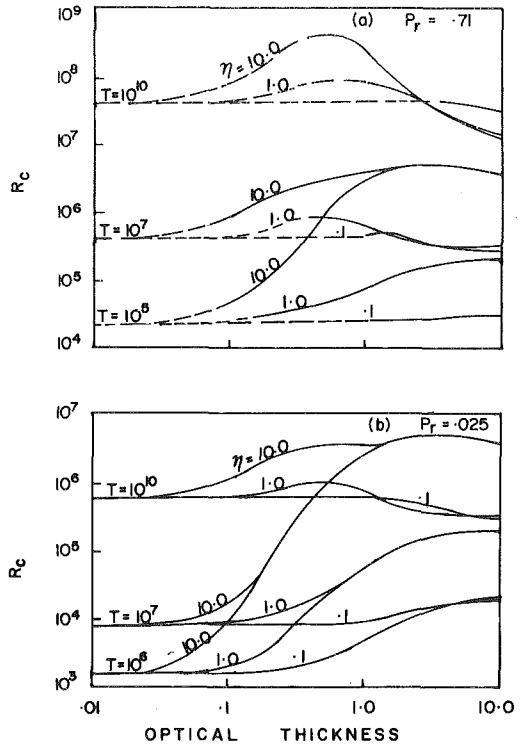

Fig. 3. Influence of the degree of nongrayness of fluid medium on critical Rayleigh number for the case $P\ell = .01$: - - - - -, Stationary convection; —— oscillatory convection: Prandtl numbers (*a*) 0.71 and (*b*) 0.025

values $R_c{}^s$ and $R_c{}^o$ from equations (25) and (26), is given by

$$Pr^* = 0.677(1 + 4\chi/3)$$

Pr* therefore increases with increasing χ (that is decreasing $P\ell$). Theoretically, $Pr^* \to \infty$ as $\chi \to \infty$. This trend is shown by the curve for $\tau = 5.0$ and $\chi = 10.0$. Hence for any significant amount of rotation ($T > 10^3$) and large χ, overstability will be the preferred mode of instability for all thick gas cases no matter what the Prandtl number of the fluid is. Figure 1 also indicates the important fact that optical thickness influences the value of χ (or $P\ell$) at which the effect of radiation becomes significant. It shows that radiative transfer influences the zones of instability when $\chi \geq 1.0$ for a medium of optical thickness 10.0 but its effect in a medium of optical thickness 0.5 is minimal even for $\chi = 10.0$.

Figures 2, 3 and 4 summarize the effect of optical thickness, Planck number, and degree of nongrayness at the onset of instability. The results are presented for two types of fluids, a low Prandtl number fluid (Pr = .025) such as mercury (liquid metal), and a moderate Prandtl number fluid (Pr = .71) such as air (gaseous medium). As the optical thickness is increased from the optically thin case the critical Rayleigh number increases from its nonradiating value and reaches a maximum value at some intermediate optical thickness. The extremum is appreciable for cases of high Taylor number, low Planck number and high η. Increasing τ produces two effects which are known to work in opposition. It is known to flatten the initial temperature distribution which induces a stabilizing effect. It also reduces the effective Prandtl number of the medium. This reduction of the effective Prandtl number reduces the magnitude of the viscous forces and hence induces a destabilizing effect. For the thin gas case, the first effect dominates and so critical Rayleigh number increases with τ. At some intermediate τ the two effects are equal and cancel each other and this is where the maximum critical Rayleigh number occurs. For greater values of τ, the second effect dominates and the critical Rayleigh number decreases asymptotically to its optically thick limit value.

The results for the low Prandtl number fluid show that the critical Rayleigh number is independent of Taylor number at large optical

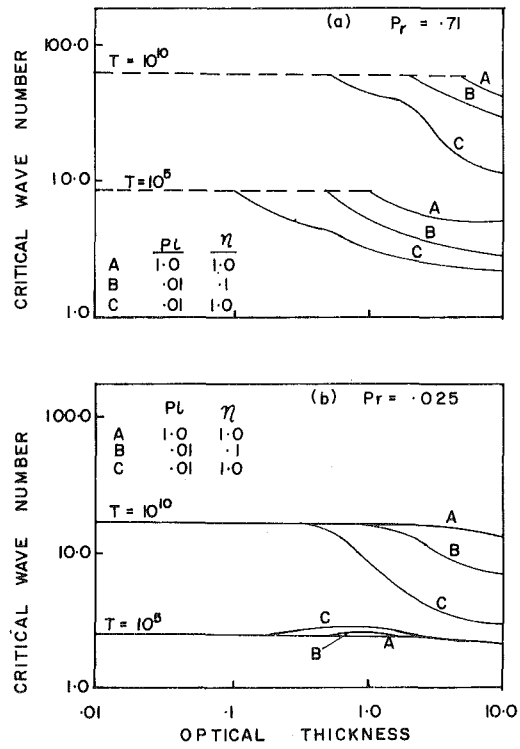

Fig. 4. The effect of Taylor number, Planck number and degree of nongrayness of fluid medium on critical wave number: - - - -, Stationary convection; —— oscillatory convection; Prandtl numbers (*a*) 0.71 and (*b*) 0.025

thickness. It was shown earlier that the thick gas radiation problem is the same as the nonradiating problem with Prandtl number reduced by $(1 + 4\chi/3)$. If a Prandtl number of 0.025 is reduced by $(1 + 4\chi/3)$ where $\chi = 10.0$, say, the effective Prandtl number becomes 0.0018 which may be neglected in equation (24) to obtain

$$R^o = \frac{2(\pi^2 + a^2)^3(1 + 4\chi/3)}{a^2 S}$$

This is independent of the Taylor number and is twice the value of the Rayleigh number for stationary convection for the case of radiation without rotation obtained by setting T = 0 in equation (23). The critical wave numbers for these two cases are the same and are given by $a^2 = \pi^2/2$. This same relationship is known to exist between R^o and R^s for nonradiating fluids as $Pr \to 0$.

The effects of other radiation parameters on stability can be explained in terms of their effects on the initial temperature distribution. Results indicate that problems with mirror boundaries are more stable than their corresponding problems with black boundaries. Viskanta and Grosh [7] have shown that, for mirror boundaries, temperature gradient is steep near the boundaries and flat near the core. The bulk of the fluid is therefore subjected to little temperature gradient and this effect is stabilizing. For this same reason, decreasing the Planck number and increasing the degree of nongrayness of the fluid stabilize the fluid.

Figure 4 shows that when stationary convection is the preferred mode of instability, the critical wave number is independent of radiative transfer. However, when overstability becomes the preferred mode of instability at higher values of optical thickness, the critical wave number is less than that for stationary convection and decreases with increasing optical thickness.

Conclusions

The Galerkin method was applied to the Benard problem of rotating radiating nongray fluids, and the problem was studied for both stationary and oscillatory convection. Results show that radiation in the presence of rotation increases the region in which overstability is the preferred mode of instability. For a thick gas this effect of radiative transfer becomes significant when the parameter $\chi = \eta/P\ell$ is greater than 1 and for a thin gas radiative effects start becoming significant for χ values greater than 10. While critical wave number for stationary convection is not affected by radiation parameters, the critical wave number for overstability for the thick gas is a function of χ.

References

1 Arpaci, V. S., and Gozum, D., "Thermal Stability of Radiating Fluids: The Benard Problem," *Physics of Fluids,* Vol. 16, 1973, pp. 581–588.

2 Chandrasekhar, S., *Hydrodynamic and Hydromagnetic Stability,* Oxford University Press, Oxford, 1961, Chapter 3.

3 Niiler, P. P., and Bisshopp, F. E., "On the Influence of Coriolis Force on the Onset of Thermal Convection," *Journal of Fluid Mechanics,* Vol. 22, 1965, pp. 753–761.

4 Khosla, P. K., and Murgai, M. P. "A Study of the Combined Effect of Thermal Radiative Transfer and Rotation on the Gravitational Stability of a Hot Fluid," *Journal of Fluid Mechanics,* Vol. 16, 1962, pp. 97–107.

5 Vincenti, W. G., and Kruger, C. H., *Introduction to Physical Gas Dynamics,* John Wiley and Sons, New York, 1965.

6 Finlayson, B. A., "The Galerkin Method Applied to Convective Instability Problems," *Journal of Fluid Mechanics,* Vol. 33, 1968, pp. 201–208.

7 Viskanta, R., and Grosh, R. J., "Effect of Surface Emissivity on Heat Transfer by Simultaneous Conduction and Radiation," *International Journal of Heat and Mass Transfer,* Vol. 5, 1962, pp. 729–734.

Magdy A. El-Hawary
Postdoctoral Fellow,
Department of Mechanical Engineering,
University of Waterloo,
Waterloo, Ontario, Canada
Mem. ASME

Effect of Combined Free and Forced Convection on the Stability of Flow in a Horizontal Tube

The effect of wall heating on the stability of low Reynolds number flows in a horizontal tube is investigated in the present study. Experiments were conducted for the flow of water in a tube with length to diameter ratio of 300. Wide ranges of mass flow rate and heating power were examined under constant wall heat flux. Stability was detected by examining signals of a thermocouple probe and a hot-film annemometer probe placed in the flow at the test section outlet. The onset of a turbulent flow was also marked by significant increases in the value of pressure drop measured across the test section. Results revealed regions of laminar flows, turbulent flows, and flows intermediate in behavior between laminar and fully turbulent. A stability map is presented showing regions of different flows on nondimensional co-ordinates representing forced and natural convection effects.

1 Introduction

The flow in tubes at low Reynolds number is a subject of particular significance when heat is transferred through the tube walls. It is encountered in a variety of engineering situations including compact heat exchangers, solar energy collectors, and heat exchangers designed for viscous fluids in chemical and food industries. Heat is transferred by combined free and forced convection as buoyancy influences become significant. The secondary motion created in the tube distorts the isothermal parabolic velocity profile which influences its stability. The shape of the distorted profile is decided by the orientation of the tube and the flow direction. Numerous experimental and theoretical studies are available in the literature for the flow field in both horizontal tubes [1–12] and vertical tubes [13–18]. Buoyancy also affects the exchange coefficients at the wall; it increases both of the friction coefficient [1, 2], and the heat transfer coefficient [1–5], for laminar flows in horizontal tubes. Similar effects were obtained for flows in vertical tubes when buoyancy acts in the same direction as the flow [13–15]. These increases are further multiplied by the onset of early transition to a turbulent flow when the convection process is dominated by natural convection.

Stability of the flow has attracted the attention of several workers; Mori, et al. [6], Nagendra [7], Petukhov and Polyakov [8], and Yao and Catton [9] for flows in horizontal tubes, and Hallman [16], Scheele and Hanratty [17], Scheele [18], and others for flows in vertical tubes. Different techniques were used for the experimental study of stability: visual observations by dye injection [17, 18], monitoring wall temperature fluctuations [18], monitoring fluid temperature fluctuations [7], or observing signals of hot-wire annemometer probe placed in the flow [6]. Stability results are normally presented in terms of critical values of the parameters controlling the shape of the velocity profile. The stability relation to velocity profile distortion was experimentally verified in different situations; for instance, the same stability results were obtained for flows in vertical tubes in the two cases of heating in upflow as well as cooling in downflow when the velocity profiles were similarly distorted [17]. Stability depends also on the level of turbulence at the inlet to the heated tube; the relation becomes insignificant when instability is caused mainly by thermal effects rather than hydrodynamic effects [6, 7].

The object of the present study is to experimentally investigate the influence of wall heating on the laminar-turbulent transition mechanism for water flows in a horizontal tube with constant flux wall heating. Experiments were conducted for different values of flow rate and heat flux. The nature of the flow was determined by examining signals from a thermocouple probe and a hot-film probe placed in the flow, as well as monitoring the pressure drop across the test section. Simultaneous measurements of temperature, velocity, and pressure drop allowed accurate classification of the flow nature under different conditions. Stability results are compared to those of Mori, et al. [6] for air flows in a horizontal tube, and to those of Scheele and Hanratty [17] for water flows in a vertical tube.

2 Experimental Equipment and Techniques

2.1 Apparatus. A schematic of the heat transfer loop is shown in Fig. 1. Water from the overhead tank moved down an insulated pipe to the test section, then through a cooler, flow meter, and a throttling valve to the sump tank. A variable speed pump delivered water from the sump tank back to the overhead tank where the level was kept constant by an overflow tube. The test section was formed of an inconel tube of 6.35 mm o.d. and 0.254 mm wall thickness. Cables were connected to its ends through copper flanges for ohmic wall heating. Power from the main supply was controlled using a voltage regulator and a variable auto transformer. The heated test section was 176 cm long, preceded by an unheated length of 35 cm to serve as a hydrodynamic approach. To minimize heat losses, the heated tube was placed inside a vacuum chamber and connected through teflon parts at both ends. Separate heating coils were used to raise the temperatures of the power cables to eliminate heat leakage through them. A U-tube manometer was connected across the test section for pressure drop measurements.

The overhead tank provided steady flow through the loop. In addition, it was equipped with a small cooling coil and an electrical heater for fine temperature control to maintain constant temperature at the test section inlet.

The inside diameters of the test section, hydrodynamic approach, and teflon connectors were carefully matched and aligned to minimize

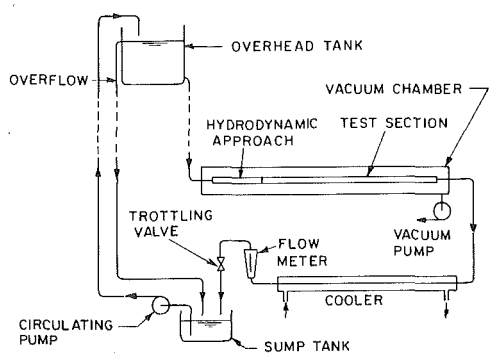

Fig. 1 Schematic of the heat transfer loop

Contributed by the Heat Transfer Division for publication in the JOURNAL OF HEAT TRANSFER. Manuscript received by the Heat Transfer Division, June 22, 1979.

flow disturbances. Mixing chambers were provided before the hydrodynamic approach and at the test section exit for fluid bulk temperature measurements.

2.2 Measuring Devices and Calibrations. Copper-constantan thermocouples were inserted in the fluid at different parts of the loop and spot welded to the test section walls. At each axial location two thermocouples were welded to the top and bottom sides of the tube where temperature difference is created due to buoyancy. Fluctuations in the flow were measured using a thermocouple probe and a hot-film probe placed at the test section exit, before the mixing chamber.

All thermocouples were calibrated before mounting on the loop. Heat losses were measured by applying small values of power to the drained test section; a linear correlation was obtained between power lost and average wall temperature. When the thermocouple wires welded to the test section were used as power leads, a linear axial voltage distribution was obtained for different power levels indicating uniform heat flux distributions.

2.3 Experimental Procedure and Observations. Flow stability is influenced by the two independent parameters: flow rate and heating power. Two series of testing were performed to examine the influence of each parameter separately; for tests of each series, one parameter was kept constant while the other gradually increased until transition was obtained. Figures 2 and 3 show the transition results for two tests representing these series. Values of the skin friction factor are plotted against Reynolds number for each test with samples of the recorded temperature and velocity fluctuations given at different experimental points. Fluctuations detected by the thermocouple probe are shown for 25 s periods, while those detected by the hot-film probe are shown for the short period of 0.05 s. Three records of the later fluctuations, taken approximately 2 s apart, are shown in the same frame to describe the relatively low frequency variations. When the flow velocity was gradually increased at constant heating power (results of Fig. 2) the f-Re variation obtained was similar to that known for isothermal flows. No significant temperature or velocity fluctuations were obtained in the laminar range of Re. This was followed by a short transition zone where successive periods of laminar and turbulent flows were obtained. The turbulent periods, although short, were clearly indicated by simultaneous fluctuations of pressure, temperature, and velocity. The flow intermittency can be clearly observed from the temperature fluctuations presented at the flow velocity of 0.491 (m/s); five periods of laminar flows were obtained in 25 s, each of which was followed by a turbulent period that has approximately the same duration. Two values of the skin friction coefficient are shown for each experimental point in this zone to show the limits of the intermittency fluctuations. When the flow velocity was further increased, fully turbulent flow was obtained as indicated by values of the skin friction factor. This flow is characterized by a remarkable reduction in the amplitudes of all fluctuations obtained for pressure, temperature, and velocity.

When the flow velocity was kept constant while increasing the heating power, the flow experienced a laminar-turbulent transition as well. In this case, however, some fluctuations were detected (in particular by the hot-film probe) at a value of heating power smaller than that required to produce turbulent-like values of the skin friction factor. Samples of these results are presented in Fig. 3 where the inlet

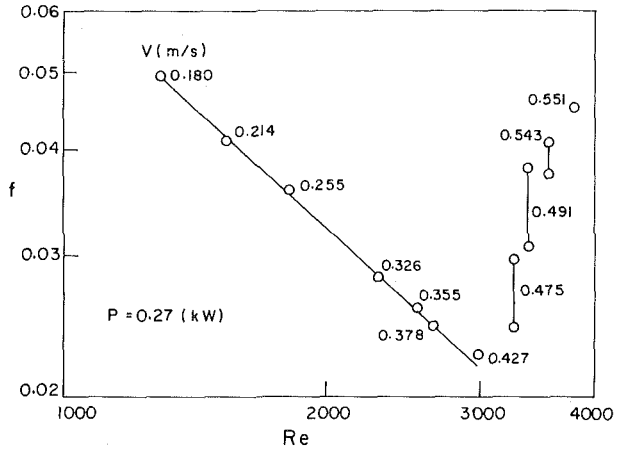

Fig. 2(*a*) *f*-Re variation

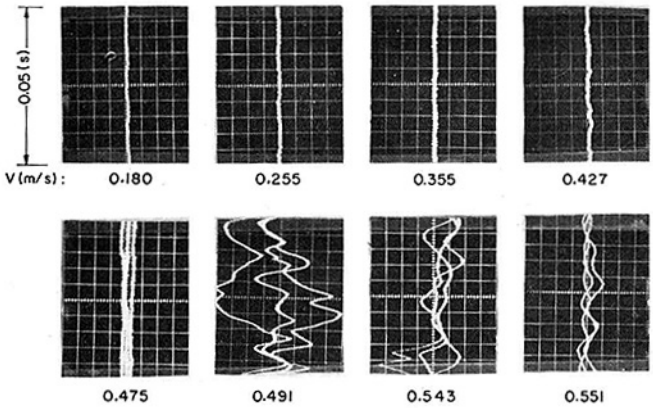

Fig. 2(*b*) Hot-film probe signals

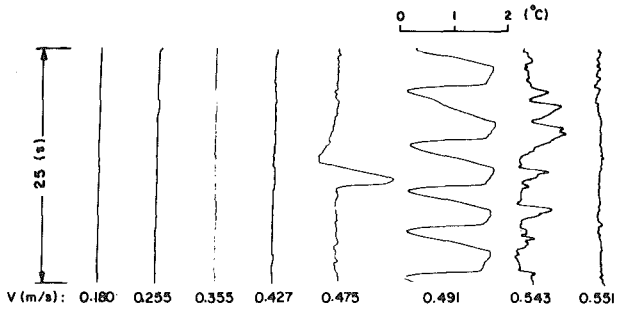

Fig. 2(*c*) Thermocouple probe signals

Fig. 2 Pressure drop results and recorded fluctuations for a test of the first series—heating power held constant

Nomenclature[1]

c_p = specific heat at constant pressure
D = tube inside diameter
f = coefficient of skin friction, $2D\Delta p/(\rho L V^2)$
g = gravitational acceleration
h = coefficient of heat transfer, $P/\pi DL(T_w - T_b)$
k = fluid thermal conductivity
L = heated length of test section
P = test section heating power
Δp = pressure drop across test section
T = local temperature
V = average velocity
x = axial coordinate along heated length
α = thermal diffusivity, $k/\rho c_p$
β = coefficient of thermal expansion
μ = dynamic viscosity
ν = kinematic viscosity, μ/ρ
ρ = density

Subscripts

b = bulk or mixed mean fluid conditions
w = conditions at tube walls
Gr^+ = modified Grashof number, $g\beta PD^3/8Lk\nu^2 = \pi/32$ ReRa
Nu = Nusselt number, hD/k
Pr = Prandtl number, ν/α
Ra = Rayleigh number, $g\beta(dT_b/dx)D^4/\alpha\nu$
Re = Reynolds number, VD/ν

[1] All properties are evaluated at the average value of the two bulk fluid temperatures measured at the inelt and outlet of the test section unless otherwise specified.

velocity was kept constant at 0.296 (m/s) while the Reynolds number based on the mean fluid temperature increased as the heating power increased. No fluctuations of any kind were obtained until the heating power reached a value of 0.59 (kW) where fluctuations of significant amplitudes were obtained. As the heating power was further increased to a value of 0.99 (kW), large pressure fluctuations were obtained accompanied by much larger velocity and temperature fluctuations which marked the transition to a fully turbulent flow. The transition period is similar in character to that obtained in Fig. 2 with the difference that fluctuations are characterized by sharp spikes of variable amplitudes. The successive periods of flows of different nature are clearly shown in the temperature fluctuations recorded at 0.99 (kW) where large oscillations of about 1.5 (°C) in amplitude are superimposed on smaller fluctuations of a maximum amplitude of 0.1 (°C). For higher values of heating power fully turbulent flow was obtained after the short transition period. This flow is also characterised by continuous fluctuation of much smaller amplitudes when compared to the flow during the transition period.

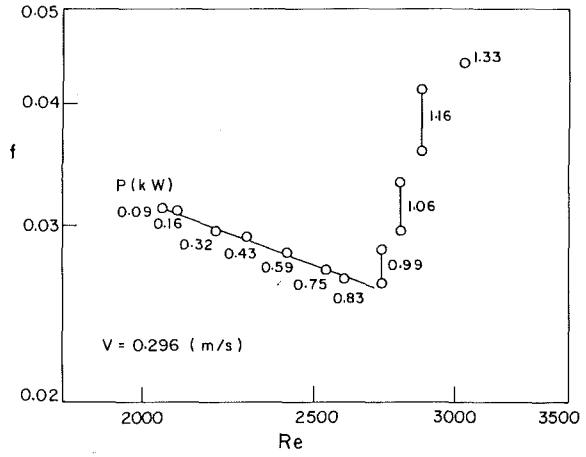

Fig. 3(*a*) *f*-Re variation

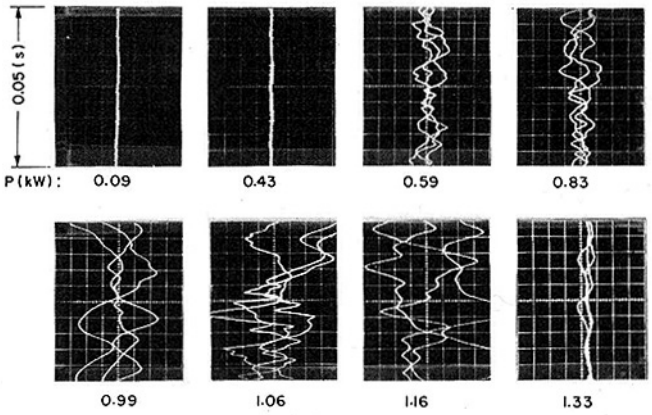

Fig. 3(*b*) Hot-film probe signals

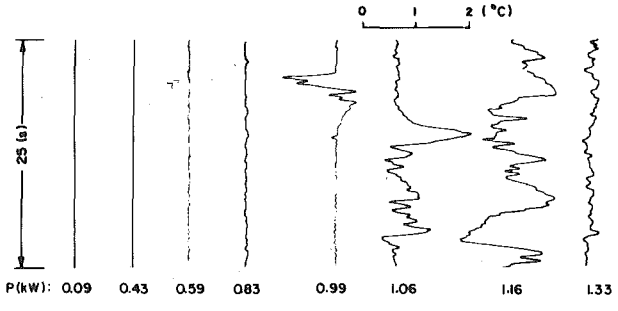

Fig. 3(*c*) Thermocouple probe signals

Fig. 3 Pressure drop results and recorded fluctuations for a test of the second series—flow velocity held constant

3 Results

3.1 Stability Results. Results obtained from both series of testing are presented in Fig. 4. For each test of the first series (heating power kept constant), values of the two velocities indicating the beginning and end of the laminar-turbulent transition period are shown on the lines A_1A_1 and A_2A_2, respectively. For tests of the second series (flow velocity kept constant), three points are plotted for each test: one on the line CC indicating the onset of significant fluctuations, and two on the lines B_1B_1 and B_2B_2 indicating the boundaries of the transition period to fully turbulent flow. Experimental points on A_1A_1 and B_1B_1 indicate conditions where turbulent fluctuations were first detected by the three measuring devices, while those on A_2A_2 and B_2B_2 indicate conditions where turbulent fluctuations became continuously observed. By extrapolation, the transition regime is confined by $A_1A_1B_1B_1$ and $A_2A_2B_2B_2$, with the flow intermittency close to zero on the first line and unity on the second line. The flow is turbulent for the region outside $A_2A_2B_2B_2$ while the region inside $A_1A_1B_1B_1$ is divided to two subregions by the line CC. Flows to the right of CC are laminar as no fluctuations of any kind were observed. Those to the left of CC have velocity and temperature fluctuations with laminar-like pressure drop values. The term "disturbed" used by Scheele [18] is presently adopted for the last region.

The transition regime is labelled "thermal transition" when the effect of free convection is predominant, and "hydraulic transition" when the axial bulk fluid motion is the direct cause for instability.

The parameter ReRa was found by Mori, et al. [6] to characterize the shape of the distorted velocity profiles for air flows in a horizontal tube with heated walls. The same parameter was recently expressed as the modified Grashof number, Gr^+, by Patankar, et al. [11]; it was found to govern buoyancy effects for the combined convection in a horizontal tube. Results obtained in the first series of testing were compared to those of Mori, et al. in Fig. 5. The parameter Gr^+Pr was used to express buoyancy effects; it offers good quantitative agreement between results obtained for both air and water as working mediums. Critical values of Re measured in the present experiment are intermediate between those obtained by Mori, et al. for two different levels of inlet turbulence. Their results were obtained with and without a turbulence generator placed at the test section inlet, as compared to a thermocouple probe holder placed in a similar position in the present test. Critical values of Re were slightly increased as natural convection effects increased for both of the present results

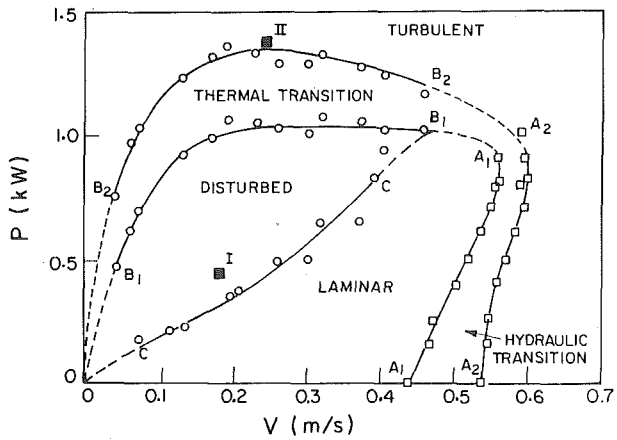

Fig. 4 Critical values of the two experimental variables flow velocity and heating power

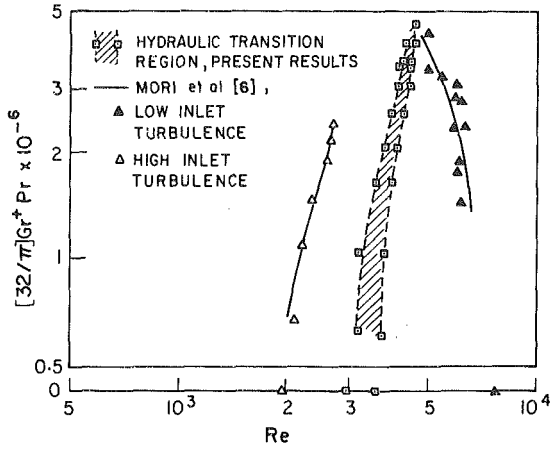

Fig. 5 Comparison of present laminar-turbulent transition results to those of Mori, et al. [6]

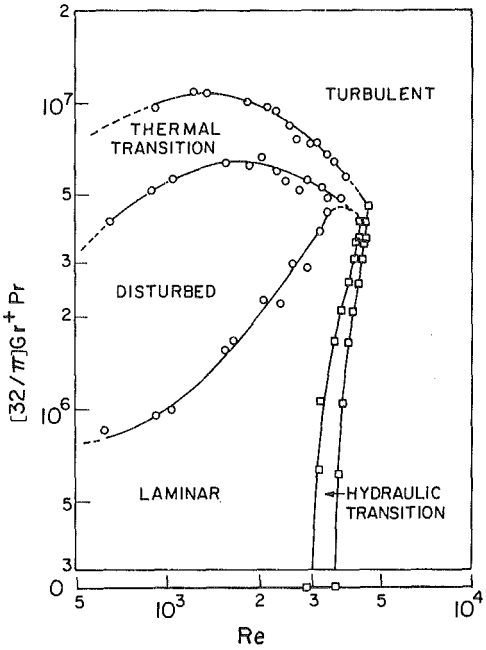

Fig. 6 Boundaries of flows of different natures on nondimensional co-ordinates representing forced and natural convection

and those of Mori, et al. for high level of inlet turbulence. However, the influence of natural convection on critical Re is generally small for all values of inlet turbulence presented. As natural convection effects increased, the effect of inlet turbulence gradually diminished, and values of critical Re appear to approach a single value at Gr^+Pr of about 5×10^5.

Stability results from both series of testing are presented on nondimensional co-ordinates in Figs. 6 and 7. Flow regimes of different natures are shown in Fig. 6 described by parameters representing the effects of free and forced convection. Transition due to thermal causes is observed to occur at values of Gr^+Pr that are little dependent on the value of Re for the range presented. On the other hand, resuls of Fig. 7 indicate that laminar flow becomes disturbed (by heating) at nearly a constant value of RaPr for all Re.

Turbulent flows were obtained in the present study at values of Re as low as 644. A value of the critical Re of 50 was reported by Scheele [18] for flows in vertical tubes with high enough heating power. Present experimental ranges of power and flow could not be extended to cover such small values of critical Re because of the limits imposed by the secondary motion in the tube. The nonuniform angular temperature distribution applied to the thin tube walls caused it to bow for extreme conditions of low flows and high heating powers.

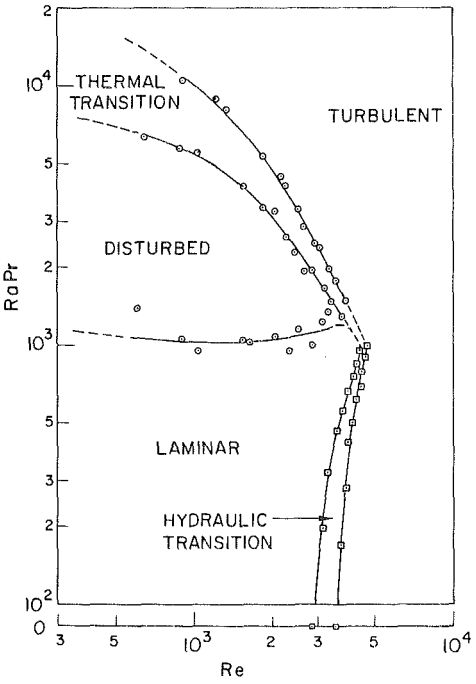

Fig. 7 Influence of Rayleigh number on flow characteristics

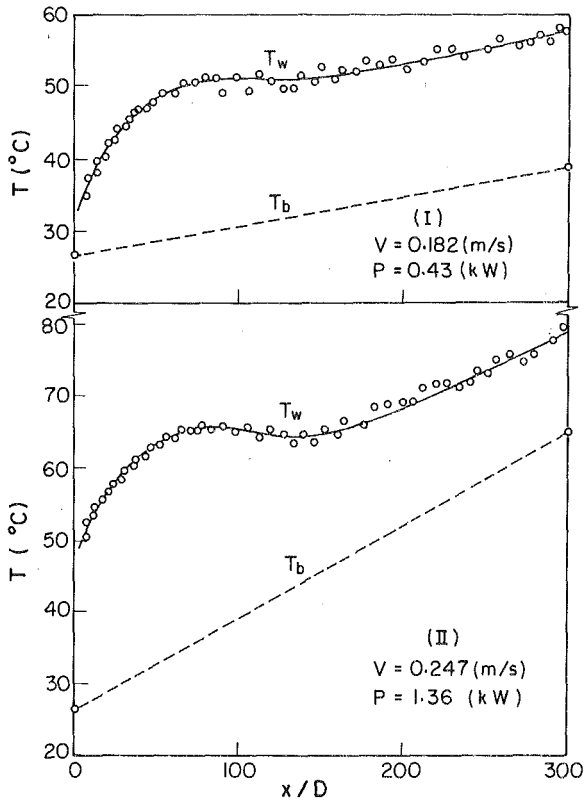

Fig. 8 Axial temperature distributions measured at experimental conditions marked I and II in Fig. 4

3.2 Exchange Coefficients at the Wall. The influence of buoyancy on the heat transfer coefficient can be clearly observed by examining the axial temperature distributions. Samples are presented in Fig. 8 for a flow in the disturbed region and another in the turbulent region. Condition of these flows are marked I and II, respectively, in Fig. 4. The wall-fluid temperature difference ($T_w - T_b$) increased with the axial distance to a peak value, then gradually decreased to reach some value along the heated tube that remained almost constant for further downstream locations. The reduction in wall-fluid tempera-

ture difference is the direct implication of an increase in the heat transfer coefficient. Certain length of the heated tube is required for the secondary flow patterns to become fully developed and have steady influence on the flow. This influence is clearly much more significant for the turbulent flow (case II) as comapred to the disturbed flow (case I).

Values of the heat transfer coefficient were calculated for the experimental points shown in Fig. 4, with $(T_w - T_b)$ values evaluated at the test section exit. Nusselt number obtained for points in the disturbed flow zone (line CC) are shown in Fig. 9 as compared to data available in the literature for laminar flows under combined free and forced convection effects. Agreement is acceptable in regard with the large scatter displayed by data of the literature. Generally, all values obtained for Nu are larger than the theoretical value for isothermal laminar flows, 48/11, and are progressively increased as buoyancy increased. The influence of turbulence on the Nu is explicitly presented in Fig. 10. Values of Nu calculated for the disturbed flow zone (shown in Fig. 9 to be comparable to the laminar values) are shown on line CC in Fig. 10 as well as values calculated for flows in the transition zones with 50 percent intermittency; points on line AA are for the hydraulic transition zone and those on line BB are for the thermal transition zone. Line BB is almost a smooth continuation of line AA; they both indicate much higher values of Nu when compared to line CC.

Buoyancy has similar effects on the friction factor; values obtained for laminar flows are higher than the isothermal value as shown in Fig. 11. This figure also shows comparison of present results to data available in the literature; maximum deviation obtained in fRe values is about 3 percent. Further significant increases of the friction factor occur upon the onset of thermal transition to a turbulent flow as presented in Fig. 3.

3.3 Flow Stability as Compared to Flows in Vertical Tubes. It is understood that the influence of buoyancy on the transition mechanism is quite dependent on the tube orientation. For practical purposes, however, present results are compared to those of Scheele and Hanratty [17] for water flows in a vertical tube with uniform heat flux. Results obtained are presented in Fig. 12. Ra was used by the last authors to represent natural convection effects as it was found to characterize the shape of the distorted velocity profiles. Experimental points on line CC in Fig. 4 were used for this comparison since they represent flows with characteristics considered by Scheele and Hanratty as unstable. Using a dye technique, the last authors reported transition when the dye filament injected in the flow first deviated from its streamline motion. This is considered equivalent to the first detection of significant flow fluctuations for the present comparison. The non-isothermal flow in a horizontal tube is less stable than that in a vertical tube; at the same value of Re instability occurs at less buoyancy effects (smaller value of Ra) for the flow in a horizontal tube.

4 Discussion of Results

Results of the present study revealed regions of laminar, disturbed, and turbulent flows that are obtained for different combinations of flow rate and wall heat flux. The disturbed flow is practically similar to the laminar flow, although characterized by significant fluctuation it exhibits laminar-like values of the exchange coefficients at the wall. Each of the two flows could be changed into a turbulent flow through short transition period. The change could be obtained by increasing the flow rate, the wall heat flux, or both. Transition periods are characterized by flows of intermittent nature for both laminar-turbulent transition and disturbed-turbulent transition. Both zones were therefore connected by extrapolation of experimental results (Figs. 4, 6 and 7). Turbulent flows obtained are quite similar in both cases; they have velocity and temperature fluctuations of similar character, and values of the exchange coefficients at the wall distinguishly higher than the laminar values. Furthermore, values of Nu obtained for both turbulent flows form a nearly continuous correlation with Gr^+Pr that represents natural convection effects (Fig. 10). This correlation, although appears meaningless as Nu is not necessarily related to Gr^+ for turbulent flows, shows that the two flows are of the same nature.

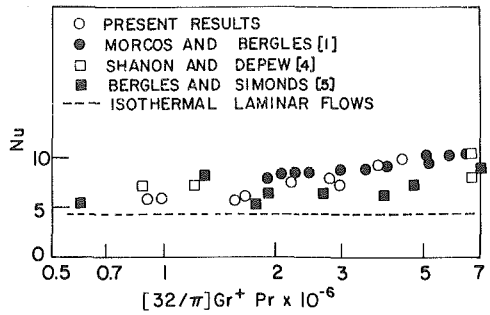

Fig. 9 Values of Nusselt number for disturbed flows as compared to values available in the literature for laminar flows

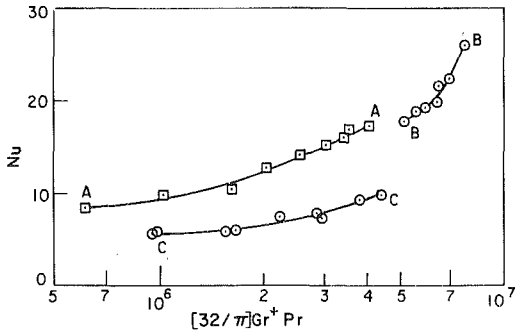

Fig. 10 Values of Nusselt number for disturbed flows as compared to values for flows in the transition regimes with 50 percent intermittency (AA hydraulic transition, BB thermal transition, and CC disturbed)

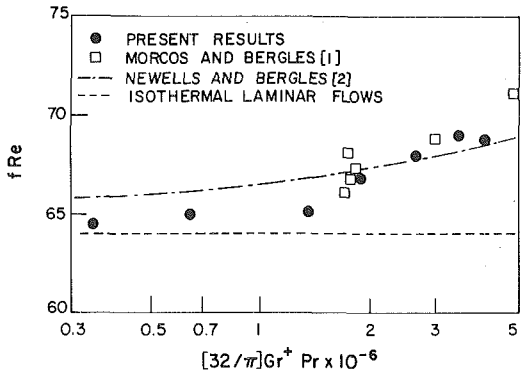

Fig. 11 Values of the skin friction factor for laminar flows as compared to values available in the literature

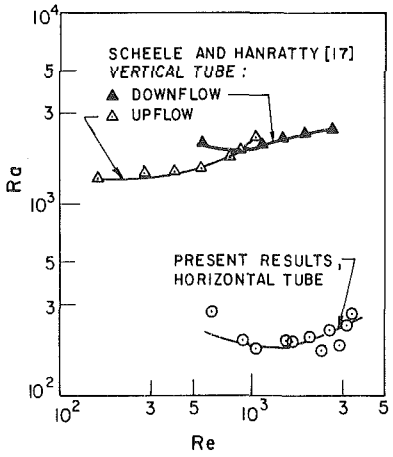

Fig. 12 Comparison between present stability results for horizontal tubes and those for vertical tubes available in the literature

No subdivision was intended for the turbulent flow zone presented in the stability maps of Figs. 4, 6 and 7.

Fluctuations obtained in the disturbed flow region are apparently due to initial transition of natural convection that is later developed into complete hydrodynamic instability with further wall heating or more flow rate. The later instability causes the classical jump in the wall exchange coefficients.

Critical values of Re obtained for the hydraulic transition zone depend on the level of inlet turbulence as earlier presented. For isothermal flows, wide range of critical values of Re is obtained for different experimental conditions. Although the value 2300 is quite common, a value as high as 40,000 was reported for tube inlet exceptionally free from disturbances [19]. No limit was reported for the maximum value of this parameter while 2000 seems to be the minimum value. For nonisothermal flows, the effect of inlet turbulence decreases as natural convection increases. The following modifications are therefore suggested in cases where the critical value of Re for the isothermal flow is known to be significantly different from the value reported in Fig. 6. The hydraulic transition zone should be shifted to pass through the known value at $Gr^+Pr = 0$. At higher values of the last parameter the shift should be smaller and finally reduces to zero at Gr^+Pr of about 5×10^5. No modifications are required for the thermal transition zone since, according to Nagendra [7], critical values of the controlling parameters are insensitive to the level of inlet turbulence for this zone.

The axial temperature variations of Fig. 8 suggest that the flow becomes fully developed somewhere between one third and one half the length of the heated tube. The flow is stable near the thermal entrance and becomes unstable further downstream, with the result of higher heat transfer coefficient and lower fluid-wall temperature difference. Axial temperature variations reported by Shanon and Depew [3] displayed similar depression in the fluid-wall temperature difference. For experimental work available in the literature where the test section length was 150 tube diameters or less, transition results depended on the downstream distance at which stability was detected [8]. It may therefore be concluded that the present stability results are valid for fully developed flows obtained at streamwise distances larger than the thermal entrance length. Hong, et al. [12] reported that the thermal entrance length depends on Ra, Re, and Pr; according to their results, the entrance length was estimated as 100 and 120 tube diameters approximately for flows I and II of Fig. 8, respectively. These values are close to the values indicated by the present temperature measurements. When the tube length is shorter than the thermal entrance length, more heating is required to cause enough flow distortion for instability to be detected.

Comparison of present results to those for the flow in a vertical tube (Fig. 12) shows that horizontal tubes are recommended for situations where turbulent flows are required for low Re applications.

5 Conclusions

Turbulent flows could be obtained in tubes with heated walls at values of Reynolds number much smaller than the isothermal critical value. Fluctuations are observed in the originally laminar flow at certain values of heating power. Turbulent-like exchange coefficients at the wall are obtained when the power is further increased to higher values. A map is presented to show flow regions of different natures under different forced and natural convection effects. Results could be used for design purposes if the flow nature is to be controlled at low values of Reynolds number.

6 Acknowledgments

Experiments were performed at the University of British Columbia, Vancouver, Canada. Financial support of the National Research Council of Canada is gratefully acknowledged. Thanks are due to Professor M. Iqbal for his help during the experimental study.

References

1 Morcos, S. M., and Bergles, A. E., "Experimental Investigation of Combined Forced and Free Laminar Convection in Horizontal Tubes," ASME JOURNAL OF HEAT TRANSFER, Vol. 97, 1975, pp. 212–219.

2 Newell, P. H., Jr., and Bergles, A. E., "Analysis of Combined Free and Forced Convection for Fully Developed Laminar Flow in Horizontal Tubes," ASME JOURNAL OF HEAT TRANSFER, Vol. 92, 1970, pp. 83–93.

3 Shanon, R. L., and Depew, C. A., "Combined Free and Forced Laminar Convection in a Horizontal Tube with Uniform Heat Flux," ASME JOURNAL OF HEAT TRANSFER, Vol. 90, 1968, pp. 353–357.

4 Shanon, R. L., and Depew, C. A., "Forced Laminar Flow Convection in a Horizontal Tube with Variable Viscosity and Free Convection Effects," ASME JOURNAL OF HEAT TRANSFER, Vol. 91, 1969, pp. 251–258.

5 Bergles, A. E., and Simonds, R. R., "Combined Forced and Free Convection for Laminar Flow in Horizontal Tubes with Uniform Heat Flux," *International Journal of Heat and Mass Transfer*, Vol. 14, 1971, pp. 1989–2000.

6 Mori, Y., Futagami, K., Tokuda, S., and Nakamura, M., "Forced Convective Heat in Uniformly Heated Horizontal Tubes; 1st Report Experimental Study on the Effect of Buoyancy," *International Journal of Heat and Mass Transfer*, Vol. 9, 1966, pp. 453–463.

7 Nagendra, H. R., "Interaction of Free and Forced Convection in Horizontal Tubes in the Transition Regime," *Journal of Fluid Mechanics*, Vol. 57, pt. 2, 1973, pp 269–288.

8 Petukhov, B. S., and Polyakov, A. F., "Flow and Heat Transfer in Horizontal Tubes under Combined Effect of Forced and Free Convection," International Heat Transfer Conference (Paris), Vol. 4, Paper No. N-C3.7, 1970.

9 Yao, L. S., and Catton, I., "The Buoyancy and Variable Viscosity Effects on a Water Laminar Boundary Layer Along a Heated Longitudinal Horizontal Cylinder," *International Journal of Heat and Mass Transfer*, Vol. 21, 1978, pp. 407–414.

10 Hussain, N. A., and McComas, S. T., "Experimental Investigation of Combined Convection in a Horizontal Circular Pipe with Uniform Heat Flux," International Heat Transfer Conference (Paris), Vol. 4, paper no. N-C4, 1970.

11 Patankar, S. V., Ramadhyani, S., and Sparrow, E. M., "Effect of Circumferentially Nonuniform Heating on Laminar Combined Convection in a Horizontal Tube," ASME JOURNAL OF HEAT TRANSFER, Vol. 100, 1978, pp. 63–70.

12 Hong, S. W., Morcos, S., and Bergles, A. E., "Analytical and Experimental Results for Combined Forced and Free Laminar Convection in Horizontal Tubes," *Heat Transfer 1974*, Tokyo, Japan, Vol. 4, NC 4.6.

13 Mullin, T. E., and Gerhard, E. R., "Heat Transfer to Water in Down Flow in a Uniform Wall Temperature Vertical Tube at Low Graetz Numbers," ASME JOURNAL OF HEAT TRANSFER, Vol. 99, 1977, pp. 586–589.

14 Chen, T. S., and Mucoglu, A., "Boundary Effects on Forced Convection Along a Vertical Cylinder," ASME JOURNAL OF HEAT TRANSFER, Vol. 97, 1975, pp. 198–203.

15 Hetherington, H. J., and Patten, T. D., "Laminar Flow Natural Convection from the Open Vertical Cylinder with Uniform Heat Flux at the Wall," *International Journal of Heat and Mass Transfer*, Vol. 19, 1976, pp. 1121–1125.

16 Hallman, T. M., "Combined Free and Forced Convection in Vertical Tube," Ph.D. Thesis, Purdue University, Indiana, 1958.

17 Scheele, G. F., and Hanratty, T. J., "Effect of Natural Convection on Stability of Flow in Vertical Pipe," *Journal of Fluid Mechanics*, Vol. 14, 1962, pp. 244–256.

18 Scheele, G. F., "The Effect of Natural Convection on Transition to Disturbed Flow in a Vertical Pipe," Ph.D. Thesis, University of Illinois, Urbana, 1963.

19 Schlichting, H., *Boundary Layer Theory*, McGraw-Hill, New York, 1968, pp. 432.

Analysis of Heat Transfer in Slightly Eccentric Annuli

L. S. Yao

Department of Mechanical and Industrial Engineering, 144 Mechanical Engineering Building, University of Illinois at Urbana-Champaign, Urbana, IL 61801

The regular perturbation solution of heat transfer is developed for slightly eccentric annuli. The numerical results demonstrate that the heat transfer in slightly eccentric annuli can be predicted from the solution of concentric annuli by a simple radial coordinate transformation when the ratio of the radius of the inner cylinder and the characteristic gap width is not too small. The regular perturbation solution breaks down when this ratio approaches zero.

Introduction

Natural convection in concentric annuli has been extensively studied for the past half century due to its wide applications in various engineering devices. A comprehensive and extensive review of the previous works has been given by Kuehn and Goldstein [1], and is not repeated here. One of the governing parameters of the problem is the Raleigh number, Ra. It has been demonstrated that a regular perturbation solution [2–5] can be obtained for $\mathrm{Ra} < 10^4$. For $\mathrm{Ra} > 10^4$, the finite-difference solution [1] has been favorably compared with the experimental data before the flow becomes unsteady.

Relatively little research has been reported for eccentric annuli except two recent experiments [6, 7]. In the paper, we study the natural convection in slightly eccentric annuli for small Ra. The physical model considered is an annulus bounded by two eccentric cylinders (Fig. 1). The surface temperatures of the inner cylinder and the outer cylinder are held constant, say at T_i and T_o, respectively. First, the general formulation is given for annuli bounded by an inner circular cylinder and an outer cylinder of arbitrary shapes. Then the perturbation equations are formulated for the outer cylinder whose contour has a small deviation from a circular cylinder which sets slightly eccentric to the inner circular cylinder. Finally, the perturbation solution is given for annuli bounded by two slightly eccentric circular cylinders.

In the Appendix, the expansion procedure developed is compared with the traditional expansion procedure which expands the boundary conditions. It shows that the expansion procedure reported here can satisfy the boundary conditions exactly and converges faster than the traditional expansion procedure.

The solution procedure can be easily extended to the case where both the inner and outer cylinders are not circular. The extension is straight-forward; therefore, it is not included. The transient problem of natural convection in phase change thermal storage materials can also be studied by a similar transformation and is reported separately [8].

Mathematical Formulation

The equations governing the stream function and the energy transportation in cylindrical coordinates are

$$\frac{1}{r}\frac{\partial[\bar{f},\nabla^2\bar{f}]}{\partial(r,\psi)} = \beta g\left[\sin\psi\cdot\frac{\partial T}{\partial r}+\frac{\cos\psi}{\bar{r}}\frac{\partial T}{\partial\psi}\right]+\nu\nabla^4\bar{f} \tag{1a}$$

$$\frac{1}{r}\frac{\partial[\bar{f},T]}{\partial(\bar{r},\psi)} = \alpha\nabla^2 T \tag{1b}$$

where

$$\frac{\partial[A,B]}{\partial[\bar{r},\psi]} = \frac{\partial A}{\partial\bar{r}}\frac{\partial B}{\partial\psi}-\frac{\partial A}{\partial\psi}\frac{\partial B}{\partial\bar{r}}, \tag{2a}$$

and

$$\nabla^2 = \frac{\partial^2}{\partial\bar{r}^2}+\frac{1}{\bar{r}}\frac{\partial}{\partial\bar{r}}+\frac{1}{\bar{r}^2}\frac{\partial^2}{\partial\psi^2}\cdot$$

$\bar{f}$ is the stream function and is related to the velocities by

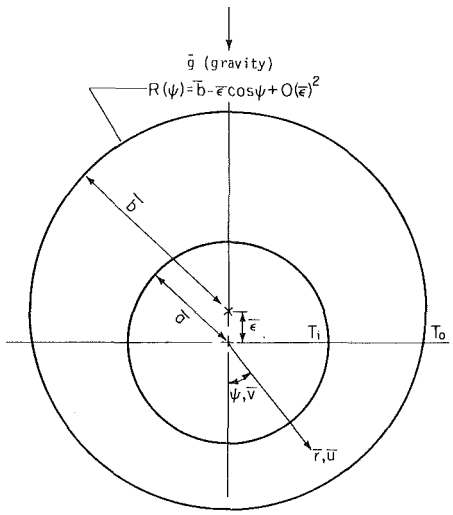

Fig. 1 Physical model and coordinates

$$\left.\begin{aligned}\bar{u} &= \frac{-1}{\bar{r}}\frac{\partial\bar{f}}{\partial\psi},\\ \bar{v} &= \frac{\partial\bar{f}}{\partial\bar{r}}\cdot\end{aligned}\right\} \tag{2b}$$

The associated boundary conditions are

$$\left.\begin{aligned}&\text{(i) } \bar{r}=0,\ \bar{u}=\bar{v}=0, \quad \text{and } T=T_i;\\ &\text{(ii) } \bar{r}=R(\psi),\ \bar{u}=\bar{v}=0, \quad \text{and } T=T_0\end{aligned}\right\} \tag{3}$$

The dimensionless variables which are used to nondimensionalize equations (1) and transform the eccentric annulus into a unit circle are

$$f=\bar{f}/\alpha \qquad \text{(stream function)} \tag{4a}$$

$$\theta=\frac{T-T_o}{T_i-T_o} \qquad \text{(temperature)} \tag{4b}$$

$$r=\frac{\bar{r}-\bar{a}}{R(\psi)-\bar{a}}, \qquad \text{(radial coordinate)} \tag{4c}$$

$$B(\psi)=\frac{R(\psi)-\bar{a}}{h},\ h=R(\psi_o)-\bar{a} \qquad \text{(gap function)} \tag{4d}$$

$$\mathrm{Ra}=\frac{\beta\bar{g}(T_i-T_o)h^3}{\alpha\nu} \qquad \text{(Rayleigh number)} \tag{4e}$$

$$\mathrm{Pr}=\nu/\alpha \qquad \text{(Prandtl number)} \tag{4f}$$

ψ_o is the reference azimuthal angle where the characteristic gap width, h, is determined. The choice of ψ_o is arbitrary; however, it would be wise to select ψ_o where h is minimum. Substitution of equations (4) into equations (1) results in the dimensionless governing equations inside a unit circle. They are

Contributed by the Heat Transfer Division for publication in the JOURNAL OF HEAT TRANSFER. Manuscript received by the Heat Transfer Division July 27, 1979.

$$\frac{1}{\Pr}\frac{1}{r+a/B}\cdot\frac{\partial[f,\nabla_1^2 f]}{\partial[r,\psi]} = \mathrm{Ra}\cdot B^3\cdot\left[\sin\psi\cdot\frac{\partial\theta}{\partial r}+\frac{\cos\psi}{r+a/B}\left(\frac{\partial\theta}{\partial\psi}-\frac{rB'}{B}\frac{\partial\theta}{\partial r}\right)\right] + (\nabla_1^4 - L)f, \tag{5a}$$

$$\frac{1}{(r+a/B)}\left[\frac{\partial f}{\partial r}\cdot\left(\frac{\partial\theta}{\partial\psi}-\frac{rB'}{B}\frac{\partial\theta}{\partial r}\right)-\left(\frac{\partial f}{\partial\psi}-\frac{rB'}{B}\frac{\partial f}{\partial r}\right)\cdot\frac{\partial\theta}{\partial r}\right] (\nabla_1^2 - M)\theta, \tag{5b}$$

where

$$\nabla_1^2 = \frac{\partial}{\partial r^2}+\frac{1}{r+a/B}\frac{\partial}{\partial r}+\frac{1}{(r+a/B)^2}\frac{\partial^2}{\partial\psi^2} \tag{6a}$$

$$\begin{aligned}L = {} & +\frac{1}{(r+a/B)^2}\left(\nabla_1^2\left(\frac{2rB'}{B}\frac{\partial^2}{\partial r\partial\psi}\right)+\nabla_1^2\left(\frac{rB''}{B}\frac{\partial}{\partial r}\right)\right)\\ & +\frac{1}{(r+a/B)^4}\left[4+\frac{2}{(r+a/B)}\frac{rB''}{B}\right]\left[\frac{2rB'}{B}\frac{\partial^2}{\partial r\partial\psi}+\frac{rB''}{B}\frac{\partial}{\partial r}\right]\\ & -\frac{1}{(r+a/B)^4}\left(\frac{2rB'}{B}\right)\frac{\partial^2}{\partial r\partial\psi}\left[\frac{2rB'}{B}\frac{\partial^2}{\partial r\partial\psi}+\frac{rB''}{B}\frac{\partial}{\partial r}\right]\\ & +\frac{1}{(r+a/B)^4}\left(\frac{rB''}{B}\right)\frac{\partial}{\partial r}\left[\frac{2rB'}{B}\frac{\partial^2}{\partial r\partial\psi}+\frac{rB''}{B}\frac{\partial}{\partial r}\right]\\ & +\frac{1}{(r+a/B)^2}\left[\frac{2rB'}{B}\frac{\partial^2}{\partial r\partial\psi}(\nabla_1^2)-\frac{rB''}{B}\frac{\partial}{\partial r}(\nabla_1^2)\right]\\ & +\frac{1}{(r+a/B)^2}\left[\frac{6B'^2}{B^2}-\frac{2B''}{B}\right](\nabla_1^2)\\ & +\frac{1}{(r+a/B)^5}\left(\frac{2a}{B}\right)\left[B''-\frac{4B'^2}{B}+\frac{3aB'^2}{B^2(r+a/B)}\right]\left(\frac{2rB'}{B}\frac{\partial^2}{\partial r\partial\psi}+\frac{rB''}{B}\frac{\partial}{\partial r}\right)\\ & -\frac{1}{(r+a/B)^4}\left(\frac{2}{B}\right)\left[B''-\frac{3B'^2}{B}+\frac{2aB'^2}{B^2(r+a/B)}\right]\left(\frac{2rB'}{B}\frac{\partial^2}{\partial r\partial\psi}+\frac{rB''}{B}\frac{\partial}{\partial r}\right)\\ & -\frac{1}{(r+a/B)^5}\left(\frac{2B'}{B}\right)\left(\frac{2rB'}{B}\right)\left[\frac{3a}{B(r+a/B)}-2\right]\\ & \times\left(\frac{2rB'}{B}\frac{\partial^2}{\partial r\partial\psi}+\frac{rB''}{B}\frac{\partial}{\partial r}\right)\end{aligned} \tag{6b}$$

$$M = \frac{1}{(r+a)^2}\left[\frac{2rB'}{B}\frac{\partial^2\theta}{\partial r\partial\psi}+\left(\frac{B''}{B}-\frac{B'^2}{B^2}\right)\cdot r\frac{\partial\theta}{\partial r}+\frac{r^2B'^2}{B^2}\frac{\partial^2\theta}{\partial r^2}\right], \tag{6c}$$

and the superscribed prime on B denotes the derivative with respect to ψ.

Equations (5) are general and valid for any shapes of the outer cylinder. The effects of the eccentricity and the irregular shape of the outer cylinder are represented by the terms which contain the derivatives of B in equations (5). Equations (5) reduces to the governing equations for natural convection within concentric annuli when $B = 1$ and $B' = B'' = 0$.

The associated boundary conditions are

$$\text{(i) } r = 0, \quad \theta = 1, \quad \text{and } \frac{\partial f}{\partial r} = \frac{\partial f}{\partial\psi} = 0; \tag{7a}$$

$$\text{(ii) } r = 1, \quad \theta = \frac{\partial f}{\partial\psi} = \frac{\partial f}{\partial r} = 0. \tag{7b}$$

For a strong convection in a large eccentric annulus, equations (5) can be readily solved by a numerical method without tangling with complex geometries. For a slightly eccentric annulus, the terms multiplied by the derivatives of B can be ignored. Verification of the suggested approximation is discussed in the Appendix. In the following, we will concentrate on the natural convection in slightly eccentric annuli for small Ra.

Slightly Eccentric Circular Annuli

For a slightly eccentric annulus, the problem can be solved by a perturbation method in terms of the double series of ϵ and Ra when Ra is small. First, let us assume that the outer cylinder deviates only slightly from a circle whose radius is $\bar{b}$ and sets eccentrically to the inner cylinder by $\bar{\epsilon}$. Its contour can be expressed as

$$R(\psi) = \bar{b} + \bar{\epsilon}\cdot g(\psi). \tag{8a}$$

ψ_o can be selected such that $h = \bar{b} - \bar{a}$, and

$$B(\psi) = 1 + \epsilon g(\psi), \tag{8b}$$

where $\epsilon = \bar{\epsilon}/h$. Equation (8b) suggests that the solution can be expanded as the following forms:

$$\theta = (\theta_{00} + \epsilon\theta_{01} + \ldots) + Ra(\theta_{10} + \epsilon\theta_{11} + \ldots) + \ldots, \tag{9a}$$

$$f = Ra(f_{10} + \epsilon f_{11} + \ldots) + \ldots. \tag{9b}$$

Substituting equations (8b) and (9) into equations (5) and (7), and collecting terms of equal order of ϵ give

Ra°:

$$\epsilon^\circ:\ \nabla_{10}^2\theta_{00} = 0 \tag{10}$$

$$\epsilon':\ \nabla_{10}^2\theta_{01} = \frac{1}{(r+a)^2}\left[(rg''+ag)\frac{\partial\theta_{00}}{\partial r} + 2rg'\frac{\partial^2\theta_{00}}{\partial r\partial\psi}-\frac{2ag}{r+a}\frac{\partial^2\theta_{00}}{\partial\psi^2}\right] \tag{11}$$

Ra:

$$\epsilon^\circ:\ \nabla_{10}^2\theta_{10} = \frac{-1}{r+a}\left[\frac{\partial f_{10}}{\partial\psi}\frac{\partial\theta_{00}}{\partial r}-\frac{\partial f_{10}}{\partial r}\frac{\partial\theta_{00}}{\partial\psi}\right], \tag{12a}$$

$$\nabla_{10}^4 f_{10} = \frac{\cos\psi}{r+a}\frac{\partial\theta_{00}}{\partial\psi}-\sin\psi\frac{\partial\theta_{00}}{\partial r}, \tag{12b}$$

$$\begin{aligned}\epsilon:\ \nabla_{10}^2\theta_{11} = {} & -\frac{ag}{(r+a)^2}\cdot\left[\left(\frac{\partial\theta_{10}}{\partial r}+\frac{2}{r+a}\frac{\partial^2\theta_{10}}{\partial\psi^2}\right)\right.\\ & \left.+\left(\frac{\partial f_{10}}{\partial\psi}\frac{\partial\theta_{00}}{\partial r}-\frac{\partial f_{10}}{\partial r}\frac{\partial\theta_{00}}{\partial\psi}\right)\right]\\ & +\frac{r}{(r+a)^2}\cdot\left[2g'\frac{\partial^2\theta_{10}}{\partial r\partial\psi}+g''\frac{\partial\theta_{10}}{\partial r}\right]\\ & +\frac{1}{(r+a)}\cdot\left[\frac{\partial(f_{10},\theta_{01})}{\partial(r,\psi)}-\frac{\partial(f_{11},\theta_{00})}{\partial(r,\psi)}\right]\end{aligned} \tag{13a}$$

Nomenclature

A,C,D,E,F = constants
$\bar{a}$ = radius of inner cylinder, Fig. 1
$a = \bar{a}/h$
$\bar{b}$ = radius of outer cylinder, Fig. 1
B = gap functions, equation (4d)
f = stream function, equation (4a)
g = contour of outer cylinder, equation (8)
$\bar{g}$ = gravitational acceleration
h = characteristic gap width, equation (4d)
Pr = Prandtl number, equation (4f)
r = radial coordinate
$\bar{r}$ = dimensionless radial coordinate, equation (A-1)
R = dimensional contour of outer cylinder, Fig. 1
T = temperature
θ = dimensionless temperature, equation (4b)
ν = kinematic viscosity
α = thermal diffusivity
β = thermal expansion coefficient
ψ = azimuthal coordinate
ψ_0 = reference angle

Subscripts

i = inner cylinder
o = outer cylinder
number = indication of the expansion order

Superscripts

$^-$ = dimensional quantities
$' = \frac{\partial}{\partial\psi}$ in the text and $\frac{\partial}{\partial\bar{r}}$ in the Appendix

$$\nabla_{10}^4 f_{11} = -\nabla_{10}^2\left[\frac{ag}{(r+a)^2}\left(\frac{\partial f_{10}}{\partial r}+\frac{2}{r+a}\frac{\partial^2 f_{10}}{\partial \psi^2}\right)\right] - \frac{ag}{(r+a)^2}\left[\frac{\partial}{\partial r}+\frac{2}{r+a}\frac{\partial^2}{\partial \psi}\right]\nabla_{10}^2 f_{10} - 3g\left[\sin\psi\frac{\partial\theta_{00}}{\partial r}+\frac{\cos\psi}{r+a}\frac{\partial\theta_{00}}{\partial\psi}\right] - \left[\sin\psi\frac{\partial\theta_{01}}{\partial r}+\frac{\cos\psi}{r+a}\frac{\partial\theta_{01}}{\partial\psi}+\left(3g\sin\psi-\frac{rg'\cos\psi}{r+a}\right)\frac{\partial\theta_{00}}{\partial r} + \frac{\cos\psi}{r+a}\cdot\left(1+\frac{ag\sin\psi}{r+a}\right)\cdot\frac{\partial\theta_{00}}{\partial\psi}\right] + L_{11}(r,\psi) \quad (13b)$$

where

$$\nabla_{10}^2 = \frac{\partial^2}{\partial r^2}+\frac{1}{r+a}\frac{\partial}{\partial r}+\frac{1}{(r+a)^2}\frac{\partial^2}{\partial\psi^2}, \quad (14a)$$

and

$$L_{11}(r,\psi) = \frac{1}{(r+a)^2}\left[\nabla_1^2\left(2rg'\frac{\partial^2 f_{10}}{\partial r\partial\psi}\right)+\nabla_1^2 rg''\frac{\partial^2 f_{10}}{\partial r}\right] + \frac{4}{(r+a)^4}\left[zrg'\frac{\partial^2 f_{10}}{\partial r\partial\psi}+rg''\frac{\partial f_{10}}{\partial r}\right]+\frac{1}{(r+a)^2}\left[zrg'\frac{\partial^2}{\partial r\partial\psi}(\nabla_{10}^2 f_{10}) - rg''\frac{\partial}{\partial r}(\nabla_{10}^2 f_{10}) - 2g''(\nabla_{10}^2 f_{10})\right] \quad (14b)$$

The higher-order equations can be obtained similarly. For slightly eccentric annuli, the contribution of the higher-order terms is expected to be small. We will demonstrate later that the series solution converges very fast with respect to ϵ. For small ϵ and Ra, the zeroth-order term plus the first-order term of Ra are sufficient.

From equations (13), it is apparent that the solution of equal to or higher than $0(\epsilon)$ depend on the actual contour of the outer cylinder, g, which has to be second-order continuous. The ψ-dependence of the solutions, θ_{01}, θ_{11}, and f_{11}, etc., can be separated out only for certain classes of g. We do not intend to classify those functions which can give separable solutions. Instead, we will study the case of two slightly eccentric circular cylinders (see Fig. 1). The contour of the outer cylinder can be approximated by

$$R(\psi) = \bar{b} - \bar{\epsilon}\cos\psi + 0(\bar{\epsilon}^2), \quad (15a)$$

if $\psi_0 = 0$ is selected; and correspondingly,

$$g = -\cos\psi \quad (15b)$$

The boundary conditions, equations (7), become

$$\text{(i) } r = 0,\ \theta_{00} = 1,\ \theta_{01} = \theta_{10} = \theta_{11} = f_{10} = \frac{\partial f_{10}}{\partial r} = f_{11} = \frac{\partial f_{11}}{\partial r} = 0, \quad (16a)$$

$$\text{(ii) } r = 1,\ \theta_{00} = \theta_{01} = \theta_{10} = \theta_{11} = f_{10} = \frac{\partial f_{10}}{\partial r} = f_{11} = \frac{\partial f_{11}}{\partial r} = 0. \quad (16b)$$

The solutions of equations (10–14), after replacing g by $-\cos\psi$, and satisfying conditions (16), are

Ra°:

$$\epsilon^\circ:\ \theta_{00} = 1 - A_1\cdot\ln(1+r/a), \quad (17)$$

where $A_1 = 1/\ln(1+1/a)$.

$$\epsilon:\ \frac{\theta_{01}}{\cos\psi} = A_1\cdot\left[1-\frac{r+a}{1+2a}-\frac{a(1+a)}{(1+2a)}\cdot\frac{1}{r+a}\right] \quad (18)$$

Ra:

$$\epsilon^\circ:\ f_{10}/\sin\psi = A_1\left[\frac{(r+a)^3}{16}\cdot[\ln(r+a)-(1.25-C_2)] + \frac{C_1}{4}(r+a)\cdot[2\cdot\ln(r+a)-1]+\frac{C_3}{2}(r+a)+\frac{C_4}{r+a}\right], \quad (19)$$

where

$$C_1 = \frac{[(1+a)^4-a^2]-4a^2(1+a)^2\cdot\ln(1+1/a)}{16[|(1+a)^2+a^2|\cdot\ln(1+1/a)-[(1+a)^2-a^2]]}, \quad (20a)$$

$$C_2 = 1-\frac{[(1+a)^2\cdot\ln(1+a)-a^2\ln a]+4\cdot C_2\cdot\ln(1+1/a)}{[(1+a)^2-a^2]}, \quad (20b)$$

$$C_3 = \frac{a^2(1+a)^2\cdot\ln(1+1/a)-4\cdot C_2\cdot[(1+a)^2\cdot\ln a-a^2\ln(1+a)]}{4\cdot[(1+a)^2-a^2]}, \quad (20c)$$

$$C_4 = \frac{C_2}{4}\frac{a^2(1+a)^2}{(1+a)^2+a^2}-\frac{a^4(1+a)^4\cdot\ln(1+1/a)}{16[(1+a)^4-a^4]}. \quad (20d)$$

$$\theta_{10}/\cos\psi = A_1^2\cdot\left[\frac{(r+a)^3}{64}\cdot\left[\frac{\ln(r+a)}{2}-1+\frac{C_1}{2}\right] + \frac{(r+a)}{8}\cdot[C_2\cdot[\ln(r+a)-1]^2+C_3[2\cdot\ln(r+a)-1]] - \frac{C_4}{2}\cdot\frac{\ln(r+a)}{(r+a)}\right]+\frac{D_1}{2}(r+a)+\frac{D_2}{r+a}, \quad (21)$$

where

$$D_1 = \frac{2a}{[(1+a)^2-a^2]}\cdot[D_3-D_4(1+1/a)] \quad (22a)$$

$$D_2 = \frac{a^2(1+a)}{[(1+a)^2-a^2]}\cdot[D_4-D_3(1+1/a)] \quad (22b)$$

$$D_3 = \frac{a^3}{64}\cdot\left[\frac{\ln a}{2}-1+\frac{C_2}{2}\right]+\frac{1+a}{8}\cdot[C_1\cdot(\ln a+1)^2 + C_3(2\ln a-1)] - \frac{C_4\cdot\ln a}{2a}, \quad (22c)$$

$$D_4 = \frac{(1+a)^3}{64}\cdot\left[\frac{\ln(1+a)}{2}-1+\frac{C_2}{2}\right] + \frac{(1+a)}{8}\cdot[C_2\cdot[\ln(1+a)-1]^2 + C_3\cdot[2\cdot\ln(1+a)-1]]-\frac{C_4\cdot\ln(1+a)}{2(1+a)} \quad (22d)$$

The higher-order solutions can be obtained similarly. The extension is straightforward; but the algebra becomes very complex and tedious. The computer extension method [9] may be the best choice to obtain the higher-order terms, which can rule out the possibility of hand calculation errors which often occur in solving those extremely long equations. Since the perturbation solution is valid for small ϵ and Ra, only the solutions up to the first order of ϵ and Ra are presented. Rigorously, the solution of $0(\epsilon\cdot\text{Ra})$ should be included in order to make the solution complete up to the first order of ϵ. Since the contribution due to the terms of $0(\epsilon\cdot\text{Ra})$ is very small and does not have practical interest (see Appendix), they are excluded.

As explained in the Appendix, the solutions of 0(1) and 0(Ra) are not for concentric annuli only; instead, they include significant parts of the eccentric effect. This can be demonstrated by transforming the solutions of 0(1) and 0(Ra) back to the physical coordinate through equation (4c). Therefore we believe that the solutions of 0(1) and 0(Ra) are in fact sufficient for slightly eccentric annuli say $\epsilon < 0.1$. A detailed discussion can be found in the Appendix. For those ϵ and Ra which are not small, a direct numerical solution of equations (5) is probably necessary.

Results and Discussion

Equations (10–13) show that the natural convection in slightly eccentric annuli depends on a, g, and Ra. The solution does not depend on Pr up to $0(\text{Ra}^2)$. However, there is an implicit restriction of Pr on the mathematical formulation that Pr cannot be too small. For fluid of very small Pr, the diffusion of energy and momentum depend

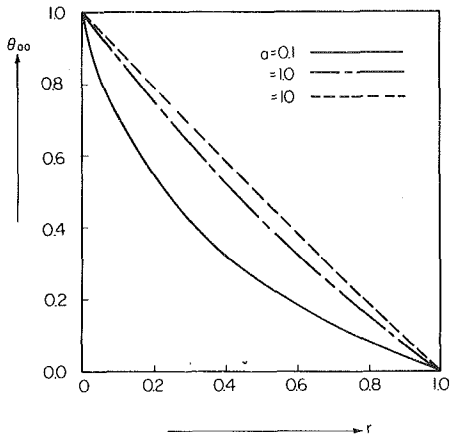

Fig. 2 Temperature function θ_{00}

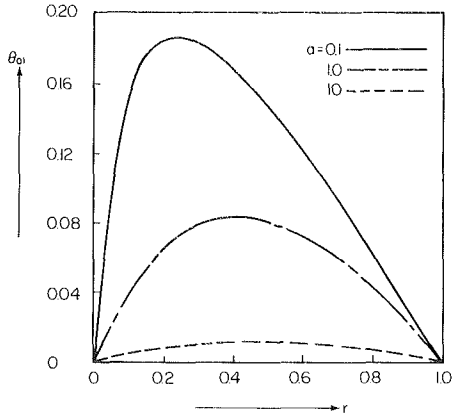

Fig. 3 Temperature function θ_{01}

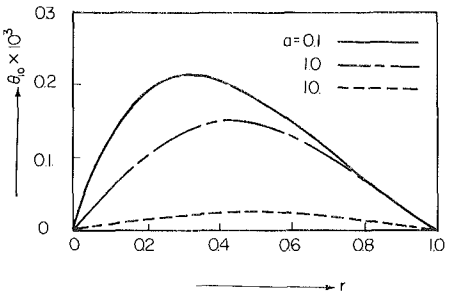

Fig. 4 Temperature function θ_{10}

strongly on the kinematic viscosity. Grashof and Prandtl numbers may be more appropriate parameters than Ra. a is the ratio of the radius of the inner cylinder and the characteristic gap width of the annulus, and represents the curvature effects. g is the dimensionless contour of the outer cylinder. Not all g allows a separable solution for equations (11) and (13). Circular functions are among those functions which allow a separable solution. In the Appendix, we demonstrate that the contribution due to terms equal to or higher than $0(\epsilon)$ is very small and can be ignored for many practical problems. For those kinds of engineering problems, the actual form of g function does not restrict the analytical solution reported in the paper.

Equation (17) is plotted for $a = 0.1$, 1.0, and 10 in Fig. 2. For large a, say 10, the temperature distribution due to conduction alone in the transformed coordinates is very close to a stright line. This is expected since the curvature effects on the temperature distribution are very small when the gap is narrow compared with the radius of the inner cylinder. As the value of a decreases, the temperature distribution becomes curved due to the participation of the curvature effects.

The first-order eccentric effect on the temperature distribution, θ_{01}, is shown in Fig. 3. The eccentric effect is more important for wider gaps. It is worthy to notice that the ratio of θ_{01} to θ_{00} is bounded by the twenty percent for $a = 0.1$; the ratio decreases when the value of a increases. The range of ϵ for which the perturbation solution can be applied cannot be determined from the first few terms of the perturbation series, and can only be determined by comparing the perturbation solution with the exact solution which is, unfortunately, not available. From our experience, the perturbation solution can probably give reasonable prediction for $\epsilon < 0.1$. This implies that the contribution of the terms of $0(\epsilon)$ is bounded by two percent as long as a is not smaller than 0.1. For the purpose of engineering design, two percent does not have any significance. For $a < 0.1$, the importance of the first-order eccentric effect, $0(\epsilon)$, gradually increases and will be further discussed later.

The first-order effect of natural convection on the temperature distribution, θ_{10}, is shown in Fig. 4. Comparing the maximum value of θ_{10} with that of θ_{00} shows that the perturbation solution can be safely applied up to $\mathrm{Ra} = 10^4$. However, the range of Ra for which the perturbation solution can be applied shrinks when the value of a decreases. This agrees with the criterion found by Mack and Bishop [2].

The normal gradients of the temperature θ_{00}, θ_{01}, and θ_{10} along the surfaces of the inner or the outer cylinder are plotted in Figs. 5–7 as functions of a, respectively. A comparison of $\partial\theta_{00}/\partial r$ with $\partial\theta_{01}/\partial r$ further confirms that the contribution due to the terms of higher-orders of ϵ is negligible as long as a is not small. However, the temperature gradients increase drastically as a approaches zero. Also, the ratio of $\partial\theta_{01}/\partial r$ and $\partial\theta_{00}/\partial r$ increases (it is always smaller than one). This seems to indicate that the higher order terms of ϵ gradually become dominant and $a = 0$ is a singular point. The physical meaning of a is the ratio of the radius of the inner cylinder and the characteristic gap width. There are two ways to achieve the limit that $a = 0$. One is no inner cylinder and the other is the inner cylinder embedded in an infinite fluid. None of them can be deduced from our solution. However, the case of very small a's is still interesting. This corresponds to the physical situation that a hot inner cylinder sets in a very large outer cylinder. The energy transfer between two cylinders by conduction is very weak and boundary layers may develop along the surfaces of two cylinders. The eccentricity of two cylinders cannot have much effect on the pattern of natural convection. It becomes a singular perturbation problem. This indicates that the regular perturbation solution breaks down for small values of a.

References

1 Kuehn, T. H., and Goldstein, R. J., "An Experimental and Theoretical Study of Natural Convection in the Annulus Between Horizontal Concentric Cylinders," *Journal of Fluid Mechanics*, Vol. 74, 1976, pp. 695–719.

2 Mack, L. R., and Bishop, E. H., "Natural Convection Between Horizontal Concentric Cylinders for Low Rayleigh Number," *Quarterly Journal of Mechanical and Applied Mathematics*, Vol. 21, 1968, pp. 223–241.

3 Mack, L. R., and Hardee, H. C., "Natural Convection Between Concentric Spheres at Low Rayleigh Numbers," *International Journal of Heat Mass Transfer*, Vol. 11, 1968, pp. 387–396.

4 Rotem, Z., "Conjugate Free Convection from Horizontal Conducting Circular Cylinders," *International Journal of Heat Mass Transfer*, Vol. 15, 1972, pp. 1679–1693.

5 Huetz, J., and Petit, J. P., "Natural and Mixed Convection in Concentric Annular Spaces—Experimental and Theoretical Results for Liquid Metal," 5th International Heat Transfer Conference, Tokyo, Vol. 3, 1974, pp. 169–172.

6 Kuehn, T. H., and Goldstein, R. J., "An Experimental Study of Natural Convection Heat Transfer in Concentric and Eccentric Horizontal Cylindrical Annuli," ASME JOURNAL OF HEAT TRANSFER, Vol. 100, 1978, pp. 635–640.

7 Sande, E. Van de, and Hamer, B. J. G., "Steady and Transient Natural Convection in Enclosures between Horizontal Circular Cylinders," *International Journal of Heat Mass Transfer*, Vol. 22, 1979, pp. 361–370.

8 Yao, L. S., and Chen, F. F., "A Mathematical Model of Natural Convection in a Melted Region Around a Heated Horizontal Cylinder," (in preparation), 1979.

9 Van Dyke, M., "Computer Extension of Perturbation Series in Fluid Mechanics," *SIAM Journal of Applied Mathematics*, Vol. 28, No. 3, 1974, pp. 720–733.

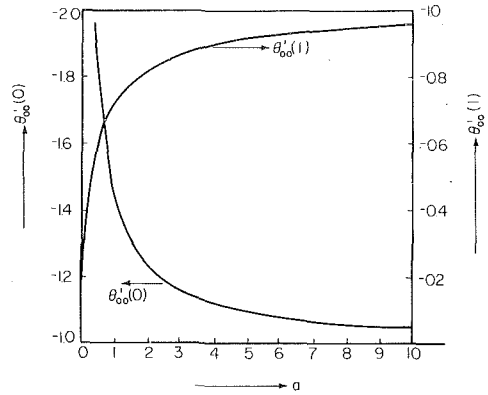

Fig. 5 Zeroth-order surface temperature gradient

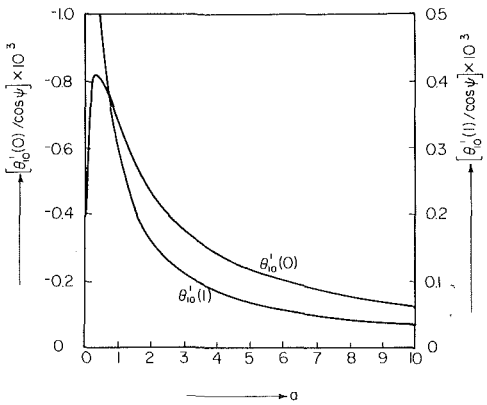

Fig. 6 First-order surface temperature gradient due to eccentricity

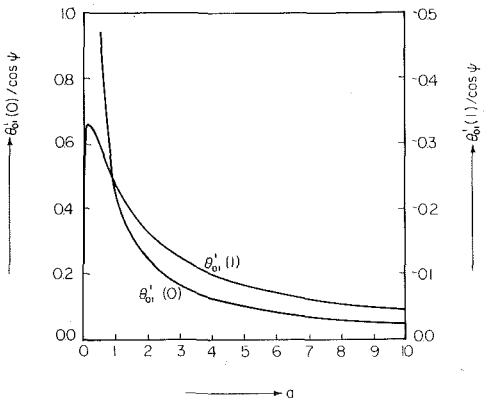

Fig. 7 First-order surface temperature gradient due to natural convection

APPENDIX

The heat conduction problem between two slightly eccentric circular cylinders (i.e., $Ra \equiv 0$) is solved by a different expansion procedure. The expansion procedure is similar to that used in solving problems of the fluid flow passing a slender body or a thin wing. This expansion procedure is designated as the expansion II to distinguish the expansion procedure described in the paper, which is referred to as the expansion I in the following discussions.

The dimensionless radial coordinate, which is used to nondimensionalize the steady conduction equation in cylindrical coordinates, is

$$\tilde{r} = \frac{\bar{r} - \bar{a}}{\bar{b} - \bar{a}} \qquad \text{(radial coordinate)}. \tag{A-1}$$

The dimensionless heat conduction equation can be written as

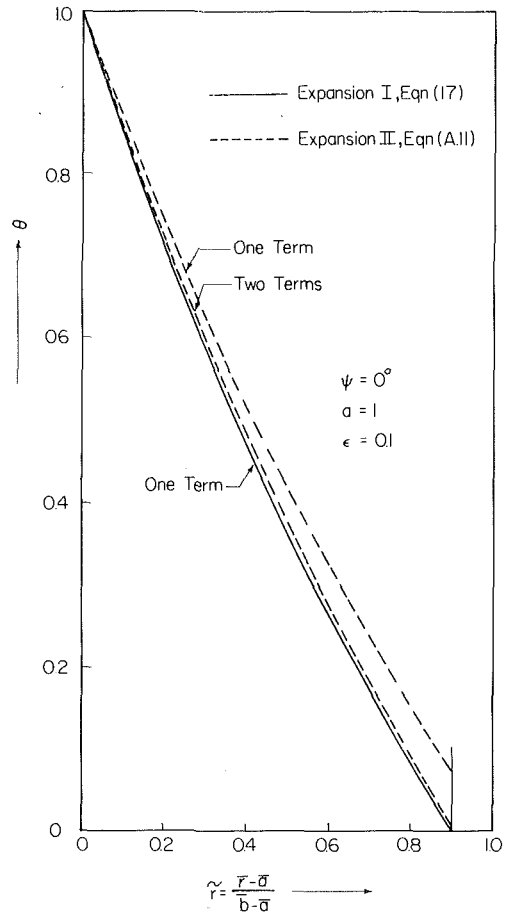

Fig. A-1

$$\frac{\partial^2\theta}{\partial\tilde{r}^2} + \frac{1}{\tilde{r}+a}\frac{\partial\theta}{\partial\tilde{r}} + \frac{1}{(\tilde{r}+a)^2}\frac{\partial^2\theta}{\partial\psi^2} = 0 \tag{A-2}$$

The associated boundary conditions are:

$$\text{(i) } \tilde{r} = 0, \quad \theta = 1, \tag{A-3}$$

$$\text{(ii) } \tilde{r} = 1 - \epsilon\cos\psi, \quad \theta = 0, \tag{A-4}$$

and the symmetry conditions along $\psi = 0$ and 180 deg.

Equation (A-4) can be expanded around $\tilde{r} = 1$ and becomes

$$\theta(1) - \epsilon\cos\psi\theta'(1) + 0(\epsilon^2) = 0 \tag{A-5}$$

where the prime denotes the derivative with respect to $\tilde{r}$.

Equation (A-5) suggests that the solution can be expanded in terms of the power series of ϵ, say

$$\theta = \tilde{\theta}_0(\tilde{r}) + \epsilon\cos\psi\,\tilde{\theta}_1(\tilde{r}) + \ldots \tag{A-6}$$

Substitution of equation (A-6) into equations (A-2, A-4), and then collection of terms of equal order of ϵ, give

$$(\epsilon^\circ): \frac{d^2\tilde{\theta}_0}{d\tilde{r}^2} + \frac{1}{\tilde{r}+a}\frac{d\tilde{\theta}_0}{d\tilde{r}} = 0,$$
$$\text{(i) } \tilde{r} = 0, \quad \tilde{\theta}_0 = 1,$$
$$\text{(ii) } \tilde{r} = 1, \quad \tilde{\theta}_0 = 0 \tag{A-7}$$

$$(\epsilon^1): \frac{d^2\tilde{\theta}_1}{d\tilde{r}^2} + \frac{1}{\tilde{r}+a}\frac{d\tilde{\theta}_1}{d\tilde{r}} - \frac{\tilde{\theta}_1}{(\tilde{r}+a)^2} = 0,$$
$$\text{(i) } \tilde{r} = 0, \quad \tilde{\theta}_1 = 0$$
$$\text{(ii) } \tilde{r} = 1, \quad \tilde{\theta}_1 = \tilde{\theta}'_0 \tag{A-8}$$

The solution of equation (A-7) is simply the heat conduction between two concentric cylinders and is

$$\tilde{\theta}_0 = 1 - \frac{\ln(1 + \tilde{r}/a)}{\ln(1 + 1/a)} \tag{A-9}$$

The solution of equation (A-8) represents the first-order eccentric effect and is

$$\tilde{\theta}_1 = \frac{1}{(1 + 2a)\ln(1 + 1/a)} \cdot \left[\frac{a^2}{\tilde{r} + a} - (\tilde{r} + a)\right] \tag{A-10}$$

Thus, the solution of the heat conduction between two slightly eccentric cylinders can be written as

$$\theta = \left|1 - \frac{\ln(1 + \tilde{r}/a)}{\ln(1 + 1/a)}\right| + \frac{\epsilon \cdot \cos\psi}{(1 + 2a)\ln(1 + 1/a)} \cdot \left|\frac{a^2}{\tilde{r} + a} - (\tilde{r} + a)\right| + 0(\epsilon^2) \tag{A-11}$$

It can be shown that the results of the expansion I can be reduced to equation (A-11) by the coordinate transformation

$$r = \frac{\tilde{r}}{1 - \epsilon \cos\psi} \tag{A-12}$$

This demonstrates that two expansion procedures are consistent and agree with each other up to the number of the terms in the expansion. For example, equation (A-11) and equations (17) and (18) agree up to $0(\epsilon)$ and differ only by the terms bounded by $0(\epsilon^2)$.

In the following, we will show that the expansion I can supply more accurate results in a practical computation. The reason is obviously that the expansion I satisfies the boundary condition exactly. The results of the two expansion procedures are plotted in Fig. A-1 for $\epsilon = 0.1$ and $a = 1$ at $\psi = 0$ where the terms of $0(\epsilon)$ make the most contribution. The second term of the expansion II, equation (A-10), contributed substantially. This is because the maximum values of $\tilde{\theta}_0$ and $\tilde{\theta}_1$ are about same. For $\epsilon = 0.1$, the term of $0(\epsilon)$, $\tilde{\theta}_1$, can contribute as much as twenty percent of θ. However, the one-term result of the expansion I, θ_{00}, is fairly close to the two-term result of the expansion II, equation (A-11). The two-term result of the expansion I lays slightly above the one-term result of the expansion I, and is hardly shown on the scale of Fig. A-1; therefore, it is not included. A careful comparison of the distribution of θ_{00} and θ_{01} reveals that the ratio of θ_{01} and θ_{00} is always bounded by 20 percent. This shows that for $\epsilon = 0.1$, the term of $0(\epsilon)$ obtained by the expansion I can contribute at most 2 percent which is a quite small fraction. This also shows that the series generated by the expansion I converges much faster than that by the expansion II. The one-term result of the expansion I may be more accurate than the two-term result of the expansion II. The reason that the expansion I produces more accurate results is unclear, but may be due to that the first term of the expansion I actually contains incomplete terms of the series which are equal to or higher than $0(\epsilon)$. Those terms are not complete, but contain significant parts of the higher-order terms, and can pull the solution closer to the exact solution. This may be the reason that the series obtained by the expansion I converge fast. The first terms alone can supply data within the accuracy required by engineers.

G. Yee
Research Staff Member,
Science Applications, Inc.,
San Leandro, Calif.
Mem.ASME

R. Chilukuri
Graduate Research Student,
Mem. ASME

J. A. C. Humphrey
Assistant Professor,
Mem. ASME

Department of Mechanical Engineering,
University of California,
Berkeley, Calif. 94720

Developing Flow and Heat Transfer in Strongly Curved Ducts of Rectangular Cross Section

A numerical study of heat transfer in 90 deg, constant cross section curved duct, steady, laminar, flow is presented. The work is aimed primarily at characterizing the effects on heat transfer of duct geometry and entrance conditions of velocity and temperature by considering, especially, the role of secondary motions during the developing period of the flow. Calculations are based on fully elliptic forms of the transport equations governing the flow. They are of engineering value and are limited in accuracy only by the degree of computational mesh refinement. A comparison with calculations based on parabolic equations shows how the latter can lead to erroneous results for strongly curved flows. Buoyant effects are excluded from the present study so that, strictly, the results apply to heat transfer flows in the absence of gravitational forces such as arise in spacecraft.

Introduction

Considerable effort has been expended on the experimental measurement and calculation of flows in curved ducts of rectangular cross section, principally because of the practical significance of such flows. Curved duct geometries frequently arise in engineering configurations where, besides providing a necessary conduit for the fluid, it may be required to enhance heat and/or mass transport processes. In curved ducts this is achieved mainly due to the prolonged residence times of fluid elements which must move along spiraling paths as they evolve in the main (longitudinal) flow direction. Thus, the centrifugal force-radial pressure gradient imbalance acting on the slow moving fluid near the side walls of the duct induces a motion of the fluid along the side walls and directed from the outer towards the inner curvature wall. In turn, faster moving fluid in the core region of the flow moves along the center (symmetry) plane of the duct, being directed from the inner to the outer curvature wall. The cross-stream motion just described is commonly referred to in the literature as secondary motion of the "first kind" or, simply, secondary motion [1]. It is obvious that the extent to which heat and mass transport can be enhanced in curved duct flows will be a strong function of the intensity and spatial variation of the secondary motion.

Even though experimental works on curved duct flows abound (a recent review may be found in [2]), data availability for engineering purposes is often deficient or simply inadequate. Whereas considerable work has been carried out to obtain useful design correlations for pressure losses and friction coefficients [3, 4] there is no equivalent body of knowledge describing three-dimensional velocity, energy, and mass transport phenomena in sufficient detail and over a wide enough range of relevant dimensionless flow parameters. That this should be the case is due primarily to the laborious and time consuming task of obtaining experimental measurements even for very specific geometries and flow conditions.

Whereas experimentation in curved duct geometries may be laborious (and complex), it is possible, in principle, to compute these flows quite accurately in the laminar regime. This has been shown by, among others, Cheng and Akiyama [5], Cheng, et al. [6], and Joseph, et al. [7] for fully developed flow; and by Ghia and Sokhey [8] and Humphrey, et al. [9] for developing flow. Calculations for turbulent regime have been performed by Pratap and Spalding [10] using a semi-elliptic numerical procedure. However, the agreement between calculations and measurements of velocity is less satisfactory in this case. Although the authors attribute the discrepancies to failings in the model of turbulence employed in the calculations, it is possible that their neglect of higher order curvature terms in the equations of motion may have contributed to the under-prediction of secondary velocity components. Of the above, only the procedure used by Humphrey, et al. [9] is based on fully elliptic forms of the equations of motion. While parabolic calculation procedures are numerically more exact (because of the finer computational grids they allow), they lead to physically erroneous results in curved duct flows with strong longitudinal pressure variation unless special treatment of the pressure field is introduced [8]. Semi-elliptic calculation procedures deal with the pressure field exactly but, like the parabolic, they cannot be used in regions of reversed flow. Although elliptic calculation procedures are completely general in their application, due to cost considerations, they are limited (at least for the present) to coarse grid computations. Generally, however, such computations are sufficiently accurate for engineering purposes.

Experimental investigations of heat transfer in curved duct flows have been described by, for example, Kreith [11], Mori, et al. [12], and Yang and Liao [13], while corresponding numerical calculations are reported by Cheng and Akiyama [5], and Cheng, et al. [6]. Except for the experimental works of Kreith [11] and Yang and Liao [13] (in turbulent regime), the remaining studies deal with the problem of fully developed laminar flow. In general, these and similar studies show that heat transfer in curved duct flow is enhanced relative to that occurring in straight ducts, with transfer rates at outer curvature walls being typically 2 to 5 times larger than corresponding values at inner walls. Nondimensionalized values of temperature profiles show trends similar to those displayed by the longitudinal velocity component, with maximum values shifted towards the outer wall. Equivalent information appears to be lacking for the case of developing laminar flow. Especially noticeable is the dearth of information for ducts with relatively strong curvature (small radius ratio: $2\,Rc/D_H < 10$) where spatial ellipticity in the flow field is pronounced.

The present study is directed toward providing (through numerical computation) some of the necessary fluid mechanical and heat transfer data for developing steady laminar flow of a nonbuoyant incompressible fluid in strongly curved ducts with 90 deg deflection angle. The calculations are of engineering accuracy and allow a relative comparison of duct performance and detailed flow characteristics as a function of relevant dimensionless parameters and boundary conditions. The neglect of buoyant effects restricts present results to gravitation-free duct flow configurations such as arise in spacecraft. Otherwise, buoyant effects would be significant over the range of parameters investigated. The experimental equivalent of this or a similar gravitation-free study would be exceedingly laborious, time consuming and expensive to perform, and substantiates the need for developing and applying calculation procedures which can be used with confidence, relatively easily and (by comparison to experiments) at moderate costs. The numerical procedure used in this study is presently the basis for similar calculations in turbulent flow [14].

Contributed by the Heat Transfer Division for publication in the JOURNAL OF HEAT TRANSFER. Manuscript received by the Heat Transfer Division June 25, 1979.

Calculation Procedure and Test Cases

The calculation procedure used to compute the flows in this study has already been described in [9]. Extension of the procedure to arbitrary orthogonal coordinate geometries and, especially, its application to developing curved pipe flows of strong curvature have been documented by Humphrey [15]. Detailed information concerning the derivation of the difference equations, their numerical solution and results for various test cases solved to evaluate the procedure are reported in the above two references and in [2]. This section presents a summary of the essential features characterizing the calculation method together with a description of its application to flows in curved ducts with heat transfer.

Equations, Boundary Conditions and Procedure for Numerical Solution. Mass conversion, momentum and energy equations for three-dimensional, steady, incompressible laminar flow in curved ducts of cylindrical geometry corresponding to Fig. 1 are given by

$$\frac{\partial v_r}{\partial r} + \frac{1}{r}\frac{\partial v_\phi}{\partial \phi} + \frac{\partial v_z}{\partial z} + \frac{v_r}{r} = 0. \tag{1}$$

$$\rho\left[v_r\frac{\partial v_r}{\partial r} + \frac{v_\phi}{r}\frac{\partial v_r}{\partial \phi} + v_z\frac{\partial v_r}{\partial z} - \frac{v_\phi^2}{r}\right] = -\frac{\partial P}{\partial r} + \mu\left[\nabla^2 v_r - \frac{v_r}{r^2} - \frac{2}{r^2}\frac{\partial v_\phi}{\partial \phi}\right], \tag{2}$$

$$\rho\left[v_r\frac{\partial v_\phi}{\partial r} + \frac{v_\phi}{r}\frac{\partial v_\phi}{\partial \phi} + v_z\frac{\partial v_\phi}{\partial z} + \frac{v_r v_\phi}{r}\right] = -\frac{1}{r}\frac{\partial P}{\partial \phi} + \mu\left[\nabla^2 v_\phi + \frac{2}{r^2}\frac{\partial v_r}{\partial \phi} - \frac{v_\phi}{r^2}\right] \tag{3}$$

$$\rho\left[v_r\frac{\partial v_z}{\partial r} + \frac{v_\phi}{r}\frac{v_z}{\partial \phi} + v_z\frac{\partial v_z}{\partial z}\right] = -\frac{\partial P}{\partial z} + \mu\nabla^2 v_z \tag{4}$$

$$\rho\, c_p\left[v_r\frac{\partial T}{\partial r} + \frac{v_\phi}{r}\frac{\partial T}{\partial \phi} + v_z\frac{\partial T}{\partial z}\right] = k\nabla^2 T \tag{5}$$

where

$$\nabla^2 = \frac{\partial^2}{\partial r^2} + \frac{1}{r}\frac{\partial}{\partial r} + \frac{1}{r^2}\frac{\partial^2}{\partial \phi^2} + \frac{\partial^2}{\partial z^2} \tag{6}$$

It is required to solve (1–5) together with various combinations of the boundary conditions as shown below:

Inlet plane ($\phi = 0$ *deg*).

$v_r = v_z = 0$, v_ϕ = plug flow or developed duct flow (7)

T = constant of $f(r)$

Exit plane (*all r and z at* $\phi = 90$ *deg*).

$$\frac{\partial v_r}{\partial \phi} = \frac{\partial v_z}{\partial \phi} = \frac{\partial v_\phi}{\partial \phi} = \frac{\partial T}{\partial \phi} = 0 \tag{8}$$

with overall continuity of mass and energy imposed.

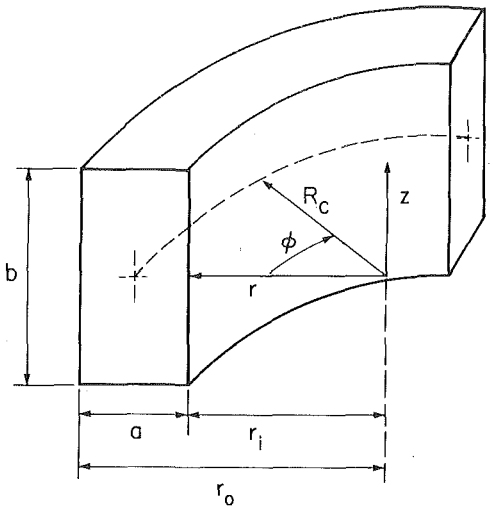

Fig. 1 Curved duct cylindrical coordinate geometry

Side walls (*all* ϕ *at* $z = \pm b/2$ *and* $r = r_i, r_o$).

$$v_r = v_z = v_\phi = 0 \tag{9}$$

T = constant or $f(\phi)$ at specified walls

$q = 0$ at specified walls

Symmetry plane (*all r and* ϕ *at* $z = 0$).

$$v_z = \frac{\partial v_r}{\partial z} = \frac{\partial v_\phi}{\partial z} = \frac{\partial T}{\partial z} = 0 \tag{10}$$

Although the boundary conditions imposed for velocity and temperature at the inlet and exit planes are inexact, the adequacy of the approximation may be assessed from Fig. 2 which shows calculated velocity and temperature profiles with and without (6 D_H length) straight tangents attached to the curved duct. The calculations correspond to Case 1 in Table 1 and indicate that for ranges of Reynolds number such that Re $\gtrsim$790, the approximation is indeed sufficiently accurate for calculations of engineering use. The adequacy of the approximation would be expected to decrease with decreasing Re number.

Finite difference equations are obtained by integrating (1–5) over volume elements or cells discretizing the flow domain. The velocity components, pressure and temperature are the dependent variables computed on a number of staggered, interconnected grids, each of which is associated with a specific variable. The general form of the finite difference expression is given by

$$\phi_p = \left(\sum_{i=1}^{6} A_i\phi_i + S_0\right)\Big/\sum_{i=1}^{6} A_i \tag{11}$$

Nomenclature

a = curved duct width
b = curved duct breadth
c_p = heat capacity at constant pressure
De = Dean number $\left(\mathrm{Re}\left[\frac{D_H/2}{Rc}\right]^{1/2}\right)$
D_H = curved duct hydraulic diameter (4 × surface/perimeter)
$\bar{h}$ = perimeter average heat transfer coefficient at ϕ plane $(\bar{q}/(Tw - \bar{T}))$
k = thermal conductivity
$\overline{\mathrm{Nu}}$ = perimeter average Nusselt number at ϕ plane $(\bar{h}D_H/k)$
P = pressure at a point in the flow
Pr = Prandtl number $\mu c_p/k$
q = heat flux at a point on the wall
$\bar{q}$ = perimeter average heat flux at ϕ plane
r = radial direction in cylindrical coordinates
r_i = inner curvature wall
r_o = outer curvature wall
Rc = duct radius of curvature $((r_i + r_o)/2)$
Re = Reynolds number $\left(\frac{D_H\rho V_B}{\mu}\right)$
T = value of temperature at a point in the flow
$\bar{T}$ = mass average temperature at ϕ plane
T_{in} = inlet temperature
T_w = wall temperature
V_B = average longitudinal velocity
v_ϕ = longitudinal velocity component
v_r = radial velocity component
v_z = axial velocity component
z = axial direction in cylindrical coordinates
θ = nondimensional temperature at a point in the flow $\left(\frac{T_w - T}{T_w - T_{\mathrm{in}}}\right)$
θ_B = nondimensional mass average temperature at ϕ plane $\left(\frac{\bar{T} - T_{\mathrm{in}}}{T_w - T_{\mathrm{in}}}\right)$
μ = viscosity
ρ = density
ϕ = longitudinal direction in cylindrical coordinates

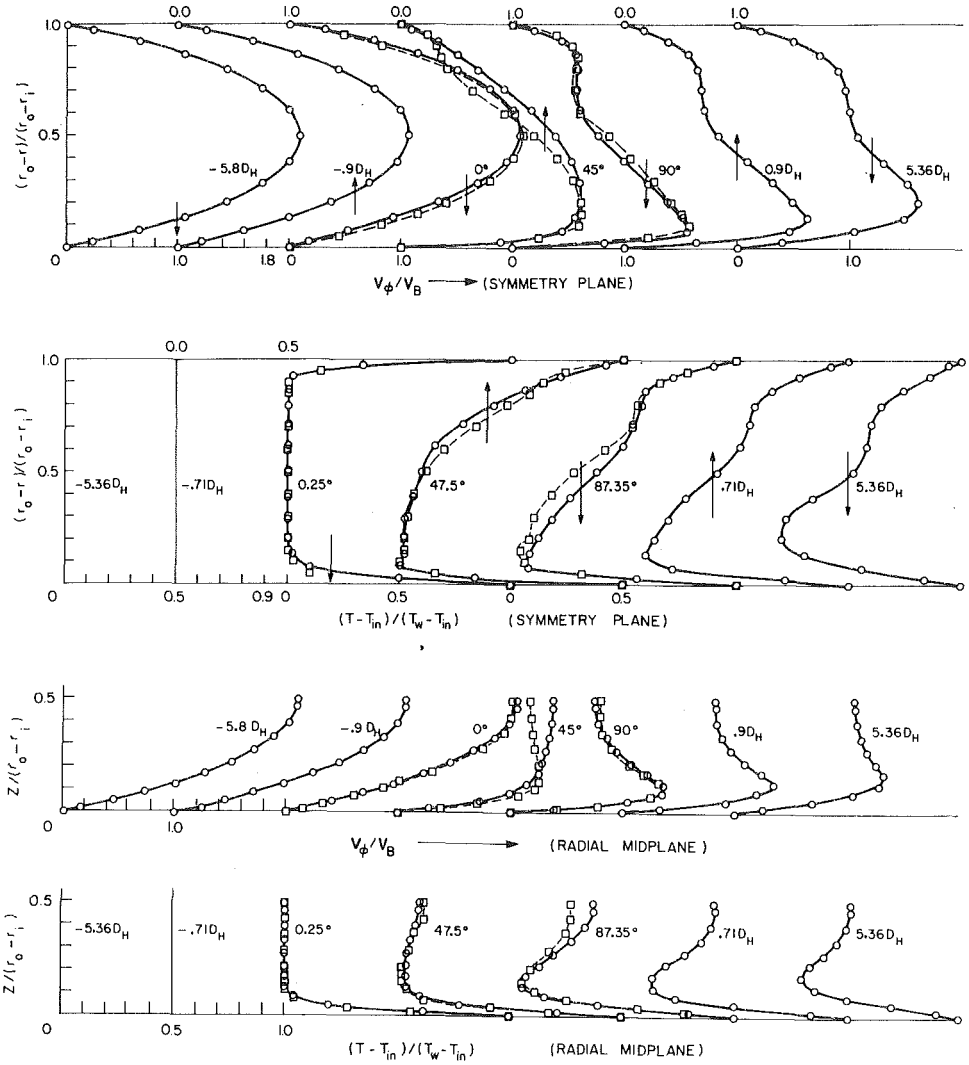

Fig. 2 Calculated velocity and temperature profiles with (○) and without (□) tangents attached to the curved duct. Re = 790, De = 368 (Case 1)

Table 1 Calculated case studies; Re = 790 and T_w = 350 K for all cases

Case No.	b/a	Rc/D_H	De	T_{in} (K)	$(v_\phi)_{in}$	Heated Walls
1	1	2.3	368	300	developed duct flow	all
1A	1	4.6	260	300	developed duct flow	all
2	3	2.3	368	300	developed duct flow	all
3	1/3	2.3	368	300	developed duct flow	all
4	1	2.3	368	300	plug flow	all
5*	1	2.3	368	290(r_i) 310(r_o)	developed duct flow	all
6*	1	2.3	368	310(r_i) 290(r_o)	developed duct flow	all
7	1	2.3	368	300	developed duct flow	r_o (remaining walls adiabatic)
8	1	2.3	368	300	developed duct flow	side (remaining walls adiabatic)
9	1	2.3	368	300	developed duct flow	r_i (remaining walls adiabatic)
10	Same as Case 1 using parabolic calculation procedure					

* Linear entrance plane temperature profiles.

where ϕ_p (velocity component, pressure or temperature) is the variable solved for at a position P in the discretized flow domain. The A_i coefficients are determined at the cell surfaces and represent the combined contributions of convection and diffusion to the balance of ϕ. Other contributions arising from pressure, body forces and temperature (sources or sinks) are contained in S_0. Detailed forms for S_0 in variable property flows are available in [16].

Solution of the system of finite difference transport equations with appropriately differenced boundary conditions is achieved by means of a cyclic series of predictor-corrector operations as described in [9, 15]. Briefly, the method involves using an initial or intermediate value of the pressure field to solve for an intermediate velocity field. A pressure correction to the pressure field is determined by bringing intermediate velocities into conformity with continuity. Corrections to the pressure and velocity fields are applied and the energy equation is solved for T (in flows where energy and momentum are not linked through temperature effects this last step can be taken after the velocity and pressure fields have been determined). The above steps are repeated until some pre-established convergence criterion is satisfied.

Testing. Extensive testing and an evaluation of the calculation procedure for predicting flows without heat transfer have been documented in [2] and reported in part in [9, 15]. It has been shown in these references that fully elliptic, three-dimensional computations of sufficient accuracy for engineering purposes can be obtained on unequally spaced grids as coarse as $12 \times 12 \times 20$ ($r \times z \times \phi$). The predictions presented in this numerical study have been performed on a slightly more refined $15 \times 12 \times 20$ mesh. While finer grids are capable of yielding more accurate results, they are increasingly more expensive to compute. Whereas numerical schemes based on parabolic or semi-elliptic froms of the transport equations will handle equivalent and finer calculation meshes at significantly less cost, for flows such as the ones of interest here where curvature effects can be pronounced, it is not possible to determine a priori whether or not reversed flow regions exist. For two interesting examples involving flow reversal in curved ducts see [9, 15].

Profiles of longitudinal velocity, calculated using elliptic and parabolic forms of the transport equations, are shown in Fig. 3 where they are compared with experimental data from [9]. The parabolic calculations were obtained by modifying the elliptic procedure of [9, 15] as explained in, for example, Launder [17]. The plots allow a relative comparison between the two approaches for a duct of relatively strong curvature (Case 1 in Table 1). Overall, the elliptic results for longitudinal velocity (and cross-stream components not shown here) are in better agreement with the measurements, especially between ϕ = 30 deg and ϕ = 90 deg where elliptic effects are strongest. Decoupling of longitudinal pressure links in the parabolic procedure leads to an inaccurate determination of pressure which, in turn, affects the velocity components. Thus, even though the velocity field is parabolic in that it contains no reversed flow zones, ellipticity in the pressure field is still strong and must be dealt with accordingly.

Testing of the calculation procedure in the presence of heat transfer effects was carried out for fully developed curved duct flow data reported by Mori et al. [12]. The results of this and a similar test related to developing heat transfer in a straight duct flow are reported by Yee [18]. In general, the agreement between calculations and experimental results of [12] was considered satisfactory given the uncertainty due to turbulence fluctuation reported in [12].

Case Studies, Results and Discussion

A summary of various case studies and conditions calculated is presented in Table 1. In all cases the temperature boundary condition was that of constant wall temperature (T_w = 350 K) except for where the adiabatic condition was enforced. Although not calculated here, variable wall temperature or variable (or constant) heat flux conditions could have been specified at the boundaries. Calculations corresponding to Re = 150 and $53 \leqslant De \leqslant 106$ will be found in [19]; because of their lower accuracy they will only be commented on briefly further below.

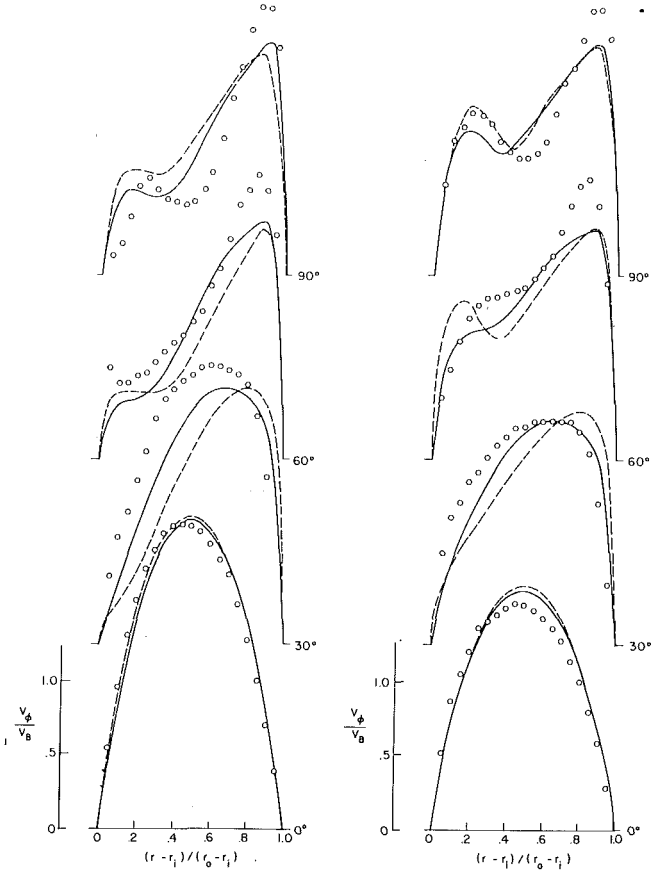

Fig. 3(*a*) $z/(b/2) = 0$ Fig. 3(*b*) $z/(b/2) = 0.5$

Fig. 3 Elliptic (——) and parabolic (- - -) calculations of longitudinal velocity. Measurements (○) are from Humphrey, et al. [9]. Re = 790, De = 368 (Case 1)

Incompressible, constant property (Pr = 1.0) flow was assumed for the calculations. While the inclusion of temperature-dependent flow properties (k, μ) is a standard feature in the numerical procedure, it does increase significantly the cost of predictions through additional storage and computing time requirements. Typical values for storage and CP times for the case studies presented here were 160 K_8 words and 235 s, respectively, on a CDC 7600. The average time for all runs required per node × sweep[1] × iteration was 1.44×10^{-5} CP s.

Velocity and Temperature Distributions. Nondimensional longitudinal velocity and temperature distributions are given in Figs. 4 and 5 in the form of equal-value contours. The profiles shown in Fig. 4(a) are typical of the bulk of the results calculated at ϕ = 90 deg and illustrate clearly the important role played by secondary motions insofar as heat and momentum transport are concerned. The similarity between longitudinal velocity and temperature contours is evident, but not surprising, in view of the convective nature of the flow.

A further indication of the possible inaccuracies arising from the application of parabolic procedures to strongly curved flows is gleaned from a comparison between Figs. 4(a) and (b). These contain plots of calculated results which are significantly dissimilar. Thus the parabolic calculations show a velocity maximum displaced from the curved duct symmetry plane which contradicts the experimental evidence in [9]. Similar differences in regard to the temperature profiles are bound to arise and will be equally incorrect.

Calculations in ducts of different aspect ratio were performed and are briefly commented on here. For b/a = 3, the cross-stream motion and heat transfer were high at all walls, but localized mainly in the

[1] Two sweeps for velocity and temperature and three for pressure were usually sufficient per iteration. Under-relaxation factors were 0.5 for velocity and temperature and 0.2 for pressure.

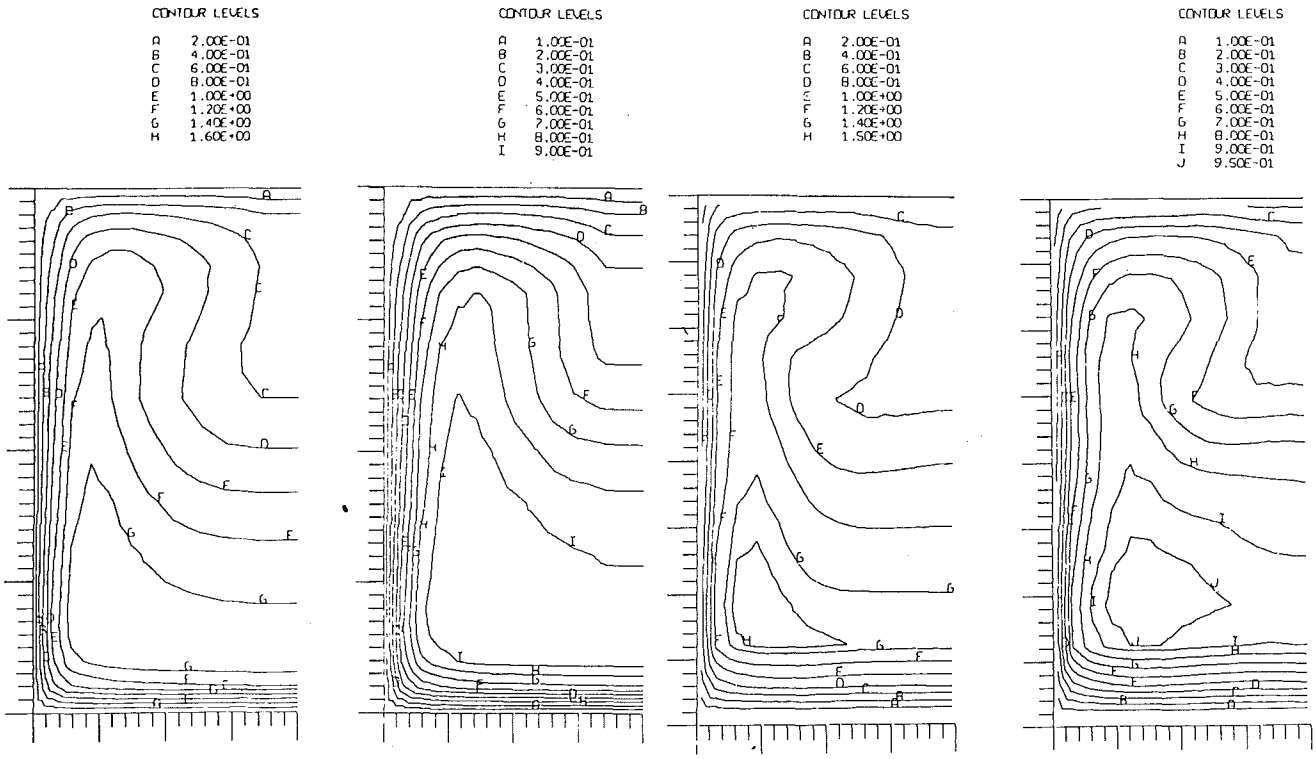

Fig. 4(*a*) Elliptic calculations

Fig. 4(*b*) Parabolic calculations

Fig. 4 Longitudinal velocity (v_ϕ/V_B) and temperature (θ) contours at ϕ = 90 deg for Case 1

region of the duct side wall. For $b/a = 1/3$, the cross-stream flow was intense along both the duct symmetry plane and side walls but, by comparison, was relatively weak at the inner- and outer-curvature walls. While longitudinal velocity and temperature contours showed distributions corresponding to the sense of the secondary motion, for $b/a = 1/3$ it is worth noting that the peak value of longitudinal velocity was displaced from the duct symmetry plane. A corresponding peak in the temperature distribution was not observed and is probably due to a relatively large contribution to heat transfer through conduction along the z axis. Similar calculations using a plug flow velocity entrance condition in a duct of $b/a = 1$ showed longitudinal velocity and temperature distributions slow to develop due to the small magnitude of the induced cross-stream flow. This was the cause for a net reduction in heat transfer relative to an equivalent flow with a parabolic velocity entrance condition.

Figure 5 shows temperature distributions at 90 deg for cases 7, 8 and 9 in Table 1 where only one of the two curved walls or both of the side walls were heated while keeping the remaining walls adiabatic. The fluid mechanics of these cases correspond to case 1, Fig. 4(a), but the manner in which the temperature fields evolve are strikingly different. In all cases the cross-stream flow scoops heated fluid from the vicinity of the hot wall and convects it in the sense of the secondary motion. It would appear however, that this is achieved most successfully when heat enters the duct through the outer curvature or side walls. The point that emerges clearly from the comparison is that heat transfer rates through the three types of walls present in curved duct flow can, and in general will, differ markedly depending on flow conditions, geometrical characteristics and fluid properties.

Pressure loss (C_p) and friction (C_f) coefficients corresponding to the various case studies were also calculated. Overall, C_p was found to decrease with increasing duct angle ϕ, decreasing De and decreasing b/a.

In all cases, the friction coefficient at the outer wall ($r = r_o$) increased (at least initially) with increasing duct angle. However, the rate of increase was largest for $b/a = 1$ and smallest for $b/a = 1/3$. High values of C_f at $r = r_o$ were initially favored by low values of De, but the reverse was true for $\phi \gtrsim 1.2$ radians. At the inner curvature wall, C_f appeared to be relatively insensitive to changes in De and for $\phi \gtrsim 0.7$ was largest for $b/a = 3$. The plug flow entrance profile case showed C_f decreasing at $r = r_o$ and increasing at $r = r_i$, respectively, and was due to the boundary layer growth occurring on these walls.

Variation of Temperature and Nusselt Number. Figure 6 shows the effects of duct aspect ratio and entrance profile conditions on Nusselt number and average temperature respectively. Also shown are the ϕ dependence of Nusselt number and average temperature for parabolic calculations corresponding to Case 1 in Table 1. In the plots the Nusselt number has been calculated from

$$\overline{\mathrm{Nu}} = \frac{\overline{h} D_H}{k} \tag{7}$$

where $\overline{h}$ is the (local) heat transfer coefficient averaged over the duct perimeter at a duct angle ϕ. Thus,

$$\overline{h} = \overline{q}/(T_w - \overline{T}) \tag{8}$$

where $\overline{q}$ is the (perimeter) averaged heat flux at the ϕ plane and T_w and $\overline{T}$ are the wall temperature and average flow temperatures, respectively, at the same longitudinal position.

In all cases except one (the plug flow entrance profile case), $\overline{\mathrm{Nu}}$ decreases with curved duct length until the cross-stream flow develops to a point where it significantly enhances heat transfer. The result is for a minimum in $\overline{\mathrm{Nu}}$ to appear at about 30 deg in the curved duct flows for Re = 790 and De = 368. Although not shown here, the minimum $\overline{\mathrm{Nu}}$ depends on the values of De and, in general, the values of $\overline{\mathrm{Nu}}$ and θ_B at a given bend angle ϕ were found to increase with De. Further discussion of this point is available in [19]. It may be concluded that, for certain conditions, short ducts with strong curvature and intense secondary motions can transfer heat as effectively as long ducts with mild curvature and weaker cross-stream flows. This conclusion is supported by total heat balance analyses performed for Cases 1 and 1A in Table 1. Thus, for conditions of equal arc length, 1.15 times more heat was transferred to the duct with higher De. From Fig. 6 it is also seen that $\overline{\mathrm{Nu}}$ is highest for $b/a = 1$ for $\phi \gtrsim 0.3$ radians. It would appear that initial heat transfer gains through increased surface area are eventually offset by reductions due to weaker cross-

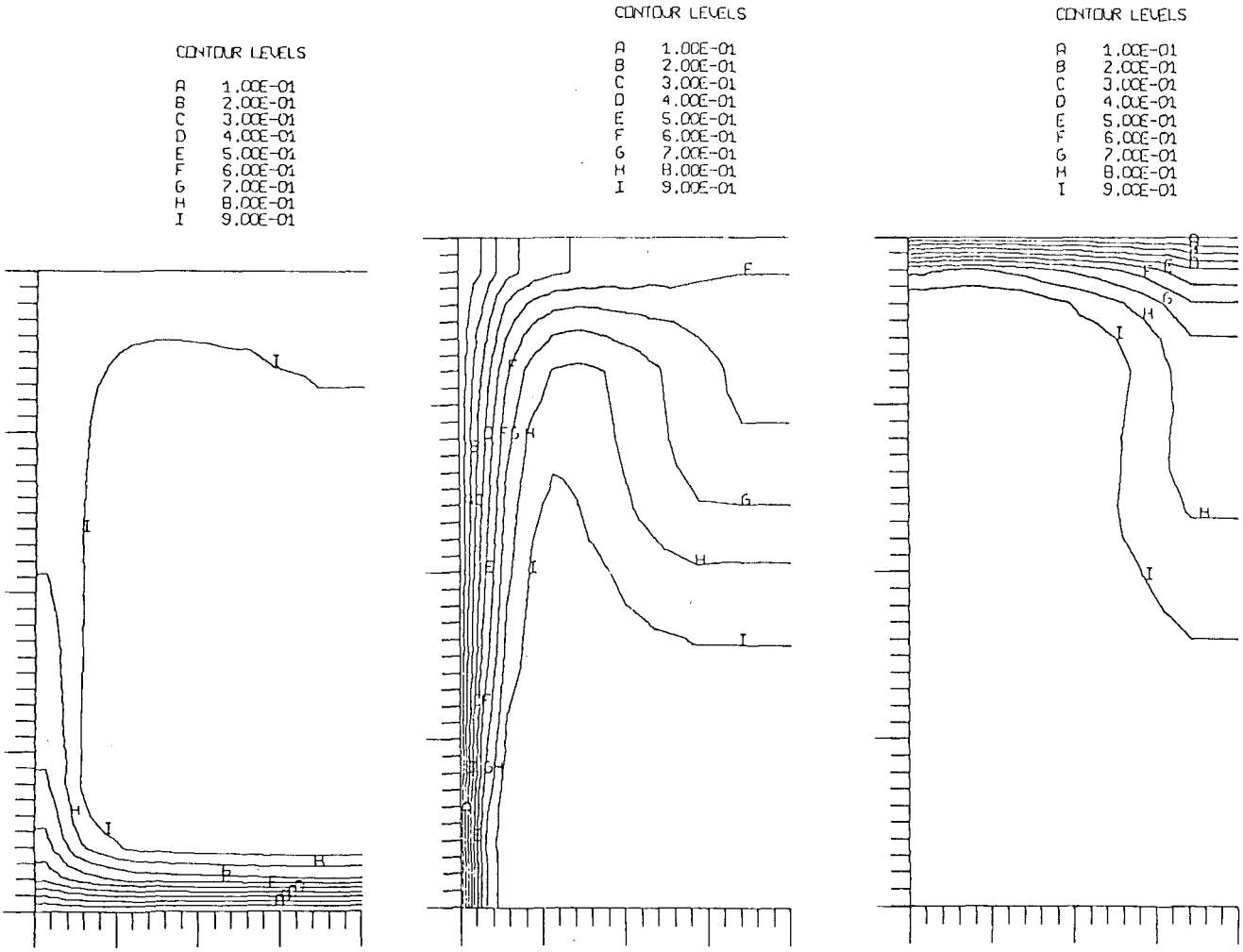

Fig. 5(*a*) Outer radius wall heated (Case 7)

Fig. 5(*b*) Side wall heated (Case 8)

Fig. 5(*c*) Inner radius wall heated (Case 9)

Fig. 5 Temperature (θ) contours at ϕ = 90 deg

stream flows for both $b/a = 3$ and $b/a = 1/3$. The plots indicate that temperature gradients at the other radius wall have a more pronounced effect on the rate of heat transfer than corresponding gradients at the inner wall. This is partly due to a surface effect, but also to the presence of higher gradients of velocity at the outer radius wall.

A relative comparison between parabolic and elliptically derived $\overline{Nu}$ and θ_B in Fig. 6 reflects the inaccuracy of the parabolic approach in the present flows. Thus, the parabolic approach leads to overpredicted values of θ_B, and $\overline{Nu}$ in most of the curved duct, due to a stronger (but incorrectly predicted) cross-stream flow.

In order to assess the relative contributions to heat transfer arising from separate duct walls during flow development, calculations were performed for the conditions corresponding to Cases 7, 8 and 9 in Table 1. Due to space considerations detailed results are not presented here, but are available in [18] and [19]. The results do indicate, however, that the highest rates of heat transfer occur through the side and outer radius walls in curved duct flow, due to the high values of secondary motion which arise at these locations. Energy balances for these three cases showed that total heat transferred through the outer radius wall was about 1.58 times larger than total heat transferred through the inner radius wall. In turn, total heat transferred through the side walls (allowing for the fact that there were two) was 1.02 times larger than the heat transferred through the outer radius wall.

Conclusions

Several conclusions may be derived from this study and are summarized below.

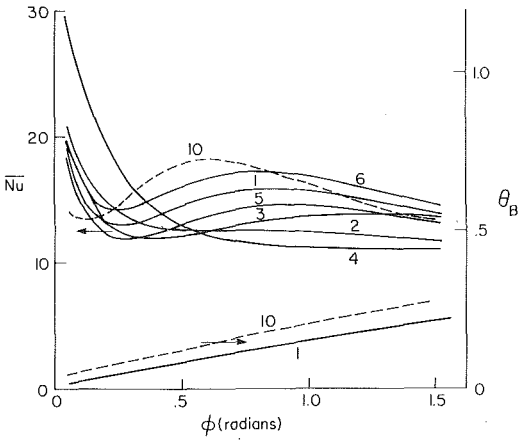

Fig. 6 Longitudinal variation of average Nusselt ($\overline{Nu}$) and temperature (θ_B). $b/a = 1/3$ (Case 3), $b/a = 1$ (Case 1), $b/a = 3$ (Case 2), entrance plug flow (Case 4), linear entrance temperature (Cases 5 and 6). Parabolic calculations (Case 10)

After an initial period of decreased heat transfer culminating in a minimum value at about 30 deg, developing cross-stream flows in curved ducts are responsible for significantly enhanced rates of heat transfer. Short ducts with intense secondary motions can be as effective in transferring heat as long ducts with weak cross-stream flows. High rates of heat transfer are favored by large De, $b/a \simeq 1$ and parabolic velocity entrance conditions. The highest rates of heat transfer

arise at outer curvature and side walls in developing curved duct flow.

Whereas elliptic schemes are presently costly in computer storage and calculation times, they are straightforward in application and deal directly with reversed flow regions when they arise. Parabolic schemes are numerically more exact, but must be modified to account for ellipticity in the pressure field of strongly curved duct flows. Neither parabolic nor semi-elliptic schemes can predict regions of reversed flow which may arise in curved ducts.

The present study is limited to heat transfer flows in which gravitational effects, and hence buoyancy, are absent. Such systems arise in, for example, spacecraft to which the results apply directly. In the presence of gravitation, buoyancy effects would make the curved duct flow structure orientation dependent and significantly alter the results presented.

Acknowledgments

The present study was made possible through NSF Grant No. ENG 78-27007 and through financial support provided by the Division of Materials Sciences, Office of Basic Energy Services, U. S. Department of Energy under contract number W-7405-ENG-48. We are grateful to Mr. R. Wylie for his help in providing the results corresponding to the parabolic flow case. Thanks are due to Ms. B. O'Hanlon for the typing of this manuscript.

References

1 Bradshaw, P., ed., "Turbulence," *Topics in Applied Physics,* 2nd ed., Vol. 12, Springer-Verlag, New York, 1978, pp. 118–123.

2 Humphrey, J. A. C., "Flow in Ducts with Curvature and Roughness," Ph.D. Thesis, University of London, 1977.

3 Ward-Smith, A. J., *Pressure Losses in Ducted Flows,* Butterworth, London, 1971.

4 Ito, H., "Friction Factors for Turbulent Flow in Curved Pipes," ASME, *Journal of Basic Engineering,* Vol. 11, 1959, p. 123.

5 Cheng, K. C. and Akiyama, M., "Laminar Forced Convection Heat Transfer in Curved Rectangular Channels," *International Journal of Heat Mass Transfer,* Vol. 13, 1970, p. 471.

6 Cheng, K. C., Lin, R. C. and Ou, J. W., "Graetz Problem in Curved Rectangular Channels with Convective Boundary Conditions—The Effect of Secondary Flow on Liquid Solidification—Free Zone," *International Journal of Heat Mass Transfer,* Vol. 18, 1975, p. 996.

7 Joseph, B., Smith, E. P., and Adler, R. J., "Numerical Treatment of Laminar Flow in Helically Coiled Tubes of Square Cross-Section," *AIChE Journal,* Vol. 21, No. 5, 1975, p. 965.

8 Ghia, K. N. and Sokhey, J. S., "Laminar Incompressible Viscous Flow in Curved Ducts of Rectangular Cross-Sections," ASME *Journal of Fluids Engineering* 1, Vol. 99, 1977, pp. 640–648.

9 Humphrey, J. A. C., Taylor, A. M. K., and Whitelaw, J. H., "Laminar Flow in a Square Duct of Strong Curvature," *Journal of Fluid Mechanics,* Vol. 83, Part 3, 1977, pp. 509–527.

10 Pratap, V. S. and Spalding, D. B., "Numerical Computation of the Flow in Curved Ducts," *Aeronautical Quarterly,* Vol. 26, 1975, p. 219.

11 Kreith, F., "The Influence of Curvature on Heat Transfer to Incompressible Fluids," *Trans. ASME,* Vol. 77, 1955, p. 1247.

12 Mori, Y., Uchida, Y., and Ukon, T., "Forced Convective Heat Transfer in a Curved Channel with a Square Cross-Section," *International Journal of Heat Mass Transfer,* Vol. 14, 1971, p. 1787.

13 Yang, J. W. and Liao, N., "Turbulent Heat Transfer in Rectangular Ducts with 180° Bend," *Proceedings of the 5th International Heat Transfer Conference,* JSME, 1974, p. 169.

14 Humphrey, J. A. C., Whitelaw, J. H., and Yee, G., "Turbulent Flow in a Square Duct with Strong Curvature," University of California, LBL Report No. 9650, 1979.

15 Humphrey, J. A.C., "Numerical Calculation of Developing Laminar Flow in Pipes of Arbitrary Curvature Radius," *Canadian Journal of Chemical Engineering,* Vol. 56, 1978, pp. 151–164.

16 Humphrey, J. A. C., "Numerical Calculation of Variable Property Flows in Curvilinear Orthogonal Coordinates," *Canadian Journal of Chemical Engineering,* Vol. 56, 1978, pp. 624–626.

17 Launder, B. E., ed., *Studies in Convection,* Vol. 1, Academic Press, New York, 1975, pp 1–78.

18 Yee, G., "Heat Transfer in Strongly Curved Duct Flow," Mechanical Engineering Project Report, University of California, Berkeley, 1979.

19 Yee, G. and Humphrey, J. A. C., "Developing Flow and Heat Transfer in Strongly Curved Ducts of Rectangular Cross-Section," University of California, LBL Report No. 9092, 1979.

Influence of Streamwise Molecular Heat Conduction on the Heat Transfer Coefficient for Liquid Metals in Turbulent Flow between Parallel Plates

S. Faggiani
Professor of Technical Physics,
Faculty of Engineering,
Pisa, Italy

Fabio Gori
Assistant Professor of Technical Physics,
Faculty of Engineering,
Florence, Italy

The energy equation for mechanically fully developed turbulent flow between parallel plates is numerically solved taking into account the term of streamwise heat conduction. Solutions are presented for Re = 7060 and 73620, and for Pr ranging from 0.001 to 0.1. Generally the influence of the streamwise molecular conduction results in a remarkable decrease of the Nusselt number in the thermal inlet.

Introduction

The problem of heat transfer and temperature distribution in mechanically fully developed turbulent flow between parallel plates was extensively studied in recent years. In particular, Hatton and Quarmby [1] examined the effect of the boundary conditions on the heat transfer coefficient; later, Hatton, et al. [2] extended the study to the influence of the turbulent Prandtl number. An analytical solution for the thermal entrance region in annuli was obtained by Chen and Yu [3] under the condition of a step-function wall heat flux. Different methods of solving the energy equation were employed by Leckner [4] in order to study the local heat transfer coefficient in the thermal inlet region. Finally the problem was analyzed by Sakakibara and Endoh (5) and by Shibani and Ozisik [6] under the condition of uniform wall temperature. In all the aforementioned studies, the case of liquid metals was included; however, the molecular heat conduction in axial direction, the importance of which has been qualitatively pointed out by Rohsenow in a recent conference [7], was always neglected. The streamwise turbulent heat transport was not taken into account either.

Regarding the last quantity, the experimental data reported by Hochreiter and Sesonke (8) showed that the streamwise eddy conduction decreased near the wall for decreasing Prandtl number. Conversely, in the remaining part of the pipe section it showed an opposite trend for the liquid metals. The experiments reported in [8] seemed to have been influenced by natural convection; then additional measurements in axial direction were considered necessary by the authors. Because of these uncertainties, only an order of magnitude estimate seems possible for the streamwise eddy conduction. Such an estimate has been performed under the hypothesis of isotropy for the eddy conduction (see Appendix C) and has led to the conclusion that the turbulent contribution in the streamwise direction is markedly smaller than the molecular contribution.

According to these considerations, in the present work the turbulent heat transport in the axial direction is not taken into account. Therefore, the objective of this work is to study the influence of the streamwise molecular conduction on the heat transfer coefficient in mechanically fully developed turbulent flow between parallel plates; however, it is plausible that the results of the present analysis can be employed beyond these rigorous limits.

Equations

Assuming that the fluid properties are constant and neglecting the turbulent heat transport in flow direction, the energy equation for the coordinate system of Fig. 1 can be written as:

$$\bar{u}\frac{\partial \overline{T}}{\partial x} = \beta\left(\frac{\partial^2 \overline{T}}{\partial x^2} + \frac{\partial^2 \overline{T}}{\partial y^2}\right) + \frac{\partial}{\partial y}\left(\epsilon_h \frac{\partial \overline{T}}{\partial y}\right) \tag{1}$$

If the lower wall for $-\infty \le x \le \infty$ and the upper one for $-\infty \le x \le 0$ are adiabatic, and the entering wall heat flux per unit area, G, is positive and constant for $0 \le x \le \infty$, equation (1) must be solved under the following conditions:

$$\frac{\partial \overline{T}}{\partial y} = 0 \quad \text{at } y = 0 \quad \text{and} \quad -\infty \le x \le \infty \tag{2}$$

$$\frac{\partial \overline{T}}{\partial y} = 0 \quad \text{at } y = 2L \quad \text{and} \quad x < 0 \tag{3}$$

$$\frac{\partial \overline{T}}{\partial y} = G/k \quad \text{at } y = 2L \quad \text{and} \quad x \ge 0 \tag{4}$$

$$\lim_{x \to -0}\left(\frac{\partial \overline{T}}{\partial x}\right) = \lim_{x \to +0}\left(\frac{\partial \overline{T}}{\partial x}\right) \quad \text{for } 0 \le y \le 2L \tag{5}$$

$$\lim_{x \to -0} \overline{T} = \lim_{x \to +0} \overline{T} \quad \text{for } 0 \le y \le 2L \tag{6}$$

$$\frac{\partial \overline{T}}{\partial x} = \frac{G}{2\rho c_p v_m L} \quad \text{for } x = \infty \tag{7}$$

$$\overline{T} = T_0 \quad \text{for } x = -\infty \tag{8}$$

being

$$v_m = \frac{1}{2L}\int_0^{2L} \bar{u}(y)dy. \tag{9}$$

Equation (1) with conditions (2–8) can be solved (see Appendices A and B) provided that the fully developed velocity profile, $\bar{u}(y)$, the momentum eddy diffusivity, ϵ_m, and the turbulent Prandtl number, $P_t = \epsilon_m/\epsilon_h$, are fixed.

About this topic a comprehensive critical analysis was done by

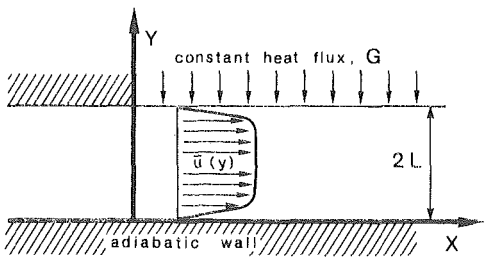

Fig. 1 Coordinate system

Contributed by the Heat Transfer Division for publication in the JOURNAL OF HEAT TRANSFER. Manuscript received by The Heat Transfer Division February 2, 1979.

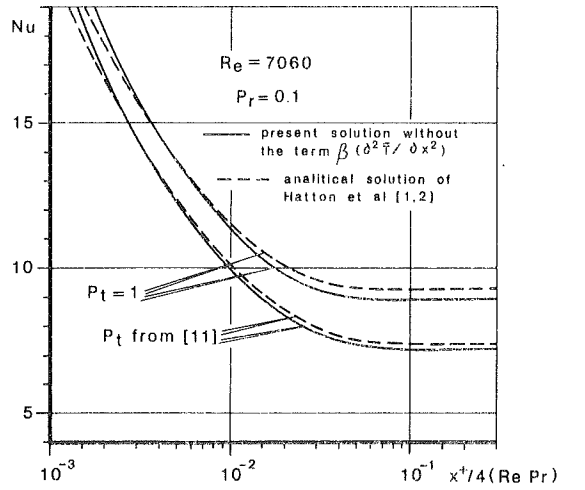

Fig. 2 Comparison of the present solution, obtained with $\beta(\partial^2\overline{T}/\partial x^2) = 0$, with the analytical solution of Hatton, et al. [1-2]

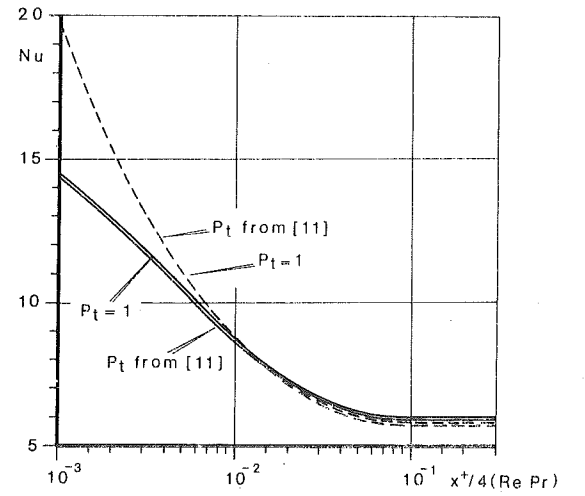

Fig. 3 Nu versus $x^+/4$ Re Pr for Re = 7060 and Pr = 0.002

Fuchs [9], on the basis of which the Reichardt's [10] expressions

$$u^+ = \frac{\overline{u}}{\sqrt{(\Sigma_w/\rho)}} = 2.5\ln(1+0.4y^+) + 2.5\ln\{1.5(1+\{1-y^+/L^+\})/(1+2\{1-y^+/L^+\}^2)\} + 7.8\{1 - \exp(-y^+/11) - y^+/11\exp(-0.33\,y^+)\} \quad (10)$$

$$\epsilon_m/\nu = 2.7\,10^{-5}(y^+)^5 \quad \text{for } y^+ \le 6$$

$$\epsilon_m/\nu = 0.4\{y^+ - 11\tanh(y^+/11)\} \quad \text{for } 6 < y^+ \le 50 \quad (11)$$

$$\epsilon_m/\nu = L^+\,0.4/3\{0.5 + (1-y^+/L^+)^2\}\{1-(1-y^+/L^+)^2\} \quad \text{for } y^+ \ge 50$$

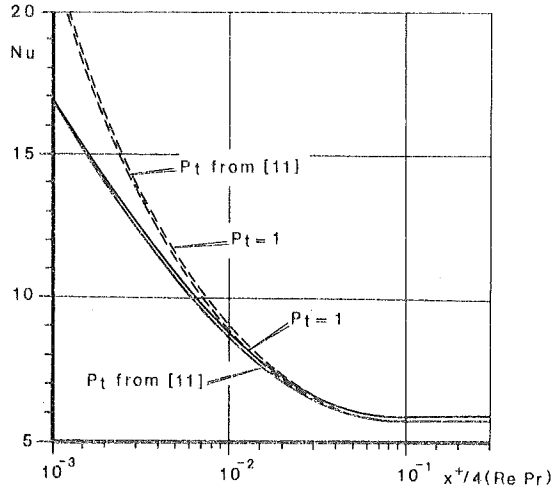

Fig. 4 Nu versus $x^+/4$ Re Pr for Re = 7060 and Pr = 0.005

have been selected for velocity and momentum eddy diffusivity. Briefly the reason of this choice is that the above expressions are in good agreement with experiments and also explicit: therefore, they do not introduce difficulties to numerical calculations. However, some results have been obtained on the basis of Mizushina's [11] velocity profile and compared with those based on Reichardt's expressions: for the trend of the Nusselt number in the thermal entrance region, i.e., the objective of this work, the differences are less than 2 percent.

Concerning the choice of P_t, in agreement with Blom's proposal [12], fully developed expressions have been assumed for the thermal entrance too. In fact, the recent measurements of Snijders, et al. [13], although in qualitative disagreement with those of Blom [12], did not suggest a different choice. As with $\overline{u}$ a check has been done for P_t using several expressions reported by Reynolds [14].

The conclusions of this check can be summarized as follows:

1 The trend of the local Nusselt number in the thermal inlet is negligibly influenced by the choice of P_t.

2 Concerning the employed expressions of P_t, the smallest values of Nu are those based on the P_t proposed by Azer and Chao [15], the largest ones on $P_t = 1$; the mean difference between the largest and smallest values of Nu is less than 5 percent for Pr = 0.01 and Re = 7060, and less than 14 percent for the same Pr and Re = 73620.

3 For Re = 7060 and Pr = 0.01 (Fig. 5), the fully developed Nu of this work are weakly influenced by the choice of P_t and in fairly good agreement with the experiments of Duchatelle and Vautray [16]; concerning Re = 73620 and Pr = 0.01 (Fig. 10), the experimental datum is comprised of the two results of the present investigation. (Aoki's expression [17] seems the best choice in this case.)

According to these conclusions, the results of the present work will be reported both for $P_t = 1$ and for the Azer-Chao expression:

$$P_t = \{1 + 380(\text{Re Pr})^{-0.58}\exp(-\{y^+/L^+\}^{0.25})\}/\{1 + 135\,\text{Re}^{-0.45}\exp(-\{y^+/L^+\}^{0.25})\} \quad (12)$$

Nomenclature

A = defined by equation (A13)
B = defined by equation (A20)
C = defined by equation (A21)
c_p = specific heat
D = defined by equation (A22)
E = defined by equation (A23)
F = defined by equation (A18)
G = wall heat per unit area
H = defined by equation (A17)
h = convective heat transfer coefficient
k = molecular thermal conductivity
L = half-height of the channel
L^+ = dimensionless half-height, defined by equation (A1)
$\text{Nu} = 4Lh/k$ = Nusselt number
$\text{Pr} = \nu/\beta$ = Prandtl number
$\text{Re} = 4L\upsilon_m/\nu$ = Reynolds number
P_t = turbulent Prandtl number
$\overline{T}$ = time-mean temperature
$\overline{u}$ = time-mean velocity
u^+ = dimensionless velocity, defined by equation (A1)
x, y = coordinates
x^+, y^+ = dimensionless coordinates, defined by equation (A1)
z^+ = dimensionless coordinate, defined by equation (A10)
β = thermal diffusivity
θ = dimensionless temperature, defined by equation (A1)
ϵ_h = heat eddy diffusivity
ϵ_m = momentum eddy diffusivity
Φ = defined by equation (A12)
η = defined by equation (A14)
ν = kinematic viscosity
ρ = density
Σ_w = wall shear stress

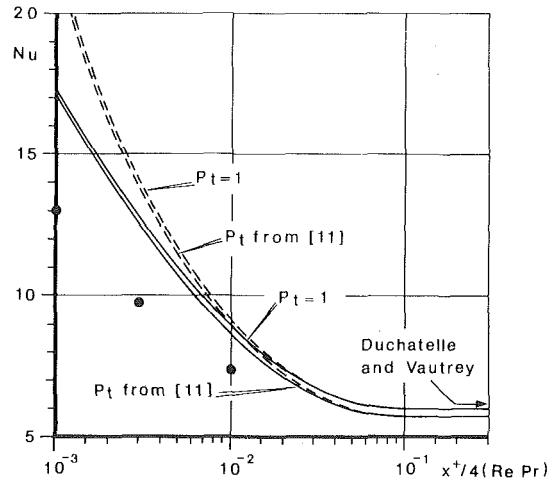

Fig. 5 Nu versus $x^+/4$ Re Pr for Re = 7060 and Pr= 0.01

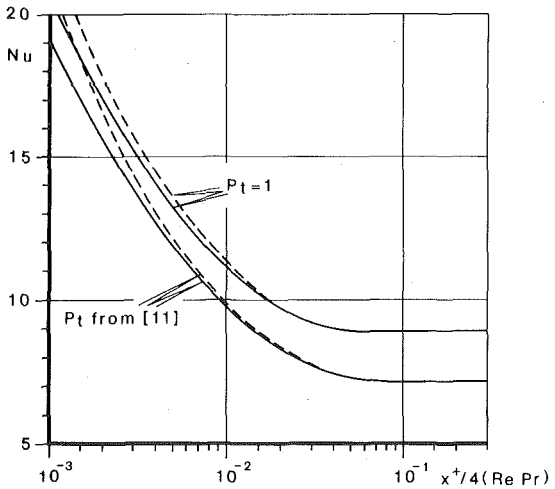

Fig. 6 Nu versus $x^+/4$ Re Pr for Re = 7060 and Pr = 0.1

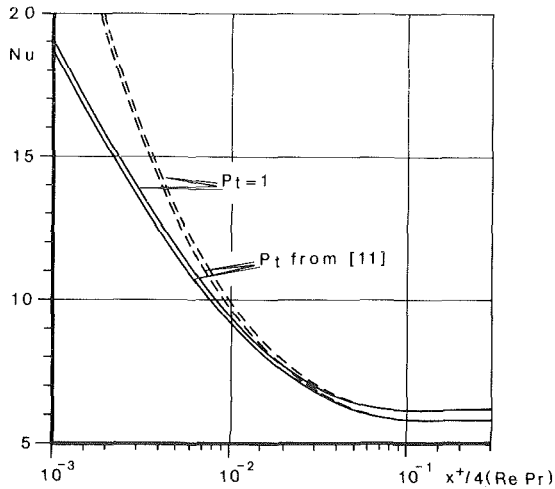

Fig. 7 Nu versus $x^+/4$ Re Pr for Re = 73620 and Pr = 0.001

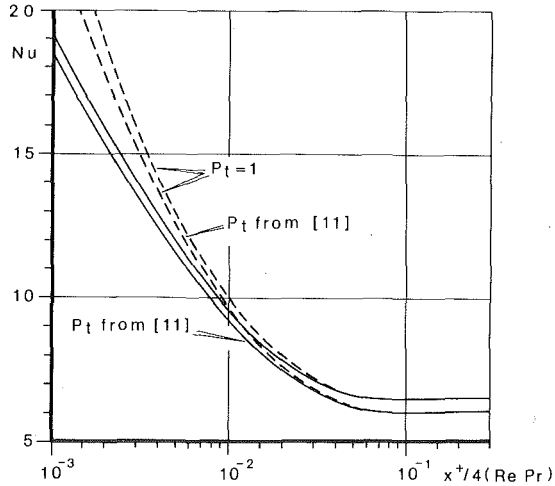

Fig. 8 Nu versus $x^+/4$ Re Pr for Re = 73620 and Pr = 0.002

Results and Conclusions

Equation (1) with conditions (2–8) have been solved numerically (see Appendices A and B) for two values of Re (7060 and 73620) and for Prandtl's numbers between 0.001 and 0.1. Additional solutions have been obtained putting $\beta(\partial^2\overline{T}/\partial x^2) = 0$ in order both to point out the effect of this term and to allow comparison with some analytical solutions [1–2]; consequently, a check of the numerical method of solution used in the present work. This comparison led to the conclusion that the aforementioned analytical solution and the results of this investigation are in agreement within 5 percent in the whole range of Re and Pr examined in this work. An example of this comparison is shown in Fig. 2.

The results of the numerical calculations are reported in Figs. 3–10. In particular Nu versus $x^+/4$ Re Pr is plotted for $P_t = 1$ and for the Azer-Chao expression in each figure; for the sake of comparison, the solution obtained without the term of streamwise heat conduction, $\beta(\partial^2\overline{T}/\partial x^2) = 0$, is reported too. Finally, in Figs. 5, 9, and 10, the arrows indicate the fully developed and the dots the thermal entry Nu from experiments of Duchatelle and Vautrey [12], whose experimental results were obtained for Pr = 0.01 − 0.02 and Pe = Re Pr = 70 − 1200. As shown in Figs. 5 and 10, the differences between predictions and experiments are reduced with the introduction of the streamwise molecular heat conduction.

The influence of the streamwise heat conduction is confined in the thermal entrance region, according to condition (7). It decreases with increasing Pr: for instance, the difference between the Nu obtained with the term of streamwise conduction (solid line) and that one without this term (dotted line) is larger than 27 percent for $x^+/4$ Re Pr = 10^{-3}, Re = 7060, and Pr = 0.002 (Fig. 3), larger than 10 percent for Pr = 0.1 and the same values of $x^+/4$ Re Pr and Re (Fig. 6). Comparison of Figs. 3, 4, 5 with Figs. 8, 9, 10, respectively, shows that this influence decreases with increasing Re as well.

Another interesting aspect of the influence of the streamwise conduction is evident in Fig. 3: The Nu obtained with the term $\beta(\partial^2\overline{T}/\partial x^2)$ is smaller than that obtained without this term for $x^+/4$ Re Pr $< 1.5\ 10^{-2}$, but becomes larger for $x^+/4$ Re Pr $> 1.5\ 10^{-2}$. This aspect, which vanishes with increasing Re and Pr, was pointed out by Hennecke [18] for the laminar flow.

Concluding, the most interesting results of the present investigation can be summarized as follows:

1 For small values of Pr and small or moderately large values of Re, the streamwise heat conduction has a remarkable influence on the Nusselt number in the thermal inlet region.

2 This influence results in a strong decrease of the Nu, excepting the case of very small Pr and Re, where the trend is like that previously found for the laminar flow.

3 From the engineering viewpoint the above influence is important for heat transfer to liquid metals, namely to fluids for which Pr ranges in the limits considered in this work.

References

1 Hatton, A. P., and Quarmby, A., "The Effect of Axially Varying and Unsymmetrical Boundary Conditions on Heat Transfer with Turbulent Flow Between Parallel Plates," *International Journal of Heat and Mass Transfer*, Vol. 6, 1963, pp. 903–914.

2 Hatton, A. P., Quarmby, A., and Grundy, I., "Further Calculations on the Heat Transfer with Turbulent Flow Between Parallel Plates," *International Journal of Heat and Mass Transfer*, Vol. 7, 1964, pp. 817–823.

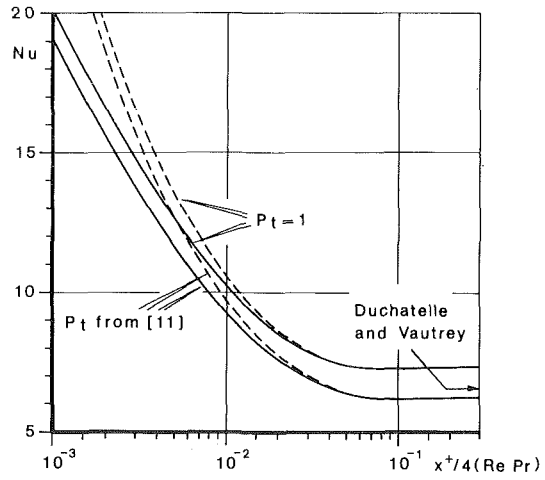

Fig. 9 Nu versus $x^+/4$ Re Pr for Re = 73620 and Pr = 0.005

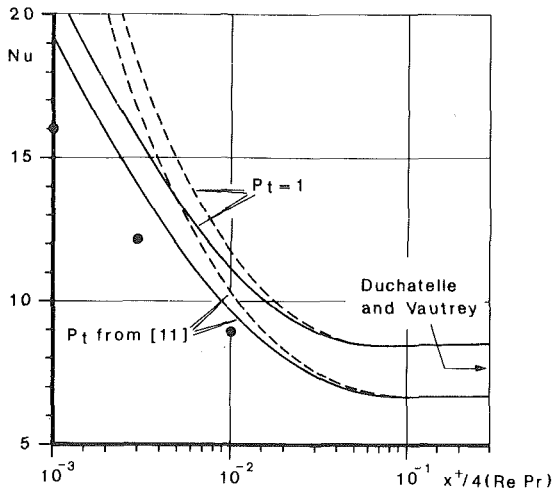

Fig. 10 Nu versus $x^+/4$ Re Pr for Re = 73620 and Pr = 0.01

3 Chen, J. C., and Yu, W. S., "Entrance Region and Variable Heat Flux Effects in Turbulent Heat Transfer to Liquid Metals Flowing in Concentric Annuli," *International Journal of Heat and Mass Transfer*, Vol. 13, 1970, pp. 667–680.

4 Leckner, B., "Heat Transfer in the Entrance Region with Fully Developed Turbulent Flow Between Parallel Plates," *International Journal of Heat and Mass Transfer*, Vol. 15, 1972, pp. 35–42.

5 Sakakibara, M., and Endoh, K., "Analysis of Heat Transfer in the Entrance Region with Fully Developed Turbulent Flow Between Parallel Plates," *Heat Transfer-Japanese Research*, 1976, pp. 54–61.

6 Shibani, A. A., and Özisik, M. N., "A Solution to Heat Transfer in Turbulent Flow Between Parallel Plates," *International Journal of Heat and Mass Transfer*, Vol. 20, 1977, pp. 565–573.

7 Rohsenow, W. M., "Heat Transfer in Turbulent Flow," Advanced Study Institute on Turbulent Forced Convection in Channels and Rod Bundles, Instanbul, Turkey, ASI Proc. Lec., 1978.

8 Hochreiter, L. E., and Sesonke, A., "Turbulent Structure of Isothermal and Nonisothermal Liquid Metal Pipe Flow," *International Journal of Heat and Mass Transfer*, Vol. 17, 1974, pp. 113–123.

9 Fuchs, H., "Heat Transfer to Flowing Sodium. Theoretical and Experimental Investigations on Temperature Profiles and Turbulent Temperature Fluctuations in a Tube," Eidg. Institut für Reaktorforschung Würelingen, Aug. 1973, Schweiz.

10 Reichardt, H., "Vollständige Darstellung der turbulenten Geschwindigkeisverteilung in glatten Leitungen," *Zeitschrift fuer Angewandte Mathematik und Mechanik*, Bd. 31, N. 7, July 1951, 208–219.

11 Mizushina, T., and Ogino, F., "Eddy Viscosity and Universal Velocity Profile in Turbulent Flow in a Straight Pipe," *Journal of Chemical Engineering of Japan*, Vol. 3, N. 2, 1970, pp. 166–170.

12 Blom, J., "An Experimental Determination of the Turbulent Prandtl Number in a Developing Boundary Layer," Ph.D. Thesis, Eindhoven University of Technology, Netherlands, 1970.

13 Snijders, A. L., Koppius, A. M., Nieuwelt, C., and deVries, D. A., "An Experimental Determination of the Turbulent Prandtl Number in the Inner Boundary Layer for Air Flow over a Flat Plate," International Heat Transfer Conference, Toronto, Canada, 1978, FC(a)-6, pp. 519–523.

14 Reynolds, A. J., "The Prediction of Turbulent Prandtl and Schmidt Numbers," *International Journal of Heat and Mass Transfer*, Vol. 18, 1975, pp. 1055–1069.

15 Azer, N. Z., and Chao, B. T., "A Mechanism of Turbulent Heat Transfer in Liquid Metals," *International Journal of Heat and Mass Transfer*, Vol. 1, 1960, pp. 121–138.

16 Duchatelle, L., and Vautrey, L., "Détermination des Coefficients de Convection d'un Alliage NaK en Ecoulement Turbulent entre Plaques Planes Parallèles," *International Journal of Heat and Mass Transfer*, Vol. 7, 1964, pp. 1017–1031.

17 Aoki, S., "A Consideration on the Heat Transfer in Liquid Metal," *Bulletin of the Tokyo Institute of Technology*, N. 54, 1963, pp. 63–73.

18 Hennecke, D. K., "Heat Transfer by Hagen-Poiseuille Flow in the Thermal Development Region with Axial Conduction," *Wärme-und Stoffübertragung*, Bd. 1, 1968, S. 177–184.

19 Vrentas, J. S., Duda, J. L., and Bargeron, K. G., "Effect of Axial Diffusion of Vorticity on Flow Development in Circular Conduits: Part I. Numerical Solutions," *AIChE Journal*, Vol. 12, N. 5, Sept. 1966, pp. 837–844.

20 de G. Allen, D. N., and Southwell, R. V., "Relaxation Methods Applied to Determine the Motion, in two Dimensions, of a Viscous Fluid past a Fixed Cylinder," *Quarterly Journal of Mechanics and Applied Mathematics*, Vol. VIII, Pt 2, 1955, pp. 129–145.

21 Schmidt, F. W., and Zeldin, B., "Laminar Heat Transfer in the Entrance Region of Ducts," *Applied Science Research*, 23, Oct. 1970, pp. 73–94.

22 Berezin, I. S., and Zhidkov, N. P., *Computing Methods*, Pergamon Press, 1965.

Appendix A

Introducing the dimensionless variables

$$x^+ = x/L;\ y^+ = y\frac{\sqrt{(\Sigma_w/\rho)}}{\nu};\ L^+ = L\frac{\sqrt{(\Sigma_w/\rho}}{\nu};$$

$$u^+ = \frac{u}{\sqrt{(\Sigma_w/\rho)}};\quad \theta = (\overline{T} - T_0)k/GL \tag{A1}$$

equation (1) and conditions (2–8) become:

$$u^+\frac{\partial\theta}{\partial x^+} = \frac{1}{L^+}\frac{\partial}{\partial x^+}\left\{\frac{1}{\mathrm{Pr}}\frac{\partial\theta}{\partial x^+}\right\} + L^+\frac{\partial}{\partial y^+}\left\{\left(\frac{\epsilon_h}{\nu} + \frac{1}{\mathrm{Pr}}\right)\frac{\partial\theta}{\partial y^+}\right\} \tag{A2}$$

$$\frac{\partial\theta}{\partial y^+} = 0 \quad \text{at } y^+ = 0 \quad \text{and} \quad -\infty \le x^+ \le \infty \tag{A3}$$

$$\frac{\partial\theta}{\partial y^+} = 0 \quad \text{at } y^+ = 2L \quad \text{and} \quad x^+ < 0 \tag{A4}$$

$$\frac{\partial\theta}{\partial y^+} = \frac{1}{L^+} \quad \text{at } y^+ = 2L \quad \text{and} \quad x^+ \ge 0 \tag{A5}$$

$$\lim_{x^+\to-0}\frac{\partial\theta}{\partial x^+} = \lim_{x^+\to+0}\frac{\partial\theta}{\partial x^+} \quad \text{for } 0 \le y^+ \le 2L^+ \tag{A6}$$

$$\lim_{x^+\to-0}\theta = \lim_{x^+\to+0}\theta \quad \text{for } 0 \le y^+ \le 2L^+ \tag{A7}$$

$$\frac{\partial\theta}{\partial x^+} = \frac{k}{2\rho c_p \upsilon_m L} = \frac{2}{\mathrm{Re\ Pr}} \quad \text{for } x^+ = \infty \tag{A8}$$

$$\theta = 0 \quad \text{for } x^+ = -\infty \tag{A9}$$

u^+ and ϵ_h/ν being defined by equations (10) and (11) and by the already discussed expressions of P_t.

According to Vrentas, et al. [19] the infinite interval $-\infty \le x^+ \le \infty$ can be transformed in the finite one $-1 \le z^+ \le 1$ by putting

$$z^+ = \tanh(mx^+) \tag{A10}$$

with m integer and positive. In this way equation (A2) is rewritten as:

$$\left(\frac{dz^+}{dx^+}\right)^2 \Phi + \eta = 0 \tag{A11}$$

with

$$\Phi = \frac{\partial^2\theta}{\partial z^{+2}} - \frac{\partial\theta}{\partial z^+}A \tag{A12}$$

$$A = \left(u^+L^+\,\mathrm{Pr}\frac{dz^+}{dx^+} - \frac{d^2z^+}{dx^{+2}}\right)\Big/\left(\frac{dz^+}{dx^+}\right)^2 \tag{A13}$$

$$\eta = L^{+2}\,\mathrm{Pr}\frac{\partial}{\partial y}\left\{\left(\frac{\epsilon_h}{\nu} + \frac{1}{\mathrm{Pr}}\right)\frac{\partial\theta}{\partial y^+}\right\} \tag{A14}$$

Following the finite difference technique first proposed by Allen and Southwell [20] and recently applied by Schmidt and Zeldin [21] to laminar flow, equation (A12) can be written with reference to the node i,j as follows:

$$\Phi = \frac{1}{\Delta z^{+2}} \frac{A\Delta z^+}{1 - \exp(-A\Delta z^+)} \{(\theta_{i-1,j} - \theta_{i,j}) + (\theta_{i+1,j} - \theta_{i,j}) \exp(-A\Delta z^+)\} \quad \text{(A15)}$$

Similarly equation (A14) leads to:

$$\eta = \Pr L^{+2} \frac{(\theta_{i,j+1} - \theta_{i,j})F(j,j-1) - (\theta_{i,j} - \theta_{i,j-1})F(j+1,j)}{H(j+1,j)F(j,j-1) - H(j,j-1)F(j+1,j)} \quad \text{(A16)}$$

being

$$H(j+1,j) = \int_j^{j+1} \frac{y^+}{\epsilon_h/\nu + 1/\Pr} dy^+ \quad \text{(A17)}$$

$$F(j+1,j) = \int_j^{j+1} \frac{dy^+}{\epsilon_h/\nu + 1/\Pr} \quad \text{(A18)}$$

and analogous expressions for $H(j,j-1)$ and $F(j,j-1)$. The integrals (A17) and (A18) can be numerically calculated by using an extension of the Simpson method reported by Berezin and Zhidkov [22].

Finally, substituting the expressions (A14) and (A15) in equation (A10), the following finite difference expression is obtained:

$$(B + C + D + E)\theta_{i,j} = B\theta_{i-1,j} + C\theta_{i+1,j} + D\theta_{i,j+1} + E\theta_{i,j-1} \quad \text{(A19)}$$

with

$$B = \left(\frac{dz^+}{dx^+}\right)^2 \frac{1}{\Delta z^{+2}} \frac{A\Delta z^+}{1 - \exp(-A\Delta z^+)} \quad \text{(A20)}$$

$$C = B \exp(-A\Delta z^+) \quad \text{(A21)}$$

$$D = \frac{L^{+2} \Pr F(j,j-1)}{H(j+1,j)F(j,j-1) - H(j,j-1)F(j+1,j)} \quad \text{(A22)}$$

$$E = D \frac{F(j+1,j)}{F(j,j-1)} \quad \text{(A23)}$$

Concerning the dimensionless mixing temperature, θ_m, and the local Nusselt number: Once determined, the temperature profile, θ, calculations have been carried out by means of the following definitions:

$$\theta_m = \frac{\int_0^{2L} \theta\bar{u}dy}{\int_0^{2L} \bar{u}dy} = \frac{\int_0^{2L^+} \theta u^+ dy^+}{\int_0^{2L^+} u^+ dy^+} = (T_m - T_0)k/GL \quad \text{(A24)}$$

$$\mathrm{Nu} = 4\,hL/k = 4\,LG/k(T_w - T_m) = 4/(\theta_w - \theta_m) \quad \text{(A25)}$$

where T_m, T_w, and θ_w are the mixing, the upper wall temperature, and the dimensionless upper wall temperature, respectively.

Appendix B

The region between the parallel plates has been divided using 60 subdivisions in both z^+ and y^+ directions. Constant intervals have been considered for z^+ because the transformation (A10), with an appropriate choice of m, insures a finer grid in the neighborhood of the inlet region. To verify the grid independence the constant m in (A10) has been changed within ten times in each series of calculations. In accordance with the proposal of Vrentas, et al. [19], the constant m has been selected to give the higher accuracy of the finite difference approximation: specifically, 2–3 percent for the results of this work. Conversely, for the y^+ direction, the following logarithmic subdivision has been used:

$$\frac{\exp\{n(1 - y^+/L^+)\} - 1}{\exp(n) - 1} = \frac{J - M}{1 - M}$$

J being the index and M the number of the grid points. For Re = 7060, $L^+ = 116$, and $n = 1$, the first grid point is $y^+ = 2.5$; while for Re = 73620 and $L^+ = 886$, the first point is $y^+ = 6$ with $n = 5$.

The finite difference equations have been solved according to a successive over-relaxation scheme by means of a 7600 CDC computer. In particular, the iterative process has been stopped when the maximum difference between two successive iterations was lower than 10^{-5}; in some cases 400 iterations were sufficient to reach the above maximum difference; in other cases, 1500 iterations have been necessary.

In conclusion, solutions of the differential equation (1) with conditions (2–8) have been considered to be the numerical solutions which satisfied both the above degree of convergence and the grid independence test.

Appendix C

If turbulent heat transport in a streamwise direction is taken into account, the term

$$\frac{1}{L^+} \frac{\partial}{\partial x^+} \left(\frac{1}{\Pr} \frac{\partial \theta}{\partial x^+}\right)$$

of equation (A2) must be substituted by

$$\frac{1}{L^+} \frac{\partial}{\partial x^+} \left\{\left(\frac{\epsilon'_h}{\nu} + \frac{1}{\Pr}\right) \frac{\partial \theta}{\partial x^+}\right\}$$

ϵ'_h being the eddy conduction in the axial direction. As has already been pointed out, the scarcety of information and some uncertainties do not allow the use of an appropriate expression for ϵ'_h; however, a rough estimate of the influence of this quantity can be obtained by assuming the hypothesis of isotropy and $P_t = 1$, and consequently by employing for ϵ'_h the expression chosen for ϵ_h, i.e., Reichardt's expressions. Accepting such an hypothesis, it can be seen that:

$$(\epsilon'_h/\nu)_{\max} = (\epsilon_h/\nu)_{\max} = 8.7 \quad \text{for Re} = 7060$$

while 1/Pr = 500; 200; 100
for the first three values of Pr, respectively; and

$$(\epsilon'_h/\nu)_{\max} = (\epsilon_h/\nu)_{\max} = 66 \quad \text{for Re} = 73620$$

while 1/Pr = 1000; 500
for the first two values of Pr corresponding to Re = 73620. Then neglecting the eddy conductivity seems reasonable in these five cases. Furthermore, for Re = 7060 and Pr = 0.1, and for Re = 73620 and Pr = 0.01, equation (A2) with the term ϵ'_h and $P_t = 1$ has been numerically solved by means of the aforementioned method. This additional computation has led to the conclusions that the influence of ϵ'_h on the Nusselt number is less than 0.1 percent.

T. C. Chawla
Reactor Analysis and Safety Division,
Argonne National Laboratory,
Argonne, Ill. 60439

S. H. Chan
Department of Mechanical Engineering,
University of Wisconsin—Milwaukee,
Milwaukee, Wisc. 53201

Combined Radiation Convection in Thermally Developing Poiseuille Flow with Scattering

The solution for thermally developing Poiseuille flow with scattering is obtained by using the method of collocation. The results show that scattering tends to decrease radiation component without affecting the convective component at low optical thicknesses. For moderate to high values of optical thicknesses, both the convective and radiation components are reduced. The relative effect of scattering both on convective and radiation Nusselt numbers appears to be unaffected by a change in the surface emissivity. A significant feature of combined radiation-convection in thermally developing flows appears to be that the total Nusselt number increases downstream of position of minimum rather than approaching an asymptotic value as is the case with corresponding pure convection. Another departure in the behavior appears to be the lack of existence of similarity in the temperature profiles, particularly at low values of conduction-radiation parameter.

Introduction

A number of analyses of channel flows with combined radiation convection modes of heat transfer have been performed [1–17]. A significant number among these analyses [2–9] have assumed fully developed temperature distribution which reduces the partial integro-differential equation to an ordinary integro-differential equation. This equation is identical in appearance to that for the combined radiation-conduction problem for the same geometry, except for the presence of a source term (as a function of local and bulk mean temperatures). Therefore, the equation can be solved by the same techniques as used for combined radiation-conduction problems. This assumption of fully developed temperature profile to simplify the problem has been carried over from channel flows with heat transfer by convection mode only. However, recently Lii and Ozisik [1] have shown that the thermally fully developed state for the slug flow between the parallel plates does not occur for the cases when the radiation effects are strong. Similar findings, particularly regarding the existence of a fully developed temperature profile, have been reported in analyses by Liu and Thorsen [11] and by Pearce and Emery [12]. Recently Balakrishnan and Edwards [10] compared their results for radiation and total Nusselt numbers at large distances from entry to the results of Wassel and Edwards [9] for thermally and hydrodynamically established turbulent flow in a pipe. These authors found that maximum errors in these Nusselt numbers were 2.2 percent and 7 percent, respectively, corresponding to radiation-to-conduction ratio of 10. It is clear that not all of the authors agree on the validity of the assumption of fully developed temperature profile. It is, therefore, one of the objectives of this paper to provide an appraisal of this assumption by comparing the temperature profiles at various axial locations for a variety of conditions of interest.

In addition, both Lii and Ozisik [1] and Kurosaki [14] have found that total Nusselt numbers increase downstream of the position of minimum rather than approach in asymptotic value as is the case with corresponding pure convection. However, in the study by Balakrishnan and Edwards [10] for nongray gases in thermally developing laminar and turbulent flows contrary to these studies, does not show the same trend. In the present analysis we make an attempt to resolve this controversy.

When the effect of scattering by participating flow is included, the solution of the resulting heat transfer problem becomes extremely complicated due to the presence of the additional integral equation which must be solved simultaneously with the nonlinear partial differential equation. To date, the only solutions [1, 13] which have been presented deal with the case of slug flow between parallel plates. The second objective of the present paper is to obtain the solution including the effect of scattering for the case of thermally developing laminar or Poiseuille flow between the parallel plates using spline collocation method [18].

Statement of Problem

Consider thermally developing flow of an absorbing, emitting, isotopically scattering, gray, and incompressible constant-property fluid between two parallel infinite plates. The bounding surfaces are opaque, gray, diffuse, and at a distance L apart. Figure 1 shows the geometry and coordinate system used. The governing equations in nondimensional form can be given as [19]

$$u(\eta)\frac{\partial\Theta}{\partial\xi} = \frac{\partial^2\Theta}{\partial\eta^2} - \frac{1}{4N}\frac{\partial q_R^*}{\partial\eta} \tag{1}$$

where

$$q_R^* = 2\chi_1 E_3(\eta) - 2\chi_2 E_3(\eta_0 - \eta) + 2\int_0^\eta \left[(1-\omega_0)\Theta^4(\eta') + \frac{\omega_0}{4}\Phi(\eta')\right] E_2(\eta-\eta')d\eta' - 2\int_\eta^{\eta_0}\left[(1-\omega_0)\Theta^4(\eta') + \frac{\omega_0}{4}\Phi(\eta')\right] E_2(\eta'-\eta)d\eta' \tag{2}$$

$$-\frac{\partial q_R^*}{\partial\eta} = (1-\omega_0)[\Phi(\eta) - 4\Theta^4(\eta)] \tag{3}$$

$$\chi_1 = \epsilon_1\Theta_1^4 + 2(1-\epsilon_1)\left\{\chi_2 E_3(\eta_0) + \int_0^{\eta_0}\left[(1-\omega_0)\Theta^4(\eta') + \frac{\omega_0}{4}\Phi(\eta')\right] E_2(\eta')d\eta'\right\} \tag{4}$$

$$\chi_2 = \epsilon_2\Theta_2^4 + 2(1-\epsilon_2)\left\{\chi_1 E_3(\eta_0) + \int_0^{\eta_0}\left[(1-\omega_0)\Theta^4(\eta') + \frac{\omega_0}{4}\Phi(\eta')\right] E_2(\eta_0-\eta')d\eta'\right\} \tag{5}$$

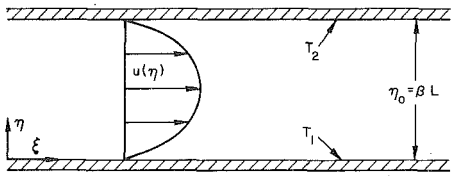

Fig. 1 Coordinate system for thermally developing flow in a parallel plate channel

Contributed by the Heat Transfer Division for publication in The JOURNAL OF HEAT TRANSFER. Manuscript received by The Heat Transfer Division August 25, 1979.

$$\Phi(\eta) = 2\chi_1 E_2(\eta) + 2\chi_2 E_2(\eta_0 - \eta) + 2\int_0^{\eta_0}\left[(1-\omega_0)\Theta^4(\eta') + \frac{\omega_0}{4}\Phi(\eta')\right] E_1(|\eta - \eta'|)d\eta' \quad (6)$$

The definition of the other symbols used is given in the Nomenclature. Substituting equation (3) into equation (1), we obtain

$$u(\eta)\frac{\partial\Theta}{\partial\xi} = \frac{\partial^2\Theta}{\partial\eta^2} - \frac{(1-\omega_0)}{N}\left[\Theta^4(\eta) - \frac{1}{4}\Phi(\eta)\right] \quad (7)$$

The boundary conditions on equation (7) with symmetry about the axis are given as:

$$\Theta(0, \xi) = \Theta_1 = \Theta_w, \quad \Theta(\eta_0, \xi) = \Theta_2 = \Theta_w \text{ for } \xi > 0 \quad (8)$$

$$\Theta(\eta, 0) = \Theta_0 \text{ for } 0 < \eta < \eta_0. \quad (9)$$

The solution of equations (7) and (6) is obtained by the spline collocation method which is described in detail in reference [18].

Heat Transfer Parameters

The heat transfer parameters of interest are the radiative q_{rw}* and the convective q_{cw}* components of the total heat flux at the wall and the corresponding Nusselt numbers. The radiation heat flux q_{rw}* is obtained from equations (2, 8), and (5) and the following symmetry conditions about the axis

$$\epsilon_1 = \epsilon_2 = \epsilon, \quad \chi_1 = \chi_2 = \chi_w, \quad \Theta_1 = \Theta_2 = \Theta_w \quad (10)$$

$$q_{rw}^* = R_0 + \omega_0\left[(1-\epsilon)R_2 - \frac{1}{2}\right] I_0 \quad (11)$$

where

$$R_0 = 2R_2[\epsilon\Theta_w^4 + 2(1-\omega_0)(1-\epsilon)I_2] - 2(1-\omega_0)I_2 \quad (12)$$

$$I_0 = \int_0^{\eta_0}\Phi(\eta')E_2(\eta')d\eta', \quad R_2 = [E_3(0) - E_3(\eta_0)]/\Lambda \quad (13)$$

The Nusselt number is defined as

$$\mathrm{Nu} = \frac{q_w D_h}{K(T_w - T_b)} = \frac{\eta_0 q_w^*}{2N(\Theta_w - \Theta_b)} \quad (14)$$

$$\mathrm{Nu} = \frac{\eta_0}{2N(\Theta_w - \Theta_b)}\left[-4N\frac{\partial\Theta}{\partial\eta} + q_r^*\right]_{\eta=0} = \mathrm{Nu}_C + \mathrm{Nu}_R \quad (15)$$

Approximate Expressions. For the purpose of establishing the behavior of radiation heat flux at small and large distances from the channel entrance, an approximate expression can be obtained by postulating that the whole fluid in the duct radiates at the bulk mean temperature Θ_b and that the effect of scattering is small and $\epsilon \simeq 1$. We may note that the temperature distribution is approximately uniform in the bulk of the fluid both near the entry and at distances far off from the entry, therefore there exists some basis for representing the fluid temperature by its bulk mean temperature. A number of other investigators have made similar assumptions to arrive at approximate expressions for the radiation heat flux. For example, Viskanta [2] has used the mean of temperature distribution to the fourth power, the use of bulk mean temperature has previously been made by Kurosaki [14]. If the wall temperature is chosen as the reference temperature for nondimensionalizing, that is $\Theta_w = 1$, it can easily be shown that equation (11) reduces to

$$q_{rw}^* = 2[E_3(0) - E_3(\eta_0)][1 - \Theta_b^4] \quad (16)$$

The use of the above expression into the definition (14) of Nusselt number gives

$$\mathrm{Nu}_R = \frac{1}{N}[E_3(0) - E_3(\eta_0)][1 + \Theta_b + \Theta_b^2 + \Theta_b^3] \quad (17)$$

Computational Results

The results of computation are presented in Tables 1–3 and in Figs. 2–5. Tables 1–3 give the results for total Nusselt numbers and individual components due to radiation and convection; these tables also show the corresponding component heat fluxes. Each of these tables also contains results for $\omega_0 = 1$ which represents pure scattering and the energy equation is uncoupled from radiation. Consequently, the solution of energy equation corresponds to $N \to \infty$. We may, however, note that the Nusselt number for the case of $\omega_0 = 1$ is not a function of η_0, but is a function of ζ only. In each of the tables, the values of N were varied from $N = 0.01$ to $N = 0.5$ with a choice of two values of ϵ, namely $\epsilon = 1.0$ and $\epsilon = 0.5$, and with ω_0 varied from zero to 1. Table 1 gives the results for $\eta_0 = 0.2$, Table 2 for $\eta_0 = 2.0$ and Table 3 for $\eta_0 = 10$.

The results corresponding to $N \to 0$ are given in Ref. 20 and no discussion of these will be given here.

Table 1 shows that at small values of η_0, i.e., optically thin fluids, the contribution of radiation to the total Nusselt number is small and decreases as the value of N increases. This latter behavior is qualitatively well represented by equation (17) which shows an inverse relationship with N. This equation also shows that radiation Nusselt number decreases with decreasing η_0. We must, however, caution against the use of this equation for quantitative predictions as it represents a very crude approximation to the radiation Nusselt number. At low values of η_0, the coupling between radiation and convection mode is very weak implying the convective components is nearly equal to the Nusselt number corresponding to the uncoupled case, i.e., $\omega_0 = 1$. However, as η_0 increases, the coupling appears to increase and the convective component decreases, relative to the uncoupled case as can be seen in Tables 2 and 3. As expected the coupling also increases as N decreases. For each of the cases studied, the effect of scattering is to decrease the radiation component significantly as ω_0 increases; on the other hand, the convective component remains approximately unaffected near the entry region as can be seen in Table 2 and 3. However, as the distance from entry in-

Nomenclature

C_p = specific heat at constant pressure
$D_h = 2L$, hydraulic diameter
$E_n(\eta)$ = nth exponential integral
$I_2 = \int_0^{\eta_0}\Theta^4(\eta')E_2(\eta')d\eta'$
K = thermal conductivity of fluid
L = distance between parallel plates
$N = K\beta/(4\sigma T_r^3)$, conduction-radiation parameter
$\mathrm{Nu} = q_w D_h/K(T_w - T_b)$, Nusselt number
q = heat flux
$q^* = q/\sigma T_r^4$, nondimensional heat flux
$\mathrm{Pr} = C_p\mu/K$, Prandtl number
$\mathrm{Re} = \rho U_m D_h/\mu$, Reynolds number
T = absolute temperature
$T_b = \int_0^L U(y)T(y)dy \Big/ \int_0^L U(y)dy$, bulk mean temperature
T_r = arbitrary reference temperature
$U(y)$ = local velocity
U_m = average velocity
$u(\eta) = U(y)/U_m = 6[\eta/\eta_0 - (\eta/\eta_0)^2]$
x = axial distance along the length of channel
$\beta = \kappa + \gamma$, extinction coefficient
γ = scattering coefficient
ϵ = emissivity of a surface
$\eta = \beta y$, optical variable
$\eta_0 = \beta L$, optical thickness
$\Theta(\eta) = T/T_r$, dimensionless temperature
Θ_0 = dimensionless temperature at $\xi = 0$
Θ_b = nondimensional bulk mean temperature
κ = absorption coefficient
μ = dynamic viscosity of fluid
$\xi = K\beta^2 x/(\rho C_p U_m) = 4\eta_0^2(x/D_h)/R_e\mathrm{Pr}$,
$\Phi(\eta)$ = dimensionless function defined by equation (6)
χ = dimensionless radiosity
$\Lambda = 1 - 2(1-\epsilon)E_3(\eta_0)$
ω_0 = albedo of scattering
$\zeta = \xi/4\eta_0^2 = (x/D_h)/\mathrm{RePr}$

Subscripts

C, c = pertaining to convection
R, r = pertaining to radiation
w = pertaining to wall

Table 1 The effect of scattering, emissivity and of conduction-radiation parameter on heat transfer in laminar flow at various axial locations along the length of a channel corresponding to $\eta_0 = 0.2$

			ξ								
			5×10^{-5}			1×10^{-3}			1×10^{-2}		
N	ε	ω_0	Nu_R (q^*_{rw})	Nu_c (q^*_{cw})	Nu	Nu_R (q^*_{rw})	Nu_C (q^*_{cw})	Nu	Nu_R (q^*_{rw})	Nu_C (q^*_{cw})	Nu
0.01	1.0	0	2.9243	18.1540		3.5458	7.7636		9.1000	7.3441	
			(0.2817)	(1.7485)	21.0783	(0.2510)	(0.5495)	11.3093	(0.0268)	(0.0217)	16.4441
		0.65	1.1233	18.2677		1.4537	7.9937		3.5895	7.3232	
			(0.1188)	(1.7630)	19.4990	(0.1073)	(0.5901)	9.4474	(0.0279)	(0.0569)	10.9127
		1.0									
			(0.0)	(1.7743)	18.3582	(0.0)	(0.6228)	8.1929	(0.0)	(0.1042)	7.5407
	0.5	0	2.2549	18.2296		2.7080	7.9485		6.9384	7.8447	
			(0.2174)	(1.7571)	20.4845	(0.1946)	(0.5711)	10.6565	(0.0279)	(0.0316)	14.7831
		0.5	1.4357	18.2631		1.7010	7.9930		4.2452	7.4661	
			(0.1385)	(1.7621)	19.6988	(0.1249)	(0.5868)	9.6940	(0.0289)	(0.0509)	11.7113
0.1	1.0	0	0.2917	18.3377		0.3384	8.1493		0.7940	7.5096	
			(0.2818)	(17.717)	18.6294	(0.2554)	(6.1524)	8.4877	(0.0964)	(0.9114)	8.3036
		0.65	0.1230	18.3491		0.1426	8.1727		0.3318	7.5174	
			(0.1189)	(17.731)	18.4721	(0.1081)	(6.1950)	8.3152	(0.0435)	(0.9851)	7.8492
	0.5	0	0.2251	18.3453		0.2608	8.1675		0.6101	7.5555	
			(0.2175)	(17.725)	18.5703	(0.1972)	(6.1750)	8.4283	(0.0759)	(0.9396)	8.1656
		0.65	0.1094	18.3507		0.1267	8.1765		0.2947	7.5272	
			(0.1057)	(17.733)	18.4600	(0.0961)	(6.1998)	8.3032	(0.0388)	(0.9914)	7.8219
0.5	1.0	0	0.0583	18.3541		0.0674	8.1842		0.1557	7.5339	
			(0.2819)	(88.687)	18.4124	(0.2558)	(31.066)	8.2516	(0.1049)	(5.0743)	7.6896
		0.65	0.0246	18.3564		0.0285	8.1888		0.0658	7.5368	
			(0.1189)	(88.702)	18.3810	(0.1081)	(31.108)	8.2172	(0.0450)	(5.1526)	7.6026
	0.5	0	0.0450	18.3556		0.0520	8.1877		0.1200	7.5441	
			(0.2175)	(88.696)	18.4006	(0.1974)	(31.088)	8.2396	(0.0812)	(5.1051	7.6641
		0.35	0.0344	18.3560		0.0398	8.1883		0.0920	7.5392	
			(0.1664)	(88.699)	18.3905	(0.1513)	(31.099)	8.2281	(0.0626)	(5.1290)	7.6312

Table 2 The effect of scattering emissivity and of conduction-radiation parameter on heat transfer in laminar flow at various axial locations along the length of the channel corresponding to $\eta = 2.0$

			ξ											
			5×10^{-4}			1.7×10^{-2}			7.5×10^{-2}			5×10^{-1}		
N	ε	ω_0	Nu_R (q^*_{rw})	Nu_C (q^*_{cw})	Nu	Nu_R (q^*_{rw})	Nu_C (q^*_{cw})	Nu	Nu_R (q^*_{rw})	Nu_C (q^*_{cw})	Nu	Nu_R (q^*_{rw})	Nu_C (q^*_{cw})	Nu
0.01	1.0	0	91.0227	35.1323		108.3816	12.5372		258.8502	27.1356				
			(0.8937)	(0.3449)	126.1550	(0.6698)	(0.0775)	120.9187	(0.0784)	(0.0082)	285.9858			
		0.35	80.3893	35.5244		95.7876	10.1306		220.3061	19.7468				
			(0.7903)	(0.3492)	115.9138	(0.6229)	(0.0659)	105.9182	(0.1195)	(0.0107)	240.0529			
		0.65	62.9454	36.3293		73.9548	8.4215		151.9194	11.0586				
			(0.6201)	(0.3579)	99.2747	(0.5220)	(0.0594)	82.3762	(0.1941)	(0.0141)	162.9780			
		1.0												
				(0.3871)	38.9934		(0.1165)	12.5945		(0.0691)	8.6249		(0.0267)	7.5415
	0.5	0	46.8842	39.5080		53.2029	18.6333		118.6515	36.8720				
			(0.4227)	(0.3899)	86.3923	(0.3933)	(0.1378)	71.8362	(0.1838)	(0.0571)	155.5235			
		0.65	38.2953	38.1617		43.0596	12.3321		77.9556	15.8528				
			(0.3784)	(0.3771)	76.4570	(0.3367)	(0.0964)	55.3917	(0.2173)	(0.0442)	93.8084			
0.1	1.0	0	9.0636	38.5617		9.0143	11.7570		10.2726	7.9753		24.3608	11.2641	
			(0.8988)	(3.8239)	47.6253	(0.8051)	(1.0500)	20.7713	(0.6994)	(0.5430)	18.2479	(0.0901)	(0.0416)	35.6249
		0.35	7.9995	38.6219		8.0563	11.7918		9.2216	7.8108		21.6512	9.6201	
			(0.7934)	(3.8303)	46.6214	(0.7224)	(1.0573)	19.8482	(0.6400)	(0.5421)	17.0324	(0.1152)	(0.0512)	31.2713
		0.65	6.2651	38.7182		6.3766	11.9343		7.2876	7.8098		16.6160	7.9666	
			(0.6215)	(3.8407)	44.9834	(0.5755)	(1.0771)	18.3108	(0.5219)	(0.5593)	15.0974	(0.1505)	(0.0722)	24.5825
	0.5	0	4.6721	39.0329		4.6267	12.8491		5.1727	9.3959		12.0830	13.9247	
			(0.4635)	(3.8725)	43.7049	(0.4193)	(1.1645)	17.4758	(0.3756)	(0.6822)	14.5686	(0.1058)	(0.1220)	26.0078
		0.65	3.8174	38.9057		3.8661	12.4267		4.3456	8.5302		9.4918	9.3705	
			(0.3788)	(3.8604)	42.7232	(0.3520)	(1.1315)	16.2928	(0.3237)	(0.6353)	12.8758	(0.1387)	(0.1370)	18.8623
0.5	1.0	0	1.8120	38.9064		1.7774	12.4096		1.9103	8.4260		3.4607	7.8419	
			(0.8992)	(19.307)	40.7184	(0.8162)	(5.6990)	14.1870	(0.7421)	(3.2734)	10.3363	(0.4481)	(1.0154)	11.3025
		0.35	1.5992	38.9188		1.5878	12.4247		1.7207	8.4228		5.1325	7.6306	
			(0.7936)	(19.314)	40.5180	(0.7297)	(5.7103)	14.0125	(0.6708)	(3.2832)	10.1435	(0.4226)	(1.0293)	10.7632
		0.65	1.2525	38.9382		1.2586	1.2459		1.3741	8.4480		2.4986	7.4638	
			(0.6216)	(19.324)	40.1907	(0.5792)	(5.7335)	13.7179	(0.5387)	(3.3119)	9.8221	(0.3592)	(1.0729)	9.9624
	0.5	0	0.9341	39.0011		0.9154	12.6377		0.9803	8.7399		1.7326	8.3873	
			(0.4636)	(19.356)	39.9352	(0.4216)	(5.8204)	13.5531	(0.3853)	(3.4355)	9.7201	(0.2492)	(1.2064)	10.1199
		0.65	0.7635	38.9758		0.7662	12.5587		0.8337	8.5942		1.4868	7.7450	
			(0.3788)	(19.344)	39.7391	(0.3532)	(5.7893)	13.3249	(0.3293)	(3.3942)	9.4280	(0.2283)	(1.1893)	9.2318

Table 3 The effect of scattering, emissivity and of conduction-radiation parameter on heat transfer in laminar flow at various axial locations along the length of a channel corresponding to $\eta = 10.0$

			ξ												
			1.25×10^{-2}			2.5×10^{-1}			8.375×10^{-1}			2.5		
N	ϵ	ω_0	Nu_R (q^*_{rw})	Nu_C (q^*_{cw})	Nu	Nu_R (q^*_{rw})	Nu_C (q^*_{cw})	Nu	Nu_R (q^*_{rw})	Nu_C (q^*_{cw})	Nu	Nu_R (q^*_{rw})	Nu_C (q^*_{cw})	Nu
0.01	1.0	0	336.451	30.9170		293.360	24.9554		705.287	58.6069				
			(0.6379)	(0.0586)	363.368	(0.2772)	(0.0236)	318.316	(0.0218)	(0.0018)	763.894			
		0.35	331.271	27.1307		292.743	21.9597		699.767	51.3043				
			(0.6295)	(0.0516)	358.401	(0.2787)	(0.0209)	314.703	(0.0230)	(0.0017)	751.071			
		0.65	315.291	22.389		288.715	17.6454		681.115	40.525				
			(0.6015)	(0.0427)	337.681	(0.2803)	(0.0171)	306.360	(0.0270)	(0.0016)	721.639			
		1.0												
				(7.7418)	38.9934		(2.7981)	14.7732		(1.8384)	10.4147		(1.2457)	8.1928
	0.5	0	197.356	56.1964		182.410	47.6085		443.441	111.117				
			(0.3809)	(0.1085)	253.552	(0.2087)	(0.0545)	230.018	(0.0545)	(0.0137)	554.580			
		0.65	191.099	40.0439		185.968	33.5402		439.102	76.0301				
			(0.3702)	(0.0776)	231.143	(0.2195)	(0.0396)	219.508	(0.0627)	(0.0109)	515.132			
0.1	1.0	0	41.0017	33.6106		28.7041	11.9899		25.4755	9.8368		32.9264	12.3051	
			(0.8102)	(0.6641)	74.6123	(0.5056)	(0.2112)	40.6940	(0.3613)	(0.1395)	35.3123	(0.2460)	(0.0191)	45.2315
		0.35	38.8772	33.8291		28.9679	11.0942		26.0249	8.8970		33.4095	10.9491	
			(0.7684)	(0.6686)	72.7062	(0.5116)	(0.1959)	40.0621	(0.3711)	(0.1269)	34.9219	(0.2531)	(0.0829)	44.3585
		0.65	34.7813	34.7027		28.5074	10.3389		26.3809	7.7581		33.4725	9.1562	
			(0.6878)	(0.6862)	69.4840	(0.5058)	(0.1835)	38.8463	(0.3800)	(0.1118)	34.1390)	(0.2606)	(0.0713)	42.6287
	0.5	0	20.9258	40.0977		16.1797	18.1575		14.8275	15.4511		18.3103	18.4329	
			(0.4143)	(0.7939)	61.0234	(0.2912)	(0.3268)	34.3372	(0.2217)	(0.2311)	30.2786	(0.1598)	(0.1609)	36.7432
		0.65	19.6944	38.2081		17.0401	14.8006		16.3170	11.9335		19.8900	13.5552	
			(0.3901)	(0.7568)	57.9024	(0.3089)	(0.2683)	31.8407	(0.2490)	(0.1821)	28.2505	(0.1844)	(0.1257)	33.4452
0.5	1.0	0	8.3981	37.3034		6.6385	13.2808		5.8628	9.2051		5.6132	7.5752	
			(0.8329)	(3.7393)	46.1014	(0.6197)	(0.1240)	19.9193	(0.4958)	(0.7785)	15.0679	(0.3778)	(0.5099)	13.1884
		0.35	7.900	37.8237		6.5267	13.2349		5.9047	9.0549		5.7609	7.3319	
			(0.7835)	(3.7514)	45.7232	(0.6096)	(1.2361)	19.7617	(0.5000)	(0.7668)	14.9596	(0.3889)	(0.4950)	13.0928
		0.65	7.0088	38.0728		6.1376	13.3507		5.7651	9.0118		5.8140	7.1093	
			(0.6952)	(3.7765)	45.0816	(0.5738)	(1.2481)	19.4883	(0.4893)	(0.7648)	14.7768	(0.3945)	(0.4824)	12.9232
	0.5	0	4.2153	39.1708		3.4121	15.1690		3.0731	11.0400		2.9835	9.3648	
			(0.4182)	(3.8863)	43.3861	(0.3199)	(1.4222)	18.5811	(0.2627)	(0.9438)	14.1132	(0.2059)	(0.6464)	12.3483
		0.65	3.9496	38.8142		3.4932	14.5670		3.3186	10.3334		3.3797	8.4963	
			(0.3919)	(3.8513)	42.7639	(0.3280)	(1.3677)	18.0602	(0.2849)	(0.8872)	13.6520	(0.2361)	(0.5935)	11.8761

creases, scattering tends to decrease also the convective component. On the other hand up to moderate values of η_0, the relative (to the case of $\omega_0 = 0$) effect of scattering on the radiation component stays roughly about the same at all values of N (see Tables 1 and 2). However, at high values of η_0, the relative effect of scattering on radiative component decreases as can be seen in Table 3. Consequently, in each case the net effect of scattering is to decrease the total Nusselt number.

The relative (to the case of $\omega_0 = 0$) effect of scattering on radiation component decreases as emissivity decreases; this can be clearly seen by comparing values at $\epsilon = 1$ with those at $\epsilon = 0.5$ in each of three tables. At high values of η_0, the relative effect of scattering on radiation component decreases also with decrease in emissivity, in fact, further downstream the effect of scattering on radiative component disappears altogether where as the relative effect on convective component stays approximately undiminished even at distances far from the entry. The net effect of decrease in emissivity is to decrease the total Nusselt number at all values of η_0 and ω_0.

One significant feature of interaction of radiation with convection is to increase the total Nusselt number downstream after reaching a minimum rather than approaching an asymptotic value as is the case with pure convection. This increase becomes more significant both with increasing η_0 and decreasing N. This behavior was also found by Lii and Ozisik [1] for the case of thermally developing slug flow. This behavior can be explained qualitatively by referring to equation (17) which shows that radiation Nusselt must increase as the bulk temperature increases. This can be more clearly seen by referring to Fig. 2 which shows the plot of radiative Nusselt number and bulk temperature both as a function of ξ. This figure clearly shows that the sharp increase in radiation Nusselt number coincides with the corresponding increase in the bulk temperature. The plot of convective Nusselt number Nu_C as a function of axial distance for the case $\eta_0 = 2.0$ and $N = 0.01$ in Fig. 3 shows that it tends to increase slightly downstream of a minimum, though this increase is substantially less than the corresponding increase in radiation Nusselt number. Consequently, total Nusselt number increases beyond a minimum with the downstream distance.

This behavior of Nusselt number can further be elaborated upon by referring to Figs. 4 and 5, which show plots of temperature profiles expressed in convectional similarity variable, namely $(T_1 - T)/(T_1 - T_b)$ as a function of optical depth η at several axial distances. Figure 4 shows the lack of invariance of the temperature profile with axial distance which is contrary to the behavior for the case of pure convection. However, as the value of N increases, the temperature profiles appear to merge together more so than for small values of N. This, in turn, implies the use of similarity assumption as made previously by various authors [2–9] is more valid at high values of N and less so as the value of N decreases.

Another interesting feature of radiation Nusselt number appears to be that it nearly remains constant (see Fig. 2) up to significant distances near the entry, this behavior again appears to be explainable qualitatively by equation (17) which shows at vanishingly small values of bulk temperature (that is near the entry region) radiation Nusselt number remains approximately constant.

Concluding Remarks

The results for the case of Poiseuille flow show that radiation scattering tends to decrease the radiation component as well as convective component of heat transfer significantly at moderate to low values of optical thickness, whereas at high values of optical thickness, the effect of scattering on the radiation component appears to be less pronounced, and the effect on the convective component remains undiminished. The relative (to $\omega_0 = 1$) effect of scattering both on convective and radiation Nusselt numbers appears to be unaffected by change in the surface emissivity, although the effect of scattering decreases relative to the case of $\epsilon = 1$. The net effect of scattering is to decrease the total Nusselt number. A significant feature of the interaction between radiation and convection is that total Nusselt number appears to increase significantly downstream of the location of its minimum, particularly at low values of conduction-radiation

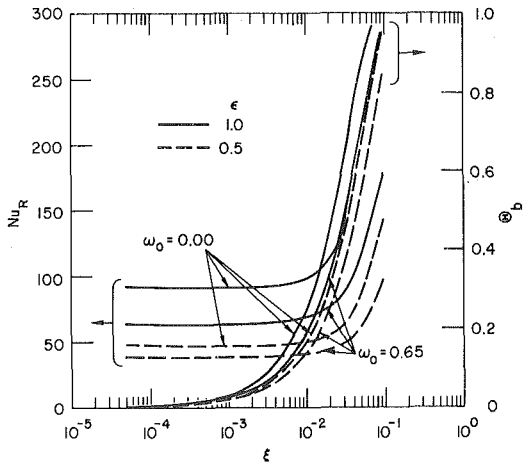

Fig. 2 Variation of radiation Nusselt number and bulk temperature as a function of axial distance for $\eta_0 = 2.0$ and $N = 0.01$

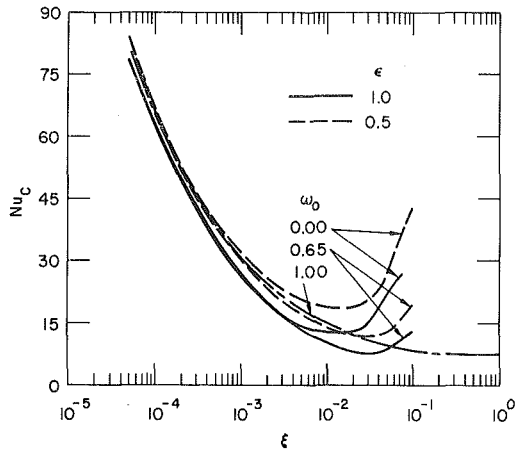

Fig. 3 Variation of convective Nusselt number as a function of axial distance for $\eta_0 = 2.0$ and $N = 0.01$

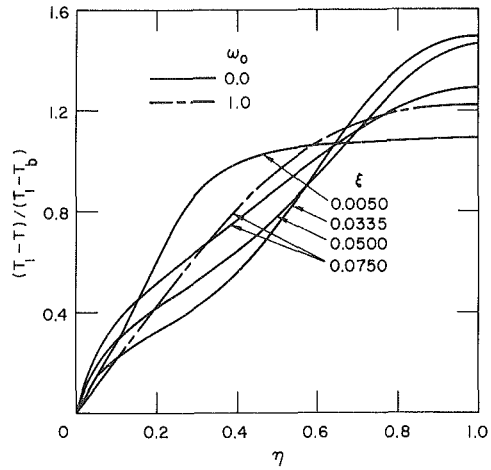

Fig. 4 Variation of temperature profile in terms of similarity variables as a function of optical depth at various axial locations along the length of channel for $\eta_0 = 2.0$, $N = 0.01$, $\epsilon = 1.0$, and $\omega_0 = 0,1$

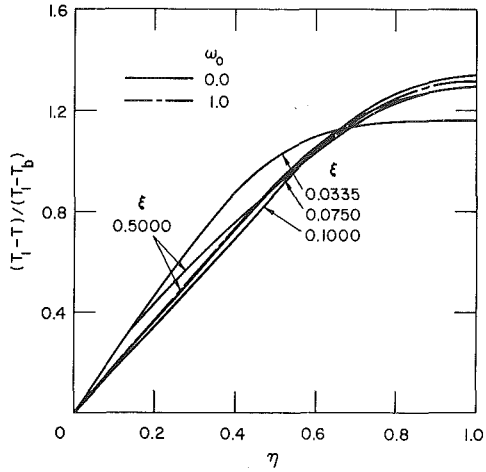

Fig. 5 Variation of temperature profile in terms of similarity variables as a function of optical depth at various axial locations along the length of channel for $\eta_0 = 2.0$, $N = 0.1$, $\epsilon = 1$, and $\omega_0 = 0,1$

parameter and at moderate to high values of optical thicknesses. This occurs mostly due to the increase in radiation component with approach of nearly uniform temperature profile or with sharp increase in the bulk temperature. This behavior is contrary to that of corresponding (i.e., with the same boundary conditions) pure convection in where the Nusselt number approaches an asymptotic value. Because of the presence of radiation mode, the similarity in the temperature profile appears to exist only at moderate to high values of conduction-radiation parameter.

Acknowledgment

This work was performed under the auspices of the U.S. Department of Energy.

References

1 Lii, C. C. and Ozisik, M. N., "Heat Transfer in an Absorbing, Emitting and Scattering Slug Flow Between Parallel Plates," ASME Paper No. 73-HT-13, ASME-AIChE Heat Transfer Conference, Atlanta, GA, Aug. 1973.

2 Viskanta, R., "Interaction of Heat Transfer by Conduction, Convection, and Radiation in a Radiating Fluid," ASME JOURNAL OF HEAT TRANSFER, Vol. 85, No. 4, 1963, pp. 318–328.

3 Viskanta, R., "Heat Transfer in a Radiating Fluid with Slug Flow in a Parallel Plate Channel," *Applied Scientific Research,* Sec. A, Vol. 13, 1964, pp. 291–311.

4 Viskanta, R. and Grosh, R. J., "Temperature Distribution in Couette Flow with Radiation," *ARS Journal,* Vol. 31, No. 6, 1961, pp. 839–840.

5 DeSoto, S. and Edwards, D. K., "Radiative Emission and Absorption in Non-Isothermal Nongray Gases in Tubes," *Proceedings of the 1965 Heat Transfer and Fluid Mechanics Institute,* Stanford University Press, Palo Alto, CA, 1965, pp. 358–372.

6 Balakrishnan, A. and Edwards, D. K., "Established Laminar and Turbulent Channel Flow of a Radiating Molecular Gas," *Heat Transfer 1974,* Vol. I, Fifth Int. Heat Transfer Conference, Tokyo, Sept. 1974, pp. 93–97.

7 Edwards, D. K. and Balakrishnan, A., "Nongray Radiative Transfer in a Turbuent Gas Layer," *International Journal of Heat and Mass Transfer,* Vol. 16, 1973, pp. 1003–1015.

8 Edwards, D. K. and Balakrishnan, A., "Self-Absorption of Radiation in Turbulent Molecular Gases," *Combustion and Flame,* Vol. 20, 1973, pp. 401–417.

9 Wassel, A. T. and Edwards, D. K., "Molecular Radiation in a Laminar or Turbulent Pipe Flow," ASME JOURNAL OF HEAT TRANSFER, Vol. 98, 1976, pp. 101–107.

10 Balakrishnan, A. and Edwards, D. K., "Molecular Gas Radiation in the Thermal Entrance Region of a Duct," ASME JOURNAL OF HEAT TRANSFER, Vol. 101, 1979, pp. 489–495.

11 Liu, S. T. and Thorsen, R. S., "Combined Force Convection and Radiation Heat Transfer in the Thermal Entrance Region of a Non-Isothermal Parallel Plate Channel-Optically Thin Gases," ASME Paper No. 73-HT-14, ASME-AIChE Heat Transfer Conference, Atlanta, GA, Aug. 1973.

12 Pearce, B. E. and Emery, A. F., "Heat Transfer by Thermal Radiation and Laminar Forced Convection to an Absorbing Fluid in the Entry Region of a Pipe," ASME JOURNAL OF HEAT TRANSFER, Vol. 92, No. 2, 1970, pp. 221–230.

13 Chen, J. C., "Simultaneous Radiative and Convective Heat Transfer in an Absorbing, Emitting, and Scattering Medium in Slug Flow Between Parallel Plates," *AIChE Journal,* Vol. 2, No. 2, 1964, pp. 253–259.

14 Kurosaki, Y., "Heat Transfer by Radiation and Other Transport Mechanisms," *Bulletin of the JSME,* Vol. 14, 1971, pp. 572–580.

15 Kurosaki, Y., "Heat Transfer by Simultaneous Radiation and Convection in an Absorbing and Emitting Medium in a Flow Between Parallel Plates," *Heat Transfer 1970,* Vol. III, Fourth International Heat Transfer Conference, Paris, 1970.

16 Echigo, R., Kamiuto, K., and Hasegawa, S., "Analytical Method on Composite Heat Transfer with Predominant Radiation—Analysis by Integral

Equation and Examination on Radiation Slip," *Heat Transfer 1974,* Vol. I, Fifth International Heat Transfer Conference, Tokyo, Sept. 1974, pp. 103–107.

17 Greif, R. and McEligot, D. "Influence of Optically Thin Radiation on Heat Transfer in the Thermal Entrance Region of a Narrow Duct," ASME JOURNAL OF HEAT TRANSFER, Vol. 93, No. 4, 1971, pp. 473–475.

18 Chawla, T. C. and Chan, S. H., "Spline Collocation Solution of Combined Radiation Convection in Thermally Developing Flows with Scattering," to be published in *Numerical Heat Transfer.*

19 Sparrow, E. M. and Cess, R. D., *Radiation Heat Transfer*, Augmented Edition, Hemisphere Publishing Corporation, Washington, 1978, pp. 255–275.

20 Chawla, T. C. and Chan, S. H., "Solution of Radiation-Conduction Problems with Collocation Method Using B-splines as Approximating Functions," *International Journal of Heat and Mass Transfer,* Vol. 22, 1979, pp. 1657–1668.

Heat Transfer by Conduction and Radiation in a One-Dimensional Absorbing, Emitting and Anisotropically-Scattering Medium

W. W. Yuen
Assistant Professor.

L. W. Wong
Graduate Student.

Department of Mechanical and Environmental Engineering,
University of California,
Santa Barbara, Calif. 93106

Heat transfer by simultaneous conduction and radiation in an absorbing, emitting and anisotropically-scattering material is investigated theoretically. Consideration is given to a one-dimensional system bounded by two parallel gray, diffuse and isothermal walls. Assuming a physical model of linear-anisotropic scattering, the resulting integral-differential equation is solved by a successive approximation technique similar to the method of undetermined parameters. The solution method is demonstrated to be relatively simple and yields solution converging qucikly to the exact results. Results show that for the present one-dimensional system, the common approach of treating the total heat transfer as a simple addition of separate independent contributions from conduction and radiation is quite inaccurate for certain cases. This approach is thus ineffective in illustrating the general effect of scattering. Both the scattering albedo and the forward-backward scattering parameters are shown to have some interesting effects on the total heat transfer and the medium's temperature. The magnitude of these effects depends on the surface emissivity of the two boundaries.

Introduction

Heat transfer by simultaneous conduction and radiation between two reflecting surfaces with an intervening medium capable of absorbing, emitting and scattering thermal radiation is a problem of considerable practical importance. It serves as the basis, for example, in the analysis of the thermal performance of porous insulating materials such as fibers, powders, foams and many others. A great deal of work have been reported in this area [1–8], but most of them have only limited success largely because of the complexity of the problem.

Mathematically, the problem of simultaneous conduction and raidation is quite formidable as it involves the complex interaction between the radiative properties of the boundary surface and the thermal and optical properties of the material. The analysis requires a difficult solution of a nonlinear integral-differential equation. Many approximation methods have been proposed [1–4]. But nearly all of these methods were successful only in generating limiting expressions for the total heat flux. Few can predict the temperature profile accurately and none of them consider the effects of anisotropic scattering. Numerically, the only successful solution appears to be that of Viskanta and Grosh [6, 7]. Using an iterative method, they analyzed numerically the problem of combined conduction radiation in a one-dimensional absorbing, emitting, but nonscattering medium bounded by two parallel gray isothermal surfaces. The effect of the various system parameters on heat transfer were established and the calculation was later generalized to include the effect of isotropic scattering [8]. But the effect of anisotropic scattering is again neglected. While it is well known that the scattering of thermal radiation by real particles is by no means isotropic [9] and that anisotropic scattering can play a significant role on the overall heat transfer, all of the existing work on anisotropic-scattering media [10–12] avoid much of the mathematical complexities by considering only the effect of radiative transfer. None of them consider the simultaneous effect of conduction.

The objective of the present work is to obtain accurate solutions to the problem of simultaneous conduction and radiation in an absorbing emitting medium with anisotropic scattering. Assuming a model of linear-anisotropic scattering, successive approximate solutions converging to the exact result are generated. The solution method is similar to a technique which was utilized successfully in some recent analyses of radiative transfer [10, 11]. Unlike those analyses, the present method does not assume a differential formulation for the radiative intensity. Instead, the governing integral-differential equation is solved exactly. The difficult question concerning the convergence of the differential formulation is thus avoided. As in the previous approaches, the governing equation and its associated boundary conditions are reduced to a set of nonlinear algebraic equations at each step of the successive approximations. Solutions are obtained quickly and efficiently by simple iterations. In the limit of pure radiation, the present technique is identical to the method of undetermined parameters [5].

Results indicate clearly the effect of various system parameters on the heat transfer and the temperature profile of the medium. The common practice of treating the total heat transfer as a sum of separate independent contributions from conduction and radiation is demonstrated to be inappropriate except for some special limiting situations. In general, scattering can have an important effect on the total heat transfer and the medium's temperature profile. In some instances, differences between the anisotropic-scattering result and the isotorpic-scattering result are quite significant.

Mathematical Formulation. The physical system chosen and its associated coordinate system for the present analysis are identical to those considered in references [11] and [12]. Utilizing the same set of physical assumptions, the equation of transfer may be written as

$$\frac{di}{d\tau} + i = (1 - \omega_0)i_b + \frac{\omega_0}{2}\int_{-1}^{1} i d\mu + \frac{\omega_0 x}{2}\int_{-1}^{1} i\mu d\mu \qquad (1)$$

where i denotes the radiation intensity, i_b the blackbody intensity, ω_0 the single scattering albedo, x the forward-backward scattering parameter, $\mu \equiv \cos\theta$ and τ is the optical thickness defined by

$$d\tau = \beta\, dz \qquad (2)$$

with z being the axis of symmetry and β the extinction coefficient. For combined conduction radiation, the energy equation is

$$\frac{d}{d\tau}\left[2\tau\int_{-1}^{1} i\mu d\mu - K\beta\frac{dT}{d\tau}\right] = \frac{H}{\beta} \qquad (3)$$

where k is the thermal conductivity of the medium, T the temperature

Contributed by the Heat Transfer Division for publication in the JOURNAL OF HEAT TRANSFER. Manuscript received by the Heat Transfer Division April 20, 1979.

and H is the internal heat generation rate.

Introducing the following dimensionless variables:

$$\theta = \frac{T}{T_1},\ \theta_H^4 = \frac{H}{\beta\sigma T_1^4},\ I = \frac{\pi i}{\sigma T_1^4},\ G = 2\int_{-1}^{1} I d\mu,\ Q = 2\int_{-1}^{1} I\mu d\mu \quad (4)$$

where T_1 is the temperature of the lower wall and σ is the Stefan-Boltzmann constant, equations (1) and (3) can be written as

$$\mu\frac{dI}{d\tau} + I = (1-\omega_0)\theta^4 + \frac{\omega_0}{4}G + \frac{\omega_0 x\mu}{4}Q \quad (1a)$$

$$\frac{d}{d\tau}\left[Q - 4N_1\frac{d\theta}{d\tau}\right]\theta_H^4 \quad (3a)$$

where $N_1 = k\beta/4\sigma T_1^3$ is the familiar conduction-radiation parameter.

Equation (1a) can be integrated over μ to give

$$\frac{1}{2}\frac{dQ}{d\tau} + \frac{1}{2}G = 2(1-\omega_0)\theta^4 + \frac{\omega_0}{2}G \quad (5)$$

Together with equation (3a), the dimensionless average intensity G can be expressed as

$$G = 4\theta^4 - \left[\theta_H^4 + 4N_1\frac{d^2\theta}{d\tau^2}\right]/(1-\omega_0) \quad (6)$$

Assuming a constant heat generation rate, equation (3a) can be integrated over τ to yield

$$Q = 4N_1\frac{d\theta}{d\tau} + \theta_H^4\tau - 4N_1\left(\frac{d\theta}{d\tau}\right)_0 + Q_0 \quad (7)$$

Utilizing equation (6) and (7), equation (1a) becomes,

$$\mu\frac{dI}{d\tau} + I = S(\tau,\mu) \quad (8)$$

where

$$S(\tau,\mu) = \theta^4 - \left(\frac{\omega_0}{1-\omega_0}\right)\left(N_1\frac{d^2\theta}{d\tau^2} + \frac{\theta_H^2}{4}\right) + \omega_0 x\mu\left[N_1\frac{d\theta}{d\tau} + \frac{\theta_H^4}{4} - N_1\left(\frac{d\theta}{d\tau}\right)_0 + \frac{Q_0}{4}\right] \quad (9)$$

Formally, the solution to equation (8) is

$$I_+ = I_+\left(-\frac{L}{2}\right)e^{(-(\tau+L/2)/\mu)} + \int_{-\frac{L}{2}}^{\tau} S(\tau^*,\mu)e^{-((\tau-\tau^*)/\mu)}\frac{d\tau^*}{\mu},\ 0 \le \mu \le 1 \quad (10a)$$

$$I_- = I_-\left(\frac{L}{2}\right)e^{-(\tau-L/2/\mu)} - \int_{\tau}^{\frac{L}{2}} S(\tau^*,\mu)e^{((\tau^*-\tau)/\mu)}\frac{d\tau^*}{\mu},\ -1 \le \mu \le 0 \quad (10b)$$

Equations (6, 9, 10a, 10b) and the definition of G can be combined to give the following integral-differential equation for the dimensionless temperature θ:

$$\theta^4 - \frac{N_1}{1-\omega_0}\frac{d^2\theta}{d\tau^2} - \frac{1}{2}\int_0^1\left[\int_{-\frac{L}{2}}^{\tau} S(\tau^*,\mu)e^{-((\tau-\tau^*)/\mu)} \times d\tau^* + \int_{\tau}^{\frac{L}{2}} S(\tau^*,-\mu)e^{-(\tau^*-\tau/\mu)}d\tau^*\right]\frac{d\mu}{\mu}$$
$$= \frac{1}{2}\left[I_+\left(\frac{-L}{2}\right)E_2\left(\frac{L}{2}+\tau\right) + I_-\left(\frac{L}{2}\right)E_2\left(\frac{L}{2}-\tau\right)\right] + \frac{\theta_H^4}{4} + \frac{\omega_0\theta_H^4}{8(1-\omega_0)}\left[E_2\left(\frac{L}{2}+\tau\right) + E_2\left(\frac{L}{2}-\tau\right)\right]$$
$$+ \frac{\omega_0 x}{2}\left[\frac{Q_0}{4} - N_1\left(\frac{d\theta}{d\tau}\right)_0\right]\left[E_3\left(\frac{L}{2}+\tau\right) - E_3\left(\frac{L}{2}-\tau\right)\right] + \frac{\omega_0 x\theta_H^4}{8}\left\{-\frac{2}{3} + \frac{L}{2}\left[E_3\left(\frac{L}{2}+\tau\right) + E_3\left(\frac{L}{2}-\tau\right)\right] + E_4\left(\frac{L}{2}+\tau\right) + E_4\left(\frac{L}{2}-\tau\right)\right\} \quad (11)$$

where $E_n(x)$ is the exponential-integral function defined by

$$E_n(x) = \int_0^1 \mu^{n-2}e^{-x/\mu}d\mu \quad (12)$$

Utilizing equations (10a) and (10b) again, the constant θ_0, $I_+(-L/2)$ and $I_-(L/2)$ in equation (11) can be expressed in terms of θ as

$$\theta_0\left\{1 - \omega_0 x\left[\frac{1}{3} - E_4\left(\frac{L}{2}\right)\right]\right\} = 2E_3\left(\frac{L}{2}\right)\left(1-\theta_2^4\right) - 4N_1\omega_0 x\left[\frac{1}{3} - E_4\left(\frac{L}{2}\right)\right]\left(\frac{d\theta}{d\tau}\right)_0 + 2\int_0^1\left[\int_{-\frac{L}{2}}^{0} S(\tau^*,\mu)e^{\tau^*/\mu}d\tau^* - \int_0^{\frac{L}{2}} S(\tau^*,-\mu)e^{-\tau^*/\mu}d\tau^*\right]d\mu \quad (13)$$

$$I_+\left(-\frac{L}{2}\right)[1 - 4(1-\epsilon_1)(1-\epsilon_2)E_3^2(L)] = \epsilon_1 + 2(1-\epsilon_1)\left\{\epsilon_2 E_3(L)\theta_2^4 + \int_0^1\int_{-\frac{L}{2}}^{\frac{L}{2}}\left[S(\tau^*,-\mu)e^{-L/2-\tau^*/\mu} + 2(1-\epsilon_2)S(\tau^*,\mu)e^{-(L/2+\tau^*)/\mu}\right]d\tau^* d\mu\right\} \quad (14)$$

Nomenclature

A_n = expansion coefficient defined by equation (19)
B_n = expansion coefficient defined by equation (20)
d = thickness of the one-dimensional slab
G = dimensionless average intensity defined by equation (4)
E_N = exponential function defined by equation (12)
H = internal heat generation rate
i = radiative intensity
i_b = blackbody intensity
I = dimensionless radiative intensity defined by equation (4)
J = Jacobian matrix
k = thermal conductivity
$L = \beta d$
M_1 = new conduction-radiation parameters N_1/L^2
N_1 = conduction-radiation parameter, $k\beta/4T_1{}^3$
Q = dimensionless radiative heat flux defined by equation (4)
$Q_0 = Q$ evaluated at $\tau = 0$
Q_t = total heat flux defined by equation (22)
S = source function defined by equation (9)
T = temperature
T_1 = temperature of the lower wall
x = forward-backward scattering parameter
$X_{i,j}$ = matrix element defined in equation (21)
$Y_{i,j}$ = matrix element defined in equation (21)
Z_i = vector defined in equation (21)
z = spacial coordinate
β = extinction coefficient
ϵ = surface emissivity
θ = dimensionless temperature, T/T_1
$\theta_m = \theta$ evaluated at τ_m
$\theta_H = H/\beta\sigma T_1{}^4$
$\theta_0 = \theta$ at $\tau = 0$
θ_2 = dimensionless upper wall temperature
$\mu = \cos\theta$
τ = optical thickness defined by equation (2)
ω_0 = scattering albedo

$$I_- \left(\frac{L}{2}\right)[1 - 4(1 - \epsilon_1(1 - \epsilon_2)E_3^2(1)]$$

$$= \epsilon_2\theta_2^4 + 2(1 - \epsilon_2)\Big\{\epsilon_1 E_3(L)\theta_2^4 + \int_0^1 \int_{-\frac{L}{2}}^{\frac{L}{2}} \Big[S(\tau^*, \mu)e^{-(L/2+\tau^*)/\mu} + 2(1 - \epsilon_1)S(\tau^*, -\mu)e^{-(L/2-\tau^*)/\mu}\Big] d\tau^* d\mu\Big\} \quad (15)$$

The boundary conditions for θ are

$$\theta\left(-\frac{L}{2}\right) = 1, \theta\left(\frac{L}{2}\right) = \theta_2 \quad (16)$$

Equations (11) and (13–15) constitute a complete mathematical description for the present one-dimensional problem.

Method of Solution. Analytical solution to equations (11) and (16) are clearly impossible to obtain. Numerically, Viskanta [6–8] had demonstrated that for cases with no-scattering or isotropic scattering, solutions can be generated by a direct iterative method. While this same technique will probably be effective also for the case with anisotropic scattering, the present work chooses to use a different solution procedure. Unlike the iterative method, each solution in the present successive approximation series is developed independently. At each step of the approximation, equation (11) is reduced to a set of finite non-linear algebraic equations which can be readily solved. In contrast to the direct iterative method, the present method has the advantages that it is mathematically simple and solutions generated converge quickly independent of values of the various system parameters.

Mathematically, the present solution method is based on a simple observation that if θ and θ^4 are expressed as power series, the various integrals appeared in equations (11) and (14–15) can be carried out analytically in terms of the exponential integral function. Evaluating equation (11) at different values of τ, a system of algebraic equations can be generated to determine the unknown expansion parameters. From a computational point of view, these equations will have the same degree of complexity as a finite-difference formulation of a nonlinear ordinary differential equation. They can thus be readily solved.

In the Jth approximation, the unknown parameters are assumed to be the temperature at $2J + 1$ distinct locations in the medium as follows:

$$\theta_m = \theta(\tau_m) \quad (17)$$

where

$$\tau_m = \frac{mL}{2(J + 1)} \quad m = 0, \pm 1, \ldots, \pm J \quad (18)$$

In terms of the τ_m's, the temperature profile is expanded as a $(2J + 3)$ term power series. This gives

$$\theta = \sum_{n=0}^{2J+2} A_n \tau^n \quad (19)$$

Evaluating equation (19) at τ_m's and at the two boundaries, the coefficients A_n's can be expressed as linear functions of τ_m's. In a similar manner, θ^4 is approximated by

$$\theta^4 = \sum_{n=0}^{2J} B_n \tau^n \quad (20)$$

But unlike equation (19), equation (20) is not required to satisfy the noslip temperature boundary conditions. Results show that this relaxing of the temperature boundary condition for θ^4 greatly improves the accuracy of the solution for the lower order approximation. This is not surprising because in the limit of a large radiative effect, a θ^4 distribution which satisfies the no-slip temperature boundary condition will always yield an inaccurate radiative heat flux prediction in the optically thin limit. In the higher order approximation ($J \to \infty$), equations (19) and (20) clearly reduce to two consistent relations.

By assuming θ and θ^4 to be separate power series, the present work also reduces greatly the complexity of the computation since only θ_m and ${\theta_m}^4$ will appear in the final matrix equation. If only equation (18) is utilized, all possible products of τ_m's up to the fourth power will appear. In all considered cases, the accuracy of the solution generated by the present method is better than or at least equal to those generated by assuming a simple power series for θ and θ^4. The computational time is always much less.

Substituting equations (19) and (20) into equation (11) and evaluated at τ_m's, a nonlinear matrix equation of the following general form results.

$$\begin{bmatrix} X_{1,1} & \cdots & X_{1,2J+1} \\ \vdots & & \vdots \\ X_{2J+1,1} & \cdots & X_{2J+1,2J+1} \end{bmatrix} \begin{bmatrix} \theta_0 \\ \theta_1 \\ \theta_{-1} \\ \vdots \\ \theta_J \\ \theta_{-J} \end{bmatrix} + \begin{bmatrix} Y_{1,1} & \cdots & Y_{1,2J+1} \\ \vdots & & \vdots \\ Y_{2J+1,1} & \cdots & Y_{2J+1,2J+1} \end{bmatrix} \begin{bmatrix} \theta_0^4 \\ \theta_1^4 \\ \theta_{-1}^4 \\ \vdots \\ \theta_J^4 \\ \theta_{-J}^4 \end{bmatrix} = \begin{bmatrix} Z_1 \\ Z_2 \\ Z_3 \\ \vdots \\ Z_{2J} \\ Z_{2J+1} \end{bmatrix} \quad (21)$$

The solution can be generated by any common iterative technique.

Results and Discussion. Because of the large number of physical parameters involved even for a simple one-dimensional problem, the present consideration will be limited to those cases with $\epsilon_1 = \epsilon_2 = \epsilon$, $\theta_H = 0$ and $\theta_2 = 0.5$. It is recognized that situations with $\epsilon_1 \neq \epsilon_2$ and other values of θ_2 and θ_H can differ significantly from those considered in the present work. They will be investigated in the future.

Results show that the present solution method yields converging results very quickly. At each step of the successive approximations no more than 4 iterations are required for the solution of the nonlinear matrix. The number of iterations required for the higher-order approximation is even less since the previous-order result, which is already quite accurate, can be used as an initial guess. The successive approximation is carried out until two consecutive approximate solutions differ by less than 0.001 both in its prediction for the temperature profile and the radiative heat flux. In all considered cases, the above convergence criteria is achieved at no higher than the sixth-order approximation. Tables 1 and 2 illustrate the rate of convergence of the temperature profile for two typical cases. It is interesting to note the first-order result, which is generated by the solution of a simple 3×3 nonlinear matrix, already yields a resonably accurate description of the medium's temperature. The heat flux prediction is also quite satisfactory and superior to the common approach which treats the total heat flux as a sum of separate independent contributions from conduction and radiation. Utilizing a recently developed closed-form approximation for pure radiative transfer in an aniso-

Table 1 The first six-order approximate temperature profile θ with $N_1 = 0.01$, $L = 1.0$, $\epsilon_1 = \epsilon_2 = 0.5$ and $\omega_0 = 0$

τ/L	1st	2nd	3rd	4th	5th	6th
0.5	0.500	0.500	0.500	0.500	0.500	0.500
0.3	0.756	0.769	0.769	0.771	0.773	0.773
0.1	0.827	0.818	0.819	0.820	0.822	0.822
0.0	0.835	0.832	0.833	0.835	0.836	0.837
−0.1	0.842	0.845	0.846	0.848	0.849	0.849
−0.3	0.886	0.874	0.874	0.876	0.877	0.878
−0.5	1.000	1.000	1.000	1.000	1.000	1.000

tropically-scattering medium, the addition-solution suggests the following expression for the total heat flux

$$Q_t = \frac{4N_1}{L}(1-\theta_2) + \frac{1-\theta_2^4}{\frac{2}{\epsilon} - 1 + \left(\frac{3}{4} - \frac{\omega_0 x}{4}\right)L} \tag{22}$$

A direct comparison between the first-order results, equation (22) and the higher order exact results obtained in the present work is shown in Table 3. It is apparent that the error of equation (22) can be quite substantial, particularly for cases with scattering and small emissivity.

Table 3 also shows that the present exact results differ slightly from the previously reported numerical results [7]. The discrepancy is not too unexpected since the previous computation was done nearly 20 years ago with a small IBM 650 computer [14]. The computer was slow and had a small core. Experience in the present calculation indicates that the accuracy of the exponential integral function. In a pure numerical computation with a small computer, slight error in the exponential integral function and consequently in the result of the calculation can be readily generated. The present work, on the other hand, utilizes a much larger and more efficient IBM 360 computer. All exponential integral functions are tabulated exactly up to eight significant figures using known analytical expressions and serves as the input of the calculation. The result should thus be more accurate and reliable.

The effect of the scattering albedo ω_0 and the forward-backward scattering parameter x on the medium's temperature profile is illustrated by Fig. 1, in which results of the temperature profiles for cases with $L = 1.0$, $\epsilon = 1.0$ and various values of N_1, ω_0 and x are presented. It readily demonstrates that scattering can have a significant effect on the medium's temperature. When $\omega_0 = 0$, the medium only absorbs and emits radiation. The interaction of conduction and radiation causes the temperature to rise above that of the pure conduction case. When $\omega_0 = 1.0$, the medium only scatters and does not either absorb or emit radiation. The temperature profile becomes linear. For intermediate values of ω_0, the temperature profile falls between the above two extreme cases. For $N_1 = 0.1$, the value of x has only a minor effect on the medium's temperature. As N_1 decreases, the effect of anisotropic scattering increases and is at a maximum at $N_1 = 0$. As expected, a strong forward scattering ($x = 1.0$) leads to an increase of the temperature near the cold wall and a decrease of the temperature near the hot wall. The opposite trend is observed for media with a strong backward scattering ($x = -1.0$). In all cases, the effect of x is quite negligible compared to the effect of ω_0.

The effect of scattering on heat transfer is illustrated by results presented in Tables 4 and 5. For the scattering albedo ω_0, its effect on heat transfer is most significant for systems with small N_1 and small surface emissivities. At $N_1 = 0.01$, $\epsilon = 0.1$ and $L = 1.0$, for example, the heat transfer result with $\omega_0 = 1.0$ represents a nearly 50 percent reduction from the result with $\omega_0 = 0$. At $\epsilon = 1.0$, on the other hand, the maximum variation of the total heat flux as ϵ_0 is changed from 0 to 1.0 is less than 10 percent. Unlike its almost negligible effect on the medium's temperature, the forward-backward scattering parameter also has a noticable effect on the heat transfer. But in contrast to the effect of ω_0, the effect of x is large for systems with large surface emissivity. At $\epsilon = 1.0$, $N_1 = 0.1$, $L = 1.0$ and $\omega_0 = 0.5$, for example, the total heat transfer in a strongly backward-scattering medium ($x = -1.0$) is about 10 percent less than that in a strongly forward-scattering medium ($x = 1.0$). At $\epsilon = 0.1$, however, the effect of x is almost negligible. At $L = 10.0$, the effect of ω_0 and x on the heat transfer results follows a similar pattern.

Physically, the above effect of ω_0 and x on the total heat transfer is not difficult to understand. For systems with small surface emissivity, energy leaving the hot bottom wall must travel many times across the medium before it is totally absorbed. There is an effective increase in the optical thickness. The effect of scattering is multiplied and thus becomes more apparent. The effect of ω_0 is therefore large for systems with small surface emissivity. But the multiple reflections by the two boundaries also cause a given ray of radiative energy to

Table 2 The first five-order approximate temperature profile θ with $N_1 = 1.0$, $L = 10.0$, $\epsilon_1 = \epsilon_2 = 1.0$, $\omega_0 = 0.5$ and x = 1.0

τ/L	1st	2nd	3rd	4th	5th
0.5	0.500	0.500	0.500	0.500	0.500
0.3	0.631	0.632	0.632	0.632	0.632
0.1	0.744	0.743	0.743	0.743	0.743
0.0	0.794	0.792	0.792	0.792	0.792
−0.1	0.840	0.838	0.837	0.837	0.837
−0.3	0.924	0.920	0.919	0.918	0.918
−0.5	1.000	1.000	1.000	1.000	1.000

Table 3 Comparison between the first-order result, equation (22), and the higher-order exact result. Values in parenthesis are numerical results reported in reference [6] ($L = 1$)

N_1	ω_0	x	First-order results equation (22)		Exact			
			$\epsilon = 1.0$	$\epsilon = 0.1$	$\epsilon = 1.0$	$\epsilon = 0.1$	$\epsilon = 1.0$	$\epsilon = 0.1$
							2.572	2.221
	0		2.569	2.202	2.536	2.047	(2.600)	(2.245)
1.0		1.0	2.592	2.149	2.577	2.048	2.594	2.157
	0.5	0	2.549	2.145	2.536	2.047	2.550	2.154
		−1.0	2.511	2.142	2.500	2.047	2.512	2.150
							0.769	0.402
	0		0.765	0.371	0.736	0.247	(0.798)	(0.393)
0.1		1.0	0.792	0.335	0.777	0.248	0.793	0.349
	0.5	0	0.748	0.333	0.736	0.247	0.750	0.346
		−1.0	0.711	0.330	0.700	0.247	0.712	0.343

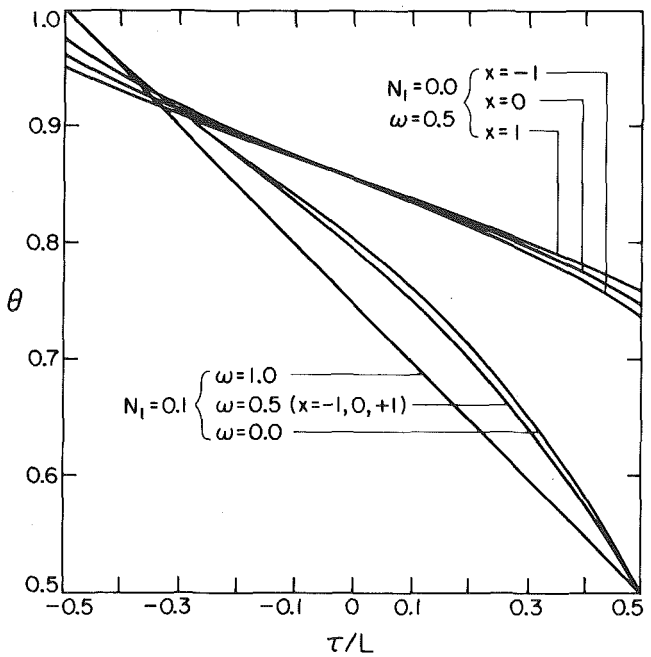

Fig. 1 The effect of anisotropic scattering on the medium's temperature with $L = 1.0$ and $\epsilon = 1.0$

Table 4 Effect of system parameters on the heat transfer result with $L = 1.0$

	N_1	$\epsilon_1 = \epsilon_2 = 1.0$			$\epsilon_1 = \epsilon_2 = 0.1$		
ω_0	x	1.0	0.1	0.01	1.0	0.1	0.01
0	0	2.572	0.769	0.567	2.221	0.403	0.158
	1.0	2.594	0.793	0.600	2.157	0.349	0.131
0.5	0	2.550	0.750	0.559	2.154	0.346	0.130
	−1.0	2.512	0.712	0.523	2.150	0.343	0.129
	1.0	2.602	0.802	0.622	2.048	0.248	0.068
1.0	0	2.519	0.719	0.539	2.047	0.247	0.067
	−1.0	2.456	0.656	0.476	2.047	0.247	0.067

Table 5 Effect of system parameters on the heat transfer result with $L = 10.0$

	M_1	$\epsilon_1 = \epsilon_2 = 1.0$			$\epsilon_1 = \epsilon_2 = 0.1$		
ω_0	x	1.0	0.1	0.01	1.0	0.1	0.01
0	0	20.115	2.115	0.315	20.105	2.106	0.305
	1.0	20.134	2.134	0.335	20.118	2.118	0.316
0.5	0	20.114	2.114	0.314	20.100	2.101	0.299
	−1.0	20.099	2.098	0.299	20.088	2.088	0.287
	1.0	20.155	2.155	0.355	20.039	2.039	0.239
1.0	0	20.110	2.110	0.310	20.035	2.035	0.235
	−1.0	20.085	2.085	0.285	20.032	2.032	0.232

totally change its direction repeatedly. After many reflections, the energy ray effectively "loses its sense of direction." The anisotropic effect of the scattering process becomes randomzied. The forward-backward scattering parameter x thus has only a relatively minor effect for systems with small surface emissivity.

Finally, it is interesting to note that for anisotropic-scattering media, an increase in the scattering albedo ω_0 does not necessarily lead to a reduction on the total heat transfer as it was suggested by the existing isotropic-scattering result [8] and confirmed by results shown in Tables 4 and 5 with $x = 0$. For many cases with $x \neq 0$, the total heat flux for a scattering medium ($\omega_0 \neq 0$) is actually greater than that of the corresponding nonscattering case ($\omega_0 = 0$). For cases considered in the present work, this unexpected behavior of anisotropic-scattering on heat transfer appears for systems with $\epsilon = 1.0$. Physically, this phenomenon can be explained by noting that a strong forward-scattering ($x = 1.0$) generally increases heat transfer. For systems with large surface emissivity in which the overall effect of ω_0 is small, the increase in heat transfer due to forward-scattering may, in some instances, be large enough to cause a net increase in the overall heat transfer. This rather "abnormal" effect of scattering does not appear for systems with $\epsilon = .1$. For those systems, the drop of the heat transfer due to the increase in ω_0 is large enough that even when $x = 1.0$, the heat transfer is less than that of the pure absorption case.

Concluding Remarks. The problem of simultaneous conduction and radiation through absorbing, emitting and anisotropically-scattering material is considered. The problem is solved by a successive approximation technique similar to the tradiational method of undetermined parameter. The conclusions that may be drawn from the presetn study are as follows:

1 The temperature profile of an anisotropically-scattering medium depends a great deal on the scattering albedo ω_0. The forward-backward scattering parameter x has only a minor effect on the medium's temperature.

2 Both ω_0 and x have important effects on the total heat transfer. The realtive importance of these effects depend on the surface emissivity of the boundaries. When ϵ is small, ω_0 has a significant effect on heat transfer and the effect of x is relatively unimportant. Scattering generally decreases heat transfer. When ϵ is large, on the other hand, the effect of ω_0 on the heat transfer is small and the effect of x becomes significant. The net heat transfer in a scattering medium can be greater or smaller than that of the pure absorption case depending on the value of x.

References

1 Schuster, A., "Radiation Through a Foggy Atmosphere," *Astrophysics Journal,* Vol. 21, 1905, pp. 1–22.

2 Van der Held, E. M. F., "Contribution of Radiation to Conduction of Heat," *Applied Science Research,* Vol. 3A, 1953, pp. 237–249.

3 Larkin, B. K. and Churchill, S. W., "Heat Transfer by Radiation Through Porous Insulation," *AIChE Journal,* Vol. 5, 1959, pp. 467–474.

4 Glaser, P. E., "Heat Transfer Mechanisms in Evacuated Powder Insulation," *International Developments in Heat Transfer,* Part IV, ASME, New York, 1961, pp. 829–837.

5 Viskanta, R. and Grosh, R. J., "Heat Transfer in a Thermal Radiation Absorbing and Scattering Medium," *International Developments in Heat Transfer,* Part IV, ASME, New York, 1961, pp. 820–828.

6 Viskanta, R. and Grosh, R. J., "Heat Transfer by Simultaneous Conduction and Radiation in an Absorbing Medium," ASME JOURNAL OF HEAT TRANSFER, Vol. 84, 1962, pp. 63–72.

7 Viskanta, R. and Grosh, R. J., "Effect of Surface Emissivity on Heat Transfer by Simultaneous Conduction and Radiation," *International Journal Heat Mass Transfer,* Vol. 5, 1962, pp. 729–734.

8 Viskanta, R., "Heat Transfer by Conduction and Radiation in Absorbing and Scattering Materials," ASME JOURNAL OF HEAT TRANSFER, Vol. 87, 1965, pp. 143–150.

9 van der Hurlst, *Light Scattering by Small Particles,* John Wiley & Sons, New York, 1957.

10 Dayan, A. and Tien, C. L., "Heat Transfer in a Gray Planar Medium with Linear Anisotropic Scattering," ASME JOURNAL OF HEAT TRANSFER, Vol. 97, 1975, pp. 391–396.

11 Yuen, W. W. and Tien, C. L., "A Successive Approximation Approach to Problems in Radiative Transfer with a Differential Formulation," accepted for publication in ASME JOURNAL OF HEAT TRANSFER.

12 Yuen, W. W. and Wong, L. W., "A Parametric Study of Radiative Transfer with Anisotropic Scattering in a One-dimensional System," accepted for publication in the *Journal of Quantitative Spectroscopy and Radiative Transfer.*

13 Siegel, R. and Howell, J. R., *Thermal Radiation Heat Transfer,* McGraw-Hill, New York, 1972.

14 Private communication with Professor R. Viskanta.

J. C. McWhorter, III
Aerospace Engineering.

M. H. Sadd[1]
Mechanical Engineering,
Mem. ASME

Mississippi State University,
Mississippi State, Miss.

Numerical Anisotropic Heat Conduction Solutions Using Boundary-Fitted Coordinate Systems

A numerical method is presented and applied to the solution of two-dimensional steady-state, anisotropic heat conduction problems. The solution method employs the boundary-fitted coordinate system technique which transforms the region under study onto a fixed rectangular domain where computations are done easily. Consequently, the procedure eliminates the shape of the boundary as a complicating factor. The method is quite general and can handle any multiply-connected, arbitrary-shaped region. Two examples, a solid disk and an eccentric annulus, are worked out to demonstrate the utility of the method. Isotherm results check with previously published solutions.

Introduction

The mechanical and thermomechanical behavior of composite materials has been of great interest in recent years due to the wide spread use of such materials. This interest produces a need to find solutions to various anisotropic continuum theories. Many of these theories have been developed several years ago, but only recently, with the increased use of composites, have these theories had significant applications. This paper is concerned with the thermal response of such materials when they act as conductors of heat.

Because of the anisotropy, the heat conduction equation is more complicated when compared with isotropic theory, and hence anisotropic solutions are difficult to attain. Recent investigations into anisotropic heat conduction have produced solutions by employing a variety of methods. Solution methods include: transformation theory [1–3]; Green's functions [4–6]; complex variable theory [7, 8]; finite differences [9]; and others. Experimental work in this area is very sparse, and is probably due to the fact that two-and commonly three-dimensional data must be gathered to correlate with theoretical solutions.

Many of the previous solution methods run into difficulty when applied to finite-sized, irregular-shaped bodies. For example, the common transformation technique of transforming the given coordinates into principal ones is not useful for problems in bounded regions because the boundary will be deformed and conditions thereon will become more complicated. This is especially true for boundary conditions of the second and third kinds. Consequently, although many of these previous solution techniques will be successful for a class of problem types, they are not universally applicable to all problems.

This present work is concerned with a numerical method using boundary-fitted coordinates to solve steady-state, two-dimensional, anisotropic problems. The boundary-fitted curvilinear coordinate method was developed several years ago and has been applied in other areas of engineering science. The procedure contains an automatic numerical generation of a curvilinear coordinate system with coordinate lines coincident with all boundaries of the region under study. The region can be a general multiconnected two-dimensional domain, with irregular boundaries which may even be time dependent. In addition the technique is not necessarily restricted to two dimensions.

After presenting the boundary-fitted coordinate method and how it can be applied to the two-dimensional steady-state heat conduction equation, two examples, one simply connected and one doubly-connected, are worked out. Example results check with previously published solutions.

Boundary-Fitted Coordinate Method

The technique of boundary-fitted coordinate systems is based on a method of automatic numerical generation of a general curvilinear coordinate system having a coordinate line coincident with each boundary of a general multiconnected domain under study. Through this new coordinate generation, a coordinate transformation is thus produced. The procedure is not in general a conformal mapping and is not limited to boundaries generated by complex transformations. Consequently the basic method is not limited to two-dimensions. The curvilinear coordinates are generated as the solution of a system of elliptic partial differential equations, one coordinate being specified to be constant on each boundary, with monotonic variations of the other coordinates along the boundaries. The coordinate system so generated is not necessarily orthogonal; however, as will be seen later, orthogonality is not really necessary in order to use the method in problem solution.

The basic idea of numerically generating boundary-fitted coordinates by solving an elliptic boundary value problem has been developed previously for simply connected domains by several investigators [10–14]. Thompson and his co-workers [15–16] extended Chu's [12] approach and have developed the method into a rather general and sophisticated technique for the solution of fluid mechanics problems. The method, of course, is useful for any boundary value problem involving partial differential equations. Our work here utilizes much of developments due to Thompson, et al. [15–16].

Once the curvilinear coordinates have been generated, any set of partial differential equations may be solved on this new coordinate system by transforming the equations and boundary conditions and solving the resulting set of equations. The important point is that this generated coordinate system produces a rectangular domain in the transformed space. Consequently, regardless of the shape and number of boundaries, all computations, both to generate the coordinate system and to solve the differential equations of interest, can be done on a rectangular domain in the transformed space. This property then allows very simple finite difference methods to be applied in the actual computations. The transformed differential equations will become more complicated; however, the boundary conditions in the transformed domain are now specified on straight coordinate boundaries.

Restricting the discussion to two dimensions, consider the doubly-connected region D, bounded by two simple closed contours Γ_1 and Γ_2 as shown in Fig. 1. Through the generated curvilinear coordinates, it is required that Γ_1 map onto Γ^*_1, Γ_2 onto Γ^*_2, Γ_3 onto Γ^*_3, and Γ_4 onto Γ^*_4, where the transformed region is also illustrated in Fig. 1. Region D will be referred to as lying in the physical plane, while D* will lie in the transformed plane. It is important to note that the

[1] Presently at University of Rhode Island, Mechanical Engineering and Applied Mechanics Department, Kingston, RI 02881.

Contributed by the Heat Transfer Division for publication in the JOURNAL OF HEAT TRANSFER. Manuscript received by the Heat Transfer Division October 12, 1979.

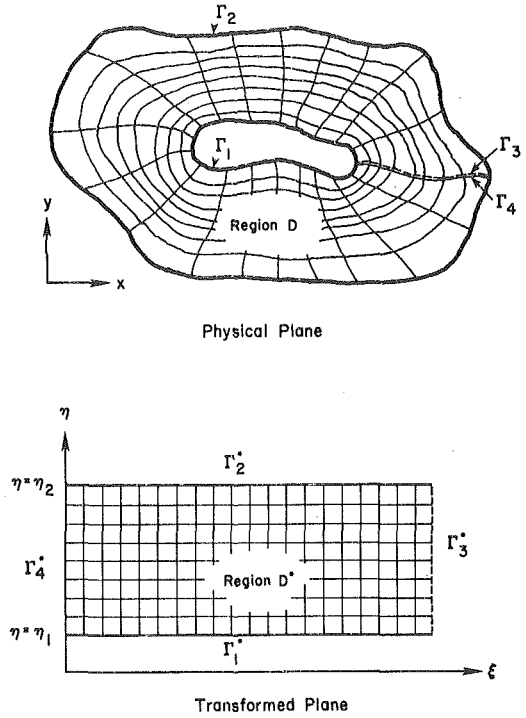

Fig. 1 Transformation geometry

transformed boundaries will be straight coordinate lines.

The general transformation from the physical x,y-plane to the transformed ξ,η-plane is specified by $\xi = \xi(x,y)$, $\eta = \eta(x,y)$ or by the inverse relations $x = x(\xi,\eta)$, $y = y(\xi,\eta)$. Derivatives in the physical plane are transformed by the relations

$$f_x = \frac{\partial(f,y)}{\partial(\xi,\eta)} \Big/ \frac{\partial(x,y)}{\partial(\xi,\eta)} = (y_\eta f_\xi - y_\xi f_\eta)/J$$
$$f_y = \frac{\partial(x,f)}{\partial(\xi,\eta)} \Big/ \frac{\partial(x,y)}{\partial(\xi,\eta)} = (-x_\eta f_\xi + x_\xi f_\eta)/J, \tag{1}$$

where J is the Jacobian of the transformation, i.e., $J = x_\xi y_\eta - x_\eta y_\xi$. Higher order derivatives are obtained by repeated applications of (1). A comprehensive set of transformed operators, unit vectors, and other useful relations are given in [16].

The basic idea of the method is to generate transformation functions $\xi(x,y)$ and $\eta(x,y)$ so that all physical boundaries coincide with ξ,η coordinate lines. In order to accomplish this task, $\xi(x,y)$ and $\eta(x,y)$ are required to be solutions of some suitable elliptic boundary value problem with one of these coordinates constant on the boundaries. An elliptic system is used because the solution of such a system is completely defined in the interior of the region by its values on the boundary. Following the work of Thompson [16], the curvilinear coordinates are taken to be solutions of the system

$$\xi_{xx} + \xi_{yy} = P(\xi,\eta)$$
$$\eta_{xx} + \eta_{yy} = Q(\xi,\eta) \tag{2}$$

where P and Q are coordinate control functions which are used to concentrate coordinate lines in areas of expected high gradients. Thompson has done extensive numerical studies to determine various choices for the coordinate control functions P and Q. The results of these studies indicated that exponential functions would produce very good control, and this choice was made for the present work (see [16] for details).

Since it is desired to perform all numerical computations on the uniform rectangular transformed plane, the dependent and independent variables in equation (2) must be interchanged, resulting in

$$\alpha x_{\xi\xi} - 2\beta x_{\xi\eta} + \gamma x_{\eta\eta} + J^2(Px_\xi + Qx_\eta) = 0$$
$$\alpha y_{\xi\xi} - 2\beta y_{\xi\eta} + \gamma y_{\eta\eta} + J^2(Py_\xi + Qy_\eta) = 0 \tag{3}$$

where

$$\alpha = x_\eta^2 + y_\eta^2, \qquad \gamma = x_\xi^2 + y_\xi^2 \tag{4}$$
$$\beta = x_\xi x_\eta - y_\xi y_\eta.$$

The transformed boundary conditions are

$$\begin{Bmatrix} x \\ y \end{Bmatrix} = \begin{Bmatrix} f_1(\xi,\eta_1) \\ f_2(\xi,\eta_1) \end{Bmatrix}, \quad \text{on } \Gamma^*_1$$
$$\begin{Bmatrix} x \\ y \end{Bmatrix} = \begin{Bmatrix} g_1(\xi,\eta_2) \\ g_2(\xi,\eta_2) \end{Bmatrix}, \quad \text{on } \Gamma^*_2 \tag{5}$$

The functions $f_{1,2}$ and $g_{1,2}$ are determined by the shape of the contours Γ_1 and Γ_2 and the specified distribution of ξ thereon. Boundary data are neither required nor allowed along the re-entrant boundaries Γ^*_3 and Γ^*_4.

Equations (3) can then be solved on the rectangular mesh by using a second-order central finite difference routine. The equations are solved by point SOR iteration, and thus produce the curvilinear coordinates $\xi(x,y)$, $\eta(x,y)$. The actual values of the coordinates, however, are irrelevant to the subsequent use of the coordinate system in the numerical solution of a system of partial differential equations. The mesh widths in the transformed plane, $\Delta\xi$ and $\Delta\eta$, simply cancel out of all difference expressions and are therefore taken as unity for convenience. Once the ξ,η-system is obtained we may then solve any set of partial differential equations on this coordinate system by solving the transformed equations on the rectangular transformed field.

Application to Anisotropic Heat Conduction

The previous boundary-fitted coordinate method is now applied to the solution of two-dimensional, steady-state, anisotropic heat conduction. The governing conduction equation using dimensionless variables reads

$$k_{xx}T_{xx} + 2k_{xy}T_{xy} + k_{yy}T_{yy} = 0. \tag{6}$$

where k_{xx}, k_{xy} and k_{yy} are the dimensionless thermal conductivities such that the flow of heat in the x and y directions is given by

$$q_x = -k_{xx}T_x - k_{xy}T_y$$
$$q_y = -k_{xy}T_x - k_{yy}T_y \tag{7}$$

Using the transformation (1), the conduction equation (6) becomes

$$A_1T_{\xi\xi} + A_2T_{\eta\eta} + A_3T_{\xi\eta} + A_4T_\xi + A_5T_\eta = 0, \tag{8}$$

where

$$A_1 = k_{xx}y_\eta^2 - 2k_{xy}x_\eta y_\eta + k_{yy}x_\eta^2$$
$$A_2 = k_{xx}y_\xi^2 - 2k_{xy}x_\xi y_\xi + k_{yy}x_\xi^2$$
$$A_3 = 2[-k_{xx}y_\eta y_\xi - k_{yy}x_\eta x_\xi + k_{xy}(x_\xi y_\eta + x_\eta y_\xi)] \tag{9}$$
$$A_4 = k_{xx}C_1 + k_{yy}C_2 + 2k_{xy}C_3$$
$$A_5 = k_{xx}C_4 + k_{yy}C_5 + 2k_{xy}C_6.$$

Nomenclature

J = transformation Jacobian
k_{xx}, k_{xy}, k_{yy} = dimensionless thermal conductivities
P, Q = coordinate control functions
q_x, q_y = dimensionless heat flux components
r, θ = dimensionless polar coordinates
T = dimensionless temperature
x,y = dimensionless Cartesian coordinates
ξ,η = dimensionless transformed coordinates

$$C_1 = y_\eta y_{\xi\eta} - y_\xi y_{\eta\eta} + (y_\xi y_\eta J_\eta - y_\eta{}^2 J_\xi)/J$$
$$C_2 = x_\eta x_{\xi\eta} - x_\xi x_{\eta\eta} + (x_\xi x_\eta J_\eta - x_\eta{}^2 J_\xi)/J$$
$$C_3 = x_\xi y_{\eta\eta} - x_\eta y_{\xi\eta} + (x_\eta y_\eta J_\xi - x_\xi y_\eta J_\eta)/J \tag{10}$$
$$C_4 = y_\xi y_{\xi\eta} - y_\eta y_{\xi\xi} + (y_\xi y_\eta J_\xi - y_\xi{}^2 J_\eta)/J$$
$$C_5 = x_\xi x_{\xi\eta} - x_\eta x_{\xi\xi} + (x_\xi x_\eta J_\xi - x_\xi{}^2 J_\eta)/J$$
$$C_6 = x_\eta y_{\xi\xi} - x_\xi y_{\xi\eta} + (x_\xi y_\xi J_\eta - x_\eta y_\xi J_\xi)/J.$$

The transformed conduction equation (8) is now to be solved numerically on the rectangular mesh shown in Fig. 1. In order to do this, equation (8) is written in finite difference form using central differences,

$$T_{i,j} = D_1[T_{i-1,j+1} + T_{i+1,j-1} - T_{i+1,j+1} - T_{i-1,j-1}] + D_2 T_{i,j+1} + D_3 T_{i-1,j} + D_4 T_{i+1,j} + D_5 T_{i,j-1},$$

where

$$D_1 = -A_3/8(A_1 + A_2)$$
$$D_2 = (A_2 + A_5/2)/2(A_1 + A_2)$$
$$D_3 = (A_1 - A_4/2)/2(A_1 + A_2) \tag{12}$$
$$D_4 = (A_1 + A_4/2)/2(A_1 + A_2)$$
$$D_5 = (A_2 - A_5/2)/2(A_1 + A_2).$$

In equation (11), $i = 1,2, \ldots i_{\max}$, $j = 1,2, \ldots j_{\max}$ corresponds to the ranges of ξ and η, respectively, (i.e., $\xi_1 \le \xi \le \xi_2$ and $\eta_1 \le \eta \le \eta_2$). For problem solution, equation (11) would be solved by SOR iteration on the transformed rectangular mesh. Particular boundary conditions to be coupled with the problem would also be transformed in exactly the same manner, and used along the straight coordinate boundaries as shown in Fig. 1.

Example Problems

The procedures developed in the previous sections are now applied to some example problems. Two examples, one simply connected and one doubly connected are worked out to demonstrate the utility of the method. A solid circular disk and an eccentric annulus both with temperature boundary conditions are solved. These problems were deliberately chosen so as to provide a comparison with the results of Chang, et al. [4]. Output in the form of isotherm results will be presented.

Solid Circular Disk. Consider a solid circular disk of unit radius with temperature boundary conditions specified according to

$$T(1,\theta) = \begin{cases} \sin\theta, 0 \le \theta \le \pi \\ 0 \quad \pi \le \theta \le 2\pi \end{cases}, \tag{13}$$

with respect to the polar coordinates r and θ.

In order to solve this problem using the boundary-fitted coordinate method, the coordinates ξ and η must first be generated. For the solid circular region under study, the circular boundary $r = 1$ is mapped onto portions of the rectangular region in the transformed plane. As mentioned previously the actual values of the coordinates are not really needed to use the method. However, with regard to coordinate control, the distribution of the coordinate lines is useful to know. For this particular problem, the region near or along the boundary would seem to be the zone of relatively high temperature gradients. Consequently in this region the coordinates were contracted (distributed more closely) by using appropriate forms for the control functions P and Q in equations (2) and (3). A plot of the ξ and η coordinate mesh in the physical plane is shown in Fig. 2.

Solving equation (11) with the boundry condition (13) yields results as shown in Fig. 3. Isotherm plots for various values of thermal conductivities are illustrated and isotherm warpage from the isotropic case is readily apparent. The results for the case $k_{xx} = 1.0$, $k_{xy} = 0.5$ and $k_{yy} = 1.2$ agree quite well with the work of Chang, et al. [4], as indicated in Fig. 4.

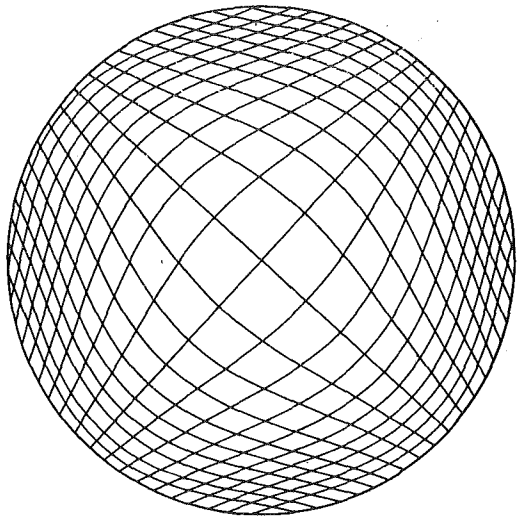

Fig. 2 Boundary-fitted coordinate system for the unit circular disk

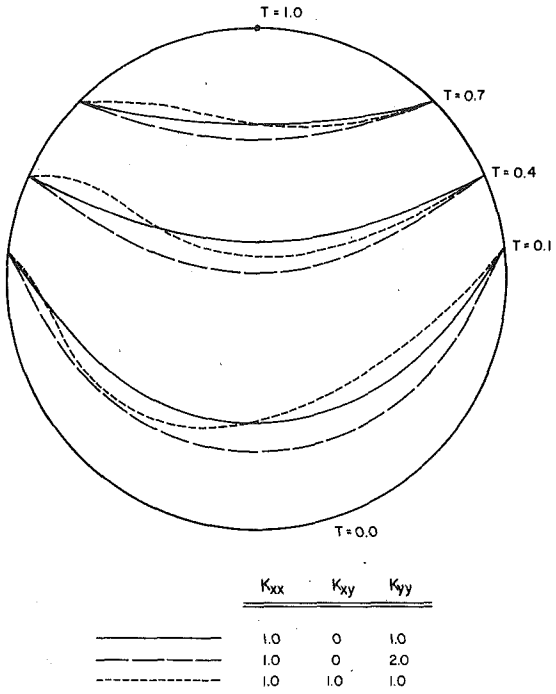

Fig. 3 Anisotropic temperature isotherms for the unit circular disk

Eccentric Circular Annulus. As a second example, the method is applied to a doubly connected region of an eccentric circular annulus. The diameter ratio of outer boundary to inner boundary is taken as 16:5, and the eccentricity is specified as 7/16 the outer radius. The boundary conditions are

$$T = \begin{cases} 1.0, & \text{on inner boundary} \\ 0.1, & \text{on outer boundary.} \end{cases} \tag{14}$$

Isotherm results for anisotropic and isotropic cases are shown in Fig. 5. A direct comparison with the results from [4] was impossible to make for this case because of the lack of specific dimensions in [4].

Discussion

The boundary-fitted coordinate system method has been applied to two-dimensional, anisotropic steady-state conduction problems. This particular method has been developed, refined and applied to problems in fluid mechanics. To the authors' knowledge, this is the first application to problems of heat conduction in solids. The two example problems were solved quite easily requiring about 3 min each

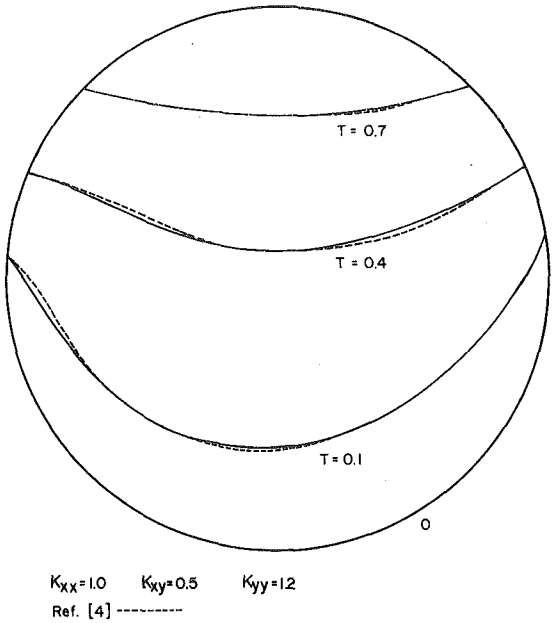

Fig. 4 Comparison of isotherms with those in reference [4]

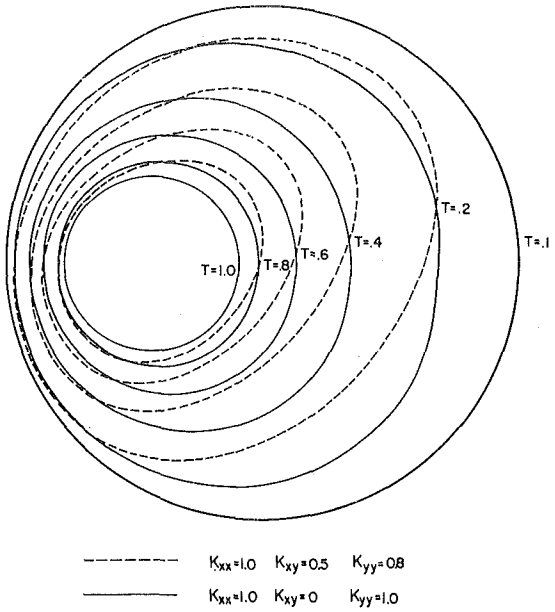

Fig. 5 Anisotropic temperature isotherms for the eccentric circular annulus

on a UNIVAC 1108 computer. The solution times necessary for more complicated shapes would probably be about the same, and consequently we believe that this method is quite efficient.

By transforming all computations onto the rectangular domain in the ξ,η-plane, finite difference techniques can be used without any interpolation between grid points. Hence the procedure eliminates the shape of the boundary as a complicating factor. It should be pointed out that poor representation of the boundary conditions is a primary source of inaccuracy in discretization techniques. This aspect of the method represents its most important contribution.

Other advantages of the method include the ability of handling time dependent boundaries, so as to analyze melting or deforming bodies. Although the boundary-fitted coordinate method has been developed and refined for two-dimensional problems, in principle the technique is also valid for three dimensions as well. Three-dimensional development is currently underway by Thompson, et al. [17].

Generalizing a bit, the boundary-fitted coordinate method can be applied to transient as well as steady state conduction. Furthermore, thermal stress analysis can also be handled by this technique. Hence the thermo-mechanical response of composite materials can be analyzed. These problems are currently being investigated and will appear in future publications.

References

1 Poon, K. C., and Chang, Y. P., "Transformation of Heat Conduction Problems from Anisotropic to Isotropic," *Letters in Heat Mass Transfer* Vol. 5, 1978, p. 215.

2 Mulholland, G. P., and Gupta, B. P., "Orthonormal Polynomial Solution of the Anisotropic Heat Transfer Equation", *Proceedings Fifth Canadian Congress of Applied Mechanics,* Fredericton, N.B., Canada, May 1975, p. 545.

3 Cobble, M. H., "Nonlinear Anisotropic Temperature Distribution in a Wedge," *International Journal Heat Mass Transfer,* Vol. 17, 1974, p. 379.

4 Chang, Y. P., Kang, C. S., and Chen, D. J., "The Use of Fundamental Green's Functions for the Solution of Problems of Heat Conduction in Anisotropic Media," *International Journal Heat Mass Transfer,* Vol. 16, 1973, p. 1905.

5 Chang, Y. P., "Analytical Solution for Heat Conduction in Anisotropic Media in Infinite, Semi-Infinite and Two-Plane-Bounded Regions," *International Journal Heat Mass Transfer,* Vol. 20, 1977, p. 1019.

6 Chang, Y. P., and Tsou, R. C. H., "Heat Conduction in an Anisotropic Medium Homogeneous in Cylindrical Regions—Unsteady State," ASME JOURNAL OF HEAT TRANSFER, Vol. 99, 1977, p. 41.

7 Clements, D. L., "Thermal Stress in an Anisotropic Elastic Half Space," *SIAM Journal Applied Mathematics,* Vol. 24, 1973, p. 332.

8 Tauchert, T. R. and Akoz, A. Y., "Stationary Temperature and Stress Fields in Anisotropic Elastic Slab," *ASME Journal Applied Mechanics,* Vol. 42, 1975, p. 647.

9 Katayama, K., Saito, A., and Kobayashi, N., "Transient Heat Conduction in Anisotropic Solids," *Proceedings International Conference Heat Mass Trans.,* Tokyo, Japan, 1974, p. 137.

10 Winshow, A. M., "Numerical Solution of the Quasi-Linear Poisson Equation in a Non-Uniform Triangular Mesh," *Journal Computational Physics,* Vol. 2, 1966, p. 149.

11 Barfield, W. D., "An Optimal Mesh Generator for Lagrangian Hydrodynamic Calculations in Two Space Dimensions," *Journal Computational Physics,* Vol. 6, 1970, p. 417.

12 Chu, W. H., "Development of a General Finite Difference Approximation for a General Domain, Part I: Machine Transformation," *Journal Computational Physics,* Vol. 8, 1971, p. 392.

13 Amsden, A. A., and Hirt, C. W., "A Simple Scheme for Generating General Curvilinear Grids," *Journal Computational Physics,* Vol. 11, 1973, p. 348.

14 Godunov, S. K., and Prokopov, G. P., "The Use of Moving Meshes in Gas Dynamics Computations," *USSR Computational Mathematics and Mathematical Physics,* Vol. 12, 1972, p. 182.

15 Thompson, J. F., Thames, F. C. and Mastin, C. W., "Automatic Numerical Generation of Body-Fitted Curvilinear Coordinate System for Fields Containing Any Number of Arbitrary Two-Dimensional Bodies," *Journal Computational Physics,* Vol. 15, 1974, p. 299.

16 Thompson, J. F., Thames, F. C. and Mastin, C. W., "TOMCAT—A Code for Numerical Generation of Boundary-Fitted Curvilinear Coordinate Systems on Fields Containing any Number of Arbitrary Two-Dimensional Bodies," *Journal Computational Physics,* Vol. 24, 1977, p. 274.

17 Mastin, C. W. and Thompson, J. F., "Three Dimensional Body-Fitted Coordinate Systems for Numerical Solution of the Navier-Stokes Equations," AIAA Paper No. 78-1147, AIAA 11th Fluid and Plasma Dynamics Conference, Seattle, Wash., July 1978.

Adnan H. Nayfeh

Department of Aerospace Engineering, and Applied Mechanics, University of Cincinnati, Cincinnati, OH

Continuum Modeling of Low Frequency Heat Conduction in Laminated Composites with Bonds

Two model analyses are constructed in order to determine the influence of bonding materials on the heat diffusion in otherwise bilaminated composites. The geometric arrangement of the composite with the bond is treated as a special type of trilaminated composite in which each of its major constituents is sandwiched between two bonding layers. In the first model, the recently developed continuum mixture theories of heat conduction in bilaminated composites [1] are extended to treat the trilaminated composite. Here details of the diffusion process in the major components and also in the bonding layers are derived. In the second model, the entire effect of the bonds is treated as a modifier to interfacial continuity conditions. In this model the details of the diffusion process in the bonding material are ignored. It is found that the results of both models correlate well with each others and also with some exact solutions especially for low frequency ranges.

Introduction

In recent years, both theoretical and experimental studies of composite structures have suggested that composite materials could be superior to metals in many structural applications. This is particularly true when high strength to weight and stiffness to weight ratios are desirable.

In the special case of heat diffusion studies very restricted classes of composites are treated. These consist of two components combined in the form of either periodically laminated plates or fiber reinforced matrix structures [1–4]. According to recently developed continuum mixture theories of heat diffusion in such composites [1, 4], the diffusion process can be approximately described by systems of two coupled partial differential equations. Such systems retain the integrity of the diffusion process in each constituent and allow them to coexist under derived coupling terms.

As mentioned above, such continuum theories only treat two component structures and, hence, do not take into consideration the possible influence of bonding agents on the overall behavior of the composite. In assessing the possible damage (perhaps in the form of debonding) in composites when subjected to various mechanical and thermal loadings, one may find it necessary to investigate the influence of bonding on the behavior of such composites. In such a case, and in the case of laminated composites, the geometrical arrangement of the composite can be thought of as a special type of trilaminated wave guide. Specifically, the laminates, which now represent three different materials, are assumed to be periodically stacked in such a way that any layer of materials 1 or 2 (the major constituents) is sandwiched between two layers of the bonding material (hereafter designated as material 0) as illustrated in Fig. 1.

In order to investigate the influence of the bonding material on the behavior of the composite we shall first extend the continuum theory [1] and analyze the trilaminated composite of Fig. 1. Horvay, et al. recently derived and discussed the exact characteristic equation of the trilaminated composite [6].[1] It is expected that the behavior of this composite will be described by a system of three coupled partial differential equations which retain the integrity of the diffusion process in the three components. Namely, details as to the distribution of temperature in each individual component (including the bonding components) will be readily available.

In actual applications, however, it is probably reasonable to assume that the thicknesses of the bonding components are much smaller than the thicknesses of the major components. For such a case, the detailed analysis of the diffusion process that takes place in the bonding components may well be unnecessary in light of the expectation that the variations of temperature across their thicknesses will be small. As an alternative, one may be able to construct a model analysis which ignores detailed processes in the bonding material but reflects its presence and influence in some fashion.

In our subsequent analysis we shall also present further simplifications under which thin bonding components may manifest themselves as modifiers to the interfacial continuity conditions between materials 1 and 2. Under these further simplifications, the behavior of the composite will be described by a system of two coupled partial differential equations which modifies the system presented in [1], namely in the absence of the bonding material. In our subsequent analysis we shall refer to this model as the reduced model. The results of both the trilaminated composite and its reduced model will be compared both analytically and numerically. Here we also indicate

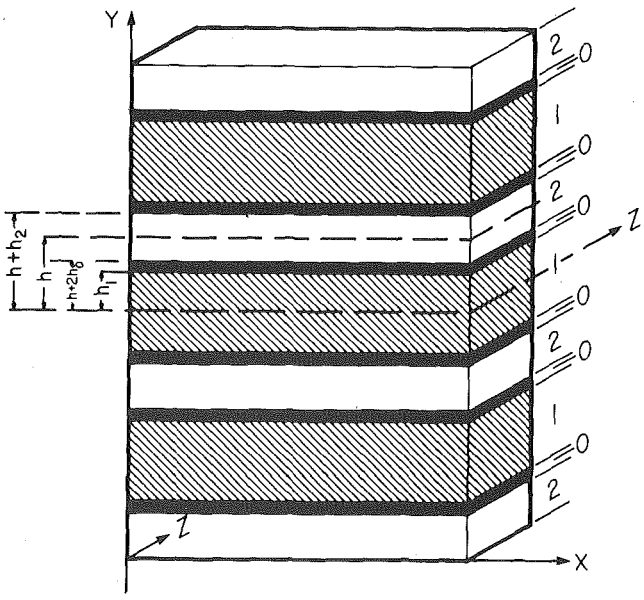

Fig. 1 Composite geometry

[1] The exact characteristic equation can also be easily obtained as an adaptation of the exact relation which we derived earlier for shear wave propagation in trilaminated composites [7].

Contributed by the Heat Transfer Division for publication in the JOURNAL OF HEAT TRANSFER. Manuscript received by The Heat Transfer Division February 20, 1979.

that we have recently investigated such a role of the bonds in the study of wave propagation in laminated composites [5].

The Trilaminated Model

Formulation of Problem. We consider heat diffusion in the direction parallel to the layering of a periodic array of linear, homogeneous, and isotropic trilaminated composite. The laminates which represent three different materials are assumed infinite in the x-z plane and are stacked normal to the y-axis in such a manner that any layer of material 1 or material 2 is sandwiched between two layers of material 0 as illustrated in Fig. 1. This specific periodicity arrangement best simulates the case in which material 0 acts as a bonding agent for materials 1 and 2. The laminates of material α, ($\alpha = 0, 1, 2$), will be identical and have the thickness $2h_\alpha$, the density ρ_α, the specific heat c_α and the conductivity k_α.

With reference to Fig. 1, the origin of the coordinate system is chosen at the centroid of one of the layers of material 1 such that the composite occupies the region $-\infty < y < \infty$. Without any loss in generality, we shall assume that no diffusion occurs in the z-direction. This is a consequence of the fact that the layers are assumed to extend to infinity in the z-direction.

Within the context of linear heat flow, the thermal field is described by the local energy balance

$$-\left(\frac{\partial q_{x\alpha}}{\partial x}+\frac{\partial q_{y\alpha}}{\partial y_\alpha}\right)=\rho_\alpha c_\alpha \frac{\partial T_\alpha}{\partial t}, \quad \alpha = 0, 1, 2 \tag{1}$$

and the constitutive equations for conduction

$$q_{x\alpha} = -k_\alpha \frac{\partial T_\alpha}{\partial x} \tag{2}$$

$$q_{y\alpha} = -k_\alpha \frac{\partial T_\alpha}{\partial y_\alpha} \tag{3}$$

Here $q_{x\alpha}$ and $q_{y\alpha}$ are the components of the heat flux vector; T_α denotes the change in the absolute temperature $T_{\alpha 0}$ and y_α is a local coordinate measured from the center line of the corresponding laminate. In addition to equations (1–3), the complete specification of the diffusion requires the continuity conditions

$$T_1 = T_0, \quad q_{y1} = q_{y0} \quad \text{at} \quad y = h_1, \tag{4}$$

$$T_0 = T_2, \quad q_{y0} = q_{y2} \quad \text{at} \quad y = h_1 + 2h_0; \tag{5}$$

the asymmetry conditions[2]

$$q_{y1}(x, h_1, t) = -q_{y1}(x, -h_1, t), \tag{6a}$$

$$q_{y2}(x, h + h_2, t) = -q_{y2}(x, h - h_2, t); \tag{6b}$$

where

$$h = h_1 + 2h_0 + h_2, \tag{7}$$

designates the microdimension of the composite; and finally appropriate initial and boundary conditions. These conditions need not, however, be specified at this stage. The conditions (6a, b), if used in conjunction with (3) imply the symmetry of T_1 and T_2, namely

$$T_1(x, -h_1, t) = T_1(x, h_1, t), \tag{8a}$$

$$T_2(x, h - h_2, t) = T_2(x, h + h_2, t). \tag{8b}$$

In the following, we shall combine equations (1–6b) into a single system of three equations which satisfies the continuity and asymmetry conditions (6a, b) and, hence, describes the diffusion process of the composite as that of an equivalent continuum. But first, since conditions (4–6b) do not involve the x-coordinate, we eliminate $q_{x\alpha}$ from equations (1) and (2) and obtain

$$\rho_\alpha c_\alpha \frac{\partial T_\alpha}{\partial x} - k_\alpha \frac{\partial^2 T}{\partial x^2} = -\frac{\partial q_{y\alpha}}{\partial y_\alpha} \tag{9}$$

which together with (3) constitute the complete field equations.

Continuum Mixture Equations. Following the procedure of [1], we couch the analysis in a continuum mixture format, by eliminating the y dependence of T_α and defining the so-called effective quantities. These are the values of the temperatures averaged over their respective laminate transverse dimension h_α. By so doing, we reduce the problem to a quasi-one-dimensional one, but limit the accuracy of our solution somewhat; i.e., averaged rather than actual field quantities are computed over the composite microdimension.

To this end, if we average equation (9) for $\alpha = 1$, 0, and 2, respectively, according to

$$\overline{(\ )}_1 = \frac{1}{h_1}\int_0^{h_1} (\ )_1\, dy, \tag{10}$$

$$\overline{(\ )}_0 = \frac{1}{2h_0}\int_{h_1}^{h_1+2h_0} (\ )_0\, dy, \tag{11}$$

$$\overline{(\ )}_2 = \frac{1}{h_2}\int_{h}^{h+h_2} (\ )_2\, dy, \tag{12}$$

and use the asymmetry and continuity conditions for $q_{y\alpha}$ as listed in (4–6b) we get

$$h_1\left[k_1\frac{\partial^2 \overline{T}_1}{\partial x^2} - \rho_1 c_1 \frac{\partial \overline{T}_1}{\partial t}\right] = q_{10} \tag{13}$$

$$2h_0\left[k_0\frac{\partial^2 \overline{T}_0}{\partial x^2} - \rho_0 c_0 \frac{\partial \overline{T}_0}{\partial t}\right] = q_{02} - q_{10} \tag{14}$$

$$h_2\left[k_2\frac{\partial^2 \overline{T}_2}{\partial x^2} - \rho_2 c_2 \frac{\partial \overline{T}_2}{\partial t}\right] = -q_{02} \tag{15}$$

where q_{10} and q_{02} define interfacial fluxes according to

$$q_{10} = q_{y1}(h_1) = q_{y0}(h_1) \tag{16}$$

$$q_{02} = -q_{y2}(h + h_2) = q_{y2}(h - h_2) = q_{y0}(h - h_2) \tag{17}$$

Here q_{10} and q_{02} constitute the transfer interaction terms between the three composite constituents.

The constitutive relation (3) together with the T_α continuity conditions listed in (4) and (5) will now be utilized to determine q_{10} and q_{02} as functions of $\overline{T}_1$, $\overline{T}_0$ and $\overline{T}_2$. Once this is done the problem described by equations (13–15) reduces to a one-dimensional one whose dependent variables, namely $\overline{T}_1$, $\overline{T}_0$ and $\overline{T}_2$ are functions of x only.

[2] These are assured by the symmetry of the geometric layering with respect to the center lines of layers 1 and 2 as may be easily seen from Fig. 1.

Nomenclature

c_α = specific heat at constant pressure for composite component α, $\alpha = 0, 1, 2$
h_α = half thickness of layer α
$h = h_1 + 2h_0 + h_2$
k_α = thermal conductivity of component α
ℓ = nondimensionalizing length
$n_\alpha = h_\alpha/h$, volume fractions, $n_0 = 2h_0/h$
$q_{x\alpha}$, $q_{y\alpha}$ = components of the heat fluxes
q_{10}, q_{02} = interfacial fluxes (interaction terms)
t = time
T = mixture temperature (zero frequency limit)
T_∞ = reference temperature
T_α = temperature of component α measured from T_∞
$\overline{T}_\alpha$ = average of T_α over the thickness h_α
$T^*_\alpha = \overline{T}_\alpha/T_\infty$ (nondimensional temperature)
x, y = space coordinates
$\alpha = 0, 1, 2$, a subscript designating the three composite components
γ = attenuation coefficient
$\epsilon = h/\ell$
ν = composite mixture diffusivity (equation (33))
ν_α = diffusivity of component α
$\bar{\nu}_\alpha = \nu_\alpha/\nu$, nondimensional diffusivity for component α
$\bar{\nu}$ = composite frequency dependent nondimensional diffusivity
ρ_α = density of component α
$\bar{\rho}_1$, $\bar{\rho}_2$, $\bar{\rho}_{12}$ = density dependent parameters (equation (45))
$\tau = t\,\nu/\ell$; nondimensional time
ω = nondimensional frequency

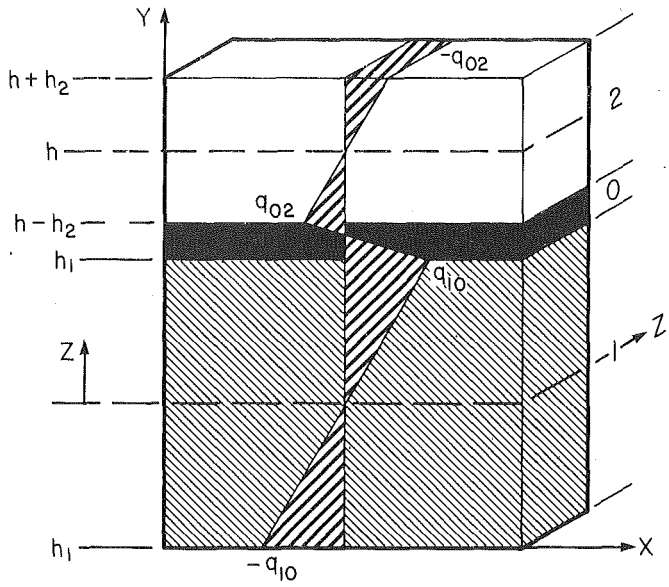

Fig. 2 Heat flux distribution

In order to do so we assume, guided by the asymmetry conditions (6*a*) and (6*b*), that q_{y1} and q_{y2} vary linearly with y according to[3]

$$q_{y1} = A_1 y, \tag{18}$$

$$q_{y2} = A_2(y - h). \tag{19}$$

Assuming also that q_{y0} varies linearly across its layers thickness, and using (18) and (19) together with the continuity conditions on q_{y0} dictates that q_{y0} takes the form (see Fig. 2)

$$q_{y0} = A_1 h_1 - \frac{(A_1 h_1 + A_2 h_2)\,(y - h_1)}{2h_0}. \tag{20}$$

Notice, in light of (16) and (17), that

$$q_{10} = A_1 h_1 \text{ and } q_{02} = -A_2 h_2. \tag{21a, b}$$

Substituting from (18) into (3) for $\alpha = 1$, multiplying the resulting equation by y, integrating according to (10) by parts and finally using (21*a*) gives

$$T_1(h_1) - \overline{T}_1 = -\frac{h_1}{3k_1} q_{10} \tag{22}$$

Similarly, substituting from (19) into (3) followed by multiplying the resulting equation by $(y - h)$, integrating according to (12) by parts and using (21*b*) gives

$$T_2\,(h + h_2) - \overline{T}_2 = \frac{h_2}{3k_2} q_{02} \tag{23}$$

Now, substituting from (20) into (3) for $\alpha = 0$, multiplying both sides by $(y - h_1)$, integrating according to (11) by parts, followed by using (21*a, b*) gives, after some algebraic reductions and manipulations

$$T_0(h_1 + 2h_0) - \overline{T}_0 = -\frac{2h_0}{k_0}\left\{\frac{q_{10}}{6} + \frac{q_{02}}{3}\right\}. \tag{24}$$

Finally, another relation similar to (24) which relates the difference between the value of $T_0(h_1)$ (at the materials 1 and 0 interface) and $\overline{T}_0$ to q_{10} and q_{02} can be obtained. Symmetry dictates that such an equation can also be obtained by interchanging $T_0(h_1 + 2h_0)$ by $T_0(h_1)$ and the role of q_{10} and q_{02} in (24) resulting in

$$T_0(h_1) - \overline{T}_0 = \frac{2h_0}{k_0}\left\{\frac{q_{02}}{6} + \frac{q_{10}}{3}\right\}. \tag{25}$$

Using the temperature continuity conditions (4) and (5), together with the symmetry relations (8*a, b*), equations (22–25) can be combined and solved for q_{10} and q_{02} to yield

$$q_{10} = \frac{1}{h}\,[D_1(\overline{T}_1 - \overline{T}_0) - D_0(\overline{T}_0 - \overline{T}_2)] \tag{26}$$

$$q_{02} = \frac{1}{h}\,[D_2\,(\overline{T}_0 - \overline{T}_2) - D_0(\overline{T}_1 - \overline{T}_0)] \tag{27}$$

where

$$D_1 = \frac{12k_1\,k_0\,(n_2k_0 + n_0k_2)}{M} \tag{28a}$$

$$D_0 = \frac{6k_1k_0k_2n_0}{M} \tag{28b}$$

$$D_2 = \frac{12k_0k_2(n_1k_0 + n_0k_1)}{M} \tag{28c}$$

with

$$M = 4(n_1k_0 + n_0k_1)(n_2k_0 + n_0k_2) - n_0^2k_1k_2 \tag{28d}$$

$$n_1 = \frac{h_1}{h}, \quad n_0 = \frac{2h_0}{h}, \quad n_2 = \frac{h_2}{h} \tag{28e}$$

Substitution from (26) and (27) into (13–15) yields

$$k_1n_1\frac{\partial^2\overline{T}_1}{\partial x^2} - \rho_1n_1c_1\frac{\partial\overline{T}_1}{\partial t} = \frac{1}{h^2}\,[D_1(\overline{T}_1 - \overline{T}_0) - D_0\,(\overline{T}_0 - \overline{T}_2)] \tag{29}$$

$$k_0n_0\frac{\partial^2\overline{T}_0}{\partial x^2} - \rho_0n_0c_0\frac{\partial\overline{T}_0}{\partial t} = \frac{1}{h^2}[(D_0 + D_2)\,(\overline{T}_0 - \overline{T}_2) - (D_1 + D_0)\,(\overline{T}_1 - \overline{T}_0)] \tag{30}$$

$$k_2n_2\frac{\partial^2\overline{T}_2}{\partial x^2} - \rho_2n_2c_2\frac{\partial\overline{T}_2}{\partial t} = \frac{1}{h^2}\,[D_0\,(\overline{T}_1 - \overline{T}_0) - D_2\,(\overline{T}_0 - \overline{T}_2)] \tag{31}$$

The three coupled equations (29–31) comprise a mixture system for the laminated composite. In general, these equations retain the integrity of the diffusion process in the individual constituents (including the bonds) and allow them to coexist under the derived interaction (26) and (27). In particular, information as to the distribution of the temperature in the individual constituent is readily obtainable.

As a further observation, assuming that the left hand sides of (29–31) remain finite while letting $h \to 0$ leads to the restriction that $\overline{T}_1 = \overline{T}_0 = \overline{T}_2 = T$. For this limiting case the sum of equations (29–31) yields the single equation

$$\nu\frac{\partial^2T}{\partial x^2} - \frac{\partial T}{\partial t} = 0 \tag{32}$$

in which the mixture diffusivity ν is given by

$$\nu = \frac{k_1n_1 + k_0n_0 + k_2n_2}{\rho_1c_1n_1 + \rho_0c_0n_0 + \rho_2c_2n_2} \tag{33}$$

This limit which can also be designated as the strong coupling limit is equivalent to the so-called zero frequency limit of laminated composites. In equation (32), we effectively replaced the actual composite by a homogenized continuum whose properties, as reflected in the definition of ν, are weighted functions of the individual constituent's properties and volume fractions.

Finally, in the limit as $h \to \infty$, (also can be designed as a weak coupling case), the temperatures in (29–31) uncouple and diffuse with the three distinct diffusivities ν_α, $\alpha = 0, 1, 2$. This limit is equivalent to the high frequency limit in laminated composites.[4] Both the weak and strong coupling limits are also predicted by the exact analysis as developed in [6] and discussed in the following sections.

[3] For a justification of such approximations we refer the reader to [1, 4]. This also implies that subsequent analysis will be valid at low frequency ranges.

[4] Although our analysis correctly predicts the results as the frequency approaches infinity the bulk of our results, as implied by the approximations (18–20) are valid for moderately low frequencies.

The Reduced Model

The system of the three equations (29–31) is algebraically cumbersome especially when compared with the relatively simple system of the two equations derived for the bilaminated composite in [1]. This is, of course, due to the inclusion of the detailed analysis of the diffusion process in the bonding components (material 0). However, since we are interested in this problem mainly when the thickness of the bonding agent, $2h_0$, is small compared with the thickness of the major components, we can proceed in a much less cumbersome way in which we treat the entire effect of the bond as a nonzero homogeneous term in the interfacial continuity conditions (hereafter we shall refer to as the reduced model). To this end, and before investigating the general behavior of the continuum model of the trilaminated composite (equations (29–31)) numerically, we shall first develop the results under the above assertion.

The idea here is to assume that $2h_0$ is so small (but not zero) such that variations in the temperature T_0 across the thickness of the bonding component can be neglected. This limit allows us to adopt the following approximations

$$T_0\,(h_1 + 2h_0) = \overline{T}_0 \equiv T_0, \quad T_0(h_1) = \overline{T}_0 \equiv T_0 \tag{34}$$

Moreover, the relations (34) together with the continuity relations (4) and (5) and symmetry relations (8a,b) imply

$$T_1(h_1) = T_0(h_1) = T_0 = T_2\,(h - h_2) = T_2\,(h + h_2) \tag{35}$$

Substituting from (35) into (22) and (23) yields

$$T_0 - \overline{T}_1 = -\frac{h_1}{3k_1}\,q_{10} \tag{36}$$

$$T_0 - \overline{T}_2 = \frac{h_2}{3k_2}\,q_{02} \tag{37}$$

By adding and subtracting equations (36) and (37) we get

$$T_0 = \frac{1}{2}\,(\overline{T}_1 + \overline{T}_2) + \frac{1}{6}\left(\frac{h_2}{k_2}\,q_{02} - \frac{h_1}{k_1}\,q_{10}\right) \tag{38}$$

$$\overline{T}_1 - \overline{T}_2 = \frac{h_1}{3k_1}\,q_{10} + \frac{h_2}{3k_2}\,q_{02} \tag{39}$$

Once we identify $\overline{T}_0$ with T_0, equation (14) becomes of most importance since it is the only equation which reflects the presence of the bonding material. Specifically it states the modified interfacial continuity relation. In the absence of the bonding material, namely, for $h_0 = 0$, it reduces to the bilaminated composite continuity relation $q_{10} = q_{02}$ as expected.

Now, by eliminating T_0 ($\overline{T}_0 \equiv T_0$) from between (14) and (38) the resulting equation can be combined with (39) to solve for q_{10} and q_{02} individually as

$$(s - 2s_1s_2h_0L_0)q_{10} = (1 - 2h_0s_2L_0)\,\overline{T}_1 - \overline{T}_2 \tag{40a}$$

$$(s - 2s_1s_2h_0L_0)q_{02} = \overline{T}_1 - (1 - 2s_1h_0L_0)\,\overline{T}_2 \tag{40b}$$

where

$$s_1 = \frac{h_1}{3k_1}, \quad s_2 = \frac{h_2}{3k_2}, \quad s = s_1 + s_2 \tag{41a}$$

and L_0 is a space-time operator given by

$$L_0 = k_0\frac{\partial^2}{\partial x^2} - \rho_0c_0\frac{\partial}{\partial t} \tag{41b}$$

Formally, equations (13, 15, 40a) and (40b) comprise the complete system which describes the behavior of the reduced model as reflected in the nonvanishing of h_0. Here the details of the diffusion process in the bonding material have been neglected.

Now, guided by our basic philosophy of approximations as reflected in the expansions (18–20) and justified in references [1, 4] as valid at low frequencies and large distances from boundaries (far field), we can still simplify the results (40a) and (40b) further. Here the low frequency and far field ranges insure that the terms involving $2h_0L_0$ are small in comparison with the remaining terms in equations (40a) and (40b). Hence to the first order of approximation in powers of h_0, equations (40a) and (40b) take the forms

$$q_{10} = \frac{1}{s^2}\,[s(\overline{T}_1 - \overline{T}_2) - 2s_2h_0L_0\,(s_1\overline{T}_2 + s_2\overline{T}_1)] \tag{42a}$$

$$q_{02} = \frac{1}{s^2}\,[s(\overline{T}_1 - \overline{T}_2) + 2s_1h_0L_0\,(s_1\overline{T}_2 + s_2\overline{T}_1)] \tag{42b}$$

Combination of equations (13, 15) and (42a, b) yields, after rearrangements, the two coupled equations

$$a_{11}\frac{\partial^2\overline{T}_1}{\partial x^2} - \bar{\rho}_1\frac{\partial\overline{T}_1}{\partial t} + a_{12}\frac{\partial^2\overline{T}_2}{\partial x^2} - \bar{\rho}_{12}\frac{\partial\overline{T}_2}{\partial t} = \frac{1}{hs}\,(\overline{T}_1 - \overline{T}_2) \tag{43}$$

$$a_{22}\frac{\partial^2\overline{T}_2}{\partial x^2} - \bar{\rho}_2\frac{\partial\overline{T}_2}{\partial t} + a_{12}\frac{\partial^2\overline{T}_1}{\partial x^2} - \bar{\rho}_{12}\frac{\partial\overline{T}_1}{\partial t} = -\frac{1}{hs}\,(\overline{T}_1 - \overline{T}_2) \tag{44}$$

where

$$a_{11} = n_1k_1 + n_0k_0\kappa_2^2, \quad \bar{\rho}_1 = \rho_1c_1n_1 + \rho_0c_0n_0\kappa_2^2 \tag{45a}$$

$$a_{22} = n_2k_2 + n_0k_0\kappa_1^2, \quad \bar{\rho}_2 = \rho_2c_2n_2 + \rho_0c_0n_0\kappa_1^2 \tag{45b}$$

$$a_{12} = n_0k_0\kappa_1\kappa_2, \quad \bar{\rho}_{12} = n_0\rho_0c_0\kappa_1\kappa_2,$$

$$\kappa_i = \frac{s_i}{s}, \quad i = 1, 2 \tag{45c}$$

The two coupled equations (43) and (44), comprise the continuum mixture description of the reduced composite model in which the entire effect of the bonding material is taken as a modifier to the interface continuity relations. In the final analysis, as it is seen from equations (43) and (44), this leads to modifications of the effective properties of the major two composite components as is obvious from the definitions of the parameters (45). For the special case where $h_0 = 0$, ($n_0 = 0$), the entire effect of the bonding material disappears and equations (43) and (44) reduce identically, except for some notational differences, to the system of equations derived for the bilaminated composite [1].

As in the case of the trilaminated continuum model we observe that as $h \to 0$ the temperatures $\overline{T}_1$ and $\overline{T}_2$ of equations (43) and (44) approach each other. For this limiting case the addition of equations (43) and (44) leads identically to the single mixture equation (32) with the same diffusivity (33). Thus, both of our models agree in predicting the effective mixture diffusivity ν which is also the same as may be obtained from the exact characteristic equation of [6].

Plane Harmonic Temperature-Comparison of Present Models with Exact Results

In order to ascertain the domain of validity of the foregoing mixture models we shall now compare their resultss with some corresponding exact solutions. Perhaps the easiest solutions of equations (1–7) to obtain are those corresponding to harmonic temperature excitations. This results in a characteristic equation which demonstrates the dependence of the diffusivity ν on the frequency of excitation ω, as developed in reference [6].

For the sake of convenience in our subsequent analysis, we shall now nondimensionalize the two systems of equations (29–31) and (43) and (44). To this end, we introduce the new variables

$$\xi = x/\ell, \; T_\alpha^* = \overline{T}_\alpha/T_\infty, \tag{46a}$$

$$\tau = \frac{t\nu}{\ell^2}, \quad \epsilon = h/\ell \tag{46b}$$

where ℓ designates a characteristic length and T_∞ denotes a reference constant temperature. Substituting from (46) into (29–31) yields, for the trilaminated model, the system of equations

$$\bar{\nu}_1\frac{\partial^2T_1^*}{\partial\xi^2} - \frac{\partial T_1^*}{\partial\tau} = \frac{1}{\nu\rho_1c_1n_1\epsilon^2}\,[D_1\,(T_1^* - T_0^*) - D_0(T_0^* - T_2^*)] \tag{47}$$

$$\bar{\nu}_0\frac{\partial^2T_0^*}{\partial\xi^2} - \frac{\partial T_0^*}{\partial\tau} = \frac{1}{\nu\rho_0c_0n_0\epsilon^2}\,[(D_0 + D_2)\,(T_0^* - T_2^*) - (D_1 + D_0)\,(T_1^* - T_0^*)] \tag{48}$$

$$\bar{\nu}_2 \frac{\partial^2 T_2^*}{\partial \xi^2} - \frac{\partial T_2^*}{\partial \tau} = \frac{1}{\nu \rho_2 c_2 n_2 \epsilon^2} [D_0 (T_1^* - T_0^*) - D_2 (T_0^* - T_2^*)] \quad (49)$$

where

$$\nu_\alpha = \frac{k_\alpha}{\rho_\alpha c_\alpha}, \quad \bar{\nu}_\alpha = \frac{\nu_\alpha}{\nu}, \quad \alpha = 0, 1, 2 \quad (50)$$

denote the diffusivity and the normalized diffusivity of the component α respectively. Similarly, substituting from (46a, b) into (43) and (44) yields, for the reduced model, the system

$$a_{11} \frac{\partial^2 T_1^*}{\partial \xi^2} - \bar{\rho}_1 \nu \frac{\partial T_1^*}{\partial \tau} + a_{12} \frac{\partial^2 T_2^*}{\partial \xi^2} - \bar{\rho}_{12} \nu \frac{\partial T_2^*}{\partial \tau} = \frac{1}{\epsilon^2 s^*} (T_1^* - T_2^*) \quad (51)$$

$$a_{22} \frac{\partial^2 T_2^*}{\partial \xi^2} - \bar{\rho}_2 \nu \frac{\partial T_2^*}{\partial \tau} + a_{12} \frac{\partial^2 T_1^*}{\partial \xi^2} - \bar{\rho}_{12} \nu \frac{\partial T_1^*}{\partial \tau} = -\frac{1}{\epsilon^2 s^*} (T_1^* - T_2^*) \quad (52)$$

where

$$s^* = \frac{n_1}{3k_1} + \frac{n_2}{3k_2}. \quad (53)$$

For harmonic temperature excitations, we consider a half-space initially at rest and subject at time zero to a harmonic boundary which is symmetric with respect to the x-axis. Accordingly we consider solutions in the form

$$T_\alpha^* = A_\alpha e^{(i\omega\tau + q\xi)}, \quad \alpha = 0, 1, 2 \quad (54)$$

where we define the diffusivity, $\nu_e(\omega)$, and the attenuation parameter, $\gamma(\omega)$, as

$$\nu_e(\omega) = \omega / Im(q^2), \quad \gamma(\omega) = -\mathrm{Re}(q) \quad (55)$$

Subsequently, we substitute from (54) into (47–49) and obtain the characteristic equation of the trilaminated model as

$$\epsilon^4 (\bar{\nu}_1 q^2 - i\omega)(\bar{\nu}_0 q^2 - i\omega)(\bar{\nu}_2 q^2 - i\omega) - \epsilon^2 [a_3 q^4 - a_2 i\omega q^2 - a_1 \omega^2] + a_4 (q^2 - i\omega) = 0 \quad (56)$$

with

$$a_1 = \frac{1}{\nu} \left[\frac{D_1}{\rho_1 c_1 n_1} + \frac{D_1 + 2D_0 + D_2}{\rho_0 c_0 n_0} + \frac{D_2}{\rho_2 c_2 n_2} \right] \quad (57a)$$

$$a_2 = \frac{1}{\nu} \left[\frac{D_1 (\bar{\nu}_0 + \bar{\nu}_2)}{\rho_1 c_1 n_1} + \frac{(D_1 + 2D_0 + D_2)(\bar{\nu}_1 + \bar{\nu}_2)}{\rho_0 c_0 n_0} + \frac{D_2 (\bar{\nu}_1 + \bar{\nu}_0)}{\rho_2 c_2 n_2} \right] \quad (57b)$$

$$a_3 = \frac{1}{\nu} \left[\frac{D_1 \bar{\nu}_0 \bar{\nu}_2}{\rho_1 c_1 n_1} + \frac{(D_1 + 2D_0 + D_2)\bar{\nu}_1 \bar{\nu}_2}{\rho_0 c_0 n_0} + \frac{D_2 \bar{\nu}_1 \bar{\nu}_0}{\rho_2 c_2 n_2} \right] \quad (57c)$$

$$a_4 = \frac{D_1 D_2 - D_0^2}{\nu} \frac{\rho_1 c_1 n_1 + \rho_0 c_0 n_0 + \rho_2 c_2 n_2}{\rho_1 c_1 n_1 \rho_0 c_0 n_0 \rho_2 c_2 n_2} \quad (57d)$$

Similarly, we substitute from (54) for $\alpha = 1, 2$ into (51) and (52) and obtain, after some algebraic reductions and manipulations, the characteristic equation of the reduced model as

$$F_3 (A_1 q^2 - i\omega)(A_2 q^2 - i\omega) - (q^2 - i\omega) = 0 \quad (58)$$

where

$$F_3 = \frac{(\bar{\rho}_1 \bar{\rho}_2 - \bar{\rho}_{12}^2) \nu^2 s^*}{a_{11} + a_{22} + 2a_{12}}, \quad A_{1,2} = \frac{F_2 \pm \sqrt{F_2^2 - 4F_1}}{2} \quad (59a)$$

with

$$F_1 = \frac{a_{11} a_{22} - a_{12}^2}{(\bar{\rho}_1 \bar{\rho}_2 - \bar{\rho}_{12}^2)\nu^2}, \quad F_2 = \frac{\bar{\rho}_1 a_{22} + \bar{\rho}_2 a_{11} - 2a_{12}\bar{\rho}_{12}}{(\bar{\rho}_1 \bar{\rho}_2 - \bar{\rho}^2)\nu} \quad (59b)$$

Discussions and Numerical Results

Equations (56, 58) and (A10) define the characteristic equations of the trilaminated, reduced and exact models, respectively. These equations demonstrate the dependence of the diffusivity ν_e and the attenuation coefficient γ on the frequency ω. This is in contrast with the corresponding results for a homogeneous material where the diffusivity is a constant independent of all frequencies and that the attenuation coefficient is zero. Composite materials, however, behave like homogeneous materials only in the limit as the frequency approaches zero. Thus, in the limit as $\omega \to 0$, the three characteristic equations (56, 58) and (A10) lead to the obvious conclusion that $\nu_e = 1$ which, in dimensional form, is given by the mixture diffusivity (33).[5] For all nonvanishing frequencies, the trilaminated reduced and exact characteristic equations will admit three, two and infinite roots, respectively. The bulk behavior of the composite will be dominated by the lowest order mode, however [1, 2].

Table 1

	Quartz	Phenolic resin
$\rho(g/cm^3)$	2.2	1.19
$k\left(\frac{ergs}{cm\ s\ °C}\right)$	1.38×10^5	1.46×10^4
$c\left(\frac{ergs}{gm\ °C}\right)$	7.54×10^6	1.76×10^7

In our numerical illustrations we are mainly concerned with two issues. In the first we demonstrate the influence of bonding agents on the diffusion characteristic of the otherwise bilaminated composite. In the second we compare the results of modeling such an influence as per the trilaminated or reduced models with some exact results. We choose for our numerical illustrations a quartz-phenolic bilaminated composite whose properties are taken from our previous paper [1] and are listed in Table 1. As for the bonding agent, no specific material is chosen, but various arbitrary sets of properties are assigned to it. In Figs. 3(a), 4(a), and 5(a) we depict the nondimensional diffusivity versus the nondimensional frequency for the lowest order mode of the trilaminated, reduced and exact models. In Figs. 3(b), 4(b) and 5(b) we depict the corresponding variations of the nondimensional attenuation coefficients with the nondimensional frequencies. In all of our calculations we choose $\epsilon = 0.1$, $n_0 = 0.1$ with $n_1 = n_2 = 0.45$. As for the remaining properties of the bonds we assigned, without loss in generality, $\rho_0 = \rho_1$, $c_0 = c_1$, and left the conductivity k_0 of the bond as the only variable. The three values of k_0 used in generating the results of Figs. 3, 4 and 5 are chosen, respectively, as 1.38×10^4, 1.38×10^6, 5.52×10^6 ergs/(cm s C). The numerical results of the exact characteristic equation were obtained by using Newton iteration schemes. As may be seen from the figures both of the approximate models correlate well with each other and also with the exact results especially in the case of the attenuation coefficients where the solutions are practically indistinguishable.

Conclusions

We developed two continuum mixture models in order to investigate heat conduction processes in laminated composites with bonds. The geometric arrangement of the composite with the bond is treated as a special type of a trilaminated composite in which each of its major constituents is sandwiched between two bonding layers. In the first model, the recently developed continuum mixture theories of heat conduction in bilaminated composites [1] are extended to treat the trilaminated composite (see the system of equations (29–31)). Here details of the diffusion process in the major components and also in the bonding layers are derived. In the second model, the entire effect of the bonds is treated as a modifier to interfacial continuity conditions. In this model the details of the diffusion process in the bonding material are ignored (see the system of equations (43) and (44)).

[5] In the case of the exact solution this limit can be obtained by using the small angle approximation relation $\tan(\epsilon n_\alpha \gamma_\alpha) \approx \epsilon n_\alpha \gamma_\alpha$.

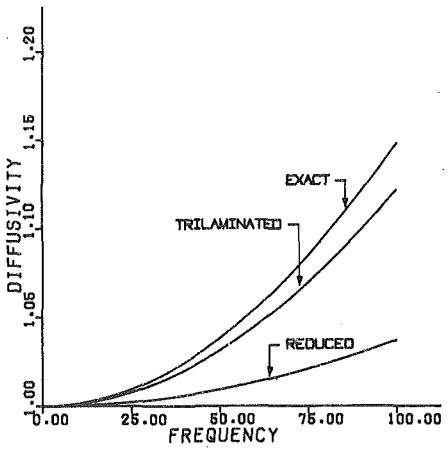

Fig. 3(*a*) Comparison of results for the variation of nondimensional diffusivity ν_e with the nondimensional frequency ω for the three models using the properties of Table 1 with $n_0 = 0.1$, $n_1 = n_2 = 0.45$, $\epsilon = 0.1$, $\rho_0 = \rho_1$, $c_0 = c_1$ and $k_0 = 0.1\ k_1$

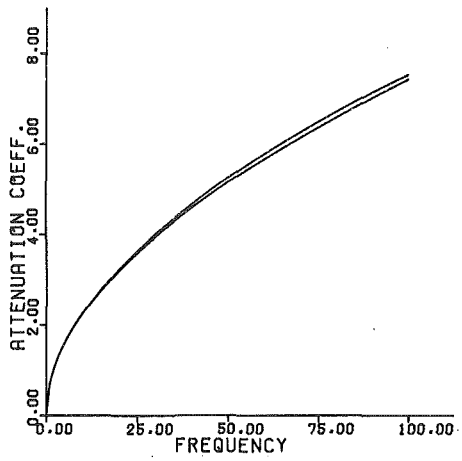

Fig. 3(*b*) Comparison of results of variation of the nondimensional attenuation coefficient γ with the nondimensional frequency ω for the three models using the properties of Table 1 with $n_0 = 0.1$, $n_1 = n_2 = 0.45$, $\epsilon = .1$, $\rho_0 = \rho_1$, $c_0 = c_1$ and $k_0 = 0.1k_1$ (the results of the three models are practically indistinguishable)

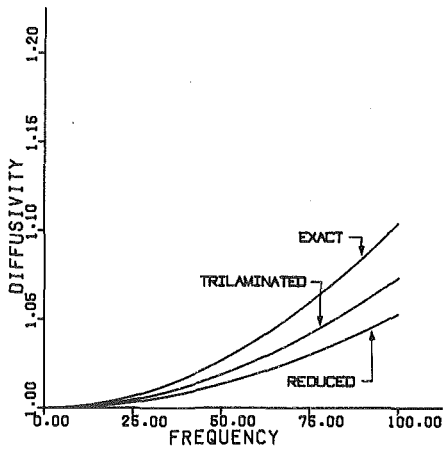

Fig. 4(*a*) Comparison of results for the variation of nondimensional diffusivity ν_e with the nondimensional frequency ω for the three models using the properties of Table 1 with $n_0 = 0.1$, $n_1 = n_2 = 0.45$, $\epsilon = .1$, $\rho_0 = \rho_1$, $c_0 = c_1$ and $k_0 = k_1$

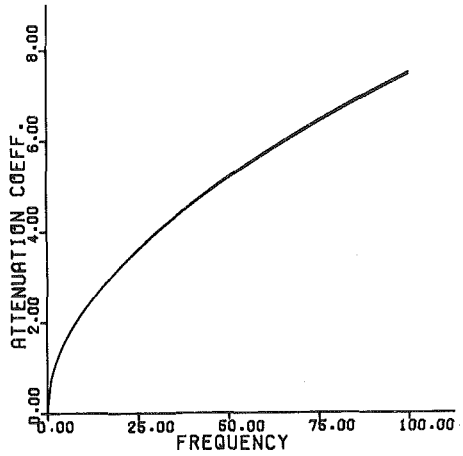

Fig. 4(*b*) Comparison of results of variation of the nondimensional attenuation coefficient γ with the nondimensional frequency ω for the three models using the properties of Table 1 with $n_0 = 0.1$, $n_1 = n_2 = 0.45$, $\epsilon = .1$, $\rho_0 = \rho_1$, $c_0 = c_1$ and $k_0 = k_1$ (the results of the three models are practically indistinguishable)

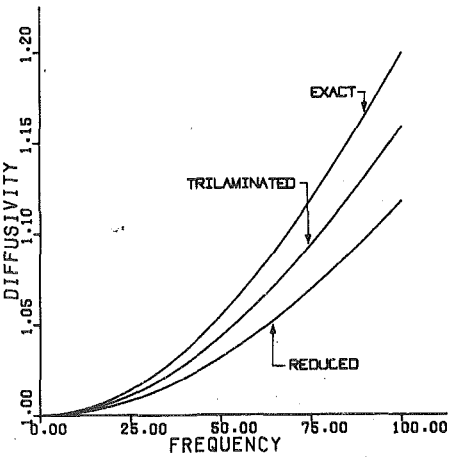

Fig. 5(*a*) Comparison of results for the variation of nondimensional diffusivity ν_e with the nondimensional frequency ω for the three models using the properties of Table 1 with $n_0 = 0.1$, $n_1 = n_2 = 0.45$, $\epsilon = .1$, $\rho_0 = \rho_1$, $c_0 = c_1$ and $k_0 = 4k_1$

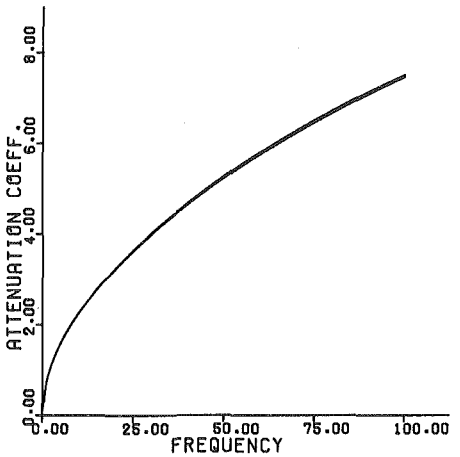

Fig. 5(*b*) Comparison of results of variation of the nondimensional attenuation coefficient γ with the nondimensional frequency ω for the three models using the properties of Table 1 with $n_0 = 0.1$, $n_1 = n_2 = 0.45$, $\epsilon = .1$, $\rho_0 = \rho_1$, $c_0 = c_1$ and $k_0 = 4k_1$ (the results of the three models are practically indistinguishable)

References

1 Nayfeh, A. H., "A Continuum Mixture Theory of Heat Conduction In Laminated Composites," ASME *Journal of Applied Mechanics,* Vol. 42, No. 2, 1975, pp. 399–404.

2 Horvay, G., "Transient Heat Conduction In Laminated Composites," ASME JOURNAL OF HEAT TRANSFER, Vol. 95, No. 3, 1973, pp. 309–316.

3. Maewal, A., Bache, T. C., and Hegemier, G. A., "A Continuum Model for Diffusion Laminated Composite Medial," ASME JOURNAL OF HEAT TRANSFER, Vol. 98, No. 1, 1976, pp. 133–138.

4. Maewal, A., Gurtman, G. A., and Hegemier, G. A., "A Mixture Theory for Quasi-One Dimensional Diffusion in Fiber-Reinforced Composites," ASME *Journal of Heat Transfer,* Vol. 100, 1978, pp. 128–133.

5. Nayfeh, A. H., and Nassar, E. M., "Simulation of the Influence of Bonding Materials on the Dynamic Behavior of Laminated Composites," ASME *Journal of Applied Mechanics,* Vol. 45, No. 4, 1978, pp. 822–828.

6. Horvay, G., Gold, B., and Kaczenski, E. S., "Longitudinal Heat Propagation in Three-Phase Laminated Composites at High Exciting Frequencies," ASME JOURNAL OF HEAT TRANSFER Vol. 100, 1978, pp. 281–287.

7. Nayfeh, A. H., and Loh, J.-I. J., "On Continuum Mixture Theories for Shear Wave Propagation in Trilaminated Wave Guides," *Journal of Sound and Vibration,* Vol. 55, No. 1, 1977, pp. 19–26.

Maria Comninou
Associate Professor,
Department of Civil Engineering,
University of Michigan,
Ann Arbor, Mich. 48109
Mem. ASME

J. Dundurs
Professor,
Department of Civil Engineering,
Northwestern University,
Evanston, Ill. 60201
Fellow ASME

On Lack of Uniqueness in Heat Conduction through a Solid to Solid Contact

If two solids are pressed together and made to exchange heat by conduction, one possible steady state corresponds to the solids remaining in contact along the entire interface. It is shown that this state is not unique, and that it is possible to construct solutions involving localized separation if heat flows in one of the two possible directions.

Introduction

The question about the possible lack of uniqueness when two contacting solids exchange heat by conduction was raised by Barber [1]. It is also implicit in the results presented by Dundurs and Panek [2, p. 734]. The object of this article is to demonstrate actual nonuniqueness in steady-state heat conduction by means of a specific example.

Consider for this purpose two semi-infinite solids that are pressed together and made to conduct heat through the contact interface. One possible steady state is that of the solids remaining in contact along the whole interface which results in simple linear temperature distributions normal to the interface. We show, however, that another steady-state solution involving a localized separation zone at the interface and satisfying the customary boundary conditions, as well as the appropriate inequalities, can be constructed for heat flowing across the interface in one of the two possible directions. Moreover, the solutions for full contact and localized separation satisfy the same far-field boundary conditions. We also give a solution for a periodic array of separation zones which appears to be of fundamental importance.

The existence of competing steady-state solutions immediately creates new questions about history dependence, stability, and the rate at which possible disturbances grow if the process of heat conduction between two solids is viewed developing in time. There is also the matter of whether the lack of uniqueness demonstrated in this article is due to the strongly idealized boundary conditions (no resistance to heat flow in zones of solid to solid contact, no heat transfer between the solids in the separation zones) and the fact that the contacting bodies are treated as semi-infinite solids. Except for a few comments made at the end, which anticipate some of the answers, we must leave these issues unresolved at the present time.

The Problem and Its Formulation

Consider two semi-infinite solids that are forced together by the applied pressure, p, and carry the remotely established uniform heat flux, q^∞, in the direction normal to the interface. As mentioned before, one steady-state solution for the thermal and elastic fields corresponds to the solids remaining in contact along the whole interface. We seek here the steady-state solutions, satisfying identical boundary conditions, but which involve localized separation between the solids. The problem is posed in the framework of linear thermoelasticity [3], assuming plane strain conditions. For simplicity, the interface is taken as frictionless.

The coordinate system is placed in relation to the two bodies as shown in Fig. 1; subscripts or superscripts 1 and 2 are used to distinguish the field quantities and physical constants of the two materials. The thermal conductivity is denoted by k, the coefficient of thermal expansion by α, the shear modulus by μ, and Poisson's ratio by ν. The quantity

$$\delta = \frac{\alpha(1+\nu)}{k} \tag{1}$$

is called the distortivity of a material [2].

Assuming that the two materials are homogeneous and isotropic, the steady-state temperature distribution is a plane harmonic function, viz.,

$$\frac{\partial^2 T}{\partial x^2} + \frac{\partial^2 T}{\partial y^2} = 0 \tag{2}$$

in the absence of internal heat generation [4]. Written in the customary indicial notation for the sake of compactness, the pertinent equations for the elastic fields, under the assumption of plane strain [3, Sec. 4.2], consist of the equilibrium conditions

$$\partial_j \sigma_{ji} = 0 \tag{3}$$

on the stress components, the relation between the total strain and displacement

$$\epsilon_{ij} = \frac{1}{2}(\partial_i u_j + \partial_j u_i) \tag{4}$$

and Hooke's law

$$\epsilon_{ij} = \frac{1}{2\mu}(\sigma_{ij} - \nu\sigma_{kk}\delta_{ij}) + \alpha(1+\nu)T\delta_{ij} \tag{5}$$

Herein, $i, j, k = 1, 2$; $(x_1 = x, x_2 = y)$; $\partial_i = \partial/\partial x_i$; and repeated indices imply summation over the values 1 and 2. The first term on the right side of (5) constitutes the elastic strain, and the second term is the strain due to thermal expansion.

The boundary conditions to be imposed in the *contact zones* are

$$T_1(x, 0) = T_2(x, 0) \tag{6}$$

$$k_1 \frac{\partial T_1(x, 0)}{\partial y} = k_2 \frac{\partial T_2(x, 0)}{\partial y} \tag{7}$$

$$u_y{}^{(1)}(x, 0) = u_y{}^{(2)}(x, 0) \tag{8}$$

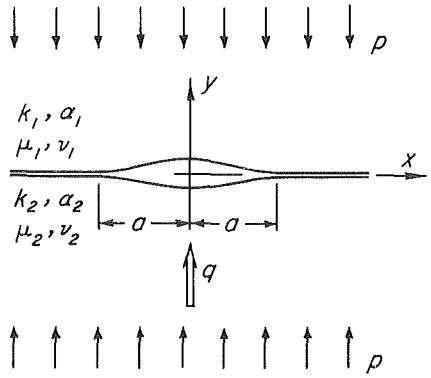

Fig. 1 Contacting solids with a single separation zone

Contributed by the Heat Transfer Division for Publication in the JOURNAL OF HEAT TRANSFER. Manuscript received by the Heat Transfer Division August 29, 1979.

$$\sigma_{xy}^{(1)}(x, 0) = \sigma_{xy}^{(2)}(x, 0) = 0 \tag{9}$$

$$\sigma_{yy}^{(1)}(x, 0) = \sigma_{yy}^{(2)}(x, 0) \leq 0 \tag{10}$$

Equation (6) reflects the idealization that the interface offers no resistance to heat flow in the regions of solid to solid contact. The next boundary condition is simply a statement that no heat is generated at the interface. The boundary condition (8) on the normal components of displacements insures that the bodies are in contact. Equations (9) and (10) express Newton's third law, the assumption of no friction, and the condition that contacting bodies can only exert pressure on each other and that the surface tractions cannot be tensile.

The boundary conditions used in the *separation zones* are

$$\frac{\partial T_1(x, 0)}{\partial y} = \frac{\partial T_2(x, 0)}{\partial y} = 0 \tag{11}$$

$$\sigma_{xy}^{(1)}(x, 0) = \sigma_{xy}^{(2)}(x, 0) = 0 \tag{12}$$

$$\sigma_{yy}^{(1)}(x, 0) = \sigma_{yy}^{(2)}(x, 0) = 0 \tag{13}$$

$$u_y^{(1)}(x, 0) - u_y^{(2)}(x, 0) \geq 0 \tag{14}$$

Equation (11) expresses the assumption that no heat is transmitted across the gaps in the separation zones. The next two boundary conditions insure that the surfaces of the bodies are free of traction in the separation zones. Condition (14) reflects the requirement that the gap between the bodies cannot be negative. It is important to note that the inequalities (10) and (14) make the problem nonlinear.

The boundary conditions at infinity will be discussed after the solutions are constructed.

The field equations (2–5) and the boundary conditions (6–10) are satisfied for full contact by the following temperature, heat flux, displacement and stress distributions:

$$T = -\frac{q^\infty}{k} y \tag{15}$$

$$q_x = 0, q_y = q^\infty \tag{16}$$

$$u_x = \frac{\nu p}{2\mu} x, u_y = -\frac{(1-\nu)p}{2\mu} y - \frac{q^\infty \delta}{2(1-\nu)} y^2 \tag{17}$$

$$\sigma_{xx} = \frac{2\mu q^\infty \delta}{1-\nu} y, \sigma_{xy} = 0, \sigma_{yy} = -p \tag{18}$$

where subscripts 1 or 2 must be attached to k, δ, μ and ν, depending on the region considered. The arbitrary datum for temperature has been adjusted so that the contact interface is at zero temperature. The linearly distributed σ_{xx} or bending stress must be applied in order to prevent the bodies from globally warping away from each other. The behavior of the field quantities at infinity is clear from the explicit formulas.

Single Separation Zone

Next, we construct a steady-state solution in which the solids are allowed to separate over an interface segment of length $2a$. The separation zone is expected to disturb the temperature and stresses only locally. We assume that no heat is transmitted across the gap, and there is no contact resistance outside the separation zone, so that the boundary conditions (11) and (6) apply in $|x| < a$ and $|x| > a$, respectively.

There is no need to start at the level of the field equations and the boundary conditions other than (11) and (13), because we can take advantage of a Green's function for exterior thermoelastic contact that consists of a thermoelastic field (heat vortex) and a purely elastic field (edge dislocation at a freely slipping interface) [5]. The full expressions for the field quantities associated with the Green's function are given in [5] and of immediate interest are only the relationships at the interface.

An isolated heat vortex of strength ω acting at the point $(\xi, 0)$ leads to the following quantities at the interface:

temperature discontinuity across the interface

$$\tau(x) = T_2(x, 0) - T_1(x, 0) = \omega H(x - \xi) \tag{19}$$

heat flux through the interface

$$q_y(x, 0) = -\frac{\omega}{\pi} \frac{k_1 k_2}{k_1 + k_2} \frac{1}{x - \xi} \tag{20}$$

gap between the solids

$$g(x) = u_y^{(1)}(x, 0) - u_y^{(2)}(x, 0) = 0 \tag{21}$$

and the normal tractions

$$\sigma_{yy}(x, 0) = 2\omega M(\delta_1 - \delta_2) \frac{k_1 k_2}{k_1 + k_2} \mathrm{H}(x - \xi) \tag{22}$$

where H( ) is the Heaviside step function, and

$$M = \frac{\mu_1 \mu_2}{2[\mu_1(1 - \nu_2) + \mu_2(1 - \nu_1)]} \tag{23}$$

The edge dislocation with the Burgers vector b_y leads to no thermal quantities, but gives

$$g(x) = -b_y \mathrm{H}(x - \xi) \tag{24}$$

$$\sigma_{yy}(x, 0) = \frac{2b_y M}{\pi} \frac{1}{x - \xi} \tag{25}$$

The desired solution for the single separation zone can be constructed by correcting the fields given by (15–18) for the full contact between the solids. In order to cancel the heat flux through the separation zone, we distribute heat vortices with the density $\Omega(x)$ over the interval $-a < x < a$. On the basis of (20), this leads to the relation

$$q^\infty - \frac{1}{\pi} \frac{k_1 k_2}{k_1 + k_2} \int_{-a}^{a} \frac{\Omega(\xi) d\xi}{x - \xi} = 0, |x| < a \tag{26}$$

From (19), it also follows that

$$\tau(x) = \int_{-\infty}^{x} \Omega(\xi) d\xi \tag{27}$$

and consequently

$$\Omega(x) = \frac{d\tau(x)}{dx} \tag{28}$$

If the temperature jump is to vanish outside the inteval $-a < x < a$, We must have

$$\int_{-a}^{a} \Omega(\xi) d\xi = 0 \tag{29}$$

Nomenclature

a = half length of separation zone
b_y = Burgers vector of an isolated dislocation
B_y = intensity of distributed dislocations
g = gap between the solids
h = half length of period
k = thermal conductivity
M = bimaterial constant (see equation (23))
p = applied pressure
q^∞ = heat flux at infinity
q_x, q_y = components of heat flux
T = temperature above the datum at which contact is established
u_i = displacement vector
x, y = cartesian coordinates
α = coefficient of thermal expansion
δ_{ij} = Kronecker delta
$\delta = \alpha(1 + \nu)/k$ = distortivity
ϵ_{ij} = strain tensor
μ = shear modulus
ν = Poisson's ratio
σ_{ij} = stress tensor
τ = temperature jump across the interface
ω = strength of an isolated heat vortex
Ω = intensity of distributed heat vortices

Equation (26) is a Cauchy singular integral equation, and its solution with the constraint (29) is known [6]:

$$\Omega(x) = -\frac{q^\infty(k_1+k_2)}{k_1k_2}\frac{x}{(a^2-x^2)^{1/2}}, \quad |x| < a \tag{30}$$

It follows then using (22) that the distributed heat vortices give the following interface tractions:

$$\sigma_{yy}(x, 0) = \begin{cases} 2Mq^\infty(\delta_1-\delta_2)(a^2-x^2)^{1/2}, & |x| < a \\ 0, & a < |x| \end{cases} \tag{31}$$

The final task is to cancel the normal tractions in the separation zone and allow for the gap. This is done by introducing a distribution $B_y(x)$ of edge dislocations in the interval $-a < x < a$. Thus, from (25) and (31),

$$-p + 2Mq^\infty(\delta_1-\delta_2)(a^2-x^2)^{1/2} + \frac{2M}{\pi}\int_{-a}^{a}\frac{B_y(\xi)d\xi}{x-\xi} = 0, \quad |x| < a \tag{32}$$

Using (24), we also get

$$g(x) = -\int_{-\infty}^{x} B(\xi)d\xi \tag{33}$$

and

$$B_y(x) = -\frac{dg(x)}{dx} \tag{34}$$

Since the gap between the solids must vanish in the contact zones

$$\int_{-a}^{a} B(\xi)d\xi = 0 \tag{35}$$

Due to the symmetry of the problem, $B_y(x)$ must be odd in x, and (35) is automatically satisfied, but this will be verified a posteriori. Moreover, $B_y(x)$ must be bounded at $x = \pm a$ [7], which also insures that the interface tractions vanish at the ends of the separation zone.

A bounded solution of a Cauchy singular integral equation is possible only if the right side of the equation satisfies a so-called consistency condition [6]. The consistency condition for (32) is

$$\int_{-a}^{a}\{-p + 2Mq^\infty(\delta_1-\delta_2)(a^2-\xi^2)^{1/2}\}(a^2-\xi^2)^{-1/2}d\xi = 0 \tag{36}$$

Carrying out the elementary integrations, (36) reduces to

$$-\pi p + 4Mq^\infty(\delta_1-\delta_2)a = 0 \tag{37}$$

Equation (37) determines the length of the separation zone. It also shows that a solution is possible (viz., $a > 0$) only when $q^\infty(\delta_1-\delta_2) > 0$, or when heat flows into the material with the larger distortivity ($q^\infty > 0$ corresponds to heat flowing in the direction of increasing y).

The solution of (32) is [6]

$$B_y(x) = -\frac{1}{2\pi M}(a^2-x^2)^{1/2}\int_{-a}^{a}\frac{2Mq^\infty(\delta_1-\delta_2)(a^2-\xi^2)^{1/2}-p}{(a^2-\xi^2)^{1/2}(\xi-x)}d\xi$$
$$= \frac{1}{\pi}q^\infty(\delta_1-\delta_2)(a^2-x^2)^{1/2}\log\left|\frac{a+x}{a-x}\right|, \quad |x| < a \tag{38}$$

It is seen that $B_y(x)$ is odd in x, as expected, and that (35) is satisfied. The gap between the solids can be obtained from (33) and (38) by numerical integration. Using (25), the normal tractions between the solids in the contact zones are seen to be

$$\sigma_{yy}(x, 0) = -p + \frac{2M}{\pi}\int_{-a}^{a}\frac{B_y(\xi)d\xi}{x-\xi}, \quad a < |x| \tag{39}$$

Substituting (38) into (39), and carrying out the integrations [8], we obtain

$$\sigma_{yy}(x, 0) = -\frac{p}{2a}(\text{sgn}x)(x^2-a^2)^{1/2}\log\left|\frac{x+a}{x-a}\right|, \quad a < |x| \tag{40}$$

The normal tractions are seen to be compressive for $q^\infty(\delta_1-\delta_2) > 0$.

The shape of the gap and the distribution of normal tractions are shown in Figs. 2 and 3.

It follows from (29) and (35) that the far field behavior of the disturbance caused by the separation zone is the same as that of a doublet of heat vortices and a doublet of dislocations. From the expressions given in [5], we can readily deduce that a doublet of heat vortices gives a temperature change and stresses that are of order $1/R$ as $R \to \infty$, where R is the distance from the doublet. A doublet of dislocations gives stresses that decay as $1/R^2$. It is clear, therefore, that the solution with a separation zone satisfies the same boundary conditions at infinity as the temperature and stress fields for full contact.

Periodic Array of Separation Zones

Another solution of fundamental importance is that involving a periodic array of separation zones. It can be constructed by means similar to those used in the previous section. As before, the initially unknown lengths of the separation zones are denoted by $2a$. The length of a period is taken to be $2h$.

The heat conduction part of the problem for a periodic array of insulated segments can first be written as

$$q^\infty - \frac{1}{\pi}\frac{k_1k_2}{k_1+k_2}\int_{-\infty}^{\infty}\frac{\Omega(\xi)d\xi}{x-\xi} = 0 \tag{41}$$

Taking advantage of the periodicity [9], we obtain

$$q^\infty + \frac{1}{2h}\frac{k_1k_2}{k_1+k_2}\int_{-a}^{a}\Omega(\xi)\cot\frac{\pi(\xi-x)}{2h}d\xi = 0, \quad |x| < a \tag{42}$$

In addition, we must require that

$$\int_{-a}^{a}\Omega(\xi)d\xi = 0 \tag{43}$$

Equation (42) can be transformed to a Cauchy singular integral equation for the new unknown function

$$\Phi(u) = \frac{\Omega(u)}{1+c^2u^2} \tag{44}$$

by the following change of variables

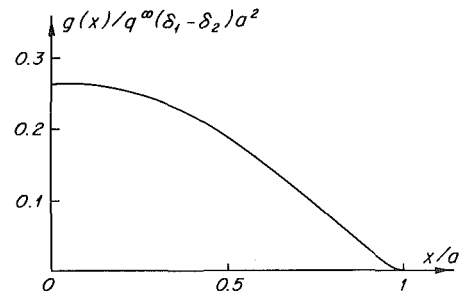

Fig. 2 Shape of the gap for a single separation zone

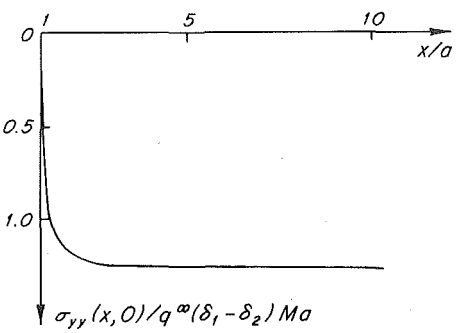

Fig. 3 Contact pressure for a single separation zone

$$\tan\frac{\pi\xi}{2h} = cu,\ \tan\frac{\pi x}{2h} = cs,\ c = \tan\frac{\pi a}{2h} \tag{45}$$

Condition (43) then becomes

$$\int_{-1}^{1} \Phi(u)du = 0 \tag{46}$$

Omitting the details which can be found in reference [9], the solution is

$$\Omega(s) = -\frac{q^\infty(k_1+k_2)(1+c^2)^{1/2}}{k_1k_2}\frac{s}{(1-s^2)^{1/2}},\ |s|<1 \tag{47}$$

The interface tractions corresponding to the periodic array of heat vortices can be obtained with the aid of (22). After some integrations, the result is

$$\sigma_{yy}(x,0) = \begin{cases} \dfrac{2Mh}{\pi}q^\infty(\delta_1-\delta_2)I(x), & |x|<a \\ 0, & a<|x|<h \end{cases} \tag{48}$$

where

$$I(x) = \log\left|\frac{\cos\dfrac{\pi x}{2h} + \left(\cos^2\dfrac{\pi x}{2h} - \cos^2\dfrac{\pi a}{2h}\right)^{1/2}}{\cos\dfrac{\pi x}{2h} - \left(\cos^2\dfrac{\pi x}{2h} - \cos^2\dfrac{\pi a}{2h}\right)^{1/2}}\right| \tag{49}$$

Next we introduce a distribution $B_y(x)$ of edge dislocations to cancel the normal tractions in the separation zones given by (48) and thus obtain the following singular integral equation:

$$-p + \frac{2Mh}{\pi}q^\infty(\delta_1-\delta_2)I(x) - \frac{M}{h}\int_{-a}^{a} B_y(\xi)\cot\frac{\pi(\xi-x)}{2h}d\xi = 0,\ |x|<a \tag{50}$$

with the constraint

$$\int_{-a}^{a} B_y(\xi)d\xi = 0 \tag{51}$$

Using the change of variables given by (45), defining a new unknown function

$$\Psi(u) = \frac{B_y(u)}{1+c^2u^2} \tag{52}$$

and proceeding as in the case of a single separation zone, we first obtain from the consistency condition that

$$\frac{p}{Mq^\infty(\delta_1-\delta_2)a} = \frac{2h}{\pi^2 a}(1+c^2)^{1/2}R(c) \tag{53}$$

where

$$R(c) = \int_{-1}^{1}\frac{F(u,c)du}{(1-u^2)^{1/2}(1+c^2u^2)^{1/2}} \tag{54}$$

and

$$F(u,c) = \log\left|\frac{(1+c^2)^{1/2}+c(1-u^2)^{1/2}}{(1+c^2)^{1/2}-c(1-u^2)^{1/2}}\right| \tag{55}$$

The solution of the transformed integral equation (50) together with (53) yields

$$\frac{\Psi(s)}{q^\infty(\delta_1-\delta_2)a} = -\frac{h}{\pi^2 a}(1-s^2)^{1/2}\left\{\frac{c^2R(c)s}{1+c^2s^2} + \int_{-1}^{1}\frac{F(u,c)du}{(1-u^2)^{1/2}(1+c^2u^2)(u-s)}\right\} \tag{56}$$

Equation (53) determines a for given p. Alternatively, it gives directly the pressure p required to produce a specified a. The integral in (54) can be evaluated by the Gauss-Jacobi quadrature [10] and the singular integral in (56) by the related quadrature developed by Erdogan and Gupta [11]. Finally, the normal tractions in the new variables are

$$\sigma_{yy}(s) = -p - \frac{2M}{\pi}(1+c^2u^2)\int_{-1}^{1}\frac{\Psi(u)du}{u-s} \tag{57}$$

Substituting (53) and (56) into (57) and performing some integrations, we obtain in the contact zones

$$\frac{\sigma_{yy}(s)}{Mq^\infty(\delta_1-\delta_2)a} = \frac{2h}{\pi^2 a}(s^2-1)^{1/2}\left\{c^2R(c)|s| + (\mathrm{sgns})(1+c^2s^2)\int_{-1}^{1}\frac{F(u,c)du}{(1-u^2)^{1/2}(1+c^2u^2)(u-s)}\right\},\ |s|>1 \tag{58}$$

The results are shown in Figs. 4–6 in the original variables. Figure 4 shows how the dimensionless parameter $p/Mq^\infty(\delta_1-\delta_2)a$ depends on a/h. As $a/h \to 0$, we recover the results for the single separation zone. Figure 5 shows the shapes of the gaps and Fig. 6, the contact pressure for various values of a/h.

If the rate of heat flow is to be the same for full contact and separation, the periodic array of gaps requires a larger far-field difference in temperatures. The additional temperature differential needed is readily extracted from the expressions given in [2], and it is

$$\Delta T = -\frac{2q^\infty h}{\pi}\left(\frac{1}{k_1}+\frac{1}{k_2}\right)\log\left[\sin\frac{\pi(h-a)}{2h}\right] \tag{59}$$

Conclusion

We have shown that two bodies that are pressed together and exchange heat by conduction may not necessarily remain in full contact and can separate locally if heat flows into the material with the larger distortivity. The questions raised in the Introduction cannot be answered in the present mathematical context due to its general complexity. However, insight into the phenomena involved can be gained by using materials that have a simpler response than that of the elastic solids conducting heat. A particularly simple model for this purpose was suggested to us by Aldo [12]. It consists of two blocks with dif-

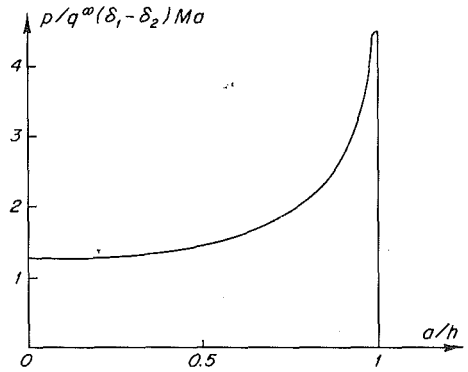

Fig. 4 Dependence of $p/q^\infty(\delta_1-\delta_2)Ma$ on a/h

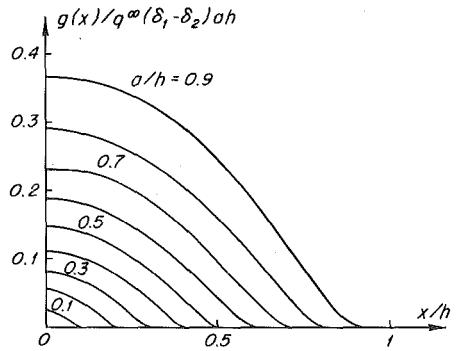

Fig. 5 Shapes of gaps for periodic arrays of separation zones for a/h from 0.1 to 0.9

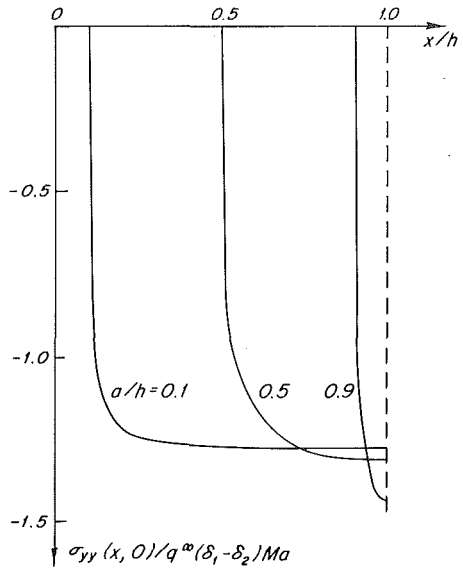

Fig. 6 Contact pressure for periodic arrays of separation zones with $a/h = 0.1$, 0.5 and 0.9

ferent properties. Each block is an assemblage of thin rods with insulated and frictionless sides, so that heat is conducted only in the direction of the rods and there are no shearing stresses when the blocks are deformed. The contact interface is normal to the rods. An investigation using the Aldo model has revealed the following behavior:

1 The steady state involving full contact is always possible. The state with partial separation becomes possible when the imposed temperature differential exceeds a certain critical value.

2 The state with partial separation corresponds to a lower level of total mechanical energy.

The details of this study are beyond the scope of the present article and will be published at a later time.

The Aldo model consisting of two finite blocks shows quite clearly that the nonuniqueness demonstrated here does not arise from the consideration of semi-infinite solids. Some very recent work by Barber [13], using a simplified model but a general and physically much more realistic contact condition for heat transfer between the solids, has shown that the lack of uniqueness is not caused by the idealized boundary conditions (6) and (11). Thus it appears that the lack of uniqueness for heat flowing into the material with the larger distortivity is not purely mathematical, that it has a physical basis, and that it signals possible instabilities.

It may be interesting to note in conclusion that there is also some difficulty with heat flowing between the contacting solids in the opposite direction, or into the material with the smaller distortivity. In such cases, the difficulty is exactly the opposite or connected with existence rather than uniqueness. It appears, however, that lack of existence is connected only with the highly idealized boundary conditions (6) and (11), and that existence can be achieved by appropriately modifying the conditions imposed at the contact interface [14, 15].

Acknowledgment

One of the authors (M.C.) is pleased to acknowledge the support of the National Science Foundation under the Grant ENG-7725032 during the course of this research.

References

1 Barber, J. R., "The Effect of Thermal Distortion on Constriction Resistance," *International Journal of Heat and Mass Transfer,* Vol. 14, 1971, pp. 751–766.

2 Dundurs, J. and Panek, C., "Heat Conduction Between Bodies With Wavy Surfaces," *International Journal of Heat and Mass Transfer,* Vol. 19, 1976, pp. 731–736.

3 Boley, B. A. and Weiner, *Theory of Thermal Stresses,* John Wiley and Sons, New York, 1960.

4 Carslaw, H. S. and Jaeger, J. C., *Conduction of Heat in Solids,* Clarendon Press, Oxford, 1947.

5 Dundurs, J. and Comninou, M., "Green's Functions for Planar Thermoelastic Contact Problems—Exterior Contact," *Mechanics Research Communications,* Vol. 6, 1979, pp. 309–316.

6 Muskhelishvili, N. I., *Singular Integral Equations,* P. Noordhoff, Groningen, 1953.

7 Dundurs, J. and Comninou, M., "Some Consequences of the Inequality Conditions in Contact and Crack Problems," *Journal of Elasticity,* Vol. 9, 1979, pp. 71–82.

8 Gradshteyn, I. S. and Ryzhik, I. M., *Table of Integrals, Series and Products,* Academic Press, New York, 1965.

9 Schmueser, D. and Comninou, M., "The Periodic Array of Interface Cracks and Their Interaction," *International Journal of Solids and Structures,* Vol. 15, 1979, pp. 927–934.

10 Stroud, A. H. and Secrest, D., *Gaussian Quadrature Formulas,* Prentice Hall, Englewood Cliffs, N. J., 1966.

11 Erdogan, F. and Gupta, G., "On the Numerical Solution of Singular Integral Equations," *Quarterly of Applied Mathematics,* Vol. 29, 1972, pp. 525–539.

12 Aldo, K. A. T., Private Communication.

13 Barber, J. R., Private Communication.

14 Barber, J. R., "Indentation of the Semi-Infinite Elastic Solid by a Hot Sphere", *International Journal of Mechanical Sciences,* Vol. 15, 1973, pp. 813–819.

15 Barber, J. R., "Contact Problems Involving a Cooled Punch," *Journal of Elasticity,* Vol. 8, 1978, pp. 409–423.

A Methodology of Predicting Cavity Geometry Based on Scanned Surface Temperature Data—Prescribed Surface Temperature at the Cavity Side[1]

C. K. Hsieh
Mechanical Engineering Department,
University of Florida,
Gainesville, FL 32611

K. C. Su
Bell Laboratories,
Whippany, New Jersey 07981

The scanned surface temperature data from a body are used to predict the cavity lying underneath the surface. The basic system under investigation is a plane wall having a rectangular cavity at the back surface. The front surface dissipates heat by convection; this is also the surface whose temperature is scanned. For a prescribed surface temperature specified on the cavity side, a numerical solution is found convenient to predict the cavity top and the approximate location of the cavity wall. A recheck of the cavity wall position calls for matching the recalculated surface temperature with the measured temperature. The data are found to be well behaved to the extent that an interpolation is possible when the mesh size chosen happens to miss the wall position. The methodology can also be extended to prediction of holes in a three-dimensional body.

Introduction

In the classic problem of heat conduction, the system configuration has to be specified. The governing equation can be formulated based on the physics of the problem. Then, if the boundary conditions are given, the problem can be solved to determine the temperature distribution at each point interior to the system. There is another type of problem in which either the temperature, or the temperature-time history is given at some interior points, and it is desirable to find either the surface temperature or the surface heat flux at boundaries. This latter type of problem is often termed the inverse problem and is encountered in quenching process, calorimetry, and convection studies, among others [1–7]. Seldom investigated in the heat transfer literature is a third type of problem which, although also related to the inverse problem, serves a totally different purpose. In this third problem, the system has a partly unknown configuration and one of the system boundaries has an additional measurable temperature in addition to a convective condition (boundary condition of the third kind) that is imposed on this surface. The purpose of the problem is to determine the configuration of the boundary opposite to this surface [8–13].

The third type of problem has received interest only recently when, in nondestructive testing using infrared scanning, one can scan the surface temperature of a body that dissipates heat by convection (including radiation) to the surroundings. The inner boundary is subjected to varied boundary conditions, and the purpose of performing infrared scanning is to determine the cavity, if any, at the inner boundary. The problem is, in fact, of contemporary interest. With the development of the computerized axial tomography (CAT), the infrared scanning carries promise of being a viable alternative to x-ray scanning [14–18].

It should be noted that, while both CAT and infrared scanning can be used to map the interior of a body, their mechanisms of operation are different. CAT operates on the extinction characteristics of the material; with the body tissues made up primarily of radiation absorbers, classical methods such as matrix inversions and the Fourier transforms of images are useful to reestablish images of nonhomogenity in the medium [19]. In contrast, the infrared scanning method monitors the surface radiosity as a function of the diffusion of heat in the medium. With the transverse coupling in heat diffusion that is as important as the longitudinal heat propagation, the heat penetration in the medium is in more than one direction. Hence, the infrared image cannot be analyzed in the same way as those used in the analysis of CAT images. This dissimilarity makes the problem a real challenge to investigation.

It is worth noting that, while the inverse problem as stated appears to be well known in the field of nondestructive testing, an exact solution of the problem has not been found in the literature. Indeed, an analytical solution of the problems having irregular boundaries subjected to a convective boundary conditions defies an exact solution by either a conformal mapping or a Schwarz-Christoffel transformation. Numerical methods such as the Schwarz iteration technique are also handicapped because of the appearance of a convective condition at the surface. The problem as stated can, of course, be solved numerically using a finite difference or a finite element method. This requires, however, the presumption of a cavity geometry, and the problem must be solved numerically for this particular cavity to yield a surface temperature in order to match the observed temperature. Such a gross trial and error solution falls within the category of template matching schemes in the pattern recognition process [20]. The method, although functional [3–10, 21, 22], is time consuming from the computation standpoint and, therefore, is of no concern to us in this study.

In this paper a method is presented that is strictly useful to predict cavities that have a prescribed temperature. The basic system under investigation consists of a plane wall having a rectangular cavity on the bottom surface, see Fig. 1. The top surface dissipates heat by convection (including radiation through a suitable h). This is also the surface whose temperature is monitored by an infrared scanner; therefore, this temperature is known. The left and right edges of the system are insulated. Physically, these edges simulate sections remote from the cavity where the temperature gradients are negligible. On the bottom boundary the surface temperature is prescribed. For the system under investigation, because of temperature symmetry, only one half of the system is needed for analysis. It is further assumed that the system is in steady state. Variations of temperatures in z direction (perpendicular to the plane of Fig. 1), as well as the thermophysical properties with temperatures, are ignored.

[1] Work supported by NSF through Grant No. ENG-7710630
Contributed by the Heat Transfer Division and presented at the Winter Annual Meeting, December 2–7, 1979, New York, New York of THE AMERICAN SOCIETY OF MECHANICAL ENGINEERS. Manuscript received by the Heat Transfer Division November 14, 1979. Paper No. 79-WA/HT-45.

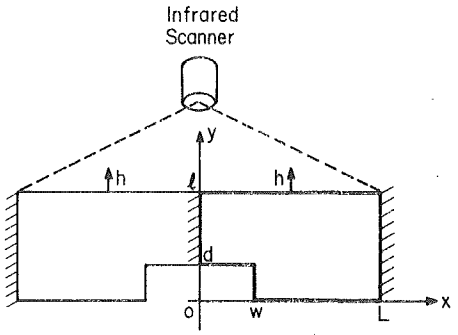

Fig. 1. Schematic of a basic system under investigation

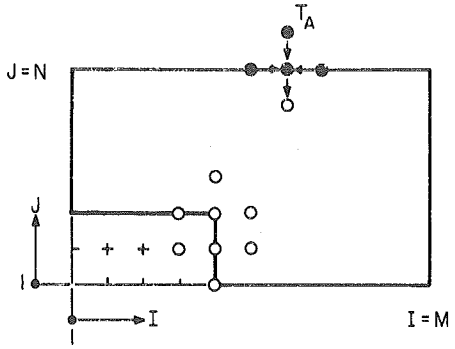

Fig. 2 Nodal points lay-out

Methodology

For a specified temperature T_B imposed on the cavity side, the problem is simplified by the fact that the boundary temperature at the top surface provides a clue to identify the cavity geometry. It has been noted earlier that the top surface dissipates heat by convection to the surroundings and the top surface temperature is also measured. This permits the use of the surface temperature and the ambient temperature to determine the nodal temperatures inside the system, see Fig. 2. The computation commences with the first row of interior nodes right underneath the top surface. The nodal temperatures are calculated one row after another in a downward direction until one (or more) temperatures in one row of nodes reach (or exceed) the prescribed level (T_B). In this way, if the nodal temperature calculated at one point exceeds the boundary temperature, this point must be lying inside the cavity region. Then, an interpolation scheme must be used to recheck the cavity location.

A further continuation of computation downward will evaluate nodal temperatures inside the cavity region. While these temperatures have no bearing on the determination of the cavity top, these temperatures will upset data near the cavity (side) wall. This point can be better illustrated by reference to Fig. 2. Say, the cavity is located $1 \le I \le 5$ and $1 \le J \le 3$, and the mesh size chosen is good; then the computation yields acceptable data up to row $J = 3$, inclusive. Proceeding further downward will yield temperatures at nodes (1 to 5, 2) higher than the prescribed levels. Particularly, the high temperature at node (5,2) will raise the temperature at node (5,1) above the prescribed level. As a result, the prediction of the corner location will be in error. It is also noted that, since it takes four nodes above a given point to predict the nodal temperature in question, the overprediction of temperatures for corner nodes will not be affected whether the computation of temperatures is from left to right or right to left.

For the rectangular cavity addressed in this study one would be inclined to say that the predicted nodal temperatures at row $J = 3$ (still using the previous example) should give sufficient indication as to where the cavity wall is located. Unfortunately, this is not so. Because of the rapid propagation of numerical errors (to be examined later), a data smoothing routine must be employed. As such, the temperature calculated at the cavity re-entrant corner will not be precisely at the prescribed level. While the approximate location of this corner can be identified based on the calculated nodel temperature, its actual location must still be verified. This can be done by picking a cavity wall position and resolving the problem, this time for a *top* surface temperature. If this calculated temperature matches the initially measured one, the assumed wall location is correct. A small trial and error is still needed. But, since the cavity top position has been identified, and the approximate position of the cavity wall is also known, the time involved in the trial and error can be greatly curtailed. An example will be provided later to illustrate these points.

Analysis

The analysis is facilitated by reference to Fig. 2. For the system shown, under a steady-state condition, only two general nodal equations are needed to calculate the interior nodal temperatures. For nodes in row $J = N - 1$,

$$T_{I,N-1} = \frac{(\Delta y)}{(\Delta x)}\left\{\left[\frac{h(\Delta x)}{k} + \frac{(\Delta y)}{(\Delta x)} + \frac{(\Delta x)}{(\Delta y)}\right]T_{I,N} - \frac{h(\Delta x)}{k}T_A - \frac{(\Delta y)}{2(\Delta x)}\left(T_{I+1,N} + T_{I-1,N}\right)\right\} \quad (1)$$

For nodes in rows $J \le (N - 2)$,

$$T_{I,J} = \frac{(\Delta y)}{(\Delta x)}\left\{2\left[\frac{(\Delta y)}{(\Delta x)} + \frac{(\Delta x)}{(\Delta y)}\right]T_{I,J+1} - \frac{(\Delta x)}{(\Delta y)}T_{I,J+2} - \frac{(\Delta y)}{(\Delta x)}\left(T_{I-1,J+1} + T_{I+1,J+1}\right)\right\} \quad (2)$$

where (Δx) and (Δy) are mesh sizes in x and y directions, respectively; h is the convective heat transfer coefficient, k, the thermal conductivity, and T_A, the ambient temperature. Since both T_A and $T_{I,N}$ are known, the numerical solution is self starting. The above two equations can also be rearranged to solve for interior nodal temperatures when the problem is reworked to find the top surface temperature.

Error Analysis

It has been shown in the methodology that the nodal temperatures will be used as a vehicle to determine the cavity boundary; the accuracy of the prediction thus relies heavily on the accuracy of the nodal temperatures that can be calculated in the analysis. Among those parameters that have a bearing on the results, the thermal conductivity and the convective heat transfer coefficient are important. The thermal conductivity can be measured within an accuracy of 1.5 to 3 percent, depending on the method used, according to the current state of the art [23]. The uncertainty in the convective coefficient is usually larger. However, since these two parameters always appear together in the equation (see equation (1)), it is convenient to consider the error of the dimensionless group $h(\Delta y)/k$ as presented below.

Nomenclature

Bi = hL/k
$D = [(\Delta y)/(\Delta x)]^2$
d = depth of cavity
e = error
h = convective coefficient
I,J = index in x, y directions, respectively
k = thermal conductivity
L = length of system in x direction; $[1 + D + h(\Delta y)/k]e_T$
ℓ = thickness of system in y direction
M = upper limit of index I
N = upper limit of index J
$P = -De_T/2$
$S = 1 + D$
T = temperature; true temperature
V = computed temperature
w = width of cavity
x,y = independent variables
ϵ = convergence criterion
Δ = mesh size of what follows

Subscripts

A = ambient
B = boundary or $h(\Delta y)/k$
S = surface
T = temperature

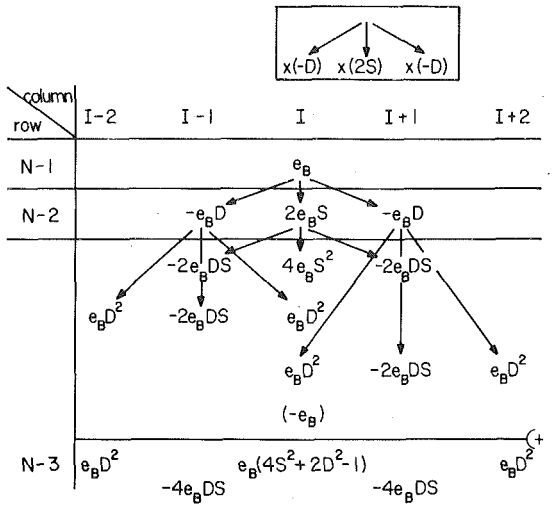

Fig. 3 Chart of error propagation due to $h(\Delta y)/k$ uncertainty

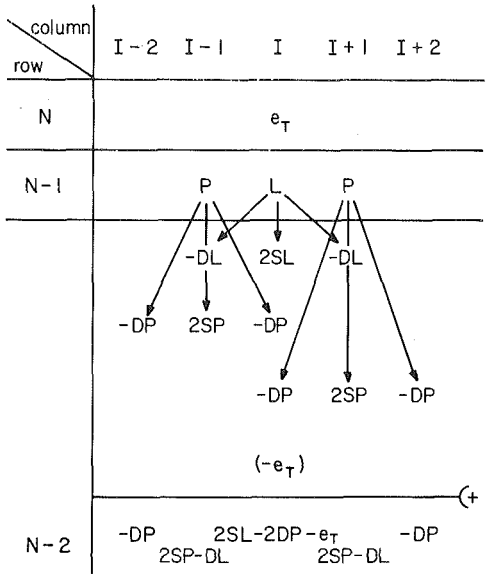

Fig. 4 Chart of error propagation due to surface temperature uncertainty

If the actual $h(\Delta y)/k$ value used in the analysis is off by a dimensionless quantity e_B and all the temperatures are evaluated in excess of T_A, then the difference between the computed temperature V and the true temperature T for nodes in row $(N-1)$ can be derived using equation (1) and expressed in terms of $T_{I,N}$ as

$$V_{I,N-1} - T_{I,N-1} = e_B T_{I,N} \tag{3}$$

This error will propagate to nodes $(I,N-2)$ and cause errors there, given as

$$V_{I,N-2} - T_{I,N-2} = 2e_BST_{I,N} - e_BD(T_{I-1,N} + T_{I+1,N}) \tag{4}$$

where

$$D = \left[\frac{(\Delta y)}{(\Delta x)}\right]^2, \quad S = 1 + D$$

The errors at nodes $(I,N-3)$ become more complicated and can again be expressed in terms of the surface temperatures as

$$V_{I,N-3} - T_{I,N-3} = e_B(4S^2 + 2D^2 - 1)T_{I,N} - 4e_BSD(T_{I-1,N} + T_{I+1,N}) + e_BD^2(T_{I-2,N} + T_{I+2,N}) \tag{5}$$

By comparing these three equations, a pattern of error propagation can be found as depicted in Fig. 3. At the top of the figure a set of coefficient multipliers is given in a boxed chart. This chart can be used to develop coefficients for T on the right of equations (4) and (5) as follows:

Using equation (3), one obtains the coefficient for $T_{I,N}$ term as e_B (see row $(N-1)$ in Fig. 3). Using this e_B and the multiplier chart, one finds the coefficients for $T_{I,N}$, $T_{I-1,N}$ (or $T_{I+1,N}$) terms in equation (4) as $2e_BS$ $(=e_B \times 2S)$, $-e_BD[=e_B \times (-D)]$, respectively. Somewhat peculiar is the presence of $(-e_B)$ in column I in the tabulation for $(N-3)$ row. This additional coefficient arises from the fact that, in the formulation of the temperature equation for row $(N-3)$, terms of temperature for row $(N-1)$ also enter into the equation. By the same token, if one derives the equation for $(V_{I,N-4} - T_{I,N-4})$, those coefficients contained in row $(N-2)$ will also appear in the equation (not shown) and, therefore, be subtracted from the $T_{I-1,N}$, $T_{I,N}$ and $T_{I+1,N}$ terms. It is noted that in the foregoing analysis, the errors in the interior nodal temperatures have all been expressed in terms of the surface temperatures (see equations (3–5)). Also the examples given here have been made based on the propagation of errors from temperatures at points $(I,N-1)$.

Another error arises from the surface temperature uncertainty. The surface temperature measured using an infrared scanner is susceptible to errors due to surface irregularities such as rough spots, rusts, etc. Hence, an error analysis is also needed to examine how a singular surface temperature irregularity could affect the temperatures at interior nodes.

If the true temperature at point (I,N) is denoted as $T_{I,N}$ and the observed value there is $T_{I,N}(1 + e_T)$, the error at the point can be represented by $e_TT_{I,N}$ where e_T denotes the percent error in T value. One can use equation (1) to prove that the difference between the computed temperature V and the true temperature T at point $(I,N-1)$ due to the singular temperature uncertainty at point (I,N) is

$$V_{I,N-1} - T_{I,N-1} = LT_{I,N} \tag{6}$$

where

$$L = \left[1 + D + \frac{h(\Delta y)}{k}\right]e_T$$

The uncertainty at point $(I+1, N-1)$ can also be derived and expressed in terms of the surface temperature as

$$V_{I+1,N-1} - T_{I+1,N-1} = PT_{1,N} \tag{7}$$

where

$$P = -(1/2)De_T$$

The multiplier chart given in Fig. 3 is again useful to derive the temperature error equations for nodes deep inside the system. For example, at point $(I,N-2)$

$$V_{I,N-2} - T_{I,N-2} = (2SL - 2DP - e_T)T_{I,N} \tag{8}$$

which can be obtained from the multiplication table given in Fig. 4.

Example and Discussion

A series of tests was made to validate the methodology presented in this paper. The top surface temperatures were calculated for some test cases having known cavity geometries. The method used in the calculation was an iteration scheme that is commonly employed in the numerical solution of heat conduction problems. These surface temperatures calculated were subsequently used as inputs to a computer program to solve inversely the nodal temperatures underneath the surface which, in turn, were used to reconstruct the cavity configuration. A sample test is shown in Fig. 5 where the test parameters are listed in the legend.

Attention is first directed to the calculated surface temperature appearing on the top of the figure. Because of the presence of the cavity the surface has a hot spot above the cavity, which is not unexpected. It is noted that the inflection point on the temperature data does not coincide with the location of the cavity (side) wall; this point is always displaced away from the cavity center. This phenomenon can be ascribed to the fact that additional heat flux is needed to

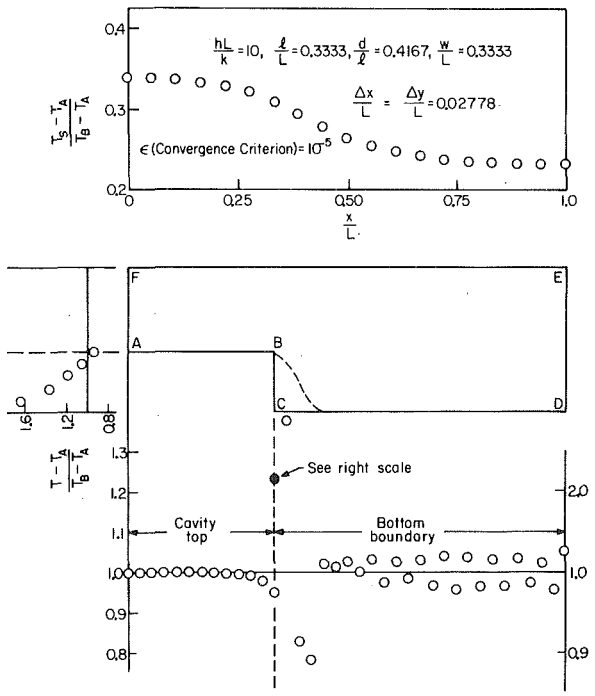

Fig. 5 Use of surface temperatures to predict cavity geometry

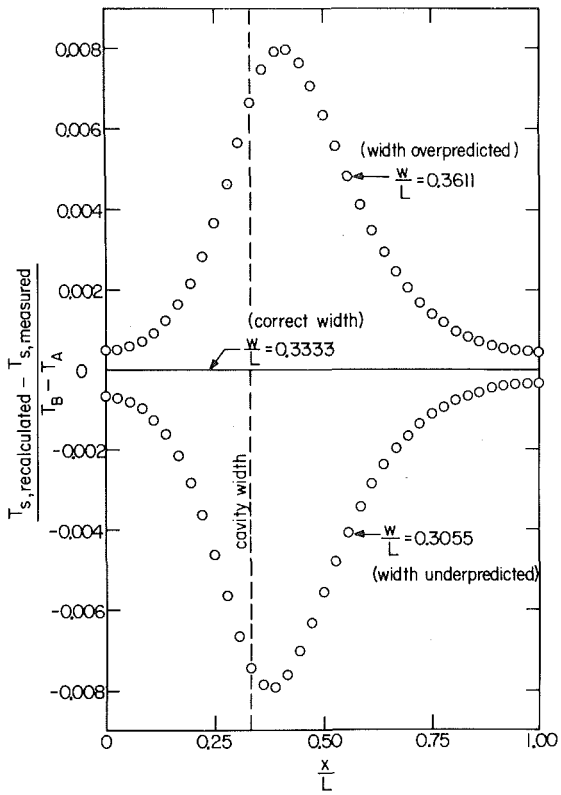

Fig. 6 Recheck of cavity wall position

maintain the cavity wall at a prescribed temperature. This additional flux crosses the system boundary and raises the temperatures near the wall.

The calculated surface temperature was next used in an inverse problem to predict the cavity geometry. In the middle diagram a cross-section of the analyzed system is shown, where the solid line at lower left corner depicts the actual cavity location. If the interior nodal temperatures are calculated one row after another covering the entire region and, if the isotherm at T_B (prescribed) is plotted in the figure, the dashed line is obtained. Clearly, this scheme of predicting the cavity geometry yields acceptable results at the cavity top, but the cavity re-entrant corner is in error and the width of the cavity base is also overpredicted. To facilitate viewing of the disagreement between the predicted nodal temperatures and the prescribed temperature (T_B) along the cavity boundary, two additional temperature plots are given as shown in the bottom and left of the figure. The bottom figure compares the calculated nodal temperatures with T_B along the cavity top (AB) and the bottom boundary (CD); the left figure makes a similar comparison for the cavity wall (BC). As shown in the bottom figure, starting from point A, the prediction of the cavity top is indeed accurate (agreement within 0.1 percent). Toward the cavity re-entrant corner (B), the calculated nodal temperatures are slightly lower; (see both bottom and left figures; note different scales used in these plots). Moving down along the cavity wall (BC), the calculated nodal temperatures increase rapidly (see left figure). Of particular interest is the observation of temperature oscillations along the bottom boundary (CD), see the bottom figure. This demonstrates the characteristics of the numerical method used in the solution. Since the nodal temperature at any point is calculated based on those at four nodes right above the point (see Fig. 2), a minute temperature fluctuation at the node right above the point of investigation tends to amplify rapidly downward and affect those temperatures calculated below the fluctuating point. Unlike the conventional solution by iteration method, in which the nodal temperatures at a point are calculated based on those temperatures in their immediate vicinity and, as such, for successive computations, any temperature fluctuations tend to damp out, the numerical method used in the present study computes temperatures one row after another in a fixed direction. Hence, any temperature fluctuation at a point will not damp out but will amplify and show markedly in a succeeding row at the same column position. This problem must be resolved and the method found successful was to apply a noise removal routine that is commonly used in the field of image processing [20,22]. According to the method, a moving average of temperatures is computed using

$$T_{I,J(\text{smoothed})} = \frac{T_{I-1,J} + 6T_{I,J} + T_{I+1,J}}{8} \tag{9}$$

which was derived based on averaging $T_{I,J}$ with $T_{I-1,J}$ (or $T_{I+1,J}$) to get the first pair of means, which are, in turn added to $T_{I,J}$ itself to compute a second set of means. Equation (9) computes the third order mean value based on the previously calculated means. This equation provides sufficient weight to the original $T_{I,J}$ data to retain its characteristics while producing a desired smoothing function satisfactory for a wide range of cases including small mesh size and shallow cavities. It is also noted that, since the slope of the surface temperature plot near the cavity center is negligibly small, this data smoothing routine will not affect the determination of the position of the cavity top. However, the nodal temperatures calculated near the cavity (side) wall are somewhat smeared to the extent that the exact position of the cavity re-entrant corner cannot be identified based on the computed nodal temperatures. This also explains why the calculated nodal temperature at the cavity re-entrant corner is slightly lower than prescribed (refer to Fig. 5). A recheck of the corner position is in order.

Based on the foregoing analysis, a cavity wall position can be assumed. Experience suggests that the cavity re-entrant corner should be located beyond the point where the nodal temperatures show a trend of dropping. With this assumed cavity wall, temperatures inside and on the surface of the system are recalculated and the latter plotted as shown in Fig. 6.

If the assumed wall position is one mesh size (Δx) displaced inward from the actual location (i.e., cavity width underpredicted), the recalculated surface temperature T_S is lower than the measured as is shown in the lower half of the figure. An overprediction by one mesh size moves the data to the top. The solid line across the figure represents where data are located when the prediction is correct. Moreover, the data located in the top half of the figure appear to form a mirror image below the solid line, signifying that an interpolation is again

possible in the searching process. According to the trend of data shown, the interpolation appears to be most effective near the temperature inflection point where the data vary most rapidly.

With the discussion of the prediction of cavity geometry complete, attention is now directed to the error analysis. Tests were made with the $h(\Delta y)/k$ value overestimated 5 percent. For this case, the computer data reveal that the predicted cavity is 6.5 percent deeper. A value of $h(\Delta y)/k$ 5 percent lower will lead to a prediction of cavity depth 7.4 percent shallower. On the other hand, because of the method of numerical solution used in this work, any erroneous temperature detected on the surface of the test specimen is found to have a marked effect in upsetting the temperatures computed for interior nodes. The region affected spreads out covering an angle $\theta = 2 \tan^{-1} (\Delta x)/(\Delta y)$ with the point of irregularity positioned at the apex. Fortunately, such an irregular temperature can often be detected in practice and can therefore be corrected before analysis.

A point of interest is that, because of the plane wall system addressed in this study, two limiting cases occur. The surface temperature observed at the edge of the system (i.e., point E in Fig. 5) is expected to asymtotically reach that of a plane wall of thickness ℓ, if the cavity width is small, i.e.

$$\frac{T_S - T_A}{T_B - T_A} = 1 - \frac{1}{1 + \dfrac{k}{h\ell}} \tag{10}$$

By the same token, the surface temperature observed at the center of the cavity will reach asymtotically that of a plane wall of thickness (ℓ-d), if the cavity is large. These limiting cases permit one to find a better k/h value and use it in the analysis. This point can be illustrated by referring to the surface temperature data given in Fig. 5. Using the surface temperature at point E and equation (10) one finds hL/k = 9.9238, an error of 0.76 percent (note the correct value is 10). If the surface temperature at point F is used, the predicted hL/k is 10.0793, again a small error of 0.79 percent. It is noted that the cavity shown in Fig. 5 is a middle size one. A wider cavity will make the prediction based on the surface temperature at the cavity center even more accurate, and vice versa. One should be cautioned, however, that in the present study the convective coefficient has been assumed to be a constant. In the event that a deep cavity is encountered, the surface temperature differential between center and edge of the system may become appreciable. Under these conditions, the variation of h with T should also be considered and an accurate prediction becomes more difficult.

As a point of further interest, the accuracy of the cavity size can also be estimated by statistical means. Say, the measured surface temperature has an error of ±1.5 percent. It follows from the preceding analysis that this error will lead to an uncertainty in Biot number (hL/k) estimation of 1.95 percent based on the temperature at point E. This Biot number uncertainty, together with the surface temperature error, will have a cumulative effect of raising the cavity depth uncertainty to 4.3 percent. A recheck of the cavity width will require computation of least squares between the recalculated and the measured temperatures on the surface.

Extension to Three-Dimensional Systems

The analysis presented above can be extended to predict cavity geometry in a three-dimensional system such as a rectangular cross-sectioned hole in a parallelepiped. If the length of this body is very long along the hole axis such that the temperature variation along this axis is negligible, the interior nodal temperatures can be computed in a two-dimensional array. There are four surfaces now available for measuring temperatures; each of these surface temperatures can be used to compute interior nodal temperatures with one set calculated for each direction of computation. In this way the position of the nearest hole boundary that is parallel to the surface can be determined. By superimposing these four arrays of temperatures the hole configuration can be identified. In fact, chores of recalculating and matching surface temperatures in this three-dimensional system can be totally eliminated in the process. It should be noted that, while the

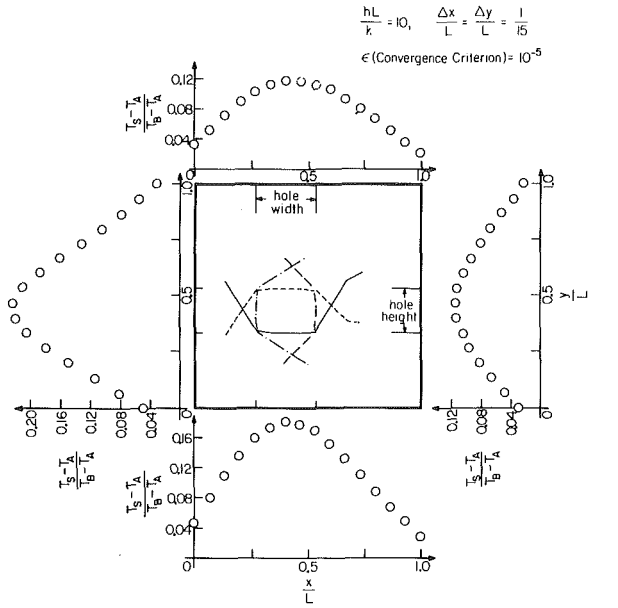

Fig. 7 Prediction of hole geometry in a three-dimensional system

method of prediction of cavity geometry becomes easier for this three-dimensional system, the accuracy of prediction becomes heavily dependent on the h/k value used in the analysis. Of major concern to users is the fact that, for three-dimensional systems, there are no limiting cases (as one had before) to check this h/k value.

A sample case is shown in Fig. 7 where the test conditions are specified in the legend. Before the numerical experiment, the surface temperature data were calculated using an iteration scheme and plotted in the figure as open circles surrounding the test body. These surface temperatures were subsequently used as inputs to predict the hole geometry. For example, the isotherm at $(T - T_A)/(T_B - T_A)$ = 1 predicted based on the bottom surface temperature is plotted using solid lines inside the center figure; the computation approaches from below. By superimposing four isotherms the geometry of the hole can be identified. The predicted hole agrees well with the actual hole (see tick marks on the body boundaries) except the corners are slightly rounded, a result of the data smoothing as has been discussed previously. Clearly, the method presented here is convenient to use and is more accurate than any other methods reported in the literature.

Concluding Remarks

It is well known in nondestructive testing using infrared scanning that the uncertainty in flaw detection is larger for small cavities located deep down the surface. With the methodologies presented in this paper this observation takes a new perspective.

For a small cavity located deep below the surface, the numerical method becomes inaccurate to predict the cavity depth. The predicted nodal temperatures near the cavity re-entrant corner drop off at the same rate as the computation steps are increased; eventually, the nodal temperatures near the center of the cavity will be affected. This will lead to an erroneous prediction of the cavity depth and width. Furthermore, the propagation of errors due to h/k can also be serious, as has been discussed previously.

The methods presented above are strictly valid for cavities having a prescribed temperature. Methodologies for other types of boundary conditions have been developed and will be reported in separate papers.

Acknowledgment

The authors acknowledge support of a grant (Grant No. ENG-7710630) from the National Science Foundation, which made this study possible.

References

1 Stolz, G., Jr., "Numerical Solutions to an Inverse Problem of Heat Conduction for Simple Shapes," ASME JOURNAL OF HEAT TRANSFER, Vol.

82, 1960, pp. 20–26.
2 Frank, I., "An Application of Least Squares Method to the Solution of the Inverse Problem of Heat Conduction," ASME JOURNAL OF HEAT TRANSFER, Vol. 85, 1963, pp. 378–379.
3 Burggraf, O. R., "An Exact Solution of the Inverse Problem in Heat Conduction Theory and Applications," ASME JOURNAL OF HEAT TRANSFER, Vol. 86, 1964, pp. 373–382.
4 Sparrow, E. M., Haji-Sheikh, A., and Lundgren, T. S., "The Inverse Problem in Transient Heat Conduction," ASME *Journal of Applied Mechanics,* Vol. 86, 1964, pp. 369–375.
5 Beck, J. V., Discussion to "the Inverse Problem in Transient Heat Conduction," ASME *Journal of Applied Mechanics,* Vol. 87, 1965, pp. 472–473.
6 Beck, J. V., and Wolf, H., "The Nonlinear Inverse Heat Conduction Problem," ASME Paper No. 65-HT-40, 1965.
7 Beck, J. V., "Nonlinear Estimation Applied to the Nonlinear Inverse Heat Conduction Problem," *International Journal of Heat and Mass Transfer,* Vol. 13, 1970, pp. 703–716.
8 Hsieh, C. K. and Ellingson, W. A., "The Feasibility of Using Infrared Scanning to Test Flaws in Ceramic Materials," *Proceedings of the Fifteenth International Thermal Conductivity Conference,* Plenum Press, 1978, pp. 11–22.
9 Hsieh, C. K., Ellingson, W. A., and Su, K. C., "A Model Study for Quantitative Flaw Detection Using Infrared Scanning," *British Journal of Non-destructive Testing,* July 1979, pp. 185–192.
10 Hsieh, C. K., Ellingson, W. A., and Su, K. C., "Computer Modeling of Heat Transfer Through Refractory Lined Transfer Lines in Coal Gasification System," Argonne National Laboratory Technical Report, in press.
11 Kutzscher, I. W., and Zimmermann, K. H., "Scanning Infrared Inspection System Applied to Nondestructive Testing of Bonded Aerospace Structures," *Applied Optics,* Vol. 7, No. 9, 1968, pp. 1715–1720.
12 Dixon, R. D., Lassahn, G. D., and DiGiallonardo, "Infrared Thermography of Subsurface Defects," *Materials Evaluation,* Vol. 30, No. 4, 1972, pp. 73–86.
13 MuCullough, L. D., and Green, D. R., "Electrothermal Nondestructive Testing of Metal Structures," *Materials Evaluation,* Vol. 30, No. 4, 1972, pp. 87–95.
14 Barnes, R. B., "Diagnostic Thermography," *Applied Optics,* Vol. 7, No. 9, 1968, pp. 1673–1685.
15 Ryan, J., "Thermography," *Australian Radiology,* Vol. 13, No. 1, 1969, pp. 23.
16 Herma van Voss, S. I. C., and Thomas, P. *Medical Thermography,* S. Karger, Switzerland, 1969.
17 Haberman, J. D., "Image Analysis of Medical Infrared Thermograms," *CRC Critical Reviews in Radiological Sciences,* 1971, pp. 427–465.
18 Chen, M. M., Pedersen, C. O., and Chato, J. C., "On the Feasibility of Obtaining Three-Dimensional Information from Thermographic Measurements," ASME *Journal of Biomedical Engineering,* Vol. 99, No. 2, 1977, pp. 58–64.
19 Gambarelli, J., Guerinel, G., Chevrot, L., and Mattei, M., *Computerized Axial Tomography,* Springer-Verlag, Berlin, Heidelbert, 1978.
20 Tou, J. T., and Gonzalez, R. C., *Pattern Recognition Principles,* Addison-Wesley, 1974, pp. 17.
21 Hsieh, C. K., Yang, M. C. K., Farber, E. A., and Jorolan, A., "A Feasibility Study to Test Structure Integrity by Infrared Scanning Technique," *Thermal Conductivity Proceedings of the Fourteenth International Conference on Thermal Conductivity,* Plenum Press, 1975, pp. 521–530.
22 Yang, M. C. K., and Hsieh, C. K., "A Three Component Method of Data Analysis for Nondestructive Testing by Infrared Scanning," *Proceedings of the Society of Photo-Optical Instrumentation Engineers,* Vol. 95, 1976, pp. 212–216.
23 Private communication with TPRC, Purdue University.

Transient Solidification in Flow into a Rod Bundle

M. Epstein
L. J. Stachyra
G. A. Lambert

Reactor Analysis and Safety Division,
Argonne National Laboratory,
9700 South Cass Avenue,
Argonne, Ill. 60439

Transient solidification of a liquid in axial flow into and through a cold rod bundle was investigated. Experiments are described in which the amount of liquid displaced through the rod bundle before freezing shut as a function of pressure drop was measured. Simple relations for the liquid mass displaced into or through the rod bundle were derived by combining the notion of a time-dependent hydraulic diameter with an available approximate method for treating transient solidification in a tube flow. The relations are shown to be approximately consistent with the experimental data.

1 Introduction

Previous engineering research on internal flows with solidification has been confined almost exclusively to flow between parallel plates [1–3] or in a circular tube [4–18]. However, some channels used in engineering structures (where freezing of the process fluid is a problem) and some molds used for casting materials have cross sections such that the flow cannot be regarded as parallel or circular. With odd-shaped cross-sections, the problem of predicting the rate of flow constriction due to solidification by a direct theoretical attack on the governing partial differential equations presents insurmountable mathematical difficulties. It is well known that, in the absence of solidification, the concept of the hydraulic diameter permits circular and noncircular cross-sections to be treated with equal facility. A study of the applicability of the "hydraulic diameter approach" to problems involving transient solidification in turbulent flow through channels of complex cross-section would seem appropriate.

The main purpose of this investigation was to determine the utility of the hydraulic diameter concept for predicting the amount of liquid displaced into and, perhaps, through a cold channel of complex cross-section before freezing shut. To this end, an experimental study was made of the transient solidification of a liquid as it penetrates axially into a steel *rod bundle* initially cooled to the liquid nitrogen boiling temperature (−196°C). In the interests of simplicity and understanding the liquid temperature was restricted to its fusion temperature. The amount of liquid displaced into or through the bundle as a function of injection pressure was measured. This was compared with predictions obtained by combining the notion of a time-dependent hydraulic diameter with a formulation recently used successfully by one of the authors to treat solidification into a penetrating tube flow [16].

Rod bundle geometry was selected for this study because of its extensive use in heat exchanger design. Moreover, the development of a simple predictive technique for the amount of liquid mass that can flow through a rod bundle before freezing shut is essential to fast-nuclear-reactor safety studies [19]. A series of tests in which a chemically produced mixture of high-pressure nitrogen gas, 3200°C molten uranium dioxide and metallic molybdenum was injected into a steel rod bundle is reported in references [20, 21]. However, owing to the complex nature of this multi-phase mixture, it is not possible to derive any information from these data which can be used to examine the hydraulic diameter concept.

2 Analysis

Figure 1 is a sketch of the flow and freezing system to be analyzed. We consider a turbulent liquid flow at its freezing temperature T_{mp} flowing axially from a large reservoir at constant pressure P_0 into an initially empty rod bundle at temperature $T_0 (T_0 \ll T_{mp})$. Freezing of the liquid takes place on the inner walls of the bundle flow "tube" as well as on the surfaces of the rods. In keeping with our objectives, we focus attention on a "representative subchannel" within the rod bundle and imagine that it can be regarded as a simple parallel-plate channel having a hydraulic diameter equal to the hydraulic diameter of the bundle, D_h, as illustrated in Fig. 1. Our choice of a parallel-plate channel rather than, say, a circular-tube representation is motivated by the fact that the freezing law for parallel-plate geometry is relatively easy to deal with analytically.[1] Moreover, solidification in a rod bundle is well-represented by a one-dimensional treatment, since the crust thickness is uniform and is not an appreciable fraction of the radius of the rods during the time span in which most of the reduction in flow area takes place (see below).

The main quantity of interest is the amount of liquid displaced into or through the rod bundle before solidification is complete in the inlet region.

The local mean hydraulic diameter of the rod bundle, $D(z,t)$, decreases with the transient growth of the solid phase. Based on our parallel-plate idealization, the penetrating liquid forms solid layers of mean thickness $[D_h - D(z,t)]/4$ which varies with both time and position along the walls of the bundle. With the exception that we are now dealing with parallel-plate geometry, our model is similar to the model reported in [16] for liquid penetration and freezing in a cold tube, the validity of which has been established from experimental and theoretical studies [16–18]. As in reference [16], we make the assumptions that (1) the temperature at the liquid-solid interface is equal to the equilibrium solidification temperature; (2) all physical properties are constant and the densities of the liquid and frozen deposit are taken to be the same; (3) the liquid-injection pressure, P_0, is sufficiently large so that most of the liquid displacement occurs under turbulent flow conditions; (4) liquid flow inertia and entrance

[1] It can be shown that the results obtained with these two representations do not differ very much from each other.

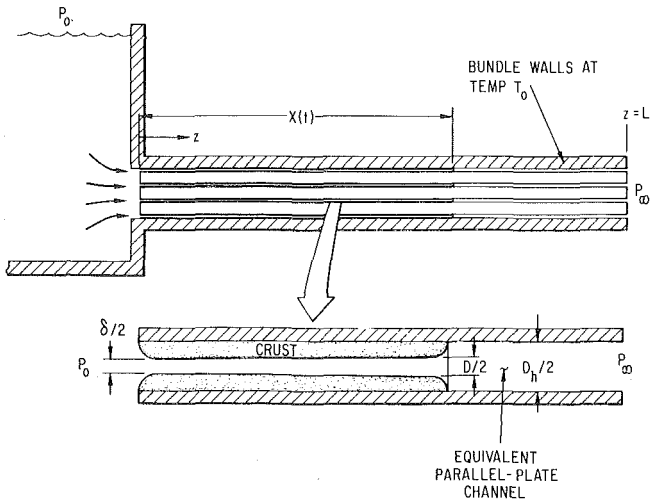

Fig. 1 Solidification in liquid flow into a rod bundle and into its equivalent parallel-plate configuration

Contributed by the Heat Transfer Division for publication in the JOURNAL OF HEAT TRANSFER. Manuscript received by the Heat Transfer Division September 21, 1979.

losses are small relative to the frictional pressure drop; and (5) the liquid penetration or flow rate is insensitive to details of the crust shape. The following additional assumptions are made relative to the rod bundle geometry: (6) the solid rods and the outer flow channel wall are maintained at constant temperature; and (7) the wetted perimeter of the rod bundle cross-section, C, is considered constant during the injection period.

Assumptions 1–5 have been discussed in some detail in references [16, 17]. Criteria for the validity of assumptions 3 and 4 are presented in [16]. Assumption 5 is verified theoretically in [17]. Assumption (7) is justified during most of the transient in view of the extremely large wetted perimeter-to-hydraulic diameter ratio, C/D_h, characteristic of rod bundles. For example, for a bundle containing seven rods of the type employed in fast reactor safety experiments (see Fig. 2), simple geometry considerations reveal that a reduction of 80 percent in the cross-sectional area for liquid flow due to uniform crust growth along the bundle walls amounts to only a 16 percent reduction in the wetted perimeter. It is clear that this assumption breaks down late in the freezing transient just before the frozen material fills the entire cross-sectional area for liquid flow.

According to our model, the liquid shear at the solid-liquid interface is well-described locally by (assumption 3)

$$\tau = \tfrac{1}{2} f \rho u^2 \tag{1}$$

Available channel flow data for annular channels including parallel-plate channels [22] suggest that the friction factor, f, be obtained from the Blasius formula:

$$f = 0.0791 \left(\frac{uD}{\nu}\right)^{-1/4} \tag{2}$$

In the above expressions, a slug-flow axial velocity profile $u = u(z,t)$ is assumed, and ν is the kinematic viscosity of the liquid. The applicability of equations (1) and (2) in the presence of transient crust growth is discussed in reference [16]. Briefly, we require the time necessary for the development of the turbulent velocity profile to be small compared with the time it takes for solidification to be complete at the channel entrance. In almost all cases of practical interest, this requirement is met.

The momentum balance between pressure and frictional forces over the instantaneous freezing length, $X(t)$, takes the form

$$\Delta P = \int_0^{X(t)} \frac{4\tau(z,t)}{D(z,t)}\, dz, \tag{3}$$

We assume a square-root function for the axial variation of the crust shape (assumption 5):

$$\frac{D}{D_h} = 1 - \left(1 - \frac{\delta}{D_h}\right)\left(1 - \frac{z}{X}\right)^{1/2} \tag{4}$$

where $\delta(t)$ is the hydraulic diameter of the rod-bundle at the inlet location $z = 0$ (see Fig. 1) and is given by the familiar square-root crust growth law:

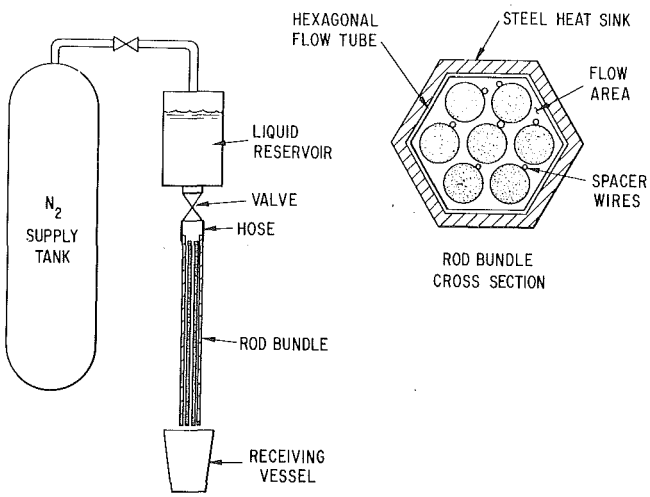

Fig. 2 Schematic drawing of the experimental apparatus and cross-sectional view of rod-bundle flow path

$$\tfrac{1}{4}[D_h - \delta(t)] = 2\lambda(\alpha_s t)^{1/2} \tag{5}$$

For crust growth on an isothermal wall, the "growth constant" λ is given by the implicit relation [23]

$$\sqrt{\pi}\lambda e^{\lambda^2} erf(\lambda) = \frac{c_s(T_{mp} - T_0)}{h_{\ell s}}$$

where $h_{\ell s}$ is the heat of fusion of the liquid material and c_s is the heat capacity of the solid phase.

The definition of the mean hydraulic diameter provides the expression:

$$A(z,t) = \tfrac{1}{4} C D(z,t) \tag{6}$$

and, finally, an overall mass balance on the incompressible advancing flow between z and $X(t)$ leads to the following relation between the local axial velocity u and the velocity of the leading edge, dX/dt:

$$Du = D_h \frac{dX}{dt} \tag{7}$$

Substituting equations (1, 2) and (4) into equation (3), performing the indicated integration, and solving the result for the liquid velocity yields

$$u(z,t) = \frac{\nu}{D(z,t)}\left[\left(\frac{1}{0.1582}\right)\left(\frac{\Delta P D_h^3}{\rho \nu^2}\right)\left(\frac{\delta^2(t)}{D_h^2 X(t)}\right)\right]^{4/7} \tag{8}$$

Equation (8) takes one of the following two forms of interest, depending on whether or not liquid emerges from the opposite end of the rod bundle at $z = L$ before freezing shut. Early in the injection

Nomenclature

A = instantaneous cross-sectional area for liquid flow
A_s = cross-sectional area of frozen blockage material
A_w = cross-sectional area of bundle wall material
c_s = heat capacity of frozen material
c_w = heat capacity of bundle wall material
C = wetted perimeter of rod bundle
D = instantaneous hydraulic diameter of rod bundle
D_h = initial hydraulic diameter of rod bundle
f = friction factor, equation (2)
$h_{\ell s}$ = latent heat of fusion
L = axial length of rod bundle freezing section
m = instantaneous mass of liquid displaced through rod bundle
m_p = total liquid mass displaced through rod bundle before freezing shut
P_0 = reservoir or injection pressure
P_∞ = initial pressure in empty rod bundle (atmospheric pressure)
t = time
t^* = time leading edge of liquid flow reaches the bundle exit
T_{mp} = fusion temperature of flowing liquid
T_0 = temperature of rod bundle walls during flow transient
T_w = final temperature of rod bundle walls, equation (13)
u = axial component of liquid velocity
X = instantaneous location of advancing liquid front
z = axial coordinate measured from rod bundle inlet, Fig. 1
α_s = thermal diffusivity of frozen material
δ_c = thickness of frozen layer
$\Delta P = P_0 - P_\infty$, total pressure drop
λ = growth constant, equation (5)
ν = kinematic viscosity of flowing liquid
ρ = density of flowing material
τ = shear stress, equation (1)

period, when $X(t) < L$, the advancing liquid flow satisfies an equation of motion obtained by eliminating the product uD between equations (7) and (8):

$$X^{4/7}\frac{dX}{d(\delta/D_h)} = -\frac{\nu D_h}{32\lambda^2\alpha_s}\left[\left(\frac{1}{0.1582}\right)\left(\frac{\Delta P D_h^3}{\rho\nu^2}\right)\right]^{4/7}\left(\frac{\delta}{D_h}\right)^{8/7}\left(1-\frac{\delta}{D_h}\right) \quad (9)$$

where time t has been eliminated in favor of the instantaneous hydraulic diameter, $\delta(t)$, at the bundle inlet. Beyond the time defined by $X(t^*) = L$, we concentrate on the instantaneous liquid mass flow rate through the rod bundle, $dm/dt = \rho uA$, or from equations (5–8):

$$\frac{dm}{d(\delta/D_h)} = -\frac{\rho\nu C D_h^2}{128\lambda^2\alpha_s}\left[\left(\frac{1}{0.1582}\right)\left(\frac{\Delta P D_h^3}{\rho\nu^2 L}\right)\right]^{4/7}\left(\frac{\delta}{D_h}\right)^{8/7}\left(1-\frac{\delta}{D_h}\right) \quad (10)$$

When the supply pressure ΔP is sufficiently low, the rod bundle freezes shut before the liquid can advance to the bundle exit at $z = L$. The final liquid penetration length, X_p, is found by integrating equation (9) between the limits $X = 0$ when $\delta = D_h$ and $X = X_p$ when $\delta = 0$ to obtain

$$\frac{X_p}{D_h} = 0.085\left(\frac{\nu}{\lambda^2\alpha_s}\right)^{7/11}\left(\frac{\Delta P D_h^2}{\rho\nu^2}\right)^{4/11} \quad (11)$$

At high injection pressures, an amount of liquid mass m_p will emerge from the rod-bundle exit before the inlet region is closed by the solidified layers. The mass of liquid displaced through the cold bundle is obtained by performing two integrations. First, we integrate equation (9) between the limits $X = 0$ when $\delta = D_h$ and $X = L$ when $\delta = \delta(t^*)$, where $\delta(t^*)$ is simply the hydraulic diameter of the rod-bundle inlet at the instant the leading edge of the liquid flow reaches the channel exit. Second, we integrate equation (10) from $m = 0$ when $\delta = \delta(t^*)$ to $m = m_p$ when $\delta = 0$. By eliminating $\delta(t^*)$ between the two resulting algebraic relationships, we obtain m_p as a function of known quantities:

$$\frac{m_p}{\rho L C D_h} = 3.33\times10^{-3}\left(\frac{D_h\nu}{\lambda^2\alpha_s L}\right)\left(\frac{\Delta P D_h^3}{\rho\nu^2 L}\right)^{4/7} - 0.159 \quad (12)$$

At some reduced driving pressure ΔP, equation (12) indicates that $m_p = 0$. For supply pressures smaller than this value, the rod bundle will freeze shut before the leading edge of the flow reaches the bundle exit. In this situation, the flow penetration length X_p is of interest and is estimated using equation (11).

3 Experimental Investigation

A schematic diagram of the experimental apparatus is shown in Fig. 2. Briefly, a valve separated a 97 cm-long rod bundle from a liquid reservoir.

A stainless-steel vessel made from 4 in. schedule 40 pipe (10.23-cm i.d.), approximate capacity of 6000 cm^3, served as the liquid reservoir. Water was selected as the principal working fluid for the solidification study since its low-temperature, solid-phase characteristics are extensively documented. In addition to water, p-xylene and pentadecane were also used as working fluids to study the effects of physical properties on flow penetration and freezing. Unfortunately, as will be discussed below, major difficulties were encountered in the use of p-xylene and pentadecane as test materials. Two thermocouples were located at different levels within the reservoir to check that a uniform temperature was attained prior to a run. The liquid in the reservoir was regarded as ready for a run when its temperature was reduced to about 0.3°C above its fusion value. The reservoir was connected at the top to a large 3×10^5-cm^3 tank pressurized with nitrogen gas to maintain a constant injection pressure. A pressure transducer was installed in the reservoir.

A 9.0 cm-long thick-rubber tube (hose) of 3.175 cm i.d. provided the connection between the valve and the rod-bundle inlet. A thermocouple and a pressure transducer were installed in this section to monitor the liquid-flow temperature and pressure just before the liquid entered the rod bundle. This instrumentation insured liquid temperature and pressure uniformity between the reservoir and the bundle inlet.

The rod bundle itself consisted of seven stainless-steel tubes arranged in a hexagonal array (see Fig. 2). The tubes were contained inside a 0.051-cm-thick hexagonal flow channel fabricated from stainless-steel with each of the inner hexagonal flats of width 1.176 cm. The tubes were prototypic fast-reactor-cladding of 0.584-cm o.d. The tubes were spaced by wrapping each tube with a wire on a 30.0-cm pitch; the wire-wrap diameters were 0.142 cm for the center tube and 0.0835 cm for the edge tubes. This tube/wire-wrap arrangement resulted in a flow cross-section between tubes of 1.67 cm^2, a wetted perimeter of 21.91 cm (which includes the hexagonal channel walls) and, therefore, a hydraulic diameter of 0.305 cm.

Two steps were taken in the design of the rod bundle to ensure continuous solid phase growth both on the inner walls of the hexagonal flow channel and along the outside surfaces of the tubes. First, each tube was filled with liquid mercury to provide the desired heat sink within the tubes. Second, a 0.635-cm thick heat sink shrouded the hexagonal flow channel. This heat sink was formed from six steel plates, welded together along the outer surfaces of the channel. The length of the rod bundle freezing section was 95 cm.

The experiment was begun by placing the entire hexagonal rod bundle in a liquid-nitrogen bath. The bundle was cooled to the liquid nitrogen boiling temperature, −196°C, and mounted on the apparatus by inserting the (upper) end of the rod bundle into the inlet rubber hose. The pressure level in the nitrogen gas tank and liquid reservoir was adjusted, and the valve connecting the reservoir to the rod bundle was open, allowing the liquid at its fusion temperature to enter the cold rod bundle. The liquid penetration length before solidification was obtained by simply measuring the mass of the frozen plug within the rod bundle. This was accomplished by allowing the solidified plug to melt and drain out at the bottom of the rod bundle into a glass beaker. At high injection pressures, liquid was observed to flow through the rod bundle and into the receiving vessel (see Fig. 2). The mass of the liquid collected in the receiving vessel was also measured. The experiments covered reservoir (injection) pressures from 0.0064 MPa (~0.06 atm) to 1.03 MPa (~10.0 atm).

4 Results and Discussion

A comparison between equation (11) and the experimental results for the water flow penetration length (dimensionless) into the rod bundle versus dimensionless reservoir pressure is shown in Fig. 3. The line represents the theoretical solution, while the points represent the experimental values. The physical properties are evaluated at the average ice crust temperature $(T_{mp} + T_0)/2$. When the injection pressure exceeded 0.055 MPa (~0.54 atm), water was observed to emerge from the bundle exit. Equation (12) and the experimental results for the dimensionless mass displaced through the rod bundle versus dimensionless reservoir pressure are shown in Fig. 4. The theory is seen to be in reasonable agreement with experiment; however, the theoretical curve tends to underestimate the measurements. This may be due to the difficulty in maintaining the walls of the rod bundle at constant temperature. Equation (5) is valid only if the temperature rise in the bundle walls, $T_w - T_0$, at the moment the bundle freezes shut is not an appreciable fraction of the initital temperature difference, $T_{mp} - T_0$; that is, only if

$$\frac{T_w - T_0}{T_{mp} - T_0} = \frac{1 + \dfrac{2h_{\ell s}}{c_s(T_{mp} - T_0)}}{1 + 2\dfrac{A_w\rho_w c_w}{A_s\rho_s c_s}} \ll 1.0 \quad (13)$$

where A_w and A_s are the cross-sectional areas of wall material and frozen blockage material, respectively, and $h_{\ell s}$ is the heat of fusion of the frozen material. Equation (13) follows from a thermal balance which equates the total heat lost from the flowing liquid during the freezing period to the increase of enthalpy of the bundle walls. Criterion (13) presumes that at the moment solidification is complete, the average temperature of the frozen blockage is $(T_{mp} + T_w)/2$. In-

troducing the pertinent property values for the bundle geometry shown in Fig. 3 and an ice blockage, we estimate $(T_w - T_0)/(T_{mp} - T_0) = 0.27$. While small, this is probably not small enough to render variable wall-temperature effects negligible. As the value of T_0 was increased from the liquid-nitrogen boiling temperature to about −30°C, predicted values of m_f were observed to fall substantially below measured values. This is in accord with inequality (13), indicating that we have imposed a severe limitation on the model by assuming T_0 is constant. Nevertheless, it is felt that the insights gained regarding the hydraulic diameter concept, together with the asymptotic applicability of the present theory to large initial temperature differences, $T_{mp} - T_0$, amply justify our preliminary study of the constant T_0 case.

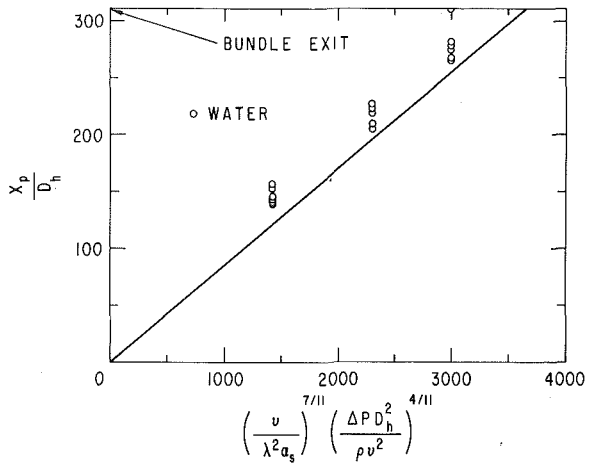

Fig. 3 Liquid penetration length into rod bundle versus reservoir pressure

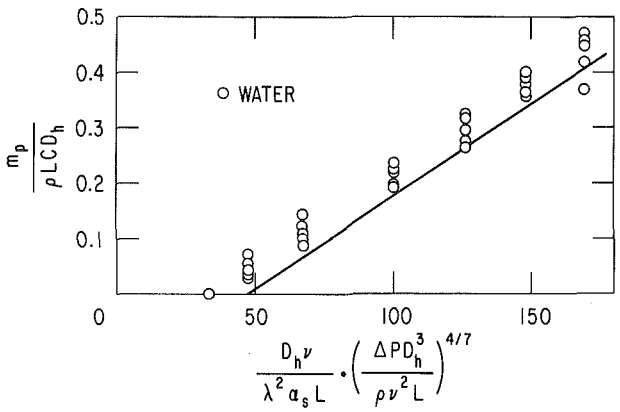

Fig. 4 Mass displaced through rod bundle versus reservoir pressure

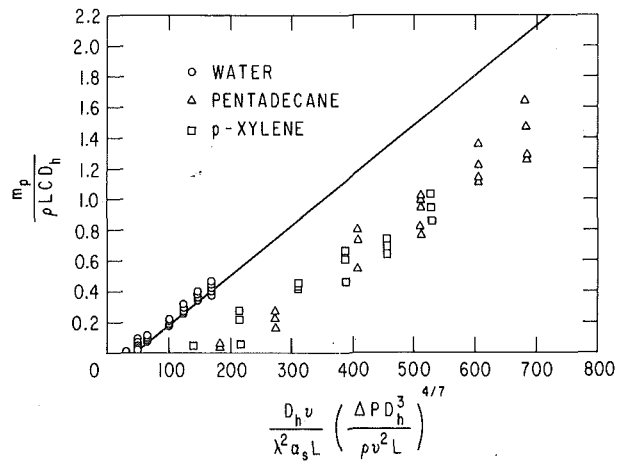

Fig. 5 Mass displaced through rod bundle versus reservoir pressure

It is important to note that the condition for a single rod to remain at constant temperature is also given by equation (13). By substituting the appropriate values of A_w and A_s into (13) we arrive at the same conclusion given above for the rod bundle temperature; namely, while the temperature rise within a mercury-filled tube is not completely negligible, it is small enough to justify the constant surface temperature assumption. Utilizing criterion (13) and our solutions, it can be shown that the liquid will travel almost 80 percent of its final penetration length before there is a perceptible rise in bundle surface temperature.

The measured liquid mass of p-xylene or pentadecane displaced through the rod bundle is plotted as a function of injection pressure in Fig. 5 in the form suggested by equation (12). The experimental data obtained from the water injection tests have also been plotted in Fig. 5 for comparison purposes. The data obtained with the organic liquids exhibit considerable scatter. Moreover, while the trend of the data seems to be consistent with the theory, specifically at high injection pressures, equation (12) is seen to over-predict the liquid mass displaced, m_p. In other words, the simple theory presented here indicates a slower rate of solidification within the rod bundle than observed experimentally.

Because of financial reasons, it was not possible to fill the liquid reservoir with pentadecane or p-xylene of the highest purity and, therefore, only practical grade organic liquids were used. The pentadecane showed a tendency to foam after passing through the cold rod bundle, while a yellow granular precipitate was observed at the bottom of the receiving vessel at the conclusion of the p-xylene tests. The amount of foam (or precipitate) collected showed a wide variation from test to test. In no test did the quantity of foam or precipitate exceed about 5 percent of the liquid mass collected. Foaming of pentadecane happens presumably because of the ability for this material to trap or dissolve air. In the case of p-xylene, the yellow precipitate might be caused by the rejection of impurities at the solid-liquid interface during crust growth.

Another difficulty with the organic liquids was the absence of the thermo-physical property values needed to evaluate the theory. The properties of these materials are only tabulated in the literature for the liquid phase at room temperature. These properties were used in the construction of Fig. 5. In some simple bench tests, an attempt was made to determine directly the product $\lambda^2 \alpha_s$ that appears in equations (11) and (12) at the low-temperature conditions of interest by growing a frozen layer of p-xylene or pentadecane in a one-dimensional manner. A thick brass plate, initially cooled in a liquid nitrogen bath, was immersed in a beaker containing the organic liquid at its fusion temperature and then removed after a predetermined time interval t. The thickness of the frozen deposit on the surface of the plate, δ_c, was measured with a caliper and compared with the Stefan solution for solidification; namely, $\delta_c = 2\lambda\sqrt{\alpha_s t}$. The $\lambda^2 \alpha_s$ values obtained in this manner showed appreciable scatter but, in general, were 30 to 60 percent higher than the values inferred from the available room-temperature physical-property measurements. It is speculated that this difference in the frozen layer growth rate is related to the formation of voids or air pockets in the solid phase, rather than to any dependence of the physical properties on temperature.

In concluding this section it should be stressed that the discrepancy between theory and experiment must be attributed to impurities in the organics and their effects on physical properties. This inference is based on three important observations mentioned in this section, which may be summed up as follows: First, the model is in good agreement with the water penetration data. Water is a well-behaved liquid and its solid-phase physical properties are extensively documented. Second, the foam and precipitate collected in the receiving vessel following each test suggest that impurities play an important role in the solidification of the organic materials. Finally, significantly better agreement between theory and experiment is obtained when the product $\lambda^2 \alpha_s$ is based on the one-dimensional bench-tests rather than on tabulated room-temperature physical-property measurements for the liquid phase.

5 Conclusions

The effect of transient solidification along the inner surfaces of a rod bundle upon turbulent axial flow has been investigated experimentally and analytically for the case of constant bundle wall temperature and liquid at its fusion temperature.

Expressions for the amount of liquid displaced into or through the rod bundle before freezing shut in terms of injection pressure and bundle temperature have been derived. A primary feature of the analysis is the assumption that the rate of reduction of the mean hydraulic diameter of the bundle due to solidification is approximately equal to that of a parallel-plate channel having the same initial hydraulic diameter and temperature.

In the case of the solidification of water there is good agreement between theoretical and experimental results, but with organic liquids, namely n-pentadecane and p-xylene, the measured amount of liquid displaced is somewhat below the theoretical values. Uncertainty in estimating the physical properties due to the presence of dissolved gas and other impurities seems to account for a large portion of the discrepancy with the organic materials. Thus, in general, it can be concluded that the model presented is useful for estimating the extent of axial penetration of flowing liquids into very cold rod bundles before freezing shut.

Acknowledgment

This work was performed under the auspices of the U. S. Department of Energy.

References

1 Shibani, A. A., and Ozisik, M. N., "A Solution of Freezing of Liquids of Low Prandtl Number in Turbulent Flow Between Parallel Plates," ASME JOURNAL OF HEAT TRANSFER, Vol. 99, 1977, pp. 20–24.

2 Cheng, K. C., and Wong, S., "Asymmetric Solidification of Flowing Liquid in a Convectively Cooled Parallel-Plate Channel," *Applied Science Research,* Vol. 33, 1977, pp. 309–335.

3 Jongenelen, F. C. H., and Heertjes, P. M., "Crystallization on a Cooled Wall with Forced Convection in the Melt," *Chemical Engineering Science,* Vol. 33, 1978, pp. 55–63.

4 Zerkle, R. D., and Sunderland, J. E., "The Effect of Liquid Solidification in a Tube Upon the Laminar-Flow Heat Transfer and Pressure Drop," ASME JOURNAL OF HEAT TRANSFER, Vol. 90, 1968, pp. 183–190.

5 Depew, C. A., and Zenter, R. C., "Laminar Flow Heat Transfer and Pressure Drop with Freezing at the Wall," *International Journal of Heat Mass Transfer,* Vol. 12, 1969, pp. 1710–1714.

6 DesRuisscaux, N., and Zerkle, R. D., "Freezing of Hydraulic Systems," *Can. J. of Chem. Eng.*, Vol. 47, 1969, pp. 233–237.

7 Ozisik, M. N., and Mulligan, J. C., "Transient Freezing of Liquids in Forced Flow Inside Circular Tubes," ASME JOURNAL OF HEAT TRANSFER, Vol. 91, 1969, pp. 385–391.

8 Mulligan, J. C., and Jones, D. D., "Experiments on Heat Transfer and Pressure Drop in a Horizontal Tube with Internal Solidification," *International Journal of Heat and Mass Transfer,* Vol. 19, 1976, pp. 213–218.

9 Bilenas, J. A., and Jiji, L. M., "Variational Solution of Axisymmetric Fluid Flow in Tubes with Surface Solidification," *Journal of the Franklin Institute,* Vol. 289, 1970, pp. 265–279.

10 Martinez, E. P., and Beaubouef, R. T., "Transient Freezing in Laminar Tube Flow," *Canadian Journal of Chemical Engineering,* Vol. 50, 1972, pp. 445–449.

11 Chun, M. H., Gasser, R. D., Kazimi, M. S., Ginsberg, T., and Jones, Jr., O. C., "Dynamics of Solidification of Flowing Fluids with Applications to LMFBR Post-Accident Fuel Relocation," in *Proceedings of the International Meeting on Fast Reactor Safety and Related Physics,* Vol. IV, USERDA, Conf. No. 761001, Chicago, Oct. 1976, pp. 1808–1818.

12 Szekely, J. and DiNovo, S. T., "Thermal Criteria for Tundish Nozzle or Taphole Blockage," *Metallurgical Transactions,* Vol. 5, 1974, pp. 747–754.

13 Thomason, S. B., Mulligan, J. C., and Everhart, J., "The Effect of Internal Solidification and Pressure Drop in a Horizontal Tube," ASME JOURNAL OF HEAT TRANSFER, Vol. 100, 1978, pp. 387–394.

14 Cheung, F. B., and Baker, Jr. L., "Transient Freezing of Liquids in Tube Flow," *Nuclear Science Engineering,* Vol. 60, 1976, pp. 1–9.

15 Madejski, J., "Solidification in Flow Through Channels and Into Cavities," *International Journal of Heat Transfer,* Vol. 19, 1976, pp. 1351–1356.

16 Epstein, M., Yim, A., and Cheung, F. B., "Freezing-Controlled Penetration of a Saturated Liquid into a Cold Tube," ASME JOURNAL OF HEAT TRANSFER, Vol. 99, pp. 233–238.

17 Epstein, M., and Hauser, G. M., "Freezing of an Advancing Tube Flow," ASME JOURNAL OF HEAT TRANSFER, Vol. 99, 1977, pp. 687–689.

18 Epstein, M., and Hauser, G. M., "Solidification of a Liquid Penetrating into a Convectively Cooled Tube," *Letters in Heat and Mass Transfer,* Vol. 5, 1978, pp. 19–28.

19 Epstein, M., "Melting, Boiling and Freezing: The "Transition Phase" in Fast Reactor Safety Analysis," in *Symposium on the Thermal and Hydraulic Aspects of Nuclear Reactor Safety,* Vol. 2—*Liquid Metal Fast Breeder Reactors,* ASME Press, New York, 1977, pp. 171–193.

20 Epstein, M., Henry, R. E., Grolmes, M. A., Fauske, H. K., Goldfuss, G. T., Quinn, D. J., and Roth, R. L., "Analytical and Experimental Studies of Transient Fuel Freezing," in *Proceedings of the International Meeting on Fast Reactor Safety and Related Physics,* Vol. IV, USERDA Conf. No. 761001, Chicago, Oct. 1976, pp. 1788–1798.

21 Spencer, B. W., Roth, R. L., Goldfuss, G. T., and Henry, R. E., "Results of Fuel Freezing Tests with Simulated CRBR-Type Fuel Pins" *Transactions of the American Nuclear Society,* Vol. 30, 1978, p. 446.

22 Rohsenow, W. M., and Hartnett, J. P., eds. *Handbook of Heat Transfer,* McGraw Hill, New York, 1970, p. 64.

23 Carslaw, H. S., and Jaeger, J. C., *Conduction of Heat in Solids,* Oxford University Press, Second ed., 1959.

On the Minimum Film Boiling Conditions for Spherical Geometries

F. S. Gunnerson[1]
A. W. Cronenberg[2]

Dept of Chemical and Nuclear Engineering,
University of New Mexico,
Albuquerque, N.M.

An analytical method is presented for predicting the minimum heater temperature and the minimum heat flux at the onset of film boiling for spherical and flat plate heaters in saturated and subcooled liquids. Consideration is given to a variety of factors known to affect the minimum film boiling point, including transient liquid-heater contact, interfacial wettability, heater geometry, and liquid subcooling. The theoretical correlations developed are the first known predictions for spherical geometries. A comparison of theory with experimental data indicates good agreement for the minimum heat flux and the minimum film boiling temperature. Results indicate that the minimum conditions may span a wide range depending upon the thermophysical nature of the heater surface and the boiling liquid.

I Introduction

The wall superheat at the minimum heat flux is called the minimum film boiling temperature $\Delta T_{\min}$, and is defined by the expression

$$\Delta T_{\min} = (T_w - T_{\text{sat}})_{\min} = \frac{(Q/A)_{\min}}{h_t} \tag{1}$$

where $(Q/A)_{\min}$ is the total minimum heat flux and h_t the total heat transfer coefficient.

In this paper, a summary of the method for predicting $\Delta T_{\min}$ and $(Q/A)_{\min}$ for spherical and flat plate geometries is presented. The details of the method can be found in references [12] and [41]. The method uses, as its foundation, the relationship given by equation (1), where

$$(Q/A)_{\min} = \begin{bmatrix}\text{Energy}\\ \text{Transport}\\ \text{per Bubble}\end{bmatrix} \cdot \begin{bmatrix}\text{Heater Area}\\ \text{Producing}\\ \text{Bubbles}\end{bmatrix}^{-1} \cdot \begin{bmatrix}\text{Minimum}\\ \text{Frequency of}\\ \text{Bubble Release}\end{bmatrix} + \begin{bmatrix}\text{Heat Transferred}\\ \text{into Subcooled}\\ \text{Liquid per Unit}\\ \text{Area per Unit Time}\end{bmatrix} + \begin{bmatrix}\text{Heat Flux Due}\\ \text{to Transient,}\\ \text{Liquid-Heater}\\ \text{Contact}\end{bmatrix} \tag{2}$$

The first three terms represent the film boiling, no contact heat flux; the second major term is the subcooling contribution; and the final term is the liquid-heater contact contribution. Each term is geometry dependent, and utilizes the minimum frequency of vapor bubble release (determined from hydrodynamic, Taylor-instability considerations) as its minimizing parameter. The total heat transfer coefficient is likewise estimated via a contributory sum as

$$h_t = \left(\frac{h_{fb}\,\Delta T_{fb}}{\Delta T_{min}}\right)\Sigma_1 + \left(\frac{h_{\text{cont}}\,\Delta T_{\text{cont}}}{\Delta T_{\min}}\right)\Sigma_2 \tag{3}$$

where h_{fb} is the film boiling heat transfer coefficient which incorporates conduction, convection and radiation across the vapor gap with subcooling considerations, and h_{cont} the effective, transient liquid-heater contact heat transfer coefficient. ΔT_{fb} and ΔT_{cont} are the temperature variance over which each heat transfer process is considered. Weighting factors (Σ_1, Σ_2) are included to account for the spacial and time dependence of the heat transfer modes and are estimated from liquid-heater contact considerations.

II Model—General Considerations

It has been experimentally observed that the diameter of the departing vapor bubbles from large cylinders [4, 5] and flat plates [6, 7], and large spheres [9, 10] is proportional to a characteristic wavelength and may be approximated as:

$$\lambda_c/2 \le D_B \le \lambda_{MD}/2 \tag{4}$$

For small spheres, however [8–10] no large scale sinusoidal liquid-vapor interface, is observed. Figure 1 illustrates this behavior and the corresponding idealized models used here. The spherical geometries are categorized, according to size and vapor removal mechanisms as:

1 *Small Spheres.* single vapor column, where from hydrostatic considerations (buoyancy and surface tension force balance)

$$D_s \le 2\sqrt{3\beta} \tag{5}$$

2 *Intermediate Spheres.* single vapor dome, which, from hydrostatic and thermodynamic considerations [12][3]

$$2\sqrt{3\beta} < D_s < \frac{16\sqrt{\beta}}{3} \tag{6}$$

3 *Large Spheres.* multiple vapor domes (similar to a flat plate), where[4]

$$\frac{16\sqrt{\beta}}{3} \le D_s < 10\,\lambda_c \tag{7}$$

4 *Very Large Spheres = Flat Plate.* multiple vapor domes

$$D_s \ge 10\,\lambda_c \tag{8}$$

II-1 Vapor Bubble Size. For small spheres, the diameter of the released vapor bubbles (assumed spherical) is approximated via a bouyancy-surface tension force balance to yield:

$$D_B = \left(\frac{6\,D_S\sigma}{(\rho_L - \rho_V)g}\right)^{1/3} \tag{9}$$

For very large spheres (i.e., flat plates) the diameter is given by

---

[1] Present Address: EG&G Idaho, Inc., P. O. Box 1625, Idaho Falls, ID 83415.

Contributed by the Heat Transfer Division and presented at the 18th AIChE/ASME National Heat Transfer Conference, August 6–8, 1979, San Diego, Calif. Revised manuscript received by the Heat Transfer Division August 25, 1979. Paper No. 79-HT-45.

[2] Present address: Engineering Science and Analysis, 836 Claire View St., Idaho Falls, Id. 83401.

[3] The upper limit of the intermediate size sphere range is considered the sphere diameter at which multiple vapor domes appear. Its derivation is given by Hendricks and Baumeister [10].

[4] When the sphere diameter equals or exceeds ten times the liquid's critical wavelength a flat plate vapor removal mechanism is assumed. The choice of such a limit is arbitrary and has little effect on the final results.

equation (4), and for intermediate and large spheres the bubble diameter is approximated by the linear relationship

$$D_B = \frac{\lambda/2 - C\sqrt{\beta}}{10\,\lambda_c - 2\sqrt{3\beta}}\,(D_S - 2\sqrt{3\beta}) + C\sqrt{\beta} \qquad (10)$$

where $C = 6^{1/3}\,2^{1/3}\,3^{1/6} = 2.75$.

Figure 2 illustrates a comparison of bubble diameters, as determined from experiment [8, 9] and from theory (equations (4, 9) and (10)). As shown, theory compares favorably with experiment. The shaded area illustrates the magnitude of the bubble diameter uncertainty that occurs from using the hydrodynamic wavelength.

II-2 Transient Liquid-Heater Contact. Until recently, liquid-solid contact was assumed to exist into the film boiling region under most conditions, however, recent evidence [8, 19, 20] indicates that, for small spheres, such may not be the case. Figure 3 illustrates experimentally determined values of $\Delta T_{\min}$ for various spheres in water. In the region of small and intermediate spheres $\Delta T_{\min}$ decreases with increasing sphere diameter. Near large sphere (multiple vapor domes) diameters (equation (7)) $\Delta T_{\min}$ increases by an order of magnitude, indicating some highly influencing parameter, perhaps liquid-heater contact.

Based on experiment observations [8, 19, 20] and Fig. 2, it is assumed that *liquid-solid contact begins* when multiple vapor domes appear, that is, for large spheres and flat plates, and a single contact occurs at the release of each vapor bubble.

II-3 Area and Duration of Transient Liquid-Heater Contacts. The experimental work of Yao and Henry [18] indicates that the area and the duration of transient contacts decrease with increasing interfacial temperature T_I (see equation (13)) and span several orders of magnitude at any given value of T_I. For the purpose of this analysis (see references [12] or [41] for details), *the area of liquid-solid contact is approximated as*

$$A_c = \begin{cases} \dfrac{\pi}{4} D_B{}^2 & T_I \le T_{\text{sat}} \\ \dfrac{\pi}{4} D_B{}^2 \left(\dfrac{T_{\max,s} - T_I}{T_{\max,s} - T_{\text{sat}}}\right) & T_{\text{sat}} < T_I < T_{\max,s} \\ 0 & T_I \ge T_{\max,s} \\ 0 & \text{No wetting, all } T_I \end{cases} \qquad (11)$$

and the *period of transient, liquid-solid contact* as

$$t_c = \begin{cases} \infty & T_I \le T_{\text{sat}} \\ \le 1/2\, f_{\min} & T_{\text{sat}} < T_I < T_{\max,s} \\ 0 & T_I \ge T_{\max,s} \\ 0 & \text{No wetting, all } T_I \end{cases} \qquad (12)$$

where $f_{\min}$ is the frequency of bubble release (see Section III-3), and the contact interface temperature is given by:

$$T_I = \frac{T_w\,(k/\sqrt{\alpha})_w + T_L\,(k/\sqrt{\alpha})_L}{(k/\sqrt{\alpha})_w + (k/\sqrt{\alpha})_L} \qquad (13)$$

Table 1 compares the theoretically determined areas and durations of transient liquid-heater contact with those determined experimentally [18]. As indicated, experimental results generally bound the values determined from theory.

III Minimum Heat Flux, $(Q/A)_{\min}$

III-1 Energy Transport per Bubble. The thermal energy transported by each bubble is

$$\begin{pmatrix}\text{Energy Transport}\\ \text{per Bubble}\end{pmatrix} = \rho_V\,(h_{fg} + C_{PL}\,\Delta T_{SC} + C_{PV}\,\Delta T_{SH})\,\frac{\pi D_B{}^3}{6} \qquad (14)$$

III-2 [Heater Area Producing Bubble(s)]$^{-1}$. Based on experimental observations [6, 7], Zuber [2, 15] concluded that the distribution of vapor bubbles on a flat horizontal surface may be viewed as a square lattice, where the side of each element is equal to a chracteristic wavelength, and that the inverse heating area producing two bubbles is given by:

$$\left[\begin{matrix}\text{Heater Area}\\ \text{Producing}\\ \text{Bubble(s)}\end{matrix}\right]^{-1}_{\text{Plate}} = \frac{1}{\lambda^2} \qquad (15)$$

For small and intermediate size spheres, those with single points of bubble release, the entire spherical heater area should contribute to a single bubble per cycle. For large spheres, the flat plate expression, equation (15), should be approached as a sphere diameter becomes very large. Assuming the inverse heater area producing the bubble(s) cannot be less than that of a flat plate:

$$\left[\begin{matrix}\text{Heater Area}\\ \text{Producing}\\ \text{Bubble(s)}\end{matrix}\right]^{-1}_{\text{Spheres}} = \frac{1}{\pi D_s{}^2} + \frac{1}{\lambda^2} \qquad (16)$$

For small spheres, the first term of equation (16) dominates and for large spheres, the second term is dominant. As $D_S \to \infty$, equation (16) reduces to that of a flat plate, equation (15).

III-3 Frequency of Vapor Bubble Release. Theoretically, the frequency of bubble release is given by [11, 13]

Nomenclature

a = constant (= 1 for nonmetals, = 2 for liquid metals)
A_c = area of transient, liquid-heater contact
A_{LV} = liquid-vapor interfacial area
c = constant
C_p = heat capacity
D = diameter
f = frequency
Gr* = modified Grashof number,. $D^{3\rho}{}_V\,(\rho_L - \rho_V)\,g/\mu_V^2$
h = heat transfer coefficient
h_{fg} = latent heat of vaporization
k = thermal conductivity
Nu = Nusselt number
Pr* = modified Prandtl number, $\mu_V\,h_{fg}/k_V\,(T_w - T_{\text{sat}})$
Q = heat flow per area
Q/A = heat flux
Ra* = modified Rayleigh number = Gr*·Pr*
T = temperature
t = time
U = velocity
X = frequency parameter
α = thermal diffusivity
β = property parameter, $\sigma/g\,(\rho_L - \rho_V)$, or slip coefficient
ϵ = emmissivity
λ = wavelength
μ = viscosity
ρ = density
σ = surface tension
Σ = weighting factor
τ = period, f^{-1}
Φ = subcooling parameter, $\Delta T_{SC}/\Delta T$
ψ = thermal conductivity ratio, k_L/k_V

Subscripts

B = bubble
C = convection
cont = liquid-heater contact
fb = film boiling
I = interface
L = liquid
min = minimum
max,s = maximum, metastable superheat
MD = most dangerous
ML = microlayer
MP = melting point
r,R = radiative
S = sphere
SC = subcooling
SH = vapor superheat
sat = saturation
t = total
V = vapor or vapor dome
W = wall or heater

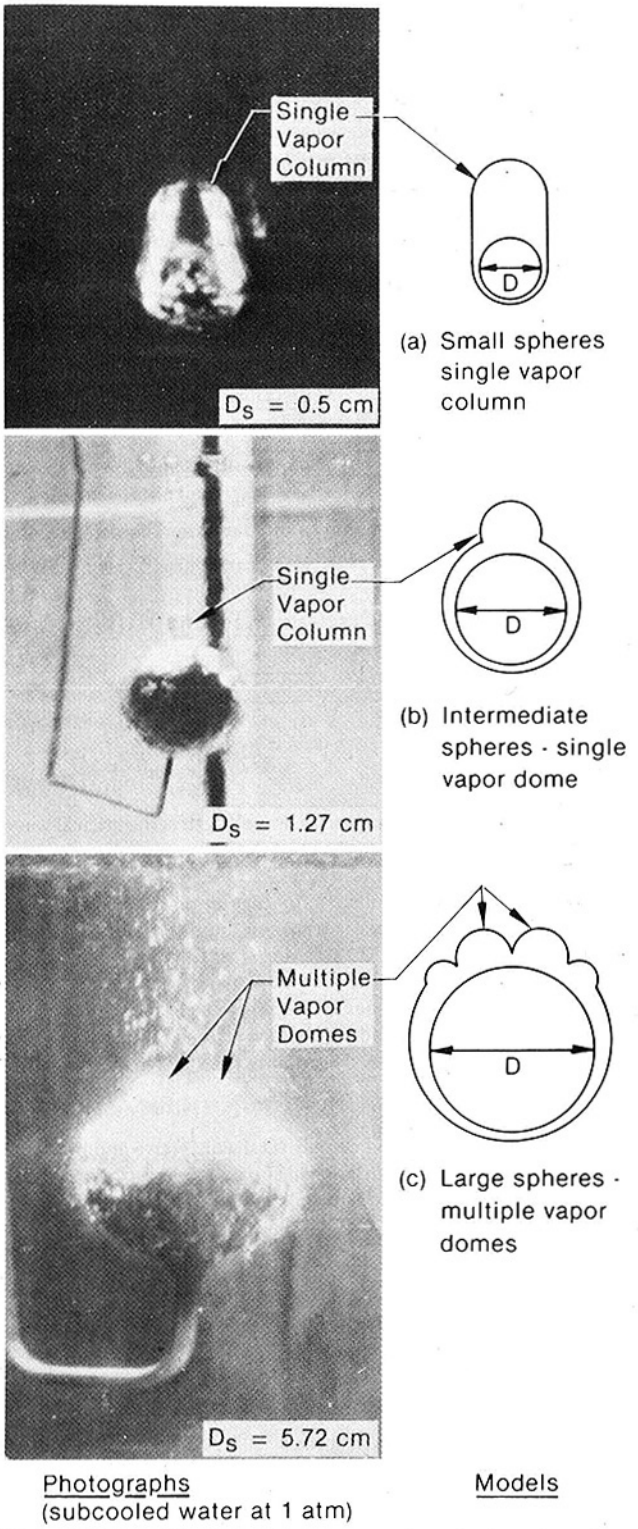

Fig. 1 Experimentally observed vapor removal mechanisms for spheres undergoing film boiling and corresponding idealized models

$$f = \frac{1}{t_w + t_g} \tag{17}$$

Jakob and Linke [14] experimentally observed that at low nucleate heat fluxes, $t_w \approx t_g$, and that

$$fD_B = C \tag{18}$$

It was also observed [14] that while the bubble continues to adhere to the interface its center of gravity rises with almost the same velocity

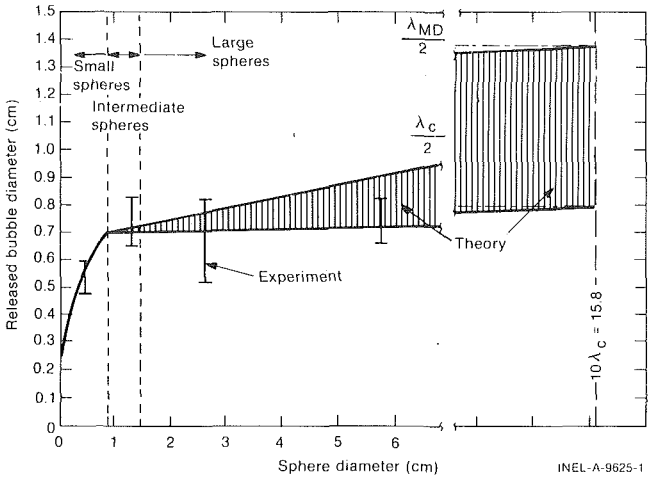

Fig. 2 Comparison of released bubble diameters versus sphere diameter as determined from theory and experiment for water at 1 atm

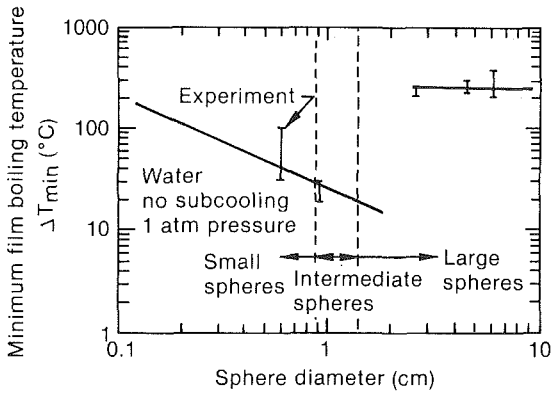

Fig. 3 Experimentally determined minimum film boiling temperatures for spherical heaters in saturated water

Table 1 Comparison of theory with experiment for area and duration of interfacial contact near minimum film boiling point

Fluid	Area of Contact (cm^2) Theory[a]	Area of Contact (cm^2) Experiment [18]	Contact Period (ms) Theory[b]	Contact Period (ms) Experiment [18]
Ethanol	0.114	0.017–8.58	0–31.2	10–100
Water	0.609	$1.1(10)^{-4}$–0.443	0–39.7	1–10

[a] From equation (11) at T_I = 145°C (ethanol), T_I = 220°C (water)
[b] From equation (12), T_I as above.

as that of the later departing bubble. This implies that

$$\frac{D_B}{t_g} \approx U \tag{19}$$

is approximately valid at low nucleate boiling heat fluxes, where U is the rise velocity of the departing bubble.

From a study of Taylor-instability theory, Lewis [16] concluded that the minimum vapor rise velocity occurs during the final growth stage of the instability, when vapor columns (bubbles) commence penetration into the liquid, and may be estimated as

$$U_{\min} = \frac{2}{3}\left(\frac{D_V g(\rho_L - \rho_V)}{2\rho_L}\right)^{1/2} \tag{20}$$

where D_V is the diameter of the bubble vertex. For small spheres, $D_V \approx D_S$ (Fig. 1). For very large spheres (flat plates), the penetrating diameter is not too different than the bubble, thus, $D_V \approx D_B$. For intermediate and large size spheres a combination of small to flat plate penetrating diameters is assumed,

$$D_V = \frac{\lambda/2 - 2\sqrt{3\beta}}{10\lambda_c - 2\sqrt{3\beta}}(D_s - 2\sqrt{3\beta}) + 2\sqrt{3\beta} \tag{21}$$

Large spheres and flat plates, which have multiple vapor domes, produce two bubbles per unit heater area in each oscillation (Section III-2). Therefore, the *minimum frequency of bubble release* is found by combining equations (17–20) to yield:

$$f_{\min} = \frac{1}{3D_B}\left(\frac{D_V\, g(\rho_L - \rho_V)}{2\rho_L}\right)^{1/2} X \tag{22}$$

where:

$$X = \begin{cases} 1 & \text{For small spheres} \\ \dfrac{D_s - 2\sqrt{3\beta}}{\dfrac{16\sqrt{\beta}}{3} - 2\sqrt{3\beta}} + 1 & \text{For intermediate spheres} \\ 2 & \text{For large spheres and flat plates} \end{cases}$$

As shown in Table 2, theory (equation (22)) compares favorably with experiment.

III-4 Subcooling Contribution. If the bulk liquid is subcooled, heat will be transferred from the liquid-vapor interface (assumed to be at T_{sat}) into the cooler liquid. Assuming: (1) the heat transfer may be modeled as a conduction process using a semi-infinite slab analysis, and (2) upon departure of the vapor bubbles, sufficient turbulence and intermixing occurs within the bulk liquid to reestablish the initial temperature profile, then the temperature profile in the liquid is:

$$T(x,t) = T_{sat} - \Delta T_{SC}\,\text{erf}\left(\frac{x}{2\sqrt{\alpha_L t}}\right) \tag{23}$$

The heat flow into the liquid during the period of bubble release may be estimated by integrating the temperature gradient (evaluated at $x = 0$) over the period of bubble release and multiplying by the time averaged liquid-vapor interfacial area ($\overline{A}_{LV}$) and the inverse unit heater area (equation (16)). The subcooling contribution to the minimum heat flux then becomes

$$(Q/A)_{SC} = \frac{2k_L\,\Delta T_{SC}\overline{A}_{LV}\sqrt{f_{\min}}}{\sqrt{\pi\alpha_L}}\left(\frac{1}{\pi {D_s}^2} + \frac{1}{\lambda^2}\right) \tag{24}$$

Figure 4 illustrates a method for estimating $\overline{A}_{LV}$ for a single bubble period. Assuming the vapor gap thickness to be much less than the sphere's diameter, the average interfacial area during the waiting period is minimum and given by: $A_{LV,\min} = [1/\pi {D_s}^2 + 1/\lambda^2]^{-1}$, where the first term ($1/\pi {D_s}^2$) dominates for small spheres, and the second term ($1/\lambda^2$) dominates for large spheres and flat plates.

Following the waiting period, the bubble(s) commences to grow. Assuming spherical bubble growth, the interfacial area during the growth period increases linearly. Thus,

$$\overline{A}_{LV} = \left[\frac{1}{\pi {D_S}^2} + \frac{1}{\lambda^2}\right]^{-1} + \frac{\pi {D^2}_{BH}}{8} \tag{25}$$

where $D_{BH} = 3^3\sqrt{2}\,D_B = 1.26\,D_B$.

III-5 Transient, Liquid-Heater Contact Contribution. If the sphere diameter obeys equations (7) or (8), then it is assumed (Section II-2) that the potential for liquid-heater contact exists.

Assuming that the contacting period is sufficiently short so that a semi-infinite slab analysis applies, the minimum additional heat flux required to thermally recover from a transient contact is estimated as

$$(Q/A)_{\text{cont}} = \frac{2\,k_L\,(T_I - T_L)\sqrt{t_c}\,A_c}{\sqrt{\pi\alpha_L}}\left(\frac{1}{\pi {D_s}^2} + \frac{1}{\lambda^2}\right) f_{\min} \tag{26}$$

Combining equations (2, 14, 16, 24) and (26) yields the following for the total *minimum heat flux for spherical and flat plate geometries:*

$$(Q/A)_{\min} = \rho_V\,(h_{fg} + C_{PL}\,\Delta T_{SC} + C_{PV}\,\Delta T_{SH})\frac{\pi {D_B}^3}{6}\left(\frac{1}{\pi {D_s}^2} + \frac{1}{\lambda^2}\right) f_{\min} + \frac{2\,k_L\,\Delta T_{SC}\,\overline{A}_{LV}\sqrt{f_{\min}}}{\sqrt{\pi\alpha_L}}\cdot\left(\frac{1}{\pi {D_s}^2} + \frac{1}{\lambda^2}\right) + \frac{2\,k_L(T_I - T_L)\sqrt{t_c}\,A_c\,f_{\min}}{\sqrt{\pi\alpha_L}}\left(\frac{1}{\pi {D_s}^2} + \frac{1}{\lambda^2}\right) \tag{27}$$

When the sphere diameter becomes very large, and liquid subcooling and vapor superheat effects are neglected, equation (27) reduces to that for *flat plates*:

$$(Q/A)_{\min} = \rho_V\,h_{fg}\frac{\pi}{24}\frac{\sqrt{2\pi}\,C}{3}\left(\frac{\sigma g(\rho_L - \rho_V)}{\rho_L^2}\right)^{1/2} + \frac{k_L\,(T_I - T_L)\,A_c}{3\sqrt{2}\pi^3 C^2}\sqrt{\frac{t_c}{\alpha_L\,\rho_L c}}\left(\frac{g(\rho_L - \rho_V)}{\sigma}\right)^2\left(\frac{\sigma^3}{g(\rho_L - \rho_V)}\right)^{1/4} \tag{28}$$

where $C = 1$ when the characteristic wavelength is the critical wavelength (λ_c) and $C = \sqrt{3}$ when the most dangerous wavelength (λ_{MD}) is employed. Equation (28) is identical to the well-known $(Q/A)_{\min}$ expression developed by Zuber [2, 15] for flat plates, except for the second term which accounts for transient, liquid-heater contact.

IV Total Heat Transfer Coefficient

IV-1 Small and Intermediate Spheres. For small and intermediate spheres, Farahat and El Halfawy [27] showed that the total heat transfer coefficient may be estimated as

$$[\text{Nu}_t - \psi\phi Nu_c]\,[\text{Nu}_c - Nu_r]^3 = \beta^*\text{Ra}^* \tag{29}$$

where the subscripts, t, c and r imply total, convective and radiative, respectively. The modified interfacial slip parameter, β^*, is assumed to be a function of the liquid subcooling and given by [12, 27]

$$\beta^* = (0.5625\,\beta)^{-1} \tag{30}$$

where

$$\beta = \begin{cases} 12 - \dfrac{18\,\Delta T_{SC}}{(T_{sat} - T_{MP})} & 0 \le \Delta T_{SC} \le \dfrac{T_{sat} - T_{MP}}{2} \\ 3 & \Delta T_{SC} > \dfrac{T_{sat} - T_{MP}}{2} \end{cases} \tag{31}$$

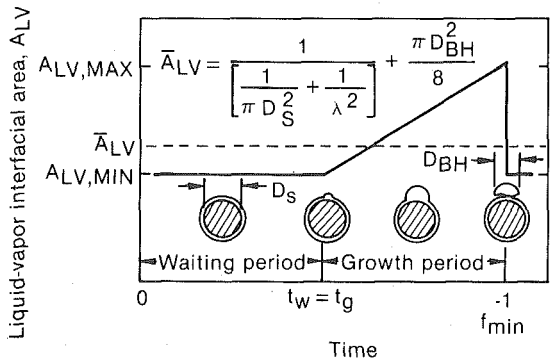

Fig. 4 Surface area of liquid-vapor interface during bubble lifetime

Table 2 Comparison of bubble release frequency near the minimum film boiling point (1 atm)

Geometry	Fluid	Frequency (s^{-1}) Theory (equation (22))	Experiment	
Sphere (2.54 cm)	Water	16.8–17.6	6.0–21.8	[9]
Sphere (5.7 cm)	Water	15.4–17.4	9.7–19.4	[9]
Plate	Water	12.7–16.7	10–20	[18]
Plate	Methanol	15.8–20.8	16.7	[7]

Note: As the sphere diameter becomes very large (i.e., flat plate), the frequency expression given by equation (22) reduces to that developed by Zuber [2] for a flat plate.

The solution of equation (29), therefore, provides h_t for small and intermediate size spheres.

IV-2 Large Spheres and Flat Plates. Table 3 illustrates experimentally determined heat transfer coefficients for large spheres and flat plates in saturated water near the minimum heat flux. As can be seen, the values for large spheres and flat plates are numerically similar, thus, *it is assumed that an analysis similar to that used for flat plates may also be applied to large spherical geometries.*

The total heat transfer coefficient is approximated by the relationship (which is similar to that used by references [1, 6] and [31]):

$$h_t = \frac{(Q/A)_{\min}}{\Delta T_{\min}} = \left(\frac{h_c\,\Delta T_c}{\Delta T_{\min}} + \frac{h_r\,\Delta T_R}{\Delta T_{\min}} + \frac{h_{SC}\,\Delta T_{SC}}{\Delta T_{\min}}\right)\Sigma_1 + \left(\frac{h_{\text{cont}}\,\Delta T_{\text{cont}}}{\Delta T_{\min}}\right)\Sigma_2 \quad (32)$$

where the weighing factors (Σ_1, Σ_2) account for the spacial and time dependence of the heat transfer modes, and given by

$$\Sigma_1 = 1 - \left(\frac{\text{contact area}}{\text{unit heater area}}\right)\left(\frac{\text{contact time}}{\text{period of bubble release}}\right) = 1 - A_c\left(\frac{1}{\pi {D_s}^2} + \frac{1}{\lambda^2}\right) t_c\, f_{\min} \quad (33)$$

and $\Sigma_2 = 1 - \Sigma_1$.

The heat transfer coefficients for each mode of heat loss are considered separately as follows:

1 Based on the work of references [1] and [31], the *convection coefficient*, h_c is given by

$$\text{Nu}_c = C\,(\text{Gr}^*\,\text{Pr}^{*a})^{1/4} \quad (34)$$

where $a = 1$ for nonmetals, $a = 2$ for liquid metals and $C = 0.41$.

2 Assuming a shape factor of unity for two concentric spheres, the *radiative coefficient*, h_r becomes

$$h_r = \frac{\sigma_{SB}}{\dfrac{1}{\epsilon_W} + \dfrac{1}{\epsilon_L} - 1}\left(\frac{{T_W}^4 - {T_{\text{sat}}}^4}{T_W - T_{\text{sat}}}\right) \quad (35)$$

3 The contribution due to subcooling is given by equation (24), therefore, the effective heat transfer coefficient for subcooling heat loss, h_{SC} is given by

$$h_{SC} = \frac{(Q/A)_{SC}}{\Delta T_{SC}} = \frac{2k_L\,\overline{A}_{LV}\sqrt{f_{\min}}}{\sqrt{\pi\alpha_L}}\left(\frac{1}{\pi {D_s}^2} + \frac{1}{\lambda^2}\right) \quad (36)$$

4 For transient liquid-heater contact equation (26) is used, and the liquid-heater conduction coefficient, h_{cont} is expressed as

$$h_{\text{cont}} = \frac{(\text{Q/A})_{\text{cont}}}{\Delta T_{LS}} = \frac{2k_L\,(T_I - T_L)\sqrt{t_c}A_c}{\sqrt{\pi\alpha_L}\,(T_I - T_L)}\left(\frac{1}{\pi {D_s}^2} + \frac{1}{\lambda^2}\right) f_{\min} \quad (37)$$

Combining equations (32–37) yields the following for the *total heat transfer coefficient, h_t, for large spheres and flat plates:*

$$h_t = \left\{\frac{0.41\,k_V}{\sqrt{\sigma/g(\rho_L - \rho_V)}}\left(\frac{(\sigma/g\,(\rho_L - \rho_V))^{3/2}\,\rho_V(\rho_L - \rho_V)g}{\mu_V^2}\cdot\left(\frac{\mu_v h_{fg}^*}{k_V\,(T_W - T_{\text{sat}})}\right)^a\right)^{1/4} + \frac{\sigma_{SB}}{\dfrac{1}{\epsilon_L} + \dfrac{1}{\epsilon_w} - 1}\left(\frac{{T_W}^4 - {T_{\text{sat}}}^4}{T_W - T_{\text{sat}}}\right) + \frac{2k_L\,\Delta T_{SC}\,\overline{A}_{LV}\sqrt{f_{\min}}}{\sqrt{\pi\alpha_L}\,(T_W - T_{\text{sat}})}\left(\frac{1}{\pi {D_s}^2} + \frac{1}{\lambda^2}\right)\right\}\Sigma_1 + \left\{\frac{2k_L\,(T_I - T_L)\sqrt{t_c}\,A_c}{\sqrt{\pi\alpha_L}\,(T_W - T_{\text{sat}})}\left(\frac{1}{\pi {D_s}^2} + \frac{1}{\lambda^2}\right) f_{\min}\right\}\Sigma_2 \quad (38)$$

Table 3 Total film boiling heat transfer coefficients for saturated water near the minimum heat flux (1 atm)

Geometry	Liquid–Solid	h_t (cal/cm^2 · s · °C) Experimental*	
Sphere (2.54 cm)	H_2O–S.S.	1.2–4.5 $(10)^{-3}$	(26)
Sphere (4.50 cm)	H_2O–S.S.	6.9–10.2 $(10)^{-3}$	(28)
Plate	H_2O–S.S.	4.1–4.77 $(10)^{-3}$	(18)
Plate	H_2O–AL	4.2–4.8 $(10)^{-3}$	(30)

* $h_t = (Q/A)_t/\Delta T$

V Minimum Film Boiling Temperature

Knowing $(Q/A)_{\min}$ and h_t, the solution to equation (1) is obtained, where $(Q/A)_{\min}$ is given by equation (27) for all size spherical and flat plate geometries and h_t is given by equation (29) for small and intermediate size spheres or equation (38) for large spheres and flat plates.

Equation (1) is transcendental in nature, that is, both $(Q/A)_{\min}$ and h_t are functions of $\Delta T_{\min}$. In addition, $(Q/A)_{\min}$, h_t, and $\Delta T_{\min}$ span a range of values due to the uncertainty inherent in the hydrodynamic wavelength ($\lambda_c \le \lambda \le \lambda_{MD}$) and transient, interfacial wettability. As a result, the minimum point parameters are given as a range of values where the upper limit stems from using the maximum wavelength (λ_{MD}) with complete interfacial wetting, and the lower limit of the minimum point parameters stems from using the minimum wavelength (λ_c) with a no-wetting condition.

VI Comparison of Theory and Experiment

Figures 5 and 6 show close correspondence of theory and experiment for $(Q/A)_{\min}$ and $\Delta T_{\min}$ for copper spheres in saturated liquid nitrogen. The shaped regions illustrate the uncertainty inherent in hydrodynamic wavelength. The general trend is decrease in minimum point parameters with increase in sphere diameter. The effects of transient contact are minimal since $k_L/k_w \ll 1$.

Figure 7 illustrates the general trend of increase $(Q/A)_{\min}$ for increase in water subcooling and stainless spheres. Uncertainty in theory stems from hydrodynamic wavelength and assumed interfacial wettability.

Figure 8 shows diameter dependence of $\Delta T_{\min}$ for stainless spheres (0.635 and 0.904 cm sphere data for nickel and aluminum, respectively) in saturated water, and large sphere data for highly modified spherical geometries, i.e., large or multiple thermocouple support probes. Since vapor removal mechanisms for large spheres and flat plates are similar (multiple vapor domes), $\Delta T_{\min}$ values are not strongly diameter dependent in these regions.

Figure 9 shows approximately linear dependence of $(Q/A)_{\min}$ for tantalum sphere in subcooled liquid sodium. Transient contact and interfacial wettability effects are highly influential.

VII Summary and Conclusions

The first known theoretical correlation for quantitatively assessing $\Delta T_{\min}$ and $(Q/A)_{\min}$ for spherical geometries was developed. Incorporated within the development are a variety of factors known to influence $\Delta T_{\min}$. One such factor, transient, liquid-heater contact, a phenomenon known to exist well into the film boiling region under most experimental conditions, but never before quantified, was assessed. It was shown that transient, liquid-heater contact would most likely occur for large sphere and flat plate geometries where the vapor removal mechanism is characterized by multiple vapor domes, and that such contacts may occur at the release of each vapor bubble. The quenching effect of transient contact on $(Q/A)_{min}$ for well-wetting and no-wetting situations was assessed from a single-dimension, heat conduction analysis. Results indicate that for film boiling of high thermal conductivity liquids, such as liquid metals, the heat transferred during the contact periods is a major fraction of the total heat transferred. In contrast, for film boiling of liquids with low thermal conductivities, such as certain cryogenic fluids, the heat transfer due to transient contacts is minimal, and may be neglected.

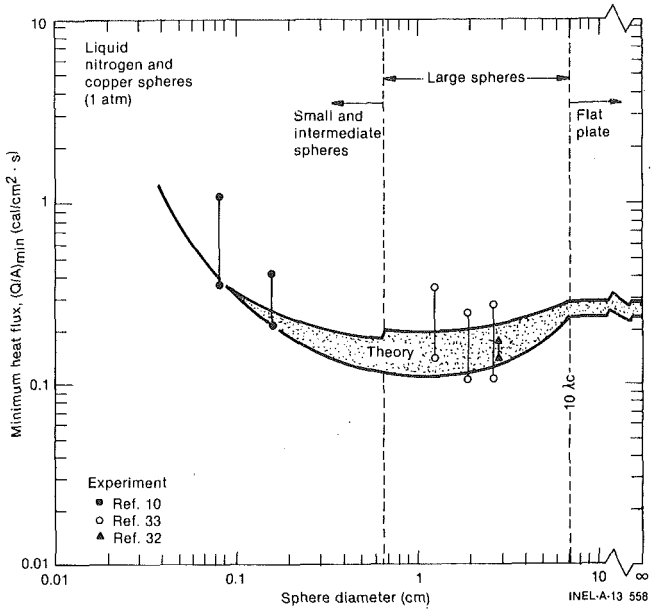

Fig. 5 Comparison of theory with experiment for $(Q/A)_{min}$ for spheres in saturated liquid nitrogen

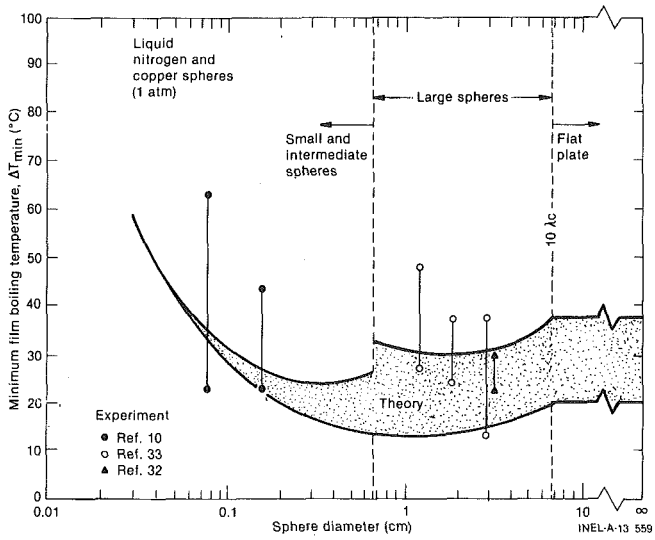

Fig. 6 Comparison of theory with experiment for ΔT_{min} in saturated liquid nitrogen for small spheres

The effects of liquid subcooling on $(Q/A)_{min}$ and ΔT_{min} were assessed as a single-dimension heat conduction process, where heat is transferred from the liquid-vapor interface (considered to be at a saturation temperature) into the cooler bulk liquid. Comparison of theory with experimental data at various liquid subcoolings indicates good agreement.

An application of these results to an important question relating to nuclear reactor safety, namely an assessment of the film boiling conditions considered necessary for initiation of energetic fuel-coolant interactions, is presented in reference [42].

References

1 Berenson, P. J., "Transition Boiling Heat Transfer from a Horizontal Surface," Technical Report No. 17, Massachusetts Institute of Technology, Cambridge, Mass., Mar. 1, 1960.

2 Zuber, N., "Hydrodynamic Aspects of Boiling Heat Transfer," Ph.D. Thesis, University of California at Los Angeles, June 1959.

3 Baumeister, K. J. and Simon, F. F., "Leidenfrost Temperature Its Correlation for Liquid Metals, Cryogens, Hydrocarbons and Water," ASME JOURNAL OF HEAT TRANSFER, May 1973, pp. 166–173.

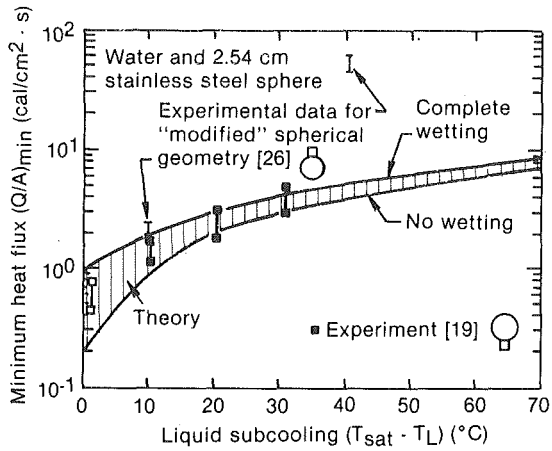

Fig. 7 Comparison of theory with experiment for $(Q/A)_{min}$ versus liquid subcooling for 2.54 cm stainless steel spheres in saturated and subcooled water (1 atm)

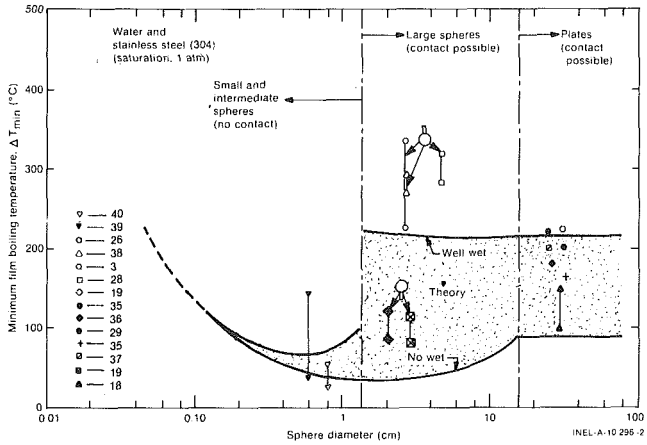

Fig. 8 ΔT_{min} as a function of sphere diameter for stainless steel spheres in saturated water

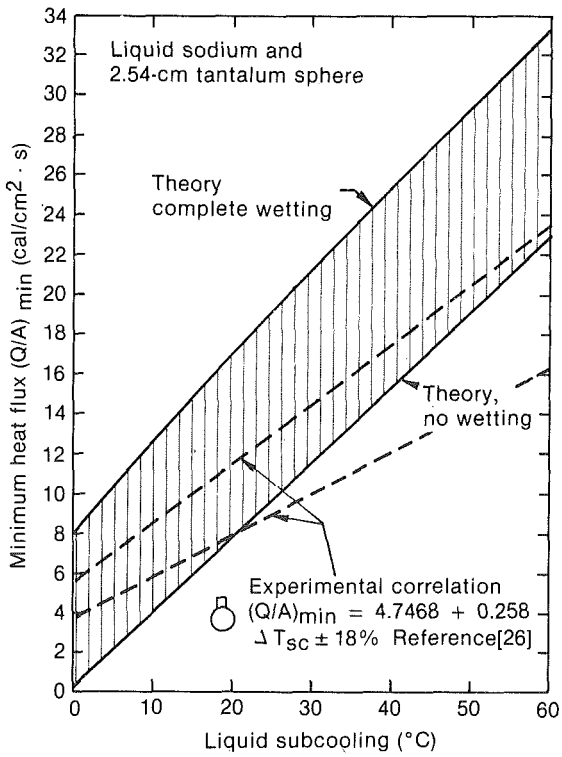

Fig. 9 $(Q/A)_{min}$ versus liquid subcooling for sodium and 2.54 cm tantalum sphere

4 Bromley, L., "Heat Transfer in Stable Film Boiling," *Chemical Engineering Progress,* Vol. 46, 1950, pp. 221.

5 Lienhard, J. H. and Wong, P. T. Y., "The Dominant Unstable Wavelength and Minimum Heat Flux During Film Boiling on a Horizontal Cylinder," ASME JOURNAL OF HEAT TRANSFER, Vol. 86, No. 2, 1964, pp. 220–226.

6 Chang, Y. P., "Wave Theory of Heat Transfer in Film Boiling," ASME JOURNAL OF HEAT TRANSFER, Feb. 1959, pp. 1–12.

7 Westwater, J. W. and Santangelo, J. G., "Photographic Study of Boiling," *Industrial Engineering Chemistry,* Vol. 47, 1955, pp. 1605.

8 Frohlich, G. and Osswald, H., "Aufbau und Abbau des Leidenfrost-Phanomens in Wasser an Kugelformigen Flachen mit und ohne Storstellen," Bericht Nr. 2–15, Institut fur Kernenergetik (IKE), Universitat Stuttgart, Stuttgart, West Germany, June 1975.

9 Gunnerson, F. S., "Photographic Study of Film-Transition Boiling on Spheres in Water," unpublished results, University of New Mexico, Feb. 1977.

10 Hendricks, R. C. and Baumeister, K. J., "Film boiling from Submerged Spheres," NASA TN D-5124, Washington, D.C., June 1969.

11 Hsu, Y. Y. and Grahm, R. W., *Transport Processes in Boiling and Two-Phase Systems,* McGraw-Hill, New York, 1976.

12 Gunnerson, F. S., "Film Boiling Destabilization from Hydrodynamic and Thermodynamic Considerations," Ph.D. Thesis, University of New Mexico, Albuquerque, NM, 1979.

13 Tong, L. S., *"Boiling Heat Transfer and Two-Phase Flow,"* Robert E. Krieger Publishing Company, Huntington, New York, 1975.

14 Jakob, M. and Linke, W., "Der Warmeubergang von einer Waagerechten Platte and Siedenes Wasser," *Forschung,* 4 Bd., Heft 2, 1933, pp. 75.

15 Zuber, N., "On the Stability of Boiling Heat Transfer," ASME JOURNAL OF HEAT TRANSFER, Vol. 80, 1958, p. 711.

16 Lewis, D. J., "The Instability of Liquid Surfaces When Accelerated in a Direction Perpendicular to their Planes II," *Proceedings of the Royal Society of London,* London, England, A-202, 1950, pp. 81.

17 Farrar, L. C. and Marshall, E., "Film Boiling in a Scaling Liquid," ASME JOURNAL OF HEAT TRANSFER, May 1976, pp. 173–177.

18 Yao, S. and Henry, R. E., "An Investigation of the Minimum Film Boiling Temperature on Horizontal Surfaces," ASME JOURNAL OF HEAT TRANSFER, Vol. 100, May 1978, pp. 260–267.

19 Dhir, V. K. and Purohit, G. P., "Subcooled Film-Boiling Heat Transfer from Spheres," ASME Paper No. 77-HT-78, presented at AIChE-ASME Heat Transfer Conference, Salt Lake City, Utah, Aug. 15–17, 1977.

20 Benz, R., Private communication, based on experimental results for film boiling from spheres in water, IKE-University of Stuttgart, West Germany, Nov. 1977.

21 Gunnerson, F. S. and Cronenberg, A. W., "On the Thermodynamic Superheat Limit for Liquid Metals and Its Relation to the Leidenfrost Temperature," ASME JOURNAL OF HEAT TRANSFER, Vol. 100, Nov. 1978, pp. 734–737.

22 Baumeister, K. J., Hendricks, R. C. and Hamill, T. D., "Metastable Leidenfrost States," NASA TN D-3226, 1966.

23 Carslaw, H. S. and Jaeger, J. C. *Conduction of Heat in Solids,* Oxford Press, 2nd ed. 1959.

24 Moore, F. D. and Mesler, R. B., "The Measurement of Rapid Temperature Fluctuations During Nucleate Boiling of Water," *AIChE Journal,* Vol. 7, No. 4, Dec. 1961, pp. 620–624.

25 Olander, R. R. and Watts, R. G., "An Analytical Expression of Microlayer Thickness in Nucleate Boiling," ASME JOURNAL OF HEAT TRANSFER, Feb. 1969, pp. 178–180.

26 Farahat, M. M., "Transient Boiling Heat Transfer from Spheres to Sodium," PhD Thesis Northwestern University, Evanston, Ill., 1971, ANL-7909.

27 Farahat, M. M. and El Halfawy, F. Z., "Film Boiling Heat Transfer from Spherical Particles to Subcooled Liquids," *Atomkernenergie* (ATKE), Bd. 26, Lfg. 4, 1975, pp. 235–241.

28 Lauer, H. and Hufschmidt, W., "Heat Transfer and Surface Rewet During Quenching," NATO Two-Phase Flow and Heat Transfer Conference, Istanbul, Turkey, August 16–27, 1976.

29 Tamura, Z. and Tanasawa, Y., "Evaporation and Combustion of a Drop in Contact with a Hot Surface," 7th International Symposium on Combustion, Butterworths, London, 1959, pp. 509–522.

30 Hosler, E. R. and Westwater, J. W., "Film Boiling on a Horizontal Plate," *ARS Journal,* Vol. 32, No. 4, Apr. 1962, pp. 553–558.

31 Hamill, T. D. and Baumeister, "Film Boiling Heat Transfer froma Horizontal Surface as an Optimal Boundary Value Process," *Proceedings of the 3rd International Heat Transfer Conference,* Vol, 4, 19066, pp. 59–64.

32 Merte, H. and Clark, J. A., "Boiling Heat Transfer with Cryogenic Fluids at Standard, Fractional, and Near Zero Gavity," ASME JOURNAL OF HEAT TRANSFER, Vol. 86, 1964, pp. 351–359.

33 Rhea, L. G. and Nevins, R. G., "Film Boiling Heat Transfer from an Oscillating Sphere," ASME JOURNAL OF HEAT TRANSFER, May 1969, pp. 267–272.

34 Farahat, M. M., Armstrong, D. R. and Eggen, D. T., "Transient Heat Transfer Between Hot Metal Spheres and Subcooled Water, *Atomkernenergie* (ATKE), Bd. 29, Lfg. 1. 1977, pp 17–22.

35 Godliski, E. S. and Bell, K. J., "The Leidenfrost Phenomenon for Binary Liquid Solutions," *Proceedings of the Third International Heat Transfer Conference,* Vol. 4, AIChE, New York, New York, 1966, pp. 51–58.

36 Gottfried, B. S., Lee, C. J. and Bell, K. J., "The Leidenfrost Phenomena: Film Boiling of Liquid Droplets on a Flate Plate," *International Journal of Heat and Mass Transfer,* Vol. 9, Nov. 1966, pp. 1167–1187.

37 Patel, B. M. and Bell, K. J., "The Leidenfrost Phenomenon for Extended Liquid Masses," *Chemical Engineering Progress Symposium Series,* Vol. 62, No. 64, 1966, pp. 62–71.

38 Farahat, M. M., Armstrong, D. R. and Eggen, D. T., "Pool Boiling in Subcooled Sodium at Atmospheric Pressure," *Nuclear Science and Engineering,* 1974, pp. 240–253.

39 Walford, F. J., "Transient Heat Transfer from a Hot Nickel Sphere Moving Through Water," *International Journal Heat and Mass Transfer,* Vol. 12, 1969, pp. 1621–1625.

40 Witte, L. C. and Henningson, P. J., "Identification of Boiling Regimes with Reaction-Force Apparatus," *Journal of Scientific Instruments* (Journal of Physics E), Series 2, Vol. 2, 1969, pp. 1101–1103.

41 Gunnerson, F. S. and Cronenberg,A. W., "A Prediction of the Minimum Film Boiling Conditions for Spherical and Horizontal Flat Plate Heaters," ASME Paper No. 79-HT-45, 1979.

42 Gunnerson, F. S., and Cronenberg, A. W., "Film Boiling and Vapor Explosion Phenomena," to be published in *Nuclear Technology,* Aug. 1980.

An Experimental Study of Falling Liquid Film Breakdown on a Horizontal Cylinder During Heat Transfer

E. N. Ganic
Asst. Professor of Heat Transfer.

M. N. Roppo
Research Assistant.

Department of Energy Engineering,
University of Illinois at Chicago Circle,
Chicago, IL 60680

In this study, an experimental investigation was conducted with subcooled water film flowing over an electrically heated horizontal cylinder. The combinations of film flow rate and heat flux at which film breakdown occurs (i.e., dry patches appear on the surface) were determined. At the conditions prior to dry patch formation, the heat transfer coefficient was determined as well. The results showed that the heat flux needed to cause a dry patch increases with film flow rate. Also, prior to dry patch formation, the heat transfer coefficient increases with film flow rate. The effects of the tube spacing and the liquid film inlet temperature on the breakdown heat flux and heat transfer coefficient were also studied.

1 Introduction

When a liquid is distributed uniformly on the outside of a horizontal tube, it flows in layer form around the periphery and falls off the bottom. In this case we have a gravity-driven liquid layer or falling film. Falling liquid films have long been used in the heat transfer industry and in some chemical engineering operations. They are characterized by high heat transfer rates at low flow rates and temperature differences.

When the flow rate of a thin film running over a heated surface is very low and/or the surface is very hot, the liquid film breaks down. That is, dry patches form on the surface. These dry patches can be rewetted by upstream disturbances at low heat fluxes, but at higher heat fluxes the dry areas eventually persist. This results in an abrupt decrease in the heat transfer coefficient, and it may also cause overheating of the surface.

One of the main difficulties encountered in designing falling-film heat exchangers is maintaining the complete wettability of the tubes. The minimum wetting rate (i.e., the minimum liquid flow rate required to wet the tube surface at a given local heat flux) should be known in order to determine the minimum liquid recycling ratio. This is especially important in the case of heat exchangers like those used for solar energy application. Such exchangers require very large heat transfer areas to compensate for the low ΔT's, and the pumping power needed to recycle the liquid affects the efficiency and feasibility of these systems.

Experimental data for the liquid film breakdown on horizontal tubes do not exist in the open literature. On the other hand, experimental investigations of film breakdown on vertical tubes have been conducted and the results reported in [1–5]. Since the wetting flow rates depend very much on the method of introducing the liquid film on the wall, the data for horizontal and vertical tubes will not be the same.

Falling-film breakdown on an adiabatic vertical surface and subsequent rewetting of the dry patch were studied initially by Hartley and Murgatroyd [6], who investigated the equilibrium of forces acting at the upstream stagnation point of the dry patch. The force balance included the inertial force due to bringing the upstream liquid to rest at the stagnation point, and the surface tension force due to a nonzero contact angle between the liquid and solid surface. By solving the force balance equation, the undisturbed film thickness (film thickness upstream of the dry patch) was obtained with the contact angle as a parameter. This work has been improved by many researchers who included the gravitational body force, the thermocapillary force (a force resulting from the variation of surface tension with temperature), the wall shear force, the vapor thrust if there is evaporation at the film interface, and the interfacial shear force [2, 5, 7].

A second model, also reported in [6], was based on the assumption that a stable film configuration corresponds to a minimum power transmission by the film in the form of kinetic and surface energy. A substantial improvement of this criterion was made in [8].

A third approach employed in the film breakdown studies is classified as the small perturbation theory model and is summarized in [5].

In spite of a large number of published studies, until more experimental data on dry patches and the contact angle at the dry patch conditions are obtained, the precise nature of film breakdown and its prediction will remain largely unexplored [4, 5, 8]. This is especially true for the situation in which films are undergoing heat transfer [9].

Most previous work on heat transfer to falling films has been concerned with evaporating films as summarized in [10]. Studies of heat transfer to subcooled liquid films have been reported in [11–15]. However, experimental investigations of the heat transfer coefficient have not been specifically conducted at subcooled film flow rates in the close vicinity of the minimum wetting rates.

In the present investigation, a systematic study of falling-film breakdown on a heated horizontal tube was undertaken. Data on the heat transfer coefficient prior to film breakdown were also obtained. The tube spacing and the film inlet temperature were parameters. The liquid film flow rates in this study were much smaller than those reported in similar studies.

2 The Experiments

2.1 Experimental Apparatus. The apparatus used in this investigation is shown in Fig. 1. The test fluid (distilled water) is heated to a constant temperature in reservoir 1 and delivered by pump 2 to overhead reservoir 3 (head tank) located six feet above the ground. This reservoir, equipped with two overflow systems, assures a constant potential head and is open to the atmosphere. All plumbing employs copper tubing of 12.7 mm o.d. These tubes are heavily insulated, as are all other metal surfaces where conduction losses could be significant. The delivery tube to reservoir 3 is wrapped with a heating tape capable of delivering an additional 1100 W to the flow. From reservoir 3, the flow is directed to horizontal spray tube 7 by means of needle valve 6. Leaving valve 6, the flow passes through a flexible rubber tube, capable of withstanding high fluid temperatures, to the inlet section of the horizontal spray tube. The inlet section is a diverging nozzle

Contributed by the Heat Transfer Division for publication in the JOURNAL OF HEAT TRANSFER. Manuscript received by the Heat Transfer Division August 10, 1979.

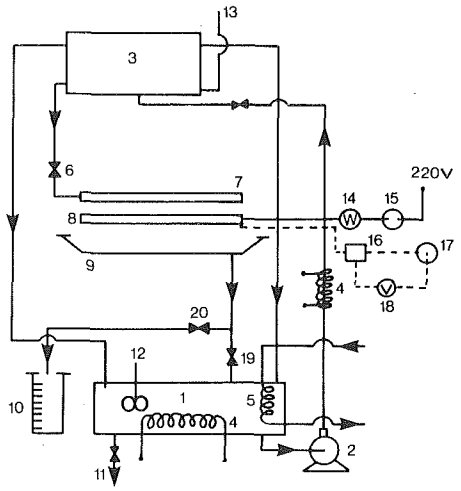

1.CONST.TEMP.RESERVOIR; 2.PUMP; 3.HEAD TENK; 4.HEATER 5.TAP WATER COOLER; 6.NEEDLE VALVE; 7.SPRAYTUBE; 8.TEST SECTION 9.RESERVOIR; 10.MEASURING FLASK; 11.DRAIN; 12.MIXER; 13.SIGHT LEVEL; 14.WATTMETER; 15.INPUT POWER REGULATOR; 16. THERMOCOUPLE SWITCH; 17.THERMOCOUPLE REFERENCE JUNCTION; 18.DIGITAL VOLTMETER 19., 20., VALVE

Fig. 1 Schematic of test loop

that provides a transition from the small-diameter rubber tube to the spray tube. The total length of the spray tube is 343mm; its inner diameter is 19.05mm. The fluid from inside the tube exits through a series of 1.6mm holes drilled 3.18mm apart along the length of the top of the tube. The exiting flow clings to the outside of the tube and is directed around its circumference to the bottom by means of a series of 3.18mm grooves, one draining each hole. The axial communication of the fluid from neighboring holes is restricted by the grooves.

The design and performance of the spray tube described above were studied in [16]. For all flow rates tested, there was a proper balance among (1) the kinetic energy and momentum force of the inlet flow, (2) the friction losses along the length of the tube, and (3) the pressure drop across the outlet holes; therefore, uniform flow distribution along the tube length is achieved.

The horizontal test section consists of a smooth cooper tube that is 343mm long with a 25.4mm o.d. and a 19.05mm i.d. It is electrically heated over 304.8mm of its length, by means of a cartridge heater capable of delivering up to 2000 W. The test section is clearly marked at each end by 1.6mm-deep grooves running circumferentially. These grooves prevent the liquid from flowing beyond the ends of the test section. The test section surface temperature is measured by means of thermocouples imbedded beneath the surface at 90 deg intervals around its circumference. Additional thermocouple readings are obtained at 45 deg locations by rotating the test section, which is mounted in insulated brass sleeves at each end. The spray tube has a similar alignment system.

The fluid falling on the test section flows around its circumference and is collected in reservoir 9. From reservoir 9 the flow is directed through valve 19 to constant-temperature reservoir 1, completing the cycle. By means of valve 20, the flow can also be directed to graduated cylinder 10 to measure the flow rate. Since the flow rates studied were very small, no accurate measurements were possible with available flow meters.

2.2 Experimental Procedure. Prior to running the fluid through the loop, the test section was thoroughly cleaned with detergent, rinsed, dried, and wiped with methyl alcohol. After a long period of exposure to the atmosphere, the test surface was thoroughly cleaned with very fine steel wool and the above procedure repeated. When the cleaning was completed, the test fluid was run through the system for several hours to allow it to wet the surface and achieve a steady state. The inlet temperature of the fluid was set in reservoir 1, and for the specific flow rate the power to the test section was gradually set to the desired value via voltage regulator 15. Steady-state heat transfer was signalized by steady thermocouple readings over a prolonged period of time.

For the film breakdown experiments, power to the test section was increased step-by-step until dry patches were visually observed. The power was then noted and the flow directed to graduate cylinder 10 for measurement.

3 Results and Discussion

3.1 Flow Regimes. The flow from the spray tube falls on the test section in the form of columns or droplets. At lower flow rates the droplet regime prevails (Fig. 2). At higher flow rates columns are present (Fig. 3). The transition from one flow regime to the other occurs over relatively large range of Γ. From the high-speed pictures of the flow regimes it was concluded that the droplet regime can exist within what appears to be the column regime to the human eye. At higher tube spacing values, the columns change to droplets (compare Figs. 3 and 4). The grooves on the spray tube do not appear to affect the column spacing, λ, since the same spacing was observed between the columns leaving the test tube (Fig. 3). The same is true for the droplet regime (Fig. 2). The values for λ were not affected by the flow rate or tube spacing, and they were generally below the value for λ given by the well-known Taylor wave length [17]. More recent study of λ was reported in reference [18].

As shown in Fig. 5, the film surface along the length of the horizontal test tube is wavy; it is essentially a series of crests and valleys. The valleys are positioned directly beneath the columns, and the overlapping waves from the impinging liquid form crests between adjacent columns (Fig. 5). The velocity profile within the film flowing around the tube circumference is essentially two-dimensional due to the presence of crests and valleys. By dropping a very small piece of styrofoam in the flow, it was noted that the falling-film velocity in the crest is much higher than the velocity in the valley. Visual observation also indicated that as the heat flux is increased the crests become more pronounced, since thinning of the film in the valleys occurs.

3.2 Film Breakdown. For the film breakdown measurements, after the preoperating procedure was completed the flow rate was set, steady state achieved, and the flow rate measured. Heat flux to the test section was increased in small steps (a steady state was achieved between steps) until dry patches were visually observed on the tube surface. (This point is the lowest part of the banded data; e.g., point A in Fig. 7.) After a certain period of time, dry patches that did not rewet themselves were manually rewetted. The heat flux was again increased until the next dry patch (or patches) appeared. When manually rewetted dry spots continued to reform over a period of time, a permanent dry patch was defined (the upper limit of the

Nomenclature

h = local heat transfer coefficient, W/m^2 °C
$\bar{h}$ = average heat transfer coefficient, W/m^2 °C
$\bar{h}^*$ = dimensionless heat transfer coefficient, $\bar{h}(\nu^2/gk^3)_i^{1/3}$
k = thermal conductivity, W/m °C
H = tube spacing, m
g = gravitational acceleration, m/s^2
ρ = liquid density, kg/m^3
q = heat flux, W/m^2
Re = film Reynolds number, $4\Gamma/\mu_i$
t_0 = picture exposure time, s
T_i = liquid inlet temperature, °C
T_w = wall temperature, °C
ΔT = temperature difference, °C
σ = surface tension, N/m
μ = dynamic viscosity, Ns/m^2
ν = kinematic viscosity, m^2/s
Γ = liquid film flow rate per axial unit length flowing over one side of a horizontal tube, kg/m.s
λ = liquid column spacing; Taylor wave length ($\lambda = 2\pi\sqrt{3\sigma/\rho g}$), m
θ = angle, rad
i = inlet conditions (subscript)

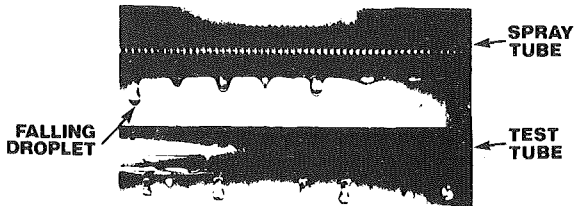

Fig. 2 Liquid droplet regime (Γ = 0.021 kg/m.s; H = 25.4 mm; T_i = 26.7°C; q = 0.0 kW/m^2; t_0 = 0.002s)

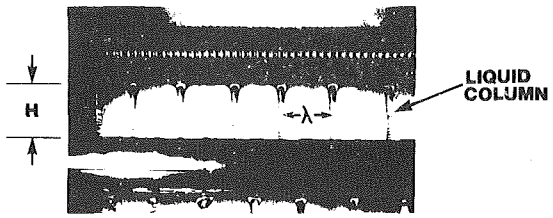

Fig. 3 Liquid column regime (Γ = 0.0383 kg/m.s; H = 25.4 mm; T_i = 26.7°C; q = 0.0 kW/m^2; t_0 = 0.002s)

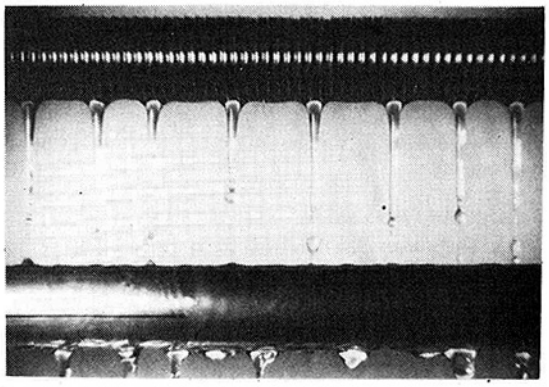

Fig. 4 Transition of liquid column regime into droplet regime (Γ = 0.0383 kg/m.s; H = 50.8 mm; T_i = 26.7°C; q = 0.0 kW/m^2; t_0 = 0.002s)

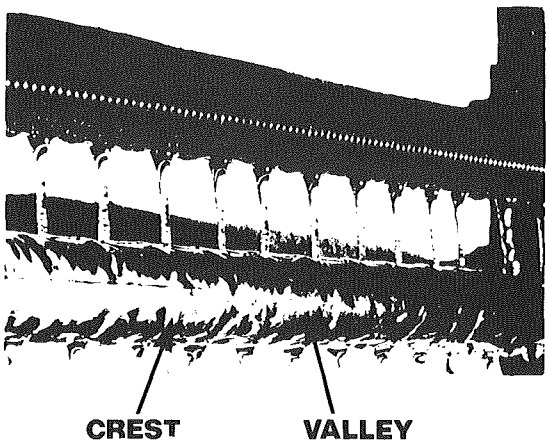

Fig. 5 Liquid film flow over horizontal tube (Γ = 0.0381 kg/m.s; H = 25.4 mm; T_i = 26.7°C; q = 38.2 kW/m^2; t_0 = 0.0005s)

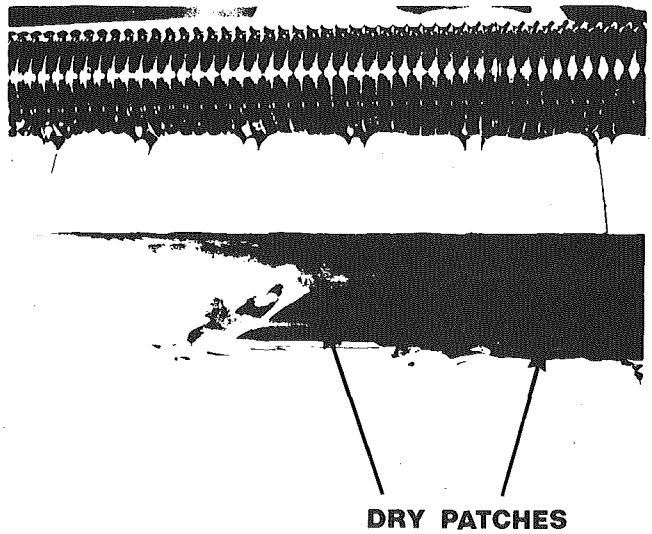

Fig. 6 Dry patch on horizontal tube (Γ = 0.0381 kg/m.s; H = 25.4 mm; T_i = 26.7°C; q = 82.3 kW/m^2; t_0 = 0.13s)

banded data; i.e., point B in Fig. 7). The same procedure was then repeated at a different flow rate. In some cases we were able to register only a permanent dry patch (e.g., point C in Fig. 7). Also, a few data points for stable dry patches were obtained by decreasing the flow rate slightly from its initial value instead of increasing the heat flux (e.g., point D in Fig. 7). A typical dry patch on the heated surface is shown in Fig. 6. The dry patches appear first on the sides of the tube. If q is increased, the dry patches will grow and eventually form a dry area around the tube—like a ring. It is reasonable to assume that the slight unsteadiness of the liquid flow patterns that was observed resulted in some scatter of the experimental data.

I Effect of Heat Flux and Flow Rate. All experimental data obtained in this study showed an increase in film breakdown heat flux with flow rate (Figs. 7–9). At higher flow rates the liquid film carries more energy (kinetic plus surface), and higher heat fluxes are required to prevent rewetting of dry patches. This is in qualitative agreement with the results of [8].

II Effect of Tube Spacing. The effect of tube spacing (i.e., distance between the tubes) on the breakdown heat flux is shown in Fig. 8. It is reasonable to assume that the velocity of the liquid falling from the spray tube to the test tube is approximately $(2gH)^{0.5}$. Therefore, increasing H increases the kinetic energy of the falling film and reduces the tendency of dry patches to form at a given surface heat flux. This is supported by the experimental data for the 12.7mm (0.5 in.) and 25.4mm (1.0 in.) tube spacing.

However, the breakdown data for 50.8mm (2.0 in.) tube spacing appear to contradict this thinking. As shown in Fig. 8, these data are not higher than those for 25.4mm spacing. The likely explanation for this phenomenon is based on observations made during the course of this investigation. In the case of 50.8mm spacing, the liquid reaching the test tube was in droplet form, except at a few high flow rates. The liquid columns had been transformed into droplets before reaching the surface (compare Figs. 3 and 4). Also, some splashing occurred as the liquid impinged on the surface. The fact that the droplet mode is more vulnerable to dry patch formation (since the liquid is not fed continuously to the test tube surface as in the case of the column regime) and the evidence of splashing are the most likely reasons that the data for 50.8mm tube spacing are not higher than those for 25.4mm spacing. In general, the instability of thin film flow is created by the liquid falling from one tube to the next and the downstream velocity field is influenced by the upstream conditions.

In any case, for most heat-exchanger applications the data on the two smaller spacings (25.4 and 12.7mm) are more relevant.

III Effect of Inlet Temperature. The experimental data on the breakdown heat flux for two different inlet temperatures of the subcooled liquid film are shown in Fig. 9. For $\Gamma < 1.2 \times 10^{-2}$ kg/m.s the breakdown heat flux was higher for a T_i value of 50°C; however, for $\Gamma > 1.2 \times 10^{-2}$ kg/m.s, no clear effect of the inlet temperature was observed. The effect of inlet temperature is associated with the effect of surface tension. At higher inlet temperatures the surface tension is smaller and the liquid film on the horizontal tube has a more uniform thickness. It is a well-known phenomenon [2] that on a wavy surface (such as that shown in Fig. 5) the region of greater film thickness (i.e., the crest) has a lower surface temperature and subsequently a higher surface tension than the thinner region. Therefore, the surface tension force draws liquid from the valley into the crest. Eventually, a liquid deficiency occurs in the thinner regions, causing film breakdown, i.e., forming a dry patch on the surface. At higher flow

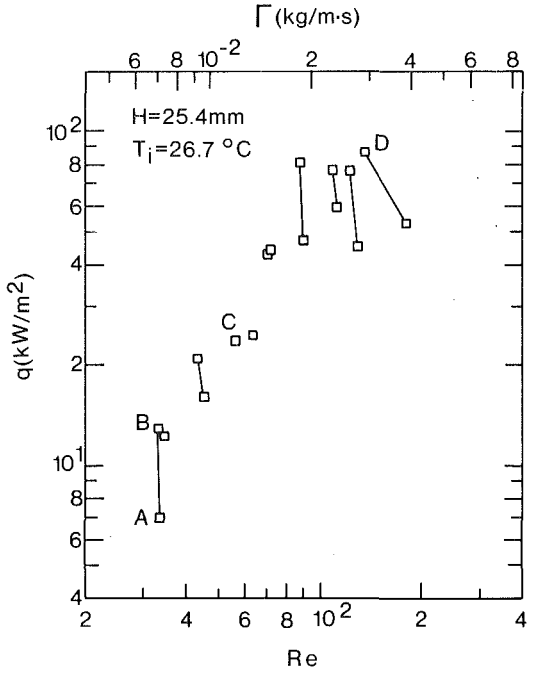

Fig. 7 Film breakdown heat flux versus liquid film flow rate

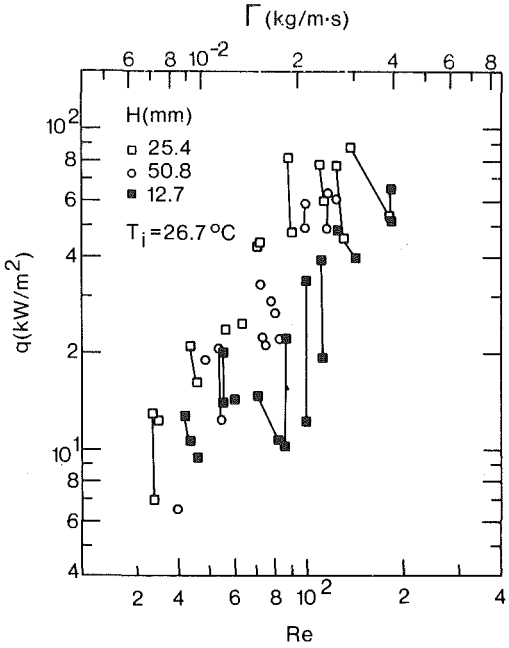

Fig. 8 Film breakdown heat flux versus liquid film flow rate (effect of tube spacing)

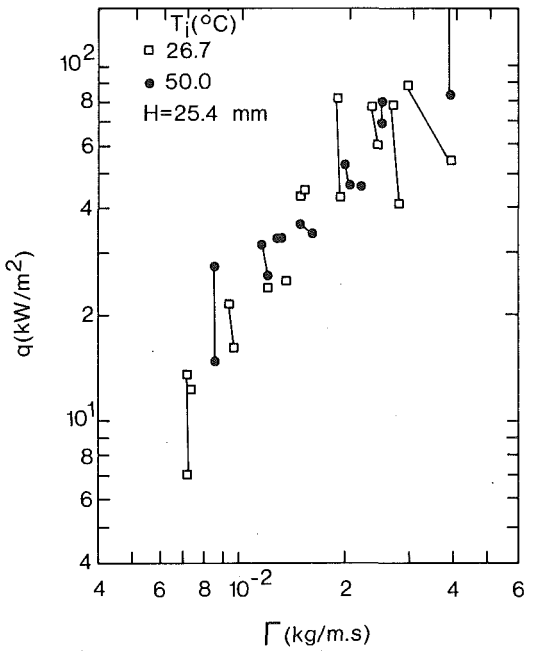

Fig. 9 Film breakdown heat flux versus liquid film flow rate (effect of liquid inlet temperature)

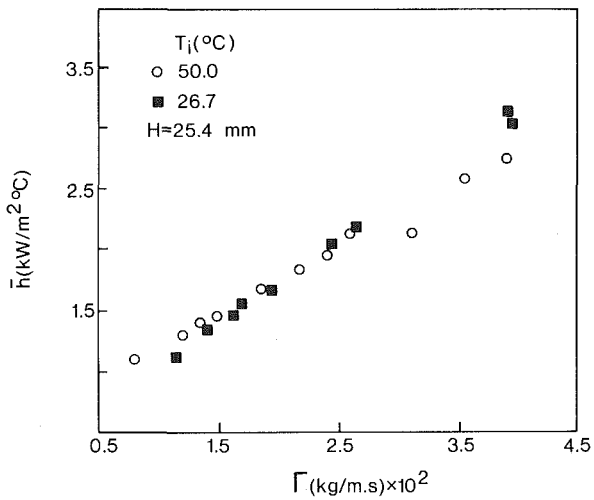

Fig. 10 Heat transfer coefficient versus liquid film flow rate (effect of liquid inlet temperature)

rates this distortion of the liquid film, due to the temperature difference set up in the film, is significantly reduced by the inertial force of the film flow.

3.3 Heat Transfer Coefficient. At conditions prior to film breakdown heat transfer measurements were taken. The local heat transfer coefficient data were presented as

$$h = q/(T_w - T_i) \tag{1}$$

and the average heat transfer coefficient was defined as

$$\bar{h} = \frac{1}{2\pi}\int_0^{2\pi} h d\theta \tag{2}$$

As shown in Figs. 10 and 11, the heat transfer coefficient increases with flow rate. The behavior of the heat transfer coefficient versus

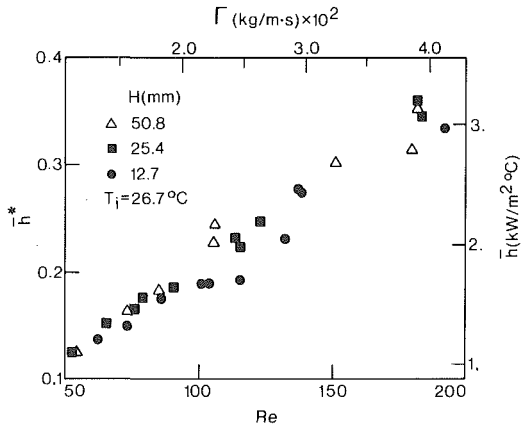

Fig. 11 Heat transfer coefficient versus liquid film flow rate (effect of tube spacing)

flow rate is different here from the classical Nusselt condensation problem. The liquid film is subcooled and also the film thickness is far from uniform. This distortion of the film reduces the heat transfer coefficient. Since the thickness of the film in the valleys is very small, the temperature of the liquid in these regions quickly approaches the tube surface temperature. Also, the falling-film velocity in the valleys is lower than in the crests due to the gradients in surface tension and density. Since the film temperature around the tube is much lower than the saturation temperature no evaporation occurs, and practically all heat from the heated tube is transferred to the subcooled liquid film, increasing its bulk temperature. The average film thickness increases with flow rate.

No systematic change in the heat transfer coefficient with inlet temperature was observed for the conditions of the experiment (Fig. 10). A certain increase in the heat transfer coefficient with tube spacing was observed at some film flow rates (Fig. 11).

Most of the data on film breakdown and heat transfer coefficient are presented in terms of the film Reynolds number ($4\Gamma/\mu$). Some of the data (Figs. 9 and 10) are presented in terms of the liquid film flow rate Γ only, since quantity ($4\Gamma/\mu$) may obliterate the effect of inlet temperature or surface tension because μ strongly depends on T. This indicates that $4\Gamma/\mu$ is not always a good correlating parameter, at least by itself.

Since the test section in this study was in contact with air, the surface tension at the liquid/air interface is generally different from what it would be at liquid/steam interface.

The stability of dry patches may be effected by the heating procedure of heat transfer surface. All data presented here are related to the prescribed heat flux condition since the test section was heated electrically.

4 Conclusions

From the results of this study the following major conclusions can be drawn.

1 For the range of flow rates studied there are basically two flow regimes associated with liquid film falling from one horizontal tube to the next: (*a*) the droplet regime which is related to lower flow rates and (*b*) the column regime related to higher flow rates. The transition from one regime to the other is effected by the tube spacing.

It is logical to expert that at extremely high film flow rates the columns will disappear and the liquid will fall from one tube to the next as a sheet.

2 As the film flow rate increases, the heat flux needed to cause a film breakdown (i.e., a dry patch) becomes higher. For the conditions of the experiment, increasing the tube spacing from 12.7mm (0.5 in.) to 25.4mm (1.0 in.) increases the breakdown heat flux. Also, at lower film flow rates ($\Gamma < 1.2 \times 10^{-2}$ kg/m.s) increasing the subcooled film inlet temperature raises the breakdown heat flux.

3 The heat transfer coefficient increases with film flow rate and with tube spacing.

The experimental results presented in this paper can be useful for various thin-film applications. The data on the film breakdown heat flux can be especially helpful in designing horizontal-tube falling-film heat exchangers, where the minimum liquid flow rate needed to wet a bank of tubes must be known in order to determine the minimum liquid recycling ratio for the exchanger.

Acknowledgment

This work was supported by the University of Illinois Research Board and the Argonne National Laboratory.

References

1 Hallett, V. A., "Surface Phenomena Causing Breakdown of Falling Liquid Films During Heat Transfer," *International Journal of Heat Mass Transfer,* Vol. 9, 1966, pp. 283–294.

2 Simon, F. F. and Hsu, Y. Y., "Thermocapillary Induced Breakdown of Falling Liquid Films," NASA TN D—5624, 1970.

3 Munakata, T., Watanabe, K. and Miyashita, K., "Minimum Wetting Rate on Wetted-Wall Column," *Journal of Chemical Engineering of Japan,* Vol. 8, No. 6, 1975, pp. 440–444.

4 Fujita, T. and Veda, T., "Heat Transfer to Falling Liquid Films and Film Breakdown" Parts I and II, *International Journal of Heat Mass Transfer,* Vol. 21, 1978, pp. 97–118.

5 Bankoff, S. G. and Chung, J., "Dryout of a Thin Heated Liquid Film," *Proceedings of International Heat Mass Transfer Center Seminar,* Dubrovnik 1978, Hemisphere Publishing, 1978.

6 Hartley, D. E. and Murgatroyd, W., "Criteria for the Break-up of Thin Liquid Layers Flowing Isothermally Over Solid Surfaces," *International Journal of Heat Mass Transfer,* Vol. 7, 1964, pp. 1003–1015.

7 Zuber, N. and Staub, F. W., "Stability of Dry Patches Forming in Liquid Films Flowing Over Heated Surface," *International Journal of Heat Mass Transfer,* Vol. 9, 1966, pp. 897–905.

8 Mikielewicz J. and Moszynski, J. R., "Minimum Thickness of a Liquid Film Flowing Vertically Down a Solid Surface," *International Journal of Heat Mass Transfer,* Vol. 19, 1976, pp. 771–776.

9 Ponter, A. B. and Aswald, K. M., "Minimum Thickness of a Liquid Film Flowing Down a Vertical Surface—Validity of Mikielewicz and Moszynski's Equation," *International Journal of Heat Mass Transfer,* Vol. 20, 1977, pp. 575–576.

10 Lorenz, J. J. and Yung, D., "A Note on Combined Boiling and Evaporation of Liquid Films on Horizontal Tubes," ASME JOURNAL OF HEAT TRANSFER, Vol. 101, 1979, pp. 178–180.

11 Wilke, W., "Warmeubergang an Rieselfilme," *Forschungen Hft. Ver. Dt. Lng. Vog.,* 490, 1962, p. B28.

12 Solan, A. and Zfati, A., "Heat Transfer in Laminar Flow of a Liquid Film on a Horizontal Cylinder," *Proceedings of Fifth International Heat Transfer Conference,* Tokyo, Japan, 1975, paper FC2.9.

13 Parken, W. H., "Heat Transfer to Thin Water Films on Horizontal Tubes," Ph.D. Thesis, Rutgers University, 1975.

14 Sernas, V., "Heat Transfer Correlation for Subcooled Water Films on Horizontal Tubes," ASME JOURNAL OF HEAT TRANSFER, Vol. 101, 1979, pp. 176–178.

15 Oosthuizen, P. H. and Chenng, T., "An Experimental Study of Heat Transfer to Developing Water Film Flow Over Cylinders," ASME JOURNAL OF HEAT TRANSFER, Vol. 99, 1977, pp. 152–155.

16 Kuhn-Zinserling, N., "Design of Fluid Uniform Distribution Pipe," Report No. EnrE–397, Dept. of Energy Engineering, University of Illinois, Chicago, 1977.

17 Lamb, H., *Hydrodynamics,* 6th ed., Dover, New York, 1945.

18 Conti, R. J., "Heat Transfer Enhancement in Horizontal Ammonia-Film Evaporators," *Proceedings of Fifth Ocean Thermal Energy Conversion Conference,* Washington, D.C., June 19–22, 1979.

M. Singh
S. C. Rajvanshi

Department of Applied Sciences,
Punjab Engineering College,
Chandigarh-160012, India

Heat Transfer between Eccentric Rotating Cylinders

The heat transfer between eccentric rotating cylinders is studied using a modified bipolar coordinate system. The energy equation has been solved by expressing the temperature in the form of a perturbation in terms of α, the dimensionless parameter defining the clearance ratio; and Rm, the modified Reynolds number. The effect of Prandtl number, eccentricity and velocity ratio on temperature distribution has been shown graphically. The results are valid for small clearance ratio. There is no restriction on eccentricity.

Introduction

Flow between eccentric cylinders forms an important part in understanding the flow in a journal bearing. A lot of work has been done in this direction since the presentation of principles of lubrication theory by Reynolds. The effects of nonzero inertia and curvature have been investigated by determining the higher order corrections in the solution of Navier-Stokes equations. Kamal [1] and Kulinski and Ostrach [2] have contributed in this area. Recently Sood and Elrod [3] have used the numerical method to solve the full Navier-Stokes equations for the flow between eccentric rotating cylinders for clearance ratio 1 only. DiPrima and Stuart [4] considered the viscous incompressible flow between eccentric rotating cylinders. They obtained the linearized inertial correction to the Stokes approximation, subject to the usual lubrication assumptions. Their emphasis is on the resultant force exerted by the fluid over the cylinders and on the distribution of these forces over the cylinders. The analysis is limited to the case of very small clearance ratio.

The theoretical and experimental investigations of the heat transfer in concentric cylinders are available in the literature. The corresponding results for eccentric cylinders are not known. Recently Kuhen and Goldstein [5] have studied experimentally the heat transfer in eccentric horizontal cylinderical annuli.

The primary object of the present theoretical investigation is to know the heat transfer between eccentric rotating cylinders with constant wall temperatures. The energy equation has been solved under the same set of assumptions as were used in [4]. The velocity profiles available therein have been used in the present work. The temperature has been expressed in the form of a perturbation in terms of α which is a measure of clearance ratio, and Rm, the modified Reynolds number. The first order corrections to temperature in terms of α and Rm have been calculated. Higher order corrections can be obtained, if desired. The temperature profiles presented in the paper are valid for small values of α, and for all values of eccentricity in the range 0 to 1 ($0 \leq \epsilon < 1$).

Governing Equations and Boundary Conditions

Following DiPrima and Stuart [4] we consider the system shown in Fig. 1, where we have two infinitely long circular cylinders of radii a and b ($b > a$) with centers set at a distance ae apart. In order to insure that the cylinders do not touch we require $ae < b\text{-}a$, which can be written as.

$$0 \leq \epsilon < 1, \tag{1}$$

where

$$\epsilon = e/\delta,\ \delta = (b - a)/a. \tag{2}$$

The parameter ϵ is the eccentricity, which measures the ratio of the distance between the centers of the two cylinders to the difference in their radii. The parameter δ, called the clearance ratio, is a measure of the ratio of the mean clearance between the cylinders to the radius of the inner cylinder. The polar coordinate system depicted in Fig. 1 has its origin at the axis of the inner cylinder with the ray $\theta = 0$ through the axis of the outer cylinder. We introduce modified bipolar coordinate system (ρ, φ). Its relationships with (r, θ) coordinate system has been discussed in detail in [4]. Let u_ρ and u_φ be the velocity components in the ρ and φ directions, respectively; and let $\overline{T}$ be the temperature at any point (ρ, φ). The boundary conditions are:

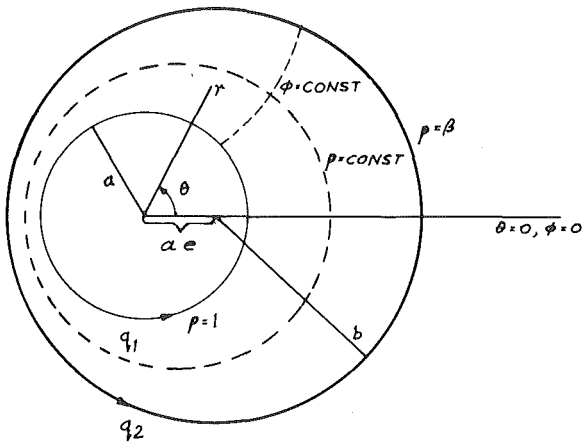

Fig. 1 Geometry and coordinate systems

$$u_\rho = 0,\ u_\varphi = q_1,\ \overline{T} = \overline{T}_1 \text{ at } \rho = 1, \tag{3}$$

and

$$u_\rho = 0,\ u_\varphi = q_2,\ \overline{T} = \overline{T}_2 \text{ at } \rho = \beta, \tag{4}$$

where $\rho = 1$ and $\rho = \beta$ (defined in [4]) denote the inner and outer cylinders, respectively. In order to exploit the fact that the clearance ratio δ is extremely small in the lubrication problem and also to facilitate the algebraic calculations, it is convenient to choose $\alpha = \beta - 1$ as the length scale. For the sake of convenience we assume

$$\rho = 1 + \alpha x. \tag{5}$$

We further define the dimensionless stream function ψ, and the temperature T in the following form:

$$\left.\begin{aligned} u_\rho &= (\alpha\, q_1 \sqrt{J/\rho})\ (\partial\psi/\partial\varphi),\ u_\varphi = -q_1 \sqrt{J}\ (\partial\psi/\partial x), \\ T &= (\overline{T} - \overline{T}_1)/(\overline{T}_2 - \overline{T}_1). \end{aligned}\right\} \tag{6}$$

Using (5) and (6) the energy equation including viscous dissipation terms for the two-dimensional, viscous, incompressible flow in (ρ, φ) coordinate system may be written as

$$\begin{aligned} (\mathrm{R}m\ J/E)\ &[(\partial\psi/\partial\varphi)(\partial T/\partial x) - (\partial\psi/\partial x)(\partial T/\partial\varphi)] \\ &= (J/\mathrm{Pr}\ E)[(\partial^2 T/\partial x^2) + \alpha\{x\ (\partial^2 T/\partial x^2) \\ &\quad + (\partial T/\partial x)\}] + [(\partial J/\partial x)(\partial\psi/\partial x) \\ &\quad + J(\partial^2\psi/\partial x^2)]^2 + \alpha[x\{(\partial J/\partial x)(\partial\psi/\partial x) \\ &\quad + J(\partial^2\psi/\partial x^2)\}^2 - 2J(\partial\psi/\partial x)\ \{(\partial J/\partial x) \\ &\quad + J\ (\partial^2\psi/\partial x^2)\}], \end{aligned} \tag{7}$$

where

Contributed by the Heat Transfer Division for publication in the JOURNAL OF HEAT TRANSFER. Manuscript received by the Heat Transfer Division June 6, 1979.

modified Reynold number $Rm = \alpha^2 a\, q_1/\nu$,
Prandtl number $Pr = \mu\, C_v/k$,
Eckert number $E = q_1^2/C_v(\overline{T}_2 - \overline{T}_1)$,
and J is the Jacobian of the transformation defined in [4].

The boundary conditions (3) and (4) for the temperature reduce to

$$T = 0 \text{ at } x = 0,$$
$$\text{and} \tag{8}$$
$$T = 1 \text{ at } x = 1.$$

The temperature T is expressed in the form of a perturbation in terms of α and Rm in the following form

$$T(x, \varphi, \epsilon, \alpha, Rm) = T_{00}(x, \varphi, \epsilon) + Rm\, T_{10}(x, \varphi, \epsilon) + \alpha\, T_{01}(x, \varphi, \epsilon) + 0(\alpha^2, Rm^2, \alpha\, Rm). \tag{9}$$

T_{00} represents the temperature distribution under Reynolds approximation. T_{10} and T_{01} give first order inertial and curvature corrections, respectively. The effect of viscous dissipation is present in all the terms, whereas the contribution of convective terms enters through T_{10}, T_{01} and higher order corrections. Since $\alpha \ll 1$ in practice, the results have been obtained up to first order approximation. As such these are expected to be valid for small values of α and Rm only.

Solutions of Equations

Equations (7–9) give

$$T_{00}(x, \varphi) = \sum_{n=0}^{4} X_{00n}(\varphi)\, x^n, \tag{10}$$

where

$$X_{000}(\varphi) = 0,$$
$$X_{001}(\varphi) = 1 + Pr\, E\,(2H^2 - 4\,G\,H + 3\,G^2),$$
$$X_{002}(\varphi) = -2\,Pr\,E\,H^2,$$
$$X_{003}(\varphi) = 4\,Pr\,E\,G\,H,$$
$$X_{004}(\varphi) = -3\,Pr\,E\,G^2.$$

$$T_{10}(x, \varphi) = \sum_{n=0}^{8} X_{10n}(\varphi)\, x^n, \tag{11}$$

where

$$X_{100}(\varphi) = 0,$$
$$X_{101}(\varphi) = -\sum_{n=2}^{8} X_{10n}(\varphi),$$
$$X_{102}(\varphi) = -4\,Pr\,E\,H\,A_{102}/C,$$
$$X_{103}(\varphi) = (1/6)\,Pr\,F + (1/6)\,Pr^2\,E\,[(2\,H^2 - 4\,H\,G + 3\,G^2)\,F - 4\,H\,F_1 C] + 4\,Pr\,E\,(A_{102}\,G - A_{103}\,H)/C,$$
$$X_{104}(\varphi) = -(1/12)\,(2+\eta)\,Pr\,F + Pr\,E\,(36\,A_{103}\,G + B_{100}\,H\,D)/6\,C + (1/12)\,Pr^2 E\,[4\,F_1\,C\,H\,(3 + 2\,H) - F\,\{2\,H^2\,(4+\eta) + G\,(2+\eta)\,(3\,G - 4\,H)\}],$$
$$X_{105}(\varphi) = (1/20)\,Pr\,F\,(1+\eta) + (1/30)\,Pr\,E\,D\,(B_{101}\,H - 9\,B_{100}\,G)/C + (1/20)\,Pr^2 E\,[F\{2\,H^2(5 + 3\,\eta) + 4\,G\,H\,(2 - \eta) + 3\,G^2(1+\eta)\} - 4\,F_1\,C(2\,H + 3\,G + 3\,G\,H + 6\,H^2)],$$
$$X_{106}(\varphi) = (1/90)\,Pr\,E\,D\,(B_{102}\,H - 6\,B_{101}\,G)/C + (1/30)\,Pr^2 E\,[4F_1 C\,(3\,G + 15\,G\,H + 4\,H^2) - 4\,F\,\{(1+\eta)\,H^2 + 3\,(2+\eta)\,G\,H + 3\,G^2\}],$$
$$X_{107}(\varphi) = (1/210)\,Pr\,E\,D\,(B_{103}\,H - 5\,B_{102}\,G)/C + (2/7)\,Pr^2\,E\,[FG\,\{(1+\eta)\,H + (2+\eta)\,G\} - F_1\,C\,G\,(4\,H + 3\,G)],$$
$$X_{108}(\varphi) = -(3/280)\,Pr\,E\,B_{103}D/C + (3/14)\,Pr^2\,E\,G^2[3\,F_1\,C - (1+\eta)F].$$

$$T_{01}(x, \varphi) = \sum_{n=0}^{5} X_{01n}(\varphi)\, x^n, \tag{12}$$

where

$$X_{010}(\varphi) = 0$$
$$X_{011}(\varphi) = -\sum_{n=2}^{5} X_{01n}(\varphi),$$
$$X_{012}(\varphi) = Pr\,E\,[H^2(1 + 2\,F_2) + 1.5\,G^2 - 2\,GH + 2H\,(1 - 2\,C - 2\,A_{012}/C)] + 0.5,$$
$$X_{013}(\varphi) = (2/3)\,Pr\,E\,[(-5 + 6\,C)\,H^2 - 6\,F_2\,G\,H - 6\,A_{013}H/C + G\,(6\,C - 1 + 6\,A_{012}/C)],$$
$$X_{014}(\varphi) = Pr\,E\,[2\,G\,H\,(4 - 5\,C) + 3\,F_2\,G^2 + 6\,A_{013}G/C - 4\,H\,B_{010}/C],$$
$$X_{015}(\varphi) = (9/5)\,Pr\,E\,G\,[(4C - 7)\,G + 4\,B_{010}/C],$$

such that

$$C(\varphi) = \sqrt{(1 - \epsilon^2)}/(1 - \epsilon\cos\varphi),$$
$$D(\varphi) = 2\,\epsilon\,(1 - \epsilon^2)\,\sin\varphi/(1 - \epsilon\cos\varphi)^2,$$
$$F(\varphi) = \epsilon\,\sqrt{(1 - \epsilon^2)}\,\sin\varphi/(1 - \epsilon\cos\varphi)^2,$$
$$F_1(\varphi) = \epsilon\,(1+\eta)\,\sin\varphi/(2 + \epsilon^2),$$
$$F_2(\varphi) = \epsilon\,(\epsilon - \cos\varphi)/[(1 - \epsilon\cos\varphi)\,\sqrt{(1 - \epsilon^2)}],$$
$$G(\varphi) = 1 + \eta - 2\,(1+\eta)(1 - \epsilon\cos\varphi)/(2 + \epsilon^2),$$
$$H(\varphi) = 2 + \eta - 3\,(1+\eta)\,(1 - \epsilon\cos\varphi)/(2 + \epsilon^2),$$
$$\eta = q_2/q_1.$$

The quantities A_{102}, A_{103}, A_{012}, B_{100}, B_{101}, B_{102}, B_{103}, B_{010} have been defined in [4]. These are not recorded here for the sake of brevity.

Results and Discussion

For numerical work the following values have been assumed

$$\alpha = 0.1,\ Rm = 0.3,\ E = 0.1. \tag{13}$$

Fig. 2 shows the variation of temperature for different values of Prandtl number Pr for $\epsilon = 0.25$, $\eta = 1.0$ and $\varphi = 0$. At low Prandtl number the ratio of the momentum transfer to heat transfer is small. Therefore the temperature profiles show a monotonic increase as we

Nomenclature

a = radius of inner cylinder
ae = displacement of the center of inner cylinder from center of outer cylinder
b = radius of outer cylinder
C_v = specific heat at constant volume
E = Eckert number, $q_1^2/C_v\,(\overline{T}_2 - \overline{T}_1)$
J = Jacobian of transformation
k = thermal conductivity
Nu = Nusselt number at the inner cylinder, $(1/\alpha)(\partial T/\partial x)_{x=0}$
Pr = Prandtl number, $\mu\, C_v/k$
q_1, q_2 = velocities of inner and outer cylinders, respectively
r, θ = polar co-ordinates
Rm = modified Reynolds number, $q_1 a \alpha^2/\nu$
T = dimensionless temperature
$\overline{T}$ = *dimensional temperature*
$\overline{T}_1, \overline{T}_2$ = temperatures of the inner and outer cylinder
u_ρ, u_φ = dimensional velocities in ρ and φ directions, respectively
x = length scale
α = dimensionless parameter, measure of clearance ratio
β, γ = dimensionless parameters
δ = clearance ratio, $(b\text{-}a)/a$
ϵ = eccentricity ratio, e/δ
μ = viscosity
σ = density
η = velocity ratio, q_2/q_1
ν = kinematic viscosity
ρ, φ = modified bipolar co-ordinates
ψ = dimensionless stream function

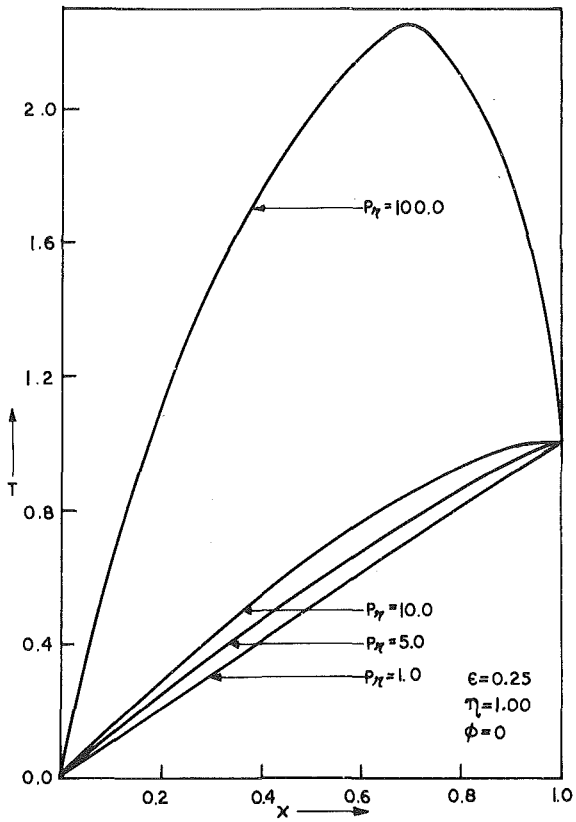

Fig. 2 Variation of T for different Pr

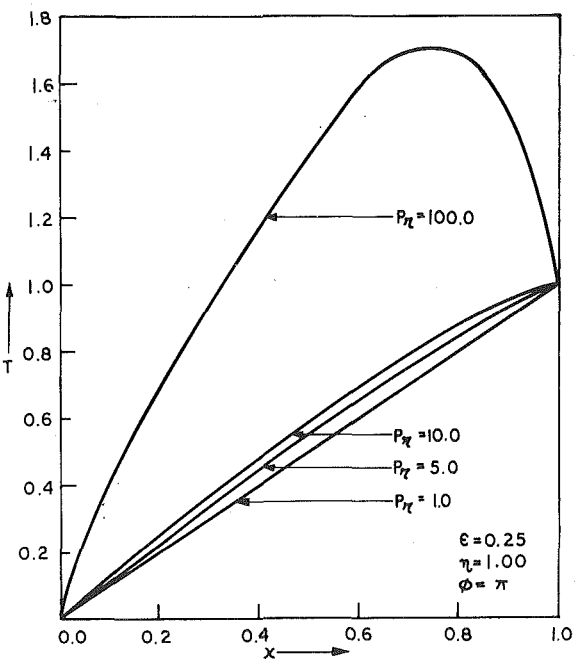

Fig. 3 Variation of T for different Pr

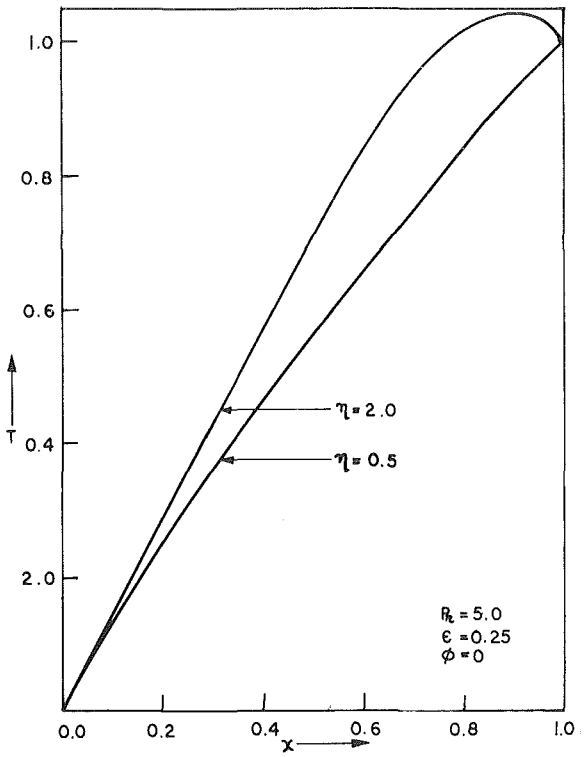

Fig. 4 Variation of T for different η

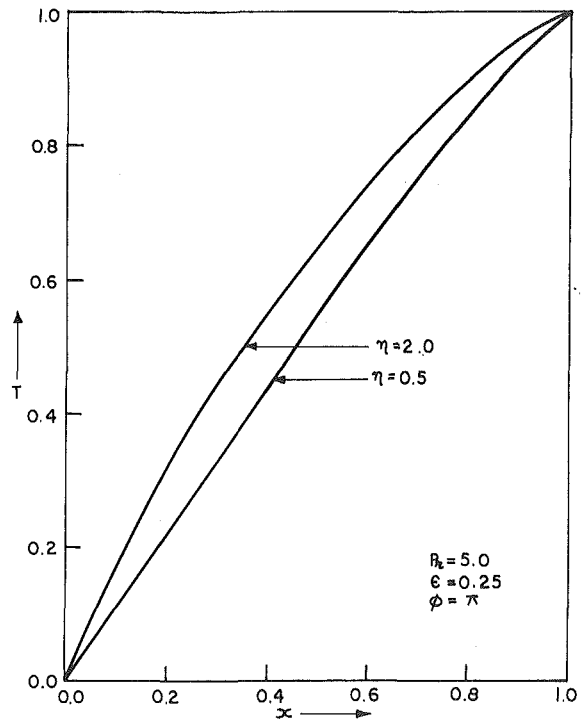

Fig. 5 Variation of T for different η

move from inner cylinder to outer cylinder. At large Prandtl number, the momentum transfer plays a dominant role. The momentum transfer attains a maxima in the region between two boundaries. With increase in momentum transfer, the convective terms dominate in the central region and the temperature attains a maximum value. Fig. 3 shows that the temperature profiles at $\varphi = \pi$ are qualitatively similar to those at $\varphi = 0$. Fig. 4 shows the effect of velocity ratio (η) on the temperature profile for Pr = 5.0, $\epsilon = 0.25$, $\varphi = 0$. With increase in η, the momentum transfer increases in the vicinity of the outer cylinder. This increase results in showing a maxima in the temperature profile in this region before attaining the prescribed value at the outer boundary. No such effect is observed in Fig. 5, which depicts the temperature distribution at $\varphi = \pi$. This may be attributed to the fact that in this region, the variation of η does not appreciably affect the momentum transfer, so that it may dominate the temperature distribution. In other words, the temperature distribution is governed by conduction terms and the convective terms have comparatively less effect. The effect of variation of eccentricity on the temperature profile is shown for Pr = 5.0, $\eta = 0.5$ in the region of maximum clearance, that is, $\varphi = 0$. The eccentricity increases the region of maximum

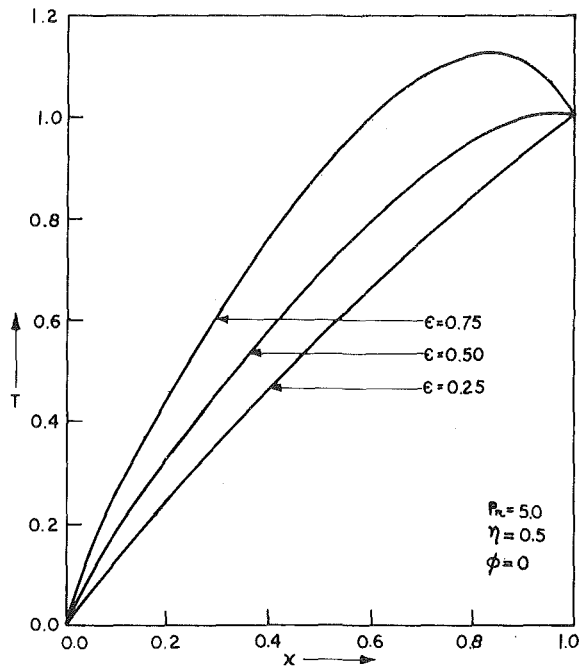

Fig. 6 Variation of T for different ϵ

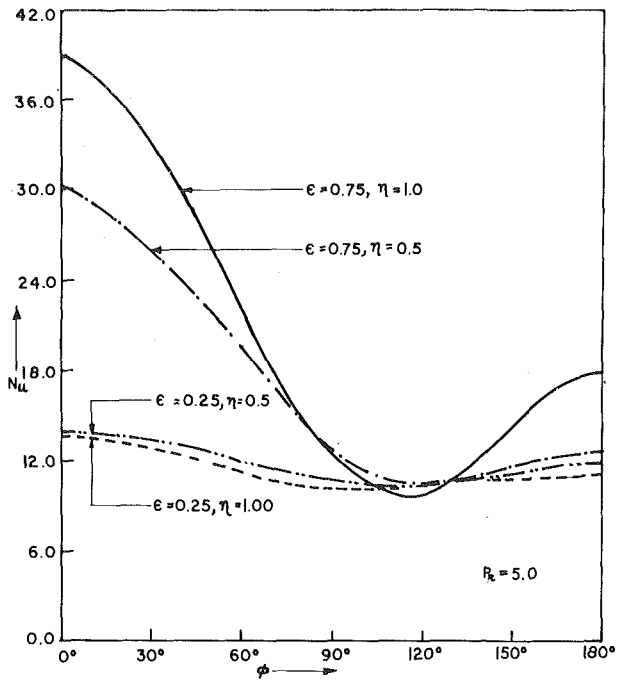

Fig. 7 Nusselt number on the inner cylinder

clearance. This induces the convective terms to dominate. The increase in momentum transfer gives rise to the geometry depicted in Fig. 6.

The heat exchange between the cylinder and the fluid is measured by means of the local coefficient of the heat transfer. Once the temperature distribution around the cylinders is known the local heat transfer coefficient can be evaluated. Using equations (5) and (6) the simplified expression for Nusselt number at the inner cylinder is given by

$$(\mathrm{Nu})_{x=0} = (1/\alpha)\,(\partial T/\partial x)_{x=0}. \tag{14}$$

Fig. 7 depicts the variation of Nu against φ on the inner cylinder for Pr = 5.0. As the momentum transfer is large in the region of maximum clearance, it will have an overriding effect, giving the maximum Nusselt number. With increase in φ, this region gets narrower and momentum transfer decreases. As it approaches π, although momentum transfer decreases, the viscous effects increase. This viscous heating results in a slight increase in Nusselt number showing the presence of a minima. These effects are more marked in the case of large eccentricity.

Acknowledgments

One of the authors (M.S.) is grateful to the University Grants Commission, New Delhi for providing the financial assistance. Thanks are due to the referees for their comments, which led to the improvement of the original draft.

References

1 Kamal, M. M., "Separation in the Flow Between Eccentric Rotating Cylinders," ASME *Journal of Basic Engineering*, Vol. 88, No. 4, Dec. 1966, pp. 717–724.

2 Kulinski, E. S., and Ostrach, S., "Journal Bearing Velocity Profiles for Small Eccentricity and Moderate Modified Reynolds Numbers," ASME *Journal of Applied Mechanics*, Vol. 89, No. 1, March 1967, pp. 16–22.

3 Sood, D. R., and Elord, H. G., "On the Flow Between Two Long Eccentric Cylinders," Report No. 17, Lubrication Research Laboratory, Columbia University, Dec. 1970.

4 DiPrima, R. C., and Stuart, J. T., "Flow Between Eccentric Rotating Cylinder," ASME *Journal of Lubrication Technology*, Vol 94, July 1972, pp. 266–271.

5 Kuhen, T. H., and Goldstein R. J., "An Experimental Study of Natural Convective Heat Transfer in, Concentric and Eccentric Horizontal Cylindrical Annuli," ASME, JOURNAL OF HEAT TRANSFER, Vol 100, No. 4, Nov. 1978, pp. 635–640.

Convective Heat Transfer Correlations for Planar, Supersonic, Separated Flows

J. P. Lamb
Professor of Mechanical Engineering,
The University of Texas at Austin,
Austin, TX 78712
Mem. ASME

Correlations are developed for minimum heat transfer levels within the separated flow fields formed by a variety of planar geometries including backsteps, open cavities, and cylinders of arbitrary cross section. Proposed correlations include the independent effects of Mach number, unit Reynolds number, and the length scale of the separated region. Both laminar and turbulent regimes are considered.

Introduction

The convective transport characteristics of a separated flow region are inherently more complex than those of an attached flow due to the occurrence of a secondary, vortical flow zone immediately adjacent to the solid surface. This additional complexity arises as a result of the coupling between the secondary flow and the external free stream; the coupling mechanisms are not only a function of Reynolds number but also of body geometry and the shape of the separated region which, in turn, is determined by a strong interaction between viscous and inviscid flow regions. These added levels of dependence have prohibited the development of any but highly complicated prediction methods [1]. Moreover, despite the existence of an extensive body of experimental data [2, 3] there has been only limited success in developing generalized correlations of heat transfer for separated regions produced by a specific geometry, e.g., a recent study [4] of slender, conical reentry geometries. In addition, there has been virtually no successful correlation of heat transfer levels for separated regions produced by different configurations.

Because of their relative simplicity, backstep or cavity geometries have often been employed to produce a separated zone. However, considerable data are available for leeward surface heat transfer to fully immersed bodies and thus the primary objective herein is to propose methods for correlating wall heat transfer rates within the separated zones of these vastly different geometries.

Fortunately for correlation purposes, the interaction process in supersonic flow is somewhat simpler than in the subsonic regime due to the hyperbolic nature of the inviscid field. Moreover, one finds in supersonic flow that the viscous-inviscid interaction (and hence the pressure field) is not highly dependent upon the thermal field within the separated zone. Thus the present approach was based on the expectation that correlations of separated heat transfer levels for different body shapes are most probable in the supersonic regime.

Flow Field Description

In general, planar separated flow fields contain two distinct regions; immediately adjacent to the leeward surface is a nearly isobaric zone which is followed by a recompression region characterized by a large positive pressure gradient. Subsequent to its separation the approaching boundary layer forms a free shear layer within the isobaric zone. Because a portion of the shear layer cannot negotiate the rising pressure of the recompression region, it is reversed toward the body surface where it impinges and is then reentrained into the free shear layer, thus creating the characteristic vortical pattern. Within the shear layer is a dividing streamline separating that portion of the flow which proceeds downstream from that portion which is continually recirculated.

Although the basic elements of each separated flow field are universal, the precise flow patterns in each case are somewhat different. For example, an open cavity flow does not contain an expansion region at the corner and hence the subsequent recompression flow is directed normally to the downstream wall rather than obliquely as in the case of base flows. Moreover, the sharp corner in a backstep geometry fixes the point of separation whereas, for cylinders having rounded leeward surfaces, the location of separation can move freely to accommodate the interaction between the recirculating inner flow (dominated by viscous effects) and the external, inviscid flow. In addition the sharp corner produces a higher degree of flow distortion than does a rounded surface. Such distortion is manifested in the external inviscid region by a complex family of both expansion and compression waves which, for high Mach numbers, may be partially embedded within the outer viscous zones [1].

Figure 1 depicts schematically the heat transfer distributions for backsteps and for cylinders as suggested by the data of [5–7]. For backstep and cavity geometries the low "separated value" of heat transfer (q_s) is followed by a sharp increase which occurs in the vicinity of reattachment. Depending upon the downstream surface configuration, there may be a peak in the distribution near reattachment which is followed by a relaxation of flow and thermal fields toward characteristic levels of attached flow. Moreover the value of q_s is directly related to the step height H for given approach flow conditions. Clearly, as H approaches zero, the value of q_s would approach the flat plate value (q_1).

As suggested by Fig. 1, the heat transfer distributions for cylinders are cross-section dependent and, due to the nature of boundary layer separation from a smooth surface, exhibit a more graduate decrease from q_1 to q_s than in flows with sharp corners. Moreover the value of q_1 is usually more difficult to define due to the slope of the heat transfer distribution. However, in the present study it was found that slight variations in the location and value of q_1 had almost no effect on the final correlation result, as will be subsequently explained (Fig. 4).

The primary mechanisms of energy transport into the recirculating inner region are shear work and thermal conduction along that portion of the dividing streamline in the nearly isobaric region. Such transport processes are dependent on profiles of velocity and enthalpy at the origin of the free layer; these free layer profiles, in turn, are related to corresponding distributions in the attached flow upstream of separation. Thus, as suggested by Charwat, et al. [8], there should be some degree of correlation between heat transfer levels before and after separation.

The present correlation scheme will therefore attempt to relate values of q_s to q_1 for various geometries and then to relate the values of q_1 (for a wide range of flow conditions) to an equivalent incompressible reference value of q_1. The relationship between q_s and q_1 is based on the observation that the lower portion of the vortex flow which determines q_s is nearly incompressible and hence is dependent primarily on the geometry of the separated zone and the inviscid flow which drives the vortex. Moreover, the relationship between q_s and q_1 has been developed largely in terms of attached flow parameters and geometric quantities. Undoubtedly this is less precise than a

Contributed by the Heat Transfer Division and presented at the Winter Annual Meeting, New York, NY, December 2–7, 1979 of THE AMERICAN SOCIETY OF MECHANICAL ENGINEERS. Revised manuscript received by the Heat Transfer Division December 19, 1979. Paper No. 79-WA/HT-13.

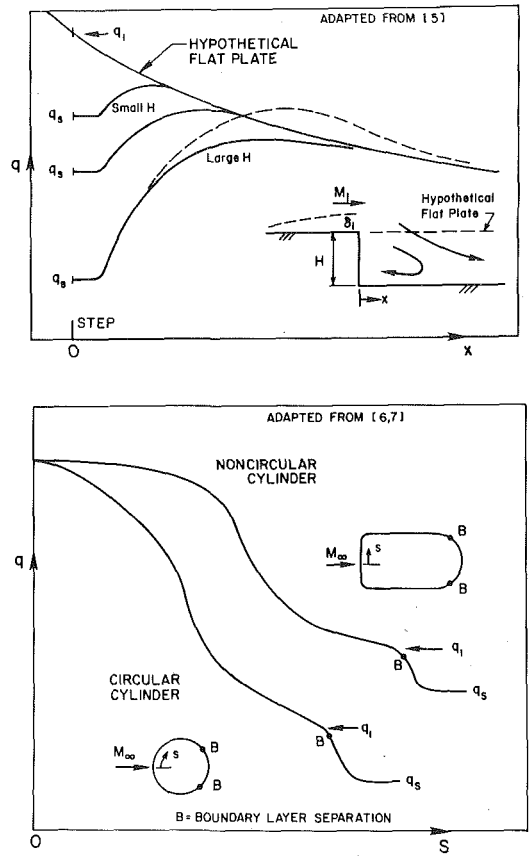

Fig. 1 Schematic representation of heat transfer distributions for backstep and cylinder geometries showing characteristic values q_1 and q_s

correlation scheme which employs flow characteristics of the separated zone itself. However, if one were able to measure or compute details of the latter region, there would be little use for the present correlations.

Despite the availability of a large number of experimental studies [2, 3], only a relatively few of these contain systematic variations of unit Reynolds number, approach Mach number and geometry parameters (such as step height H and cavity length L). Moreover, not all required parameters have been reported; thus some computed values have been utilized along with measurements to produce the desired correlation variables. Hence, the exact functional forms of the proposed correlation curves must be treated as provisional even though it is believed that physically significant correlation parameters are identified. Moreover, in view of the use of both computed and measured information, it is difficult to make estimates of uncertainty levels.

Laminar Flows

The present data base for the laminar regime includes, in addition to the aforementioned data [5–7], the backstep results of Holloway, et al. [9] and the open cavity data reported by Hahn [10], Nicoll [11], and Wieting [12].[1] Major test parameters are tabulated in Table 1 where it is seen that most flows are in the hypersonic regime and are planar except in the case of Nicoll who utilized a conical flow surface with helium as the test gas. (Nicoll's approach flow conditions were converted to equivalent planar values.)

Shown in Fig. 2 are the distributions of q_1 and q_s with $\mathrm{Re}(\delta_1)$ for the aforementioned studies. In most instances, the values of δ_1 used for Fig. 2 were predicted using relatively simple integral methods in which any unknown parameters (e.g., wall pressure distributions) could be varied until the predicted and measured values of q_1 were

[1] Only the largest L/H data are considered here in view of the diminished role of convection in extremely short or deep cavities.

Table 1 Parameters for laminar flow cases

Investigator	Geometry	M_1	$U\mathrm{Re}_1 \times 10^{-5}$	H (cm)	Gas	L/H (cavity)	
Jakubowski [5]	Backstep	4.0 4.2	0.91 0.38	0.16, 0.51, 1.02 0.16, 0.51, 1.02	air	—	
Holloway [9]	Backstep	6.2	0.47, 0.92	0.32, 0.64	air	—	
Hahn [10]	Cavity	6.3	0.010, 0.021	1.9	air	5.3, 8.0, 10.7	
Nicoll [11]	Cavity (conical surface)	6.5	2.3, 3.8, 5.3	0.32	helium	2.5 to 10	
Wieting [12]	Cavity	6.9	0.57, 0.74	2.0	combustion gas	0.52	
	Cylinders					M_∞	$U\mathrm{Re}_\infty \times 10^{-6}$
Lamb [6]	Noncircular Cyl. (width = 5.8 cm)	2.2–2.7 2.3	0.5–5.5 1.3	2.79 2.79	air air	12 16	0.4, 2, 5 2
Bertin [7]	Circular Cyl. (Rad = 1.9 cm)	2.94	0.83, 4.3	1.65	nitrogen	10	8.3, 73.8
Bertin [7]	Noncircular Cyl. (width = 3.8 cm)	2.93	0.73, 5.1	1.38	nitrogen	10	7.1, 60.6

Nomenclature

b = thickness of turbulent free shear layer in open cavity flow
c_p = specific heat at constant pressure
D = boundary layer correlation parameter, $\delta_1/(\delta_1 + H)$
H = effective width of separated region (step height, cavity depth, etc.)
L = length of cavity in flow direction
M = Mach number
q = convective heat transfer rate
$q_{\max}$ = hypothetical maximum heat transfer rate, $\rho u\, c_p(T_{aw} - T_w)$
r = recovery factor, $(T_{aw} - T)/(T_0 - T)$
Re = Reynolds number
S = surface coordinate for cylinders (Fig. 1)
St = Stanton number, $q/(q_{\max})_1$
St_{eq} = Stanton number, defined in equation (1)
T = temperature
u = flow velocity
$U\mathrm{Re}$ = unit Reynolds number (per meter)
x = longitudinal coordinate
δ = boundary layer thickness
ρ = fluid density
σ = asymptotic spread rate parameter for turbulent free shear layer
γ = ratio of specific heats, c_p/c_v

Subscripts

aw = adiabatic wall conditions
ef = effective value
fp = flat plate flow
i = incompressible flow conditions corresponding to station 1
s = separated flow region
w = wall conditions
0 = free stream stagnation conditions
1 = attached flow conditions upstream of separated region
∞ = approach flow conditions for cylinders (Fig. 1)

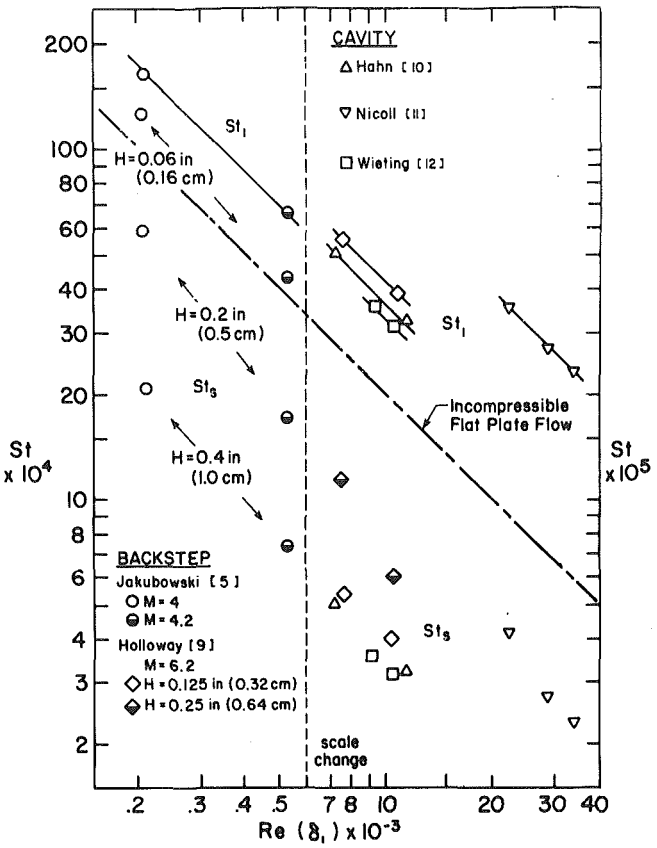

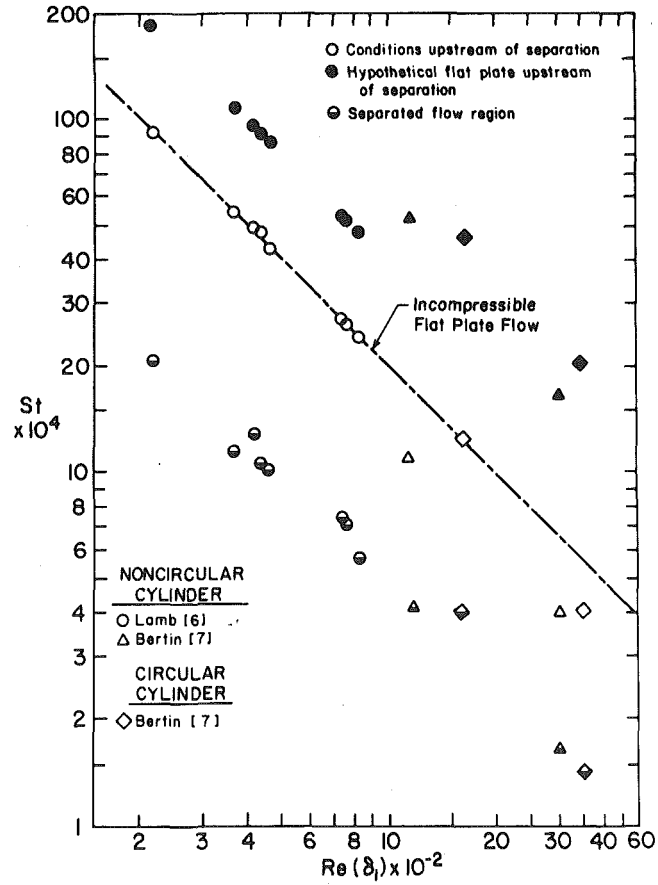

Fig. 2 Variation of Stanton numbers St_s and St_1 with Reynolds number for laminar flow

in general agreement. It is observed that the data of Jakubowski/Lewis and of Holloway include independent variations of unit Reynolds number and step height; in addition, the cylinder data include two body widths and a wide range of unit Reynolds numbers. Tests reported by Lamb [6] on a cylinder of noncircular cross-section were obtained with a model in which the wall temperature over the windward and leeward portions was controlled independently, thus allowing one to determine the extent to which the approaching thermal boundary layer affected leeward heat transfer. It is seen from Fig. 2 that this effect was well correlated by the predicted boundary layer thickness just prior to separation. It should also be noted that the apparent agreement between actual upstream values of St and the incompressible flat plate distribution is purely coincidental.

The distributions of q_s in Fig. 2 indicate that, in addition to the limiting condition ($H \to 0$) mentioned earlier, there is a lower limit on q_s which occurs when $\delta_1 \to 0$. This result suggests that a parameter of the form $\delta_1/(\delta_1 + H)$ might be useful since it varies between zero and unity for the foregoing limits. Moreover it is recognized that the overall temperature gradient $(\Delta T/\Delta y)$ across the upstream boundary layer is inversely proportional to δ_1 whereas the corresponding temperature gradient across the entire separated zone is inversely proportional to $(\delta_1 + H)$.

The data of Fig. 2 are replotted in Fig. 3 to indicate the variation of q_s/q_1 with D. The distributions of Jakubowski/Lewis for thick boundary layers do indeed exhibit the expected approach of q_s/q_1 toward unity as $H \to 0$ (i.e., $D \to 1$). For small values of D, Fig. 3 suggests a limiting value of $q_s/q_1 \simeq 0.1$ for open cavities and backsteps.[2] It is also significant that the open cavity data of Nicoll (where δ_1/L was small) show no apparent influence of L/H on q_s as compared with the results of Wieting (where δ_1/L was large) which exhibit a decrease in q_s/q_1 when δ_1/L increases above 0.1.

Figure 3 suggests that the lower limiting value of q_s/q_1 for cylinders is cross section dependent which is not unexpected since approach flow conditions (e.g., q_1) are also cross-section dependent (Fig. 1). For proper comparison of the cylinder data, therefore, it was necessary to employ, as an upstream reference, the value of q_1 for an equivalent flat plate flow. In the present cases it was found that, for equal values of displacement thickness (δ_1^*), the value of δ_1 for a hypothetical flat plate layer is much less than δ_1 for the actual (computed) boundary layer which develops in a highly accelerating flow (Fig. 1). Hence the corresponding value of $(St_1)_{fp}$ was larger than St_1. This result is indicated in Fig. 2 (closed symbols).

A comparison of the Jakubowski, Lewis and the Holloway distributions in Fig. 3 suggests a slight effect of approach Mach number. This influence has been included by using $D/(T/T_0)_1^{0.3}$ as the correlation parameter in Fig. 4 which also includes the use of $q_1(ef) = (q_1)_{fp}$ for cylinder data. The distribution of Fig. 4 therefore represents the final correlation of q_s/q_1 for laminar flows.

Use of Fig. 4 allows one to relate q_s to q_1 for a specific geometry and approach flow. Various upstream conditions can then be interrelated with the usual laminar compressibility transformation (e.g., reference temperature). In this manner all separated heat transfer data can be made to disperse about the incompressible flat plate value, i.e., $St_{eq} \simeq 2.07/\mathrm{Re}(\delta)$. A consolidated plot of St_{eq} versus $\mathrm{Re}(\delta_1)$ is presented in Fig. 5 to indicate the degree of dispersion which results from the present scheme. The value of St_{eq} can also be expressed in terms of the correlation parameters as:

$$St_{eq} = \frac{St_1}{(St_1/St_i)} \frac{(q_s/q_1)_a}{(q_s/q_1)_D} \tag{1}$$

where St_1/St_i is found from the compressibility transformation.

The parameter $(q_s/q_1)_D$ in equation (1) denotes the correlation from Fig. 4 (based on δ_1, H, and M_1) whereas the ratio $(q_s/q_1)_a$ is based on actual heat transfer levels. However, if one were using equation (1) for prediction, the latter ratio would be the primary unknown whose value would allow q_s to be estimated.

[2] It should be recognized that the apparent limit of 0.1 may also be related to measurement limitations.

Turbulent Flows

The primary source of systematic data for the turbulent regime is the open cavity study of Charwat, et al. [8]. These data have been supplemented by the open cavity and backstep results of Nestler, et al. [13], the open cavity data of Emery [14], and the measurements of Larson, et al. [15] who obtained base plane data using a planar ogive body. Major test conditions for the relevant turbulent flows are shown in Table 2.

Following the general procedure used for laminar flow one may plot the variation of St_s with $Re(\delta_1)$, as in Fig. 6, to illustrate the influences of H and of L/H. As before, the smaller value of H yields larger values of St_s which approach St_1; simultaneously, larger values of L/H reduce St_s due to a thickened boundary layer on the cavity wall as well as to the presence of a thicker shear layer which reduces the effective temperature gradient across the dividing streamline. Hence one is led to utilize the effective thickness of the shear layer $b(L)$ as a length scale for turbulent transport in lieu of δ_1 which was successful in the laminar regime.

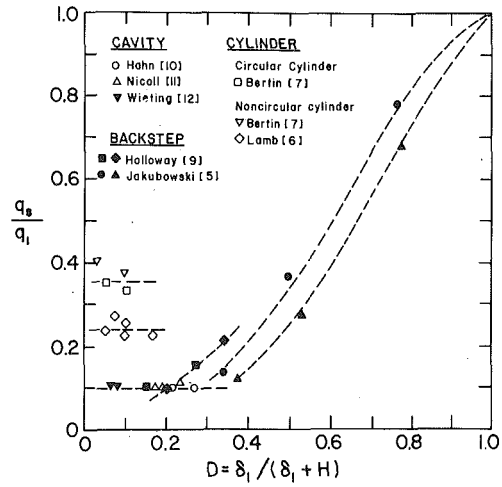

Fig. 3 Correlation of q_s/q_1 with the boundary layer parameter D for laminar flow

Figure 7 presents the Charwat data in terms of $Re(b)$ which produces a simple inverse relationship between q_s and b. Because of the relatively thick boundary layers for this set of data, the value of b was based on an outer edge growth proportional to $x^{6/7}$ (as in a wall layer) whereas the inner edge growth was estimated with the developing shear layer model of Lamb [16]. This theoretical model predicts a growth rate which increases with distance from the origin of the layer and which merges into the asymptotic, linear growth rate given by $db/dx \sim 1/\sigma$ where σ is inversely proportional to free stream Mach number.

An obvious exception to the inverse relationship of q_s and b is seen in the distribution for $M_1 = 2.1$ and $H = 0.25$ in (0.64 cm) in which the value of q_s for $L/H = 12$ is almost identical with that for $L/H = 9$. This is thought to be a result of the interference between the shear layer and the counterflowing boundary layer on the cavity surface. The result is a merging of the two shear flows which leads to a decreased thermal resistance. The present correlation does not include such a condition.

Inasmuch as $q_s \sim b^{-1}$ one must scale the ratio q_s/q_1 in order to determine the effect of δ_1/H. This is done in Fig. 8 which includes not only the Charwat data but also the measurements reported by Emery and by Nestler. As in the laminar case the expected variation of q_s and D is evident although a definite lower limit on q_s for δ_1 approaching

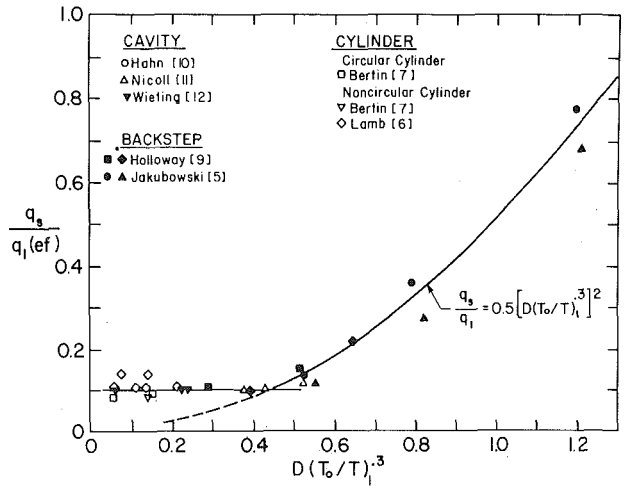

Fig. 4 Final correlation of q_s/q_1 for laminar flows

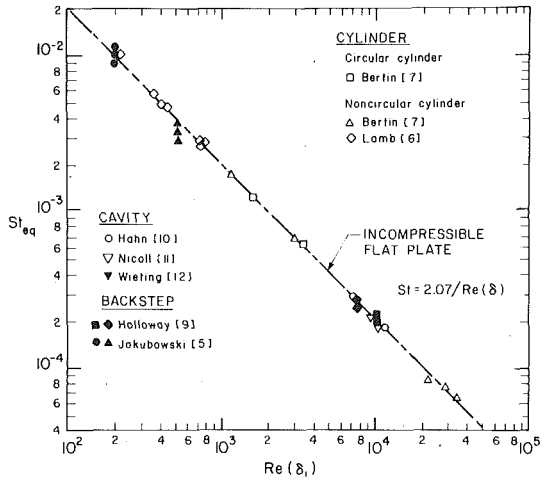

Fig. 5 Variation of equivalent Stanton number with Reynolds number using the correlation of Fig. 4

Table 2 Parameters for turbulent flow cases

Investigator	Geometry	M_1	$U\mathrm{Re}_1 \times 10^{-6}$	H (cm)	L/H
Charwat [8]	Cavity	2.1	7.6	0.64, 1.27	1, 3, 6, 9, 12
		2.9	4.7	0.64, 1.27	1, 3, 6, 9, 12
		3.5	3.1	0.64, 1.27	1, 3, 6, 9, 12
Charwat	Backstep	2.1	7.6	0.64	—
		2.9	4.7	0.64	—
		3.5	3.1	0.64	—
Nestler [13]	Cavity	6.3	13.5	2.5	5
		8.5	12.1	2.5	5
Nestler	Backstep	6.3	13.5	2.5	—
			13.5	2.0	—
Emery [14]	Cavity	2.9	42	0.5	9 to 11
Larson [15]	Base (ogive)	2.95	9.6 to 33.6	1.9	—

NOTE: Test gas in all cases was air.

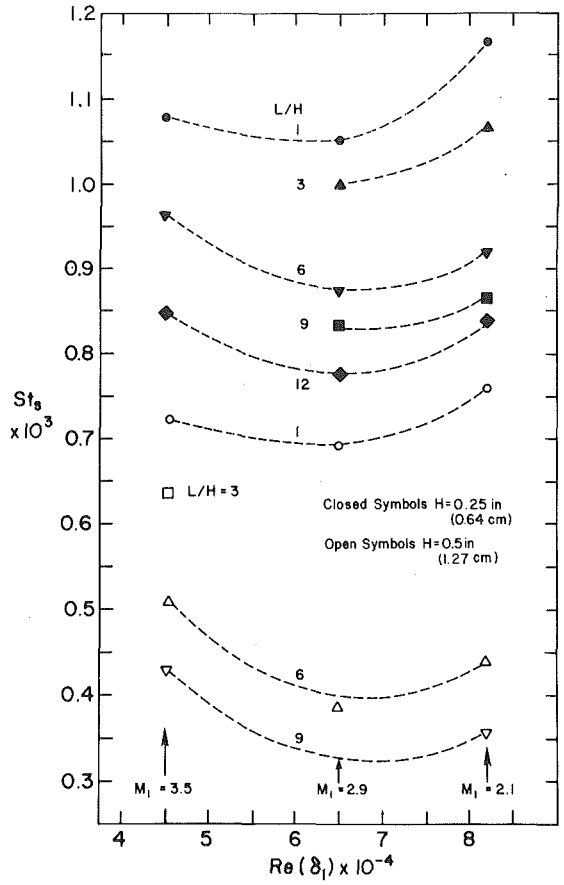

Fig. 6 Variation of minimum Stanton number in open cavities: data of Charwat, et al. [8]

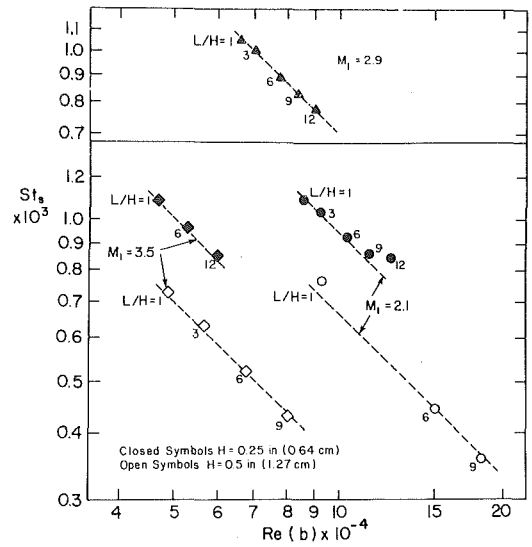

Fig. 7 Variation of minimum Stanton number in open cavities [8] with Reynolds number based on maximum thickness of free shear layer

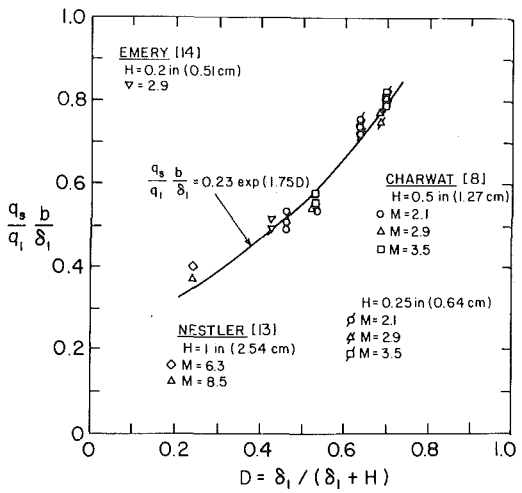

Fig. 8 Final correlation of q_s/q_1 with D for turbulent cavity flows

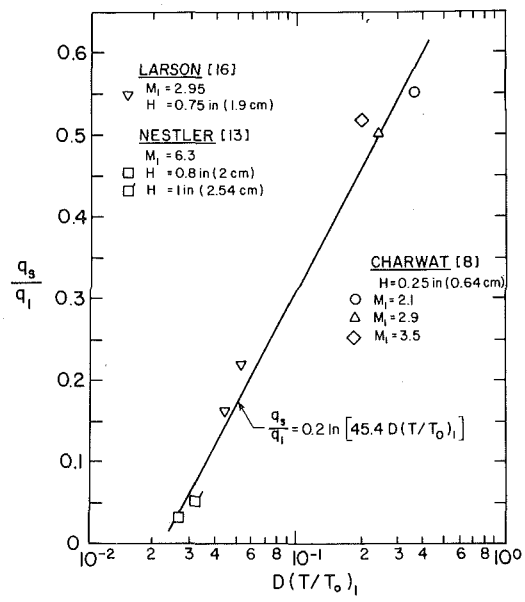

Fig. 9 Correlation of q_s/q_1 for turbulent base and backstep geometries

zero cannot be determined by the data. The final correlation for turbulent flow over cavities is therefore

$$\mathrm{St}_s = \mathrm{St}_1[\delta_1/b(L)]0.23\exp(1.75D)$$

in which all Mach number influences are apparently included in the value of δ_1 and $b(L)$.

Data showing the variation of q_s/q_1 for backsteps and blunt base flows, although sparse, indicate a strong inverse relationship between this heat transfer ratio and M_1. Such a conclusion is in agreement with the earlier theoretical results of Lamb and Hood [17] which showed that base heat transfer in the turbulent regime was almost completely controlled by flow conditions immediately downstream of the corner expansion. As in the laminar case one can use $(T_0/T)_1$ as a weighting factor for D. However for turbulent flow the inverse relationship between these two parameters requires semilogarithmic coordinates as shown in Fig. 9 which also includes a correlation curve expressed by

$$\mathrm{St}_s = 0.2\,\mathrm{St}_1 \ln[45.4\,D(T/T_0)_1].$$

Concluding Remarks

The present investigation of convective transport in supersonic separated flows has demonstrated that correlation of the minimum level of heat transfer is possible for a wide range of geometries and flow conditions. In particular it was shown that the effects of approaching boundary layer and characteristic width of the separated zone can be correlated with a single geometric parameter. Simple relationships between the geometric correlation parameter and the ratio of heat transfer rates before and after separation were demonstrated for a variety of geometries including backsteps, open cavities, and cylinders of arbitrary cross-section. For decreasing values of the characteristic width (with constant upstream boundary layer thickness) it was demonstrated that the minimum heat transfer approaches the cor-

responding upstream value in both laminar and turbulent regimes. A lower limiting value of separated heat transfer for thin boundary layers was demonstrated for laminar flow and was suggested by turbulent flow data. Use of the free shear layer thickness was demonstrated to correlate the effect of length/depth ratio for open cavities in turbulent flow whereas the corresponding correlations for base and backstep flows indicated a relatively strong influence of free stream Mach number.

The proposed correlation equations are considered as provisional until more extensive data are available. However, it is believed that physically significant correlation parameters have been identified. It is anticipated that the present approach could be extended from the consideration of a single characteristic heat transfer level (i.e., minimum value) to provide some correlation of the distribution of separated heat transfer.

References

1 Berger, S. A., *Laminar Wakes*, American Elsevier, New York, 1971.

2 Fletcher, L. S., et al., "Heat Transfer in Separated and Reattaching Flows: An Annotated Review," *Israel Journal of Technology*, Vol. 12, Mar.–Apr., 1974.

3 Chilcott, R. E., "Separated and Reattaching Flows with Heat Transfer," *International Journal of Heat and Mass Transfer*, Vol. 10, No. 6, June 1967, pp. 783–797.

4 Bulmer, B. M., "Heat-Transfer Measurements in a Separated Laminar Base Flow," *Journal of Spacecraft and Rockets*, Vol. 14, No. 11, Nov. 1977, pp. 701–702.

5 Jakubowski, A. K., and Lewis, C. H., "Rearward-Facing Steps in Laminar Supersonic Flows With and Without Suction," AIAA Paper No. 73-667, Palm Springs, CA, July 16–18, 1973.

6 Lamb, J. P., and Mruk, G. K., "Leeward Heat Transfer Experiments on the Shuttle Orbiter Fuselage," *Journal of Spacecraft and Rockets*, Vol. 13, No. 11, Nov. 1976, pp. 701–703.

7 Bertin, J. J., et al., "Flow Field Measurements for Space Shuttle-Related Cylindrical Configurations in Hypersonic Streams," AIAA Paper No. 72-294, San Antonio, TX., Apr. 10–13, 1972.

8 Charwat, A. F., et al., "An Investigation of Separated Flows—Part II: Flow in the Cavity and Heat Transfer," *Journal of Aerospace Sciences*, Vol. 28, No. 7, July 1961, pp. 513–527.

9 Holloway, P. F., et al., "An Investigation of Heat Transfer Within Regions of Separated Flow at a Mach Number of 6.0," NASA TN D-3074, Nov. 1965.

10 Hahn, M., "Experimental Investigation of Separated Flow Over a Cavity at Hypersonic Speed," *AIAA Journal.*, Vol. 7, No. 6, June 1969, pp. 1092–1098.

11 Nicoll, K. M., "A Study of Laminar Hypersonic Cavity Flows," *AIAA Journal*, Vol. 2, No. 9, Sept. 1964, pp. 1535–1541.

12 Wieting, A. R., "Experimental Investigation of Heat-Transfer Distributions in Deep Cavities in Hypersonic Separated Flow," NASA TN D-5908, Sept. 1970.

13 Nestler, D. E., et al., "Heat Transfer to Steps and Cavities in Hypersonic Turbulent Flow," *AIAA Journal*, Vol. 7, No. 7, July 1969, pp. 1368–1370.

14 Emery, A. F., *et al.*, "Heat Transfer and Pressure Distribution in Open-Cavity Flow," ASME JOURNAL OF HEAT TRANSFER, Vol. 89, No. 1, Feb. 1967, pp. 103–108.

15 Larson, R. E., et al., "Heat Transfer Below Reattaching Turbulent Flows," AIAA Paper No. 65-825, San Diego, CA, Dec. 13–15, 1965.

16 Lamb, J. P., "An Approximate Theory for Developing Turbulent Free Shear Layers," *Trans. ASME*, Vol. 89, No. 3, 1967, pp. 633–642.

17 Lamb, J. P., and Hood, C. G., "Theoretical Distributions of Heat Transfer Downstream of a Backstep in Supersonic Flow," ASME JOURNAL OF HEAT TRANSFER, Vol. 94, No. 1, Feb. 1972, pp. 87–94.

A Study of the Heat Transfer Mechanisms in Horizontal Flame Propagation

S. R. Ray
A. C. Fernandez-Pello[1]
I. Glassman

Department of Mechanical and Aerospace Engineering,
Princeton University,
Princeton, N.J. 08540

An experimental study is performed on the magnitude of the different mechanisms by which heat is transferred from the flaming region to the unburnt fuel ahead of the flame for flames propagating horizontally over the surface of a solid fuel. Measurements of the gas velocity field, temperature fields and radiant flux distribution in a particular case of laboratory scale flame spread over a thick fuel are used to determine the magnitude of the heat fluxes ahead of the flame. The results show that, for this particular case, although heat conduction through the solid is dominant, radiation from the flame contributes significantly to the heat transfer process. An analysis of the development of the fire indicates that there is a transition in the mechanisms of heat transfer as the fire grows. While in the early stages of the fire, heat conduction through the solid is dominant, radiation from the flame becomes of increased importance as the size of the fire increases.

1 Introduction

The central process in the spread of fire along the surface of a solid fuel is heat transfer from the burning region of the fuel to the unignited material. The three principal mechanisms by which this heat transfer may occur are radiation from the flame, conduction or convection through the gas ahead of the flame, and conduction through the solid. All three mechanisms are involved to some extent and it is often difficult to determine which is dominant. An understanding of the dominant mode of heat transfer will facilitate the development of simplified and accurate descriptions of the fire spread process and thus give insight into possible means of control.

When this study was begun, although a large amount of quantitative information had been reported on the mechanisms of heat transfer in downward flame spread [1–5], there were, to the knowledge of the authors, only qualitative observations on the horizontal mode of flame propagation reported in the literature [1, 3]. However, while the research was in progress, the authors became aware of a reprint [6], published in a Japanese journal, in which this problem was addressed. The present investigation was conceived with the somewhat broader scope of performing a detailed analysis of the gas phase heat transfer phenomenon as well as investigating the possible influence of radiative heat transfer from the flame in an attempt to explain the observed differences in the magnitude of the spread rate for horizontal and downward flame propagation [3]. The purpose of this paper is to present the results of our measurements, which basically agree with those of reference [6], of the magnitude of the heat conducted through the solid for a thermally thick fuel and, in addition, to illuminate certain aspects of the problem, particularly the importance of flame radiation as a function of the magnitude of the fire and its role in producing a larger flame spread rate for the horizontal mode of flame propagation.

If radiation from the flame to the nonburning fuel plays a significant role in the heat transfer process, its influence will differ according to the magnitude of the fire. In the very early stages of the flame propagation process the flame size will be small and consequently it is expected that the magnitude of the radiant flux will also be small. For large scale fires, it is valid to presume that radiation from the flames will be the dominant mode of heat transfer. This dependence of the influence of flame radiation on the magnitude of the fire brings the question of what scale of experiment would be more realistic for a fundamental study. In this work we have approached the problem by performing an accurate study of the mechanisms of gas and solid phase heat transfer, and of radiation from the flame for a particular case of laboratory scale flame propagation. This case which we define as basic in this work was selected such that a two-dimensional, steady-state flame propagation occurs. The dimensions of the fuel specimen (size of the fire) are comparable to those of other experiments for vertically downward spread [3, 5, 6] so that the differences between both modes of propagation can be analyzed. The results of this basic experiment are used in combination with measurements of flame radiative fluxes and phenomenological arguments to study the heat transfer mechanisms taking place during the initiation of the fire where a transient spread process occurs. Measurements on a somewhat larger scale experiment are used in combination with previous results to deduce by extrapolation the eventual dominant influence of radiative heat transfer in a large scale fire.

2 Experimental Installation

The main reason for the scarcity of information on the horizontal mode of flame propagation in comparison with that obtained for downward flame spread is the difficulty of attaining stable conditions of the flame plume and gas flow induced naturally by the flame. In horizontal flame spread, the fluid mechanical characteristics of the flame plume and induced gas flow are very sensitive to external perturbations making it difficult to perform the experiments with conventional methods.

To carry out the work presented in this paper, a sophisticated experimental installation has been constructed and applied to the measurement of the heat transfer parameters involved in the horizontal propagation of flames in a natural convective environment. The experiments are carried out in a quiescent test cell, with the operation of the experiment automatically controlled from outside the test cell to avoid perturbations in the flame induced flow field by environmental air currents. A schematic diagram of the experimental installation is shown in Fig. 1. The facility consists of a two-dimensional laser doppler velocimeter (LDV), a thermocouple and radiometry probing system and an optical indicator of flame location. Simultaneous measurement of the flame spread rate, the gas flow velocity, the temperature, and the arrival of the flame front at the location of the measurements are obtained and recorded in a real time data acquisition system.

Most of the experiments are performed with flat sheets of polymethylmethacrylate (PMMA) 0.30 m long, 0.15 m wide and 25 mm thick (thermally thick fuel). PMMA is used as a fuel because its properties are well known and its burning mechanisms are orderly and reproducible. Further experiments with fuel thicknesses closer to the thermally thin limit were considered unnecessary since they had been performed by the investigators of reference [6], and the results of the

[1] Present address: Department of Mechanical and Nuclear Engineering, Northwestern University, Evanston, ILL 60201.

Contributed by the Heat Transfer Division for publication in the JOURNAL OF HEAT TRANSFER. Manuscript received by the Heat Transfer Division December 6, 1979.

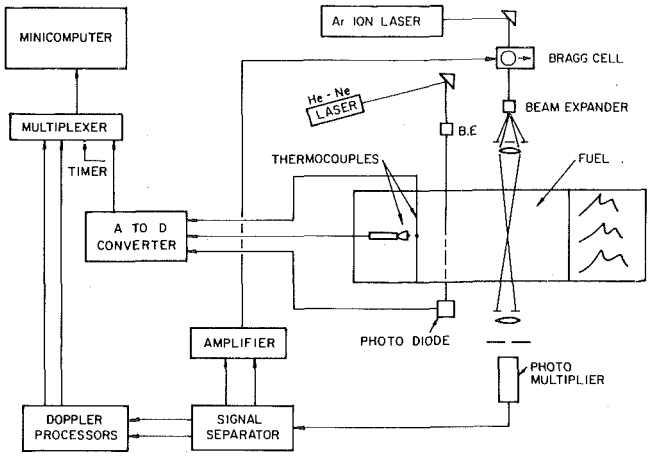

Fig. 1 Schematic diagram of the experimental installation

present work for the conductive and convective heat fluxes in a thick fuel basically agree with the results of that study. PMMA sheets 0.30 m wide are used to measure radiative heat fluxes when attempting to represent a larger scale fire.

For the experiments, the PMMA sheets are mounted in a metallic frame which is located on a lathe-bed to allow accurate positioning of the fuel specimen with respect to the experimental apparatus. The bottom surface of the fuel sheet is insulated from the metallic frame by sheets of an insulating material (fiber frax). Strips of the insulating material are also used as inhibitor along the edges of the fuel sheet to prevent preferential flame spread along the edges. The flame spreading process is initiated at one end of the fuel sheet by igniting a small amount of acetone deposited on a groove previously machined along the upstream edge of the PMMA sheet. Along the central portion of the sheet, except within approximately 10 mm of the edges, the front of the flame is a straight line, thus assuring two-dimensionality in the flame spread process.

During the experiment, the fuel and the experimental apparatus are kept stationary with respect to laboratory coordinates, and the flame moves toward the location of the measurements. Since the flame spread rate is very slow ($0(10^{-4}$ m/s)) and the characteristic time for changes in the magnitude of the parameters to be measured is large (0(1 s)), the value of the measurements practically correspond to stationary conditions. Before performing the measurements, the flame is allowed to spread for up to 0.10 m so that steady conditions are insured. We believe that this last experimental procedure is particularly important in the horizontal mode of flame propagation where the size of the flame may play a critical role not only in the magnitude of the radiant flux from the flame, but also in the magnitude of the entrained air flow. When analyzing the case of the initiation of the fire, measurements are obtained continuously from the moment that the flame has spread 5 mm from its initiation. Since the spread rate is time dependent during this period, its value is measured at 5 mm intervals.

Because the accurate knowledge of the relative position of the flame front with respect to the location of the measurements is critical in the interpretation of the results (the gradients are large near the flame front), an optical indicator employing a low power laser and a photo-diode is used to determine within 0.1 mm the position of the flame front. The arrangement of the indicator employed in this work is particularly suitable for a transparent fuel such as PMMA. It makes use of the fact that for PMMA, the flame front sharply defines two regions which have different optical properties. While the unignited PMMA is transparent to the light, the burning region is practically opaque, thus allowing the optical determination of the location of both regions. A schematic diagram of the optical indicator is shown in Fig. 1. The laser beam is directed perpendicular to the PMMA surface, passes through the PMMA and is detected by a photo-diode. The voltage output of the photo-diode is amplified and fed to the data acquisition system so that the photo-diode signal is recorded simultaneously with the output from the measuring instruments. Since the output of the photo-diode is proportional to the percentage of laser beam that passes through the PMMA, the arrival of the flame is determined by the sudden drop in the photo-diode voltage output. To increase the spatial resolution in the determination of the flame front, a 3X beam expander is used to focus the laser beam waist at the PMMA surface. The resolution of the optical indicator was determined by comparing its output to surface temperature measurements obtained from a Chromel-Alumel thermocouple 0.025 mm in diameter, the bead of which is embedded in the PMMA surface at the position of interception of the laser beam with the PMMA surface.

In the experiment, all the measuring instruments are positioned at known locations with respect to the location of the laser beam of the optical indicator. The real time data acquisition system is started by a microswitch that is triggered manually when the flame front arrives at a distance of 50 mm from the indicator laser beam. The data

Nomenclature

c = specific heat (KJ/K_g K)
F = radiant flux absorbed at the fuel surface (W/m^2)
h = total heat transfer coefficient (W/m^2 °C)
L = fuel thickness (m)
Q_{cg} = heat conducted inward through the gas at the x boundary of the control volume in the gas,

$$Q_{cg} = \int_0^\infty \lambda_g \frac{\partial T_g}{\partial x} dy \text{ (W/m)}$$

Q_{cs} = heat conducted inward through the solid at the x boundary of the control volume in the solid,

$$Q_{cs} = \int_{-L}^0 \lambda_s \frac{\partial T_s}{\partial x} dy$$

Q_{cvg} = heat convected outward through the gas at the x boundary of the control volume in the gas,

$$Q_{cvg} = \int_0^\infty \int_{-\infty}^{-x} \rho_g c_p \times \left[U_x \frac{\partial T_g}{\partial x} + U_y \frac{\partial T_g}{\partial x}\right] dxdy$$

Q_R = heat transferred by radiation up to a distance −x from the flame front,

$$Q_R = \int_{-\infty}^{-x} F dx$$

Q_{rr} = heat reradiated at the fuel surface up to a distance $-x$ from the flame front

$$Q_{rr} = \int_{-\infty}^{-x} \epsilon\sigma(T_w{}^4 - T_\infty{}^4) dx$$

Q_T = net outward heat flow in the control volume of the solid,

$$Q_T = \int_{-L}^0 \rho_s V \left[\int_{T_\infty}^T c_s dT_s\right] dy$$

Q_w = heat conducted through the solid gas interface up to a distance −x from the flame front,

$$Q_w = \int_{-\infty}^{-x} \lambda \frac{\partial T}{\partial y} dx$$

T = temperature (K)
t = time (s)
U = component of the gas velocity (m/s)
V = flame spreading velocity (m/s)
x = coordinate parallel to the fuel surface (m)
y = coordinate normal to the fuel surface (m)
ϵ = emissivity of the fuel
λ = thermal conductivity (W/m K)
ρ = density (K_g/m^3)
σ = Stefan-Boltzmann constant

Subscripts

g = gas
s = solid
x = x direction
y = y direction
w = fuel surface
∞ = ambient

acquisition is terminated by a second microswitch, triggered when the flame arrives at a distance of 10 mm after the indicator laser beam. The elapsed time marked by the triggering of the microswitches and drop in the photo-diode voltage output is used to determine the flame spread rate. The spread rate and position of flame arrival is used to convert the time dependence of the measured parameters into space dependence with respect to the position of the flame front.

3 Pathways of Heat Transfer for Basic Case

As we have mentioned before, an accurate study of the mechanisms of heat transfer is performed for a particular case of laboratory scale flame propagation. The study includes measurements of the gas velocity field, temperature fields and radiation from the flame to the fuel surface. These measurements are used to construct energy balances to determine the relative importance of the different modes of heat transfer affecting the flame spread process.

3.1 Gas Phase Velocity Measurements. Velocities of the gas flow induced by natural convection by the flame plume were measured with a two-dimensional Laser Doppler Velocimeter (LDV) facility. The LDV, which is described schematically in Fig. 1, utilizes a 2W argon-ion laser and a two-dimensional ultrasonic Bragg Cell used to split the laser beam into four components. Four beams converging into the LDV probe volume allow the determination of two components of the velocity vector. The doppler frequencies are processed in an electronic counter (burst processor) and fed to a real time data acquisition system (Hewlett-Packard 32K minicomputer). A more detailed description of the LDV facility can be found in reference [7].

The experimentally measured gas velocity field upstream from the flame front is shown in Fig. 2. The arrows correspond to the velocity vector at characteristic locations ahead of the flame. The coordinate system adapted is indicated in Fig. 6. From the results of Fig. 2, it is seen that the flow field presents a slight convergence toward the fuel surface with the horizontal component of the velocity increasing slightly toward the flame front. Measurements of the gas velocity far from the fuel surface (not represented in the figure) show that the gas velocity reaches a maximum of approximately 0.16 m/s at 20 mm from the fuel surface, and from then on decreases with the distance from the surface. It is seen from the results that the entrainment of air from the flame plume affects a considerable region of the gas field in a uniform manner.

3.2 Temperature Measurements. Solid and gas phase temperature histories upstream from the flame front were measured by means of thermocouple probing. The emf's from the thermocouples are electronically amplified to volt levels, analog to digital converted and recorded in the real time data acquisition system (see Fig. 1). The temperature histories are then translated into profiles of temperature versus distance from the flame front by use of the measured flame spread rate.

Surface and solid phase temperature histories were obtained with Chromel-Alumel thermocouples 0.025 mm in diameter. The technique described in reference [4] was used to position the thermocouples at the PMMA surface and along several isotherms within the interior of the fuel. Gas phase temperature histories were measured with Platinum-Platinum 13 percent Rhodium thermocouples 0.025 mm in diameter coated with a noncatalytic compound [8]. For the measurements the thermocouples were positioned at several distances normal to the fuel surface by means of a micro-manipulator.

The temperature profiles were used to produce the temperature fields within the solid and gas phases shown in Fig. 3. Technical difficulties involved in measuring the temperature very close to the surface in the solid [4, 5] prevented us from obtaining data at distances closer than 0.5 mm from the interface. For this reason, in Fig. 3 the temperature gradients near the fuel surface are reported as dotted lines to indicate their approximated nature. From the gas phase temperature field it is seen that there is heat input from the gas to the solid for $x > -2$ mm and from the solid to the gas for $x < -2$ mm. The solid phase temperature field shows that the heated region in the solid not only extends beyond that of the gas, but far beyond the region expected to be heated by conduction through the solid [3, 5]. This

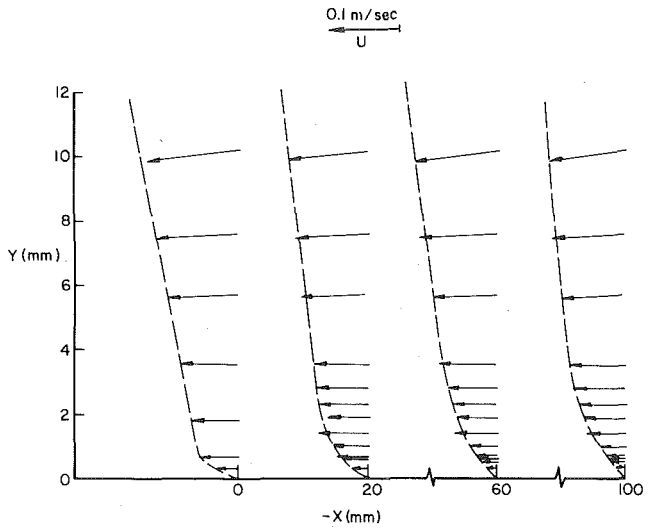

Fig. 2 Gas velocity field at several distances upstream from the flame front for horizontal flame spread along PMMA sheets 2.54 cm thick

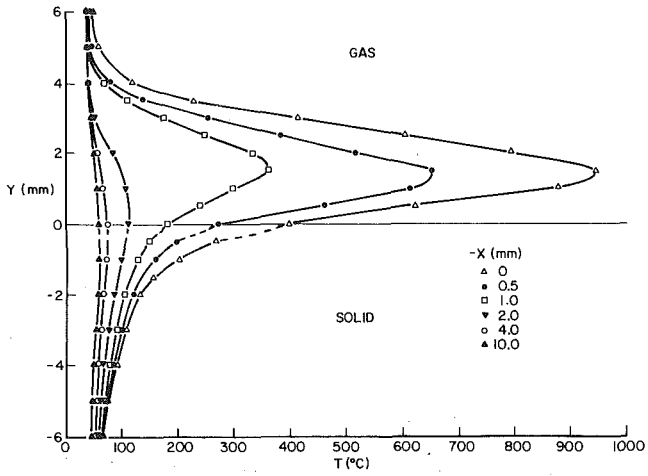

Fig. 3 Temperature fields upstream from the flame front for horizontal flame propagation along PMMA sheets 2.54 cm thick

qualitative observation suggests that radiative heat transfer from the flame to the virgin material may have a significant role in the fuel heating process. Comparison of the surface temperature profiles shown in Fig. 4 for flames spreading over the same fuel (PMMA) and thickness (25.4 mm) in the downward configuration (negligible radiation [3, 5]) and in the horizontal mode of flame propagation also shows a more extended region of elevated surface temperature for this last case, thus emphasizing the potential role of radiative heat transfer in horizontal flame spread.

3.3 Radiant Flux Measurements. From the arguments stated in the previous section, it appears that a mechanism of heat transfer that can be of significant importance in the horizontal mode of flame propagation is radiation from the flame to the unburnt fuel ahead of the flame. Radiant fluxes at the surface of the fuel in front of the flame are difficult to measure with conventional instruments because of the perturbing influence of the radiometer on the flame spread process. Commercially available radiometers are bulky and if positioned in front of the flame, the gas flow field is disturbed, changing the flame spread characteristics. If the radiometer is embedded in the fuel, the sensing element of the radiometer could lie below the fuel surface, the view angle would be distorted and the radiation reading would become meaningless. In an attempt to measure the radiant flux at the fuel surface, various techniques were used, including a nonperturbing

radiometer specifically developed for this work. The concept of operation of this radiometer is similar to that developed by Kosdon [9], but is adapted for this particular case so that the flame spread process is not disturbed. Two equal lengths (5 mm) of platinum resistance wire 0.025 mm in diameter are employed in the sensing element of the radiometer. The sensor wires are placed slightly below the fuel surface in a groove following the isothermal line perpendicular to the direction of flame propagation (Fig. 5). An Irtran II window is mounted flush to the fuel surface to avoid convective disturbances on the radiometer wires. One of the sensing wires has an absorbing coating (candle soot) while the other is uncoated. Upon exposure to radiation, the temperature of the blackened wire rises and its electrical resistance increases; the temperature of the uncoated wire changes little since it reflects radiation. The change in difference of the resistance between the two wires is therefore a function of the incident radiant flux. The resistances of the two wires form two arms of a Wheatstone bridge, which is balanced initially and whose imbalance voltage is recorded as a calibrated measure of the radiant flux. A temperature-controlled blackbody source was used, following the method described in reference [9], as the standard for the radiometer calibration.

The advantage of this radiometer is that the sensor is small enough to measure in a continuous mode essentially pointwise radiant fluxes without perturbing the flame spread process. The main problem in applying this radiometer to the present measurements is the need for approximate correlations between the calibration outputs and the actual experimental outputs. While the calibration is performed under the valid assumption that the wire sensors act as flat detectors, when the emitter has a large surface this assumption is no longer valid and corrections must be applied to account for the curvature of the wires. Further corrections are also needed to account for the absorption and reflection of radiation by the Irtran window (see Fig. 5) which are a function of the angle of incidence of the radiant flux.

To corroborate the measurements of the radiant flux obtained with the wire radiometer, several other radiometers were also used. One method uses a Sensor Inc., Type Cl thermopile which is mounted in a water cooled brass casing with the thermopile window placed flush with the casing surface. Because the active area of the thermopile is located 1.5 mm below the window, the application of this type of radiometer to the present experiment is not straightforward. If the measurements are performed with the radiometer mounted flush with the fuel surface, the sensor view angle of the flame is smaller than that of the fuel surface, and corrections are required to account for the effects of reflection by the window and smaller view angle. If the radiometer is placed vertically protruding from the fuel surface, the gas flow pattern is perturbed, the flame leans toward the radiometer and the measured radiant flux is larger because of a larger view angle and a closer flame. In this work we have approached the problem by performing the measurements in two different ways. One is to measure the radiant flux distribution with the radiometer mounted flush with the fuel surface. The other is to measure the radiant flux with the radiometer placed vertically, but exposing the radiometer to the flame for brief periods of time to minimize perturbations of the flame. Approximate corrections for view angles were then applied to this last measurement.

A third radiometer which operates on a continuous basis is manufactured by ITI. It is a solid state transducer in the form of a thin square flat plate, 12.8 mm long and 1.4 mm thick, coated with a high absorptivity ceramic. The advantage of this technique is that the detector can be placed flush with the surface so as to have the same radiation factor as the fuel surface. Although no estimates of flame shape or size are required for a view factor correction, a calibration of the radiometer is still necessary. Therefore, in principle the only difference between the radiation absorbed by the detector and a similar area of fuel is the fraction which is reflected from the fuel surface.

From the description of the radiometers used in the experiments it is seen that their application has implicit corrections which often require estimations of flame size and position with respect to the radiometer location. To further confirm the magnitude of the radiant flux at the fuel surface, we have used alternative noncontinuous

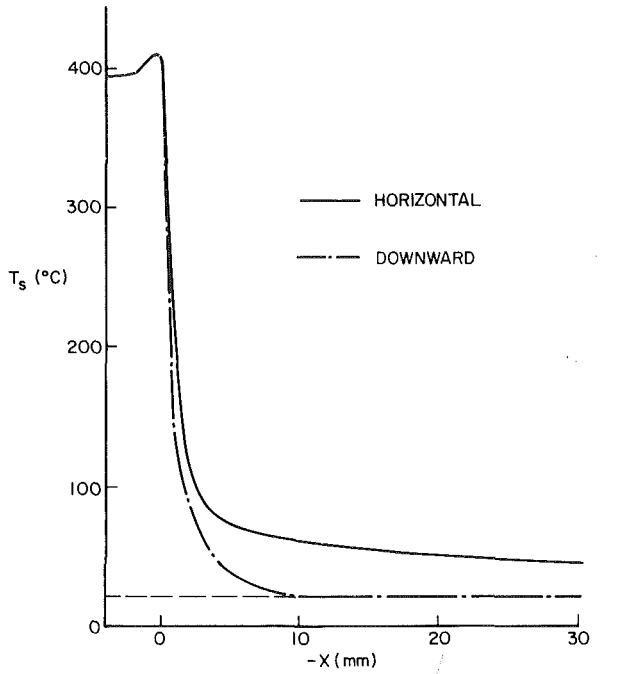

Fig. 4 Comparison of surface temperature profiles for horizontal and downward flame spread over PMMA sheets 2.54 cm thick

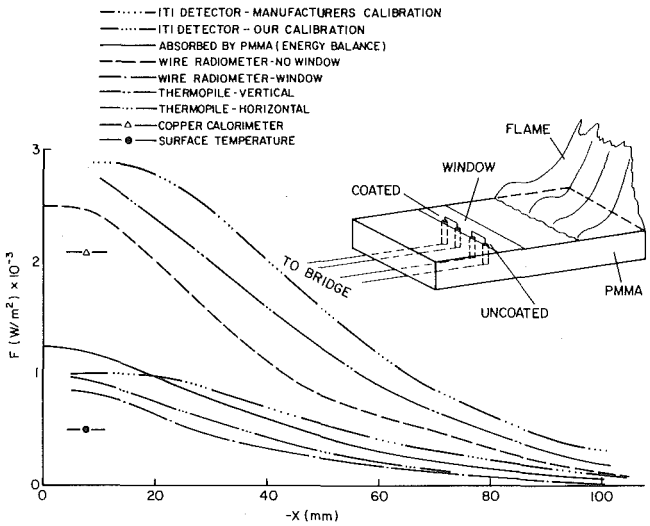

Fig. 5 Radiant flux distribution at the fuel surface ahead of the flame for horizontal flame spread along PMMA sheets 2.54 cm thick

methods to estimate quantitatively the radiant flux received by the surface near the flame front. One of the methods follows the procedure employed by Sibulkin and Hansen in the work of reference [10]. A strip of copper 5 mm wide, 60 mm long and 5 mm thick, is embedded flush with the PMMA surface following an isotherm and insulated from the PMMA by strips of an insulating material. A Chromel-Alumel thermocouple is bonded to the bottom surface of the copper strip and a black coating is applied to its top surface to ensure absorption of radiation. The copper is suddenly exposed to the flame radiation and its temperature recorded. The transient increase of the copper temperature is used in conjunction with its heat capacity to estimate the radiant energy received by the copper strip. Another indirect method used to estimate the radiant flux received by the PMMA surface near the flame front was to calculate the necessary radiant energy required to produce the measured profile of surface temperature. Since the fuel can be considered as a thermally thick

fuel, and the radiant flux within 10 mm from the flame front is practically constant (see Fig. 5), the theoretically predicted rise in surface temperature is given by [11]

$$\Delta T_s = (F/h)\{1 - \exp[h^2 t/(\lambda_s \rho_s c_s)] \cdot \mathrm{erfc}[h(t/(\lambda_s \rho_s c_s)^{1/2}]\}$$

where h is a global heat transfer coefficient-convection plus linearized radiation. The surface temperature profile of Fig. 4 is used in the above equation to calculate the radiation absorbed by the PMMA surface (h = 25 W/m^2 °C). Although there is limited information available [12, 13], both effects are complicated functions of the wavelength and angle of incidence of the flame-emitted radiation, and their consideration implies further assumptions and corrections.

From the above arguments it is seen that a large number of uncertain estimations and corrections are required in order to provide a quantitative value of the radiant energy absorbed at the PMMA surface. For this reason, in presenting the results of Fig. 5 we have opted for reporting all the results obtained with the different techniques currently used in this work. Figure 5 shows that a wide range of radiant flux distributions were obtained according to the measuring technique employed. For comparative purposes the radiant flux distribution deduced from the energy balance in the solid phase (Fig. 6) has also been included in the figure. It is seen that the results of the energy balance are within the range of the measurements. The fact that the deduced distribution agrees better with the results obtained under the conditions simulating the fuel surface, reinforces the validity of the conclusions and suggests that reflection of radiation by the PMMA surface may be significant. Further information that can be deduced from the results of Fig. 5 is that the radiant flux received by the fuel is practically constant within 10 mm from the flame front. This indicates that at such a small distance from the flame front, the fuel sees the flame as an infinite emitter.

3.4 Energy Balance. Energy balances constructed through the measurements of gas velocity, temperature and radiant flux fields are a direct means for analyzing the relative magnitude of the pathways of heat transfer from the flame to the nonburning solid. Although the energy balance for the gas phase is not necessary to determine the pathways of heat transfer, it can produce useful information about the effect of the flame induced air flow on the streamwise gas phase heat conduction. In addition, it can corroborate the results of the solid phase energy balance.

With the control volumes illustrated in Fig. 6, and the coordinate system anchored to the flame front, conservation of energy along the solid phase control volume gives (V = constant, $U_x \gg V$)

$$\int_{-L}^{0} \rho_s V[\int_{T_\infty}^{T} c_s \, dT_s]dy = \int_{-L}^{0} \lambda_s \frac{\partial T_s}{\partial x} dy + \int_{-\infty}^{-x} \lambda_g \frac{\partial T_g}{\partial y} dx + \int_{-\infty}^{-x} F dx - \int_{-\infty}^{-x} \epsilon\sigma(T_w^4 - T_\infty^4)dx \quad (1)$$

Conservation of energy along the gas phase control volume gives

$$\int_0^\infty \int_{-\infty}^{-x} \rho_g c_p \left[U_x \frac{\partial T_g}{\partial x} + U_y \frac{\partial T_g}{\partial y}\right] dxdy = \int_0^\infty \lambda_g \frac{\partial T_g}{\partial x} dy + \int_{-\infty}^{-x} \lambda_s \frac{\partial T_s}{\partial y} dx \quad (2)$$

In the above energy balances, the terms corresponding to the solid and gas reactions have been neglected. They are difficult to estimate and it is not expected that they will contribute significantly to the overall heat balance.

The results of the integration of the several terms involved in equations (1) and (2) are shown in Fig. 6. The temperature dependent thermophysical properties of PMMA used in the calculations are [5, 14]: $\rho_s = 1.19 \times 10^3$ kg/m^3, $c_s = -0.247 + 5.69 \times 10^{-3}\, T$ kJ/kg K, $\lambda_s = -1.0 + 6.32 \times 10^{-3}\, T - 1.03 \times 10^{-5}\, T^2 + 5.57 \times 10^{-9}\, T^3$ W/m K. The dependence on temperature of the thermophysical properties of air was obtained from reference [15]. The measured flame spread rate is $V = 5.98 \times 10^{-2}$ mm/s.

The quantitative results shown in Fig. 6 for the solid phase energy balance provide information about the relative importance of the different modes of heat transfer from the flaming region to the nonburning fuel ahead of the flame. Comparison of the magnitude of the terms corresponding to the net heat flow in the control volume of the solid, Q_T, and the heat conducted inward through the solid at the x = 0 boundary, Q_{cs}, shows that up to 60 percent of the total heat transferred from the flame to the unignited fuel is conducted through the solid. The computation of the heat flux at the solid-gas interface shows that the overall heat flow conducted through the gas from the flame is negligible. It can thus be concluded that up to 40 percent of the energy required to heat the solid to its pyrolyzing temperature is transferred by radiation from the flame. The difference between the calculated total heat flow, Q_T, and the heat conducted through the solid Q_{cs}, convected at the interface, Q_{wg}, and reradiated from the fuel surface, Q_{rr}, provides the radiant flux absorbed by the fuel, Q_R, which would verify the energy balance in the solid phase. The deduced value is shown in Fig. 6. It was used to obtain the radiant flux distribution absorbed at the fuel surface shown in Fig. 5. The difference between the calculated radiant flux absorbed by the fuel, Q_R, and that reradiated at the fuel surface, Q_{rr} corroborates qualitatively this result. The fact that quantitatively this difference does not balance exactly the energy conservation (its magnitude is larger than 40 percent of the net heat flow), is justified by the number of assumptions needed to estimate the radiant flux absorbed and reradiated by the fuel.

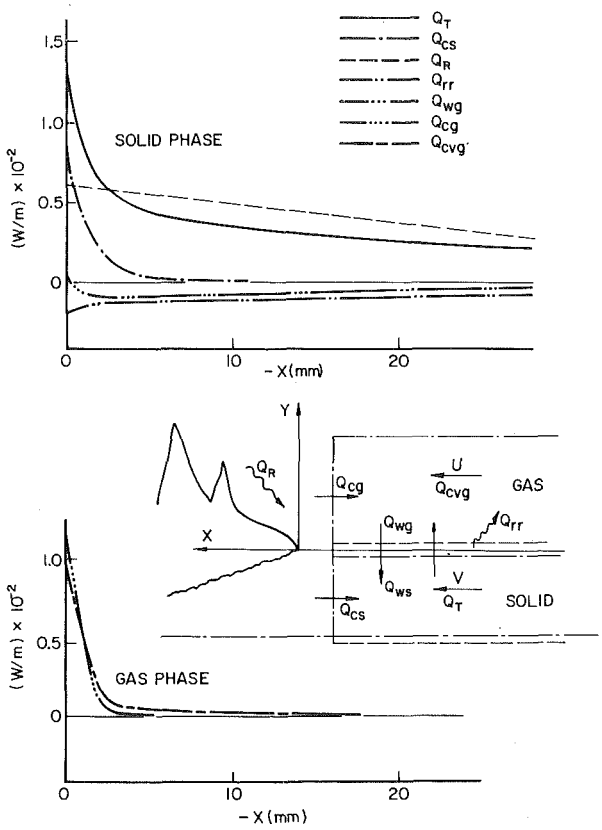

Fig. 6 Distribution of heat fluxes ahead of the flame for horizontal flame propagation along PMMA sheets 2.54 cm thick

Complementary information about the heat transfer process ahead of the flame is obtained through the results of the gas phase energy balance (Fig. 6). The heat flux at the interface, Q_{ws} is not computed because of the uncertainties of the temperature gradients in this region (Section 3.2). However, comparison of the magnitudes of the convective (or net) heat term in the gas phase, Q_{cvg}, and the heat conducted upstream through the gas at the x boundary, Q_{cg}, shows that the heat flux at the interface Q_{ws} (equation (2)) is of the same order of magnitude as Q_{wg}, thus verifying the energy balance in the solid phase control volume. The fact that the conductive term is only

slightly larger than the convective term at distances smaller than 2 mm from the flame front corroborates previous deductions that radiation from the flame is the only mechanism of heat transfer contributing to the heating of the fuel far away from the flame front. Finally, from the values of the conductive and convective terms, it is also observed that a substantial amount of the energy conducted through the gas from the flame goes into heating the incoming air flow. Thus, convective effects due to the entrainment of air by the flame plume play an important role in the ability of the heat to be conducted through the gas from the flame.

The above qualitative and quantitative information about the pathways of heat transfer in horizontal flame spread clearly indicates that, at least for thermally thick fuels, radiation energy transfer from the flame to the nonburning fuel plays a significant role in this mode of flame propagation.

It is interesting to note, however, that the heat transferred by radiation is a small but cumulative process. The radiant flux per unit area itself is small (Fig. 5) but affects a very long region ahead of the flame. When the conduction and radiation effects are compared near the flame front (Figs. 4 and 6) it is seen that the increase of heat flux due to radiation is very small in comparison with that of conduction. Thus, the influence of the flame radiation on the flame spread process could be considered approximately as a fuel preheating mechanism. Analytically, radiation could be treated as affecting only the initial temperature of the fuel, and the flame spread process could be modeled in first approximation neglecting the radiation term.

Particularly interesting is the comparison of these results with those obtained for downward flame spread over thermally thick fuels [3, 5]. While the heat conducted through the solid is approximately the same for both modes of flame propagation, this heat flux accounts for practically the whole energy transfer in downward flame spread, whereas in the horizontal mode it accounts for only 60 percent of the total heat transferred from the flame to the non-burning fuel. The additional energy is transferred into the solid by radiation from the flame. Since the fluid mechanical and thermal characteristics of the gas upstream from the flame front are similar for both modes of flame propagation, it can be concluded that radiant heat transfer from the flame is the principal reason for the larger (approximately 30 percent) flame spread rates observed for horizontal flame spread.

4 The Effect of the Fire Scale

In this section, the effect of the fire scale on the relative importance of the different mechanisms of heat transfer in horizontal flame propagation is analyzed. Partial measurements and phenomenological arguments will be used in conjunction with the results of the basic case to deduce the influence of the size of the fire in this mode of flame spread.

4.1 Early Stages of the Fire. During the initiation and very early stages of the fire, the propagation process is characterized by an initial small flame which increases in size as the flame propagates across the fuel surface. In comparison with the basic experimental case (previous section), a smaller flame will result in a small radiative flux impinging upon the fuel surface and lower entrained air velocities opposing the propagation of the flame (higher conductive fluxes through the gas phase). Since the surface temperature of the fuel already burning will be practically constant [16, 17], the heat conducted through the solid ahead of the flame will also be constant and practically independent of the size of the fire. Thus it can be expected that the flame propagation rate will increase very fast initially (until solid conduction is established) and from then on the spreading rate will increase slowly as the contribution of the radiation from the flame increases.

In an attempt to verify the above deductions we have performed some experimental measurements of the parameters we feel are more indicative of the flame spread process. The experiments were performed with PMMA sheets of the same width and thickness as in the basic case, but with the flame propagating from a fuel burning region (pyrolysis length) of 5 mm up to fire sizes of the order of those for which the basic experiment was performed. Measurements of the radiant flux at the fuel surface near the flame front as a function of the pyrolysis length (flame size) were obtained by placing the radiometer at 10 mm from the upstream edge of the fuel sheet (the edge inhibited with insulating material), and by recording continuously the radiant flux as the flame propagated in the opposite direction. The results showed the radiant flux increasing monotonically from a value of approximately 209 W/m^2 for a pyrolysis length of 5 mm up to values of the order of those measured in the basic case (2.1×10^3 W/m^2) when the pyrolysis length was approximately 70 mm. Larger pyrolysis lengths did not show any increase in the value of the radiant flux, indicating that the flame was optically thick, thus avoiding any additional transmission of radiation from the rear region of the flame. The most informative results are those of the flame spread rate measurements. It was found that at a pyrolysis length of 5 mm the spread rate was already 5×10^{-2} mm/s, i.e.: 80 percent of that measured in the basic case. As the pyrolysis length increased the spread rate also increased slowly approaching in an asymptotic manner a propagation velocity of 5.98×10^{-2} mm/s (basic experiment) for pyrolysis lengths of approximately 60 mm.

The rapid increase of the flame spread rate at the initiation of the spreading process, in combination with the low radiant fluxes and small contribution of gas phase heat conduction, indicates that heat conduction through the solid phase is the dominant mechanism of heat transfer during the very early stages of the flame propagation process over the surface of a thick fuel. The contribution of radiation heat transfer increases uniformly but slowly as the flame spreading process continues, reaching values of the order of 40 percent of the total heat transferred ahead of the flame after pyrolysis lengths of the order of 60 mm. That heat conduction through the solid is the dominant mode of heat transfer in very small fires corroborates previous deductions obtained by the authors of reference [10] for flames spreading axisymmetrically over the surface of thick PMMA sheets.

4.2 Large Fires. For large scale fires it is generally agreed that radiation from the flames is the dominant mode of heat transfer. It is also known that the core of the fire can generate strong winds opposing the direction of fire propagation. Attempting to understand how the process takes place, we have performed some experiments on a somewhat larger scale fire than that presented in Section 3. The experiments were performed with PMMA sheets of the same thickness as in the basic experiment, but with sheet widths of 0.3 m. Measurements of the distribution of radiant flux along the fuel surface were performed following a procedure similar to that described before. Although the results did not show major differences between both cases, it was found that while the radiant flux near the flame front was practically the same for both cases, the radiant fluxes far away from the flame front were slightly larger and more extended for the present case. These results corroborate previous deductions that relatively early on in the development of the fire, the fuel surface near the flame front sees the flame as an infinite emitter. The contribution of the larger flame occurs further away from the flame front by preheating the unburnt fuel over a more extended region. Because the flame spread rate is very sensitive to the initial temperature of the fuel [18, 19], preheating of the fuel could eventually enhance the flame spreading process considerably. Counteracting this effect are the facts that heat conduction through the solid will decrease as the temperature gradients along the fuel length decrease, and higher opposed gas flow velocities tend to slow down the spread process [20]. However, the propagation process is so strongly dependent on the temperature of the fuel that these counteracting effects will be of secondary importance. It can therefore be concluded that for large fires radiation from the flame will be the dominant mechanism of heat transfer and that its effect will take place primarily by raising the temperature of the fuel along large extensions of its surface.

5 Conclusion

The results of the present work, in combination with those of Hirano, et al. [6], provide comprehensive information about the heat transfer mechanisms controlling the horizontal propagation of flames over the surface of a solid fuel. It has been shown that unlike vertically downward flame propagation, radiation heat transfer from the flame

to the unburnt fuel can play a significant role in the heat transfer process for the horizontal mode of flame spread. While for downward spread buoyant forces keep the flame close to the fuel surface, for horizontal propagation buoyancy tends to lift the flame from the fuel surface, thus providing a favorable view factor for radiation to be transmitted from the flame to the unburnt fuel. It has been shown that for a comparable scale fire, the other modes of heat transfer and the characteristics of the temperature and gas velocity fields are similar for both modes of flame propagation, thus indicating that the additional contribution of radiation from the flame is the primary reason for the larger spread rates observed in the horizontal mode of flame propagation. Since the contribution of the radiant flux to the horizontal flame spread process is a function of the size of the fire, the process will be a transient one whenever a growth of the fire occurs (thick uninhibited fuels). In the early stages of the propagation process, the size of the flame is small enough for radiation to be negligible. In this case, the flame spreading process behaves similarly for horizontal and vertically downward propagation, with heat conduction through the solid being dominant for thick fuels.

At this point we believe that the grounds for the development of accurate theoretical models describing the horizontal or vertically downward modes of flame propagation in natural convective environments have been established. We would like to emphasize here that this type of analysis of the heat transfer mechanisms in flame propagation processes addresses only one basic aspect of the problem: how the heat is transferred from the burning region of the fuel to the virgin material ahead of the flame. Other aspects of the flame spreading process that must be considered if accurate descriptions of the process are attempted are the vaporization of the fuel ahead of the flame, its mixing with the incoming oxidizer, and the propagation of the flame along this mixture.

Acknowledgments

The authors wish to thank Dr. F. L. Dryer and Dr. R. J. Santoro for their helpful comments and advice concerning the experiments. The technical assistance of Messrs. J. Sivo and D. Peoples was most helpful. The research was supported by The National Bureau of Standards under Grant 7-9004.

References

1 Hirano, T., Noreikis, S. E., and Waterman, T. E. "Measured Velocity and Temperature Profiles Near Flames Spreading Over a Thin Combustible Solid," *Combustion and Flame,* Vol. 23, 1974, p. 83.

2 Sibulkin, M., and Lee, C. K., "Flame Propagation Measurements and Energy Feedback Analysis for Burning Cylinders," *Combustion Science and Technology,* Vol. 9, 1974, p. 137.

3 Fernandez-Pello, A. C., and Williams, F. A., "Laminar Flame Spread Over PMMA Surfaces," Fifteenth Symposium (International) on Combustion, The Combustion Institute, 1975, p. 217.

4 Fernandez-Pello, A. C., and Williams, F. A., "Experimental Techniques in the Study of Laminar Flame Spread Over Solid Combustibles," *Combustion Science and Technology,* Vol. 14, 1976, p. 155.

5 Fernandez-Pello, A. C., and Santoro, R. J., "On the Dominant Mode of Heat Transfer in Downward Flame Spread," Seventeenth Symposium (International) on Combustion, The Combustion Institute, 1978, p. 1201.

6 Hirano, T., Koshida, T., and Akita, K., "Flame Spread Mechanisms over PMMA Surfaces," *Bulletin of Japanese Association of Fire Science and Engineering,* Vol. 27, No. 2, 1977, (in Japanese), p. 33.

7 Santoro, R. J., Fernandez-Pello, A. C., Dryer, F. L. and Glassman, I., "An Application of a Two-Component LDV to the Measurement of Flows Induced by Flames Propagating Over Condensed Fuels," *Applied Optics, 17,* 23, 1978, p. 3843.

8 Kent, J. H., "A Noncatalytic Coating for Platinum Rhodium Thermocouples," *Combustion and Flame,* Vol. 14, 1970, p. 279.

9 Kosdon, F. J., *Combustion of Cellulose,* Ph.D. Thesis, University of California, San Diego, 1970.

10 Sibulkin, M., and Hansen, A. G., "Experimental Study of Flame Spreading Over a Horizontal Fuel Surface," *Combustion Science and Technology,* Vol. 10, 1975, p. 85.

11 Carslaw, H. S., and Jaeger, J. C., *Conduction of Heat in Solids,* Oxford Press, Oxford, 1973, p. 75.

12 *Plexiglas, Design and Fabrication Data,* Rohm & Haas Co., 1971.

13 Orloff, L., and deRis, J., "Absorption Characteristics of Colorless PMMA for PMMA Pool Fire Radiation," Factory Mutual Research Corporation, Interoffice Correspondence, June 1975.

14 Orloff, L., deRis, J., and Tewarson, A., "Thermal Properties of PMMA at Elevated Temperatures," Factory Mutual Research Corporation, Tech. Rept. 22355-2, 1974.

15 Hilsenrath, J., et al., *Tables of Thermodynamic and Transport Properties of Air,* Pergamon Press, 1960.

16 Fernandez-Pello, A. C., Kindelan, M., and Williams, F. A., "Surface Temperature Histories During Downward Propagation of Flames on PMMA Sheets," *Ingenieria Aeronautica y Astronautica,* Vol. 135, 41, 1974, Also WSS/CI Paper 73-8.

17 Kosdon, F. J., Williams, F. A. and Buman, C., "Combustion of Vertical Cellulosic Cylinders in Air," Twelfth Symposium (International) on Combustion, The Combustion Institute, 1971, p. 949.

18 McAlevy, R. F. III, and Magee, R. S., "The Mechanism of Flame Spreading over the Surface of Igniting Condensed-Phase Materials," Twelfth Symposium (International) on Combustion, The Combustion Institute, 1969, p. 215.

19 Perrins, L. E. and Pettet, K., "Measurements of Flame Spread Velocities," *Journal Fire and Flammability,* Vol. 5, 1974, p. 85.

20 Fernandez-Pello, A. C., Ray, S. R., and Glassman, I., "Downward Flame Spread in an Opposed Forced Flow," *Combustion Science and Technology,* Vol. 19, 1978, p. 19.

Journal of Heat Transfer

Technical Notes

This section contains shorter technical papers. These shorter papers will be subjected to the same review process as that for full papers.

Average Heat Transfer Coefficients for Forced Convection on a Flat Plate with an Adiabatic Starting Length

S. C. Lau[1] and E. M. Sparrow[1]

Nomenclature

$\bar{h}$ = average heat transfer coefficient for thermally active section in presence of starting length
$\bar{h}^*$ = average coefficient for isothermal plate of length L without starting section
$\bar{h}^{**}$ = average coefficient for isothermal plate of length λ without starting section
L = length of thermally active section, Fig. 1
L_0 = length of adiabatic starting section, Figs. 1 and 2
λ = overall length of plate, Fig. 2

Introduction

In engineering practice, average heat transfer coefficients are usually of more direct utility than are local coefficients. The purpose of this Note is to provide information about average coefficients for laminar boundary layer flow along a flat plate whose initial portion constitutes an unheated starting length. The thermally active portion of the plate (downstream of the starting length) is isothermal.

Local heat transfer coefficients for this situation, derived by solving the integral momentum and energy equations, are widely available in the literature (e.g., [1]), but it appears that average coefficients have not yet been presented. The objectives of the work reported here encompass not only the derivation of the average coefficients but also include performance comparisons which illuminate the impact of the starting length. Experimental data are also presented which offer qualitative support for the analytical findings.

The average coefficients are first derived by employing the local heat flux results from the aforementioned integral solution. Since the integral solution is approximate, so also are the average coefficients. The resulting modest inaccuracies are then eliminated by accounting for literature information on the local errors of the integral solution [2].

Two types of performance comparisons are made. In one, the average coefficients for a thermally active surface of given streamwise length, respectively corresponding to the absence and the presence of an added starting length, are compared. These results show the effect of adding a starting length to a given thermally active surface. The other comparison ratios the average coefficient for a thermally active surface preceded by a starting length with that for a fully thermally active plate whose overall length is the sum of the lengths of the active and inactive zones of the former. This comparison shows the effect of suppressing the heat transfer on the initial portion of a plate which previously was thermally active at all surface locations. The experimental results to be discussed are average mass transfer coefficients obtained via the naphthalene sublimation technique.

Analysis

Consideration is first given to the physical situation pictured in the upper diagram of Fig. 1, which shows a flat plate with an isothermal section of length L (temperature T_w) preceded by an adiabatic hydrodynamic starting section of length L_0. The average heat transfer coefficient for this case will be compared with that for an isothermal plate of length L (without a starting length) such as is pictured in the lower part of the diagram.

Since the section of plate between $x = 0$ and $x = L$ is isothermal, the average coefficient can be evaluated from

$$\bar{h} = (1/L) \int_0^L h_x dx \tag{1}$$

For the case in which there is an unheated starting length, an expression for the local coefficient h_x has been obtained from the integral momentum and energy equations [1]. In terms of the coordinates of Fig. 1, this expression can be written as

$$h_x = \Omega \left[(x + L_0)^{1/4}((x + L_0)^{3/4} - L_0^{3/4})^{1/3}\right]^{-1} \tag{2}$$

where

$$\Omega = 0.332k\mathrm{Pr}^{1/3}(U_\infty/\nu)^{1/2} \tag{3}$$

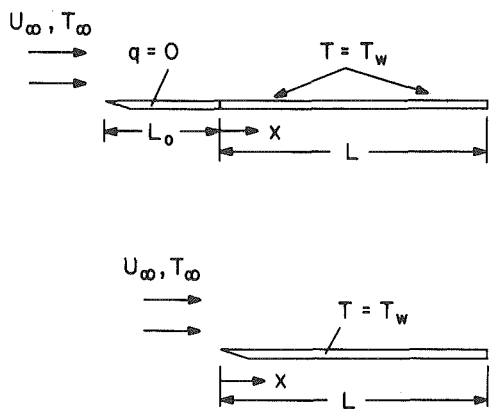

Fig. 1 Diagram of a plate having a thermally active length L, with and without an added upstream starting length.

[1] Department of Mechanical Engineering University of Minnesota, Minneapolis, Minn. 55455

Contributed by the Heat Transfer Division for publication in The JOURNAL OF HEAT TRANSFER received by The Heat Transfer Division October 1, 1979.

To facilitate the integration of equation (2), it is convenient to change variables and let

$$f = (x + L_0)^{3/4} - L_0^{3/4} \tag{4}$$

With this substitution, it follows without difficulty that

$$\bar{h}L/k = 0.664\mathrm{Pr}^{1/3}(U_\infty L/\nu)^{1/2}\,[(1 + L_0/L)^{3/4} - (L_0/L)^{3/4}]^{2/3} \tag{5}$$

For the comparison of the $\bar{h}$ of equation (5) with the average coefficient for an isothermal plate of length L without a starting length (lower diagram of Fig. 1), it appears appropriate, for consistency, to also employ the results of the integral momentum-energy analysis for the latter. If $\bar{h}^*$ denotes the no-starting length case, then

$$\bar{h}^*L/k = 0.664\mathrm{Pr}^{1/3}(U_\infty L/\nu)^{1/2} \tag{6}$$

Then, by ratioing equations (5) and (6)

$$\bar{h}/\bar{h}^* = [(1 + L_0/L)^{3/4} - (L_0/L)^{3/4}]^{2/3} \tag{7}$$

This equation will be plotted and discussed shortly.

With regard to the foregoing development, it should be noted that there is a degree of approximation since the integral momentum-energy solution is, itself, approximate. In [2], on the basis of finite difference solutions, a correction to h_x for Pr = 0.7 was determined and expressed as follows

$$h_x = (1 + F/100)h_x(\text{equation 2}) \tag{8}$$

where F is a function of $(1 + x/L_0)$ which is read from the ordinate of Fig. 1 of [2]. For the determination of $\bar{h}$, equation (8) was substituted into equation (1) and the integration was carried out numerically. Similarly, $\bar{h}^*$ was obtained by correcting equation (6) in accordance with the finite difference solution. In this way, corrected values of $\bar{h}/\bar{h}^*$ were determined as a function of L_0/L, and these will be presented shortly.

Attention is now turned to the physical situation depicted in Fig. 2. The upper diagram shows a plate with an unheated starting length which, aside from certain changes of notation, is identical to that of the upper diagram of Fig. 1. Note that the total length of the plate, encompassing the starting length and the heated length, is λ. The changes of notation were motivated by comparisons to be made with an isothermal plate of overall length λ as shown in the lower diagram of the figure.

With the local coefficient h_x from the integral solution as input, $\bar{h}$ can be evaluated for both the upper and lower diagrams of Fig. 2. The latter $\bar{h}$ is denoted by $\bar{h}^{**}$ to distinguish it from that for the lower diagram of Fig. 1 ($\bar{h}^*$ and $\bar{h}^{**}$ differ because one is for length L and the other for length λ). The final result is

$$\bar{h}/\bar{h}^{**} = [1 - (L_0/\lambda)^{3/4}]^{2/3}/[1 - (L_0/\lambda)] \tag{9}$$

It can be readily verified that equations (7) and (9) are mutually consistent.

To eliminate the approximations of the integral method, the corrected local coefficients from equation (8) can be employed. Rather than perform the requisite numerical integrations to obtain the corrected values of $\bar{h}/\bar{h}^{**}$, they can be deduced from the corrected values of $\bar{h}/\bar{h}^*$ for the previous case in accordance with the following relationship

$$\bar{h}/\bar{h}^{**} = (1 + L_0/L)^{1/2}(\bar{h}/\bar{h}^*) \tag{10}$$

where, for a given L_0/λ, the value of $\bar{h}/\bar{h}^*$ in equation (10) corresponds to an L_0/L obtained from

$$L_0/L = (L_0/\lambda)/(1 - L_0/\lambda) \tag{11}$$

Thus, with equations (10) and (11) and with the already obtained values of $\bar{h}/\bar{h}^*$, the corrected values of $\bar{h}/\bar{h}^{**}$ can be determined as a function of L_0/λ. These results, along with those from equation (9), will be presented in the next section.

Results and Discussion

The $\bar{h}/\bar{h}^*$ ratio for the situation depicted in Fig. 1 is plotted in Fig. 3 as a function of L_0/L. For the interpretation of these results, it is convenient to think of a flat plate having an isothermal portion of length L to which an upstream starting section of parametric length L_0 is added. The ratio $\bar{h}/\bar{h}^*$ compares the average heat transfer coefficients for the thermally active length L for the cases in which a starting length is either present or absent. The quantity L_0/L which appears on the abscissa of Fig. 3 measures the length of the starting section relative to the length of the thermally active zone.

Examination of Fig. 3 indicates that the addition of a starting length upstream of the thermally active surface reduces the average heat transfer coefficient for the latter. The cause of the reduction is the lower velocities which wash the thermally active surface when the starting length is in place. The reductions are quite modest when

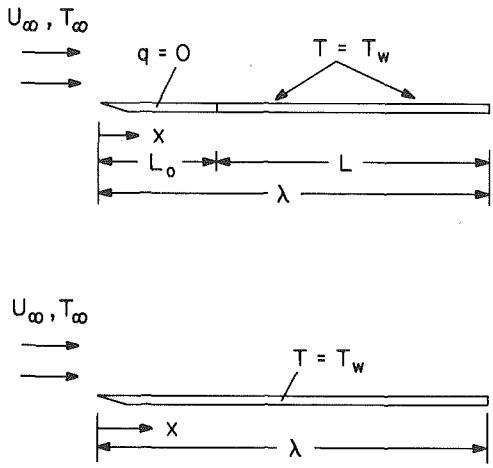

Fig. 2 Diagram of a plate having an overall length λ, with or without the initial portion being a starting length

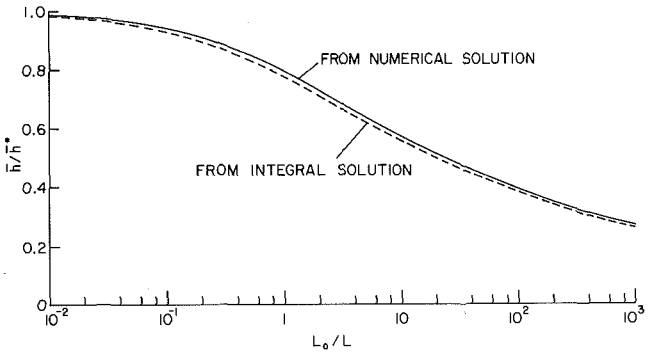

Fig. 3 Comparison of average heat transfer coefficients with and without a starting length for conditions of Fig. 1

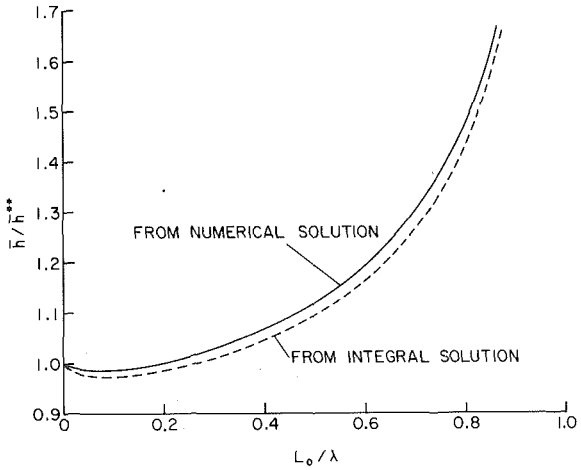

Fig. 4 Comparison of average heat transfer coefficients with and without a starting length for conditions of Fig. 2

viewed with respect to the extent of the starting section needed to achieve them. For example, when a starting section equal in length to that of the active surface is used, there is a reduction of about 20 percent in the average coefficient. To achieve a 50 percent reduction, it is necessary that the starting section be 20 times longer than the active section.

The dashed and solid lines in Fig. 3 portray the results based on the local coefficients from the integral solution and on the corrections provided by the finite difference solutions of [2], respectively. The agreement is generally good, with a maximum deviation of about three percent.

The results for the situation depicted in Fig. 2 are presented in Fig. 4. Here, it is convenient to envision a plate of length λ which, at first, is thermally active over its entire extent. Then, heat transfer may be regarded as being suppressed for a fraction L_0/λ of the total length. The ratio $\overline{h}/\overline{h}^{**}$ compares the average coefficient for the still-active length $L = (\lambda - L_0)$ to that for the original length λ. Values of $\overline{h}/\overline{h}^{**}$ are plotted in Fig. 4 as a function of L_0/λ, both for the integral solution (dashed lines) and the finite difference solution (solid lines).

The figure shows that the average heat transfer coefficient is very little affected by the starting length when $0 \leq L_0/\lambda \leq 1/4$, but for larger L_0/λ the values of $\overline{h}/\overline{h}^{**}$ exceed unity and increase rapidly. The key ingredient in this behavior is the fact that when the unheated starting length is in place, the fluid temperatures in the active-zone boundary layer are lower (for $T_w > T_\infty$) than those which would prevail when the starting length is absent. This lowering of the fluid temperature tends to increase the heat transfer coefficient. The longer the starting length, the lower are the active-zone fluid temperatures and the higher are the $\overline{h}/\overline{h}^{**}$ values.

It is interesting to note that for small L_0/λ, $\overline{h}/\overline{h}^{**}$ takes on values slightly below one. This is believed due to the effect of decreased boundary layer velocities owing to the presence of the starting length. On the other hand, the aforementioned temperature reduction effect, which would tend to increase $\overline{h}/\overline{h}^{**}$, is small for this range of L_0/λ.

The deviations between the solid and dashed curves in Fig. 4 are, at most, about three percent.

Brief mention may be made of wind tunnel experiments involving the naphthalene sublimation technique. The experiments are only qualitatively related to the work described here in that they involved a square plate (side dimension = 7.62 cm) inclined to the flow direction, the surface being tilted up by 25° relative to the horizontal wind vector. The departures of the experimental conditions from those of the analysis (finite span of plate, finite angle of attack) reflect the fact that the experimental apparatus had been originally designed and employed for another research objective.

Two sets of experiments were performed. In the first, average coefficients were measured for mass transfer taking place from the entire plate surface. In the second, mass transfer was suppressed for the forwardmost one-third of the plate. For the Reynolds number range investigated (20,000 to 80,000), it was found that

$$\overline{h}/\overline{h}^{**} = 1.08 \tag{12}$$

reflecting an increase in the transfer coefficient. This is in qualitative agreement with the results of Fig. 4 in that $\overline{h}/\overline{h}^{**} > 1$ for $L_0/\lambda = 1/3$; quantitative agreement is not expected in view of the aforementioned differences in the flow configurations.

References

1 Eckert, E. R. G. and Drake, R. M., *Analysis of Heat and Mass Transfer*, McGraw-Hill, New York, 1972.

2 Abdel-Wahed, R. M., Sparrow, E. M., and Patankar, S. V., "Mixed Convection on a Vertical Plate with an Unheated Starting Length," ASME JOURNAL OF HEAT TRANSFER, Vol. 98, 1976, pp. 576–583.

Blasius Series Solution for Heat Transfer with Nonisothermal Wall Temperature

Sun-Yuan Tsay[1] and Yen-Ping Shih[1]

Introduction

The two-dimensional laminar boundary layer forced flow past a cylindrical surface was first studied by Blasius [1] in 1908 with the introduction of power series solution and universal functions. The corresponding heat and mass transfer problem was studied by Frössling [2] and Newman [3]. Newman [3] gave an extensive table on the effect of the Schmidt number on the rate of mass transfer and asymptotic solutions for Schmidt number approaching infinity and zero. Other forms of series solutions were suggested by Görtler [4], Meksyn [5], Merk [6], and Chao and Fagbenle [7]. However, all these studies are restricted to constant wall temperature.

In this report, the work of Frössling and Newman was extended to nonisothermal wall temperature, which is assumed to be a power series of the distance from the stagnation point along the cylindrical surface. The solution is expressed in terms of universal functions for large Prandtl number. For small Prandtl number, the effect of the Prandtl number on the rate of heat transfer is tabulated.

Velocity Profiles

The governing equations for the fluid flow are the standard laminar boundary layer equations. For a symmetric cylinder with a round nose, the external velocity $U(x)$ can be expressed as a power series of the coordinate along the cylindrical surface, x:

$$U(x) = U_1 x(1 + a_2 x^2 + a_4 x^4 + a_6 x^6 + \ldots) \tag{1}$$

Universal functions for the velocity distribution are obtained by letting

$$f(x, \eta) = f_0(\eta)x + a_2 f_2(\eta)x^3 + [a_4 f_4(\eta) + a_2^2 f_{22}(\eta)]x^5 + [a_6 f_6(\eta) + a_4 a_2 f_{42}(\eta) + a_2^3 f_{222}(\eta)]x^7 + \ldots \tag{2}$$

Here

$$\psi = \sqrt{\nu U_1}\, f(x, \eta),\ \eta = y\sqrt{U_1/\nu}.$$

where ψ is the stream function, ν is the kinematic viscosity of the fluid, and y is the coordinate normal to the cylindrical surface. Numerical solutions of $f_0, f_2, f_4, \ldots$ have been given by Gadd, et al. [8].

Heat Transfer

Consider the surface temperature of the cylinder to be nonisothermal $T_w(x)$, and let

$$\theta = \frac{T - T_\infty}{T_0 - T_\infty} \tag{3}$$

where T_0 is the temperature at the stagnation point and T is the fluid temperature. The energy equation in the boundary layer becomes

$$u\frac{\partial \theta}{\partial x} + v\frac{\partial \theta}{\partial y} = \frac{k}{\rho c_p}\frac{\partial^2 \theta}{\partial y^2} \tag{4}$$

where k, c_p, and ρ are the thermal conductivity, specific heat, and density of the fluid, respectively. The boundary conditions are

$$y = 0, \theta = \theta_w(x);$$

$$y \to \infty, \theta = 0 \tag{5}$$

It is assumed that the wall temperature is described by a power series of x in the following form:

$$\theta_w(x) = 1 + b_2 x^2 + b_4 x^4 + b_6 x^6 + \ldots \tag{6}$$

For constant wall temperature, $b_2 = b_4 = \ldots = 0$.

Since a symmetrically cylindrical surface is assumed, the temper-

[1] National Cheng Kung University, Tainan, Taiwan, China.

Contributed by the Heat Transfer Division for publication in the JOURNAL OF HEAT TRANSFER. Manuscript received by the Heat Transfer Division March 23, 1977.

viewed with respect to the extent of the starting section needed to achieve them. For example, when a starting section equal in length to that of the active surface is used, there is a reduction of about 20 percent in the average coefficient. To achieve a 50 percent reduction, it is necessary that the starting section be 20 times longer than the active section.

The dashed and solid lines in Fig. 3 portray the results based on the local coefficients from the integral solution and on the corrections provided by the finite difference solutions of [2], respectively. The agreement is generally good, with a maximum deviation of about three percent.

The results for the situation depicted in Fig. 2 are presented in Fig. 4. Here, it is convenient to envision a plate of length λ which, at first, is thermally active over its entire extent. Then, heat transfer may be regarded as being suppressed for a fraction L_0/λ of the total length. The ratio $\overline{h}/\overline{h}^{**}$ compares the average coefficient for the still-active length $L = (\lambda - L_0)$ to that for the original length λ. Values of $\overline{h}/\overline{h}^{**}$ are plotted in Fig. 4 as a function of L_0/λ, both for the integral solution (dashed lines) and the finite difference solution (solid lines).

The figure shows that the average heat transfer coefficient is very little affected by the starting length when $0 \leq L_0/\lambda \leq 1/4$, but for larger L_0/λ the values of $\overline{h}/\overline{h}^{**}$ exceed unity and increase rapidly. The key ingredient in this behavior is the fact that when the unheated starting length is in place, the fluid temperatures in the active-zone boundary layer are lower (for $T_w > T_\infty$) than those which would prevail when the starting length is absent. This lowering of the fluid temperature tends to increase the heat transfer coefficient. The longer the starting length, the lower are the active-zone fluid temperatures and the higher are the $\overline{h}/\overline{h}^{**}$ values.

It is interesting to note that for small L_0/λ, $\overline{h}/\overline{h}^{**}$ takes on values slightly below one. This is believed due to the effect of decreased boundary layer velocities owing to the presence of the starting length. On the other hand, the aforementioned temperature reduction effect, which would tend to increase $\overline{h}/\overline{h}^{**}$, is small for this range of L_0/λ.

The deviations between the solid and dashed curves in Fig. 4 are, at most, about three percent.

Brief mention may be made of wind tunnel experiments involving the naphthalene sublimation technique. The experiments are only qualitatively related to the work described here in that they involved a square plate (side dimension = 7.62 cm) inclined to the flow direction, the surface being tilted up by 25° relative to the horizontal wind vector. The departures of the experimental conditions from those of the analysis (finite span of plate, finite angle of attack) reflect the fact that the experimental apparatus had been originally designed and employed for another research objective.

Two sets of experiments were performed. In the first, average coefficients were measured for mass transfer taking place from the entire plate surface. In the second, mass transfer was suppressed for the forwardmost one-third of the plate. For the Reynolds number range investigated (20,000 to 80,000), it was found that

$$\overline{h}/\overline{h}^{**} = 1.08 \tag{12}$$

reflecting an increase in the transfer coefficient. This is in qualitative agreement with the results of Fig. 4 in that $\overline{h}/\overline{h}^{**} > 1$ for $L_0/\lambda = 1/3$; quantitative agreement is not expected in view of the aforementioned differences in the flow configurations.

References

1 Eckert, E. R. G. and Drake, R. M., *Analysis of Heat and Mass Transfer*, McGraw-Hill, New York, 1972.

2 Abdel-Wahed, R. M., Sparrow, E. M., and Patankar, S. V., "Mixed Convection on a Vertical Plate with an Unheated Starting Length," ASME JOURNAL OF HEAT TRANSFER, Vol. 98, 1976, pp. 576–583.

Blasius Series Solution for Heat Transfer with Nonisothermal Wall Temperature

Sun-Yuan Tsay[1] and Yen-Ping Shih[1]

Introduction

The two-dimensional laminar boundary layer forced flow past a cylindrical surface was first studied by Blasius [1] in 1908 with the introduction of power series solution and universal functions. The corresponding heat and mass transfer problem was studied by Frössling [2] and Newman [3]. Newman [3] gave an extensive table on the effect of the Schmidt number on the rate of mass transfer and asymptotic solutions for Schmidt number approaching infinity and zero. Other forms of series solutions were suggested by Görtler [4], Meksyn [5], Merk [6], and Chao and Fagbenle [7]. However, all these studies are restricted to constant wall temperature.

In this report, the work of Frössling and Newman was extended to nonisothermal wall temperature, which is assumed to be a power series of the distance from the stagnation point along the cylindrical surface. The solution is expressed in terms of universal functions for large Prandtl number. For small Prandtl number, the effect of the Prandtl number on the rate of heat transfer is tabulated.

Velocity Profiles

The governing equations for the fluid flow are the standard laminar boundary layer equations. For a symmetric cylinder with a round nose, the external velocity $U(x)$ can be expressed as a power series of the coordinate along the cylindrical surface, x:

$$U(x) = U_1 x(1 + a_2 x^2 + a_4 x^4 + a_6 x^6 + \ldots) \tag{1}$$

Universal functions for the velocity distribution are obtained by letting

$$f(x, \eta) = f_0(\eta)x + a_2 f_2(\eta)x^3 + [a_4 f_4(\eta) + a_2^2 f_{22}(\eta)]x^5 + [a_6 f_6(\eta) + a_4 a_2 f_{42}(\eta) + a_2^3 f_{222}(\eta)]x^7 + \ldots \tag{2}$$

Here

$$\psi = \sqrt{\nu U_1}\, f(x, \eta),\ \eta = y\sqrt{U_1/\nu}.$$

where ψ is the stream function, ν is the kinematic viscosity of the fluid, and y is the coordinate normal to the cylindrical surface. Numerical solutions of $f_0, f_2, f_4, \ldots$ have been given by Gadd, et al. [8].

Heat Transfer

Consider the surface temperature of the cylinder to be nonisothermal $T_w(x)$, and let

$$\theta = \frac{T - T_\infty}{T_0 - T_\infty} \tag{3}$$

where T_0 is the temperature at the stagnation point and T is the fluid temperature. The energy equation in the boundary layer becomes

$$u\frac{\partial \theta}{\partial x} + v\frac{\partial \theta}{\partial y} = \frac{k}{\rho c_p}\frac{\partial^2 \theta}{\partial y^2} \tag{4}$$

where k, c_p, and ρ are the thermal conductivity, specific heat, and density of the fluid, respectively. The boundary conditions are

$$y = 0, \theta = \theta_w(x);$$

$$y \to \infty, \theta = 0 \tag{5}$$

It is assumed that the wall temperature is described by a power series of x in the following form:

$$\theta_w(x) = 1 + b_2 x^2 + b_4 x^4 + b_6 x^6 + \ldots \tag{6}$$

For constant wall temperature, $b_2 = b_4 = \ldots = 0$.

Since a symmetrically cylindrical surface is assumed, the temper-

[1] National Cheng Kung University, Tainan, Taiwan, China.

Contributed by the Heat Transfer Division for publication in the JOURNAL OF HEAT TRANSFER. Manuscript received by the Heat Transfer Division March 23, 1977.

Table 1 Dimensionless heat-transfer coefficients from Blasius series

Pr	0.1	0.5	0.7	1.0	2.0	5.0	10.0	20.0	50.0	100.0	200.0
$\theta'_0(0)$	−0.2195	−0.4334	−0.4959	−0.5705	−0.7437	−1.0435	−1.3389	−1.7104	−2.3529	−2.9869	−3.7855
$\theta'_2(0)$	−0.1847	−0.3866	−0.4476	−0.5210	−0.6931	−0.9937	−1.2911	−1.6656	−2.3132	−2.9518	−3.7556
$g'_2(0)$	−0.3977	−0.7507	−0.8519	−0.9724	−1.2513	−1.7331	−2.2081	−2.8059	−3.8401	−4.8608	−6.1469
$\theta'_4(0)$	−0.2304	−0.5025	−0.5859	−0.6868	−0.9246	−1.3418	−1.7556	−2.2772	−3.1797	−4.0698	−5.1899
$g'_4(0)$	−0.5025	−0.9318	−1.0545	−1.2004	−1.5382	−2.1218	−2.6975	−3.4221	−4.6761	−5.9137	−7.4737
$\theta'_{22}(0)$	0.0675	0.1613	0.1906	0.2262	0.3106	0.4595	0.6077	0.7950	1.1196	1.4402	1.8441
$g'_{22}(0)$	−0.2864	−0.5806	−0.6671	−0.7704	−1.0109	−1.4277	−1.8390	−2.3566	−3.2514	−4.1334	−5.2476
$\theta'_6(0)$	−0.2678	−0.6006	−0.7036	−0.8284	−1.1235	−1.6427	−2.1587	−2.8098	−3.9367	−5.0484	−6.4474
$g'_6(0)$	−0.5805	−1.0657	−1.2041	−1.3688	−1.7499	−2.4088	−3.0588	−3.8772	−5.2933	−6.6910	−8.4534
$\theta'_{42}(0)$	0.1808	0.4479	0.5319	0.6341	0.8772	1.3075	1.7372	2.2809	3.2245	4.1573	5.3330
$g'_{42}(0)$	−0.3219	−0.5321	−0.5943	−0.6687	−0.8422	−1.1436	−1.4411	−1.8154	−2.4620	−3.0984	−3.9055
$g'_{24}(0)$	−0.3539	−0.7035	−0.8052	−0.9264	−1.2079	−1.6952	−2.1758	−2.7805	−3.8260	−4.8561	−6.1699
$\theta'_{222}(0)$	−0.0682	−0.1741	−0.2075	−0.2482	−0.3450	−0.5169	−0.6890	−0.9071	−1.2863	−1.6613	−2.1340
$g'_{222}(0)$	0.1279	0.2834	0.3298	0.3855	0.5158	0.7430	0.9680	1.2517	1.7435	2.2305	2.8378

ature profile can be expressed as a Blasius series:

$$\theta = \theta_0(\eta) + [a_2\theta_2(\eta) + b_2g_2(\eta)]\,x^2 + [a_4\theta_4(\eta) + b_4g_4(\eta) + a_2^2\theta_{22}(\eta) + a_2b_2g_{22}(\eta)]\,x^4 + [a_6\theta_6(\eta) + b_6g_6(\eta) + a_4a_2\theta_{42}(\eta) + a_4b_2g_{42}(\eta) + a_2b_4g_{24}(\eta) + a_2^3\theta_{222}(\eta) + a_2^2b_2g_{222}(\eta)]\,x^6 + \ldots \quad (7)$$

The functions, $\theta_0, \theta_2, \ldots, g_{222}$ are dependent on the Prandtl number which is the only parameter. Table 1 shows the numerical results of $\theta'_0(0), \theta'_2(0), \ldots, g'_{222}(0)$.

The local rate of heat transfer from the wall $q(x)$ and the local heat transfer coefficient $h(x)$ is related as follows:

$$q(x) = -k\left.\frac{\partial T}{\partial y}\right|_{y=0} = h(x)\,(T_0 - T_\infty) \quad (8)$$

Defining local Nusselt number, $\mathrm{Nu}_x = hx/k$ and local Reynolds number $\mathrm{Re}_x = U_1x^2/\nu$, equations (7–8) give:

$$\mathrm{Nu}_x(\mathrm{Re}_x)^{-1/2} = -\{\theta'_0(0) + [a_2\theta'_2(0) + b_2g'_2(0)]\,x^2 + [a_4\theta'_4(0) + b_4g'_4(0) + a_2^2\theta'_{22}(0) + a_2b_2g'_{22}(0)]\,x^4 + [a_6\theta'_6(0) + b_6g'_6(0) + a_4a_2\theta'_{42}(0) + a_4b_2g'_{42}(0) + a_2b_4g'_{24}(0) + a_2^3\theta'_{222}(0) + a_2^2b_2g'_{222}(0)]\,x^6 + \ldots\} \quad (9)$$

The calculation of local heat transfer rate can thus be easily performed using equation (9) and Table 1. An example is given below.

For a circular cylinder of radius R and free-stream velocity U_∞ parallel to the x-axis, the external velocity is given by [1, p. 158]

$$U(x) = 2U_\infty \sin\frac{x}{R} = 2U_\infty\left[\frac{x}{R} - \frac{1}{3!}\left(\frac{x}{R}\right)^3 + \frac{1}{5!}\left(\frac{x}{R}\right)^5 - \frac{1}{7!}\left(\frac{x}{R}\right)^7 + \ldots\right] \quad (10)$$

From equation (9) we have [1, p. 190]

$$\mathrm{Nu}_D(\mathrm{Re}_D)^{-1/2} = \left(\frac{hD}{k}\right)\left(\frac{DU_\infty}{\nu}\right)^{-1/2} = -2\{\theta'_0(0) + [a_2\theta'_2(0) + b_2g'_2(0)]\,x^2 + [a_4\theta'_4(0) + b_4g'_4(0) + a_2^2\theta'_{22}(0) + a_2b_2g'_{22}(0)]\,x^4 + [a_6\theta'_6(0) + b_6g'_6(0) + a_4a_2\theta'_{42}(0) + a_4b_2g'_{42}(0) + a_2b_4g'_{24}(0) + a_2^3\theta'_{222}(0) + a_2^2b_2g'_{222}(0)]\,x^6 + \ldots\} \quad (11)$$

where

$$a_2R^2 = -\frac{1}{3!}, a_4R^4 = \frac{1}{5!}, a_6R^6 = -\frac{1}{7!}, \ldots$$

The effect of non-isothermal wall on the heat transfer for circular cylinder in air flow is shown in Fig. 1.

Perturbation Solution for Large Prandtl Number

For large Prandtl number, the extended Lighthill approximation [9, 10] is used to calculate the temperature profile and the heat transfer rate. First, $f_0(\eta), f_2(\eta), \ldots$ of equation (2) are expanded into

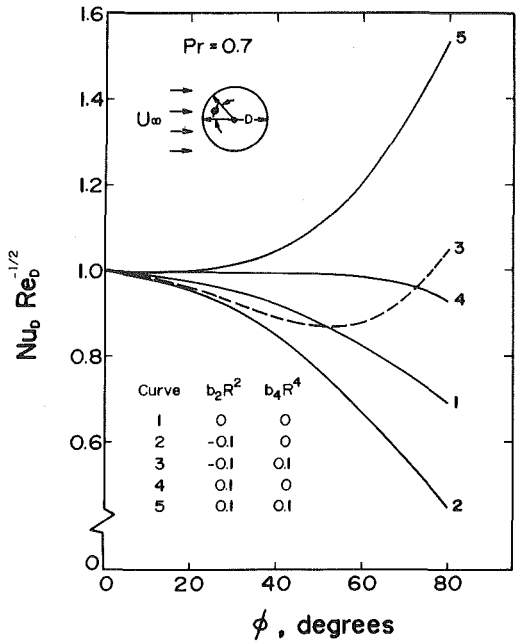

Fig. 1 Heat transfer from circular cylinder with nonisothermal surface air flow

power series of η. That is,

$$f_0(\eta) = \frac{a}{2}\eta^2 - \frac{1}{6}\eta^3 + \frac{a^2}{5!}\eta^5 - \frac{2a}{6!}\eta^6 + \frac{2}{7!}\eta^7 + \ldots \quad (12)$$

$$f_2(\eta) = \frac{b}{2}\eta^2 - \frac{2}{3}\eta^3 + \frac{ab}{30}\eta^5 - \frac{2(12a+b)}{6!}\eta^6 + \frac{32}{7!}\eta^7 + \ldots \quad (13)$$

where

$$a = 1.23259,\ b = 2.8978$$

A new independent variable ξ is defined as

$$\xi = \left(\frac{a}{6}\right)^{1/3}\mathrm{Pr}^{1/3}\eta \quad (14)$$

$\theta_0, \theta_2, g_2, \theta_4, g_4 \ldots$ of equation (7) are then expressed as function of ξ. Asymptotic expansion of these functions as a power series of $\mathrm{Pr}^{-1/3}$ gives, for example,

$$\theta_0(\xi) = \sum_{i=0}^{\infty}\theta_{0,i}(\xi)\,\mathrm{Pr}^{-i/3} \quad (15)$$

$\theta_{0,i}, \theta_{2,i} \ldots$ are universal functions. Table 2 gives the numerical results of the wall derivatives of these functions.

For Prandtl number approaches infinity, the first term on the right hand side of equation (15) is much larger than other terms. Therefore,

Table 2 Wall derivatives of the universal functions from perturbation method

$\theta'_{0,0}(0)$	−1.11984	$g'_{2,0}(0)$	−1.80549	$g'_{4,0}(0)$	−2.18998	$g'_{22,0}(0)$	−1.56088
$\theta'_{0,1}(0)$	0.12972	$g'_{2,1}(0)$	0.13662	$g'_{4,1}(0)$	0.13720	$g'_{22,1}(0)$	0.22547
$\theta'_{0,2}(0)$	0.03437	$g'_{2,2}(0)$	0.02543	$g'_{4,2}(0)$	0.02131	$g'_{22,2}(0)$	0.05865
$\theta'_{0,3}(0)$	−0.00838	$g'_{2,3}(0)$	−0.00359	$g'_{4,3}(0)$	−0.00245	$g'_{22,3}(0)$	−0.03248
$\theta'_{0,4}(0)$	−0.00047	$g'_{2,4}(0)$	−0.00011	$g'_{4,4}(0)$	−0.00005	$g'_{22,4}(0)$	0.01354
$\theta'_{2,0}(0)$	−1.12832	$\theta'_{4,0}(0)$	−1.57267	$\theta'_{22,0}(0)$	0.56589	$g'_{6,1}(0)$	−2.47384
$\theta'_{2,1}(0)$	0.21889	$\theta'_{4,1}(0)$	0.37659	$\theta'_{22,1}(0)$	−0.17936	$g'_{6,2}(0)$	0.13735
$\theta'_{2,2}(0)$	0.07593	$\theta'_{4,2}(0)$	0.12934	$\theta'_{22,2}(0)$	−0.04649	$g'_{6,3}(0)$	0.01895
$\theta'_{2,3}(0)$	−0.05862	$\theta'_{4,3}(0)$	−0.12664	$\theta'_{22,3}(0)$	0.06409	$g'_{6,4}(0)$	−0.001916
$\theta'_{2,4}(0)$	0.00962	$\theta'_{4,4}(0)$	0.02761	$\theta'_{22,4}(0)$	−0.01886	$g'_{6,5}(0)$	−0.000034

$$\theta'_0(0) = -0.66076\ \mathrm{Pr}^{-1/3},\ \mathrm{Pr} \to \infty \qquad (16)$$

It corresponds to the use of the first term of the righ-hand side of equation (12) for the velocity profile. This is known as the Lighthill approximation [11]. Other asymptotes are given in Table 3.

Table 3 Asymptotes for large Prandtl numbers

$$\theta'_0(0) = -0.66076\ \mathrm{Pr}^{1/3}$$
$$\theta'_2(0) = -0.66577\ \mathrm{Pr}^{1/3}$$
$$g'_2(0) = -1.06533\ \mathrm{Pr}^{1/3}$$
$$\theta'_4(0) = -0.92795\ \mathrm{Pr}^{1/3}$$
$$g'_4(0) = -1.29220\ \mathrm{Pr}^{1/3}$$
$$\theta'_{22}(0) = 0.33391\ \mathrm{Pr}^{1/3}$$
$$g'_{22}(0) = -0.92100\ \mathrm{Pr}^{1/3}$$
$$g'_6(0) = -1.45969\ \mathrm{Pr}^{1/3}$$

Conclusion

Blasius series solution is given for the heat transfer from a symmetrically cylindrical to a nonisothermal surface for the case of laminar boundary layer flow. Universal functions are given for large Prandtl number using perturbation technique. For small Prandtl number, an extensive table is given for the coefficients in Blasius series for heat transfer. However, the limitation of Blasius series solution for slender cylindrical surface is also encountered in our method [1, p. 154].

References

1 Schlichting, H., *Boundary Layer Theory*, McGraw-Hill, New York, Sixth edition, 1968.

2 Frössling, N., "Evaporation, Heat Transfer, and Velocity Distribution in Two-Dimensional and Rotationally Symmetrical Laminar Boundary Layer flow," NACA, TM1432, 1958.

3 Newman, J., "Blasius Series for Heat and Mass Transfer," *International Journal of Heat and Mass Transfer*, Vol. 9, 1966, pp. 705–709

4 Görtler, H., "A New Series for the Calculation of Steady Laminar Boundary Layer Flows," *Journal of Mathematics and Mechanics*, Vol. 6, No. 1, 1957, pp. 1–66.

5 Meksyn, D., *New Method in Laminar Boundary Layer Theory*, Pergamon Press, Oxford, 1961.

6 Merk, H. J., "Rapid Calculation for Boundary Layer Transfer Using Wedge Solutions and Asymptotic Expansions," *Journal of Fluid Mechanics*, Vol. 5, 1959, pp. 460–480.

7 Chao, B. T. and Fagbenle, R. O., "On Merk's Method of Calculating Boundary Layer Transfer," *International Journal of Heat and Mass Transfer*, Vol. 17, 1974, pp. 223–240.

8 Gadd, G. E., Jones, C. W. and Watson, E. J., "Approximate Methods of Solution," in *Laminar Boundary Layers*, Ed. by Rosenhead, L., Oxford University Press, 1963.

9 Tsay, S. Y., and Shih, Y. P., "Perturbation Solution for the Effect of Prandtl Number on Heat Transfer from a Non-isothermal Rotating Disk," *Letters in Heat and Mass Transfer*, Vol. 4, 1977, pp. 53–62.

10 Tsay, S. Y., "Effect of Prandtl Number on the Heat Transfer in Wedge Flow," *Journal of the Chinese Institute of Chemical Engineers*, Vol. 8, 1977, pp. 9–25.

11 Lighthill, M. L., "Contributions to the Theory of Heat Transfer Through a Laminar Boundary," *Proceedings of the Royal Society*, London, Vol. 202A, 1950, pp. 359–377.

Higher-Order Boundary Layer Effects in Plane Horizontal Natural Convection Flows

R. L. Mahajan[1] and B. Gebhart[2]

Nomenclature

G = modified Grashof number = $(\mathrm{Gr}_x)^{1/5}$

Q = total heat transfer rate from surface between leading edge and local x (per side per unit width)

$T = (t - t_\infty)/\Delta T$

X = Stokes radius = $\left(\dfrac{\upsilon^2}{g\beta_t N}\right)^{1/n+3}$

$\Delta T = t_0 - t_\infty = Nx^n$

ϕ = angular coordinate measured from plate

β_t = coefficient of thermal expansion

1 Introduction

There have been several investigations of the higher-order boundary layer effects for buoyancy induced flows adjacent to vertical surfaces [1–5]. The isothermal surface was considered in [1–4], while Mahajan and Gebhart [5] considered the uniform flux surface condition. There is, however, no prior investigation of the higher-order effects for natural convection flow adjacent to a horizontal surface. This paper treats this perturbation problem for a power law surface temperature variation. Matched asymptotic expansions are used to construct three term inner and outer expansions for velocity, temperature and pressure. The leading term is taken as the well known zeroth-order boundary layer solution treated earlier by Stewartson [6], Gill, et al. [7] and Rotem [8]. The eigenvalues and their eigenfunctions associated with the boundary layer expansions have been determined, together with a global momentum and energy analysis. Numerical results are then presented for flow and heat transfer quantities for Pr = 0.72 and 6.7 for isothermal surface condition.

2 Analysis

We consider a plane flow which is generated over an extensive horizontal surface downstream from a straight leading edge at $x = 0$. Gravity is taken to act in the negative y-direction and the surface temperature variation is given by ΔT. The treatment of this problem to higher-order approximations is similar in approach to that given in [5] and will be outlined here only briefly. The perturbation parameter ϵ in this case is $1/G$ and the inner expansions, valid in the boundary layer, and outer expansions, valid in the inviscid region are of the following forms.

Inner:

$$\psi = U\delta(f_0(\eta) + \epsilon f_1(\eta) + \epsilon^2 f_2(\eta) + C_m\epsilon^{\lambda m}F_m(\eta) + \ldots) \qquad (1a)$$

$$t - t_\infty = \Delta T(T_0(\eta) + \epsilon T_1(\eta) + \epsilon^2 T_2(\eta) + C_m\epsilon^{\lambda m}\theta_m(\eta) + \ldots) \qquad (1b)$$

$$p - p_\infty = \rho U^2(g_0(\eta) + \epsilon g_1(\eta) + \epsilon^2 g_2(\eta) + C_m\epsilon^{\lambda m}G_m(\eta) + \ldots) \qquad (1c)$$

[1] Research Leader, Western Electric Company, P.O. Box 900, Princeton, NJ 08540.

[2] Professor, Mechanical Engineering, State University of New York at Buffalo, Amherst, NY 14260.

Contributed by the Heat Transfer Division for publication in the JOURNAL OF HEAT TRANSFER. Manuscript received by the Heat Transfer Division December 27, 1979.

Table 2 Wall derivatives of the universal functions from perturbation method

$\theta'_{0,0}(0)$	−1.11984	$g'_{2,0}(0)$	−1.80549	$g'_{4,0}(0)$	−2.18998	$g'_{22,0}(0)$	−1.56088
$\theta'_{0,1}(0)$	0.12972	$g'_{2,1}(0)$	0.13662	$g'_{4,1}(0)$	0.13720	$g'_{22,1}(0)$	0.22547
$\theta'_{0,2}(0)$	0.03437	$g'_{2,2}(0)$	0.02543	$g'_{4,2}(0)$	0.02131	$g'_{22,2}(0)$	0.05865
$\theta'_{0,3}(0)$	−0.00838	$g'_{2,3}(0)$	−0.00359	$g'_{4,3}(0)$	−0.00245	$g'_{22,3}(0)$	−0.03248
$\theta'_{0,4}(0)$	−0.00047	$g'_{2,4}(0)$	−0.00011	$g'_{4,4}(0)$	−0.00005	$g'_{22,4}(0)$	0.01354
$\theta'_{2,0}(0)$	−1.12832	$\theta'_{4,0}(0)$	−1.57267	$\theta'_{22,0}(0)$	0.56589	$g'_{6,1}(0)$	−2.47384
$\theta'_{2,1}(0)$	0.21889	$\theta'_{4,1}(0)$	0.37659	$\theta'_{22,1}(0)$	−0.17936	$g'_{6,2}(0)$	0.13735
$\theta'_{2,2}(0)$	0.07593	$\theta'_{4,2}(0)$	0.12934	$\theta'_{22,2}(0)$	−0.04649	$g'_{6,3}(0)$	0.01895
$\theta'_{2,3}(0)$	−0.05862	$\theta'_{4,3}(0)$	−0.12664	$\theta'_{22,3}(0)$	0.06409	$g'_{6,4}(0)$	−0.001916
$\theta'_{2,4}(0)$	0.00962	$\theta'_{4,4}(0)$	0.02761	$\theta'_{22,4}(0)$	−0.01886	$g'_{6,5}(0)$	−0.000034

$$\theta'_0(0) = -0.66076\ \mathrm{Pr}^{-1/3},\ \mathrm{Pr} \to \infty \qquad (16)$$

It corresponds to the use of the first term of the righ-hand side of equation (12) for the velocity profile. This is known as the Lighthill approximation [11]. Other asymptotes are given in Table 3.

Table 3 Asymptotes for large Prandtl numbers

$$\theta'_0(0) = -0.66076\ \mathrm{Pr}^{1/3}$$
$$\theta'_2(0) = -0.66577\ \mathrm{Pr}^{1/3}$$
$$g'_2(0) = -1.06533\ \mathrm{Pr}^{1/3}$$
$$\theta'_4(0) = -0.92795\ \mathrm{Pr}^{1/3}$$
$$g'_4(0) = -1.29220\ \mathrm{Pr}^{1/3}$$
$$\theta'_{22}(0) = 0.33391\ \mathrm{Pr}^{1/3}$$
$$g'_{22}(0) = -0.92100\ \mathrm{Pr}^{1/3}$$
$$g'_6(0) = -1.45969\ \mathrm{Pr}^{1/3}$$

Conclusion

Blasius series solution is given for the heat transfer from a symmetrically cylindrical to a nonisothermal surface for the case of laminar boundary layer flow. Universal functions are given for large Prandtl number using perturbation technique. For small Prandtl number, an extensive table is given for the coefficients in Blasius series for heat transfer. However, the limitation of Blasius series solution for slender cylindrical surface is also encountered in our method [1, p. 154].

References

1 Schlichting, H., *Boundary Layer Theory*, McGraw-Hill, New York, Sixth edition, 1968.

2 Frössling, N., "Evaporation, Heat Transfer, and Velocity Distribution in Two-Dimensional and Rotationally Symmetrical Laminar Boundary Layer flow," NACA, TM1432, 1958.

3 Newman, J., "Blasius Series for Heat and Mass Transfer," *International Journal of Heat and Mass Transfer*, Vol. 9, 1966, pp. 705–709

4 Görtler, H., "A New Series for the Calculation of Steady Laminar Boundary Layer Flows," *Journal of Mathematics and Mechanics*, Vol. 6, No. 1, 1957, pp. 1–66.

5 Meksyn, D., *New Method in Laminar Boundary Layer Theory*, Pergamon Press, Oxford, 1961.

6 Merk, H. J., "Rapid Calculation for Boundary Layer Transfer Using Wedge Solutions and Asymptotic Expansions," *Journal of Fluid Mechanics*, Vol. 5, 1959, pp. 460–480.

7 Chao, B. T. and Fagbenle, R. O., "On Merk's Method of Calculating Boundary Layer Transfer," *International Journal of Heat and Mass Transfer*, Vol. 17, 1974, pp. 223–240.

8 Gadd, G. E., Jones, C. W. and Watson, E. J., "Approximate Methods of Solution," in *Laminar Boundary Layers*, Ed. by Rosenhead, L., Oxford University Press, 1963.

9 Tsay, S. Y., and Shih, Y. P., "Perturbation Solution for the Effect of Prandtl Number on Heat Transfer from a Non-isothermal Rotating Disk," *Letters in Heat and Mass Transfer*, Vol. 4, 1977, pp. 53–62.

10 Tsay, S. Y., "Effect of Prandtl Number on the Heat Transfer in Wedge Flow," *Journal of the Chinese Institute of Chemical Engineers*, Vol. 8, 1977, pp. 9–25.

11 Lighthill, M. L., "Contributions to the Theory of Heat Transfer Through a Laminar Boundary," *Proceedings of the Royal Society*, London, Vol. 202A, 1950, pp. 359–377.

Higher-Order Boundary Layer Effects in Plane Horizontal Natural Convection Flows

R. L. Mahajan[1] and B. Gebhart[2]

Nomenclature

G = modified Grashof number = $(\mathrm{Gr}_x)^{1/5}$

Q = total heat transfer rate from surface between leading edge and local x (per side per unit width)

$T = (t - t_\infty)/\Delta T$

X = Stokes radius = $\left(\dfrac{\upsilon^2}{g\beta_t N}\right)^{1/n+3}$

$\Delta T = t_0 - t_\infty = Nx^n$

ϕ = angular coordinate measured from plate

β_t = coefficient of thermal expansion

1 Introduction

There have been several investigations of the higher-order boundary layer effects for buoyancy induced flows adjacent to vertical surfaces [1–5]. The isothermal surface was considered in [1–4], while Mahajan and Gebhart [5] considered the uniform flux surface condition. There is, however, no prior investigation of the higher-order effects for natural convection flow adjacent to a horizontal surface. This paper treats this perturbation problem for a power law surface temperature variation. Matched asymptotic expansions are used to construct three term inner and outer expansions for velocity, temperature and pressure. The leading term is taken as the well known zeroth-order boundary layer solution treated earlier by Stewartson [6], Gill, et al. [7] and Rotem [8]. The eigenvalues and their eigenfunctions associated with the boundary layer expansions have been determined, together with a global momentum and energy analysis. Numerical results are then presented for flow and heat transfer quantities for Pr = 0.72 and 6.7 for isothermal surface condition.

2 Analysis

We consider a plane flow which is generated over an extensive horizontal surface downstream from a straight leading edge at $x = 0$. Gravity is taken to act in the negative y-direction and the surface temperature variation is given by ΔT. The treatment of this problem to higher-order approximations is similar in approach to that given in [5] and will be outlined here only briefly. The perturbation parameter ϵ in this case is $1/G$ and the inner expansions, valid in the boundary layer, and outer expansions, valid in the inviscid region are of the following forms.

Inner:

$$\psi = U\delta(f_0(\eta) + \epsilon f_1(\eta) + \epsilon^2 f_2(\eta) + C_m\epsilon^{\lambda m}F_m(\eta) + \ldots) \qquad (1a)$$

$$t - t_\infty = \Delta T(T_0(\eta) + \epsilon T_1(\eta) + \epsilon^2 T_2(\eta) + C_m\epsilon^{\lambda m}\theta_m(\eta) + \ldots) \qquad (1b)$$

$$p - p_\infty = \rho U^2(g_0(\eta) + \epsilon g_1(\eta) + \epsilon^2 g_2(\eta) + C_m\epsilon^{\lambda m}G_m(\eta) + \ldots) \qquad (1c)$$

[1] Research Leader, Western Electric Company, P.O. Box 900, Princeton, NJ 08540.

[2] Professor, Mechanical Engineering, State University of New York at Buffalo, Amherst, NY 14260.

Contributed by the Heat Transfer Division for publication in the JOURNAL OF HEAT TRANSFER. Manuscript received by the Heat Transfer Division December 27, 1979.

Outer:

$$\psi = \bar{\psi}_0 + \bar{\psi}_1 + \bar{\psi}_2 \tag{2a}$$

$$t - t_\infty = H_0 + H_1 + H_2 \tag{2b}$$

$$p - p_\infty = P_0 + P_1 + P_2 \tag{2c}$$

where

$$U = \frac{\nu G^2}{x}, \delta = \frac{x}{G}$$

In the boundary layer expansions (1), λ_m is the eigenvalue associated with the eigenfunctions, $C_m \epsilon^{\lambda m} F_m$, $C_m \epsilon^{\lambda m} A_m$ and $C_m \epsilon^{\lambda m} m_{G_m}$. These functions identically satisfy the boundary conditions at $\eta = 0$ and $\eta = \infty$. The multiplying constant, C_m, was pointed out by Stewartson [6] to be associated with the stream function upstream.

The classical zeroth order boundary layer problem is given by

$$f_0''' - \frac{4n+2}{5} g_0 - \frac{n-2}{5} g_0' \eta + \frac{n+3}{5} f_0 f_0'' - \frac{2n+1}{5} f_0'^2 = 0 \tag{3a}$$

$$g_0' - T_0 = 0 \tag{3b}$$

$$\frac{T_0''}{\mathrm{Pr}} + \frac{n+3}{5} f_0 T_0' - n T_0 f_0' = 0 \tag{3c}$$

subject to the boundary conditions

$$f_0(0) = f_0'(0) = T_0(0) - 1 = 0 \tag{4}$$

Matching of 1-term inner and outer expansions, of u, p and t, provides the following conditions

$$f_0'(\infty) = g_0'(\infty) = T_0(\infty) = 0 \tag{5}$$

The asymptotic forms of the functions f_0, g_0 and T_0 as $\eta \to \infty$ are obtained to be $f_0(\eta) \sim A_0 + est$, $g_0(\eta) \sim est$, and $T_0(\eta) \sim est$, where A_0 is a constant for a given Prandtl number and est denotes exponentially small terms. In the outer region, $\bar{\psi}_0 = H_0 = P_0 = 0$.

In a manner completely analogous to that given in [3] and [5], it can be easily shown that the solution to the first order outer problem is given by

$$\bar{\psi}_1 = \frac{A_0 \upsilon}{\sin \frac{n+3}{5}\pi} \left(\frac{r}{X}\right)^{\frac{n+3}{5}} \sin \frac{n+3}{5}(\pi - \phi) \tag{6}$$

$$P_1 = -\frac{1}{2}\rho \frac{\left(\frac{n+3}{5}\right)^2}{\sin^2 \frac{n+3}{5}\pi} A_0^2 \left(\frac{\nu}{X}\right)^2 \left(\frac{X}{r}\right)^{\frac{4-2n}{5}} \tag{7}$$

Consequently, the first-order boundary layer problem is:

$$f_1''' - \frac{3n-1}{5} f_0' f_1' + \frac{n+3}{5} f_0 f_1'' = \frac{3n-1}{5} g_1 + \frac{n-2}{5} \eta g_1' \tag{8a}$$

$$g_1' = T_1 \tag{8b}$$

$$n(T_0 f_1'' + f_0' T_1) - \frac{n+3}{5}(f_0 T_1)' = \frac{T_1''}{\mathrm{Pr}} \tag{8c}$$

with

$$f_1(0) = f_1'(0) = T_1(0) = 0, f_1'(\infty) = -A_0 \frac{n+3}{5} \cot \frac{n+3}{5}\pi, g_1(\infty) = 0 = T_1(\infty) \tag{8d}$$

It follows that $f_1 \sim -A_0 n + 3/5 \cot (\frac{n}{3/5}\pi)\eta + A_1$, where A_1 is a numerically determined constant.

The second order outer problem is given by

$$H_2 \equiv 0, \nabla^2 \bar{\psi}_{(\phi=\pi)2} = 0, \bar{\psi}_{2(\phi=0)} = 0 \quad \bar{\psi}_2 = \upsilon A_1 \tag{9}$$

where the last condition is obtained from two term matching of the outer and inner stream functions. The solution $\bar{\psi}_2$ is found to be

$$\bar{\psi}_2 = A_1 \nu \left(1 - \frac{\phi}{\pi}\right) \tag{10}$$

From Bernoulli's theorem, we obtain

$$P_2 = -\frac{A_0 A_1}{\pi} \frac{n+3}{5} \frac{\cos \frac{n+3}{5}(\phi - \pi)}{\sin \frac{n+3}{5}\pi} \rho \left(\frac{\nu}{X}\right)^2 \left(\frac{X}{r}\right)^{\frac{7-n}{5}} \tag{11}$$

The next terms, f_2, g_2 and T_2 of the inner expansions, are found to satisfy

$$f_2''' - \frac{2n-4}{5} f_0' f_2' - \frac{n-2}{5} f_1' f_1' - \frac{n+3}{5} f_2 f_0'' + \frac{n+3}{5} f_0 f_2'' = \frac{2n-4}{5} g_2 + \frac{n-2}{5} \eta g_2' - \frac{4n^2-6n-4}{25} f_0' - \frac{n^2-3n+2}{5} f_0'' \eta - \frac{n^2-4n+4}{25} f_0''' \eta^2 \tag{12a}$$

$$\frac{n^2+6n+9}{25} f_0 f_0' - \frac{n^2-4n+4}{25} \eta f_0'^2 + \frac{n^2+n-6}{25} \eta f_0 f_0'' + \frac{3n-1}{5} f_0'' + \frac{n-2}{5} \eta f_0''' = T_2 - g_2' \tag{12b}$$

$$\frac{T_2''}{\mathrm{Pr}} + \frac{n+3}{5} f_0 T_2' - \frac{3n-6}{5} f_0' T_2 = n T_0 f_2' + \frac{n+3}{5} f_2 T_0' + \frac{4n-3}{5} f_1' T_1 + \frac{n(1-n)T_0}{\mathrm{Pr}} - \frac{2n(n-2)T_0'}{5\mathrm{Pr}} - \frac{(n-2)(n-7)}{25\mathrm{Pr}} \eta T_0' - \frac{(n-2)^2}{25\mathrm{Pr}} \eta^2 T_0'' \tag{12c}$$

with boundary conditions

$$f_2(0) = f_2'(0) = T_2(0) = 0 \tag{13a}$$

Matching the inner and outer expansions for u, t and p, we get

$$f_2'(\infty) = -\frac{A_1}{\pi} - \frac{(n+3)(n-2)}{25} A_0 \eta, T_2(\infty) = 0 \text{ and } g_2(\infty) = -\frac{(n+3)^2}{50} \frac{A_0^2}{\sin^2 \frac{n+3}{5}\pi} \tag{13b}$$

Eigenvalues and Eigenfunctions. The linear homogeneous equation for F_m, G_m and θ_m are obtained to be

$$F_m''' + \frac{n+3}{5}(1 - \lambda_m) f_0'' F_m + \frac{n+3}{5} \lambda_m f_0' F_m' - \frac{4n+2}{5} f_0' F_m' + \frac{n+3}{5} f_0 F_m'' = \frac{4n+2}{5} G_m - \frac{n+3}{5} \lambda_m G_m + \frac{n-2}{5} \eta G_m' \tag{14a}$$

$$\theta_m - G_m' = 0 \tag{14b}$$

$$\frac{\theta_m''}{\mathrm{Pr}} + \frac{n+3}{5} f_0 \theta_m' - f_0' \theta_m \left(n - \frac{n+3}{5}\lambda_m\right) - n T_0 F_m' + \frac{n+3}{5} F_m T_0'(1 - \lambda_m) = 0 \tag{14c}$$

subject to the following conditions

$$F_m(0) = F_m'(0) = \theta_m(0) = F_m'(\infty) = G_m(\infty) = \theta_m(\infty) = 0 \tag{15}$$

The normalization condition is taken as $F_m(\infty) = 1$.

3 Results and Discussion for the Isothermal Surface Condition

We now consider a particular case of the power law surface temperature variation, $n = 0$. This is the isothermal condition. The perturbation equations are obtained from equation (3–13).

Table 1 Numerical results for isothermal case

	$f_i''(0)$		$T_i'(0)$		A_i	
	Pr = .72	Pr = 6.7	Pr = .72	Pr = 6.7	Pr = .72	Pr = 6.7
$i = 0$	0.97840	0.42389	−0.35741	−0.62394	2.33376	0.91003
$i = 1$	0.26881	0.05679	0.	0.	−0.30498	−0.34031
$i = 2$	−7.94945	−7.47330	2.20636	10.63676		

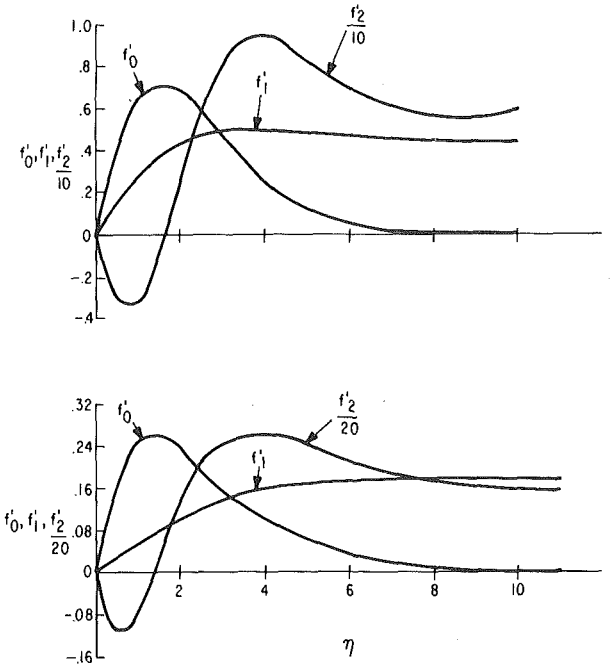

Fig. 1 Velocity function profiles for Pr = 0.72 (top) and for Pr = 6.7 (bottom)

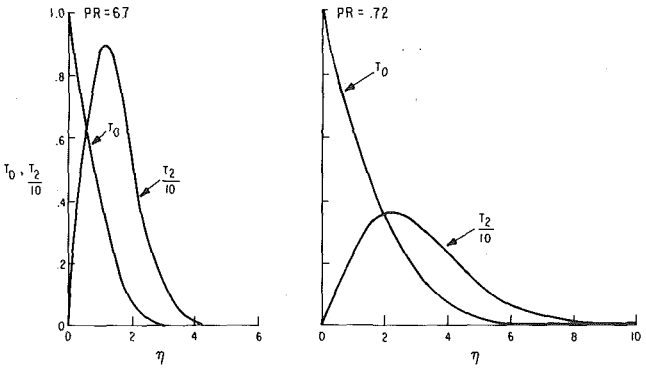

Fig. 2 Temperature function profiles

It is clear from (8*b*, 8*c*) and (8*d*), for $n = 0$, that the only solution that satisfies (8*b*) and (8*c*) is $T_1 \equiv 0 \equiv g_1$. Thus the first-order correction to both the temperature and pressure fields is identically zero. The first result is similar to that obtained for a vertical surface [3].

The zeroth to second-order boundary layers obtained in Section 2 for $n = 0$, were solved numerically using fourth-order Runge Kutta method. The integration scheme was similar to the one used in [5]. Missing values of $f_i''(0)$, $T_i'(0)$ and the values of the constants A_i for these equations for Pr = 0.72 and Pr = 6.7 are listed in Table 1.

The velocity, and temperature distributions associated with the above solutions are given in Figs. 1 and 2.

Eigenvalues and Eigenfunctions. The governing equations for the complementary functions (14), for $n = 0$, were found numerically using the boundary conditions (15). The first two eigenvalues, having values less than 2, and their associated eigenfunctions, are given in Table 2 for both Pr = 0.72 and Pr = 6.7.

Table 2

i	λ_m	$F_m''(0)$		$\theta_m'(0)$	
		Pr = .72	Pr = 6.7	Pr = .72	Pr = 6.7
1	1.5547	−0.0550	−0.0531	0.0855	0.3012
2	5/3	−0.1397	−0.1553	0.1021	0.4572

Of the two, the eigenfunctions associated with λ_2 can be explicitly determined to be

$$F_2 = \frac{1}{A_0}\left(f_0 - \frac{2}{3}\eta f_0'\right) \tag{16a}$$

$$\theta_2 = \frac{1}{A_0}\left(-\frac{2}{3}\eta T_0'\right) \tag{16b}$$

$$G_2 = \frac{1}{A_0}\left(\frac{2}{3}g_0 - \frac{2}{3}\eta g_0'\right) \tag{16c}$$

These are seen to be proportional to the x-derivative of the zeroth-order stream function, temperature and pressure, respectively. Hence, following Stewartson [6], these represent the indeterminacy associated with the location of the leading edge.

Improved Values of Local Surface Heat Flux, q_w, and Skin Friction, τ_ω

$$q_w = -kt_{y_{y=0}} = -k\frac{\Delta T}{\delta}\left[T_0'(0) + C_1\epsilon^{1.5547}\theta_1'(0) + C_2\epsilon^{5/3}\theta_2'(0) + \epsilon^2 T_2'(0) + \ldots\right] \tag{17}$$

Note that there is no first-order correction to q_w, and that the next order correction is indeterminate.

$$\tau_w = \mu u_{y_{y=0}} = \mu\frac{U}{\delta}\left[f_0''(0) + \epsilon f_1''(0) + C_1\epsilon^{1.5547}F_1''(0) + C_2\epsilon^{5/3}F_2''(0) + \epsilon^2 f_2''(0) + \ldots\right] \tag{18}$$

From the results given in Table 1, the first order correction to τ_w is positive for both values of the Prandtl number.

Total Heat Transfer Rate, Q, and the Total Drag, *D*. Following the procedure indicated in [5], these quantities are determined below.

$$Q = k\Delta T\left(\frac{0.5957}{\epsilon} + 0.3420 + 0.2569C_1\epsilon^{0.5547} + 0.2553C_2\epsilon^{2/3} + 3.6775\epsilon^2 + \ldots.\right) \text{for Pr} = 0.72 \tag{19a}$$

$$Q = k\Delta T\left(\frac{1.0399}{\epsilon} + 0.2512 + 0.9050C_1\epsilon^{0.5547} + 1.1430C_2\epsilon^{2/3} + 17.7279\epsilon^2 + \ldots.\right) \text{for Pr} = 6.7 \tag{19b}$$

From (17) and (19), it is seen that, although the first-order correction to local wall heat flux is zero, the 0 (ϵ) correction to total heat is not zero. A similar result was found by Hieber [3] for a vertical isothermal surface. Further, as shown in [3], this 0 (ϵ) correction to Q may be interpreted as the leading edge effect upon the global heat transfer rate.

$$D = \rho\frac{U}{\delta}x\left(\frac{5}{4}f_0''(0) + 5\epsilon f_1''(0) - 7.529C_1\epsilon^{1.5547}F_1''(0) - 5C_2\epsilon^{5/3}F_2''(0) - \frac{5}{2}\epsilon^2 f_2''(0) + \ldots\right) \tag{20}$$

Comparison of (20) and (18) shows that unlike the vertical flow [3], there is no 0 (1) contribution to D due to global buoyany force acting through the leading edge region. This is to be expected since the buoyant force in this case acts normal to the plate.

Acknowledgements

The authors wish to express their appreciation for the support of the National Science Foundation under Grant ENG 7721641 and the reviewers for their comments.

References

1 Yang, K. T., and Jerger, E. W., 1964, "First-Order Perturbations of Laminar Free Convection Boundary Layers on a Vertical Plate," ASME JOURNAL OF HEAT TRANSFER, Vol. 86, pp. 107–115.

2 Kadambi, V., 1969, "Singular Perturbations in Free-Convection," *Warmeund Stoffubert ragung,* Vol. 2, pp. 99–104.

3 Hieber, C. A., 1974, "Natural Convection Around a Semi-Infinite Vertical Plate: Higher Order Effects," *International Journal of Heat and Mass Transfer,* Vol. 17, pp. 785–791.

4 Riley, D. S., and Drake, D. G., 1975, "Higher Approximations to the Free Convection Flow from a Heated Vertical Flat Plate," *Applied Scientific Research,* 30(3), pp. 193–207.

5 Mahajan, R. L., and Gebhart, B., 1978, "Higher Order Approximations to the Natural Convection Flow Over a Uniform Flux Vertical Surface," *International Journal of Heat and Mass Transfer,* Vol. 21, pp. 549–555.

6 Stewartson, K., 1958, "On Free Convection from a Horizontal Plate," *ZAMP,* 9a, pp. 276–281.

7 Gill, W. N., Zeh, D. W., and Del-Casal, E., 1965, "Free Convection on a Horizontal Plate," *ZAMP,* 16, pp. 532–541.

8 Rotem, Z., and Classen, L., 1969, "Natural Convection Above Unconfined Horizontal Surfaces," *JFM,* 38, Part 1, pp. 173–192.

Buoyancy Effects in Boundary Layers on Inclined, Continuous, Moving Sheets

A. Moutsoglou[1] and T. S. Chen[1]

Introduction

The problem of heat transfer in boundary layer on a continuous, moving surface has many practical applications in manufacturing processes in industry and has been investigated by many authors (see, for example, [1–5]). However, aside from the work of Chen and Strobel [5], the buoyancy force effects resulting from the temperature differences in the fluid were neglected in all the previous studies. In the present paper, we examine analytically the buoyancy force effects on the heat transfer charactertistics of laminar boundary layer adjacent to an inclined, continuous flat sheet that moves in a fluid at rest.

Analysis

Consider now a continuous flat sheet that originates from a slot and is moving with a constant velocity u_0 in an inclined direction through an otherwise quiescent fluid at temperature T_∞. The positive x coordinate is measured along the direction of the moving sheet with the slot as the origin and the positive y coordinate is measured normal to the surface in the outward direction toward the fluid. The sheet is assumed to be either maintained at a uniform wall temperature T_w or subjected to a uniform surface heat flux q_w. The inclination of the moving sheet is measured by the acute angle γ from the vertical. The analysis applies to both heating and cooling of the sheet, with the sheet moving either upward or downward. The case of a vertically moving sheet corresponds to $\gamma = 0$ deg.

The mathematical formulation of the present problem resembles that of the problem of forced flow over an inclined, stationary plate [6], even though the two problems are physically distinct. Thus, subject to the condition $(\delta/x)\tan\gamma \ll 1$, where δ is the flow boundary layer thickness, the conservation equations are identical to equations (1, 9), and (4) of reference [6], but the boundary conditions for the velocity field are now changed to $u = u_0$ and $v = 0$ at $y = 0$ and $u \to 0$ as $y \to \infty$. Thus, with u_∞ replaced by u_0, $f'(\xi,0) = 0$ by $f'(\xi, 0) = 1$, $f'(\xi, \infty) = 1$ by $f'(\xi, \infty) = 0$, $F'(\chi, 0) = 0$ by $F'(\chi, 0) = 1$, and $F'(\chi, \infty) = 1$ by $F'(\chi, \infty) = 0$, the nomenclature and equations (10–17) and (22–31) for the stationary plate problem [6] apply as well to the present problem. It suffices to reiterate here that the local friction factor C_f and the local Nusselt number Nu_x are given, respectively, by

$$C_f \mathrm{Re}_x^{1/2} = 2f''(\xi, 0), \quad \mathrm{Nu}_x Re_x^{-1/2} = -\theta'(\xi,0) \tag{1}$$

for the case of uniform wall temperature (UWT) and by

$$C_f \mathrm{Re}_x^{1/2} = 2F''(\chi, 0), \quad \mathrm{Nu}_x \mathrm{Re}_x^{-1/2} = 1/\Phi(\chi, 0) \tag{2}$$

for the case of uniform heat flux (UHF) at the surface. In equations (1) and (2), $\mathrm{Re}_x = u_0 x/\nu$ is the Reynolds number, $f(\xi, \eta)$ and $F(\chi, \eta)$, both defined as $\psi(x, y)/(\nu u_0 x)^{1/2}$, are the respective reduced stream functions, $\theta(\xi, \eta) = (T - T_\infty)/(T_w - T_\infty)$ and $\Phi(\chi, \eta) = (T - T_\infty)\text{-}\mathrm{Re}_x^{1/2}/(q_w x/k)$ are the respective dimensionless temperatures, and the primes denote partial derivatives with respect to $\eta = y(u_0/\nu x)^{1/2}$. The respective buoyancy force parameters ξ and χ have the expressions

$$\xi = |\mathrm{Gr}_x| \cos\gamma/\mathrm{Re}_x^2, \quad \chi = |\mathrm{Gr}_x^*| \cos\gamma/\mathrm{Re}_x^{5/2} \tag{3}$$

with $\mathrm{Gr}_x = g\beta(T_w - T_\infty)x^3/\nu^2$ and $\mathrm{Gr}_x^* = g\beta q_w x^4/k\nu^2$ representing the respective local Grashof numbers for the UWT and UHF cases. Except for the changes in the boundary conditions to $f'(\xi, 0) = 1$, $f'(\xi, \infty) = 0$ and $F'(\chi, 0) = 1$, $F'(\chi, \infty) = 0$, it is noted that $f(\xi, \eta)$, $\theta(\xi, \eta)$ and $F(\chi, \eta)$, $\Phi(\chi, \eta)$ satisfy, respectively, equations (13–15) and (26–28) of reference [6].

The average friction factor $\overline{C}_f = \overline{\tau}_w/(\rho u_0^2/2)$ and the average Nusselt number $\overline{\mathrm{Nu}} = \overline{h}L/k$ over a length L of the sheet are also of practical interest. From the definitions of the average wall shear stress $\overline{\tau}_w$ and the average heat transfer coefficient $\overline{h}$

$$\overline{\tau}_w = \frac{1}{L}\int_0^L \tau_w(x)dx, \quad \overline{h} = \frac{1}{L}\int_0^L h(x)dx \tag{4}$$

it can be shown that for the UWT case

$$\overline{C}_f \mathrm{Re}_L^{1/2} = \frac{2}{\xi_L^{1/2}}\int_0^{\xi_L} f''(\xi, 0)\xi^{-1/2}d\xi,$$

$$\overline{\mathrm{Nu}}\mathrm{Re}_L^{-1/2} = \frac{1}{\xi_L^{1/2}}\int_0^{\xi_L} [-\theta'(\xi, 0)]\xi^{-1/2}d\xi \tag{5}$$

and that for the UHF case

$$\overline{C}_f \mathrm{Re}_L^{1/2} = \frac{4}{3}\frac{1}{\chi_L^{1/3}}\int_0^{\xi_L} F''(\chi, 0)\chi^{-2/3}d\chi,$$

$$\overline{Nu}Re_L^{-1/2} = \frac{2}{3}\frac{1}{\chi_L^{1/3}}\int_0^{\xi_L} [\Phi(\chi, 0)]^{-1}\chi^{-2/3}d\chi \tag{6}$$

with ξ_L and χ_L denoting, respectively, the values of ξ and χ based on the length L.

Results and Discussion

The numerical solutions of the systems of equations for the functions $f(\xi, \eta)$, $\theta(\xi, \eta)$ and $F(\chi, \eta)$, $\Phi(\chi, \eta)$ were carried out by using an efficient and accurate finite-difference method similar to but modified from that described in [7]. Results were obtained for fluids with Prandtl numbers, Pr, of 0.7 and 7, which are typical for air and water, for a range of values of the buoyancy force parameters ξ and χ. Representative values of $f''(\xi, 0)$, $\theta'(\xi, 0)$ for the UWT case and $F''(\chi, 0)$, $\Phi(\chi, 0)$ for the UHF case are listed, respectively, in Tables 1 and 2.

The variations of the local friction factor C_f and the local Nusselt number Nu_x with the buoyancy force parameters ξ and χ, respectively, for the UWT and UHF cases, can be obtained from equations (1) and (2), along with the results in Tables 1 and 2. They are, there-

[1] Department of Mechanical and Aerospace Engineering, University of Missouri-Rolla, Rolla, Mo.

Contributed by The Heat Transfer Division for publication in the JOURNAL OF HEAT TRANSFER. Manuscript received by the Heat Transfer Division September 21, 1979.

Comparison of (20) and (18) shows that unlike the vertical flow [3], there is no 0 (1) contribution to D due to global buoyany force acting through the leading edge region. This is to be expected since the buoyant force in this case acts normal to the plate.

Acknowledgements

The authors wish to express their appreciation for the support of the National Science Foundation under Grant ENG 7721641 and the reviewers for their comments.

References

1 Yang, K. T., and Jerger, E. W., 1964, "First-Order Perturbations of Laminar Free Convection Boundary Layers on a Vertical Plate," ASME JOURNAL OF HEAT TRANSFER, Vol. 86, pp. 107–115.

2 Kadambi, V., 1969, "Singular Perturbations in Free-Convection," *Warmeund Stoffubert ragung,* Vol. 2, pp. 99–104.

3 Hieber, C. A., 1974, "Natural Convection Around a Semi-Infinite Vertical Plate: Higher Order Effects," *International Journal of Heat and Mass Transfer,* Vol. 17, pp. 785–791.

4 Riley, D. S., and Drake, D. G., 1975, "Higher Approximations to the Free Convection Flow from a Heated Vertical Flat Plate," *Applied Scientific Research,* 30(3), pp. 193–207.

5 Mahajan, R. L., and Gebhart, B., 1978, "Higher Order Approximations to the Natural Convection Flow Over a Uniform Flux Vertical Surface," *International Journal of Heat and Mass Transfer,* Vol. 21, pp. 549–555.

6 Stewartson, K., 1958, "On Free Convection from a Horizontal Plate," *ZAMP,* 9a, pp. 276–281.

7 Gill, W. N., Zeh, D. W., and Del-Casal, E., 1965, "Free Convection on a Horizontal Plate," *ZAMP,* 16, pp. 532–541.

8 Rotem, Z., and Classen, L., 1969, "Natural Convection Above Unconfined Horizontal Surfaces," *JFM,* 38, Part 1, pp. 173–192.

Buoyancy Effects in Boundary Layers on Inclined, Continuous, Moving Sheets

A. Moutsoglou[1] and T. S. Chen[1]

Introduction

The problem of heat transfer in boundary layer on a continuous, moving surface has many practical applications in manufacturing processes in industry and has been investigated by many authors (see, for example, [1–5]). However, aside from the work of Chen and Strobel [5], the buoyancy force effects resulting from the temperature differences in the fluid were neglected in all the previous studies. In the present paper, we examine analytically the buoyancy force effects on the heat transfer charactertistics of laminar boundary layer adjacent to an inclined, continuous flat sheet that moves in a fluid at rest.

Analysis

Consider now a continuous flat sheet that originates from a slot and is moving with a constant velocity u_0 in an inclined direction through an otherwise quiescent fluid at temperature T_∞. The positive x coordinate is measured along the direction of the moving sheet with the slot as the origin and the positive y coordinate is measured normal to the surface in the outward direction toward the fluid. The sheet is assumed to be either maintained at a uniform wall temperature T_w or subjected to a uniform surface heat flux q_w. The inclination of the moving sheet is measured by the acute angle γ from the vertical. The analysis applies to both heating and cooling of the sheet, with the sheet moving either upward or downward. The case of a vertically moving sheet corresponds to $\gamma = 0$ deg.

The mathematical formulation of the present problem resembles that of the problem of forced flow over an inclined, stationary plate [6], even though the two problems are physically distinct. Thus, subject to the condition $(\delta/x)\tan\gamma \ll 1$, where δ is the flow boundary layer thickness, the conservation equations are identical to equations (1, 9), and (4) of reference [6], but the boundary conditions for the velocity field are now changed to $u = u_0$ and $v = 0$ at $y = 0$ and $u \to 0$ as $y \to \infty$. Thus, with u_∞ replaced by u_0, $f'(\xi,0) = 0$ by $f'(\xi, 0) = 1$, $f'(\xi, \infty) = 1$ by $f'(\xi, \infty) = 0$, $F'(\chi, 0) = 0$ by $F'(\chi, 0) = 1$, and $F'(\chi, \infty) = 1$ by $F'(\chi, \infty) = 0$, the nomenclature and equations (10–17) and (22–31) for the stationary plate problem [6] apply as well to the present problem. It suffices to reiterate here that the local friction factor C_f and the local Nusselt number Nu_x are given, respectively, by

$$C_f \mathrm{Re}_x^{1/2} = 2f''(\xi, 0), \quad \mathrm{Nu}_x Re_x^{-1/2} = -\theta'(\xi,0) \tag{1}$$

for the case of uniform wall temperature (UWT) and by

$$C_f \mathrm{Re}_x^{1/2} = 2F''(\chi, 0), \quad \mathrm{Nu}_x \mathrm{Re}_x^{-1/2} = 1/\Phi(\chi, 0) \tag{2}$$

for the case of uniform heat flux (UHF) at the surface. In equations (1) and (2), $\mathrm{Re}_x = u_0 x/\nu$ is the Reynolds number, $f(\xi, \eta)$ and $F(\chi, \eta)$, both defined as $\psi(x, y)/(\nu u_0 x)^{1/2}$, are the respective reduced stream functions, $\theta(\xi, \eta) = (T - T_\infty)/(T_w - T_\infty)$ and $\Phi(\chi, \eta) = (T - T_\infty)\text{-}\mathrm{Re}_x^{1/2}/(q_w x/k)$ are the respective dimensionless temperatures, and the primes denote partial derivatives with respect to $\eta = y(u_0/\nu x)^{1/2}$. The respective buoyancy force parameters ξ and χ have the expressions

$$\xi = |\mathrm{Gr}_x| \cos\gamma/\mathrm{Re}_x^2, \quad \chi = |\mathrm{Gr}_x^*| \cos\gamma/\mathrm{Re}_x^{5/2} \tag{3}$$

with $\mathrm{Gr}_x = g\beta(T_w - T_\infty)x^3/\nu^2$ and $\mathrm{Gr}_x^* = g\beta q_w x^4/k\nu^2$ representing the respective local Grashof numbers for the UWT and UHF cases. Except for the changes in the boundary conditions to $f'(\xi, 0) = 1$, $f'(\xi, \infty) = 0$ and $F'(\chi, 0) = 1$, $F'(\chi, \infty) = 0$, it is noted that $f(\xi, \eta)$, $\theta(\xi, \eta)$ and $F(\chi, \eta)$, $\Phi(\chi, \eta)$ satisfy, respectively, equations (13–15) and (26–28) of reference [6].

The average friction factor $\overline{C}_f = \overline{\tau}_w/(\rho u_0^2/2)$ and the average Nusselt number $\overline{\mathrm{Nu}} = \overline{h}L/k$ over a length L of the sheet are also of practical interest. From the definitions of the average wall shear stress $\overline{\tau}_w$ and the average heat transfer coefficient $\overline{h}$

$$\overline{\tau}_w = \frac{1}{L}\int_0^L \tau_w(x)dx, \quad \overline{h} = \frac{1}{L}\int_0^L h(x)dx \tag{4}$$

it can be shown that for the UWT case

$$\overline{C}_f \mathrm{Re}_L^{1/2} = \frac{2}{\xi_L^{1/2}}\int_0^{\xi_L} f''(\xi, 0)\xi^{-1/2}d\xi,$$

$$\overline{\mathrm{Nu}}\mathrm{Re}_L^{-1/2} = \frac{1}{\xi_L^{1/2}}\int_0^{\xi_L} [-\theta'(\xi, 0)]\xi^{-1/2}d\xi \tag{5}$$

and that for the UHF case

$$\overline{C}_f \mathrm{Re}_L^{1/2} = \frac{4}{3}\frac{1}{\chi_L^{1/3}}\int_0^{\xi_L} F''(\chi, 0)\chi^{-2/3}d\chi,$$

$$\overline{Nu}Re_L^{-1/2} = \frac{2}{3}\frac{1}{\chi_L^{1/3}}\int_0^{\xi_L} [\Phi(\chi, 0)]^{-1}\chi^{-2/3}d\chi \tag{6}$$

with ξ_L and χ_L denoting, respectively, the values of ξ and χ based on the length L.

Results and Discussion

The numerical solutions of the systems of equations for the functions $f(\xi, \eta)$, $\theta(\xi, \eta)$ and $F(\chi, \eta)$, $\Phi(\chi, \eta)$ were carried out by using an efficient and accurate finite-difference method similar to but modified from that described in [7]. Results were obtained for fluids with Prandtl numbers, Pr, of 0.7 and 7, which are typical for air and water, for a range of values of the buoyancy force parameters ξ and χ. Representative values of $f''(\xi, 0)$, $\theta'(\xi, 0)$ for the UWT case and $F''(\chi, 0)$, $\Phi(\chi, 0)$ for the UHF case are listed, respectively, in Tables 1 and 2.

The variations of the local friction factor C_f and the local Nusselt number Nu_x with the buoyancy force parameters ξ and χ, respectively, for the UWT and UHF cases, can be obtained from equations (1) and (2), along with the results in Tables 1 and 2. They are, there-

[1] Department of Mechanical and Aerospace Engineering, University of Missouri-Rolla, Rolla, Mo.

Contributed by The Heat Transfer Division for publication in the JOURNAL OF HEAT TRANSFER. Manuscript received by the Heat Transfer Division September 21, 1979.

Table 1 Results for $f''(\xi, 0)$ and $-\theta'(\xi, 0)$, uniform wall temperature

$\frac{Gr_x \cos\gamma}{Re_x^2}$	Pr = 0.7		Pr = 7.0	
	$f''(\xi, 0)$	$-\theta'(\xi, 0)$	$f''(\xi, 0)$	$-\theta'(\xi, 0)$
5.0	2.13988	0.59086	0.99201	1.58510
4.5	1.92062	0.57893	0.86049	1.56956
4.0	1.69652	0.56609	0.72697	1.55334
3.5	1.46692	0.55214	0.59126	1.53641
3.0	1.23103	0.53681	0.45318	1.51864
2.5	0.98772	0.51973	0.31245	1.49999
2.0	0.73552	0.50031	0.16880	1.48026
1.5	0.47214	0.47764	0.02105	1.45938
1.0	0.19425	0.45505	−0.12876	1.43712
0.5	−0.10558	0.41320	−0.28376	1.41322
0	−0.44375	0.34924	−0.44375	1.38703
−0.025	−0.46302	0.34339	−0.45191	1.38475
−0.5			−0.60988	1.35907
−1.0			−0.78353	1.32776
−1.5			−0.96689	1.29249
−2.0			−1.16352	1.25173

Table 2 Results for $F''(\chi, 0)$ and $\Phi(\chi, 0)$, uniform surface heat flux

$\frac{Gr_x^* \cos\gamma}{Re_x^{5/2}}$	Pr = 0.7		Pr = 7.0	
	$F''(\chi, 0)$	$\Phi(\chi, 0)$	$F''(\chi, 0)$	$\Phi(\chi, 0)$
5.0			0.09595	0.43893
4.5			0.04455	0.43982
4.0	1.90290	1.29536	−0.00736	0.44072
3.5	1.67430	1.31631	−0.05979	0.44165
3.0	1.43543	1.34001	−0.11278	0.44259
2.5	1.18428	1.36725	−0.16635	0.44355
2.0	0.91813	1.39925	−0.22051	0.44453
1.5	0.63276	1.43795	−0.27530	0.44554
1.0	0.32209	1.48674	−0.33072	0.44656
0.5	−0.02740	1.55428	−0.38688	0.44761
0	−0.44375	1.66240	−0.44375	0.44878
−0.05	−0.49317	1.68107	−0.44949	0.44880
−0.5			−0.50138	0.44979
−1.0			−0.55982	0.45092
−1.5			−0.61907	0.45207
−2.0			−0.67924	0.45326

fore, not illustrated in graphical form. However, it is evident from the numerical results that a positive buoyancy force (i.e., $Gr_x \cos\gamma/Re_x^2 > 0$ or $Gr_x^* \cos\gamma/Re_x^{5/2} > 0$) contributes to an increase in the local friction factor and the local Nusselt number. This results from a favorable pressure gradient that enhances the fluid motion and the rate of surface heat transfer. On the other hand, a negative buoyancy force (i.e., $Gr_x \cos\gamma/Re_x^2 < 0$ or $Gr_x^* \cos\gamma/Re_x^{5/2} < 0$) induces an adverse pressure gradient that retards the fluid motion and reduces the surface heat transfer rate, thereby giving rise to a decrease in the local friction factor and the local Nusselt number. In addition, it can be observed from the tables that for both UWT and UHF cases the local friction factor increases from a negative to a positive value as the buoyancy force increases from zero in the positive sense, but it decreases further to a more negative value with increasing negative buoyancy force.

The change in the sign of the friction factor can be best explained when reference is made to the velocity profiles, as shown in Fig. 1 for the UWT case. It can be seen from the figure that the velocity gradient at the surface is negative for $Gr_x \cos\gamma/Re_x^2 < 0$, yielding a negative wall shear stress and hence a negative friction factor. As the buoyancy force increases from zero, the fluid velocities near the surface increase and finally exceed the velocity of the moving sheet when $Gr_x \cos\gamma/Re_x^2$ becomes greater than 0.68 for Pr = 0.7 and 1.42 for Pr = 7 (see also Table 1), resulting in a positive velocity gradient at the surface. This accounts for the change to a positive value in the local friction factor. Fig. 1 also reveals that the velocity field is more sensitive to the buoyancy force effect for Pr = 0.7 than for Pr = 7.

The average friction factor $\overline{C}_f$ and the average Nusselt number $\overline{Nu}$ can be evaluated numerically from equations (5) for the UWT case and from equations (6) for the UHF case. To conserve space, only the

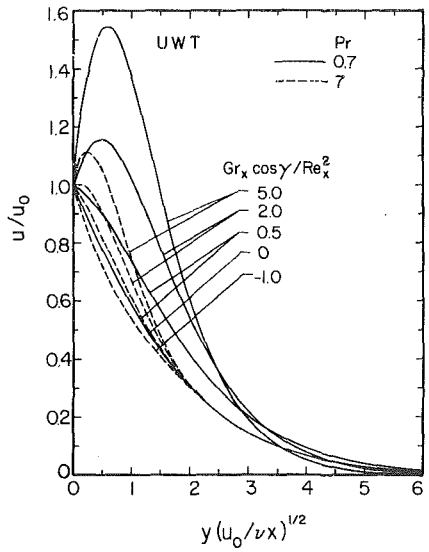

Fig. 1 Representative velocity profiles for uniform wall temperature, Pr = 0.7 and 7

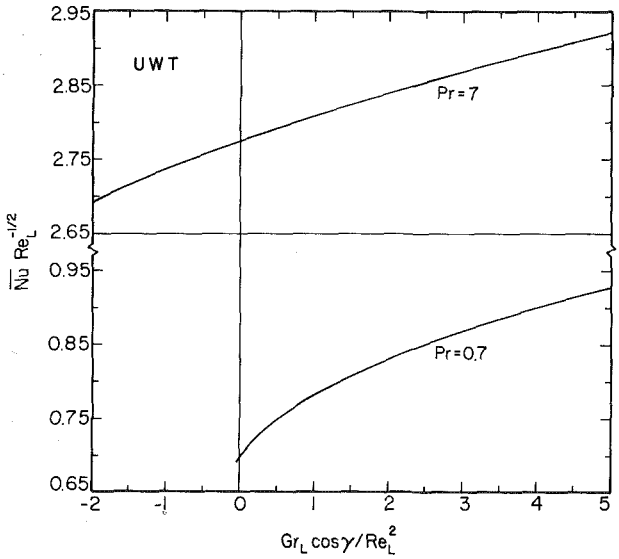

Fig. 2 Average Nusselt number results for uniform wall temperature, Pr = 0.7 and 7

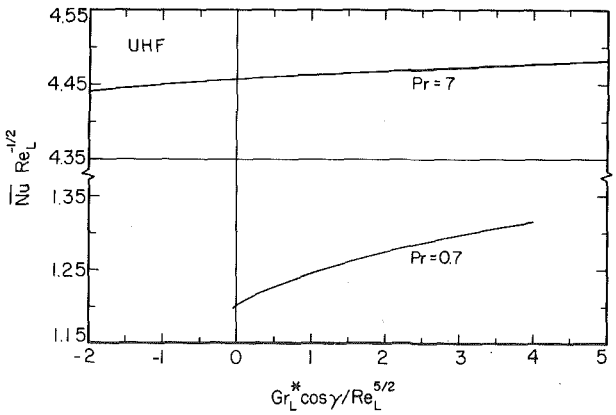

Fig. 3 Average Nusselt number results for uniform surface heat flux, Pr = 0.7 and 7

results for the average Nusselt number are illustrated in Figs. 2 and 3. It can be seen that the average Nusselt number increases with increasing buoyancy force intensity, with $Gr_L \cos\gamma/Re_L^2$ for the UWT case (Fig. 2) and with $Gr_L^* \cos\gamma/Re_L^{5/2}$ for the UHF case (Fig. 3). As is to be expected, the Nusselt numbers for fluids with Pr = 7 are larger

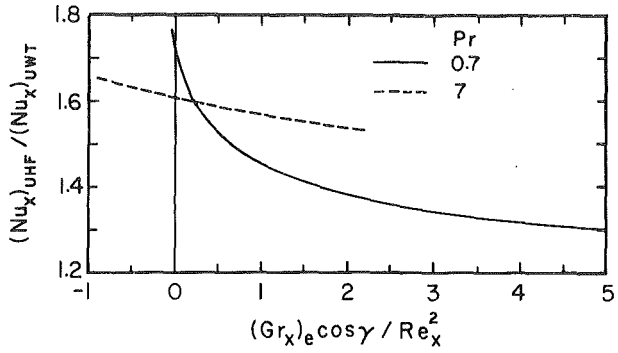

Fig. 4 A comparison of the local Nusselt numbers between uniform surface heat flux and uniform wall temperature, Pr = 0.7 and 7

than the respective values for Pr = 0.7 at a given buoyancy force intensity.

The friction factor and the Nusselt number results reduce to those for a vertically moving sheet when $\gamma = 0$ deg. Since the ratio of ξ or χ between the inclined and vertical sheets is $\cos\gamma$, it is clear that the buoyancy force effect diminishes as γ increases. This is true for both positive and negative buoyancy forces.

A comparison of the local Nusselt numbers between the UHF and UWT cases can be made in terms of an equivalent buoyancy force parameter $\xi_e = |(Gr_x)_e| \cos\gamma/Re_x^2$, where $(Gr_x)_e = g\beta[T_w(x) - T_\infty]x^3/\nu^2$ and $T_w(x) - T_\infty = (q_w x/k)Re_x^{-1/2}\Phi(\chi, 0)$. From the definition of χ, one can find $\xi_e = \chi\Phi(\chi, 0)$. Thus, for $\xi = \chi\Phi(\chi, 0)$, the Nusselt number ratio can be written as

$$(Nu_x)_{UHF}/(Nu_x)_{UWT} = -1/[\Phi(\chi, 0)\theta'(\xi, 0)] \quad (7)$$

This ratio is plotted against $(Gr_x)_e \cos\gamma/Re_x^2$ in Fig. 4 and is seen to be greater than one. Thus, heating by the uniform surface heat flux provides a higher rate of surface heat transfer than heating by the uniform wall temperature.

As a final note, the results presented in this paper are valid for values of the angle of inclination from the vertical, γ, that satisfy the condition $\tan\gamma \ll x/\delta$ or equivalently $\tan\gamma \ll Re_x^{1/2}/\eta_\delta$.

References

1 Sakiadis, B. C., "Boundary-Layer Behavior on Continous Solid Surfaces: II. The Boundary-Layer on a Continuous Flat Surface," *AIChE Journal*, Vol. 7, 1961, pp. 221–225.

2 Koldenhof, E. A., "Laminar Boundary Layer on Continuous Flat and Cylindrical Surfaces," *AIChE Journal*, Vol. 9, 1963, pp. 411–418.

3 Erickson, L. E., Fan, L. T., and Cha, L. C., "The Cooling of a Moving Continuous Sheet," *AIChE, Chemical Engineering Progress Symposium Series*, Heat Transfer—Los Angeles, Vol. 62, 1966, pp. 157–165.

4 Tsou, F. K., Sparrow, E. M., and Goldstein, R. J., "Flow and Heat Transfer in the Boundary Layer on a Continuous Moving Surface," *International Journal of Heat and Mass Transfer*, Vol. 10, 1967, pp. 219–235.

5 Chen, T. S. and Strobel, F. A., "Buoyancy Effects in Boundary Layer Adjacent to a Continuous, Moving Horizontal Flat Plate," ASME JOURNAL OF HEAT TRANSFER, (in press).

6 Mucoglu, A. and Chen, T. S., "Mixed Convection on Inclined Surfaces," ASME JOURNAL OF HEAT TRANSFER, Vol. 101, 1979, pp. 422–426.

7 Cebeci, T. and Bradshaw, P., *Momentum Transfer in Boundary Layers*, Chapter 7, Hemisphere Publishing Corp., Washington, D.C. 1977.

The Boundary Layer Behavior in Transient Turbulent Thermal Convection Flow

F. B. Cheung[1]

Nomenclature

C_p = specific heat
Fo = Fourier number, $\alpha t/L^2$
g = acceleration due to gravity
k = thermal conductivity
L = layer depth
Nu = upper surface Nusselt number, $qL^2/k\Delta T$
q = volumetric energy sources
Ra_I = internal Rayleigh number, $g\beta qL^5/k\alpha\nu$
T_c = turbulent core temperature
T_w = upper wall temperature
ΔT = temperature drop across the layer
t = time
ρ = density
δ = boundary layer thickness
θ_c = dimensionless core temperature, equation (10)
β = isobaric coefficient of thermal expansion
α = thermal diffusivity
ν = kinematic viscosity

Subscripts

I = initial condition
F = final condition
δ = upper boundary layer
w = upper wall
c = turbulent core

[1] Reactor Analysis and Safety Division, Argonne National Laboratory, 9700 S. Cass Avenue, Argonne, IL 60439.

Contributed by the Heat Transfer Division for publication in the JOURNAL OF HEAT TRANSFER. Revised manuscript received by The Heat Transfer Division June 11, 1979.

I Introduction

Turbulent thermal convection in a volumetrically heated fluid layer with an adiabatic lower boundary has received considerable attention in the studies of post-accident heat removal in fast reactors [1]. Laboratory observations [2, 3] have found the existence of a thin thermal boundary layer in the upper wall region where most changes of temperature in the fluid layer occur, indicating that majority of the thermal resistance to upward heat transfer is contained there. Accordingly, successful correlation of the steady-state heat transfer data has been obtained in terms of the boundary layer characteristics [4]. The same phenomenology has recently been employed by Cheung [5] to investigate the nature of developing and decaying turbulent convection in an internally heated fluid layer following a step change in volumetric energy generation. Under the assumption that the boundary layer would maintain its steady-state behavior during turbulent-to-turbulent transitions despite any restructuring of the flow that might take place, the time dependence of the turbulent core temperature has been determined and found to be in good agreement with measurements performed later [6]. Nevertheless, there is not enough experimental evidence to substantiate the quasi-steady argument. The actual behavior of the thermal boundary layer during flow transitions is still not clear. Further examination of the physical process is therefore needed.

II Steady-State Behavior

As a preliminary to the analysis of flow transitions, we first consider the steady process of turbulent thermal convection in a heat-generating fluid layer bounded from above by an isothermal upper wall and from below by an adiabatic lower wall. At steady-state, the upper surface heat flux must be equal to qL where q is the rate of volumetric heating and L, the layer depth. For highly turbulent flow, this heat flux may be related to the rate of heat conduction in the thermal boundary layer at the upper wall by

$$qL = k\Delta T_\delta/\delta, \quad (1)$$

where ΔT_δ is the temperature drop across the boundary layer with thickness δ and k, the thermal conductivity of the fluid. If the Rayleigh number is sufficiently high, we may assume heat transport to be independent of the layer depth. From dimensional considerations, we have

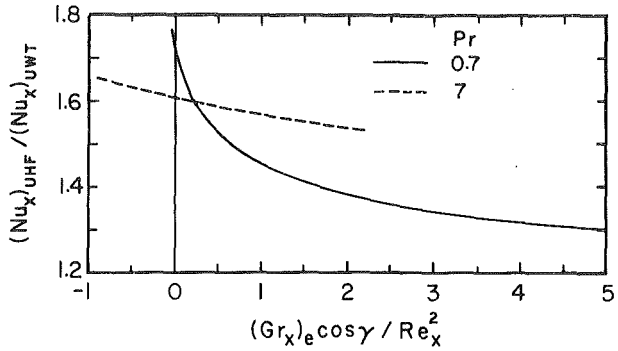

Fig. 4 A comparison of the local Nusselt numbers between uniform surface heat flux and uniform wall temperature, Pr = 0.7 and 7

than the respective values for Pr = 0.7 at a given buoyancy force intensity.

The friction factor and the Nusselt number results reduce to those for a vertically moving sheet when $\gamma = 0$ deg. Since the ratio of ξ or χ between the inclined and vertical sheets is $\cos\gamma$, it is clear that the buoyancy force effect diminishes as γ increases. This is true for both positive and negative buoyancy forces.

A comparison of the local Nusselt numbers between the UHF and UWT cases can be made in terms of an equivalent buoyancy force parameter $\xi_e = |(Gr_x)_e| \cos\gamma/Re_x^2$, where $(Gr_x)_e = g\beta[T_w(x) - T_\infty]x^3/\nu^2$ and $T_w(x) - T_\infty = (q_w x/k)Re_x^{-1/2}\Phi(\chi, 0)$. From the definition of χ, one can find $\xi_e = \chi\Phi(\chi, 0)$. Thus, for $\xi = \chi\Phi(\chi, 0)$, the Nusselt number ratio can be written as

$$(Nu_x)_{UHF}/(Nu_x)_{UWT} = -1/[\Phi(\chi, 0)\theta'(\xi, 0)] \quad (7)$$

This ratio is plotted against $(Gr_x)_e \cos\gamma/Re_x^2$ in Fig. 4 and is seen to be greater than one. Thus, heating by the uniform surface heat flux provides a higher rate of surface heat transfer than heating by the uniform wall temperature.

As a final note, the results presented in this paper are valid for values of the angle of inclination from the vertical, γ, that satisfy the condition $\tan\gamma \ll x/\delta$ or equivalently $\tan\gamma \ll Re_x^{1/2}/\eta_\delta$.

References

1 Sakiadis, B. C., "Boundary-Layer Behavior on Continous Solid Surfaces: II. The Boundary-Layer on a Continuous Flat Surface," *AIChE Journal*, Vol. 7, 1961, pp. 221–225.

2 Koldenhof, E. A., "Laminar Boundary Layer on Continuous Flat and Cylindrical Surfaces," *AIChE Journal*, Vol. 9, 1963, pp. 411–418.

3 Erickson, L. E., Fan, L. T., and Cha, L. C., "The Cooling of a Moving Continuous Sheet," *AIChE, Chemical Engineering Progress Symposium Series*, Heat Transfer—Los Angeles, Vol. 62, 1966, pp. 157–165.

4 Tsou, F. K., Sparrow, E. M., and Goldstein, R. J., "Flow and Heat Transfer in the Boundary Layer on a Continuous Moving Surface," *International Journal of Heat and Mass Transfer*, Vol. 10, 1967, pp. 219–235.

5 Chen, T. S. and Strobel, F. A., "Buoyancy Effects in Boundary Layer Adjacent to a Continuous, Moving Horizontal Flat Plate," ASME JOURNAL OF HEAT TRANSFER, (in press).

6 Mucoglu, A. and Chen, T. S., "Mixed Convection on Inclined Surfaces," ASME JOURNAL OF HEAT TRANSFER, Vol. 101, 1979, pp. 422–426.

7 Cebeci, T. and Bradshaw, P., *Momentum Transfer in Boundary Layers*, Chapter 7, Hemisphere Publishing Corp., Washington, D.C. 1977.

The Boundary Layer Behavior in Transient Turbulent Thermal Convection Flow

F. B. Cheung[1]

Nomenclature

C_p = specific heat
Fo = Fourier number, $\alpha t/L^2$
g = acceleration due to gravity
k = thermal conductivity
L = layer depth
Nu = upper surface Nusselt number, $qL^2/k\Delta T$
q = volumetric energy sources
Ra_I = internal Rayleigh number, $g\beta qL^5/k\alpha\nu$
T_c = turbulent core temperature
T_w = upper wall temperature
ΔT = temperature drop across the layer
t = time
ρ = density
δ = boundary layer thickness
θ_c = dimensionless core temperature, equation (10)
β = isobaric coefficient of thermal expansion
α = thermal diffusivity
ν = kinematic viscosity

Subscripts

I = initial condition
F = final condition
δ = upper boundary layer
w = upper wall
c = turbulent core

[1] Reactor Analysis and Safety Division, Argonne National Laboratory, 9700 S. Cass Avenue, Argonne, IL 60439.

Contributed by the Heat Transfer Division for publication in the JOURNAL OF HEAT TRANSFER. Revised manuscript received by The Heat Transfer Division June 11, 1979.

I Introduction

Turbulent thermal convection in a volumetrically heated fluid layer with an adiabatic lower boundary has received considerable attention in the studies of post-accident heat removal in fast reactors [1]. Laboratory observations [2, 3] have found the existence of a thin thermal boundary layer in the upper wall region where most changes of temperature in the fluid layer occur, indicating that majority of the thermal resistance to upward heat transfer is contained there. Accordingly, successful correlation of the steady-state heat transfer data has been obtained in terms of the boundary layer characteristics [4]. The same phenomenology has recently been employed by Cheung [5] to investigate the nature of developing and decaying turbulent convection in an internally heated fluid layer following a step change in volumetric energy generation. Under the assumption that the boundary layer would maintain its steady-state behavior during turbulent-to-turbulent transitions despite any restructuring of the flow that might take place, the time dependence of the turbulent core temperature has been determined and found to be in good agreement with measurements performed later [6]. Nevertheless, there is not enough experimental evidence to substantiate the quasi-steady argument. The actual behavior of the thermal boundary layer during flow transitions is still not clear. Further examination of the physical process is therefore needed.

II Steady-State Behavior

As a preliminary to the analysis of flow transitions, we first consider the steady process of turbulent thermal convection in a heat-generating fluid layer bounded from above by an isothermal upper wall and from below by an adiabatic lower wall. At steady-state, the upper surface heat flux must be equal to qL where q is the rate of volumetric heating and L, the layer depth. For highly turbulent flow, this heat flux may be related to the rate of heat conduction in the thermal boundary layer at the upper wall by

$$qL = k\Delta T_\delta/\delta, \quad (1)$$

where ΔT_δ is the temperature drop across the boundary layer with thickness δ and k, the thermal conductivity of the fluid. If the Rayleigh number is sufficiently high, we may assume heat transport to be independent of the layer depth. From dimensional considerations, we have

$$\delta \sim (g\beta\Delta T_\delta/\alpha\nu)^{-1/3}, \tag{2}$$

where g is the acceleration due to gravity, β the isobaric coefficient of thermal expansion, α the thermal diffusivity, and ν the kinematic viscosity. Equations (1) and (2) lead to

$$\delta/L \sim (g\beta qL^5/k\alpha\nu)^{-1/4}, \quad \text{or} \quad \delta/L \sim \mathrm{Ra}_I^{-1/4}, \tag{3}$$

where Ra_I is the internal Rayleigh number of the layer. Physically, δ/L is equivalent to the ratio of conductive heat flux to convective heat flux and is thus inversely proportional to the Nusselt number. This results in

$$\mathrm{Nu} \sim \mathrm{Ra}_I^{1/4}, \tag{4}$$

which in essence is the asymptotic law of heat transport in this class of flow. The above relation between Nusselt number and Rayleigh number, however, is valid only for very high Rayleigh number flows. Experimental studies [2, 3] with water performed at lower Rayleigh numbers clearly indicate

$$\mathrm{Nu} \sim \mathrm{Ra}_I^{0.227} \quad \text{for } 1.9 \times 10^3 < \mathrm{Ra}_I < 2.2 \times 10^{12}. \tag{5}$$

Therefore, if Ra_I is not large enough, we may expect a slight deviation from the asymptotic behavior of the thermal boundary layer. In particular, we may write

$$\delta/L \sim \mathrm{Ra}_I^{-0.227} \quad \text{or } \delta/L \sim (g\beta qL^5/k\alpha\nu)^{-0.227}. \tag{6}$$

This expression, when combined with equation (1), leads to a modified boundary layer relation, i.e.,

$$\delta/L \sim (g\beta\Delta T_\delta L^3/\alpha\nu)^{-0.293}. \tag{7}$$

Thus heat transport at a not-sufficiently-high Rayleigh number is not totally independent of the layer depth. Detailed discussions of this matter have been made by Cheung [7] from a fundamental point of view.

III Transition-State Behavior

Consider the situation in which the fluid layer of interest is initially in steady turbulent thermal convection. At a certain instant, there is a step change in volumetric heat generation of the layer, and transition to a new steady-state occurs. The initial and the final Rayleigh numbers are assumed to be large so that turbulence is the dominant mode of heat transfer during the entire transient. Under this condition, we may assume that the instantaneous core temperature of the layer, T_c, be constant[2] and that all of the thermal resistance to upward heat transfer be contained in the thin δ region at the upper surface. Using the Boussinesq approximation, the horizontally averaged energy equation may be integrated to yield

$$\rho C_p dT_c/dt = -k(T_c - T_w)/\delta L + q, \tag{8}$$

where T_w is the upper wall temperature, ρ the density, and C_p the specific heat of the fluid. In writing (8), we have neglected the variation of temperature and the volumetric heat generation within the boundary layer, which may result in an error of the order δ/L. At the initial steady-state, we have

$$q_I = k(T_{cI} - T_w)/\delta_I L. \tag{9}$$

If we let

$$\theta_c = 2k(T_c - T_w)/q_I L^2, \tag{10}$$

equations (8) and (9) can be combined to yield

$$\frac{1}{2}\frac{d\theta_c}{d\mathrm{Fo}} = -\frac{\theta_c}{\theta_{cI}}\left(\frac{\delta}{\delta_I}\right)^{-1} + \frac{\mathrm{Ra}_F}{\mathrm{Ra}_I}, \tag{11}$$

where $\mathrm{Fo} = \alpha t/L^2$ is the Fourier number and Ra_F, the final Rayleigh number. Note that at each instant we have $\Delta T_\delta \sim T_c - T_w$ so that θ_c is directly proportional to ΔT_δ. If, during the flow transition, the thermal boundary layer is indeed in a quasi-steady state, as has been thought to be the case in previous studies [5, 6], the relation given by equation (7) should hold instantaneously. This leads to

$$\frac{\delta}{\delta_I} = \left(\frac{\theta_c}{\theta_{cI}}\right)^{-0.293}, \tag{12}$$

which can be easily solved along with equation (11) to yield $\theta_c(\mathrm{Fo})$ and thus the transient rate of heat transfer. Following this simple procedure, Kulacki, et al. [6] have found that the results so obtained are in good agreement with the observed behavior. Apparently one tends to conclude that the transient boundary layer relation *is* represented by equation (12). However, further examination of equations (11) and (12) indicates that $\theta_c(\mathrm{Fo})$ is not quite sensitive[3] to changes in the term representing δ/δ_I, since it is raised to a power of -0.293. Although the gross behavior of $\theta_c(\mathrm{Fo})$ is correctly predicted, the transient relation given by equation (12) may still be in error.

To understand how the thermal boundary layer actually responds to a step change in Rayleight number, let us assume a simple power-law relation between δ and θ[4]

$$\frac{\delta}{\delta_I} = \left(\frac{\theta_c}{\theta_{cI}}\right)^{-m}, \tag{13}$$

where m is allowed to be a function of time. Note that for a given value of $\mathrm{Ra}_F/\mathrm{Ra}_I$, both θ_c/θ_{cI} and δ/δ_I are functions of Fo/θ_{cI} alone, as can be seen from equation (11). Thus it is quite reasonable to regard δ/δ_I as a function of θ_c/θ_{cI} only.[5] Manipulation of equations (11) and (13) gives

$$m(\mathrm{Fo}) = \frac{\ln(\mathrm{Ra}_F/\mathrm{Ra}_I - 0.5\, d\theta c/d\mathrm{Fo})}{\ln(\theta_c/\theta_{cI})} - 1, \tag{14}$$

which can be readily determined by experimental measurements. A typical result corresponding to the case of a step increase in Rayleigh number from 5.87×10^8 to 2.85×10^9 is shown in Fig. 1. For this particular case, the value of θ_{cI} is 0.044. The experimental data points were obtained by Kulacki, et al. [6], using water as the working fluid. These are used in conjunction with equation (14) to derive the time dependence of m which is presented in the same figure. Should the boundary layer be in a quasi-steady state, m would be constant with respect to Fo or at least nearly so and has a value of 0.293. Instead, m

[2] We shall ignore the slight variation of T_c with position which is a valid approximation at high Rayleigh numbers.

[3] Conversely, the instantaneous value of δ/δ_I is very sensitive to changes in $d\theta_c/d\mathrm{Fo}$ and thus, $\theta_c(\mathrm{Fo})$.

[4] At Fo = 0, we have $\delta/\delta_I = \theta_c/\theta_{cI} = 1$, so that the constant of proportionality must be unity.

[5] A rigorous test of this assumption, however, would require experimental results at more than just one value of θ_{cI}, which, unfortunately, do not exist at the present time.

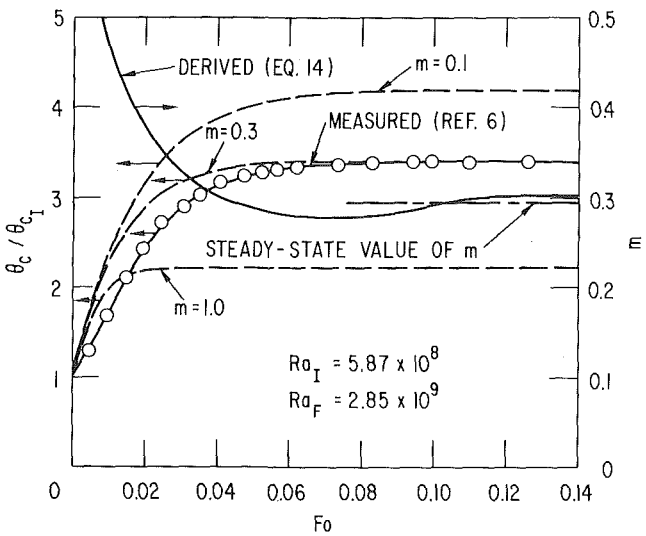

Fig. 1 The transient boundary layer behavior: empirically determined time dependence of m(Fo)

is found to be a strong function of time, especially in the earlier stage of flow development. Obviously, the quasi-steady assumption is a valid approximation only in the later transition period. To further illustrate this point, the theoretical cruves of θ_c/θ_{c_I} for $m = 0.1, 0.3$, and 1.0 are presented in the same figure. Apparently, we have $m > 0.3$ in the initial stage unless the errors in the measured data [6] are at least as large as the differences between the $m = 0.3$ (dashed) and the $m =$ variable (solid) curves. This is considered to be very unlikely since the relative error in θ_c/θ_{c_I} would almost have to exceed 30 percent (see Fig. 1). The large value of m obtained in the early transition period implies that the actual response of the thermal boundary layer to the step change in Rayleigh number is much faster than is predicted by the quasi-steady approach. Physically, this means that there is a considerable initial distortion of the boundary layer by sudden increase in volumetric heating of the layer.

It remains to be explained why the predicted behavior of $\theta_c(\mathrm{Fo})$ based upon equation (12) agrees so satisfactorily with the experiment.[6] The reason appears to be purely mathematical. From equations (11) and (13), it is quite obvious that the rate of transition is determined by the instantaneous value of $(\theta_c/\theta_{c_I})^{1+m}$. If, in a given time step, m is underestimated as in the case of using equation (12), then $d\theta_c/d\mathrm{Fo}$ would be slightly[7] overestimated. This would result in a somewhat larger value of θ_c/θ_{c_I} in the next time step, which in turn would affect the new value of $d\theta_c/d\mathrm{Fo}$. However, the two error sources are compensating. With θ_c/θ_{c_I} being overestimated while m being underestimated, $(\theta_c/\theta_{c_I})^{1+m}$ would tend to approach its true value, thus minimizing the overall error. In view of the "self-adjustable" property of equation (11), the use of equation (12) seems to be quite adequate for practical purposes. However, if one is interested in the intermediate behavior of the layer, a more elaborate analysis that permits us to improve on the present predictive capability is required.

IV Final Remarks

It has been demonstrated that in heat source-driven turbulent convection, the transient behavior of the thermal boundary layer is quite different from the corresponding steady-state behavior, especially during the initial period of transition. The early response of the boundary layer to a step change in Rayleigh number, as indicated by the time variation of its thickness, is found to be much faster than it would be in quasi-steady manner. The marked deviation from the steady-state behavior may be an indication of the fact that the effect of flow restructuring in the turbulent core region is not at all negligible upon the thermal boundary layer.

The above conclusions, however, must be regarded as preliminary ones since they were based upon a rather limited amount of data [6]. Further experimental studies are needed to verify the present results.

Acknowledgments

The author wishes to thank Professor F. A. Kulacki for providing the data of his experiment. This work was performed under the auspices of the U. S. Department of Energy.

References

1 Cheung, F. B., "Natural Convection in a Volumetrically Heated Fluid Layer at High Rayleigh Numbers," *International Journal of Heat and Mass Transfer*, Vol. 20, 1977, pp. 499–506.

2 Kulacki, F. A. and Nagle, M. Z., "Natural Convection in a Horizontal Fluid Layer with Volumetric Energy Sources," *ASME* JOURNAL OF HEAT TRANSFER, Vol. 97, 1975, pp. 204–211.

3 Kulacki, F. A. and Emara, A. A., "Steady and Transient Thermal Convection in a Fluid Layer with Uniform Volumetric Energy Sources," *Journal of Fluid Mechanics*, Vol. 83, 1977, pp. 375–395.

4 Cheung, F. B., "Correlation Equations for Turbulent Thermal Convection in a Horizontal Fluid Layer Heated Internally and from Below," *ASME* JOURNAL OF HEAT TRANSFER, Vol. 100, 1978, pp. 416–422.

5 Cheung, F. B., "Turbulent Natural Convection in a Horizontal Fluid Layer with Time Dependent Volumetric Energy Sources," Paper No. 78-HT-6, *AIAA-ASME Thermophysics and Heat Transfer Conference*, Palo Alto, CA 1978.

6 Kulacki, F. A., Min, J. H., Nguyen, A. T., and Keyhani, M., "Steady and Transient Natural Convection in Single and Multi-Fluid Layers with Heat Generation," *Proceedings Post-accident Heat Removal Information Exchange*, Ispra, Italy, 1978.

7 Cheung, F. B., "Heat Source-Driven Thermal Convection at Arbitrary Prandtl Number," *Journal of Fluid Mechanics*, now in press.

[6] Although the temperature is significantly overestimated in the early transition period [6], the end results appear to be perfectly correct.

[7] Note that $d\theta_c/d\mathrm{Fo}$ is controlled by the value of θ_c/θ_{c_I} raised to a power of $(1 + m)$, not directly to m. Insofar as $m(\mathrm{Fo})$ is not an order of magnitude different from 0.293, $d\theta_c/d\mathrm{Fo}$ is not sensitive to the error introduced in $m(\mathrm{Fo})$.

Interferometric Observation of Natural Convection During Freezing from a Vertical Flat Plate

P. D. Van Buren[1] and R. Viskanta[1]

Nomenclature

c = specific heat
Fo = Fourier number, $\alpha_\ell t/L^2$
Δh_f = latent heat of fusion
L = length of heat exchanger
Nu_x = local Nusselt number defined by equation (1)
Ra_x = local Rayleigh number based on initial temperature, $[g\beta(T_i - T_f)x^3/\nu_\ell^2](\nu_\ell/\alpha_\ell)$
Ra_L = overall Rayleigh number based on initial temperature, $[g\beta(T_i - T_f)L^3/\nu_\ell^2](\nu_\ell/\alpha_\ell)$
Ste = Stefan number, $c_s(T_f - T_w)/\Delta h_f$
T = temperature
t = time
x = distance measured downward from the air-liquid interface
α = thermal diffusivity
β = thermal expansion coefficient
ν = kinematic viscosity

Subscripts

f = refers to fusion
i = refers to initial (uniform) conditions
ℓ = refers to liquid
s = refers to solid
x = refers to local
w = refers to wall

Introduction

Solidification along a vertical plate immersed in an infinite volume of fluid at a uniform temperature has been predicted analytically for the case in which there is heat transfer by natural convection at the solid-liquid interface [1]. However, it was not until after the original submission of this Technical Note for publication that experimental evidence became available [2, 3] which clearly indicated the important effect of natural convection heat transfer on solid-liquid interface motion during the freezing of a superheated liquid around a horizontal [2] and vertical [3] cylinder in a finite-size test cell where recirculation was present. Experimental results show that freezing can be terminated by natural convection even in a slightly superheated liquid. A more complete list of references relevant to such solid-liquid phase change heat transfer processes is available [4].

The purpose of this note is to provide interferometric evidence of natural convection in a liquid undergoing freezing from a vertical wall and to complement recently published results. The study was motivated by the need to acquire basic understanding of the heat transfer processes for the design of latent heat-of-fusion thermal energy storage systems [5]. Cost effective and thermally efficient storage

[1] Heat Transfer Laboratory, School of Mechanical Engineering, Purdue University, West Lafayette, Ind. 47907

Contributed by the Heat Transfer Division for publication in the JOURNAL OF HEAT TRANSFER. Manuscript received by the Heat Transfer Division June 29, 1979.

is found to be a strong function of time, especially in the earlier stage of flow development. Obviously, the quasi-steady assumption is a valid approximation only in the later transition period. To further illustrate this point, the theoretical cruves of θ_c/θ_{c_I} for $m = 0.1, 0.3$, and 1.0 are presented in the same figure. Apparently, we have $m > 0.3$ in the initial stage unless the errors in the measured data [6] are at least as large as the differences between the $m = 0.3$ (dashed) and the $m =$ variable (solid) curves. This is considered to be very unlikely since the relative error in θ_c/θ_{c_I} would almost have to exceed 30 percent (see Fig. 1). The large value of m obtained in the early transition period implies that the actual response of the thermal boundary layer to the step change in Rayleigh number is much faster than is predicted by the quasi-steady approach. Physically, this means that there is a considerable initial distortion of the boundary layer by sudden increase in volumetric heating of the layer.

It remains to be explained why the predicted behavior of $\theta_c(\mathrm{Fo})$ based upon equation (12) agrees so satisfactorily with the experiment.[6] The reason appears to be purely mathematical. From equations (11) and (13), it is quite obvious that the rate of transition is determined by the instantaneous value of $(\theta_c/\theta_{c_I})^{1+m}$. If, in a given time step, m is underestimated as in the case of using equation (12), then $d\theta_c/d\mathrm{Fo}$ would be slightly[7] overestimated. This would result in a somewhat larger value of θ_c/θ_{c_I} in the next time step, which in turn would affect the new value of $d\theta_c/d\mathrm{Fo}$. However, the two error sources are compensating. With θ_c/θ_{c_I} being overestimated while m being underestimated, $(\theta_c/\theta_{c_I})^{1+m}$ would tend to approach its true value, thus minimizing the overall error. In view of the "self-adjustable" property of equation (11), the use of equation (12) seems to be quite adequate for practical purposes. However, if one is interested in the intermediate behavior of the layer, a more elaborate analysis that permits us to improve on the present predictive capability is required.

IV Final Remarks

It has been demonstrated that in heat source-driven turbulent convection, the transient behavior of the thermal boundary layer is quite different from the corresponding steady-state behavior, especially during the initial period of transition. The early response of the boundary layer to a step change in Rayleigh number, as indicated by the time variation of its thickness, is found to be much faster than it would be in quasi-steady manner. The marked deviation from the steady-state behavior may be an indication of the fact that the effect of flow restructuring in the turbulent core region is not at all negligible upon the thermal boundary layer.

The above conclusions, however, must be regarded as preliminary ones since they were based upon a rather limited amount of data [6]. Further experimental studies are needed to verify the present results.

Acknowledgments

The author wishes to thank Professor F. A. Kulacki for providing the data of his experiment. This work was performed under the auspices of the U. S. Department of Energy.

References

1 Cheung, F. B., "Natural Convection in a Volumetrically Heated Fluid Layer at High Rayleigh Numbers," *International Journal of Heat and Mass Transfer*, Vol. 20, 1977, pp. 499–506.

2 Kulacki, F. A. and Nagle, M. Z., "Natural Convection in a Horizontal Fluid Layer with Volumetric Energy Sources," *ASME* JOURNAL OF HEAT TRANSFER, Vol. 97, 1975, pp. 204–211.

3 Kulacki, F. A. and Emara, A. A., "Steady and Transient Thermal Convection in a Fluid Layer with Uniform Volumetric Energy Sources," *Journal of Fluid Mechanics*, Vol. 83, 1977, pp. 375–395.

4 Cheung, F. B., "Correlation Equations for Turbulent Thermal Convection in a Horizontal Fluid Layer Heated Internally and from Below," *ASME* JOURNAL OF HEAT TRANSFER, Vol. 100, 1978, pp. 416–422.

5 Cheung, F. B., "Turbulent Natural Convection in a Horizontal Fluid Layer with Time Dependent Volumetric Energy Sources," Paper No. 78-HT-6, *AIAA-ASME Thermophysics and Heat Transfer Conference*, Palo Alto, CA 1978.

6 Kulacki, F. A., Min, J. H., Nguyen, A. T., and Keyhani, M., "Steady and Transient Natural Convection in Single and Multi-Fluid Layers with Heat Generation," *Proceedings Post-accident Heat Removal Information Exchange*, Ispra, Italy, 1978.

7 Cheung, F. B., "Heat Source-Driven Thermal Convection at Arbitrary Prandtl Number," *Journal of Fluid Mechanics*, now in press.

[6] Although the temperature is significantly overestimated in the early transition period [6], the end results appear to be perfectly correct.

[7] Note that $d\theta_c/d\mathrm{Fo}$ is controlled by the value of θ_c/θ_{c_I} raised to a power of $(1 + m)$, not directly to m. Insofar as $m(\mathrm{Fo})$ is not an order of magnitude different from 0.293, $d\theta_c/d\mathrm{Fo}$ is not sensitive to the error introduced in $m(\mathrm{Fo})$.

Interferometric Observation of Natural Convection During Freezing from a Vertical Flat Plate

P. D. Van Buren[1] and R. Viskanta[1]

Nomenclature

c = specific heat
Fo = Fourier number, $\alpha_\ell t/L^2$
Δh_f = latent heat of fusion
L = length of heat exchanger
Nu_x = local Nusselt number defined by equation (1)
Ra_x = local Rayleigh number based on initial temperature, $[g\beta(T_i - T_f)x^3/\nu_\ell^2](\nu_\ell/\alpha_\ell)$
Ra_L = overall Rayleigh number based on initial temperature, $[g\beta(T_i - T_f)L^3/\nu_\ell^2](\nu_\ell/\alpha_\ell)$
Ste = Stefan number, $c_s(T_f - T_w)/\Delta h_f$
T = temperature
t = time
x = distance measured downward from the air-liquid interface
α = thermal diffusivity
β = thermal expansion coefficient
ν = kinematic viscosity

Subscripts

f = refers to fusion
i = refers to initial (uniform) conditions
ℓ = refers to liquid
s = refers to solid
x = refers to local
w = refers to wall

Introduction

Solidification along a vertical plate immersed in an infinite volume of fluid at a uniform temperature has been predicted analytically for the case in which there is heat transfer by natural convection at the solid-liquid interface [1]. However, it was not until after the original submission of this Technical Note for publication that experimental evidence became available [2, 3] which clearly indicated the important effect of natural convection heat transfer on solid-liquid interface motion during the freezing of a superheated liquid around a horizontal [2] and vertical [3] cylinder in a finite-size test cell where recirculation was present. Experimental results show that freezing can be terminated by natural convection even in a slightly superheated liquid. A more complete list of references relevant to such solid-liquid phase change heat transfer processes is available [4].

The purpose of this note is to provide interferometric evidence of natural convection in a liquid undergoing freezing from a vertical wall and to complement recently published results. The study was motivated by the need to acquire basic understanding of the heat transfer processes for the design of latent heat-of-fusion thermal energy storage systems [5]. Cost effective and thermally efficient storage

[1] Heat Transfer Laboratory, School of Mechanical Engineering, Purdue University, West Lafayette, Ind. 47907

Contributed by the Heat Transfer Division for publication in the JOURNAL OF HEAT TRANSFER. Manuscript received by the Heat Transfer Division June 29, 1979.

systems which take advantage of the latent heat-of-fusion of a phase change material are prerequisite for economic utilization of alternate energy sources (such as solar, waste heat recovery and load leveling).

Experiments

A Mach-Zehnder interferometer of typical rectangular design, having 7.3 cm dia optics, was utilized for measuring the temperature distribution in the liquid. A 10 mW He-Ne laser served as a light source, and a system of lenses produced a collimated beam. The use of a laser eliminated the need for a compensation in the reference path of the interferometer.

The test cell employed in the experiments consisted of two independent units: (1) a Plexiglass container for holding the test fluid, and (2) a flat plate heat exchanger which was installed in the test cell. The inside dimensions of the container were 10.8 cm in height, 8.51 cm in width, and 5.07 in depth. Two faces of the test cell were made of optical quality glass. Special care was taken in the design and construction of the test cell to insure that the glass windows were parallel to each other. The vertical flat plate heat exchanger was machined from a copper block by milling channels in one face of the plate and then soldering a thin copper plate over the channels. The width of the heat exchanger was such that it fitted snugly in the test cell. The heat exchanger was installed in a vertical position in the test cell adjacent to one of the walls, with the major plane of the heat exchanger perpendicular to the windows. The heat exchanger was cooled by circulating a coolant from a Kryomat® (constant temperature bath). The ambient air temperature in the laboratory where the experiments were conducted was carefully controlled and maintained at a temperature level of not more than 1°C above the fusion temperature of the phase change material. As a result of this precaution, heat gain from the surroundings to the test material was greatly reduced (but of course was not completely eliminated).

A number of copper-constantan thermocouples, calibrated against a NBS standard, were installed just under the surface of the heat exchanger in order to measure uniformity and magnitude of the surface temperature. Two calibrated thermocouples were installed to measure the reference temperature of the fluid "far" from the heat exchanger surface.

The interference fringe pattern was focused on the film plane of a 35 mm Nikon model F2AS camera, by a 177.7 mm f/1.9 television camera lens. This lens was corrected for spherical aberration and other image defects.

A paraffin (n-heptadecane, $C_{17}H_{36}$) was chosen as a test fluid, because it has a fusion temperature close to the room temperature (conducive for reducing heat gains or losses from the surroundings). Other reasons for choosing n-heptadecane are: (1) the liquid phase is transparent and sufficiently good quality for optical measurements, and (2) the physical and transport properties of n-heptadecane are fairly well documented, which allows for correlation of the data in terms of dimensionless parameters.

The test cell was filled with n-heptadecane (99 percent pure) and sufficient time was allowed for the fluid to attain a uniform temperature throughout the test cell. Interference fringes were visually observed on a screen and were counted during the cooling down (equilibration period) of the liquid to a temperature typically less than 1°C above the fusion temperature. This procedure was necessary in order to interpret the interference fringe pattern, since the index of refraction of n-heptadecane is fairly sensitive to its temperature. Thus, even a small temperature difference in the liquid can result in fringe densities at the solid-liquid interface which are too large for accurate data reduction. During the course of the experiments, the temperature variation in the liquid, just prior to initiation of freezing, was never observed to be greater than 0.07°C.

After the desired initial uniform temperature conditions were attained in the liquid and the interferometer was adjusted to an infinite fringe, ethanol (at a predetermined and constant temperature below the fusion temperature of the fluid) was circulated through the heat exchanger. Because of effective heat transfer, the surface temperature of the heat exchanger surface soon thereafter attained a steady value. Thermocouple readings were recorded and interference fringe patterns were photographed at predetermined time intervals.

The interferograms (photographs of interference fringe patterns) were enlarged to enable accurate measurement of the fringe position

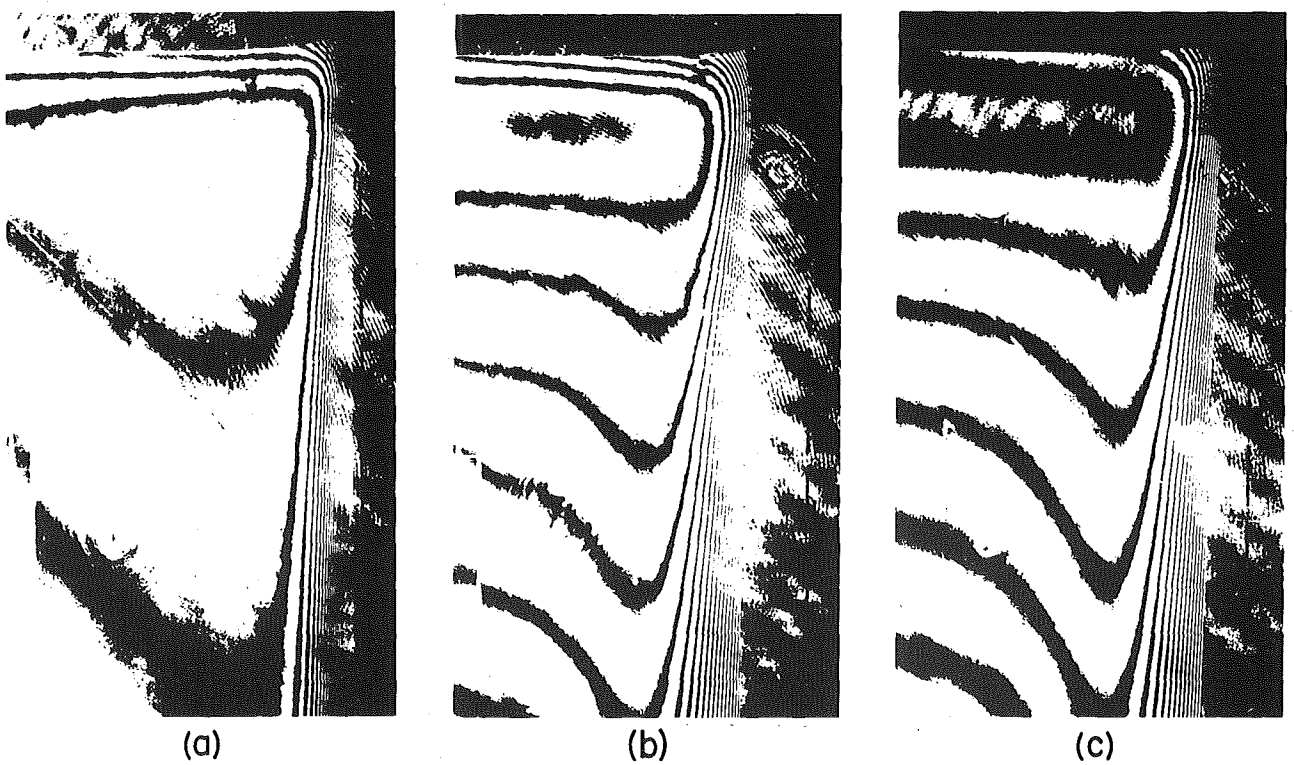

Fig. 1 Interferograms during freezing of n-heptadecane: (*a*) Ste = 0.0168, $Ra_L = 1.19 \times 10^7$ and Fo = 7.04×10^{-4}; (*b*) Ste = 0.0168, $Ra_L = 1.19 \times 10^7$ and Fo = 3.17×10^{-2}; (*c*) Ste = 0.0048, $Ra_L = 1.71 \times 10^7$ and Fo = 3.17×10^{-2}

using a vernier microscope. The temperature distribution in the liquid, the temperature gradient at the solid-liquid interface (which yields the heat transfer coefficients) were determined using the data reduction procedure described by Hauf and Grigull [6].

Results and Discussion

Some typical interferograms obtained from the experiments are shown in Fig. 1. The dashed line indicates the location of the heat exchanger surface. The solid phase of the test material is adjacent to the heat exchanger surface. The air-liquid interface curves upward in the immediate vicinity of the solid due to surface tension. These interferograms clearly show the isotherms in the liquid from which the natural circulation patterns can be inferred. The liquid flows downward along the solid-liquid interface and upward in the region away from the interface. Figure 1(a) shows that at very early time natural convection has been initiated but the liquid away from the solid-liquid interface is yet at an almost uniform temperature. This is evidenced by a few irregular fringes away from the interface. Figure 1(b) shows that as the cooling proceeds, natural convection circulation produces increased thermal stratification of the liquid phase. It also shows that continued freezing increases the solid layer thickness and decreases the heat transfer rate at the solid-liquid interface (indicated by the smaller fringe density at the interface). A comparison of Figs. 1(b) and 1(c) indicates that at the same time both the solid layer thickness and fringe density decreases with decreasing Stefan number (i.e., the elapsed freezing time for the interferograms of Figs. 1(b) and 1(c) is the same but the Stefan number for the situation shown in Fig. 1(b) is greater than that shown in Fig. 1(c).

Figure 2 shows that the minimum solid layer thickness occurs near the top of the cooled plate ($x/L \simeq 0.05$) where the flow is predominantly perpendicular to the heat exchanger surface and makes an abrupt 90° downward turn. At early times the solid thickness is nearly constant for $x/L > 0.15$; however, at later times it increases with the distance from the air-paraffin interface. The most recent published results on the effects of natural convection during freezing [3] and the results of the present study show them to be mutually supportive. A direct comparison of analytical predictions for freezing on a vertical plate suspended in an infinite volume of liquid at a constant temperature [1] with the data of this work (for freezing in a finite domain) is not meaningful since the model does not account for liquid recirculation and predicts no solid formation at the leading edge.

The variation of the heat transfer coefficient along the solid-liquid interface, given in terms of standard parameters for correlating transient natural convection in the absence of phase change [7], is shown in Fig. 3. The local Nusselt number at the interface is defined as

$$\mathrm{Nu}_x = -\left.\frac{\partial T}{\partial n}\right|_0 x/(T_f - T_i) \qquad (1)$$

where $\partial T/\partial n|_0$ is the temperature gradient in the fluid normal to the phase-change boundary and x is the distance measured from the air-liquid interface. The choice of x as a characteristic length scale may not be appropriate for transient natural convection heat transfer with liquid-solid phase change, because the volume and shape of the liquid region as well as the contour of the solid-liquid interface is continuously changing. However, this choice allows for direct comparison of the present results with those for steady and transient natural convection from a vertical plate in an infinite volume of fluid.

It should also be emphasized that the nature of the Mach-Zehnder interferometer yields only the integrated average temperature gradient $(\partial T/\partial n)_0$ over the width of the plate. Therefore, small nonuniformities in the temperature gradient at the heat exchanger surface are already accounted for, and the local heat transfer coefficients given by equation (1) must be considered as averaged over the width of the heat exchanger.

The interferograms shown in Fig. 1 indicate that the highest temperature gradients (and therefore the highest heat transfer coefficients) occur near the top of the plate where the flow makes an abrupt 90 deg turn. However, presentation of the heat transfer coefficients

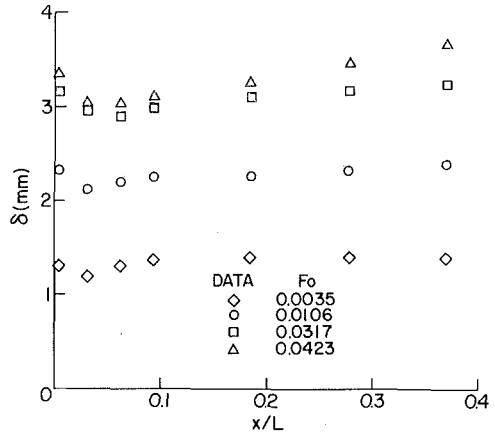

Fig. 2 Variation of solid layer thickness during freezing from a vertical wall: Ste = 0.0168, $Ra_L = 1.19 \times 10^7$, $L = 9$ cm

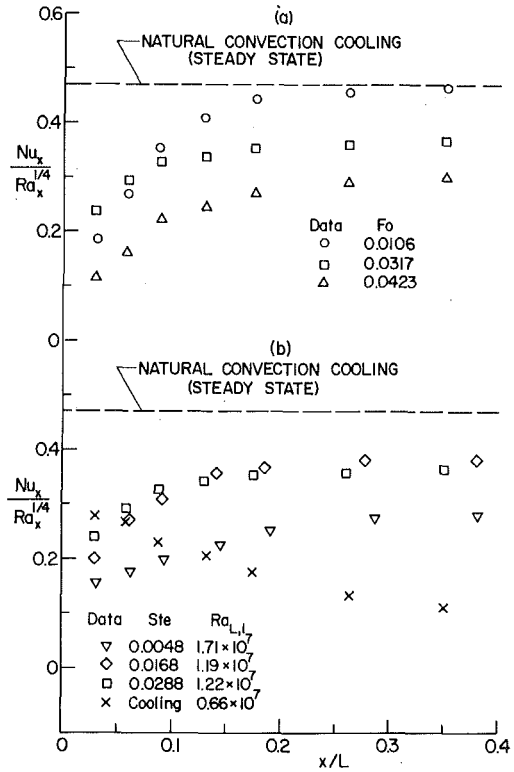

Fig. 3 Variation of heat transfer along the vertical wall during freezing: (a) effect of time, Ste = 0.0288 and $Ra_L = 1.22 \times 10^7$; (b) effect of Stefan number, Fo = 0.0317

in dimensionless group $\mathrm{Nu}_x/\mathrm{Ra}_x^{1/4}$ fails to reveal such a maximum. At very early time conduction predominates, resulting in high heat transfer rates, which decrease with time. The results are not presented for Fo < 0.00106 because the high fringe densities made accurate interpretation of the interferograms impossible.

The presence of natural convection augments the heat transfer, but the simultaneous decrease of the liquid bulk temperature and the development of thermal stratification within the fluid, results in decrease of heat transfer. The net result of the competing processes is the decrease in the local heat transfer coefficient with time. Steady-state natural convection heat transfer from a vertical plate suspended in an infinite volume of liquid as predicted by boundary layer theory in the absence of phase change [8] is included in Fig. 3 for the purpose of comparison. At early time (Fo = 0.00106) and for $x/L > 0.3$, the experimental data are seen to approach the theoretical predictions. The results are not included for $x/L > 0.4$ because the optics of the interferometer were too small to accommodate the entire length of

the plate (L = 9 cm). Based on quasi-steady convection in a liquid undergoing phase change and integral method of solution, the heat flux parameter $Nu_x/Ra_x^{1/4}$ has been analytically predicted [1]. However, a meaningful comparison with data is not possible because the two physical situations are different.

The effect of Stefan number on the local heat transfer coefficients and a comparison of results with those for transient natural convection in the absence of phase change are also included in Fig. 3(*b*). At a given time, the heat transfer results exhibit complicated trends with Stefan number. This can be attributed to a simultaneous occurrence of two main effects: (1) decrease in the liquid bulk temperature, and (2) alteration in the natural convection flow field as a result of change in liquid temperature distribution, solid layer thickness and stratification with the test cell.

For transient natural convection cooling of a liquid, the heat transfer parameter $Nu_x/Ra_x^{1/4}$ attains a maximum value in the vicinity of $x/L \simeq 0$. The trends in data for the freezing and cooling experiments are quite different. This is primarily due to a more intense stratification and a faster approach of the test material temperature to the plate surface temperature during a cooling process. The faster approach mentioned would be due to the fact that latent heat of fusion is not removed during the cooling process. As a consequence of a small temperature driving potential (buoyancy force) and resulting reduced natural convection flow, the heat transfer coefficients are lower for $x/L > 0.12$.

The results reported here and elsewhere [2, 3] provide evidence that freezing of a superheated liquid can be affected greatly by natural convection in the liquid. The results also indicate that several additional effects and parameters must be considered when correlating natural convection heat transfer data and choosing scaling parameters during liquid-to-solid phase change from a cooled vertical wall of a finite-size system.

Acknowledgments

This work was supported by the National Science Foundation Heat Transfer Program under Grant No. ENG-7811686.

References

1 Lapadula, C. A., and Mueller, W. K., "The Effect of Buoyancy on the Formation of a Solid Deposit Freezing Onto a Vertical Surface," *International Journal of Heat and Mass Transfer*, Vol. 13, 1970, pp. 13–25.

2 Bathelt, A. G., Van Buren, P. D., and Viskanta, R., "Heat Transfer During Solidification Around a Cooled Horizontal Cylinder," in *Heat Transfer—San Diego 1979*, AIChE Symposium Series, No. 189, Vol. 75, 1979, pp. 103–111.

3 Sparrow, E. M., Ramsey, J. W., and Kemink, R. G., "Freezing Controlled by Natural Convection," ASME JOURNAL OF HEAT TRANSFER, Vol. 101, Nov. 1979, pp. 578–584.

4 Hale, N. W., Jr., and Viskanta, R., "Solid-Liquid Phase-Change Heat Transfer and Interface Motion in Materials Cooled or Heated from Above or Below," *International Journal of Heat and Mass Transfer*, (in press).

5 Turner, R. H., *High Temperature Energy Thermal Storage*, Franklin Institute Press, Philadelphia, PA, 1978.

6 Hauf, W., and Grigull, W., "Optical Methods in Heat Transfer," in *Advances in Heat Transfer*, T. F. Irvine, Jr. and J. P. Hartnett, Eds, Vol. 6, Academic Press, 1970, pp. 133–366.

7 Hellums, J. D., and Churchill, S. W., "Transient and Steady State, Free and Natural Convection Numerical Solutions: Part I The Isothermal, Vertical Plate," *AIChE Journal*, Vol. 8, Nov. 1962, pp. 690–692.

8 Churchill, S. W., and Ozoe, H., "A Correlation for Laminar Free Convection from a Vertical Plate," ASME JOURNAL OF HEAT TRANSFER, Vol. 95, Nov. 1973, pp. 540–541.

A Heat Transfer Analysis for Solidification of Rounds

R. H. Tien[1]

Nomenclature

α = thermal diffusivity
C = specific heat
ϵ = location of freezing front
h = heat-transfer coefficient
k = thermal diffusivity
L = heat of fusion
r = radial distance
r_0 = radius of cylinder
t = time
T = temperature
T_c = temperature of coolant
T_m = melting temperature

$$\bar{T} = \frac{T - T_c}{T_m - T_c}$$

$$\bar{r} = \frac{r}{r_0}$$

$$\bar{\epsilon} = \frac{\epsilon}{r_0}$$

$$\bar{t} = \frac{\alpha t}{r_0^2}$$

$$H = \frac{hr_0}{k}$$

$$G = \frac{L}{C(T_m - T_c)}$$

[1] U.S. Steel Research Laboratory, Monroeville, PA 15146

Contributed by the Heat Transfer Division for publication in the JOURNAL OF HEAT TRANSFER. Manuscript received by the Heat Transfer Division November 7, 1979.

Introduction

A semi-analytical solution for the solidification of rounds with convective heat transfer at the cooling surface has been obtained by using a modified heat balance integral method. The solution includes an explicit expression for temperature distribution within the solidifying shell, hence making analysis easier when heat transfer is to be coupled with other phenomena such as thermal stress or chemical segregation.

When the conventional heat balance integral method [1] is applied to solidification problems, the boundary condition obtained from conservation of energy at the solidification front is used indirectly to

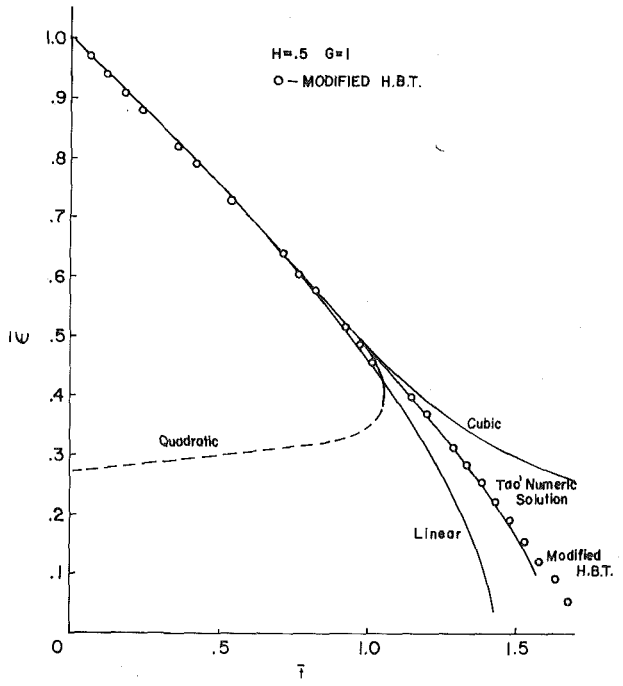

Fig. 1 Location of freezing front

the plate (L = 9 cm). Based on quasi-steady convection in a liquid undergoing phase change and integral method of solution, the heat flux parameter $Nu_x/Ra_x^{1/4}$ has been analytically predicted [1]. However, a meaningful comparison with data is not possible because the two physical situations are different.

The effect of Stefan number on the local heat transfer coefficients and a comparison of results with those for transient natural convection in the absence of phase change are also included in Fig. 3(*b*). At a given time, the heat transfer results exhibit complicated trends with Stefan number. This can be attributed to a simultaneous occurrence of two main effects: (1) decrease in the liquid bulk temperature, and (2) alteration in the natural convection flow field as a result of change in liquid temperature distribution, solid layer thickness and stratification with the test cell.

For transient natural convection cooling of a liquid, the heat transfer parameter $Nu_x/Ra_x^{1/4}$ attains a maximum value in the vicinity of $x/L \simeq 0$. The trends in data for the freezing and cooling experiments are quite different. This is primarily due to a more intense stratification and a faster approach of the test material temperature to the plate surface temperature during a cooling process. The faster approach mentioned would be due to the fact that latent heat of fusion is not removed during the cooling process. As a consequence of a small temperature driving potential (buoyancy force) and resulting reduced natural convection flow, the heat transfer coefficients are lower for $x/L > 0.12$.

The results reported here and elsewhere [2, 3] provide evidence that freezing of a superheated liquid can be affected greatly by natural convection in the liquid. The results also indicate that several additional effects and parameters must be considered when correlating natural convection heat transfer data and choosing scaling parameters during liquid-to-solid phase change from a cooled vertical wall of a finite-size system.

Acknowledgments

This work was supported by the National Science Foundation Heat Transfer Program under Grant No. ENG-7811686.

References

1 Lapadula, C. A., and Mueller, W. K., "The Effect of Buoyancy on the Formation of a Solid Deposit Freezing Onto a Vertical Surface," *International Journal of Heat and Mass Transfer*, Vol. 13, 1970, pp. 13–25.

2 Bathelt, A. G., Van Buren, P. D., and Viskanta, R., "Heat Transfer During Solidification Around a Cooled Horizontal Cylinder," in *Heat Transfer—San Diego 1979*, AIChE Symposium Series, No. 189, Vol. 75, 1979, pp. 103–111.

3 Sparrow, E. M., Ramsey, J. W., and Kemink, R. G., "Freezing Controlled by Natural Convection," ASME JOURNAL OF HEAT TRANSFER, Vol. 101, Nov. 1979, pp. 578–584.

4 Hale, N. W., Jr., and Viskanta, R., "Solid-Liquid Phase-Change Heat Transfer and Interface Motion in Materials Cooled or Heated from Above or Below," *International Journal of Heat and Mass Transfer*, (in press).

5 Turner, R. H., *High Temperature Energy Thermal Storage*, Franklin Institute Press, Philadelphia, PA, 1978.

6 Hauf, W., and Grigull, W., "Optical Methods in Heat Transfer," in *Advances in Heat Transfer*, T. F. Irvine, Jr. and J. P. Hartnett, Eds, Vol. 6, Academic Press, 1970, pp. 133–366.

7 Hellums, J. D., and Churchill, S. W., "Transient and Steady State, Free and Natural Convection Numerical Solutions: Part I The Isothermal, Vertical Plate," *AIChE Journal*, Vol. 8, Nov. 1962, pp. 690–692.

8 Churchill, S. W., and Ozoe, H., "A Correlation for Laminar Free Convection from a Vertical Plate," ASME JOURNAL OF HEAT TRANSFER, Vol. 95, Nov. 1973, pp. 540–541.

A Heat Transfer Analysis for Solidification of Rounds

R. H. Tien[1]

Nomenclature

α = thermal diffusivity
C = specific heat
ϵ = location of freezing front
h = heat-transfer coefficient
k = thermal diffusivity
L = heat of fusion
r = radial distance
r_0 = radius of cylinder
t = time
T = temperature
T_c = temperature of coolant
T_m = melting temperature

$$\bar{T} = \frac{T - T_c}{T_m - T_c}$$

$$\bar{r} = \frac{r}{r_0}$$

$$\bar{\epsilon} = \frac{\epsilon}{r_0}$$

$$\bar{t} = \frac{\alpha t}{r_0^2}$$

$$H = \frac{hr_0}{k}$$

$$G = \frac{L}{C(T_m - T_c)}$$

[1] U.S. Steel Research Laboratory, Monroeville, PA 15146

Contributed by the Heat Transfer Division for publication in the JOURNAL OF HEAT TRANSFER. Manuscript received by the Heat Transfer Division November 7, 1979.

Introduction

A semi-analytical solution for the solidification of rounds with convective heat transfer at the cooling surface has been obtained by using a modified heat balance integral method. The solution includes an explicit expression for temperature distribution within the solidifying shell, hence making analysis easier when heat transfer is to be coupled with other phenomena such as thermal stress or chemical segregation.

When the conventional heat balance integral method [1] is applied to solidification problems, the boundary condition obtained from conservation of energy at the solidification front is used indirectly to

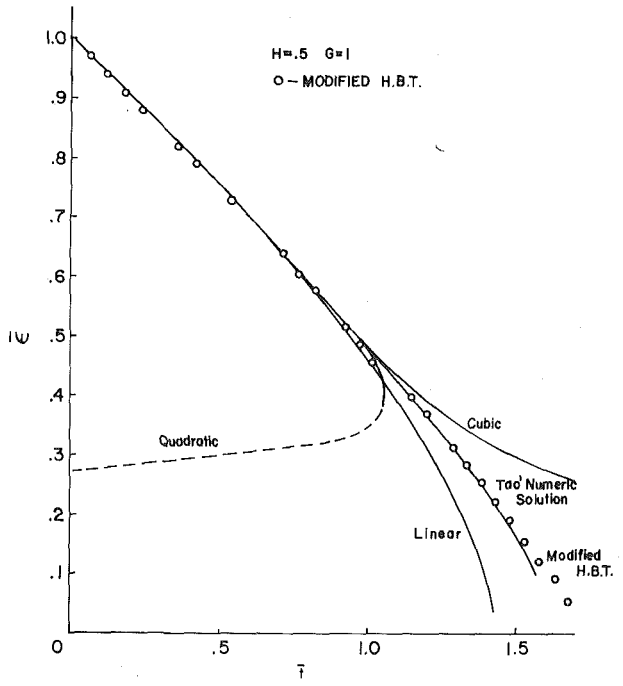

Fig. 1 Location of freezing front

derive the temperature profile, and the solutions converge as the temperature distribution is represented by polynomials of increasingly higher order. This procedure cannot be applied to problems of cylindrical coordinates, however, since solutions for the location of the freezing front diverge toward the end of solidification as shown in Fig. 1 for temperature distributions, which are assumed to be linear, quadratic, and cubic, respectively. In the modified integral method used here, the conventional integral procedure is used only at the beginning to generate an additional initial condition. This condition then allows the boundary condition obtained from conservation of energy at the freezing front to be used directly to evaluate the coefficients of the assumed temperature distribution.

Solution

The governing equation of the present problem is the usual one-dimensional heat-conduction equation in the cylindrical coordinate system. Heat transfer by convection with constant heat-transfer coefficient is used as a boundary condition. Then solutions of the temperature distribution for the quadratic case and the corresponding freezing rate for the present problem are given by:

$$\overline{T} = 1 + C_1(\bar{r} - \bar{\epsilon}) + C_2(\bar{r} - \bar{\epsilon})^2 \tag{1}$$

where

$$\begin{cases} C_1 = G\dfrac{d\bar{\epsilon}}{d\bar{t}} \\ C_2 = -\dfrac{H + C_1 + HC_1(1-\bar{\epsilon})}{(1-\bar{\epsilon})(2+H-H\bar{\epsilon})} \end{cases}$$

and

$$\frac{d^2\bar{\epsilon}}{d\bar{t}^2} = \frac{1}{B_1}\left[B_3\left(\frac{d\bar{\epsilon}}{d\bar{t}}\right)^2 + B_2\frac{d\bar{\epsilon}}{d\bar{t}} - H - HC_1(1-\bar{\epsilon}) - HC_2(1-\bar{\epsilon})^2\right] \tag{2}$$

with the initial conditions,

$$\bar{\epsilon}(\bar{t}=0) = 1$$

$$\frac{d\bar{\epsilon}}{d\bar{t}}(\bar{t}=0) = -\frac{H}{G} \text{ (obtained from conventional method)}$$

$$B_1 = \frac{G}{12}(1-\bar{\epsilon})^2\frac{5+3\bar{\epsilon}+H(1-\bar{\epsilon})}{2+H(1-\bar{\epsilon})}; \qquad B_4 = \frac{H}{(1-\bar{\epsilon})(2+H-H\bar{\epsilon})}$$

$$B_2 = -\left(\frac{2}{G}B_4B_1\right) + \bar{\epsilon}G$$

$$B_3 = \frac{G(1-\bar{\epsilon})}{12(2+H-H\bar{\epsilon})^2}[14 + 18\bar{\epsilon} + 2H(1-\bar{\epsilon})(3+7\bar{\epsilon}) + H^2(1-\bar{\epsilon})^2(1+3\bar{\epsilon})].$$

Equation (2) is solved by the simple and accurate Runge-Kutta method which was discussed in reference [3].

Discussion

A comparison of this new solution with Tau's numerical solution [2] is shown in Fig. 1 along with the results for the conventional method. The modified method is seen to give much better results.

The rate of growth of the freezing front, $d\bar{\epsilon}/d\bar{t}$, and the temperature at the surface, $\overline{T}(\bar{r}=1)$ are plotted against the shell thickness $(1-\bar{\epsilon})$ for different values of the cooling parameter H, in Fig. 2. The freezing rate increases toward the end of solidification for low values of H, that is, when the heat transfer coefficient is low or the thermal conductivity is high. This is contrary to the case of freezing of a slab, where the freezing rate decreases during the entire solidification process for all values of H. Increasing the rate of growth of the freezing front may lead to an unstable liquid-solid interface, since the freezing front under this condition may lose its restorative ability after a small perturbation.

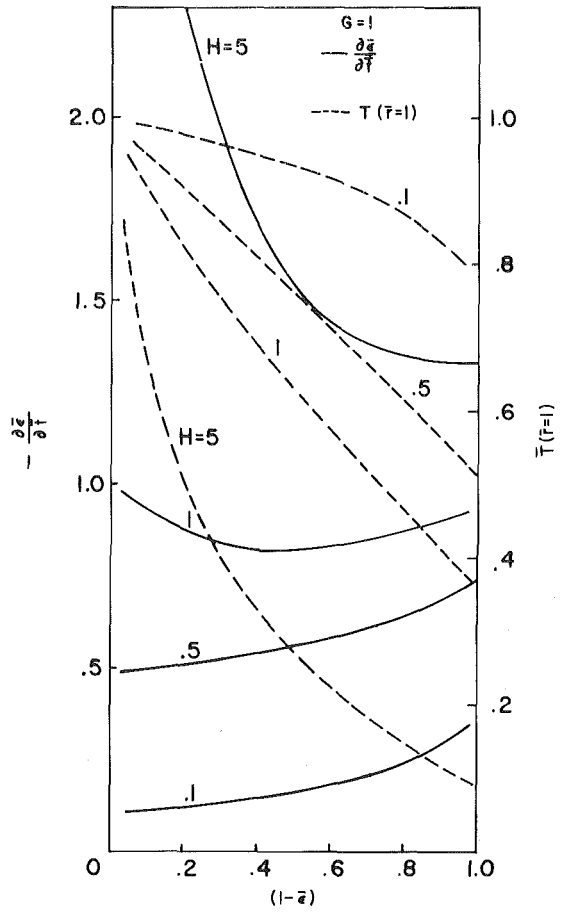

Fig. 2 Freezing rate and surface temperature of solidification of a round

The increasing of freezing rate toward the end of solidification can be explained qualitatively as follows: when the decreasing of heat flux at the freezing front due to the decreasing of surface area available for solidification exceeds the required reduction of heat flux due to the increasing of over-all thermal resistance between liquid and coolant at the large stage of solidification in a round, the rate of movement of the freezing front must increase. This becomes most noticeable for the case of high thermal conductivity (or low value of H). This, in a sense, is related to the condition of optimum thickness of insulation around a circular pipe.

Since this work demonstrates that the ordinary procedure for the integral method is not suitable for the case of freezing of a cylinder as the freezing front approaches the center, care also must be taken when the momentum integral is applied to fluid mechanical problems involving boundary layers in cylinders of small diameter.

References

1 Goodman, T. R., "The Heat Balance Integral and its Application to Problems Involving a Change of Phase," *Trans. ASME*, Vol. 30, 1958, p. 335.

2 Tao, L. C., "Generalized Numerical Solutions of Freezing a Saturated Liquid in Cylinders and Spheres," *AIChE Journal*, Vol. 13, 1967, pp. 165–169.

3 Hildebrand, F. B., *Introduction to Numerical Analysis*, McGraw-Hill, 1956, p. 237.

Sublimation of a Horizontal Slab of Dry Ice: an Analog of Pool Boiling on a Flat Plate

V. K. Dhir[1]

Nomenclature

A_H = solid dry ice or heater surface area
A_g = surface area occupied by gas or vapor
c = specific heat
D_b = bubble diameter
h = heat transfer coefficient
k = thermal conductivity
q = heat flux
T_f = freezing temperature of the liquid
T_H = pool temperature
T_I = instantaneous interface temperature, $T_I - T_{sub}/T_H - T_I = \sqrt{k_H \rho_H c_H / k_c \rho_c c_c}$
T_{min} = pool or heater temperature at film collapse
T_{sat} = saturation temperature of boiling liquid
T_{sub} = sublimation temperature of dry ice
T_w = flat plate heater temperature
ρ = density
ΔT = temperature difference, $T_H - T_{sub}$ or $T_w - T_{sat}$
ΔT_{min} = temperature difference at film collapse, $T_{min} - T_{sub}$ or $T_{min} - T_{sat}$
λ_d = fastest growing Taylor wavelength

Subscripts

c = dry ice
H = pool
max = maximum
min = minimum

Introduction

Understanding of the thermal and hydrodynamic interactions of molten core materials such as UO_2 and steel with core retention or core containment materials such as steel, MgO or concrete is important to assess the propagation or mitigation of hypothetical core disruptive accidents in nuclear reactors. In references [1] and [2] it was shown that as long as the temperature difference between an overlying pool and the supporting subliming or melting surface was greater than a certain ΔT_{min} the interfacial heat transfer was governed by Taylor instability. Partial liquid solid contact was observed to be established when the pool temperature dropped to such a value that a continuous gas or liquid film could not be maintained between the pool and the solid surface. If, in the partial liquid-solid contact region, the instantaneous contact temperature, T_I, of the overlying liquid was less than its freezing temperature [1], the overlying liquid was observed to freeze on the surface. In that region, the interfacial heat transfer decreased rapidly with decrease in pool temperature. The heat transfer rate was almost zero when a thick crust separated the overlying liquid pool from the subliming surface. The purpose of this work is to show how the heat transfer from the pool to the subliming surface would depend on ΔT, if the freezing temperature of the overlying liquid was about the same or lower than the sublimation temperature ($\simeq$194 K) of dry ice.

Experimental Apparatus and Procedure

The interfacial heat transfer experiments were conducted by forming a pool of n-Amyl alcohol $CH_3(CH_2)_4OH$ over a slab of dry ice. The freezing temperature of amyl alcohol is 194 K while the boiling temperature is 410.3 K. The experimental apparatus is similar to that described in reference [1] and is shown in Fig. 1. A 20 × 20 × 2.5 cm dry ice slab was supported on a sheet of plexiglas. A pool of amyl alcohol was formed in a 15 cm dia open ended pyrex jar. A rubber gasket was attached to the lower end of the jar while at the upper end a cross bar was used to press the glass jar against the dry ice surface. The pool temperature was measured with a 30 gage chromel-alumel thermocouple placed about ½ cm above the dry ice surface and connected to a Houston X-Y recorder.

Prior to each experiment the dry ice surface was visually examined to avoid use of an originally uneven surface. The dry ice slab was then placed on a plexiglas sheet and was leveled so that the test surface was as nearly horizontal as possible. The pyrex jar was then positioned on the dry ice surface and the nuts on the cross bar were tightened so that the jar was held tightly against the dry ice surface. About 800–1000 cc of amyl alcohol was heated on a hot plate. The temperature and precise weight of the test liquid were noted and the test liquid was poured into the pyrex jar. In the experiments, the pool height above the dry ice surface generally varied from 5–8 cm and, the agitation of rising CO_2 bubbles kept the pool well stirred. The heat transfer calculations were made by noting the time rate of change of enthalpy of the pool. The rate of change of enthalpy of the pool was calculated by multiplying the mass, the specific heat and rate of change of pool temperature with time. The raw heat transfer data so obtained were corrected for heat losses to the environment by convection and evaporation. After correcting for the heat losses, the uncertainty in data is expected to be less than ±6 percent. However, for a given pool temperature, the heat fluxes obtained from different experiments were found to be within ±15 percent.

Results and Discussion

Upon pouring n-amyl alcohol at a temperature of about 335 K, a shiny film of gas was observed to form at the surface of the dry ice. This film inhibited the liquid pool from touching the dry ice surface. Carbon dioxide bubbles were observed to leave the dry ice surface at regular intervals in a fashion similar to the one described in reference [1] for pools of water and benzene. However, the gas film was seen to break up when the pool temperature decreased to about 315 K, and the dry ice surface appeared to be crowded with bubbles smaller than those observed during pseudo-film boiling. This pattern of gas evolution continued with further decrease in pool temperature, although bubble release frequency appeared to slow down considerably.

The heat flux as a function of temperature difference between the pool and the subliming surface obtained from two of several pseudo boiling experiments is plotted in Fig. 2. In this figure, a typical heat flux curve that would be obtained if amyl alcohol at one atmosphere pressure was boiling on a flat plate is also plotted. The minimum heat flux and the minimum temperature for the boiling on a flat plate are obtained from Berenson's work [3, 4], while the peak heat flux is ob-

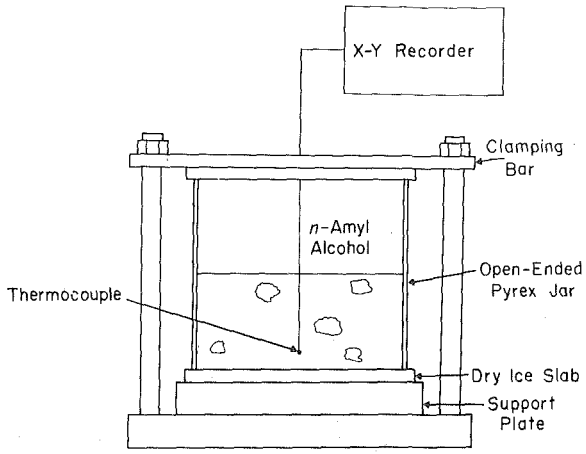

Fig. 1 Schematic diagram of the experimental apparatus

[1] School of Engineering and Applied Science, University of California, Los Angeles, Los Angeles, CA 90024.
Contributed by the Heat Transfer Division for publication in the JOURNAL OF HEAT TRANSFER. Manuscript received by the Heat Transfer Division October 17, 1979.

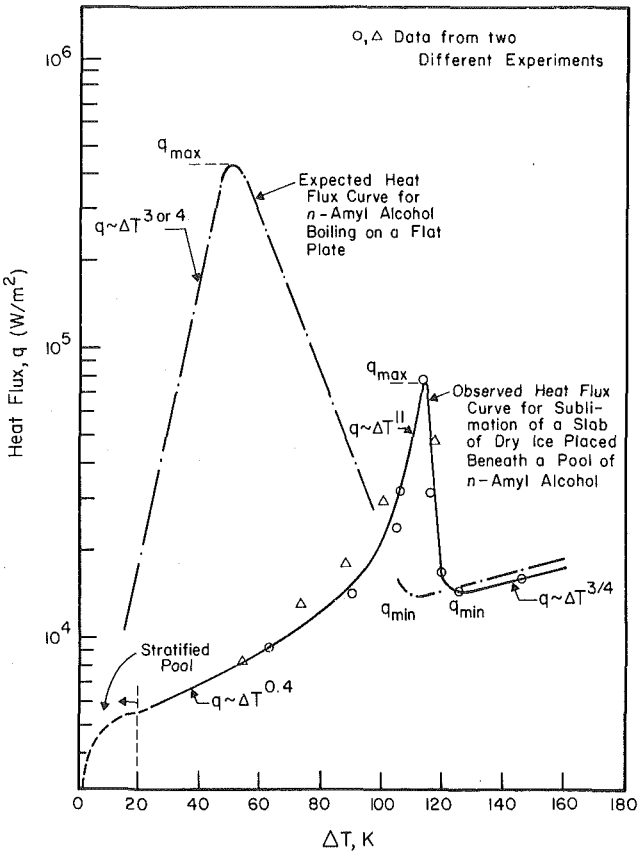

Fig. 2 Comparison of heat fluxes observed during boiling on a flat plate and during sublimation of dry ice

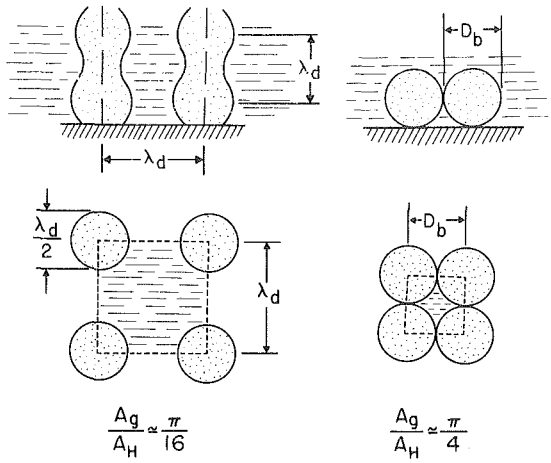

Fig. 3(*a*) Zuber's model for maximum heat flux on flat plates **Fig. 3(*b*) Suggested mode for maximum heat flux during sublimation**

Fig. 3 Models for maximum heat flux during boiling on flat plates and during sublimation of a horizontal slab of dry ice

tained by using Zuber's expression [5] improved on by Lienhard, et al. [6]. In the conventional boiling curve the peak heat flux would have been about 15 percent less had density and latent heat of sublimation of CO_2 been used instead of vapor density and latent heat of vaporization of amyl alcohol.

During the pseudo film boiling on the dry ice slab the heat flux is observed to vary as $\Delta T^{3/4}$, i.e., in the same way as for film boiling on a flat plate. The magnitude of the pseudo film boiling heat transfer coefficient near the minimum is about 15 percent less than that predicted by Berenson's expression. This is because of the release of only one bubble per λ^2 area of the solid surface, as in reference [1]. The gas film breaks up at $\Delta T \simeq 120$ K, whereas ΔT_{min} predicted from Berenson's expression is 110 K. Upon gas film collapse, the heat flux increases rapidly by about four to five times and reaches a maximum valve when the pool temperature is only about 10 K less than the initial film collapse temperature. Thereafter, the heat flux decreases as ΔT^{11}, but this dependence of heat flux on ΔT weakens rapidly as the pool temperature decreases. The liquid pool tends to stratify when the pool temperature reaches such a value that the gas generated at the solid surface is insufficient to agitate the pool. This stratification of the pool results in a liquid temperature at the interface about equal to the sublimation temperature of dry ice and in a quick drop in the interfacial heat flux. Prior to stratification of the pool the heat flux depends on ΔT only as $\Delta T^{0.4}$. In contrast, during saturated boiling on a flat plate (conventional boiling), the transition from film to nucleate boiling is gradual. The maximum heat flux may be about 25 to 30 times higher than the minimum heat flux. Nucleate boiling heat flux irrespective of ΔT varies as $\Delta T^{3 \text{ or } 4}$. Figure 2, thus, shows that the pseudo boiling on the dry ice surface and conventional boiling on a flat plate are similar as far as occurrence of a maxima and a minima is concerned. However, the physical mechanisms governing the post-film collapse behavior in the two processes may be different.

Based on visual observations, a conceptual model for the maximum heat flux during sublimation is proposed and is shown in Fig. 3. In this figure, the vapor removal configuration envisioned by Zuber [5] and subsequently corroborated and slightly modified by Lienhard, et al. [6] for peak heat flux on infinite flat plates is also shown. During nucleate boiling on a flat plate the cavities on the surface act as vapor bubble releases sites. Generally for commercial surfaces the density of these sites may vary as ΔT^6 whereas the bubble release frequency may increase as $\Delta T^{1.5}$. Transition from single bubbles to vapor jets may occur when vapor bubble release frequency is such that vapor bubbles start to merge with each other in the vertical direction. On the average, these jets locate themselves about a Taylor wavelength apart and have a diameter equal to about half of the Taylor wavelength (Fig. 3(*a*)). The peak heat flux occurs when vapor velocity in the jets reaches such a value that the jets become Helmholtz unstable and consequently inhibit locally the liquid from reaching the heater surface. As shown by Yu and Mesler [7], the main mode of transport of heat near the peak heat flux is evaporation of micro and macrolayers adjacent to the heater surface.

During the pseudo boiling process studied in this work, the energy for the phase change process is supplied by the liquid. After the collapse of the stable gas film between the liquid and the dry ice slab, continued growth of isolated bubbles is only possible if a sustained contact of the overlying liquid with the dry ice surface is maintained. Also, as the liquid next to the solid surface becomes cold, hotter liquid from the pool has to be brought to the surface. Thus, gas evolution rate at the surface will very much depend on the temperature difference between the pool and the subliming surface and on the mechanical interaction of the two fluids. The transfer process associated with fluid motion is expected to be slow, and for this reason the bubble frequency during sublimation never reaches a stage where gas bubbles start to merge with each other in the vertical direction and from a gas jet. During sublimation any location on the surface of the dry ice slab can act as an active gas evolution site. The maximum heat flux would occur when the dry ice surface is fully crowded with bubbles and the growth rate of the bubbles is maximum. The highest pool temperature, i.e., the temperature immediately after gas film collapse would be the most favored one. The process is however self limiting because for the bubble configuration shown in Fig. 3(*b*) liquid can only contact the dry ice surface through the interstitial area between the adjoining bubbles. A stronger dependence of heat flux on ΔT is expected during pseudo nucleate boiling process because the thermal potential of the liquid affects the growth rate of the bubbles which in turn influences the fluid motion near the solid surface.

It is interesting to note here that sublimation of a slab of dry ice placed beneath a liquid offers a third category of hydrodynamic transitions during pool type boiling. The first two categories being hydrodynamic transitions during boiling on a flat plate as identified by Zuber [5] and by Moissis and Berenson [8] and during electrolysis as identified by Bhattacharya and Lienhard [9]. In the work of

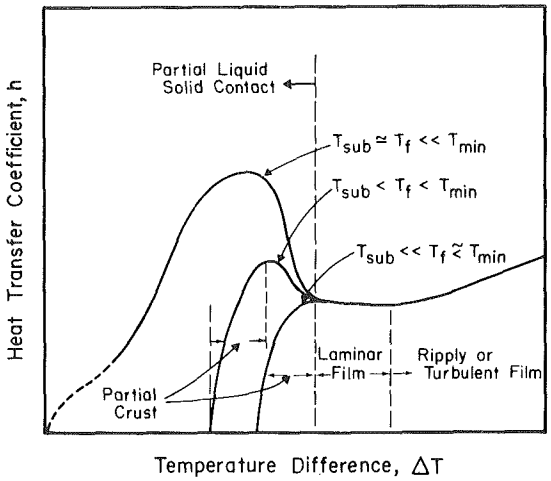

Fig. 4 Expected dependence of heat transfer coefficient on difference between pool temperature and the sublimation temperature of dry ice

Bhattacharya and Lienhard an increase in voltage across the electrodes was observed to increase the bubble release frequency (gas volume flux), which eventually resulted in merger of bubbles emanating from the electrode. Formation of a gas jet at the electrode inhibited the electrolyte from reaching the surface of the electrode. Deficiency of liquid at the electrode caused the gas volume flux to decrease from a maximum with further increase in voltage across the electrodes.

Figure 4 shows qualitatively the expected dependence of heat transfer coefficient on the temperature difference between the pool and the sublimation or melting temperature of the supporting substrate for three different freezing temperatures of the overlying liquid. The lowest curve is for the case when the freezing temperature of the liquid is slightly lower than the temperature at which gas film collapses. The next curve is for the case when the freezing temperature of the liquid is substantially lower than the film collapse temperature but is higher than the sublimation temperature. Finally, the top curve is for the case when the dry ice sublimation temperature and the freezing temperature of the liquid are about the same but both are very much lower than the gas film collapse temperature. At pool temperatures for which a stable gas film separates the solid surface from the overlying pool, the heat transfer coefficient will vary as $\Delta T^{-1/4}$ if the film is laminar. However, for a turbulent or ripply film, the heat transfer coefficient may increase at ΔT or some positive exponent of ΔT [1]. After gas film collapse, the heat transfer coefficient will decrease rapidly if the instantaneous liquid-solid temperature, T_I, is lower than the freezing temperature of the overlying liquid. The rapid decrease in heat transfer is caused by formation of a crust at the solid surface. But for liquids with freezing temperature lower than the instantaneous contact temperature, T_I, the heat transfer coefficient will go through a maxima before decreasing to almost zero when the pool temperature adjacent to the solid surface reaches either the freezing temperature of liquid or sublimation or melting temperature of the solid. The magnitude of the maximum heat transfer coefficient and subsequent functional dependence of heat transfer coefficient on the temperature will very much depend on the freezing temperature of the liquid and on the volume flux of the gas. The implication of this work to certain post accident heat removal situations is that the film boiling models presently being used [10] to describe interfacial heat transfer between a pool of molten UO_2 or steel and concrete may represent a lower limit of pool penetration rates. For example, if a pool of molten steel (melting temperature $\simeq$1800 K) is supported on a slab of concrete (melting temperature $\simeq$1200 K), the interfacial heat transfer coefficient may go through a maxima if the freezing temperature of the eutectic compound formed by molten concrete and steel in the pool is sufficiently less than the temperature at which a gas film can no longer be supported between the melt and the concrete slab.

References

1. Dhir, V. K., Castle, J. N., and Catton, I., "Role of Taylor Instability on Sublimation of a Horizontal Slab of Dry Ice," ASME JOURNAL OF HEAT TRANSFER, 1977, pp. 411–418.
2. Taghavi-Tafreshi, K., Dhir, V. K., and Catton, I., "Thermal and Hydrodynamic Phenomena Associated with Melting of a Horizontal Substrate Placed Beneath a Heavier Immiscible Liquid," ASME JOURNAL OF HEAT TRANSFER, 1979, pp. 318–325.
3. Berenson, P. J., "Film Boiling Heat Transfer from a Horizontal Surface," ASME JOURNAL OF HEAT TRANSFER, 1961, pp. 351–362.
4. Berenson, P. J., "Experiments on Pool Boiling Heat Transfer," *International Journal of Heat and Mass Transfer*, Vol. 5, No. 10, 1962, pp. 985–999.
5. Zuber, N., "Hydrodynamic Aspects of Boiling Heat Transfer," AEC Report No. AECU-4439, *Physics and Mathematics*, 1959.
6. Lienhard, J. H., Dhir, V. K., and Riherd, D. M., "Peak Pool Boiling Heat Flux Measurements on Finite Horizontal Plates," ASME JOURNAL OF HEAT TRANSFER, 1973, pp. 477–482.
7. Yu, C. L., and Mesler, R. B., "A Study of Nucleate Boiling Near the Peak Heat Flux through Measurement of Transient Surface Temperature," *International Journal of Heat and Mass Transfer*, Vol. 20, No. 8, 1977, pp. 827–840.
8. Moissis, R., and Berenson, P. J., "On the Hydrodynamic Transition in Nucleate Boiling," ASME JOURNAL OF HEAT TRANSFER, 1963, pp. 53–78.
9. Bhattacharya, A., and Lienhard, J. H., "Hydrodynamic Transition in Electrolysis," ASME *Journal of Basic Engineering*, Vol. 94, 1972, p. 804.
10. Castle, J. N., Dhir, V. K., and Catton, I., "On the Heat Transfer from a Pool of Molten UO_2 to a Concrete Slab," *ANS Transactions*, Vol. 26, 1977, pp. 356–357.

Heat Transfer to Power-Law Non-Newtonian Flow between Parallel Plates

S. H. Lin and W. K. Hsu[1]

Introduction

Studies of heat transfer characteristics to a non-Newtonian flow between parallel plates have been made before by Tien [1], Suckow, et al. [2], Vlachopoulos and Keung [3] and Kwant and van Ravenstein [4]. Tien [1] used an approximate velocity profile to describe the Graetz-Nusselt heat transfer to a power-law fluid. The problem he considered was relatively simple and was refined by Suckow, et al. [2], who considered an exact velocity distribution. These authors obtained an approximate solution by using two eigenvalues only which was later found by Vlachopolous and Keung [3] and Kwant and van Ravenstein [4] to be inadequate. In fact, according to El-Ariny and Aziz [5], the semi-analytic approach used by Tien [1] and Suckow, et al. [2], may need ten or even more eigenvalues in order to accurately predict the heat transfer characteristics. Vlachopoulos and Keung [3] also considered the effect of viscous dissipation in their work. The effect of viscous dissipation is indeed important in many practical situations.

An important assumption common to all the previous investigations is that the physical properties of the fluid are constant. In fact, the rheological properties of non-Newtonian fluid are highly temperature dependent. Variation of the fluid property in the thermal entrance region can significantly distort the velocity distribution which in turn influences appreciably the heat transfer characteristics. In other words, the interdependence of momentum and heat transfer will give results which are quite different from those under the condition of constant fluid property. In order to predict more faithfully the heat transfer characteristics of this problem, incorporation of the effect

[1] Department of Chemical Engineering, Polytechnic Institute of New York, Brooklyn, New York 11201

Contributed by the Heat Transfer Division for publication in the JOURNAL OF HEAT TRANSFER. Received by The Heat Transfer Division November 16, 1980.

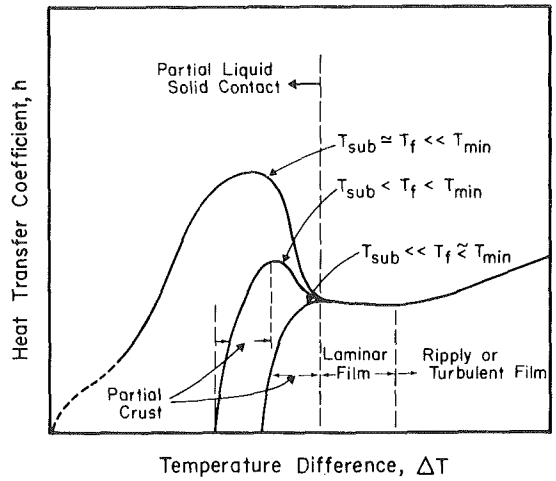

Fig. 4 Expected dependence of heat transfer coefficient on difference between pool temperature and the sublimation temperature of dry ice

Bhattacharya and Lienhard an increase in voltage across the electrodes was observed to increase the bubble release frequency (gas volume flux), which eventually resulted in merger of bubbles emanating from the electrode. Formation of a gas jet at the electrode inhibited the electrolyte from reaching the surface of the electrode. Deficiency of liquid at the electrode caused the gas volume flux to decrease from a maximum with further increase in voltage across the electrodes.

Figure 4 shows qualitatively the expected dependence of heat transfer coefficient on the temperature difference between the pool and the sublimation or melting temperature of the supporting substrate for three different freezing temperatures of the overlying liquid. The lowest curve is for the case when the freezing temperature of the liquid is slightly lower than the temperature at which gas film collapses. The next curve is for the case when the freezing temperature of the liquid is substantially lower than the film collapse temperature but is higher than the sublimation temperature. Finally, the top curve is for the case when the dry ice sublimation temperature and the freezing temperature of the liquid are about the same but both are very much lower than the gas film collapse temperature. At pool temperatures for which a stable gas film separates the solid surface from the overlying pool, the heat transfer coefficient will vary as $\Delta T^{-1/4}$ if the film is laminar. However, for a turbulent or ripply film, the heat transfer coefficient may increase at ΔT or some positive exponent of ΔT [1]. After gas film collapse, the heat transfer coefficient will decrease rapidly if the instantaneous liquid-solid temperature, T_I, is lower than the freezing temperature of the overlying liquid. The rapid decrease in heat transfer is caused by formation of a crust at the solid surface. But for liquids with freezing temperature lower than the instantaneous contact temperature, T_I, the heat transfer coefficient will go through a maxima before decreasing to almost zero when the pool temperature adjacent to the solid surface reaches either the freezing temperature of liquid or sublimation or melting temperature of the solid. The magnitude of the maximum heat transfer coefficient and subsequent functional dependence of heat transfer coefficient on the temperature will very much depend on the freezing temperature of the liquid and on the volume flux of the gas. The implication of this work to certain post accident heat removal situations is that the film boiling models presently being used [10] to describe interfacial heat transfer between a pool of molten UO_2 or steel and concrete may represent a lower limit of pool penetration rates. For example, if a pool of molten steel (melting temperature $\simeq$1800 K) is supported on a slab of concrete (melting temperature $\simeq$1200 K), the interfacial heat transfer coefficient may go through a maxima if the freezing temperature of the eutectic compound formed by molten concrete and steel in the pool is sufficiently less than the temperature at which a gas film can no longer be supported between the melt and the concrete slab.

References

1. Dhir, V. K., Castle, J. N., and Catton, I., "Role of Taylor Instability on Sublimation of a Horizontal Slab of Dry Ice," ASME JOURNAL OF HEAT TRANSFER, 1977, pp. 411–418.
2. Taghavi-Tafreshi, K., Dhir, V. K., and Catton, I., "Thermal and Hydrodynamic Phenomena Associated with Melting of a Horizontal Substrate Placed Beneath a Heavier Immiscible Liquid," ASME JOURNAL OF HEAT TRANSFER, 1979, pp. 318–325.
3. Berenson, P. J., "Film Boiling Heat Transfer from a Horizontal Surface," ASME JOURNAL OF HEAT TRANSFER, 1961, pp. 351–362.
4. Berenson, P. J., "Experiments on Pool Boiling Heat Transfer," *International Journal of Heat and Mass Transfer*, Vol. 5, No. 10, 1962, pp. 985–999.
5. Zuber, N., "Hydrodynamic Aspects of Boiling Heat Transfer," AEC Report No. AECU-4439, *Physics and Mathematics*, 1959.
6. Lienhard, J. H., Dhir, V. K., and Riherd, D. M., "Peak Pool Boiling Heat Flux Measurements on Finite Horizontal Plates," ASME JOURNAL OF HEAT TRANSFER, 1973, pp. 477–482.
7. Yu, C. L., and Mesler, R. B., "A Study of Nucleate Boiling Near the Peak Heat Flux through Measurement of Transient Surface Temperature," *International Journal of Heat and Mass Transfer*, Vol. 20, No. 8, 1977, pp. 827–840.
8. Moissis, R., and Berenson, P. J., "On the Hydrodynamic Transition in Nucleate Boiling," ASME JOURNAL OF HEAT TRANSFER, 1963, pp. 53–78.
9. Bhattacharya, A., and Lienhard, J. H., "Hydrodynamic Transition in Electrolysis," ASME *Journal of Basic Engineering*, Vol. 94, 1972, p. 804.
10. Castle, J. N., Dhir, V. K., and Catton, I., "On the Heat Transfer from a Pool of Molten UO_2 to a Concrete Slab," *ANS Transactions*, Vol. 26, 1977, pp. 356–357.

Heat Transfer to Power-Law Non-Newtonian Flow between Parallel Plates

S. H. Lin and W. K. Hsu[1]

Introduction

Studies of heat transfer characteristics to a non-Newtonian flow between parallel plates have been made before by Tien [1], Suckow, et al. [2], Vlachopoulos and Keung [3] and Kwant and van Ravenstein [4]. Tien [1] used an approximate velocity profile to describe the Graetz-Nusselt heat transfer to a power-law fluid. The problem he considered was relatively simple and was refined by Suckow, et al. [2], who considered an exact velocity distribution. These authors obtained an approximate solution by using two eigenvalues only which was later found by Vlachopolous and Keung [3] and Kwant and van Ravenstein [4] to be inadequate. In fact, according to El-Ariny and Aziz [5], the semi-analytic approach used by Tien [1] and Suckow, et al. [2], may need ten or even more eigenvalues in order to accurately predict the heat transfer characteristics. Vlachopoulos and Keung [3] also considered the effect of viscous dissipation in their work. The effect of viscous dissipation is indeed important in many practical situations.

An important assumption common to all the previous investigations is that the physical properties of the fluid are constant. In fact, the rheological properties of non-Newtonian fluid are highly temperature dependent. Variation of the fluid property in the thermal entrance region can significantly distort the velocity distribution which in turn influences appreciably the heat transfer characteristics. In other words, the interdependence of momentum and heat transfer will give results which are quite different from those under the condition of constant fluid property. In order to predict more faithfully the heat transfer characteristics of this problem, incorporation of the effect

[1] Department of Chemical Engineering, Polytechnic Institute of New York, Brooklyn, New York 11201

Contributed by the Heat Transfer Division for publication in the JOURNAL OF HEAT TRANSFER. Received by The Heat Transfer Division November 16, 1980.

of variable fluid property may be necessary. This is the main purpose of the present Technical Note.

Problem Formulation

Consider a steady-state polymer flow between parallel plates. The equation of motion describing the one-dimensional flow can be represented by

$$\frac{d\tau}{dy} = -\frac{dP}{dx} \tag{1}$$

where τ is the shear stress, y the axial coordinate, and $(-dP/dx)$ the constant axial pressure gradient. Equation (1) can be integrated to

$$\tau = \frac{y}{a}\tau_w \tag{2}$$

by using the wall boundary condition $\tau = \tau_w$ at $y = a$ to eliminate the pressure gradient. The temperature-dependent power-law equation is

$$\tau = K(T)\left(-\frac{dv}{dy}\right)^n \tag{3}$$

in which v is the velocity, $K(T)$ the temperature-dependent consistency index, and n the pseudoplastic index. Although several expressions have been available relating $K(T)$ to the temperature, the one suggested by Mizushina and Kuriwaki [6] is to be used here. The relation is represented by

$$K(T) = \frac{K_i}{[1 + \beta_i(T - T_i)]^n} \tag{4}$$

where K_i and β_i are constant parameters at a reference temperature T_i. As shown by Mizushina and Kuriwaki [6], equation (4) correlates the temperature-dependent consistency index fairly well. In fact, equation (4) was also found by the present authors to correlate well the $K - T$ relation for Carbopol solutions.

Combination of equations (2, 3) and (4) and integration gives

$$v = a\left(\frac{\tau_w}{K_i}\right)^{1/n}\int_Y^1 (1 + \beta\theta)Y^{1/n}dY = a\left(\frac{\tau_w}{K_i}\right)^{1/n} I_1(Y) \tag{5}$$

in which $Y = y/a$, $\beta = \beta_i T_i$, and $\theta = (T - T_i)/T_i$. The mean velocity is given by

$$\bar{v} = \frac{1}{a}\int_0^a v dy \tag{6}$$

Insertion of equation (5) into equation (6) leads to

$$\bar{v} = a\left(\frac{\tau_w}{K_i}\right)^{1/n}\int_0^1 I_1(Y)dY = a\left(\frac{\tau_w}{K_i}\right)^{1/n} I_2 \tag{7}$$

Dividing equation (5) by equation (7) then provides the temperature-dependent velocity distribution for the present study

$$V = \frac{v}{\bar{v}} = \frac{I_1(Y)}{I_2} \tag{8}$$

The steady-state energy balance equation neglecting the axial conduction is represented by

$$\rho C_p v\frac{\partial T}{\partial x} = k\frac{\partial^2 T}{\partial x^2} - \tau\frac{dv}{dy} \tag{9}$$

where ρ is the fluid density, C_p the heat capacity, K the thermal conductivity, and x the axial coordinate. Note that the viscous dissipation term is included here for generality as represented by the second term in the right side. Using equations (3, 4) and (5), obtains

$$-\tau\frac{dv}{dy} = \mathrm{Br}\frac{y^{(n+1)/n}(1 + \beta\theta)}{I_2{}^{n+1}} \tag{10}$$

with Br being the Brinkman number as defined by

$$\mathrm{Br} = \frac{K_i\bar{v}^{n+1}}{ka^{n-1}T_i} \tag{11}$$

Substitution of equations (8) and (10) and in terms of the dimensionless variables, equation (9) finally becomes

$$V\frac{\partial\theta}{\partial X} = \frac{\partial^2\theta}{\partial Y^2} + \mathrm{Br}\frac{Y^{(n+1)/n}(1 + \beta\theta)}{I_2{}^{n+1}} \tag{12}$$

It can be shown that for $\beta = 0$, equation (12) reduces to the model previously considered by Vlachopoulos and Keung [3]. The inlet and boundary conditions for equation (12) are

$$X = 0; \theta = 0 \tag{13}$$

$$Y = 0; \frac{\partial\theta}{\partial Y} = 0 \tag{14}$$

$$Y = 1; \theta = \phi - 1 \tag{15}$$

where $\phi = T_w/T_i$ with T_w being the wall temperature. For cooling, the wall temperature T_w is less than the inlet temperature T_i and hence ϕ is less than one. For heating, ϕ is then greater than one. Both cases are considered in the present study. The dimensionless heat transfer equation along with the inlet and boundary conditions was solved by the implicit Crank-Nicolson finite difference method [7].

The mean Nusselt number is defined as

$$\overline{\mathrm{Nu}} = \frac{2a\bar{h}}{k} \tag{16}$$

where the mean heat transfer coefficient $\bar{h}$ is given by

$$\bar{h} = \frac{C_p\int_0^a v(T - T_i)dy}{ax[T_w - (T_i + T_b)/2]} \tag{17}$$

in which T_b is the mean temperature of the fluid at the axial position x. In terms of the dimensionless variables, the mean Nusselt number is rewritten as

$$\overline{\mathrm{Nu}} = \frac{2Gz}{\theta_w - \frac{1}{2}\theta_b} \tag{18}$$

where the dimensionless mean temperature and Gz are given by

$$\theta_b = \int_0^1 \frac{I_1(Y)}{I_2}\theta dY \tag{19}$$

$$Gz = \bar{v}a^2C_p/kx \tag{20}$$

The mean Nusselt number therefore can be readily computed as a function of other characteristic parameters as shown in the following figures.

Discussion of Results

In order to insure the accuracy of the present numerical solution, a special case with constant physical property was run so that comparison could be made with those of Vlachopoulos and Keung [3]. In fact, the present solution and those of Vlachopoulos and Keung [3] for the local Nusselt number and the dimensionless mean temperature were essentially identical.

Because of temperature dependence of fluid property, the velocity profile changes during heat transfer. For heating, that is $\phi > 1.0$, increase in temperature in the wall region decreases the apparent viscosity of the fluid in this region. This leads to increased velocity near the wall and decreased center-line velocity. These effects are displayed in Fig. 1 which shows the development of the velocity profile of a non-Newtonian fluid with $n = 0.5$ as it flows down the heating parallel plates. It is noted that at a certain axial distance from the entrance, the center-line velocity reaches a minimum value before it rises again. After a sufficiently long axial distance from the entrance, the velocity profile exhibits the general characteristics of an isothermal flow since the fluid temperature becomes fully developed. For cooling at the plate wall, that is $\phi < 1.0$, the temperature effect on the velocity distribution was also observed to be very significant.

In Fig. 2, the mean Nusselt numbers for both cooling and heating cases are demonstrated for a pseudoplastic index of 0.5 and without

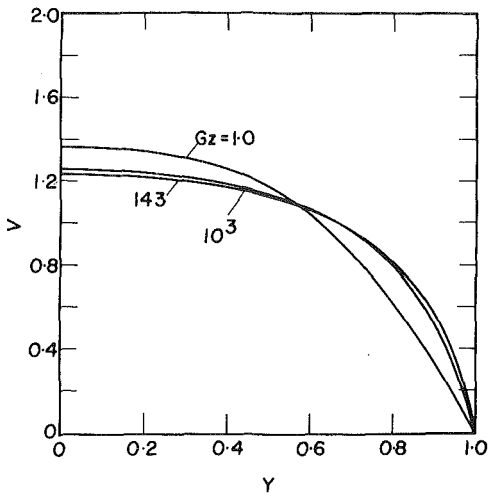

Fig. 1 Development of the velocity profile during the heating of a non-Newtonian fluid with $n = 0.5$, $\beta = 10$, Br = 1.0 and $\phi = 1.02$.

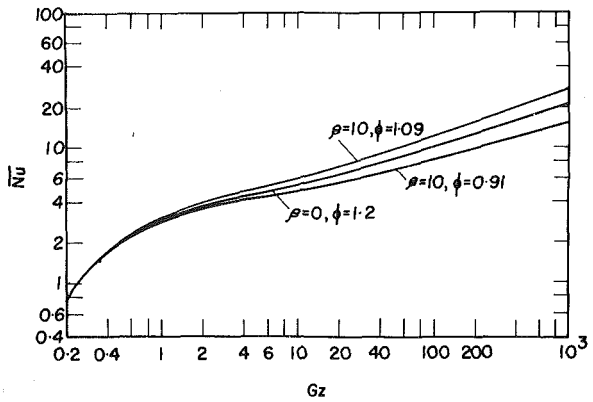

Fig. 2 $\overline{Nu}$ versus Gz for the heating and cooling of a non-Newtonian fluid with $n = 0.5$ and Br = 0

viscous dissipation. For heating, increase in the velocity profile near the wall increases the velocity gradient in this region which in turn enhances heat transfer. For a similar reason, when the plate wall is cooled, the decreased velocity profile near the wall causes a reduction in the heat transfer rate and thus in the mean Nusselt number. These effects are clearly displayed in Fig. 2.

The development of the temperature profiles in the thermal developing region for the heating case is shown in Fig. 3. It is apparent that the accelerated heat transfer rate for the variable physical property case significantly enhances the temperature development.

The effect of viscous dissipation on the mean Nusselt number is demonstrated in Fig. 4 for both heating and cooling cases and for several pseudoplastic indexes. The viscous heating is so significant for this case that even if cooling is maintained at the wall, the mean temperature of the fluid increases along the plates. According to equation (18), for $\phi < 1$, the mean Nusselt number becomes negative if θ_b is positive because of negative dimensionless wall temperature θ_w. Such a negative Nusselt number will occur if the viscous dissipation is significantly large such as in the present case. It is of interest to note that occurrence of negative Nusselt number tends to shift toward the channel entrance as the pseudoplastic index decreases.

References

1 Tien, C., "Laminar Heat Transfer of Power-Law Non-Newtonian Fluid—The Extension of Graetz-Nusselt Problem," *Canadian Journal of Chemical Engineering*, Vol. 40, 1962, p. 130.

2 Suckow, W. H., Hrycak, P., and Griskey, R. G., "Heat Transfer to Polymer Solutions and Melts Flowing between Parallel Plates," *Polymer Science and Engineering*, Vol. 11, 1971, p. 401.

3 Vlachopoulos, J., and Keung, C. K., *Journal of American Institute of Chemical Engineers*, Vol. 18, 1972, p. 1272.

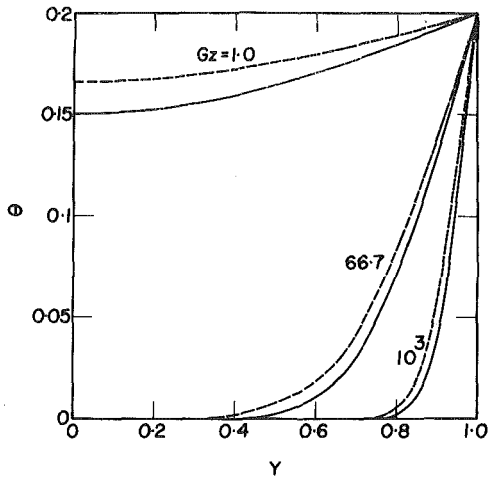

Fig. 3 Development of the temperature profile for the heating of a non-Newtonian fluid with $n = 0.5$, Br = 0 and $\phi = 1.09$. —— $\beta = 0$, - - - $\beta = 10$

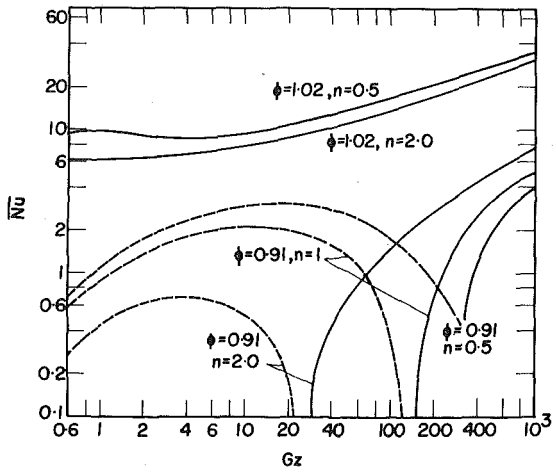

Fig. 4 $\overline{Nu}$ versus Gz for the heating and cooling of a non-Newtonian fluid with $\beta = 10$ and Br = 10 (- - - negative Nusselt number)

4 Kwant, P. B., and van Ravenstein, T. N. M., "Non-Isothermal Laminar Channel Flow," *Chemical Engineering Science*, Vol. 28, 1973, p. 1939.

5 El-Ariny, A. S., and Aziz, A., "A Numerical Solution of Entrance Region Heat Transfer in Plane Couette Flow," ASME JOURNAL OF HEAT TRANSFER, Vol. 100, 1976, p. 427.

6 Mizushina, T., and Kuriwaki, M., *Memoir of the Faculty of Engineering*, Kyoto University, Japan, Vol. 4, 1968, p. 511.

7 Von Rosenberg, D. U., *Methods for the Numerical Solution of Partial Differential Equations*, American Elsevier, 1969.

Turbulent Heat Transfer in Large Aspect Channels

F. D. Haynes[1] and G. D. Ashton[2]

Introduction

Turbulent heat transfer in round tubes has been studied extensively and correlations between heat transfer and flow rate are well established. Turbulent heat transfer in rectangular channel geometries has been studied, comparatively, less. This study was motivated by the

[1] Materials Research Engineer, U.S. Army Cold Regions Research and Engineering Laboratory, Hanover, N.H., Assoc. Mem. ASME.

[2] Supervisory Research Physical Scientists, U.S. Army Cold Regions Research and Engineering Laboratory, Hanover, N.H. 03755

Contributed by the Heat Transfer Division for publication in the JOURNAL OF HEAT TRANSFER. Manuscript received by the Heat Transfer Division February 1, 1980.

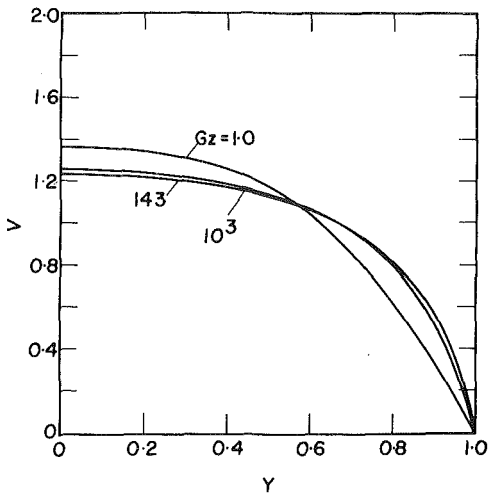

Fig. 1 Development of the velocity profile during the heating of a non-Newtonian fluid with $n = 0.5$, $\beta = 10$, Br = 1.0 and $\phi = 1.02$.

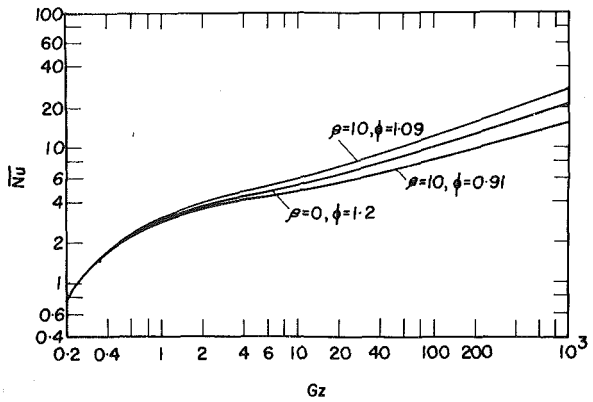

Fig. 2 $\overline{Nu}$ versus Gz for the heating and cooling of a non-Newtonian fluid with $n = 0.5$ and Br = 0

viscous dissipation. For heating, increase in the velocity profile near the wall increases the velocity gradient in this region which in turn enhances heat transfer. For a similar reason, when the plate wall is cooled, the decreased velocity profile near the wall causes a reduction in the heat transfer rate and thus in the mean Nusselt number. These effects are clearly displayed in Fig. 2.

The development of the temperature profiles in the thermal developing region for the heating case is shown in Fig. 3. It is apparent that the accelerated heat transfer rate for the variable physical property case significantly enhances the temperature development.

The effect of viscous dissipation on the mean Nusselt number is demonstrated in Fig. 4 for both heating and cooling cases and for several pseudoplastic indexes. The viscous heating is so significant for this case that even if cooling is maintained at the wall, the mean temperature of the fluid increases along the plates. According to equation (18), for $\phi < 1$, the mean Nusselt number becomes negative if θ_b is positive because of negative dimensionless wall temperature θ_w. Such a negative Nusselt number will occur if the viscous dissipation is significantly large such as in the present case. It is of interest to note that occurrence of negative Nusselt number tends to shift toward the channel entrance as the pseudoplastic index decreases.

References

1 Tien, C., "Laminar Heat Transfer of Power-Law Non-Newtonian Fluid—The Extension of Graetz-Nusselt Problem," *Canadian Journal of Chemical Engineering*, Vol. 40, 1962, p. 130.

2 Suckow, W. H., Hrycak, P., and Griskey, R. G., "Heat Transfer to Polymer Solutions and Melts Flowing between Parallel Plates," *Polymer Science and Engineering*, Vol. 11, 1971, p. 401.

3 Vlachopoulos, J., and Keung, C. K., *Journal of American Institute of Chemical Engineers*, Vol. 18, 1972, p. 1272.

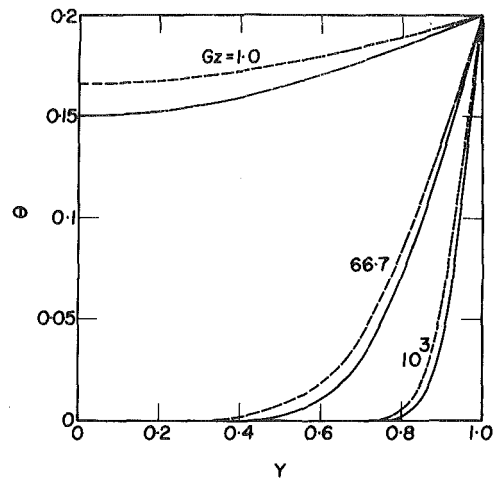

Fig. 3 Development of the temperature profile for the heating of a non-Newtonian fluid with $n = 0.5$, Br = 0 and $\phi = 1.09$. —— $\beta = 0$, - - - $\beta = 10$

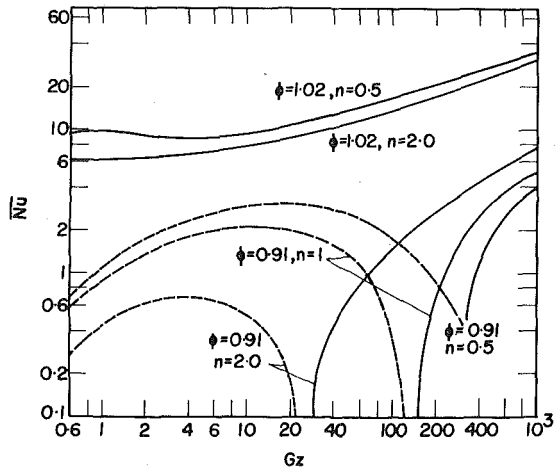

Fig. 4 $\overline{Nu}$ versus Gz for the heating and cooling of a non-Newtonian fluid with $\beta = 10$ and Br = 10 (- - - negative Nusselt number)

4 Kwant, P. B., and van Ravenstein, T. N. M., "Non-Isothermal Laminar Channel Flow," *Chemical Engineering Science*, Vol. 28, 1973, p. 1939.

5 El-Ariny, A. S., and Aziz, A., "A Numerical Solution of Entrance Region Heat Transfer in Plane Couette Flow," ASME JOURNAL OF HEAT TRANSFER, Vol. 100, 1976, p. 427.

6 Mizushina, T., and Kuriwaki, M., *Memoir of the Faculty of Engineering*, Kyoto University, Japan, Vol. 4, 1968, p. 511.

7 Von Rosenberg, D. U., *Methods for the Numerical Solution of Partial Differential Equations*, American Elsevier, 1969.

Turbulent Heat Transfer in Large Aspect Channels

F. D. Haynes[1] and G. D. Ashton[2]

Introduction

Turbulent heat transfer in round tubes has been studied extensively and correlations between heat transfer and flow rate are well established. Turbulent heat transfer in rectangular channel geometries has been studied, comparatively, less. This study was motivated by the

[1] Materials Research Engineer, U.S. Army Cold Regions Research and Engineering Laboratory, Hanover, N.H., Assoc. Mem. ASME.

[2] Supervisory Research Physical Scientists, U.S. Army Cold Regions Research and Engineering Laboratory, Hanover, N.H. 03755

Contributed by the Heat Transfer Division for publication in the JOURNAL OF HEAT TRANSFER. Manuscript received by the Heat Transfer Division February 1, 1980.

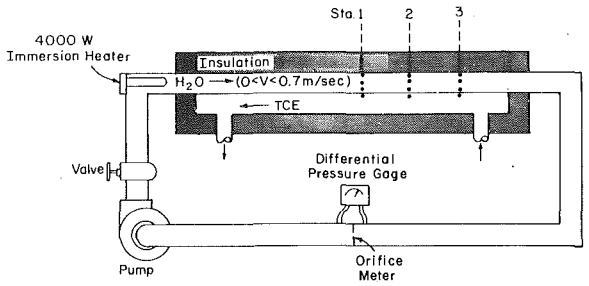

Fig. 1 Apparatus schematic

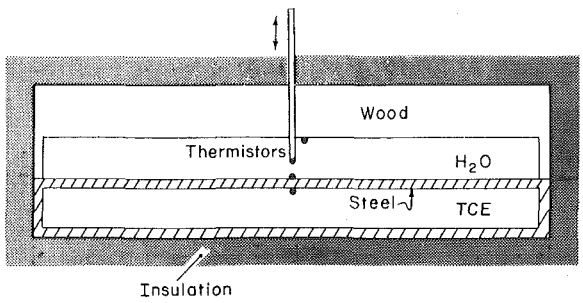

Fig. 2 Cross-section schematic of apparatus

authors' interest in heat transfer from a river to its ice cover; the cross-section geometry of the river is better specified by an aspect ratio B/D where B is the channel width and D is the flow depth. This report presents new data for a closed channel flow with $B/D = 10$ and compares these data with the earlier data of Ashton [1] and Hsu [2]. The data from the present study are underestimated by the formula of Petukhov and Popov [3], which is for a round tube.

Experiments

The experiments were conducted in a rectangular channel with width $B = 0.254$ m and flow depth $D = 0.0254$ m. A schematic of the apparatus is shown in Fig. 1 and a cross-section schematic in Fig. 2. The lower boundary of the apparatus was steel and enclosed a flow of trichloroethylene (TCE) circulated below the water channel at an inlet temperature of about −28°C. The flow depth for the refrigerant was 0.0254 m. The top and sides of the water channel were constructed of wood, and the entire channel section was insulated with urethane and fiberglass. The test section was 3.66 m long. At the inlet, a 4000 W immersion heater was controlled by a thermostat to allow control of the water temperature. The bulk temperature of the water flow was from about 3 to 7°C. Water flow rates were from 0.64×10^{-3} to 4.5×10^{-3} m^3 s^{-1} with corresponding mean flow velocities from 0.1 to 0.7 m s^{-1}. Temperatures of the water, wall, and refrigerant were measured at three stations. The distance from entry to the first station was 1.676 m. Based on the results of Hatton and Quarmby [4], the first station was well beyond the distance at which entry effects are significant. The distance between stations was 0.9144 m. After flow adjustments were made, the system was allowed to stabilize for about 30 min before temperature data were collected.

Four thermistors, each calibrated at the water-ice triple point, were positioned (see Fig. 2) at each of the three stations and the thermistor signals were read with a Keithley Model 172 Digital Multimeter in a forward-reverse-forward sequence. Based on signal ranges used and manufacturer's specifications, absolute temperatures were determined to about 0.01°C and differential resolutions to about 0.005°C. The heat transfer rate was determined from measurements of the decrease in temperature of the flow between measuring stations with the heat flux assumed to be only from the flow to the bottom steel plate. This last assumption was verified by order-of-magnitude calculations. The experiments were also conducted at wall temperatures above 0°C so that no ice formed on the wall.

Results

A total of 27 tests were conducted. Detailed results are given by Haynes and Ashton [5]. The results are shown in Fig. 3 in terms of the Prandtl number, Pr, Reynolds number, Re, and Nusselt number, Nu, defined, respectively, by

$$\mathrm{Pr} \equiv \frac{\mu C_p}{k}, \quad \mathrm{Re} \equiv \frac{UD_h\rho}{\mu}, \quad \mathrm{Nu} \equiv \frac{qD_h}{k(T_\infty - T_0)} \tag{1}$$

where U is the mean flow velocity, q is the heat flux from the flow to the wall, and $T_\infty - T_0$ is the difference between the bulk water temperature T_∞ and the wall temperature T_0. The terms μ, ρ, k, and C_p are the dynamic viscosity, density, thermal conductivity, and specific heat capacity of the water and were evaluated at T_∞. The hydraulic diameter D_h is defined in the conventional way by $D_h = 4A/P$ where A is the cross section area of the flow and P is the wetted perimeter.

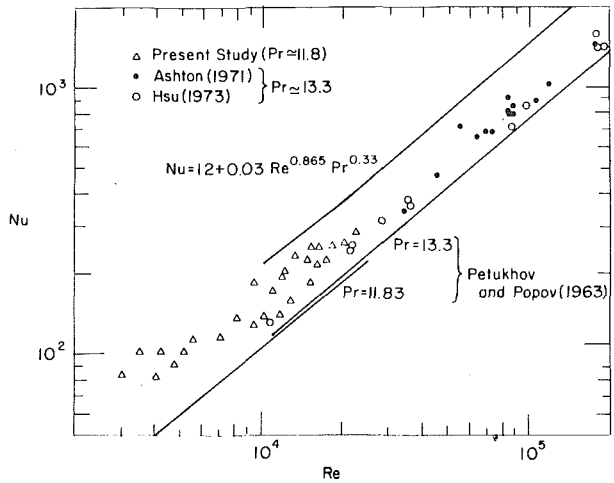

Fig. 3 Heat transfer as a function of Reynolds number

For the present experiments, $D_h = 1.818D$. All of the present experiments were in a narrow range of Prandtl number $9.90 < \mathrm{Pr} < 12.28$ with a representative Pr for most of the data of $\mathrm{Pr} \simeq 11.8$.

Ashton [1] and later Hsu [2] investigated turbulent heat transfer at the bottom of an open channel flow in a flume 0.61 m wide and 12.2 m long; most experiments were conducted with a 0.15 m flow depth. They froze an ice slab onto the bottom of the flume and measured the heat flux by calculating the change in thickness of the ice at the center of the channel and well downstream from the inlet. Their test results are shown in Fig. 3. In their experiments, $D_h = 2.667\,D$ where D is the flow depth. The range of Prandtl number was quite small ($12.34 < \mathrm{Pr} < 13.62$) with a representative value of $\mathrm{Pr} \simeq 13.3$.

Data Interpretation

All the data are plotted in Fig. 3 as a function of Re and Nu. Three of Hsu's data points overlap the data of the present study. For comparison, two analytical predictions are also plotted in Fig. 3. The formula of Petukhov and Popov [3] correlates turbulent heat transfer in round tubes quite well (± 6 percent) for a wide range of Re and Pr (see, e.g., Karlekar and Desmond [6]); it underpredicts the Hsu [2] and Ashton [1] data by about 15 percent, and the data of the present study by about 35 percent. The formula of Petukhov and Popov [3] is

$$\mathrm{Nu} = \frac{(f/8)\mathrm{RePr}}{1.07 + 12.7\,(f/8)^{1/2}(\mathrm{Pr}^{2/3} - 1)} \tag{2}$$

where f has been calculated using the Filonenko equation (see Karlekar and Desmond [6])

$$f = [1.82 \log_{10}(\mathrm{Re}) - 1.64]^{-2} \tag{3}$$

We also note that the Petukhov-Popov formula yields Nusselt numbers somewhat greater (~20 percent) than the commonly used Dittus-Boelter equation or the Colburn equation in the range of Reynolds numbers of the Hsu and Ashton data sets.

Shibani and Ozisik [7] presented an analytical solution for turbulent

heat transfer between parallel plates with top and bottom cooling and correlated their analytical predictions in the range $0.1 < Pr < 10^4$ and $10^4 < Re < 10^6$ by

$$Nu = 12 + 0.03\,Re^{a_1}\,Pr^{a_2} \tag{4}$$

where

$$a_1 = 0.88 - \frac{0.24}{(3.6 + Pr)} \tag{5}$$

$$a_2 = 0.33 + 0.5e^{-0.6Pr} \tag{6}$$

For the Prandtl numbers of the present data set, the second term in equation (6) is negligible compared with the first. In equation (5), the second term is approximately −0.015 for the Prandtl numbers of the present data set, so that the Shibani-Ozisik formula becomes

$$Nu = 12 + 0.03\,Re^{0.865}Pr^{0.33} \tag{7}$$

Equation (7) is also presented in Fig. 3 and is seen to overpredict the Nusselt number by about 50 percent.

Several reasons are offered for the differences between the data and the predictions. First, it is difficult to achieve the idealized flow conditions implicit in the analyses and there may have been a high turbulence level in the recirculating flow. We also suspect the steel plate had some roughness in the present experiments, and in the Reynolds range of these experiments, this could well have contributed to a higher Nusselt number. Second, the aspect ratio B/D_h varied from 1.5 for the Ashton-Hsu data sets to 5.5 for the present study, while the Petukhov-Popov formula is applicable to a round cross section roughly equivalent to a $B/D_h = 1$ and the Shibani-Ozisik formula is applicable to a $B/D_h = \infty$.

Conclusions

The main objectives of the present experiments were to obtain new data on the effect of aspect ratio B/D_h on heat transfer and compare the data to existing theoretical and empirical results. Existing data for round cross sections roughly equivalent to $B/D_h = 1$ are represented by various empirical formulae such as the Petukhov-Popov formula. This formula underpredicts the results of Ashton-Hsu for $B/D_h = 1.5$ and for the present data for $B/D_h = 5.5$. The Shibani-Ozisik formula, applicable to a $B/D_h = \infty$ overpredicts the heat transfer rates. However, the present data and the Ashton-Hsu data are inadequate to provide a relationship for the heat transfer rates as a function of B/D_h.

References

1 Ashton, G. D., "The Formation of Ice Ripples on the Underside of River Ice Covers," Thesis presented to the University of Iowa, Iowa City, Iowa in partial fulfillment of the requirements for the degree of Doctor of Philosophy, June, 1971.

2 Hsu, K., "Spectral Evolution of Ice Ripples," Thesis presented to the University of Iowa, Iowa City, Iowa, in partial fulfillment of the requirements for the degree of Doctor of Philosophy, Dec., 1973.

3 Petukhov, B. S., and Popov, V. N., "Theoretical Calculation of Heat Exchange and Frictional Resistance in Turbulent Flow in Tubes of an Incompressible Fluid with Variable Physical Properties," *Transactions in High Temperature*, Vol. 1, No. 1, 1963.

4 Hatton, A. P. and Quarmby, A., "The Effect of Axially Varying and Unsymmetrical Boundary Conditions on Heat Transfer with Turbulent Flow between Parallel Plates," *International Journal of Heat Mass Transfer*, Vol. 6, No. 10, Oct. 1963, pp. 903–914.

5 Haynes, F. D. and Ashton, G. D., "Turbulent Heat Transfer in Large Aspect Channels," U.S. Army CRREL Report 79-13, May 1979.

6 Karlekar, B. V., and Desmond, R. M., *Engineering Heat Transfer*, 1st ed., West Publishing, St. Paul, 1977, pp. 351–352.

7 Shibani, A. A., and Ozisik, M. N., "A Solution to Heat Transfer in Turbulent Flow between Parallel Plates," *International Journal of Heat Mass Transfer*, Vol. 20, No. 5, May 1977, pp. 565–573.

A Simplified Approach to Shape-Factor Calculation between Three-Dimensional Planar Objects

W. W. Yuen[1]

Introduction

The objective of the present work is to show that by some simple algebraic manipulation of known shape factors, the shape factor between a differential plane area element and an arbitrary three-dimensional planar object with straight edges can be written in closed-form analytically. The shape factor between two planar objects in which one of them has straight edges is reduced to a simple integration of a positive-definite nonsingular function over only one surface area. Compared to the traditional method of direct numerical integration over both surface areas, the present method represents a substantial reduction of the computational effort. A detailed example calculation is presented to demonstrate the utility of the present approach.

Analysis

The basic idea of the present approach is to express the shape factor between a differential plane area element and a three-dimensional object with straight edges in terms of known shape factors. The expression fundamental to the present analysis is the shape factor between a differential plane area element dA_0 and a right triangle A_1 in a parallel plane. Consider the two planes with the orientation and geometry as shown in Fig. 1. The shape factor between dA_0 and A_1 can be obtained from a simple contour integration [1] as

$$F_{dA_0-A_1} = \frac{u}{2\pi(u^2+d^2)^{1/2}}\tan^{-1}\frac{v}{(u^2+d^2)^{1/2}} \tag{1}$$

Equation (1) can now be utilized to calculate the shape factor between dA_0 and an arbitrary triangle A_1 with orientation as shown in Fig. 2. Using superposition, it can be readily shown that the shape factor is given by

$$F_{dA_0-\overline{A_1}} = F_{dA_0-\overline{014}} + F_{dA_0-065} - F_{dA_0-012} - F_{dA_0-023} - F_{dA_0-063} \tag{2}$$

where F_{dA_0-ijk} stands for the shape factor between dA_0 and the right triangle with vertices i, j, and k. Utilizing equation (1), and after some algebraic manipulation, equation (2) becomes

$$F_{dA_0-A} = G(x_0, x_1, x_2, y_2, d) \tag{3}$$

with $G(x_0, x_1, x_2, y_2, d)$

$$= \frac{x_1 y_2}{2\pi[(x_1^2+d^2)y_2^2 + d^2(x_1-x_2)^2]^{1/2}} \times \tan^{-1}\frac{[(x_1^2+d^2)y_2^2 + d^2(x_1-x_2)^2]^{1/2}}{[d^2+x_1x_2]} - \frac{x_0 y_2}{2\pi[(x_0^2+d^2)y_2^2 + d^2(x_0-x_2)^2]^{1/2}} \times \tan^{-1}\frac{[(x_0^2+d^2)y_2^2 + d^2(x_0-x_2)^2]^{1/2}}{[d^2+x_0x_2]} \tag{3a}$$

It is interesting to note that equation (3) is applicable for both cases with $0 \le x_0 \le x_1 \le x_2$ or $0 \le x_0 \le x_2 \le x_1$.

Equation (3) is developed basically for cases in which A_1 is a triangle with one of its edges lying on the x axis or the y axis. But with the aid of some additional shape-factor algebraic manipulation, equation (3) is sufficient to be applied for other possibilities. Consider the two triangles with arbitrary dimensions and locations as shown in Figs.

[1] Department of Mechanical and Environmental Engineering, University of California, Santa Barbara, Santa Barbara, CA 93106.

Contributed by the Heat Transfer Division for publication in the JOURNAL OF HEAT TRANSFER. Manuscript received by the Heat Transfer Division July 30, 1979.

heat transfer between parallel plates with top and bottom cooling and correlated their analytical predictions in the range $0.1 < Pr < 10^4$ and $10^4 < Re < 10^6$ by

$$Nu = 12 + 0.03\,Re^{a_1}\,Pr^{a_2} \tag{4}$$

where

$$a_1 = 0.88 - \frac{0.24}{(3.6 + Pr)} \tag{5}$$

$$a_2 = 0.33 + 0.5e^{-0.6Pr} \tag{6}$$

For the Prandtl numbers of the present data set, the second term in equation (6) is negligible compared with the first. In equation (5), the second term is approximately −0.015 for the Prandtl numbers of the present data set, so that the Shibani-Ozisik formula becomes

$$Nu = 12 + 0.03\,Re^{0.865}Pr^{0.33} \tag{7}$$

Equation (7) is also presented in Fig. 3 and is seen to overpredict the Nusselt number by about 50 percent.

Several reasons are offered for the differences between the data and the predictions. First, it is difficult to achieve the idealized flow conditions implicit in the analyses and there may have been a high turbulence level in the recirculating flow. We also suspect the steel plate had some roughness in the present experiments, and in the Reynolds range of these experiments, this could well have contributed to a higher Nusselt number. Second, the aspect ratio B/D_h varied from 1.5 for the Ashton-Hsu data sets to 5.5 for the present study, while the Petukhov-Popov formula is applicable to a round cross section roughly equivalent to a $B/D_h = 1$ and the Shibani-Ozisik formula is applicable to a $B/D_h = \infty$.

Conclusions

The main objectives of the present experiments were to obtain new data on the effect of aspect ratio B/D_h on heat transfer and compare the data to existing theoretical and empirical results. Existing data for round cross sections roughly equivalent to $B/D_h = 1$ are represented by various empirical formulae such as the Petukhov-Popov formula. This formula underpredicts the results of Ashton-Hsu for $B/D_h = 1.5$ and for the present data for $B/D_h = 5.5$. The Shibani-Ozisik formula, applicable to a $B/D_h = \infty$ overpredicts the heat transfer rates. However, the present data and the Ashton-Hsu data are inadequate to provide a relationship for the heat transfer rates as a function of B/D_h.

References

1 Ashton, G. D., "The Formation of Ice Ripples on the Underside of River Ice Covers," Thesis presented to the University of Iowa, Iowa City, Iowa in partial fulfillment of the requirements for the degree of Doctor of Philosophy, June, 1971.

2 Hsu, K., "Spectral Evolution of Ice Ripples," Thesis presented to the University of Iowa, Iowa City, Iowa, in partial fulfillment of the requirements for the degree of Doctor of Philosophy, Dec., 1973.

3 Petukhov, B. S., and Popov, V. N., "Theoretical Calculation of Heat Exchange and Frictional Resistance in Turbulent Flow in Tubes of an Incompressible Fluid with Variable Physical Properties," *Transactions in High Temperature*, Vol. 1, No. 1, 1963.

4 Hatton, A. P. and Quarmby, A., "The Effect of Axially Varying and Unsymmetrical Boundary Conditions on Heat Transfer with Turbulent Flow between Parallel Plates," *International Journal of Heat Mass Transfer*, Vol. 6, No. 10, Oct. 1963, pp. 903–914.

5 Haynes, F. D. and Ashton, G. D., "Turbulent Heat Transfer in Large Aspect Channels," U.S. Army CRREL Report 79-13, May 1979.

6 Karlekar, B. V., and Desmond, R. M., *Engineering Heat Transfer*, 1st ed., West Publishing, St. Paul, 1977, pp. 351–352.

7 Shibani, A. A., and Ozisik, M. N., "A Solution to Heat Transfer in Turbulent Flow between Parallel Plates," *International Journal of Heat Mass Transfer*, Vol. 20, No. 5, May 1977, pp. 565–573.

A Simplified Approach to Shape-Factor Calculation between Three-Dimensional Planar Objects

W. W. Yuen[1]

Introduction

The objective of the present work is to show that by some simple algebraic manipulation of known shape factors, the shape factor between a differential plane area element and an arbitrary three-dimensional planar object with straight edges can be written in closed-form analytically. The shape factor between two planar objects in which one of them has straight edges is reduced to a simple integration of a positive-definite nonsingular function over only one surface area. Compared to the traditional method of direct numerical integration over both surface areas, the present method represents a substantial reduction of the computational effort. A detailed example calculation is presented to demonstrate the utility of the present approach.

Analysis

The basic idea of the present approach is to express the shape factor between a differential plane area element and a three-dimensional object with straight edges in terms of known shape factors. The expression fundamental to the present analysis is the shape factor between a differential plane area element dA_0 and a right triangle A_1 in a parallel plane. Consider the two planes with the orientation and geometry as shown in Fig. 1. The shape factor between dA_0 and A_1 can be obtained from a simple contour integration [1] as

$$F_{dA_0-A_1} = \frac{u}{2\pi(u^2+d^2)^{1/2}}\tan^{-1}\frac{v}{(u^2+d^2)^{1/2}} \tag{1}$$

Equation (1) can now be utilized to calculate the shape factor between dA_0 and an arbitrary triangle A_1 with orientation as shown in Fig. 2. Using superposition, it can be readily shown that the shape factor is given by

$$F_{dA_0-\overline{A_1}} = F_{dA_0-\overline{014}} + F_{dA_0-065} - F_{dA_0-012} - F_{dA_0-023} - F_{dA_0-063} \tag{2}$$

where F_{dA_0-ijk} stands for the shape factor between dA_0 and the right triangle with vertices i, j, and k. Utilizing equation (1), and after some algebraic manipulation, equation (2) becomes

$$F_{dA_0-A} = G(x_0, x_1, x_2, y_2, d) \tag{3}$$

with $G(x_0, x_1, x_2, y_2, d)$

$$= \frac{x_1 y_2}{2\pi[(x_1^2+d^2)y_2^2 + d^2(x_1-x_2)^2]^{1/2}} \times \tan^{-1}\frac{[(x_1^2+d^2)y_2^2 + d^2(x_1-x_2)^2]^{1/2}}{[d^2+x_1x_2]} - \frac{x_0 y_2}{2\pi[(x_0^2+d^2)y_2^2 + d^2(x_0-x_2)^2]^{1/2}} \times \tan^{-1}\frac{[(x_0^2+d^2)y_2^2 + d^2(x_0-x_2)^2]^{1/2}}{[d^2+x_0x_2]} \tag{3a}$$

It is interesting to note that equation (3) is applicable for both cases with $0 \le x_0 \le x_1 \le x_2$ or $0 \le x_0 \le x_2 \le x_1$.

Equation (3) is developed basically for cases in which A_1 is a triangle with one of its edges lying on the x axis or the y axis. But with the aid of some additional shape-factor algebraic manipulation, equation (3) is sufficient to be applied for other possibilities. Consider the two triangles with arbitrary dimensions and locations as shown in Figs.

[1] Department of Mechanical and Environmental Engineering, University of California, Santa Barbara, Santa Barbara, CA 93106.

Contributed by the Heat Transfer Division for publication in the JOURNAL OF HEAT TRANSFER. Manuscript received by the Heat Transfer Division July 30, 1979.

3(*a*) and 3(*b*). In Fig. 3(*a*) it can be readily observed that after subdividing the triangle into seven smaller triangles, each of the smaller triangles is of the same general orientation as that of Fig. 2. Similarly, after a simple rotation of the coordinate system in Fig. 3(*b*), the two smaller triangles as shown have one of their axes lying on the x axis. Equation (3) can be applied to each of these smaller triangles. The shape factor between dA_0 and any parallel triangle can thus be written as a sum of finite numbers of terms, each of which is an expression similar to equation (3). This argument can be further extended to yield the shape factor between dA_0 and a parallel polygon. It is a well known fact in geometry that any n-sided polygon can be composed into n-2 triangles. The shape factor between dA_0 and an n-sided polygon is therefore a sum of n-2 terms, each of which is just the shape factor between dA_0 and a parallel triangle.

Finally, the shape factor between dA_0 and a polygon which is not parallel to dA_0 can also be calculated based on the present analysis. The polygon must first be projected along its different lines of sight from dA_0 to its various vertices onto a plane parallel to dA_0. The shape factor between dA_0 and an arbitrary polygon is simply equal to the shape factor between dA_0 and the line-of-sight projection of that polygon. The previous analysis can thus be applied.

For any three-dimensional planar object with straight edges, the shape factor between dA_0 and the object's different faces can now be written, based on the present approach, as a finite sum of expressions similar to equation (3). Taking dA_0 to be a differential area element on a second object, the shape factor between two finite objects can be obtained by a simple integration. It is important to note that the present approach requires integration over only one surface area. The integral, which consists of a finite number of terms similar to equation (3), is positive-definite and without any undesirable singularity. In contrast with a direct numerical integration over the general shape-factor expression, this represents a substantial reduction in computational effort. It must also be emphasized that the restriction that one of the two objects must be planar and have straight edges is really not too severe since any curve surfaces can be approximated to an arbitrary degree of accuracy by a sum of planar surfaces.

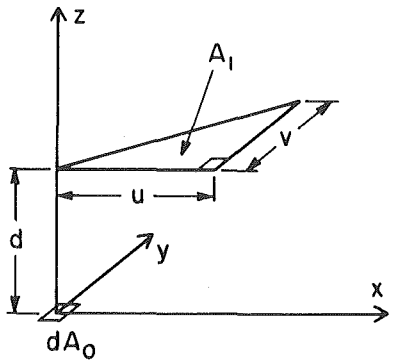

Fig. 1 Coordinate system for the calculation of shape factor between a differential plane-area element and a parallel right triangle

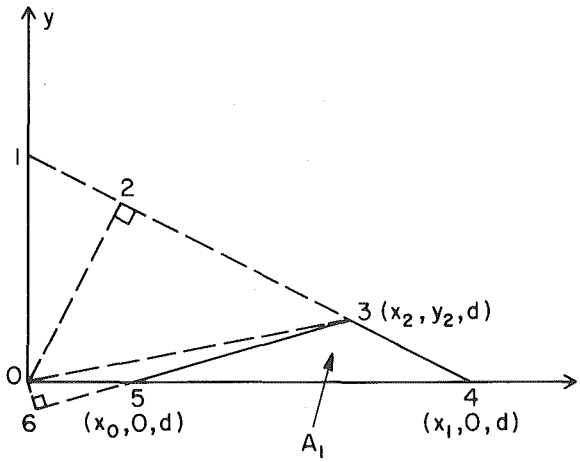

Fig. 2 The geometry and orientation of A_1 relative to the $x - y$ axis for equation (2)

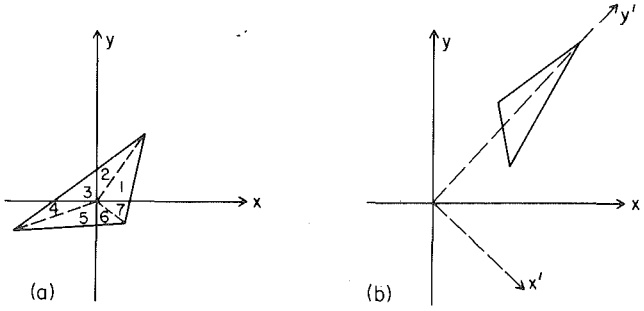

Fig. 3 Examples of how to subdivide an arbitrary triangle into smaller triangles with the general orientation and geometry as in Fig. 2(*d*)

Examples of Application

To illustrate the utility of the present approach for actual shape-factor evaluation, an example is now presented.

This example deals with the shape factor between two rectangular plates of identical dimension $a \times b$. The two plates are separated by a distance h and one of the plates is oriented at an angle β with respect to the other. The detailed coordinate system is shown in Fig. 4.

The system is clearly symmetric with respect to the x axis. It suffices, therefore, to calculate $F_{dA_I - A_{II}}$ only for values of $x > 0$ and $y > 0$. Consider now a differential area element dA_I at (x, y, o), and the line-of-sight projection of A_{II} onto the plane $z = h + b \sin \beta$ can be

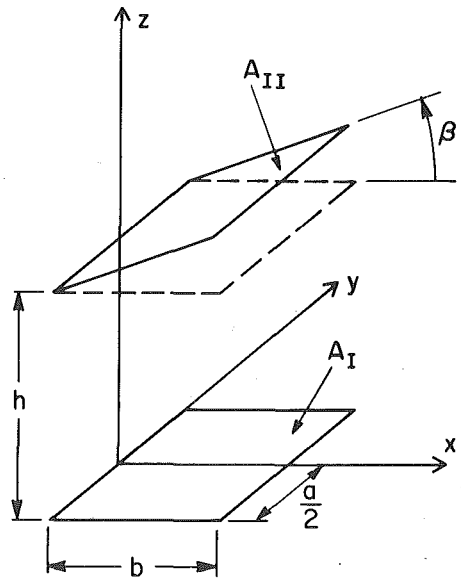

Fig. 4 Coordinate system used in the first example of shape factor calculation

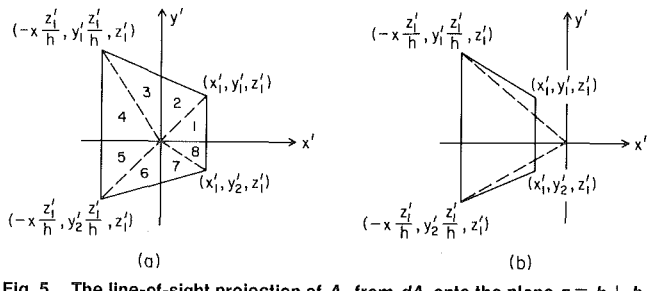

Fig. 5 The line-of-sight projection of A_{II} from dA_I onto the plane $z = h + b \sin \beta$. The coordinates (x', y', z') are measured from dA_I. ($x_1' = b \cos \beta - x$, $y_1 = a/2 - y$, $y_2' = a/2 - y$, $z_1 = h + b \sin \beta$)

readily generated. Depending on the value of x, the relative location of the projected area with respect to (x, y, o) has two possibilities as illustrated in Fig. 5. The shape factor between dA_I and A_{II} can now be readily obtained by direct application of equation (3). For $x < b \cos\beta$, the shape factor is given by

$$F_{dA_I-A_{II}} = \sum_{i=1}^{8} F_{dA_I-A_i} \tag{4}$$

where the A_i's are the smaller areas as denoted in Fig. 5(a) with

$$F_{dA_I-A_1} = G\left(0, b\cos\beta - x, b\cos\beta - x, \frac{a}{2} - y, h + b\sin\beta\right) \tag{5}$$

$$F_{dA_I-A_2} = G\left(0, m, \frac{a}{2} - y, b\cos\beta - x, h + b\sin\beta\right) \tag{6}$$

$$F_{dA_I-A_3} = G\left(0, m, \left(\frac{a}{2} - y\right)\left(1 + \frac{b}{h}\sin\beta\right), x\left(1 + \frac{b}{h}\sin\beta\right), h + b\sin\beta\right) \tag{7}$$

$$F_{dA_I-A_4} = G\left(0, x, x, \frac{a}{2} - y, h\right) \tag{8}$$

$$F_{dA_I-A_5} = G\left(0, x, x, \frac{a}{2} + y, h\right) \tag{9}$$

$$F_{dA_I-A_6} = G\left(0, n, \left(\frac{a}{2} + y\right)\left(1 + \frac{b}{h}\sin\beta\right), x\left(1 + \frac{b}{h}\sin\beta\right), h + b\sin\beta\right) \tag{10}$$

$$F_{dA_I-A_7} = G\left(0, n, \frac{a}{2} + y, b\cos\beta - x, h + b\sin\beta\right) \tag{11}$$

$$F_{dA_I-A_8} = G\left(0, b\cos\beta - x, b\cos\beta - x, \frac{a}{2} + y, h + b\sin\beta\right) \tag{12}$$

and

$$m = \frac{\left(\frac{a}{2} - y\right)(h + b\sin\beta)\cos\beta}{h\cos\beta + x\sin\beta} \tag{13}$$

$$n = \frac{\left(\frac{a}{2} + y\right)(h + b\sin\beta)\cos\beta}{h\cos\beta + x\sin\beta} \tag{14}$$

For $x > b\cos\beta$, the shape factor is

$$F_{dA_I-A_{II}} = \sum_{i=1}^{4} F_{dA_I-A_i} \tag{15}$$

where the A_i's are areas as denoted in Fig. 5(b) and

$$F_{dA_I-A_1} = G\left(0, x, x, \frac{a}{2} - y, h\right) - G\left(0, p, p, \frac{p}{x}\left(\frac{a}{2} - y\right), h + b\sin\beta\right) \tag{16}$$

$$F_{dA_I-A_2} = G\left(0, x, x, \frac{a}{2} + y, h\right) - G\left(0, p, p, \frac{p}{x}\left(\frac{a}{2} + y\right), h + b\sin\beta\right) \tag{17}$$

$$F_{dA_I-A_3} = G\left(\frac{pq}{x}, \left(1 + \frac{b\sin\beta}{h}\right)q, q - \frac{xh}{q}\cos\beta, \left(\frac{a}{2} - y\right)\frac{b}{q}\cos\beta, h + b\sin\beta\right) \tag{18}$$

$$F_{dA_I-A_4} = G\left(\frac{pr}{x}, \left(1 + \frac{b\sin\beta}{h}\right)r, r - \frac{xh}{r}\cos\beta, \left(\frac{a}{2} + y\right)\frac{b}{r}\cos\beta, h + b\sin\beta\right) \tag{19}$$

with

$$p = x - b\cos\beta \tag{20}$$

$$q = \left(x^2 + \left(\frac{a}{2} - y\right)^2\right)^{1/2} \tag{21}$$

$$r = \left(x^2 + \left(\frac{a}{2} + y\right)^2\right)^{1/2} \tag{22}$$

By a simple application of the reciprocity relation, the shape factor between A_I and A_{II} is simply given by

$$F_{A_{II}-A_I} = 2\int_0^{a/2}\int_0^{b} F_{dA_I-A_{II}}\, dxdy \tag{23}$$

Equation (23) can be readily evaluated numerically. Results for various values of a, b, h, and β are presented in Table 1. As expected, the shape factor decreases with increasing h and increasing β. For the case with $\beta = 0$ and the case with $\beta = \pi/2$ and $h = 0$, the present solution gives exact agreement with the available results [1].

Table 1 Shape factors between two rectangular plates with different aspect ratio (b/a), β, and a/h.

β	b/a a/h	0.2	0.5	1.0	2.0	5.0
$\pi/2$	0.5	0.001	0.003	0.009	0.018	0.024
	1.0	0.004	0.016	0.033	0.045	0.041
	2.0	0.017	0.052	0.076	0.078	0.057
	∞	0.271	0.240	0.200	0.149	0.087
$\pi/4$	0.5	0.010	0.023	0.040	0.060	0.071
	1.0	0.032	0.070	0.108	0.132	0.119
	2.0	0.086	0.165	0.213	0.216	0.157
	∞	0.588	0.547	0.479	0.388	0.234
0	0.5	0.015	0.036	0.069	0.117	0.178
	1.0	0.049	0.117	0.200	0.286	0.359
	2.0	0.135	0.286	0.415	0.509	0.573
	∞	1.000	1.000	1.000	1.000	1.000

Reference

1 Sparrow, E. M., and Cess, R. D., *Radiative Heat Transfer*, Brooks/Cole Publishing Company, Belmont, Calif., 1966.

Heat Transfer through Irradiated, Semi-transparent Layers at High Temperature

R. Viskanta[1] and D. M. Kim[1]

Nomenclature

D_n = function defined as $\int_0^1 \mu^{n-2}\exp(-t/\mu)\beta(\mu)d\mu$
$E_{b\lambda}$ = Planck's black body distribution function
E_n = exponential integral defined as $\int_0^1 \mu^{n-2}\exp(-t/\mu)d\mu$
$\mathcal{F}$ = radiative flux in the y-direction
F_i = external flux incident on gas-material interface
k = thermal conductivity of material
n = index of refraction
q = total (conductive + radiative) heat flux in y-direction
R_n = function defined as $\int_0^1 r_i(\mu)\mu^{n-2}\exp(-t/\mu)\beta(\mu)d\mu$
r_i = reflectivity of gas-material interface
T = temperature
t_i = transmissivity of gas-material interface
T_n = function defined as $\int_0^1 t_i(\mu')(\mu')^{n-2}\exp(-t/\mu')\beta(\mu)d\mu'$
y = distance measured from the opaque wall

[1] Heat Transfer Laboratory, School of Mechanical Engineering, Purdue University, West Lafayette, Ind. 47907.

Contributed by the Heat Transfer Division for publication in The JOURNAL OF HEAT TRANSFER. Manuscript received by The Heat Transfer Division June 21, 1979.

readily generated. Depending on the value of x, the relative location of the projected area with respect to (x, y, o) has two possibilities as illustrated in Fig. 5. The shape factor between dA_I and A_{II} can now be readily obtained by direct application of equation (3). For $x < b \cos\beta$, the shape factor is given by

$$F_{dA_I-A_{II}} = \sum_{i=1}^{8} F_{dA_I-A_i} \tag{4}$$

where the A_i's are the smaller areas as denoted in Fig. 5(a) with

$$F_{dA_I-A_1} = G\left(0, b\cos\beta - x, b\cos\beta - x, \frac{a}{2} - y, h + b\sin\beta\right) \tag{5}$$

$$F_{dA_I-A_2} = G\left(0, m, \frac{a}{2} - y, b\cos\beta - x, h + b\sin\beta\right) \tag{6}$$

$$F_{dA_I-A_3} = G\left(0, m, \left(\frac{a}{2} - y\right)\left(1 + \frac{b}{h}\sin\beta\right), x\left(1 + \frac{b}{h}\sin\beta\right), h + b\sin\beta\right) \tag{7}$$

$$F_{dA_I-A_4} = G\left(0, x, x, \frac{a}{2} - y, h\right) \tag{8}$$

$$F_{dA_I-A_5} = G\left(0, x, x, \frac{a}{2} + y, h\right) \tag{9}$$

$$F_{dA_I-A_6} = G\left(0, n, \left(\frac{a}{2} + y\right)\left(1 + \frac{b}{h}\sin\beta\right), x\left(1 + \frac{b}{h}\sin\beta\right), h + b\sin\beta\right) \tag{10}$$

$$F_{dA_I-A_7} = G\left(0, n, \frac{a}{2} + y, b\cos\beta - x, h + b\sin\beta\right) \tag{11}$$

$$F_{dA_I-A_8} = G\left(0, b\cos\beta - x, b\cos\beta - x, \frac{a}{2} + y, h + b\sin\beta\right) \tag{12}$$

and

$$m = \frac{\left(\frac{a}{2} - y\right)(h + b\sin\beta)\cos\beta}{h\cos\beta + x\sin\beta} \tag{13}$$

$$n = \frac{\left(\frac{a}{2} + y\right)(h + b\sin\beta)\cos\beta}{h\cos\beta + x\sin\beta} \tag{14}$$

For $x > b\cos\beta$, the shape factor is

$$F_{dA_I-A_{II}} = \sum_{i=1}^{4} F_{dA_I-A_i} \tag{15}$$

where the A_i's are areas as denoted in Fig. 5(b) and

$$F_{dA_I-A_1} = G\left(0, x, x, \frac{a}{2} - y, h\right) - G\left(0, p, p, \frac{p}{x}\left(\frac{a}{2} - y\right), h + b\sin\beta\right) \tag{16}$$

$$F_{dA_I-A_2} = G\left(0, x, x, \frac{a}{2} + y, h\right) - G\left(0, p, p, \frac{p}{x}\left(\frac{a}{2} + y\right), h + b\sin\beta\right) \tag{17}$$

$$F_{dA_I-A_3} = G\left(\frac{pq}{x}, \left(1 + \frac{b\sin\beta}{h}\right)q, q - \frac{xh}{q}\cos\beta, \left(\frac{a}{2} - y\right)\frac{b}{q}\cos\beta, h + b\sin\beta\right) \tag{18}$$

$$F_{dA_I-A_4} = G\left(\frac{pr}{x}, \left(1 + \frac{b\sin\beta}{h}\right)r, r - \frac{xh}{r}\cos\beta, \left(\frac{a}{2} + y\right)\frac{b}{r}\cos\beta, h + b\sin\beta\right) \tag{19}$$

with

$$p = x - b\cos\beta \tag{20}$$

$$q = \left(x^2 + \left(\frac{a}{2} - y\right)^2\right)^{1/2} \tag{21}$$

$$r = \left(x^2 + \left(\frac{a}{2} + y\right)^2\right)^{1/2} \tag{22}$$

By a simple application of the reciprocity relation, the shape factor between A_I and A_{II} is simply given by

$$F_{A_{II}-A_I} = 2\int_0^{a/2}\int_0^{b} F_{dA_I-A_{II}}\, dxdy \tag{23}$$

Equation (23) can be readily evaluated numerically. Results for various values of a, b, h, and β are presented in Table 1. As expected, the shape factor decreases with increasing h and increasing β. For the case with $\beta = 0$ and the case with $\beta = \pi/2$ and $h = 0$, the present solution gives exact agreement with the available results [1].

Table 1 Shape factors between two rectangular plates with different aspect ratio (b/a), β, and a/h.

β	b/a a/h	0.2	0.5	1.0	2.0	5.0
$\pi/2$	0.5	0.001	0.003	0.009	0.018	0.024
	1.0	0.004	0.016	0.033	0.045	0.041
	2.0	0.017	0.052	0.076	0.078	0.057
	∞	0.271	0.240	0.200	0.149	0.087
$\pi/4$	0.5	0.010	0.023	0.040	0.060	0.071
	1.0	0.032	0.070	0.108	0.132	0.119
	2.0	0.086	0.165	0.213	0.216	0.157
	∞	0.588	0.547	0.479	0.388	0.234
0	0.5	0.015	0.036	0.069	0.117	0.178
	1.0	0.049	0.117	0.200	0.286	0.359
	2.0	0.135	0.286	0.415	0.509	0.573
	∞	1.000	1.000	1.000	1.000	1.000

Reference

1 Sparrow, E. M., and Cess, R. D., *Radiative Heat Transfer*, Brooks/Cole Publishing Company, Belmont, Calif., 1966.

Heat Transfer through Irradiated, Semi-transparent Layers at High Temperature

R. Viskanta[1] and D. M. Kim[1]

Nomenclature

D_n = function defined as $\int_0^1 \mu^{n-2}\exp(-t/\mu)\beta(\mu)d\mu$
$E_{b\lambda}$ = Planck's black body distribution function
E_n = exponential integral defined as $\int_0^1 \mu^{n-2}\exp(-t/\mu)d\mu$
$\mathcal{F}$ = radiative flux in the y-direction
F_i = external flux incident on gas-material interface
k = thermal conductivity of material
n = index of refraction
q = total (conductive + radiative) heat flux in y-direction
R_n = function defined as $\int_0^1 r_i(\mu)\mu^{n-2}\exp(-t/\mu)\beta(\mu)d\mu$
r_i = reflectivity of gas-material interface
T = temperature
t_i = transmissivity of gas-material interface
T_n = function defined as $\int_0^1 t_i(\mu')(\mu')^{n-2}\exp(-t/\mu')\beta(\mu)d\mu'$
y = distance measured from the opaque wall

[1] Heat Transfer Laboratory, School of Mechanical Engineering, Purdue University, West Lafayette, Ind. 47907.

Contributed by the Heat Transfer Division for publication in The JOURNAL OF HEAT TRANSFER. Manuscript received by The Heat Transfer Division June 21, 1979.

β = function defined as $[1 - \rho_w r_i \exp(-2\tau_0/|\mu|)]^{-1}$
ϵ = emissivity of opaque wall
κ = absorption coefficient
λ = wavelength
ρ = reflectance of opaque wall
τ = optical depth, $\int_0^y \kappa dy$
τ_0 = optical thickness of layer, $\int_0^L \kappa dy$

Subscripts

i = refers to interface
λ = refers to wavelength
w = refers to wall

Introduction

Slag layers are known to form on tubes and walls of utility boilers [1], exhaust gas recuperators associated with glass melting tanks, MHD plant components [2, 3], black liquor boilers [4] and many other slagging combustion systems. For example, slag layers are expected to form in the combustor, channel, diffuser, radiant boiler, and seed recovery components of an MHD plant [3]. Dense, stable slag layers can protect structural materials from high temperature gases, corrosive products and large transient heat loads. However, the presence of slag layers on surfaces also increases thermal resistance to heat transfer thus necessitating a larger and costlier piece of equipment. The fact that a coal-ash slag is not opaque but is semitransparent to thermal radiation is not recognized [1, 5]. The semi-transparency of the slag is expected to have serious implications in the design of some MHD plant components [2]. For example, as a result of the semi-transparency, the slag will lose some of its heat protection capability, and the total heat transfer by conduction and radiation through the layer will be increased. Also, one possible reason for the failure ("burnout") of utility boiler tubes can be attributed to the melting of the slag because of changes in the system operating conditions such as use of coal having different composition and ash content. In view of the serious consequences of a tube failure in a large utility boiler, the understanding of heat transfer through an irradiated, coal-ash slag layer is of considerable practical and economic significance not only to the designer but also to the operator of a power plant.

The purpose of this note is to present a model for predicting conduction and radiation heat transfer across an irradiated layer of semitransparent material at high temperature. A model for analyzing gravity flow and heat transfer in a slag layer has been recently given [2], but the prediction of radiative transfer is too complicated for design calculations. The validity and accuracy of the model is established by comparing the predictions with those reported in the literature. Results of sample calculations are included for the purpose of determining the relative importance of radiation in comparison to the total heat transfer across the layer.

Analysis

Consider a layer of an amorphous, semi-transparent substance of uniform thickness L which is bounded on one side by an opaque wall and on the other by gases. The material may be solid, liquid or both simultaneously and be capable of absorbing, and emitting but not scattering thermal radiation. Heat transfer in the layer is predominantly in the y-direction perpendicular to the layer. The radiation characteristics of the opaque wall are assumed to be known, and the radiation characteristics of the free (gas-material) surface are predicted from Fresnel equations. The external radiation flux incident on the free surface is considered to be given. Since the interest here is to develop an approximate radiation and not the total heat transfer model, the temperatures of the opaque wall and of the gas-material interface are taken as known.

If heat transfer by convection in the liquid layer is neglected in comparison to conduction and radiation as can be readily justified [2], the energy equation becomes

$$q = -k\frac{dT}{dy} + \mathcal{J}(y) \tag{1}$$

The first term on the right-hand-side of equation (1) represents the conductive and the second the radiative fluxes, respectively. For a plane layer of semi-transparent material, either in a liquid or a solid phase, in direct contact with an opaque, diffusely reflecting wall maintained at a constant temperature T_w, the local radiative flux $\mathcal{J}(y)$ can be expressed as [2]

$$\mathcal{J}(y) = 2\int_0^\infty [\epsilon_{w\lambda} n_\lambda^2 E_{b\lambda}(T_w) f_1(\tau_\lambda) - F_{i\lambda} f_2(\tau_\lambda) + \int_0^{\tau_{0\lambda}} n_\lambda^2 E_{b\lambda}(t) G(\tau_\lambda, t) dt] d\lambda \tag{2}$$

where

$$f_1(\tau_\lambda) = [D_3(\tau_\lambda) - R_3(2\tau_{0\lambda} - \tau_\lambda)] \tag{3}$$

$$f_2(\tau_\lambda) = [T_3(\tau_{0\lambda} - \tau_\lambda) - \rho_{w\lambda} T_3(\tau_{0\lambda} + \tau_\lambda)] \tag{4}$$

and

$$G(\tau_\lambda, t) = \text{sign}(\tau_\lambda - t) E_2(|\tau_\lambda - t|) + \rho_{w\lambda} D_2(\tau_\lambda + t) + \rho_{w\lambda} R_2(2\tau_{0\lambda} + \tau_\lambda - t) - R_2(2\tau_{0\lambda} - \tau_\lambda - t) - \rho_{w\lambda} R_2(2\tau_{0\lambda} - \tau_\lambda + t) \tag{5}$$

The first term on the right-hand-side of equation (2) represents the contribution to the net radiative flux due to the emission by the wall, the second term denotes the contribution to the flux due to the external radiation flux $F_{i\lambda}$ incident on the free boundary ($y = L$) of the layer, and the final (integral) term represents the net contribution from the emission and partial absorption of radiation by the material. In deriving equation (2) all possible interreflections between the opaque wall and the transparent outer boundary at $y = L$ were taken into account.

The optical thicknesses $\tau_{0\lambda}$ of slag layers under slagging conditions are expected to be such that the Planck's function will vary slowly over the distance by which the local radiation effects will attenuate, that is,

$$\frac{dE_{b\lambda}}{dt} = \frac{dE_{b\lambda}}{dT}\frac{dT}{dt} \simeq \frac{dE_{b\lambda}}{dT}\frac{dT}{d\tau_\lambda} \tag{6}$$

for $|\tau_\lambda - t| \leq \delta$. This is equivalent to saying that the attenuation of the integro-exponential functions $[E_n(t), D_n(t), R_n(t)$ and $T_n(t)]$ is very rapid. If the third term in equation (2) is integrated by parts and the above approximation is made in the evaluation of the integral over the optical thickness ($\int_0^{\tau_{0\lambda}} \ldots dt$), the equation can be expressed as

$$\mathcal{J}(y) = \int_0^\infty \left[\mathcal{J}_{s\lambda}(y) - H_\lambda(y)\frac{dT}{dy}\right] d\lambda \tag{7}$$

where

$$\mathcal{J}_{s\lambda}(y) = 2[\epsilon_{w\lambda} n_\lambda^2 E_{b\lambda}(T_w) f_i(\tau_\lambda) - F_{i\lambda} f_2(\tau_\lambda)] + 2\{n_\lambda^2 E_{b\lambda}(T_w)[-E_3(\tau_\lambda) + \rho_{w\lambda} D_3(\tau_\lambda) + \rho_{w\lambda} R_3(2\tau_{0\lambda} + \tau_\lambda) + R_3(2\tau_{0\lambda} - \tau_\lambda) - \rho_{w\lambda} R_3(2\tau_{0\lambda} - \tau_\lambda)] + n_\lambda^2 E_{b\lambda}(T_L)[E_3(\tau_{0\lambda} - \tau_\lambda) - \rho_{w\lambda} D_3(\tau_{0\lambda} + \tau_\lambda) + \rho_{w\lambda} R_3(\tau_{0\lambda} + \tau_\lambda) - R_3(\tau_0 - \tau_\lambda) + \rho_{w\lambda} R_3(3\tau_{0\lambda} - \tau_\lambda)]\} \tag{8}$$

and

$$H_\lambda(y) = -2\{[-\tfrac{2}{3} + E_4(\tau_\lambda) - E_4(\tau_{0\lambda} - \tau_\lambda) - \rho_{w\lambda}[D_4(\tau_{0\lambda} + \tau_\lambda) - D_4(\tau_\lambda)] - \rho_{w\lambda}[R_4(\tau_{0\lambda} + \tau_\lambda) - R_4(2\tau_{0\lambda} + \tau_\lambda)] + [R_4(\tau_{0\lambda} + \tau_\lambda) - R_4(2\tau_{0\lambda} - \tau_\lambda)] + \rho_{w\lambda}[R_4(3\tau_{0\lambda} - \tau_\lambda) - R_4(2\tau_{0\lambda} - \tau_\lambda)]\}\left(\frac{n_\lambda^2}{\kappa_\lambda}\right)\left(\frac{dE_{b\lambda}}{dT}\right)_T \tag{9}$$

The first term on the right-hand-side of equation (7) represents the net contribution to the radiative flux due to the "long-range" effects of radiation emitted from the wall and external radiation transmitted into the layer of material across the free surface. The second term represents the contribution to the net flux resulting from the local emission of radiation by the material and its "diffusion" in the layer.

Substitution of the expression for the local radiative flux, equation (7), into equation (2) gives

$$q = -\left[k + \int_0^\infty H_\lambda(y)d\lambda\right]\frac{dT}{dy} + \int_0^\infty \mathcal{F}_{s\lambda}(y)d\lambda$$

$$= -(k + k_r)\frac{dT}{dy} + \mathcal{F}_s(y) \quad (10)$$

Thus, according to equation (10) the local radiative flux can be considered as consisting of diffusion and source contributions. Clearly, the basic difference between the present model and Rosseland diffusion approximation [6] is that in the analysis $\tau_{0\lambda}$ is finite and the presence of boundaries and external radiation sources are accounted for.

Equation (1) was solved numerically by imposing the temperature boundary conditions: $T = T_w$ at $y = 0$ and $T = T_L$ at $y = L$. The integro-exponential functions, except $E_n(t)$, were evaluated numerically. To reduce the computational time the functions were approximated accurately by a sum of exponentials, i.e., $D_n(t) \simeq \Sigma_i^N a_i e^{b_i t}$. The coefficients a_i and b_i were determined from a least-square fit.

Results and Discussion

A comparison of temperature distributions predicted using the exact expression for the local radiative flux, equation (2), as reported in [2] with those determined employing the approximate expression, equation (7), is given in Fig. 1. The calculations were carried out on a gray basis for a given thickness and a temperature difference across the layer. As expected, the results show that the approximate expression for the radiative flux becomes more accurate as the optical thickness of the layer is increased. The total (conductive plus radiative) fluxes predicted by the present model are 11, 6 and 3 percent higher than those reported in [2] for cases 1, 2 and 3, respectively. In agreement with results reported elsewhere [2], heat transfer by conduction was predominant only in the immediate vicinity of the opaque wall, but for $y/L > 0.2$ heat transfer was mostly (~90 percent) by radiation.

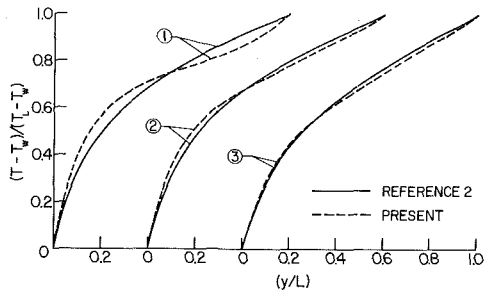

Fig. 1 Comparison of temperature profiles for different conditions T_w = 810 K, k = 1 W/m K and ϵ_w = 0.4; 1) τ_0 = 1.525 (κ = 50 cm^{-1}), T_L = 1444 K, and F_i = 393,600 W/c^2; 3) τ_0 = 4.75 (κ = 200 m^{-1}), T_L = 1483 K and F_i = 377,300 W/m^2

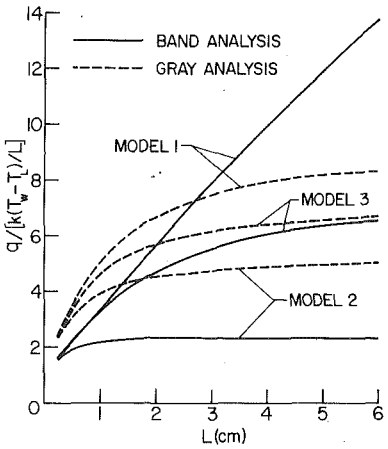

Fig. 2 Dependence of dimensionless heat flux on the layer thickness, T_w = 800 K, T_L = 1500 K, K = 1 W/mK, ϵ_w = 0.4 and F_i = 246,000 W/m^2

Table 1 Effects of temperature level and difference on heat transfer [$q/(k\Delta T/L)$] across the layer: F_i = 246,000 W/m^2, L = 1 cm, k = 1 W/m K, and ϵ_w = 0.4

$T_w(K)$	$\Delta T(K)$	Model 1	Model 2	Model 3
		a) T_L = 1500 K		
1100	400	4.55	2.74	4.42
900	600	3.67	2.33	3.50
700	800	3.14	2.05	3.05
500	1000	2.80	1.85	2.70
		b) T_L = 1800 K		
1400	400	5.42	2.78	4.55
1200	600	4.78	2.65	4.17
1000	800	4.19	2.45	3.73
800	1000	3.73	2.24	3.34

The importance of semitransparency and spectral effects on heat transfer across high temperature, irradiated layers is clearly evident from the results presented in Fig. 2 and Table 1. The sample results reported have been obtained using gray calculations based on a Planck mean absorption coefficient and band approximation. The spectral absorption coefficient models used in the calculations were:

Model 1: $\kappa_\lambda = 0.12$ cm^{-1} for $0 \le \lambda < 2.75$ μm; $\kappa_\lambda = 4.5$ cm^{-1} for $2.75 \le \lambda < 4.7$ μm; $\kappa_\lambda = \infty$ for $\lambda \ge 4.7$ μm

Model 2: $\kappa_\lambda = 4.0$ cm^{-1}, $0 \le \lambda < 2.75$ μm; $\kappa_\lambda = 5.0$ cm^{-1} for $2.75 \le \lambda < 4.7$ μm; $\kappa_\lambda = \infty$ for $\lambda \le 4.7$ μm

Model 3: $\kappa_\lambda = 1.0$ cm^{-1} for $0 \le \lambda < 1$ μm; $\kappa_\lambda = 0.8$ cm^{-1} for $1.0 \le \lambda < 2.75$ μm; $\kappa_\lambda = 5$ cm^{-1} for $2.75 \le \lambda < 4.7$ μm; $\kappa_\lambda = \infty$ for $\lambda \ge 4.7$ μm

Models 1 and 2 are intended to approximate the absorption coefficient of window and green glass and Model 3 that of slag formed as a result of coal combustion. The spectral radiation flux incident on the layer, $F_{i\lambda}$, was assumed to have a Planckian distribution with a total flux F_i = 246,000 W/m^2. This value is representative of the radiant flux expected in some components of an open-cycle, coal-fired MHD plant [2].

The sample results reported show that treatment of the slag as if it were an opaque substance could result in large underpredictions of the total heat transfer in comparison to the situation where the material of the layer is semitransparent to radiation. The findings have practical implications to the design of components of coal-fired combustion systems. Data on the spectral absorption coefficient and transport properties are required for realistic design calculations of heat transfer in combustion systems in which slag is formed on heat transfer surfaces.

References

1 Reid, W. T., *External Corrosion and Deposits*, American Elsevier Publishing Co., New York, 1971.

2 Chow, L. S. H., Viskanta, R. and Johnson, T. R., "Slag Transport Models for Radiant Heater of an MHD System," ASME Paper No. 78-WA/HT-21.

3 Postlethwaite, A. W. and Sluyter, M. M., "MHD Heat Transfer Problems—An Overview," *Mechanical Engineering*, Vol. 100, No. 3, March 1978, pp. 32–39.

4 Sheth, P. R., Lawit, R. L. and Klett, M. G., "Application of Black-Liquor Boiler Technology to MHD Heat and Seed Recovery Equipment Design," in *18th Symposium Engineering Aspects of Magnetohydrodynamics*, Butte, Montana, June 18–20, 1979, pp. C1.1–C.1.6.

5 Smith, V. L., "Coal Firing and Industrial Boiler Design—the Modern Approach," ASME *Journal of Engineering for Power*, Vol. 98, No. 3, 1976, pp. 297–304.

6 Viskanta, R. and Anderson, E. E., "Heat Transfer in Semitransparent Solids," in *Advances in Heat Transfer*, Edited by T. F. Irvine, Jr. and J. P. Hartnett, Academic Press, 1975, Volume 11, pp. 317–441.

Mean Velocity and Concentration Characteristics Downstream of Rows of Jets in a Cross-Flow

Z. A. Khan[1] and J. H. Whitelaw[1]

Introduction

Previous investigations of the flow characteristics of rows of jets in a cross-flow have been reported in references [1–5]. They encompass a range of ratios of average jet-to-crossflow velocities (V_j/U_∞) from 2.3 to 8.5 and pitch-to-diameter ratios from 2 to 12. References [1–3] were concerned mainly with temperature profiles and references [4] and [5], with mean velocity and concentration measurements but for a single configuration; the influence of the central jet asymmetry was shown, in references [4] and [5], to be significant for values greater than 0.1 times the pitch.

The present paper describes an experimental investigation which follows the approach of reference [4] and makes use of the flow configuration shown in Fig. 1. It extends the range of velocity ratios for a single row of holes from 2.0 to 0.5 and demonstrates the influence of asymmetry over this range. Also, measurements with opposing rows of holes and for a velocity ratio of 2.8 show that, with the two sets of opposed jets separated by 8 jet diameters, the interaction is negligible; thus they allow the information of the single row of holes to be extended to a velocity ratio of 2.8.

This information is relevant to the lower range of velocity ratios found in gas-turbine practice and to an opposed-jet spacing which is slightly larger than that found in most practical configurations. It provides useful guidelines for the influence of dimensional tolerances and will also be used to quantify the abilities of three-dimensional calculation procedures.

The Flow Configuration and Experimental Techniques

The wind tunnel, previously described in reference [6], was used for the present investigation but with a purpose-built, 300mm wide by 200mm high working section and traverse arrangement. The top and base plates of the working section each had five 25.4mm holes located across the 0.30m span with centers 0.30m downstream of a sandpaper trip and with a uniform pitch of 51mm. The holes were connected to 0.76m long tubes to insure fully-developed turbulent pipe flow. The central hole of the top plate could be adjusted to allow the investigation of hole eccentricity.

Measurements of the mean velocity were obtained with an impact probe of external and internal diameters of 1.1 mm and 0.61 mm, respectively. A transducer and a time-averaging voltmeter allowed a reproducibility of pressure measurement of better than ±1 percent. The local concentration of a trace of helium gas, which was injected into the central jet of the top plate, was determined by sampling through the same impact probe and passing through a thermal-conductivity cell as described in references [4–6]. Outside regions of flow recirculation, the concentration measurements are precise to within ±2 percent of the maximum measured value in the flow field. The precision of concentration measurements in regions of recirculation is difficult to quantify and these have been omitted in all but a few cases.

The Reynolds numbers of the flow in each pipe was varied from 1.8×10^4 to 5.0×10^4, corresponding to average velocities of 10 m/s and 28 m/s, respectively. The velocity profiles in the plane of the pipe exits were measured, in the absence of the freestream velocity, and were each found to be symmetric about two orthogonal planes to better than 6 percent of the local velocity values. Measurements of velocity profiles, with one and both rows of holes arranged symmetrically and operating over a range of ratios of jet-to-crossflow velocities, showed that the flow was sensibly symmetrical about the center plane and on either side of neighbouring holes up to the furthest downstream station of the present measurements, i.e., 0.20m or 8 hole diameters. The cross-flow velocity was varied between 10 m/s and 20 m/s with the minimum value corresponding to a turbulent boundary layer at the leading edge of the holes (without the jets) with a momentum thickness Reynolds number of 2.65×10^2.

Results and Discussion

For all the results reported in this section, the mean velocities have been normalized with the freestream velocity and the concentrations have been normalized with the helium concentration at the pipe exit.

With a symmetrical arrangement of the jets, cross-stream profiles of velocity and concentration were obtained at $Y/D=3$, 2 and 1 (measured from the top plate) and at a distance downstream from the center line of the jets of $X=6D$, and exhibited symmetry to better than 5 percent of the maximum velocity and 1 percent for the normalized concentration. These results were obtained with jet-to-crossflow velocity ratios (V_j/U_∞) of 0.5, 1.0 and 2.0. Measurements of velocity and concentration at $X/D=6$ for a velocity ratio of 2 were also obtained with a central jet eccentricity of $0.25D$; i.e., the central jet was moved $0.25D$ to one side but in the same lateral plane as the other four jets. The eccentricity in geometry resulted in a large eccentricity in the velocity field. Near the surface, the two jets whose center lines were closer together acted as a single jet with a common recirculation region. On the other side, the jets whose center lines were further apart merged into the free-stream by $Y/D=3$. In spite of the large asymmetry in the velocity field, it was clear that the initially eccentric jet had moved rapidly towards the symmetric position and that, by $6D$ downstream, the maxima of the concentration profiles were very close to the symmetric position. These results were generally in accord with those of reference [5].

Figures 2 and 3 present velocity and concentration profiles at X/D of 6, for a central jet eccentricity of $0.25D$ and for jet-to-crossflow

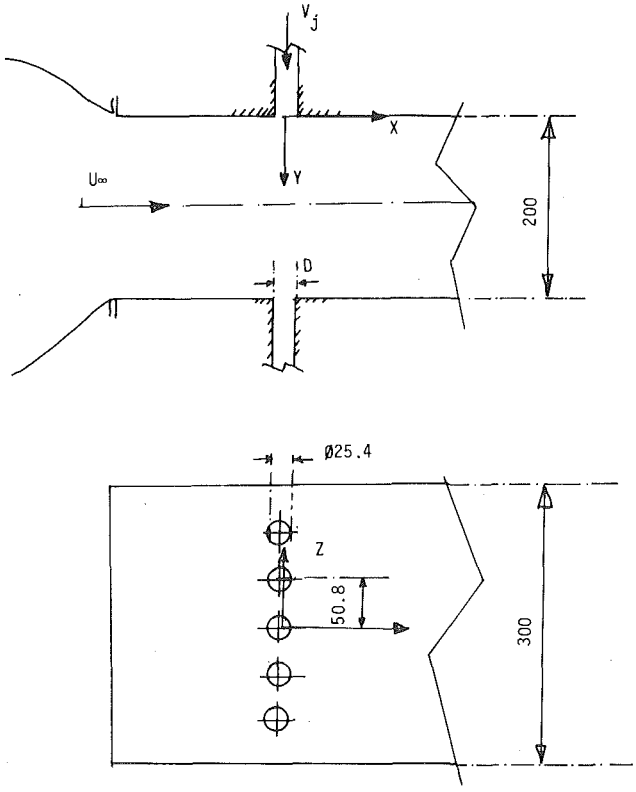

Fig. 1 Schematic of multiple jets (dimensions in mm: not to scale)

[1] Imperial College of Science and Technology, Department of Mechanical Engineering, London SW7 2BX, England

Contributed by The Heat Transfer Division for publication in the JOURNAL OF HEAT TRANSFER. Manuscript received by The Heat Transfer Division November 21, 1979.

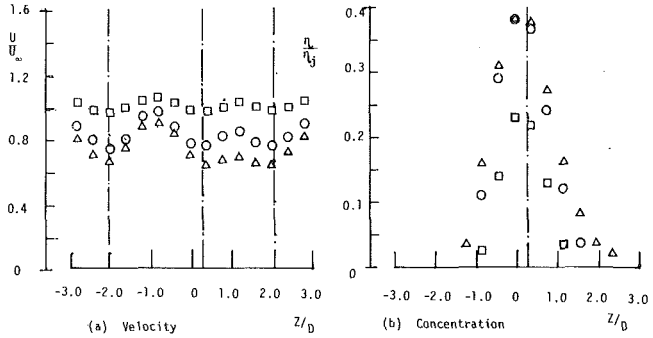

Fig. 2 Velocity and concentration distributions at $X = 6D$ for a single row of jets; eccentricity $e = 0.25D$ ($V_j/U_\infty = 1.0$, □ $Y/D = 1.5$, ○ $Y/D = 1.0$, △ $Y/D = 0.5$)

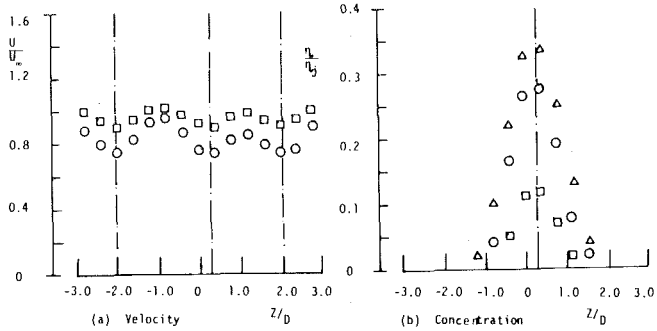

Fig. 3 Velocity and concentration distributions at $X = 6D$ for a single row of jets; eccentricity $e = 0.25D$ ($V_j/U_\infty = 0.5$, □ $Y/D = 1.0$, ○ $Y/D = 0.5$, △ $Y/D = 0.25$)

velocity ratios of 1.0 and 0.5, respectively. The asymmetry of the velocity field is not as severe as for the higher velocity ratio and the velocity profiles become less asymmetric with increasing distance from the surface. In contrast to results for the higher velocity ratio, the concentration profiles remain symmetrical about the center line of the displaced jet and this is made possible by the greater penetration of the crossflow into the region between the adjacent jets with consequent reduction in the interaction between them.

Velocity profiles were obtained for opposed rows of jets at downstream stations of $X/D=4$ and 8 with the top central jet eccentricity $e = 0.25D$, and with a jet-to-mainstream velocity ratio of 2.8. The results were similar to those obtained for a single row of jets with the same eccentricity and a velocity ratio of 2.0 and suggest that, for the present spacing between the opposing jets, their effect upon each other is negligible. The concentration profiles showed a rapid return to the symmetric position which is also in accord with the previous single-row result obtained with $V_j/U_\infty = 2.0$. Further confirmation of the lack of influence of one row of jets on the other with the present $8D$ spacing was given by the measurements obtained with a staggered arrangement of the two rows. In this case, and as shown in reference [7], measurements of mean velocity and concentration along the line of a hole center line are similar to those obtained with the in-line arrangement for $X/D>4$.

Conclusions

The following conclusions may be extracted from the preceding section.

1 The mean velocity and concentration profiles downstream of a row of jets issuing normal to a crossflow, with uniform pitch-to-diameter ratio and velocity ratios from 0.5 to 2.8 are symmetrical and stable.

2 For high jet-to-crossflow velocity ratios (2.8 and 2.0), the introduction of a geometric asymmetry leads to a highly eccentric velocity field, but the passive scalar field tends to return to symmetry with downstream distance. With lower velocity ratios (1.0 and 0.5) the asymmetry of the velocity field becomes less pronounced and the passive scalar field is no longer able to return to symmetry.

3 For the present spacing between the opposing jets of 8D and jet-to-crossflow velocity ratio of 2.8, there is no interaction between the opposing jets.

Acknowledgments

The authors gratefully acknowledge financial support from the Ministry of Defence (Procurement Executive).

References

1 Kamotani, Y., and Greber, I., "Experiments on Confined Turbulent Jets in Crossflow," AIAA Paper No. 73–647, AIAA 6th Fluid and Plasma Dynamics Conference, Palm Springs, Calif., July 16–18, 1973.

2 Cox, G. B. Jr., "Multiple Jet Correlations for Gas Turbine Engine Combustor Design," ASME *Journal of Engineering for Power*, Vol. 98, 1976, p. 265.

3 Holdeman, J. D., and Walker, R. E., "Mixing of a Row of Jets with a Confined Crossflow," *AIAA Journal*, Vol. 15, 1977, p. 243

4 Crabb, D., "Jets in Crossflow," Ph.D. Thesis, University of London, 1979.

5 Crabb, D., and Whitelaw, J. H., "The Influence of Geometric Asymmetry on the Flow Downstream of a Row of Jets Discharging normally into a Free Stream," ASME JOURNAL OF HEAT TRANSFER, Vol. 101, Feb. 1979, p. 183.

6 Rastogi, A. K. and Whitelaw, J. H., "The Effectiveness of Three Dimensional Film-Cooling Slot Measurements," *International Journal of Heat and Mass Transfer*, Vol. 16, 1973, p. 1665.

7 Khan, Z. A., and Whitelaw, J. H., "Mean Velocity and Concentration Characteristics of Rows of Jets in a Crossflow," Imperial College, Mechanical Engineering Department, Report FS/79/16.

Surface Temperature Oscillations of Electrical Resistance Heaters Supplied with Alternating Current

F. A. Jeglic,[1] K. A. Switzer,[2] and J. H. Lienhard[3]

The investigator studying convective heat transfer must often choose between alternating and direct current electrical power for his heaters. A-C can produce undesirable temperature variations, but it is usually far more convenient to use than d-c. Some years ago the first[4] and second two[5] authors independently calculated the magnitude of the surface temperature oscillations which could result in such cases and arranged the results in conventional temperature response charts. These charts are not in the accessible literature so we present them here for the convenience of our colleagues, without reproducing the underlying calculations. The charts are for two situations: flat plate heaters of thickness, δ, insulated on the bottom and cooled convectively on top; and solid cylinders of radius, δ, cooled convectively on the outside. In each case the heaters are supplied with Q W/m^3 of electric power, in the form:

$$Q = \frac{2\bar{q}}{\delta} \sin^2 \omega t, \quad \text{for the flat plate,} \tag{1}$$

or

$$Q = \frac{4\bar{q}}{\delta} \sin^2 \omega t, \quad \text{or the cylinder} \tag{1a}$$

where ω is the frequency in rad/s (usually equal to $2\pi(60)$), t is time

[1] Manager, Nuclear Equipment Engineering, Babcock and Wilcox, Barberton, OH, Mem. ASME, formerly with NASA.

[2] Deceased.

[3] Professor of Mechanical Engineering, University of Kentucky, Lexington, KY, Fellow ASME.

[4] F. A., Jeglic, "An Analytical Determination of Temperature Oscillations in a Wall Heated by Alternating Current," NASA TN D-1286, July 1962.

[5] K. A., Switzer, and J. H., Lienhard, "Surface Temperature Variations on Electrical Resistance Heaters Supplied with Alternating Current," Washington State University, Inst. of Tech., Bull. No. 280, 1964.

Contributed by the Heat Transfer Division for publication in the JOURNAL OF HEAT TRANSFER. Manuscript received by the Heat Transfer Division October 21, 1979.

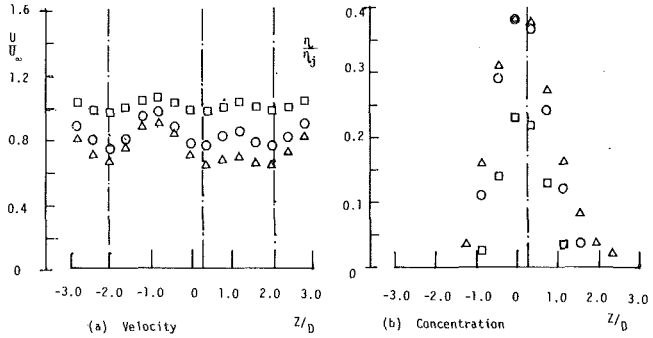

Fig. 2 Velocity and concentration distributions at $X = 6D$ for a single row of jets; eccentricity $e = 0.25D$ ($V_j/U_\infty = 1.0$, □ $Y/D = 1.5$, ○ $Y/D = 1.0$, △ $Y/D = 0.5$)

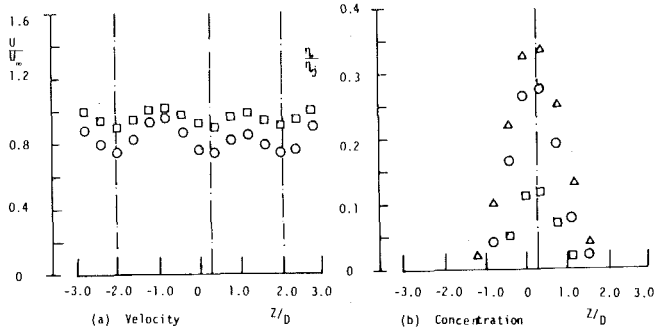

Fig. 3 Velocity and concentration distributions at $X = 6D$ for a single row of jets; eccentricity $e = 0.25D$ ($V_j/U_\infty = 0.5$, □ $Y/D = 1.0$, ○ $Y/D = 0.5$, △ $Y/D = 0.25$)

velocity ratios of 1.0 and 0.5, respectively. The asymmetry of the velocity field is not as severe as for the higher velocity ratio and the velocity profiles become less asymmetric with increasing distance from the surface. In contrast to results for the higher velocity ratio, the concentration profiles remain symmetrical about the center line of the displaced jet and this is made possible by the greater penetration of the crossflow into the region between the adjacent jets with consequent reduction in the interaction between them.

Velocity profiles were obtained for opposed rows of jets at downstream stations of $X/D=4$ and 8 with the top central jet eccentricity $e = 0.25D$, and with a jet-to-mainstream velocity ratio of 2.8. The results were similar to those obtained for a single row of jets with the same eccentricity and a velocity ratio of 2.0 and suggest that, for the present spacing between the opposing jets, their effect upon each other is negligible. The concentration profiles showed a rapid return to the symmetric position which is also in accord with the previous single-row result obtained with $V_j/U_\infty = 2.0$. Further confirmation of the lack of influence of one row of jets on the other with the present $8D$ spacing was given by the measurements obtained with a staggered arrangement of the two rows. In this case, and as shown in reference [7], measurements of mean velocity and concentration along the line of a hole center line are similar to those obtained with the in-line arrangement for $X/D>4$.

Conclusions

The following conclusions may be extracted from the preceding section.

1 The mean velocity and concentration profiles downstream of a row of jets issuing normal to a crossflow, with uniform pitch-to-diameter ratio and velocity ratios from 0.5 to 2.8 are symmetrical and stable.

2 For high jet-to-crossflow velocity ratios (2.8 and 2.0), the introduction of a geometric asymmetry leads to a highly eccentric velocity field, but the passive scalar field tends to return to symmetry with downstream distance. With lower velocity ratios (1.0 and 0.5) the asymmetry of the velocity field becomes less pronounced and the passive scalar field is no longer able to return to symmetry.

3 For the present spacing between the opposing jets of 8D and jet-to-crossflow velocity ratio of 2.8, there is no interaction between the opposing jets.

Acknowledgments

The authors gratefully acknowledge financial support from the Ministry of Defence (Procurement Executive).

References

1 Kamotani, Y., and Greber, I., "Experiments on Confined Turbulent Jets in Crossflow," AIAA Paper No. 73–647, AIAA 6th Fluid and Plasma Dynamics Conference, Palm Springs, Calif., July 16–18, 1973.

2 Cox, G. B. Jr., "Multiple Jet Correlations for Gas Turbine Engine Combustor Design," ASME *Journal of Engineering for Power*, Vol. 98, 1976, p. 265.

3 Holdeman, J. D., and Walker, R. E., "Mixing of a Row of Jets with a Confined Crossflow," *AIAA Journal*, Vol. 15, 1977, p. 243

4 Crabb, D., "Jets in Crossflow," Ph.D. Thesis, University of London, 1979.

5 Crabb, D., and Whitelaw, J. H., "The Influence of Geometric Asymmetry on the Flow Downstream of a Row of Jets Discharging normally into a Free Stream," ASME JOURNAL OF HEAT TRANSFER, Vol. 101, Feb. 1979, p. 183.

6 Rastogi, A. K. and Whitelaw, J. H., "The Effectiveness of Three Dimensional Film-Cooling Slot Measurements," *International Journal of Heat and Mass Transfer*, Vol. 16, 1973, p. 1665.

7 Khan, Z. A., and Whitelaw, J. H., "Mean Velocity and Concentration Characteristics of Rows of Jets in a Crossflow," Imperial College, Mechanical Engineering Department, Report FS/79/16.

Surface Temperature Oscillations of Electrical Resistance Heaters Supplied with Alternating Current

F. A. Jeglic,[1] K. A. Switzer,[2] and J. H. Lienhard[3]

The investigator studying convective heat transfer must often choose between alternating and direct current electrical power for his heaters. A-C can produce undesirable temperature variations, but it is usually far more convenient to use than d-c. Some years ago the first[4] and second two[5] authors independently calculated the magnitude of the surface temperature oscillations which could result in such cases and arranged the results in conventional temperature response charts. These charts are not in the accessible literature so we present them here for the convenience of our colleagues, without reproducing the underlying calculations. The charts are for two situations: flat plate heaters of thickness, δ, insulated on the bottom and cooled convectively on top; and solid cylinders of radius, δ, cooled convectively on the outside. In each case the heaters are supplied with Q W/m^3 of electric power, in the form:

$$Q = \frac{2\bar{q}}{\delta} \sin^2 \omega t, \quad \text{for the flat plate,} \tag{1}$$

or

$$Q = \frac{4\bar{q}}{\delta} \sin^2 \omega t, \quad \text{or the cylinder} \tag{1a}$$

where ω is the frequency in rad/s (usually equal to $2\pi(60)$), t is time

[1] Manager, Nuclear Equipment Engineering, Babcock and Wilcox, Barberton, OH, Mem. ASME, formerly with NASA.

[2] Deceased.

[3] Professor of Mechanical Engineering, University of Kentucky, Lexington, KY, Fellow ASME.

[4] F. A., Jeglic, "An Analytical Determination of Temperature Oscillations in a Wall Heated by Alternating Current," NASA TN D-1286, July 1962.

[5] K. A., Switzer, and J. H., Lienhard, "Surface Temperature Variations on Electrical Resistance Heaters Supplied with Alternating Current," Washington State University, Inst. of Tech., Bull. No. 280, 1964.

Contributed by the Heat Transfer Division for publication in the JOURNAL OF HEAT TRANSFER. Manuscript received by the Heat Transfer Division October 21, 1979.

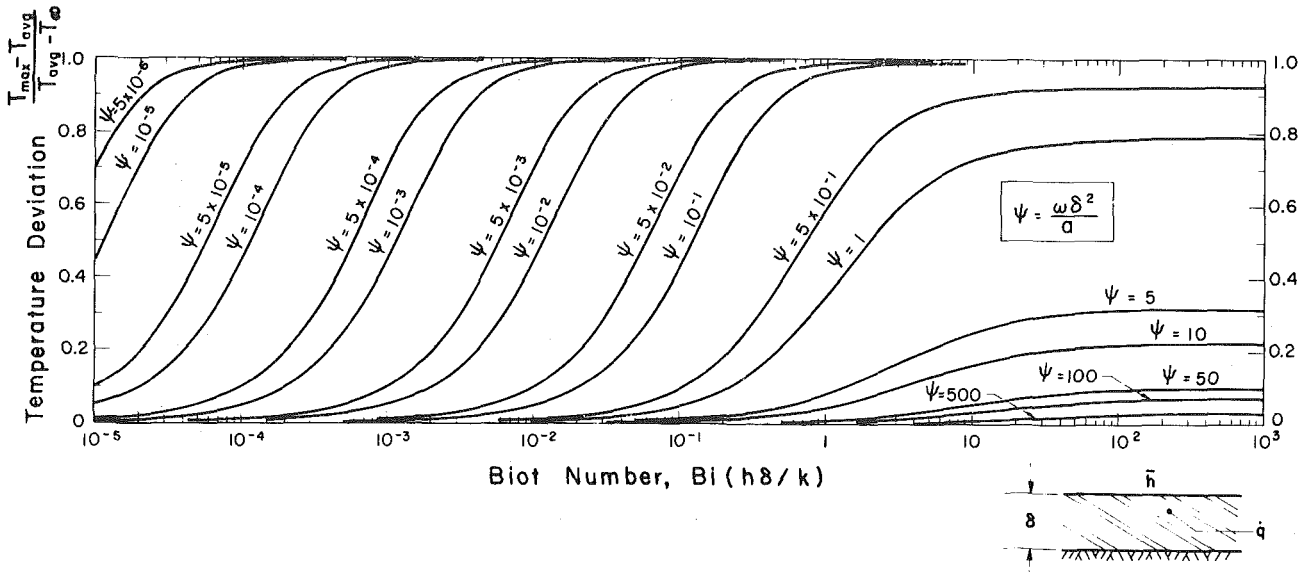

Fig. 1 Temperature deviation at the surface of a flat plate heated with alternating current

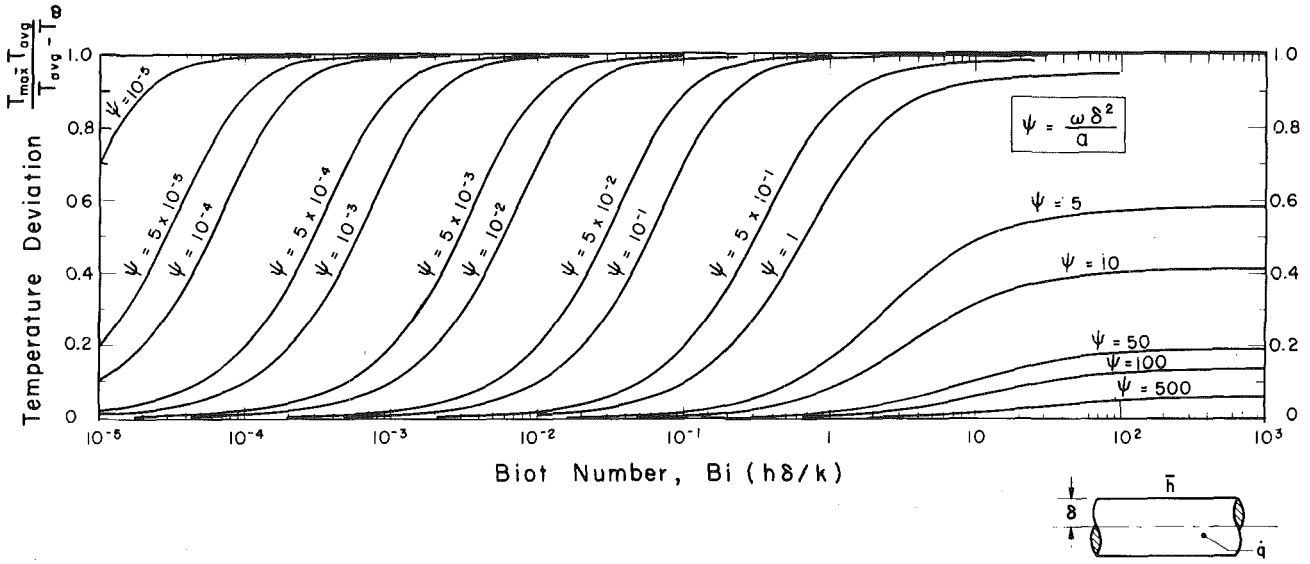

Fig. 2 Temperature deviation at the surface of a cylinder heated with alternating current

in s, and $\bar{q}$ is the average surface heat flux. The initial transient is ignored and the charts are for the steady periodic behavior.

The results of the calculation are given graphically in Figs. 1 and 2 in the form:

$$\frac{T_{max} - T_{avg}}{T_{avg} - T_\infty} = f(\mathrm{Bi}, \psi) \tag{2}$$

where $(T_{max} - T_{avg})$ is the amplitude of the surface temperature oscillation, T_{avg} is the average temperature of the surface, and T_∞ is the temperature of the coolant fluid. The Biot number, Bi, is

$$\mathrm{Bi} \equiv h\delta/k = \bar{q}\delta/k(T_{avg} - T_\infty) \tag{3}$$

where k is the thermal conductivity of the heater and h is the convective heat transfer coefficient. And ψ is a kind of inverse Fourier number:

$$\psi \equiv \omega\delta^2/a \tag{4}$$

where a is the thermal diffusivity of the heater.

Journal of Heat Transfer

Discussion

Further Developments of Dropwise Condensation Theory[1]

S. S. Sadhal.[2] In this recent contribution by Tanaka, some progress has been made in the treatment of ensembles of droplets on solid surfaces. It must be pointed out, however, that in Tanaka's analysis, Mikic's [1] expression for the heat flow across a single droplet is used outside its range of validity. The heat flow Q across a hemispherical droplet with a uniform base temperature is given by Umur and Griffith [2] to be

$$\frac{Q}{Rk_\ell(T_v - T_s)} = 2\pi \sum_{m=1,3,5,\ldots}^{\infty} \frac{m(2m+1)}{1 + (k_\ell/hR)m} \left[\int_0^1 P_m(x)dx\right]^2, \tag{1}$$

where R is the droplet radius, k_ℓ is the thermal conductivity of the liquid, T_v is the vapor temperature, T_s is the droplet base temperature, and h is the heat-transfer coefficient at the liquid-vapor interface. A useful approximation for (1) was obtained by Mikic [1] to be

$$\frac{Q}{Rk_\ell(T_v - T_s)} = \frac{4\pi}{1 + 2k_\ell/hR} \tag{2}$$

As pointed out by Sadhal [3], equation (2) is only valid for Bi = $hR/k_\ell < 10$. To illustrate this point, equations (1) and (2) are plotted on the same graph in Fig. 1. It can be clearly seen that Mikic's approximation holds very well up to Bi = 10. For Bi > 10 a strong deviation is observed, and equation (2) levels off to a value 4π. Equation (1), on the other hand appears to behave like $\sim \ell n(\text{Bi})$.

It is quite appropriate to note here that for metallic condensors (thermal conductivity, $k_s \sim 100\ k_\ell$), it was shown by Sadhal and Plesset [4] that the effect of the solid becomes quite significant for Bi > 1000. At such large values of Bi, the droplet base temperature, therefore, cannot be assumed to be uniform.

In conclusion, since Tanaka[1] has used values of Bi up to 10^4 in equation (2), the results so obtained are questionable.

Additional References

1 Mikic, B. B., "On the Mechanism of Dropwise Condensation," *International Journal of Heat and Mass Transfer*, Vol. 12, 1969, pp. 1311–1323.

2 Umur, A., and Griffith, P., "Mechanism of Dropwise Condensation," ASME JOURNAL OF HEAT TRANSFER, Vol. 87, 1965, pp. 275–282.

3 Sadhal, S. S., "Comments about Yang's Analysis on Droplets Evaporating from a Solid Surface," *Letters in Heat and Mass Transfer*, Vol. 6, 1979, pp. 149–155.

4 Sadhal, S. S., and Plesset, M. S., "Effect of Solid Properties and Contact Angle in Dropwise Condensation and Evaporation," ASME JOURNAL OF HEAT TRANSFER, Vol. 101, 1979, pp. 48–54.

[1] By H. Tanaka, published in the November 1979 issue of the JOURNAL OF HEAT TRANSFER, Vol. 101, No. 4, pp. 603–611.

[2] Department of Mechanical Engineering and Applied Mechanics, University of Pennsylvania, Philadelphia, PA 19104

Author's Closure

I acknowledge that in the strict sense Mikic's expression is only valid for Bi < 10, that is for $\xi < 5\xi_1$ in my Nomenclature. Under actual dropwise condensation including that of water, however, the size of thermodynamic critical droplet, r_{cri} is over two orders of magnitude smaller than the size $5r_1$ in my Nomenclature which corresponds to Bi = 10 (see Table 1 of my paper), and heat is transferred mainly by microscopic active drops belonging in the range Bi < 10, though a large percentage of the condensing surface is occupied by larger drops. Thus, whether we adopt Umur-Griffith's exact prediction or Mikic's approximation, we obtain almost the same value of heat-transfer coefficient for dropwise condensation. From a more theoretical point of view, it will be understood in reviewing the theory [1] that, whatever profile we may assume for the substantial growth rate $\dot{r}_e$ in the size range where $\dot{r}_e$ becomes over an order of magnitude smaller than the total rate of drop growth rate $\dot{r}_a$, results of the drop-size distribution N and the drop growth rate $\dot{r}_a$ predicted from the basic integro-differential equations remain entirely unchanged.

As for the effects of a finite thermal conductivity of a condenser material deviation of the substantial growth rate $\dot{r}_e$ due to ununiformity of the droplet base temperature in a large drop range is not important to the resultant heat-transfer coefficient for the reason stated above; but the so-called constriction resistance proposed by Mikic [2] seems to be worthy of much attention. In this respect, Hannemann and Mikic [6] have shown that in the case of dropwise condensation of steam onto a copper surface the constriction resistance is almost negligible.

Additional Reference

5 Hannemann, R. J., and Mikic, B. B., "An Analysis of the Effect of Surface Thermal Conductivity on the Rate of Heat Transfer in Dropwise Condensation," *International Journal of Heat and Mass Transfer*, Vol. 19, 1976, pp. 1299–1307.

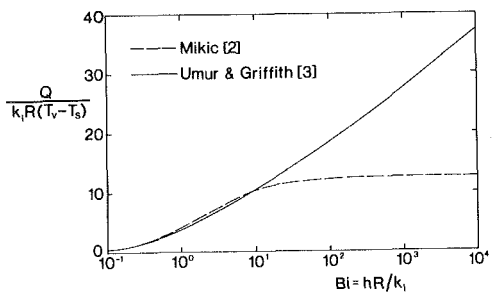

Fig. 1 Nusselt number Nu = $Q/[k_\ell R(T_v - T_s)]$ as a function of Bi = hR/k_ℓ; comparison of Umur-Griffith prediction with Mikic's approximation

Optimal Fin-Side Design of Compact Tube-in-Fin Heat Exchangers with Rippled Fins[1]

A. S. Mujumdar[2] and Y-K Li.[3] The authors have presented a very interesting and useful design methodology based on optimization theory and judicious experimentation. However, we believe that clarification of the following points will enhance the value of their contribution.

First, it is necessary to validate the boundary layer assumptions for the complex internal flow problem considered. The neglect of the diffusion terms permits use of the marching technique. We believe that for the configuration studied, it is possible to generate zones of recirculation at least for certain geometric and flow conditions. Such a possibility is precluded by reducing the full elliptic equations to a parabolic form. It is therefore necessary to provide detailed flow and/or heat transfer data to justify the boundary layer approach. Pressure drop measurements by themselves provide a rather insensitive test of the validity of a mathematical model for flow.

Second, the authors' results on the effect of variable physical properties is especially important since very few studies have reported on this aspect of the problem. It is assumed that the authors considered temperature dependence of density, viscosity, and thermal conductivity for flow of air. Clearly, the results will depend on the actual temperature ranges used and the fluid property correlations used. Figures 4 and 5 do not provide full information about their experiments or simulations. Specifically, what was the inlet fluid temperature used? Is it possible to generalize these results? Is it possible to estimate the variable property results from constant property data? Did the authors consider both heating and cooling?

Finally, does the optimal ripple configuration depend additionally on the temperature difference between the fluid and the ripple surface?

Author's Closure

Professor Mujumdar and Mr. Li's comments clarify both the advantages and the problems involved in synthesis studies of complex situations, viz. highlighting salient aspects and indicating experimental and analytic studies for the future.

Under the assumptions of laminar flow throughout, zones of recirculation would be indicated by inconsistently predicted pressure-velocity profiles. As noted, this is checked by doubly-solving the continuity equation. In a few cases, separation or possible recirculation were indicated by the solution procedure getting in a loop which would generally diverge numerically. Typically this was at fairly high Re. The need for detailed flow and/or heat transfer data is always with us—particularly to study the *phenomenon* of disturbed flow with heat exchange—but it is the prupose of the present work to indicate the ability to predict overall performance and to suggest what data are most critical.

Variable properties across and along the channel were incorporated. In the experimentation, the inlet and outlet fluid temperatures were 212°F (100°C) and 70°F (21.1°C), respectively.

The results can be generalized insofar as the nondimensional nature of the solution and results permit. This includes cooling in the appropriate flow range. Other data (ours and others) seem to support this, but we do not have exhaustive data.

From the curves, it would appear that the variable properties results are a simple multiple of the constant properties model. However, this breaks down since the scaling (nondimensional parameters) are not linear with the independent variables. Interestingly, the constant properties optima are less well-defined and the design contours are smoother and flatter. The optimum occurs in the same region, but the variable-properties optimum is relatively better than neighboring designs than is the constant properties optimum.

From experimentation—physical as well as numerical—it appears that the optimum ripple is relatively insensitive to the temperature difference between the fluid and ripple surface-at least in this general range. In other words, it appears that the flow properties dominate choice of the optimum ripple, and that in the laminar range, the predictions are consistent.

[1] By S. W. Mandel, M. A. Townsend and T. F. Parrish, Jr. published in the August issue of the ASME JOURNAL OF HEAT TRANSFER, Vol. 101, No. 3, pp. 574–520.

[2] Associate Professor, Department of Chemical Engineering, McGill University, Montreal, Canada

[3] Graduate Student, Department of Chemical Engineering, McGill University, Montreal, Canada

Perturbation Solutions to Phase Change Problem Subject to Convection and Radiation[1]

R. V. Seeniraj.[2] This paper represents a significant addition to the perturbation solutions of a moving-boundary problem subject to convection and radiation. The solutions were obtained (1) by expressing T^4 in the radiative term as a linear function and (2) by expanding it in a Taylor series about T_a. As the convection-radiation boundary condition is expressed in a linear form, the resulting solutions will give approximate values and also have limited applications. In addition, the zero-order solution which corresponds to pseudo-steady-state, is also an approximate one.

The objective of this discussion is to show that perturbation solutions can be obtained without resorting to either of the approximations for the radiative-convective boundary condition to which a finite slab is subjected to at $\chi = 0$. It is also shown that zero-order solutions are possible for the inward solidification problems discussed in [2].

The system of equations is recast in the following nondimensional form for the case of solidification.

$$\frac{\partial^2 u}{\partial \bar{\chi}^2} = \epsilon g \frac{\partial u}{\partial s}; \quad u(s, \bar{\chi} = s) = 1,$$

$$\left.\frac{\partial u}{\partial \bar{\chi}}\right|_{\bar{\chi}=0} = H'[u_s{}^4 - U_a{}^4] + \mathrm{Bi}[u_s - U_a]$$

$$g = \frac{ds}{d\tau} = \left.\frac{\partial u}{\partial \bar{\chi}}\right|_{\bar{\chi}=s},$$

$$\left.\frac{\partial u}{\partial \bar{\chi}}\right|_{\bar{\chi}=1} = 0, \quad u_s(\tau = 0) = 1 \quad (1)$$

The nondimensional variables employed here are

$$u = T/T_i, \quad \bar{\chi} = \chi/\ell; \quad s = \delta/\ell, \quad \tau = kT_i t/\rho \ell^2 L, \quad \epsilon = C_p T_i/L$$
$$\mathrm{Bi} = h\ell/k, \quad H' = \sigma \epsilon T_i{}^3 \ell/k, \quad U_a = T_a/T_i; \quad (2)$$

Note that the Stefan number ϵ, defined here corresponds to S^* and $1/B$ in [2] and [4], respectively.

Following the similar procedure reported, the solutions obtained by taking the first two terms in the series for u are presented below, for higher-order solutions become too unwieldy to manipulate.

$$u_0 = (1 - u_{0,s})\bar{\chi}/s + u_{0,s} \quad (3)$$

where $u_{0,s}$, the zero-order surface temperature is the solution of

$$u_{0,s}{}^4 + u_{0,s}(\mathrm{Bi} \cdot s + 1)/H's = (U_a \mathrm{Bi} \cdot s + 1)/H's + U_a{}^4 \quad (4)$$

The solution for $u_{0,s}$ can be calculated from Cardano's formulae [1] and it is provided in Fig. 1.

[1] By M. M. Yan and P. N. S. Huang, published in the February 1979 issue of the JOURNAL OF HEAT TRANSFER, Vol. 101, No. 1, pp. 96–100.

[2] Lecturer, Department of Mechanical Engineering, Govt. College of Technology, Coimbatore 641 013, India.

ERRATA

Erratum: J. D. Felske and C. L. Tien, "The Use of the Milne-Eddington Absorption Coefficient for Radiative Heat Transfer in Combustion Systems," published in the August 1977 issue of the JOURNAL OF HEAT TRANSFER, pp. 458–465.

In the expression for the Rosseland mean coefficient given as equation (36) in the paper, the numerical coefficient should be 4.0 instead of 3.6. The remainder of the expression is correct.